Uranium silicate complexes as models for surface immobilised uranium catalysts

Laura E. Nicholls

Submitted for the degree of Doctor of Philosophy
University of Sussex
July 2015

Declaration

I hereby declare that this thesis has not been and will not be submitted in whole or in part to another University for the award of any other degree.

Signature:

Laura E. Nicholls

Abstract

Chapter 1 provides an insight into the current areas of research that could provide answers to the global energy problems outlined in Appendix A, namely the reductive functionalisation of carbon oxides and as an extension to this, the activation of other small molecules. The review predominantly concentrates on the chemistry of the 5*f* elements which already contain examples of reductive functionalisation of carbon oxides, albeit in homogeneous phase. In addition the chapter provides an overview of the current research in surface science and by extension, the development of molecular models that mimic such surfaces. This synopsis provides an insight into the difficulties involved in this area of research and why molecular mimics are of vital importance.

Using ligating Si-O bonds to mimic a silica surface, Chapter 2 outlines the research which enabled the development of a series of uranium siloxides, centred on the previously unreported pentakis(triarylsiloxy) uranate(IV) ion. Characterisation data and full analysis are included within this chapter which provided the basis for the investigations discussed in the following chapters. This chapter also presents an interesting UV-Vis analysis of the uranium siloxides which will enable a wider understanding of the *f*-elements and the role *f*-orbitals have on the chemistry and geometry of *f*-element molecules. Chapter 2 develops a deeper understanding of these complexes by investigating the mechanisms of formation and the chemistry of the $U(Ph_3SiO)_5$ fragment using ESI techniques in con-

junction with NMR analysis.

Chapter 3 investigates the reactivities of the uranium siloxides previously developed and discusses a new dioxo species and a rare and novel U^{V} monooxo complex which was synthesised and successfully isolated. An analysis of other dioxo and monooxo complexes is included which allows the reader to develop an appreciation of how few and far between monooxo products are. In addition, previous examples of monooxo's are lacking characterisation data and are mostly products of oxygen atom donor reactions, not as a result of small molecule activation as is presented here. There is currently one previous example of such a system resulting from small molecule activation which is also discussed in this chapter.

Chapter 4 investigates a second ligand system which could be used to mimic a silica surface. Whilst the ligand, tris *tert*butoxy has been investigated previously, at the time of this work, the ligand had not been successfully used in relation to a uranium complex. The $U^{3.5}$ species, $[(U(OSi(O^{t}Bu)_3)_3)_2(\mu{-}\eta^6{:}\eta^6\text{-tol}))]$ is presented here alongside the complexes $[((^{t}BuO)_3SiO)_3U]_2(\mu^2\text{-}O)_3$ and $U(OSi(O^{t}Bu)_3)_4$. During the development of this species, very similar species were published by another group and these syntheses and characterisation data are presented here as a comparison to the species developed as part of this work.

Chapter 5 investigates the reactivities of the uranium siloxides developed in Chapter 4 including decomposition analysis and reactions with small molecules such as O_2, I_2 and CO_2 and presents the resulting complexes some of which were developed by a Masters student working in collaboration with the author.

Acknowledgements

Firstly, and most importantly, I would like to thank my supervisor, Dr. John Turner who has spent the last five years guiding, tutoring and putting up with me as I attempted to juggle a Ph.D. and a serious ultra marathon running addiction, culminating in the toughest footrace on Earth, the 'Marathon des Sables'. Thank you John, I will always be grateful to you for your help and infinite patience in the face of my many, many questions.

Thank you to Tara and Kayla who guided me through my M.Chem. and taught me everything I know. Thank you both for your support, I think my Ph.D. would have been a much tougher ride had it not been for your outstanding lessons on all things research and lab maintenance.

I also couldn't have achieved so much without the help and support of Prof. Geoff Cloke and everyone in Lab 14, especially Nikos. Their help, support, encouragement and advice has always been forthcoming even at times when they've been busy and under pressure themselves.

A special thanks to Dr. M. Roe for solving all my crystal structures, Dr. A. Abdul-Sada for running the mass spectrometry experiments and Dr. I. Day for all his advice in running and analysing NMR spectra.

To the 14 students who have spent time in the Turner lab during the course of my Ph.D.

Thank you for teaching me patience, helping me develop my skills as an educator and forgiving me when I got it wrong. I hope your time with me was rewarding and you take the skills you learnt from me forward, into incredibly successful careers. Specifically I'd like to thank James Pankhurst and Melvyn Ansell whose work during their respective masters project and summer placement complimented the work presented here.

Finally, I would like to thank Mum, Dad and my sister Emma who've been there at every twist and turn, every tearful phone call when it was all 'too much' and every celebration when I finally 'got it right'. You've shaped me into the person I am today and without you all, I couldn't have achieved half as much.

Contents

List of Figures

List of Schemes

List of Tables

List of Symbols and Constants

pK_a	acid dissociation constant
Å	angstroms
atm	atmospheric pressure
Z	atomic number
μ	bridging ligand
e	charge on an electron = 1.602176×10^{-19}C
δ	chemical shift
d	deuterated
DCM	dichloromethane
DME	dimethoxyethane
ESI	electrospray ionisation
ν	frequency
FWHH	full width half height
GEB	global energy balance
GHG	greenhouse gas
GWP	global warming potential
η	hapticity
LMCT	ligand-metal charge transfer
m_e	mass of electron = 9.10938×10^{-31} kg
MLCT	metal-ligand charge transfer
ε	molar absorptivity
M	molarity, mols per litre
ppmv	parts per million / volume
Pa	pascals
Ph	phenyl, C_6H_5
POMSS	polyhedral oligometallasilsesquioxanes
POSS	polyhedral oligosilasesquioxanes
py	pyridine
ΔG_f°	standard Gibbs free energy of formation / kg mol^{-1}
σ	sigma
s-	surface bound complex
SOLnC	surface organolanthanide chemistry
SOMC	surface organometallic chemistry
T	temperature
THF	tetrahydrofuran
tol	toluene
J	total angular momentum quantum number
TMSOTf	trimethylsilyl trifluoromethanesulfonate
W	watts
λ	wavelength

Key to X-ray Diffraction Crystallography Molecular Structures

Green	=	uranium
Red	=	oxygen
Turquoise	=	silicon
Purple	=	potassium
Dark grey	=	carbon
White	=	hydrogen
Royal blue	=	nitrogen
Yellow	=	chlorine

Chapter 1

Siloxides as surface mimics and the use of uranium in molecular models

In order to establish the motivation behind the research presented here, the global picture is first analysed and presented in Appendix A with focus on current trends in climate change and the peak oil crisis. The analysis begins with the role carbon dioxide plays within the atmosphere and the potential effects on the planet when the atmospheric composition changes. The following discussion leads on from the global picture, analysing and investigating potential solutions *via* the use of siloxides as surface mimics and the use of uranium in those molecular models which has repeatedly shown interesting and unusual chemistry when used to activate small molecules such as carbon oxides.

1.1 Atomic and physical properties of uranium

No other element has such a Jekyll and Hyde reputation[1]

The actinides and more specifically early actinides such as uranium, are distinguished from the lanthanides and transition metals in a number of aspects. One of the most significant physical properties of the actinides is the contraction of the ionic radii as the nuclear charge increases across the period. This is also observed more prominently in the lanthanide series. The lanthanide contraction is caused by the strong attraction between the electrons in a 4*f* orbital and the positively charged nucleus. This attraction is only partially shielded by the electrons in other orbitals. As the nuclear charge increases across the lanthanide series, the shielding becomes less efficient.

The 5*f* orbitals of the actinides are not as effectively shielded by the filled 6*s* and 6*p* subshells compared to the 4*f* orbitals of the lanthanides, so whilst actinide contraction is observed, it is not as pronounced as the lanthanide series. Due to the fact that the 5*f* subshell of the actinides is less effectively shielded than the lanthanides, the 5*f* electrons in actinide ions are not considered as 'inner' subshells but more closely described as part of the 'outer' subshells. For this reason, the 5*f* electrons can play a greater role in bonding than the equivalent 4*f* electrons of the lanthanides. This effectively means the 5*f*, 6*d* and 7*s* subshells can all play a role in bonding in the actinides.[2] [3]

With the 5*f*–orbitals more available for bonding and the ionic radius of uranium being comparatively large, as shown in Appendix M, compared to the later actinides, a greater number of oxidation states and higher coordination numbers available.[4] This can be further analysed by considering the electronic configuration of the oxidation states of uranium itself. A U^{III} complex would have an electronic configuration of [Rn]5f^3, U^{IV} = [Rn]5f^2 and U^{V} = [Rn]5*f* until the 5*f* orbitals are empty at U^{VI}. It is this variety of available oxidation states that provides access to different chemistry compared to the relatively restricted lanthanide series, which almost entirely relies on the Ln^{III} oxidation state.[2] [3] Due to these unusual qualities, research has developed in the field of uranium catalytic

chemistry with a number of successes in the field of small molecule activation.

1.1.1 Small molecule activation and uranium

The previously discussed characteristics and properties of uranium provide access to interesting and sometimes unpredictable chemistry. Evidence has been reported that uranium can activate small molecules efficiently and effectively and therefore the development of uranium–based catalysts has gathered pace.[1][5] The following sections examine the development of uranium–based catalysts with emphasis on small molecule activation over the last thirty years.

Dinitrogen activation

In order to activate H_2 and N_2 to synthesise NH_3, pressures of around 150–250 bar and temperatures of around 300–500 °C are needed, which are both dangerous, expensive and resource–intensive, thereby impacting greatly on environmental cycles.[6] Such conditions are due to the inert nature of dinitrogen. Dinitrogen's bond dissociation energy is 944 kJ mol^{-1} [7] making cleavage of the triple bond difficult and activating dinitrogen has proven a challenge. Dinitrogen is a non–polar molecule with tightly bound σ and π electrons. This coupled with the large gap between its HOMO and LUMO means dinitrogen will not readily accept or lose electrons. There have been examples recorded of dinitrogen activation through 'end–on' or 'side–on' bonding to actinide and transition metal centres.[1][8]

Elongation of the N–N bond within a dinitrogen complex is often taken as a measure of the degree of reduction of the N_2 moiety, albeit an indirect one. Bond elongation is commonly caused by donation of electrons from a metal orbital of appropriate symmetry into

the anti–bonding molecular orbitals of dinitrogen. Once activated, dinitrogen may then proceed to other products, resulting in functionalisation, further activation or complete cleavage. Figure 1.1 illustrates generic examples of monometallic and bimetallic bonding to dinitrogen.[7]

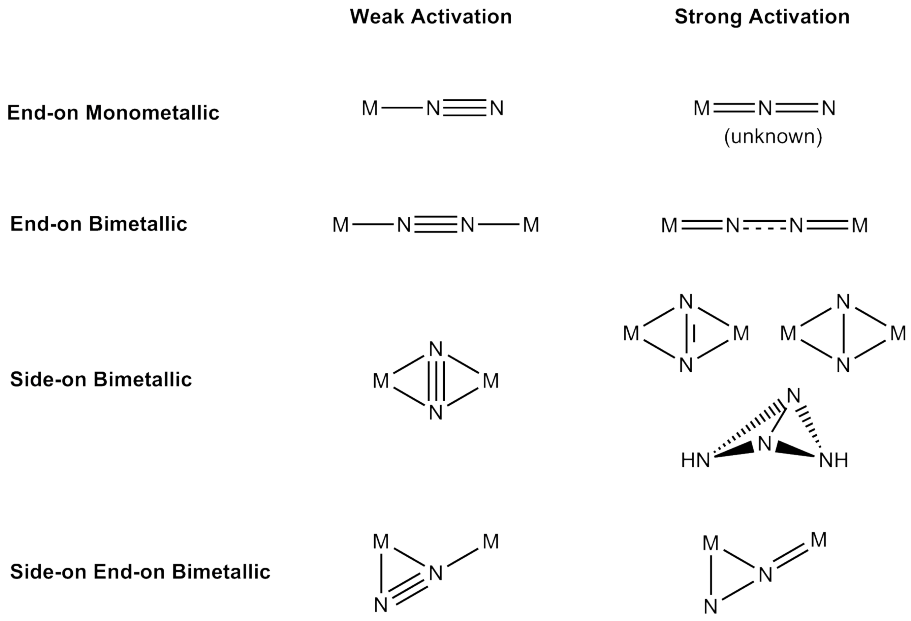

Figure 1.1: Dinitrogen binding modes in monometallic and bimetallic complexes

$[((N_3N)U)_2(N_2)]$ ($N_3N = N(CH_2CH_2NSi(^tBu)Me_2)_3$) was the first uranium, side bound dinitrogen complex and was synthesised by reacting the trivalent complex $[U(N_3N)]$ with N_2 to form a side–on bridged dinuclear uranium complex as shown in Scheme 1.1.[9] The N_2 bond length is 1.109$\pm$ 0.007 Å, which is similar to the bond length of free dinitrogen at 1.0975 Å. This comparison of data can be interpreted to indicate that little activation of the dinitrogen bond had occurred. However the data still provides evidence that uranium complexes could be used to bind dinitrogen and lead to activation of the bond.[1]

The uranium complex $(Ar(R)N)_3U(N_2)Mo(N(^tBu)Ph)_3$ (R = N–tert–butylanilide) was isolated and is an example of a stable hetero–bimetallic dinitrogen complex. $Li(N[R]Ar)(OEt_2)$ was reacted with one equivalent of $UI_3{\cdot}(THF)_4$ resulting in a yellow compound being isolated, identified as the U^{IV} complex, $(U(I)(N[R]Ar)_3)$ which could be reacted further to form

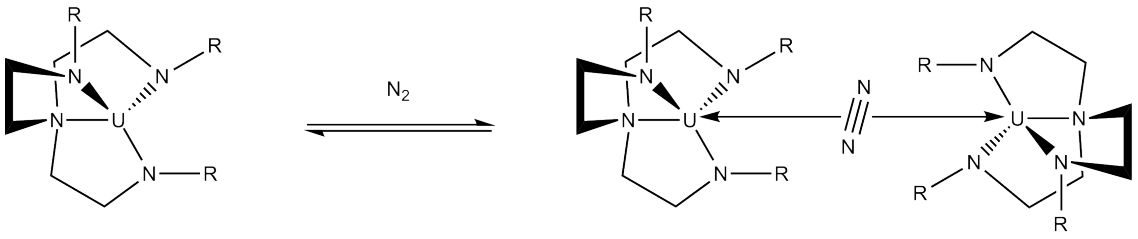

Scheme 1.1: The first example of a side–on dinitrogen U^{III} complex

$U(THF)(N[R]Ar)_3$. Activation of dinitrogen was unsuccessful and therefore the uranium complex was reacted in a 1:1 ratio with $Mo(N[^tBu]Ph)_3$ under 1 atm of nitrogen which resulted in the aforementioned nitrogen bound complex as shown in Scheme 1.2.[10] The N–N distance of the end–on bound dinitrogen is substantially longer with an observed distance of 1.232 Å, an increase of 0.13 Å. This indicates that the dinitrogen molecule had been activated by a uranium–based complex for the first time.

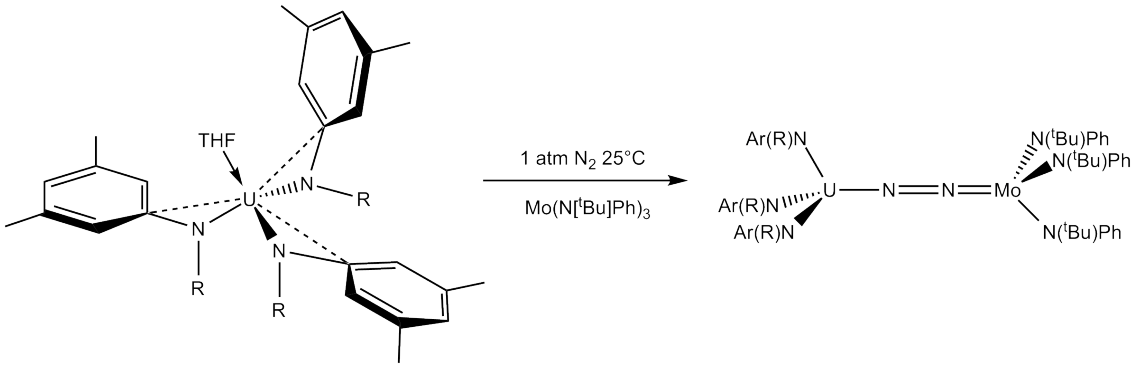

Scheme 1.2: The first example of a heterodinuclear end–on dinitrogen U^{IV} complex

Complete cleavage of dinitrogen was observed when potassium naphthalenide was reacted with $[(Et_8-calix-4-tetrapyrrole)U(dme)][K(dme)]$ and dinitrogen gas to synthesise $[(K(dme)(calix-4-tetrapyrrole)U)_2(\mu-NK)_2][K(dme)_4]$. This product was unprecedented and provided a unique example of a binuclear mixed–valent μ–nitrido U^V/U^{IV} complex in addition to providing the first example that a highly reducing uranium centre could reduce the strong dinitrogen bond when in the presence of the correct ligand environment.[11]

The first example of a mixed sandwich U^{III} complex reacting with dinitrogen is shown in

Scheme 1.3. The reaction resulted in dinitrogen bonding in a side–on manner forming a U^{IV} complex. The key N–N bond length was reported to be 1.232(10) Å, similar to a N=N double bond which suggests that the dinitrogen had been partially reduced by the uranium centre. Unfortunately this nitrogen bound complex was not stable and released N_2 very easily in both the solution and solid state resulting in the retrieval of the U^{III} starting material.[12]

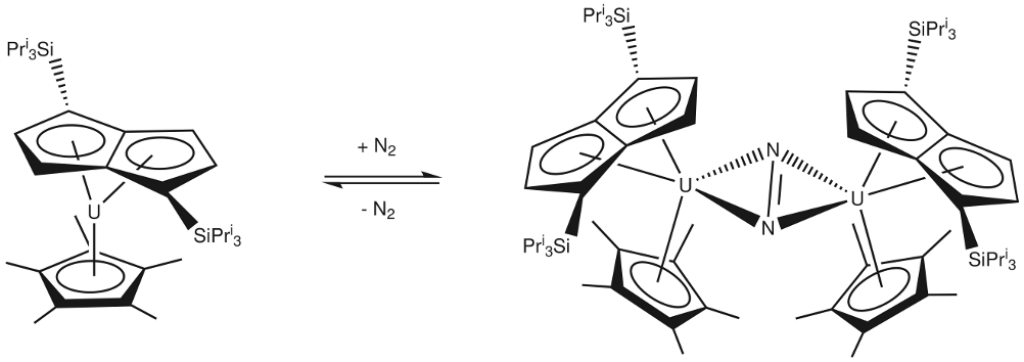

Scheme 1.3: A binuclear, side–on bridging dinitrogen unit, reducing N_2 to N_2^{2-}

By subjecting the U^{III} complex $(Cp\cdot)_3U$ to 80 psi of N_2 an example of a monometallic end–on bound dinitrogen complex was synthesised as shown in Scheme 1.4. When the pressure was reduced, C_6D_6 solutions of the uranium complex released N_2 regenerating $(Cp\cdot)_3U$. The N–N bond distance of 1.120(14) Å is relatively similar to that of free N_2 at 1.0975 Å, indicating that the N_2 molecule had not been significantly altered.[13]

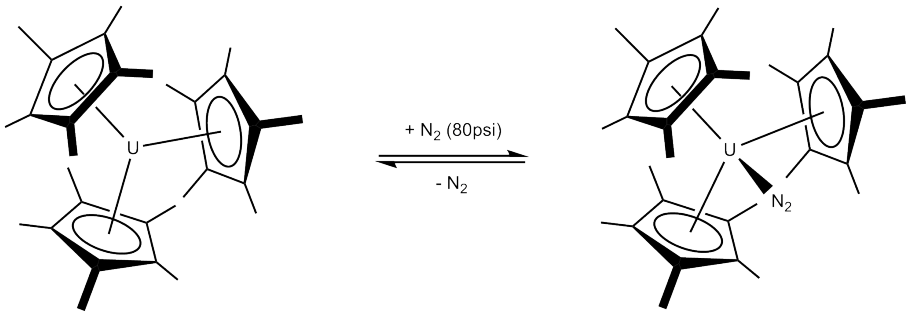

Scheme 1.4: The monometallic end–on dinitrogen U^{III} complex, $(Cp\cdot)_3U(\eta^1N_2)$

Carbon monoxide activation

The activation of carbon based small molecules is an important process especially since the development of the Fischer–Tropsch process in the 1930's. The bond energy of carbon monoxide is greater than dinitrogen at 1079 kJ mol^{-1} but the bond is more easily broken due to the polarity between the carbon and oxygen atoms causing a greater degree of ionic bonding.[14] CO can bond to a metal centre in an 'end–on' manner via the carbon or the oxygen although normally found to be via a σ–bonding interaction between the carbon and the metal with secondary π–bonding between the *d*–orbitals on the metal centre and the *p*–orbitals on the carbon.[15] Other binding modes are illustrated in Figure 1.2 with many examples on transition metals found in the literature.[16][17]

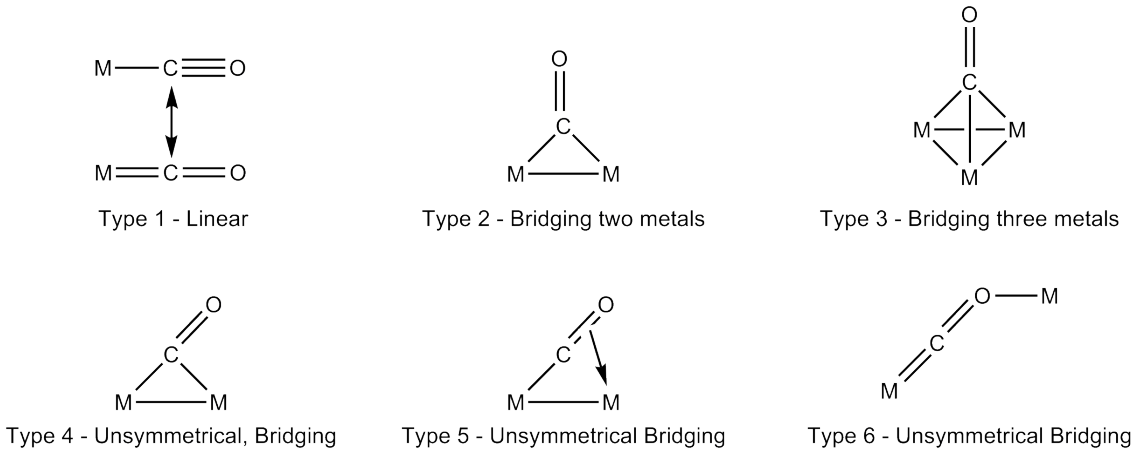

Figure 1.2: Carbon Monoxide binding modes in monometallic and bimetallic complexes

The first reported example of carbon monoxide bound to uranium was $(Me_3SiC_5H_4)_3UCO$, which was synthesised by reacting 1 atm of carbon monoxide at 20° C with $(Me_3SiC_5H_4)_3U$ and is shown in Figure 1.3. The volumetric studies carried out showed the uranium complex absorbed 1.0 $\pm$ 0.05 M equivalents of CO at 25 ° C. It was also found that the reaction could be reversed under vacuum several times with no decomposition of the uranium complex. The CO was found to be bound to the uranium centre through the carbon in a linear fashion, supported by X–ray analysis. In addition a significant reduc-

tion of the carbon monoxide stretching frequency was observed (1969 cm^{-1}), indicating a lengthening and therefore weakening of the C≡O bond.[18]

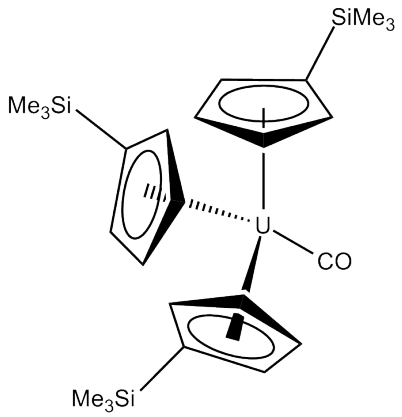

Figure 1.3: $(Me_3SiC_5H_4)_3UCO$, the first example of carbon monoxide bound to a uranium complex

The first example of a CO bridged dinuclear uranium compound is shown in Scheme 1.5.[19] Carbon monoxide was reacted with the uranium complex resulting in a pale brown solution. Infrared characterisation showed a distinct band at 2092 cm^{-1}, which is close to that of other coordinated CO complexes. X–ray diffraction analysis supported the bridged CO formulation although no reliable CO bond distance data were available due to disorder of the crystals.

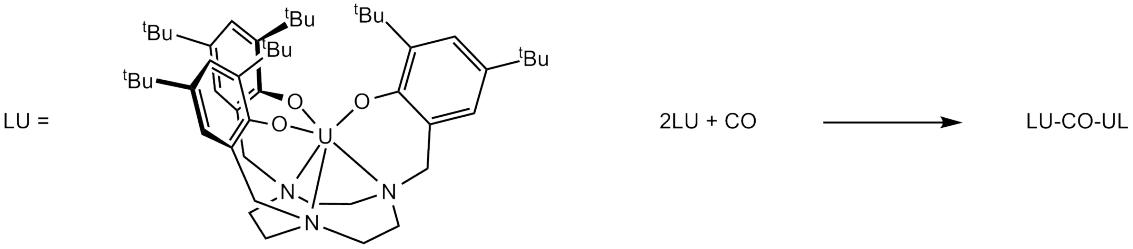

Scheme 1.5: The first example of carbon monoxide bridged dinuclear uranium complex

The previously reported complex, [U($\eta-$COT)($\eta-$Cp*)(THF)] was reacted with CO at ambient pressure to give the dimeric U^{IV} deltate complex as shown in Scheme 1.6. Most of the bond distances were unremarkable and the majority of discussion focusses on the U(C_3O_3)U planar unit. The U2–O3 bond distance was found to be slightly longer than aryloxides and the U1–O1 and U1–O2 bond lengths observed were significantly longer

(2.516(3) Å and 2.484(3) Å respectively). The C–O bond lengths were found to lie in between the average single and double CO bond lengths. In addition the C–C bond distances were also noticeably distorted with one long and two shorter bonds and this was investigated further with DFT calculations which reproduced the same distortions suggesting the distortions are effected by the sterics within the system.[20]

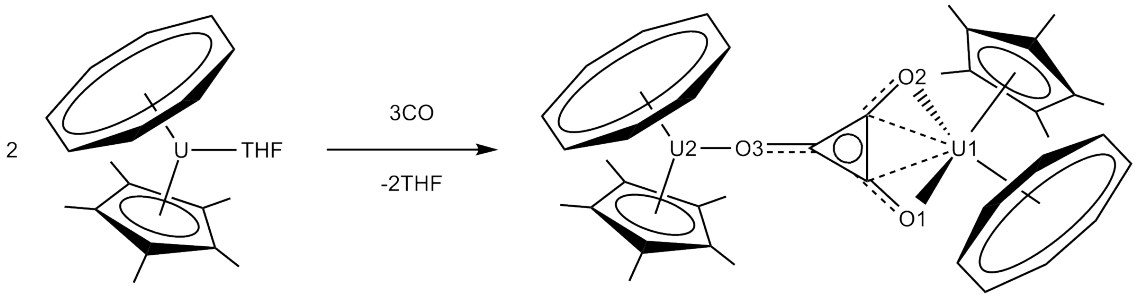

Scheme 1.6: Reductive cyclotrimerization of CO to the deltate dianion by an organometallic uranium complex

Based on the work previously reported on the deltate dianion, subtle changes in the steric or electronic properties of the starting material were utilised to investigate whether the squarate dianion was possible. By replacing the Cp* ligand with Cp^{Me_3H} to form the complex, [U($\eta-$C$_8$H$_6$(Si^{i}Pr$_3-1,4$)$_2$)($\eta-$Cp^{Me_3H})(THF)] and exposing it to ambient pressures of CO at -30 °C the squarate dianion was synthesised and is shown in Scheme 1.7. The oxocarbon unit was found to be planar like the deltate dianion and the U–O distances were observed to be almost identical to the deltate distances. The difference however, is found in the U–C distances which were longer (3.045 Å average) than those found in the deltate dianion (2.662 Å average).[21]

Scheme 1.8 shows an example of CO insertion into a uranium carbon double bond. The tetrahedral complex [(Cp)$_3$U($\eta--$COCHPMePh$_2$)] was synthesised by reacting the starting material, [(Cp)$_3$U($=$CHPMePh$_2$)] with atmospheric pressures of CO at ambient temperature. The C–O bond length of the η_2–CO fragment is 1.27 Å, the P–C distance was 1.77 Å and the C–C distance was 1.37 Å which suggest a delocalised structure as

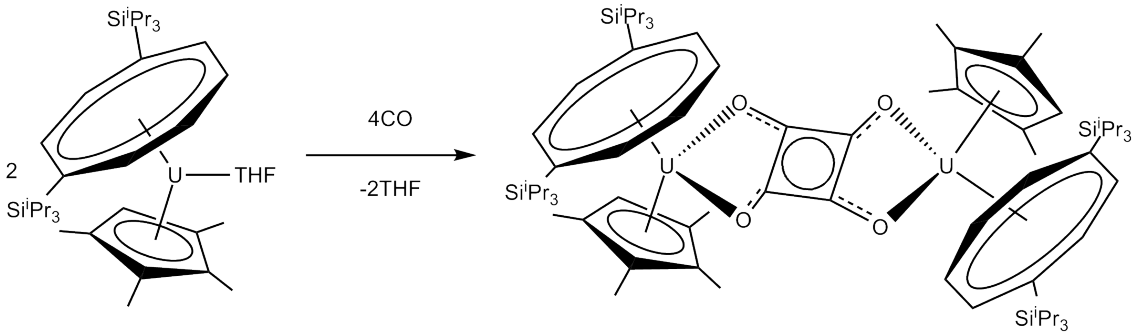

Scheme 1.7: Reductive cyclotetramerization of CO to squarate by a U^{III} complex

depicted in Scheme 1.8 as two resonance structures.[22]

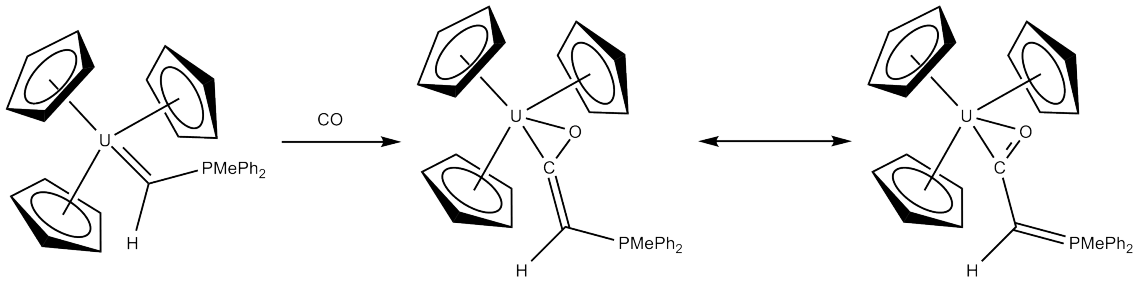

Scheme 1.8: Carbon monoxide insertion into the uranium carbon double bond

These examples show that CO can interact with uranium complexes in a variety of ways. Uranium also possesses the ability to activate the coordinated CO fragment and to functionalise the fragment providing evidence that uranium may be a suitable element to be used in a catalytic CO transformations.

Carbon dioxide activation

As discussed in section A.1, CO_2 is relatively inert. This characteristic of CO_2 requires the molecule to be activated prior to any reaction taking place and this can be achieved by bonding CO_2 to a metal centre. This can be achieved in a number of ways such as 'end–on' or bridging between two metal centres. The following section highlights some of the key uranium–based complexes that have successfully activated CO_2.

One of the first examples of a carbon dioxide insertion into a uranium methyl bond was demonstrated by reacting $[(Cp^*)_2U(Me)_2]$ with an excess of CO_2 to yield bis(acetate) complex $[(Cp^*)_2U(OAc)_2]$. In addition by adding just one equivalent of CO_2 to the same starting material, the monomeric methyl acetate complex, $[(Cp^*)_2U(Me)(OAc)]$ was synthesised.

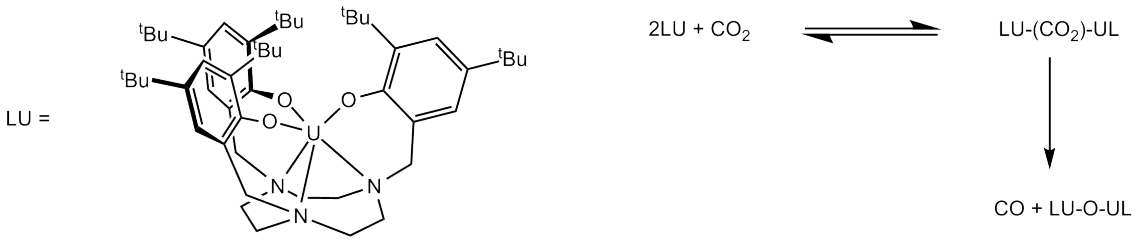

Scheme 1.9: The first example of carbon monoxide bridged dinuclear uranium complex

The complex shown in Scheme 1.9 also reacted with CO_2 to form an oxide–bridged uranium compound releasing carbon monoxide.[19] A similar complex was also investigated in the CO_2 reactivity studies. The *ortho t*–butyl substituents on the aryloxides were replaced with adamantyl substituents as shown in Scheme 1.10. This complex formed the previously unreported $\eta^1-OCO^{\bullet-}$ radical anion.

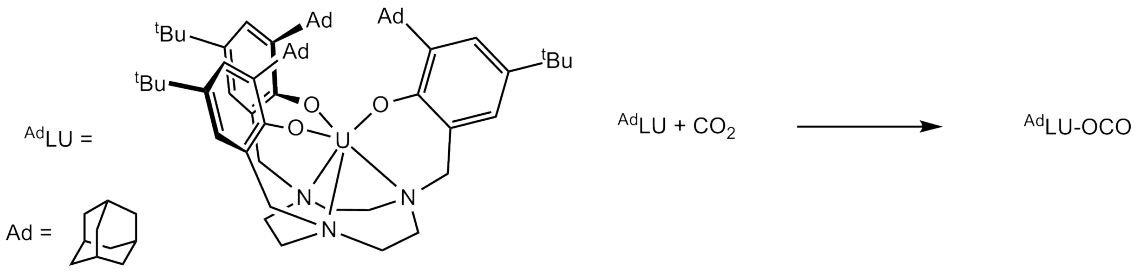

Scheme 1.10: The first example of an end–on carbon dioxide uranium complex

Characterisation of the resulting complex showed the CO_2 molecule had bound in an almost linear fashion with U–O–C and O–C–O angles of 171.1 ° and 178.0 ° respectively. The infrared vibration spectra also showed a significantly reduced frequency for CO_2 of 2188 cm^{-1} compared to free CO_2 which has a vibrational frequency of around 2349 cm^{-1}.[23]

Scheme 1.11 shows the symmetrical U^{IV} dimer $(OTtbp)_2U(\mu{-}O)(\mu{-}O_2COTtbp)_2U(OTtbp)_2$ which was synthesised from U^{III} reduction of CO_2. The O–Ar bonds were similar to other O–Ar bonds however the U–μ–O distance is 2.095(3) Å, shorter than expected and the U–O–U angles was not the predicted linear angle, but observed at 140.4(5) °. The carbonates have U–O bond distances of 2.315(7) and 2.371(7) Å and UO–C bond distances of 1.258(12) and 1.253(13) Å suggesting delocalisation of the charge.[24]

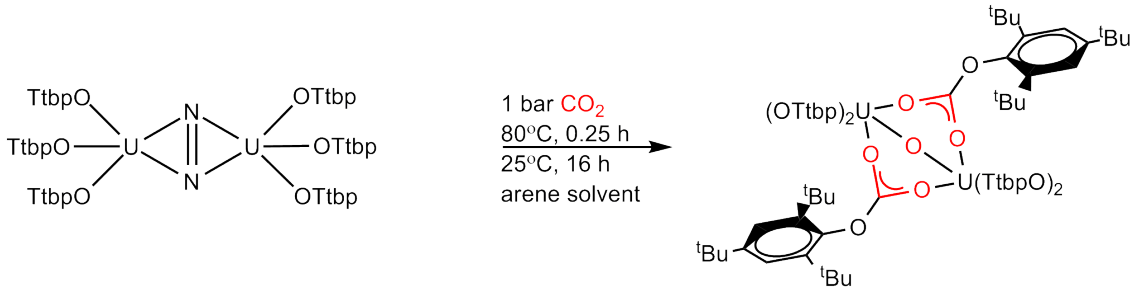

Scheme 1.11: Insertion of carbon dioxide into uranium aryloxide bonds

A more recent example shown in Scheme 1.12 highlights the reductive coupling of CO_2 to form a bridging oxalate complex. The identity of the R group and therefore the sterics of the complex are vital to the outcome of the reaction. When R = Me, two products were identified, $(U(\eta^8{-}C_8H_6(1,4{-}SiMe_3)_2)(\eta^5{-}Cp^{Me_5}))_2(\mu{-}O)$ and the bridging oxalate, $(U(\eta^8{-}C_8H_6(1,4{-}SiMe_3)_2)(\eta^5{-}Cp^{Me_5}))_2(\eta{-}\mu^2{:}\mu^2{-}C_2O_4)$. When R = Et or ^{i}Pr, the bridging carbonate complex, $(U[\eta^8{-}C_8H_6(1,4{-}SiMe_3)_2](\eta^5{-}Cp^{Me_4R}))_2(\mu{-}\eta^1{:}\eta^2{-}CO_3)$ and the bridging oxalate complex $(U[\eta^8{-}C_8H_6(1,4{-}SiMe_3)_2](\eta^5{-}Cp^{Me_4R}))_2(\mu{-}\eta^2{:}\eta^2{-}C_2O_4)$ were formed and when R = ^{t}Bu the only product observed was the bridging carbonate complex, $(U[\eta^8{-}C_8H_6(1,4{-}SiMe_3)_2](\eta^5{-}Cp^{Me_4tBu}))_2(\mu{-}\eta^1{:}\eta^2{-}CO_3)$. 1.12 specifically shows how the oxalate was synthesised as the major product when the R group size was increased (R = Me (20%), Et (30%), ^{i}Pr (60%)). The structural analysis of the oxalate complexes obviously differ depending on the R group, however the U–O bond distances ranged from 2.431(4) to 2.441(5) Å with the average C–O distances observed at 1.263 Å.[25]

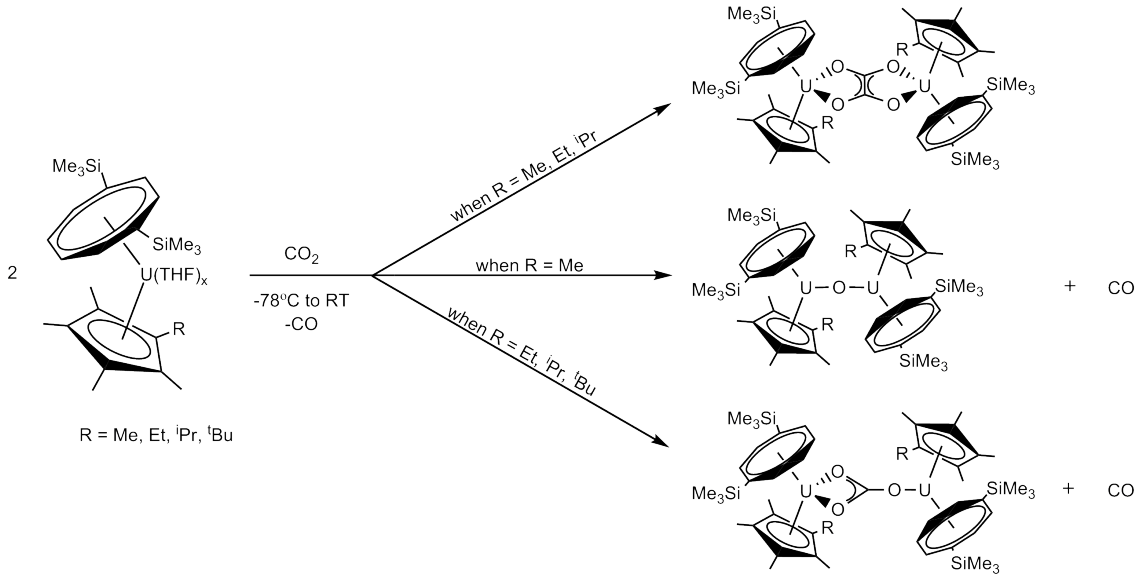

Scheme 1.12: Reductive activation of CO_2 by mixed sandwich uranium III complexes

These examples of show that uranium has been used successfully to react with small molecules such as N_2, CO and CO_2. Both sterics and electronics play a role in the synthetic outcome of these reaction. Development in this area could potentially result in some interesting and significant outcomes.

1.2 Surface sites and molecular mimics

The majority of industrial processes employ heterogeneous catalysis for several reasons. Solid catalysts, or solid–supported catalysts are mechanically robust and self–supporting, which simplifies the construction and operation of large–scale reactors. Additionally, catalytic reactions are then either gas–solid or, more rarely, gas–liquid and the removal of the catalyst is then clearly simple. Solid phase catalysts are usually thermally robust, allowing a wider range of temperatures. Approximately 90% of industrial catalytic processes are based on heterogeneous catalysis.[26]

There are several difficulties when attempting to explain fundamental aspects of surface–

mediated catalysis. The majority of the material is bulk material and conforms to the structure of the normal solid and is only indirectly involved with the catalytic mechanism, as the reaction takes place on the surface of a dense–phase catalyst. Even on the surface, reaction does not occur at every atomic position but at a subset, which means that if the average structure of the surface can be determined, little structural data may be available for the active site or sites.

Several chemical approaches have been used to circumvent these disadvantages, with the hope that increased structural and mechanistic understanding of the active site or sites will allow a rationally designed approach to catalysts with greater activity. One approach is to employ a microporous material, such as a zeolite, which is a crystalline, periodically folded surface in which every atom is at the surface or is surface–like. Structural determinations are in principle no different from a structural determination of a small molecule crystal. Within the microporous structure, catalytic sites can be introduced either as surface atoms, for example in the formation of a microporous Brønsted acid shown below where $(_{s-})$ represents the surface:

$$s - Si[SiO_4] \rightarrow s - Si_{(1-x)}[AlH]_x[SiO_4] \tag{1.2.1}$$

A second approach is to mount an atom exohedrally on the surface such that the atom is chemically bound to the surface and all the reactivity that is established by this route is determined by these surface atoms and not the unmodified support. A proportion of surface materials are based on silica and there are various types of functional group active sites on a silica surface, a number of which are shown in Figure 1.4. It is key to begin by understanding the support surface and the active sites.

The concentrations of each type of active site can be varied with treatment. Dehydroxyla-

tion transforms vicinal silanol groups into isolated groups with treatment temperatures around 700 °C. At higher temperatures in the region of 800 °C the vicinal groups are transformed into strained four membered ring siloxane bridges. The concentrations of each type of silanol or siloxane bridge are therefore dependant on the pretreatment the surface receives and can be manipulated accordingly. Silica can be considered homogeneous, with regard to its active surface sites, with R_3SiOH.[26]

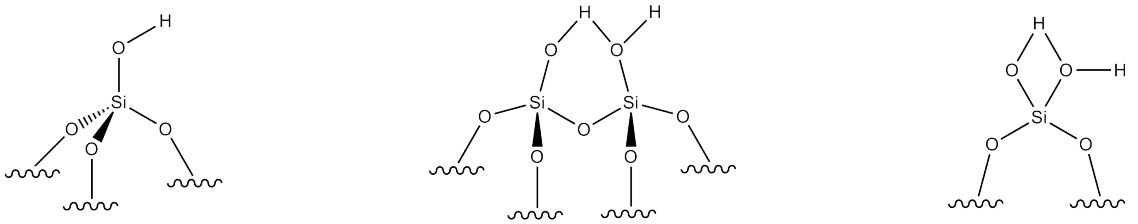

Figure 1.4: Types of surface silanol groups

In order to understand the reactivity of these groups, the tools of molecular chemistry are employed to investigate such systems. Complexes are developed that 'mimic' the surface active sites but on an organometallic, molecular level. There are key questions that should always be considered when using one system as a mimic for another. For example; does the molecular system react in identical ways to the surface it is mimicking? Can the structure of the molecular systems be rationalised in terms of the solid surface sites? Is it possible to study the steps of a reaction on the molecular mimic and is this a true reflection of the chemistry involved on the surface site?[26] Investigations into the acidity and behaviour of the Si–OH unit are therefore important.

1.2.1 Silanols as molecular mimics for surface sites

Silanols are compounds containing the Si–OH bond and are homologous with the carbon containing alcohol group, C–OH. There are three major groups within the silanol family.

First the silanol groups which contain just one Si–OH unit. Second the group of silanols containing compounds which possess one or more $Si(OH)_2$ units and finally the third group containing all the silanol compounds which possess one or more $Si(OH)_3$ units.[27] For the purposes of this work only silanols with one Si–OH unit will be considered.

In general silanols tend to be difficult to synthesise and store. There are currently two main methods used to synthesise silanols. The first is to hydrolyse compounds containing the Si–X unit (X = F, Cl, Br, I, H). The second method is to oxidise the Si–H unit of the desired compound using an oxidising agent such as $KMnO_4$, $AgNO_2$, $AgNO_3$, Ag_2O, O_3 or dioxiranes.[27]

The Si–O group also shows a tendency to undergo an intermolecular condensation reaction resulting in a very stable siloxane compound and water. This tendency means the isolation of pure silanols can be problematic and this is, to a large extent, the reason for the high price of many silanol derivatives. Solutions to this issue involve storage of the silanols at lower temperatures to reduce the rate at which the condensation reaction occurs, dilution of the silanols in order to reduce the probability of a condensation reaction and using bulky R groups on the silicon in order to stabilise the silanol kinetically.

Finally, during the preparation of most silanols, the R_3Si-Cl group is synthesised first. The hydrolysis of the Si–Cl moiety results in acidic impurities which can cause degradation of the desired silanol. Mild bases such as triethylamine or aniline can be effective in the removal of such impurities.[27]

Si–O Bonding

The σ–bonding in a Si–O bond is very different from a C–O bond. The bond dissociation energies of the two are 498 kJ/mol and 358 kJ/mol respectively showing that the C–O

single bond is weaker. The converse is observed in the case of Si=O and C=O, in which case, the bond dissociation energies are 749 kJ/mol and 803 kJ/mol respectively.[28,29]

The principle difference between these two quantities rests on the description of the constituent atomic orbitals that are assembled under the LCAO approximation. In carbon, the *p*–orbitals have no radial node, are contracted and can form π–interactions readily at the distance of a C=O bond. However, because of the strong interaction between the two atoms, the gap between the bonding and anti–bonding orbitals is substantial and any donation into a $\sigma*$–orbital is negligible. A C–O single bond therefore has single bond character only.

For a Si–O single bond, other effects are involved. The $s-p$ gap is somewhat larger, leading to a higher degree of *p*–character in the valence shell; the electronegativity difference is greater therefore:

$$\Delta\chi = \chi(O) - \chi(C) = 0.89$$

$$\Delta\chi = \chi(O) - \chi(Si) = 1.54$$

resulting in a far more polar bond and therefore a greater electrostatic contribution. In additon the radial node present in the 3*p* orbital destabilises $3p--2p$ π–interactions.

Because the bonding–antibonding gap is smaller in an Si–O bond, then the availability of the $\sigma*$–orbitals becomes important and the interaction between the *p*–rich Si bonding hybrids and the anti–bonding CH or SiH σ*–orbitals is significant.[30,31] This bonding model provides a more satisfactory explanation than the earlier hypothesis of *p*–*d* dative bonding.[32,33] This π–acidity at the Si centre also plays a role in the geometry of the M–O–Si linkage, as discussed below.

In addition, when comparing the silyl ligand, Ph_3SiOH to the alkyl ligand, Ph_3COH it has been noted that the silyl ligand is more electron withdrawing. Whilst the carbon atom is

in fact the more electronegative of the two, the silicon atom possesses a strong inductive effect which has an impact on the whole ligand. This is reflected by the acidity of the two ligands. For example Ph_3SiOH (pK_a = 16.57, DMSO) is a stronger acid than the alkoxide equivalent Ph_3COH (pK_a = 16.97, DMSO). In addition it is worth noting that the siloxide ligand binds to metal centres in a more ionic fashion than the less acidic alkoxide ligands.[34]

Si–O–M Bonding

The Si–O–M bond is normally linear, whereas the C–O–M bond is more often bent. It is generally accepted that the principle bonding between siloxides or alkoxides and the metal centre occurs through a σ–bond from the oxygen to the metal centre. There is also an argument for significant interaction between the ligand and the metal via donation from the $p\pi$–orbitals on the oxygen, see Figure 1.5 (a) and (b) respectively.[34] This type of bonding presumes a three electron donation from the ligand to the metal centre, therefore enabling the stabilisation of low coordinate and electron deficient metal centres.

The linear nature of the Si–O–M bond angle has been previously accredited to the *d*–orbitals on the silicon atom accepting electrons from the *p*–orbitals on the oxygen.[35,36] However, more recently this theory has been superseded and the linear nature of the Si–O–M bond is more accurately described by considering 'Bent's rule'[37] and electronegativity differences.[31] Bent's rule predicts that bonding *sp* hybrids to atoms of higher electronegativity will result in an increased percentage of *p* character, which will lead to smaller bond angles.[31] Therefore, because carbon has a greater electronegativity value (2.5) compared to silicon (1.9) the orbital of the oxygen atom will posses greater *p* character and lead to smaller (non–linear) bond angles.

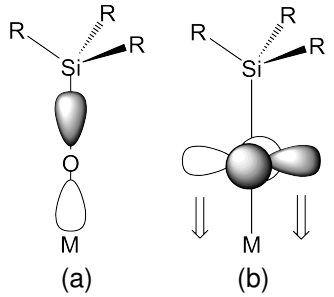

Figure 1.5: Si–O Bonding modes (a) $p\sigma$ donation and (b) $p\pi$ donation

1.2.2 Surface organometallic chemistry

As discussed in section 1.2, surface science can use the surface of a material to stabilise inorganic catalysts. Moreover, reactions that are unprecendented in solution can occur at surface–bound metal atoms. This has proved to be useful in the transformation of alkanes, which is of great interest to the petrochemical industry in their quest to transform small hydrocarbons such as methane. Because of reactions such as this, surface organometallic chemistry (SOMC) is an area of chemistry that has gained popularity and is used to anchor complexes onto surfaces such as oxides, zeolites or metals in order to use the complex further in catalysis.

There are a variety of examples of complexes bound to zeolites. Once bound, the structure of the complex is investigated along with the possible mechanism, reactivities of the complex and the catalytic properties in relation to the activation of alkanes *via* a metathesis type reaction, which is examined further here.

Metathesis of alkanes

The metathesis of alkanes is not without its issues. For example, if the metathesis of alkenes are considered for a moment, in most cases there is only one double bond for the reaction to occur. Now consider alkanes, and more specifically, C_n where $n \geqslant 3$. Each C–C

bond is a potential reaction site and therefore multiple products are to be expected.[38–40] To illustrate this point further, a complex previously reported in 1978 by Schrock and Fellmann[41] can be used as an example when the tantalum complex is bound to a dehydroxylated silica surface, represented as *s*- in Scheme 1.13. The reaction produced two silica bound tantalum compound and neopentane gas.[42]

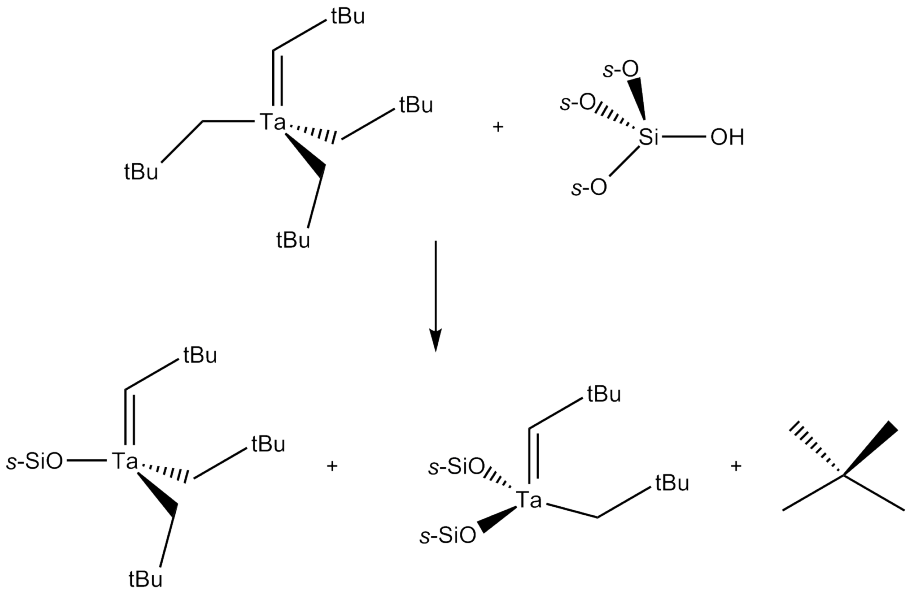

Scheme 1.13: Tantalum compound on dehydroxylated silica surface

Following this example, the synthesis of the monohydride tantalum compound[43] was synthesised by exposing the two tantalum products, depicted in Scheme 1.13, to 1 atm of hydrogen in temperatures of up to 200° C. The hydride species[38] showed no catalytic reactivity when reacted with cycloalkanes and only a Ta^{III} cyclo–alkyl species was formed with the evolution of hydrogen gas. However, when the tantalum hydride species was exposed to acyclic alkanes a catalytic metathesis reaction was observed (25° C -200° C) leading to both higher and lower homologues. For example, the metathesis of ethane simply formed methane and propane. However, as predicted, when exposed to an alkane with more than one C–C bond a mixture of products were observed and the metathesis of propane led mainly to the products n–butane and isobutane with other observed products being ethane, n–pentane, isopentane and propane.

In addition to the tantalum hydride, zirconium hydrides have also been investigated. The development of a highly electron deficient zirconium neopentyl complex, which was stabilised by being bound to the surface of dehydroxylated silica causing steric crowding, as shown in Scheme 1.14. The product was reacted with hydrogen (6 x 10^4 Pa at 150° C) to form the hydride and various reactions were observed with cyclo–octane and methane.[44] However, more interesting was the synthesis and reactivity of a zirconium monohydride and dihydride.[45] The reactivities of these complexes were reported with regard to exposure to methane. The monohydride reacted slowly and incompletely to form [$s-(SiO)_3ZrMe$] whilst in contrast the dihydride reacted quickly and completely to form the species [$s-(SiO)_2ZrMe_2$] via the intermediate [$s-(SiO)_2ZrHMe$] as shown in Scheme 1.15.

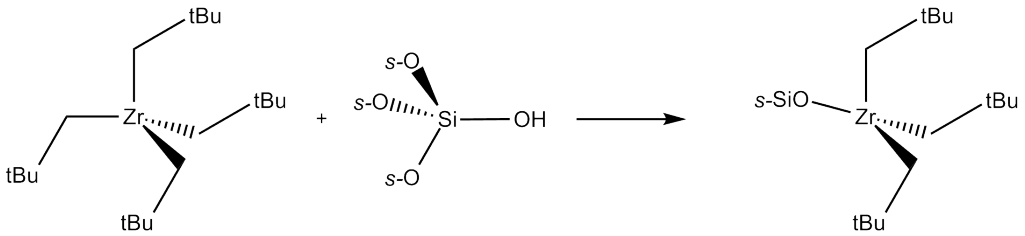

Scheme 1.14: Zirconium species on a dehydroxylated silica surface

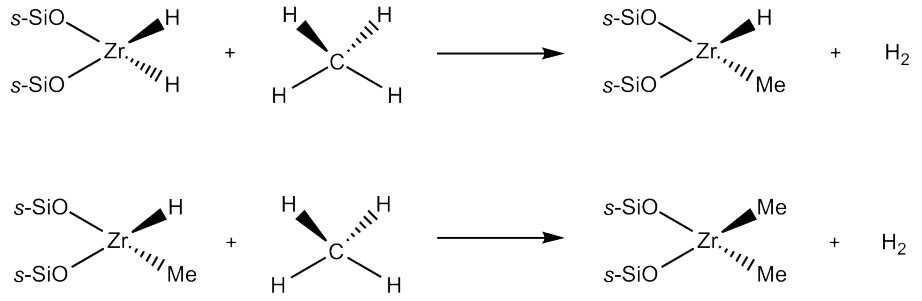

Scheme 1.15: Zirconium hydride species on a dehydroxylated silica surface reacting with methane

This observation suggests that dihydrides and perhaps polyhydrides could be used more effectively in the catalytic reactions involving methane and other alkanes.

1.3 Current molecular models for surface materials

One of dominant area of research has been on the use polyhedral oligosilasesquioxanes (POSS) as surface mimics.[46] This group of molecules are useful in this area of chemistry for two reasons. Firstly, they possess an adequate degree of oligomerisation making them relevant models for highly silaceous materials and secondly, they retain the Si–OH functionality which allows them to be used as ligands in a wide range of transition metal and main group complexes.[46] In addition, the extensive framework within POSS suggests that the electronic properties should be closer to those of silica and siliceous solids compared to conventional models such as siloxide ligands. For example, the electron withdrawing properties of the Si_8O_{12} framework are similar to CF_3 which is a stark contrast to the electron donating properties of the R_3Si derivatives. Furthermore, conventional models fail to mimic the geometry observed in silica supported species due to the metal centre being the dominant force in the ligand arrangement. A silica surface dictates its own structure due to the inflexible nature of the solid surface itself.

The first example of a transition metal containing siloxane that was designed to mimic surface sites possessed three hydroxyl groups bonded to a single metal atom.[47] The new compounds are called polyhedral oligometallasilsesquioxanes (POMSS) and synthesised by substituting transition metal atoms into the silicon oxygen framework of polyhedral oligosilasesquioxanes. One of the most notable examples in this area is a vanadium containing silsesquioxane complex.[48–50] Vanadium complexes are reported to be possible catalysts for the oxidation of methane and other hydrocarbons. In addition, a number of studies have reported that vanadium formed the elusive "three–legged" surface complexes which are preferable due to the increased stability of three anchors.

1.3.1 Triphenylsiloxide as a molecular surface mimic

Triphenylsiloxide has been used as a ligand on a number of transition metal and lanthanide complexes with a view to synthesise a mimic for a surface bound species; such complexes include both heteroleptic and homoleptic systems.

1.3.2 Lanthanides

Scheme 1.16 shows various lanthanum siloxide complexes which have been reported in the literature, the first of which was $[La(OSiPh_3)_3(THF)_3]\cdot THF$ which was synthesised by reacting $[La(N(SiMe_3)_2)_3]$ with aliquots of Ph_3SiOH at 0°C.[51] The resulting $[La(OSiPh_3)_3]_n$ was then stirred in THF and recrystallised from THF/diethyl ether mix. Derivatives of this complex were synthesised by using different solvent systems. $[La(OSiPh_3)_3(py)_3]$ was prepared by condensing pyridine onto the solid, $[La(OSiPh_3)_3]_n$ and recrystallised from a pyridine/diethyl ether mix. Finally $[La(OSiPh_3)]_n$ was stirred with $OP(^nBu)_3$ to form the complex, $[La(OSiPh_3)_3(OP(^nBu)_3)_2]$. Only one of these complexes had full characterisation data, $[La(OSiPh_3)_3(THF)_3]\cdot THF$. The complex has average La–O_{silox} bonds of 2.226(3) Å, La–O_{THF} bonds of 2.643(7) Å and Si–O bonds of 1.598(0) Å.[51]

Cerium has also been investigated and $Ce(OSiPh_3)_2(\mu-OSiPh_3)_2$ can be synthesised by reacting $Ln[N(SiMe_3)_2]_3$ (Ln = La, Ce) with Ph_3SiOH which crystallises as the dimer $[Ce(OSiPh_3)_3]_2$ with bridging siloxide ligands. The average Ce–O_{silox} bond lengths were observed at 2.163(6) Å whilst the Ce–$O_{bridging}$ were found to be slightly longer at 2.384(5) Å.[52] Secondly, $Ce(OSiPh_3)_4$ was prepared from $Ce(OPr^i)_4$ by reacting it with Ph_3SiOH in DME. Single crystals of $Ce(DME)(OSiPh_3)_4$ which were of X–ray diffraction quality were yielded from a toluene/Et_2O mix and Ce–O_{silox} bond lengths were observed at 2.11(48) Å, on average, whilst the Ce–O_{DME} were found to be slightly longer at 2.581(10) Å.[53]

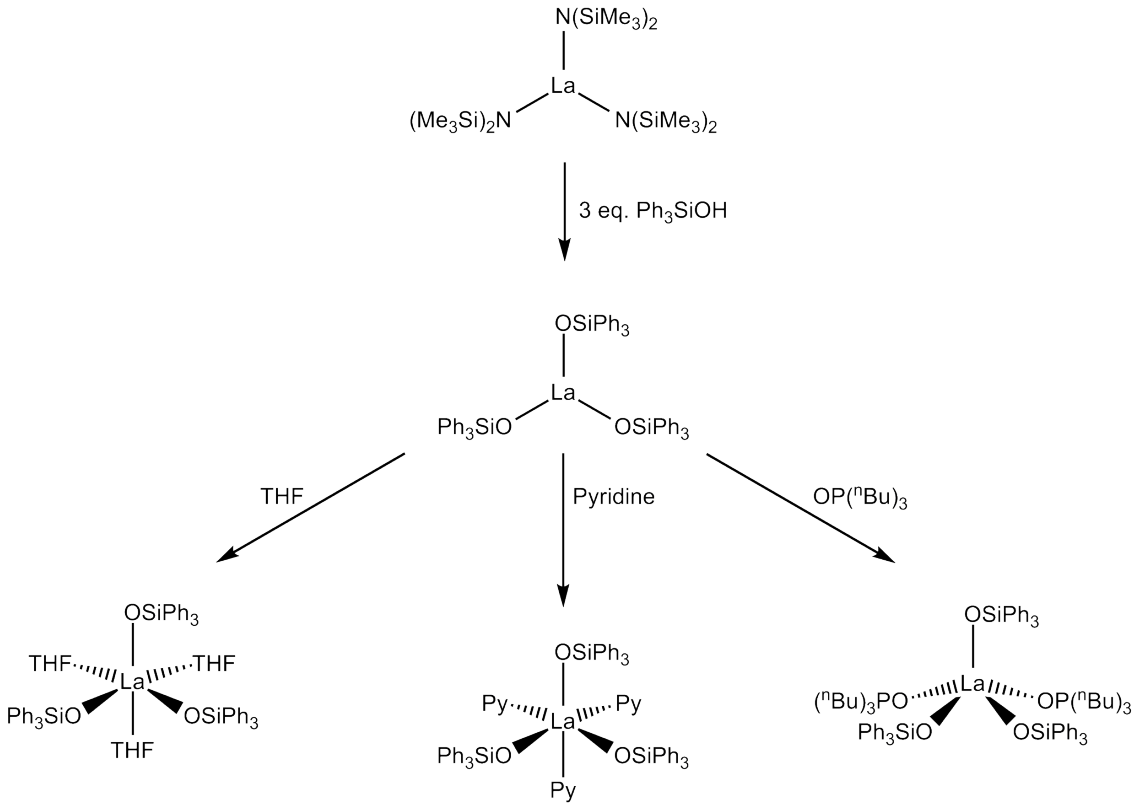

Scheme 1.16: The homoleptic triphenylsiloxide lanthanum complexes and lewis base adducts

Finally, by heating $Ln(NO_3)_3(H_2O)_y$ (Ln = Y, Ce, Nd, Pr) in the presence of NH_4NO_3 the anhydrous trivalent nitrates $(NH_4)_xLn(NO_3)_{3+x}$ were formed which could then be reacted with three equivalents of $NaOSiPh_3$ to synthesise $[Ln(OSiPh_3)_3(THF)_3](THF)$. Only the cerium compound was characterised fully, but the average Ce–O_{silox} bond lengths were observed at 2.222(4) Å whilst the Ce–O_{THF} were found to be 2.591(7) Å.[54]

An example of a samarium complex was synthesised by reacting a previously prepared solution of $[Cp^{"}{}_2SmF]_2$ in THF with Ph_3SiOH. The characterisation data showed the complex had a Sm–O_{silox} bond of 2.169(8) Å and a O–Si bond of 1.590(8) Å.[55]

Two further samarium siloxide examples were developed by reacting $Sm(N(SiMe_3)_2)_3$ with Ph_3SiOH and recrystallised from ether. By reacting $[(Ph_3SiO)_3SiO]_3Sm(THF)_3$ with $[Cp \cdot Sm(\mu{-}OSi(O^tBu)_3)_3Sm]$, a mixed polynuclear siloxide was isolated and the product, $[(Ph_3SiO)_3Sm(Cp \cdot)Sm(OSi(O^tBu)_3)_3Sm]$ is shown in Scheme 1.17. Only structural data

were published for the second complex which gave an average Sm–O_{silox} bond length of 2.161(8) Å and an Si–O bond length of 1.608(2) Å.[56]

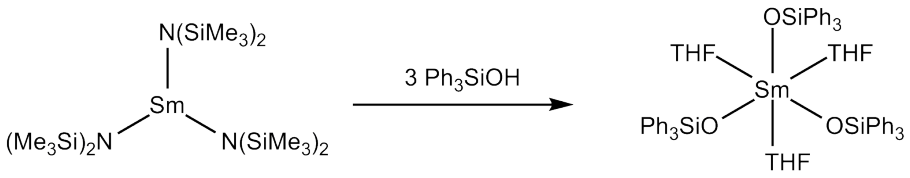

Scheme 1.17: The samarium complex, $Sm(OSiPh_3)_3(THF)_3 \cdot (THF)$

Three dysprosium complexes have been reported, which are similar to the lanthanum complexes discussed previously and shown in Figure 1.6. $[Dy(\mu-OSiPh_3)(OSiPh_3)_2]_2$ (a), $Dy(OSiPh_3)_3(THF)_3$ (b) and $Dy(OSiPh_3)_3(py)_3$ (c) were synthesised using $Dy(NR_2)_3$, Ph_3SiOH and either toluene, THF and pyridine respectively with no structural data available.[57]

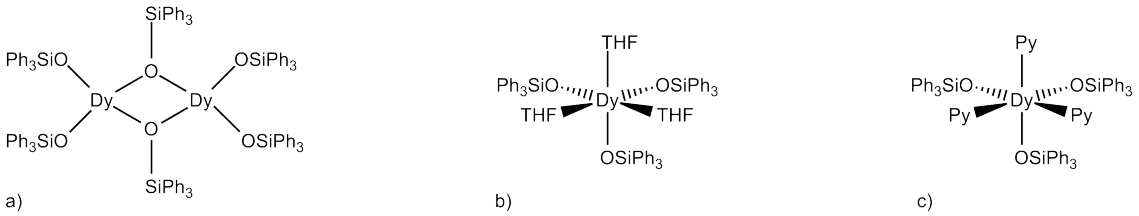

Figure 1.6: Examples of dysprosium siloxides

1.3.3 Titanium

A wide variety of titanium triphenylsiloxide complexes have been reported as surface mimics for titanium supported on silica; these compounds are summarised in Table 1.1.

Cyclopentadienyl derivatives as anchors

Large ring systems have long been investigated as ligands for their ability to stabilise otherwise reactive metal centres. The same systems are also considered mimics for

surfaces and as such, group IV metallocenes have been developed as a homogeneous, single site, metallocene anchored catalysts, as shown in Scheme 1.18. The M–O–Si IR stretch of this system was observed at 957 cm^{-1} for the Ti and Zr derivatives, whilst the Hf derivative was recorded at 977 cm^{-1}. The M–O (M = Ti, Zr, Hf) bond lengths were observed through X–ray analysis and were found to be 1.842(4) Å, 1.961(6) Å and 1.934(5) Å respectively and M–O–Si bond angles of 164.5(2)°, 173.0(4)° and 171.9(4)° respectively.[58]

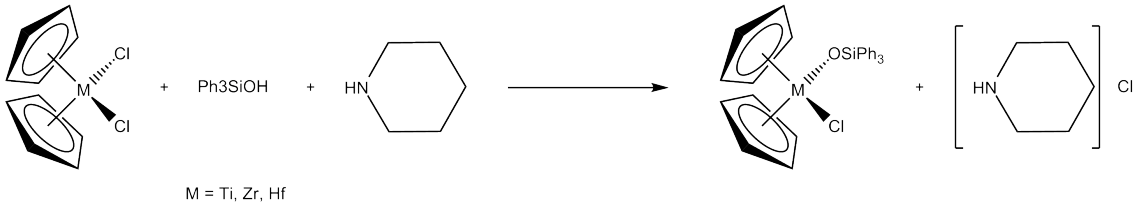

Scheme 1.18: Synthesis of a group IV metallocene chloro triphenylsilanolate

Scheme 1.19 shows the synthesis of titanasiloxanes via a hydrogen transfer process from a monosilanol such as triphenylsilanol to a titanium framework. The reaction gave good yields in the region of 71–95%.[59]

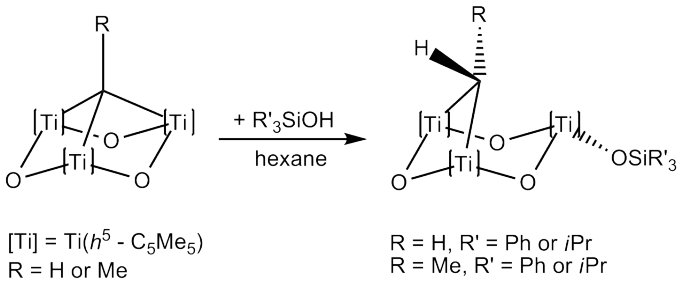

Scheme 1.19: The synthesis of titanasiloxanes using silanols

Both complexes of the general formula, $Cp^{"}(Ph_3SiO)_2TiX$ and $Cp^{"}(Ph_3SiO)TiX_2$ (X = Cl, Me, CH_2Ph) can be synthesised and are shown in Scheme 1.20. Unfortunately, only $Cp^{"}(Ph_3SiO)Ti(CH_2Ph)_2$ was reported with X–ray data showing the Si–O bond length to be 1.6430(15) Å and the Ti–O bond length to be 1.8055(15) Å.[60]

In the above examples, the titanium metal centre is in its most commonly found Ti^{IV} oxid-

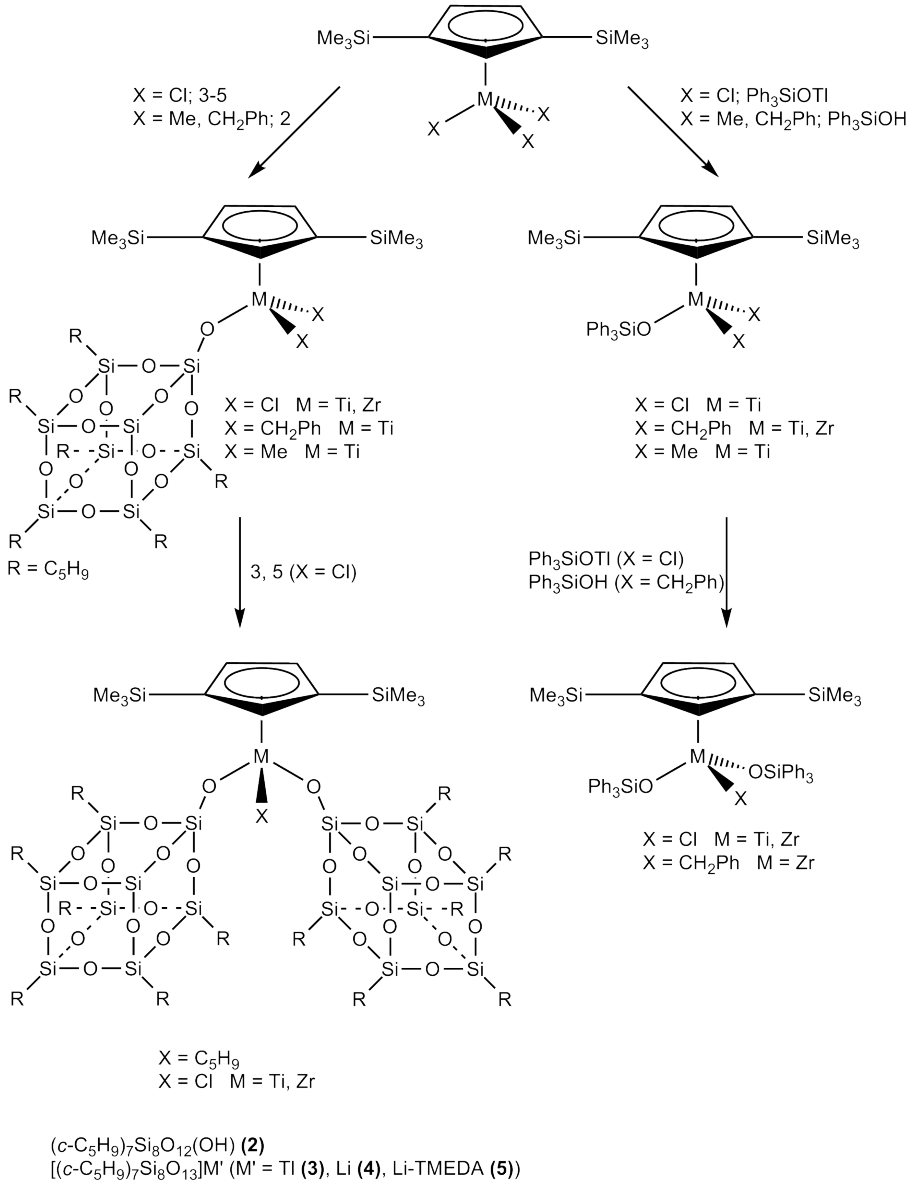

Scheme 1.20: Group 4 metal siloxy and silsesquioxane complexes: soluble model systems for silica–grafted olefin polymerization catalysts

ation state. The following provides an example of a Ti^{III} compound, $[Cp^*_2Ti(OSiPh_3)]$ of which green crystals were grown following an insertion reaction between the starting materials, permethyltitanocene $[Cp^*Ti(\eta^5{:}\eta^1\text{-}C_5Me_4CH_2)]$ and triphenylsilanol. Electronic absorption data were collected and peaks were found in the ranges 497–525, 605–665 and 1300–1800 nm. The IR data were observed as an intense absorption band at 956 cm^{-1}. X–ray data were also analysed with an observed Ti–O bond length of 1.9190(13) Å and an Si–O bond length of 1.6115(13) Å.[61]

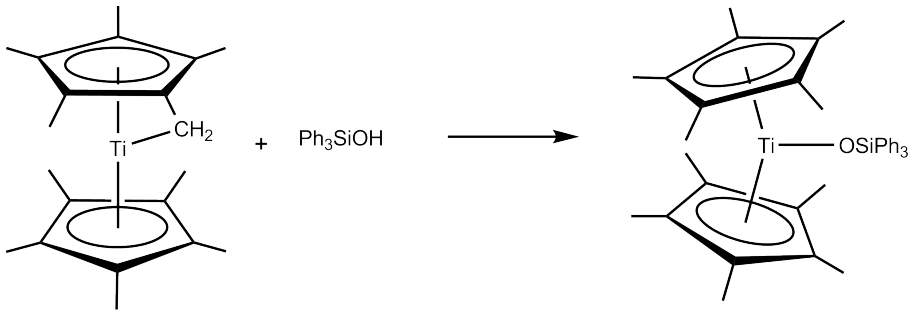

Scheme 1.21: [Cp · 2 Ti($OSiPh_3$)], synthesised by protonolysis of the titanium–methylene bond in a singly tucked–in permethyltitanocene

Other ligand systems

Whilst cyclopentadienyl derivatives are many, other ligand systems have also been investigated. The reaction between $[Mg_2(\mu{-}OSiPh_3)_2(OSiPh_3)_2(THF)_2]$ and $TiCl_4$ is shown in Scheme 1.22. Several titanium complexes can be synthesised with this method and one of the products, $[TiCl_2(OSiPh_3)_2(THF)_2] \cdot 2\,THF$, was synthesised and exhibits a distorted octahedral geometry and an Si–O bond length of 1.653(3) Å. In addition the complex has a Ti–O bond length of 1.800(3) Å.

Reacting $[Mg_2(\mu{-}OSiPh_3)_2(OSiPh_3)_2(THF)_2]$ with four equivalents of *cis*$-[TiCl_2(\eta^2{-}mal)_2]$ (mal = (*O,O*)–3–oxy–2–methyl–pyran–4–onato), $[TiCl(OSiPh_3)(\eta^2{-}mal)_2] \cdot THF$ was synthesised in 72% yield. This new complex had an observed Si–O bond length of 1.634(3) Å and a Ti–O bond length of 1.799(3) Å. Further treatment of $[TiCl(OSiPh_3)(\eta^2{-}mal)_2] \cdot THF$ with Li^{t}Bu and Ph_3SiOH resulted in two further siloxide compounds being synthesised, $[Ti(^t Bu)(OSiPh_3)(\eta^2{-}mal)_2]$ in 63% yield and $[Ti(OSiPh_3)_2(\eta^2 mal)_2]$ in 91% yield.[62]

Complexes with the general formula $[(Ph_3SiO)_2MCl_2(THF)_2](tol)_2$ (M = Ti, Zr, Hf) were synthesised from $MCl_4(THF)_2$ and two equivalents of Ph_3SiOLi in THF. X–ray analysis showed a Si–O bond length of 1.642(2) Å and a Ti–O bond length of 1.782(2) Å.[63]

$Ti(OSiPh_3)_4$ can be synthesised by reacting $Ti(O^n Bu)_4$ with triphenylsilanol in toluene at

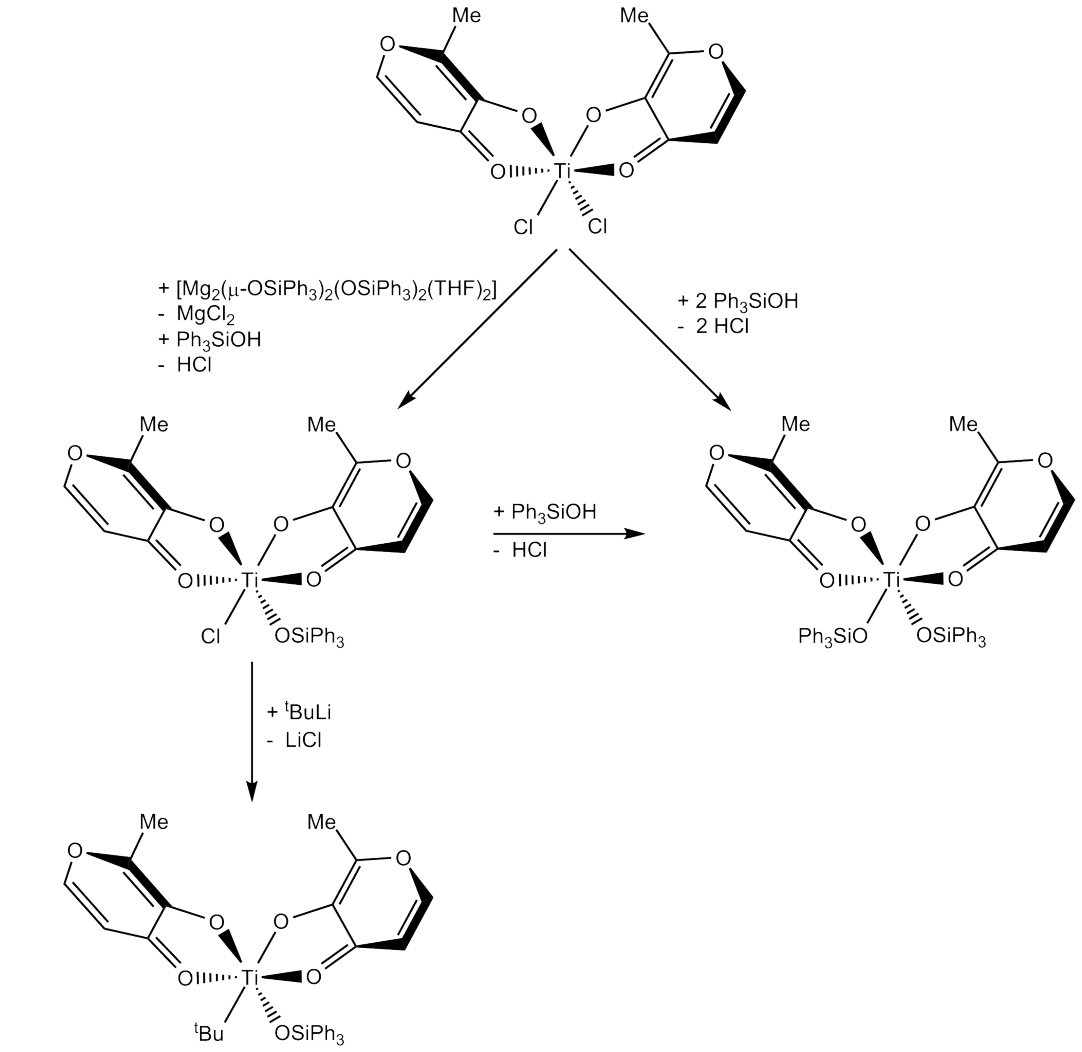

Scheme 1.22: Synthesis of various titanium siloxanes

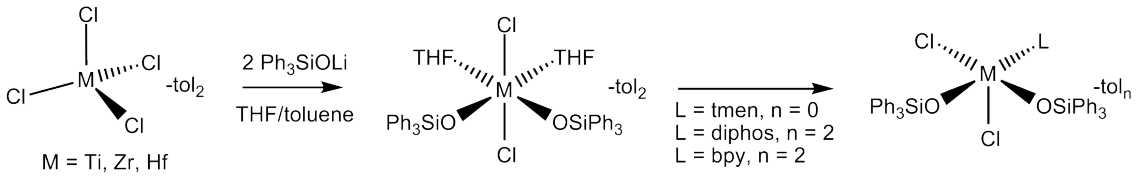

Scheme 1.23: Synthesis of group IV complexes, $[(Ph_3SiO)_2MCl_2(THF)_2](tol)_2$

ambient temperature and pressure. The Ti–O bond lengths range from 1.782(4) Å to 1.798(7) Å whilst the Si–O bond lengths range from 1.650(4) Å to 1.613(7) Å. The Ti–O–Si bond angle is observed as 148.2(3)°.[64]

Triphenylsilanol can also be reacted directly with the metal containing complex. An example of this is [PcTi($OSiPh_3$)$_2$ (shown in Scheme 1.25), an air sensitive blue/green com-

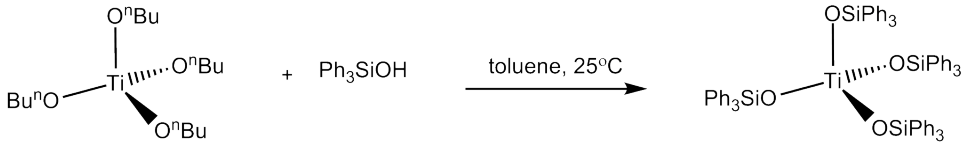

Scheme 1.24: Synthesis of the monomeric, tetrahedral, four coordinate titanium siloxide complex, $Ti(OSiPh_3)_4$

pound, which was synthesised by reacting two equivalents of Ph_3SiOH with one equivalent of the starting material, N,N'–di–4–tolylureato(phthalocyaninato)titanium(IV). From X–ray data the observed bond length for Ti–O was found to be 1.852(11) Å whilst the Si–O bond length was 1.627(11) Å. In addition, two peaks were observed in the UV–Vis spectrum at λ_{max} 741 nm and 698 nm, which were attributed to the siloxy ligands. The IR spectrum showed a band at 821 cm^{-1} which was assigned to the O–Si–O antisymmetric stretch.[65]

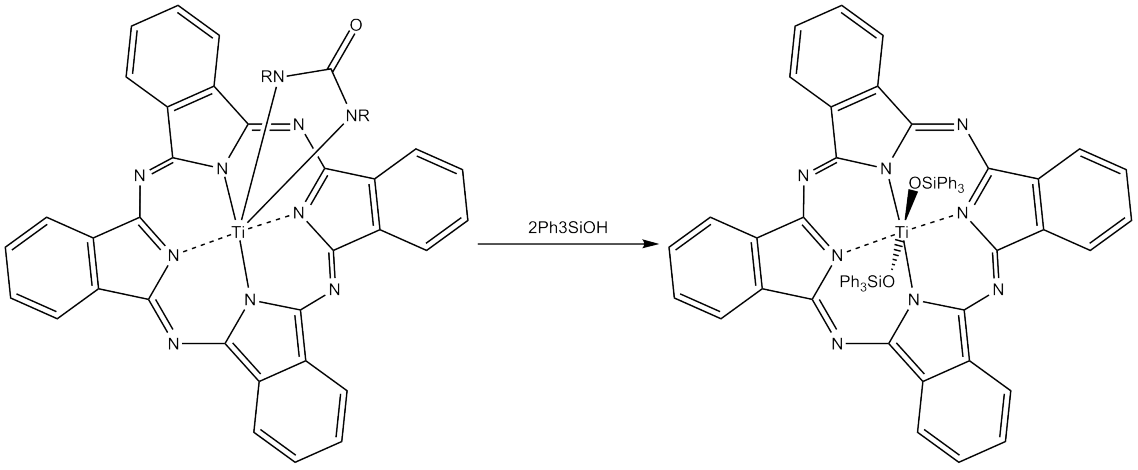

Scheme 1.25: Synthesis of *trans*–bis (triphenylsiloxy)phthalocyaninatotitanium(IV)

In addition, by adding one and a half equivalents of triphenylsilanol to one equivalent of $(PyO)_2Ti(O^iPr)_2$, the product $(PyO)_2Ti(OSiPh_3)_2$ was synthesised, although in relatively poor yields (50%). X–ray quality crystals were grown in which a Ti–O bond length of 1.85 Å was observed within the siloxy ligand. In addition the colourless compound was observed to have a UV–Vis λ_{max} value of 281 nm.[66]

Finally, a solution of $Ti(O^tBu)_4$ was stirred with triphenylsilanol and triethanolamine in THF

with the resulting product, $(Ph_3SiO)TiN(OCH_2CH_2)_3$ which was subsequently recrystallised from toluene in yields of 78%. The X–ray analysis showed an Si–O bond length of 1.608(2) Å and a Ti–O bond length of 1.834(2) Å with a perfectly linear Ti–O–Si bond angle of 180°.[67]

Titanium Compound	Oxidation State	Si–O Bond Length	Ti–O Bond Length
$[Cp^*{}_2Ti(OSiPh_3)]$[61]	III	1.6115(13) Å	1.9190(13) Å
$(Ph_3SiO)_2(pc)Ti$[65]	IV	1.627(11) Å	1.852(11) Å
$[(Cp \cdot Ti(\mu O))_3(\mu CHR)(OSiR^{'}_3)]$[59]	IV	—	—
$(OPy)_2Ti(OSiPh_3)_2$[66]	IV	—	1.85 Å
$Cp_2TiCl(OSiPh_3)$[58]	IV	—	1.842(4) Å
$[TiCl_2(OSiPh_3)_2(THF)_2] \cdot 2\,THF$[62]	IV	1.653(3) Å	1.800(3) Å
$[TiCl(OSiPh_3)(\eta^2-mal)_2] \cdot THF$[62]	IV	1.634(3) Å	1.799(3) Å
$[Ti(^tBu)(OSiPh_3)(\eta^2-mal)_2]$[62]	IV	—	—
$[Ti(OSiPh_3)_2(\eta^2 mal)_2]$[62]	IV	—	—
$Ti(OSiPh_3)_4$[64]	IV	1.632(1) Å	1.790(6) Å
$[(Ph_3SiO)_2MCl_2(THF)_2](tol)_2$[63]	IV	1.642(2) Å	1.782(2) Å
$(Ph_3SiO)TiN(OCH_2CH_2)_3$[67]	IV	1.608(2) Å	1.83(4) Å
$Cp^{"}(Ph_3SiO)Ti(CH_2Ph)_2$[60]	IV	1.6430(15) Å	1.8055(15) Å
Average Bond Length	III	1.6115(13) Å	1.9190(13) Å
Average Bond Length	IV	1.634(3) Å	1.81(74) Å

Table 1.1: Summary of key bond lengths found in examples of titanium triphenylsiloxides

1.3.4 Zirconium

Examples of triphenylsiloxides as ligands for zirconium based complexes are as abundant as the titanium based compounds and are summarised in Table 1.2 along with key bond distances.

Cyclopentadienyl derivatives as anchors

As shown in Scheme 1.18 (Section1.3.3) the compound, $Cp_2ZrCl(OSiPh_3)$ was synthesised by reacting the zirconium metallocene dichloride with triphenylsilanol and piperidine. The complex was then reacted with $K[H_2BC_8H_{14}]$ to afford the 18 electron complex $Cp_2Zr(OSiPh_3)(\mu{-}H)_2BC_8H_{14})$. X–Ray diffraction analysis showed the Zr–O bond lengthening from 1.961(6) Å in the first compound to 1.985(3) Å in the second compound, $Cp_2Zr(OSiPh_3)(\mu{-}H)_2BC_8H_{14})$. This species had an observed Si–O bond length of 1.614(3) Å. Whilst this is within the average values found for silicon oxygen bonds, no comparison can be made to the starting compound due to a lack of reported data.[58]

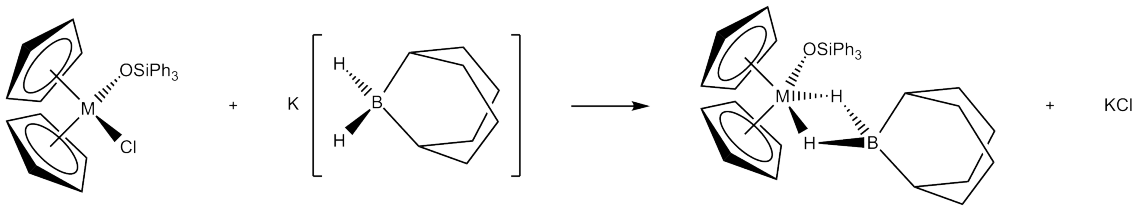

Scheme 1.26: Metathesis reaction between $Cp_2ZrCl(OSiPh_3)$ and $K[H_2BC_8H_{14}]$ to synthesise the 18 electron complex $Cp_2Zr(OSiPh_3)(\mu{-}H)_2BC_8H_{14})$

The compounds $Cp"(Ph_3SiO)_2ZrCl$, $Cp"(Ph_3SiO)Zr(CH_2Ph)_2$ and $Cp"(Ph_3SiO)_2Zr(CH_2Ph)$ were all synthesised from the starting material $Cp"ZrCl_3$ and either silsesquioxane or triphenylsiloxy and are shown in Scheme 1.20. Colourless crystals of $Cp"(Ph_3SiO)_2ZrCl$ were grown from a saturated hexane solution and X–ray diffraction analysis showed a Zr–O bond length of 1.925(5) Å.[60]

Other ligand systems

$[(\eta^7{-}C_7H_7)Zr(OSiPh_3)]_2$ was synthesised from $[(\eta^7{-}C_7H_7)Zr(N(SiMe_3)_2)]_n$ and a toluene/THF solution of Ph_3SiOH. The dimeric structure was characterised by X–ray diffraction studies revealing Zr–O bond lengths of 2.1810(9)–2.2494(9) Å, which are significantly

longer than the average Zr–O bond length reported to be *ca.* 1.93 Å in the paper.[68]

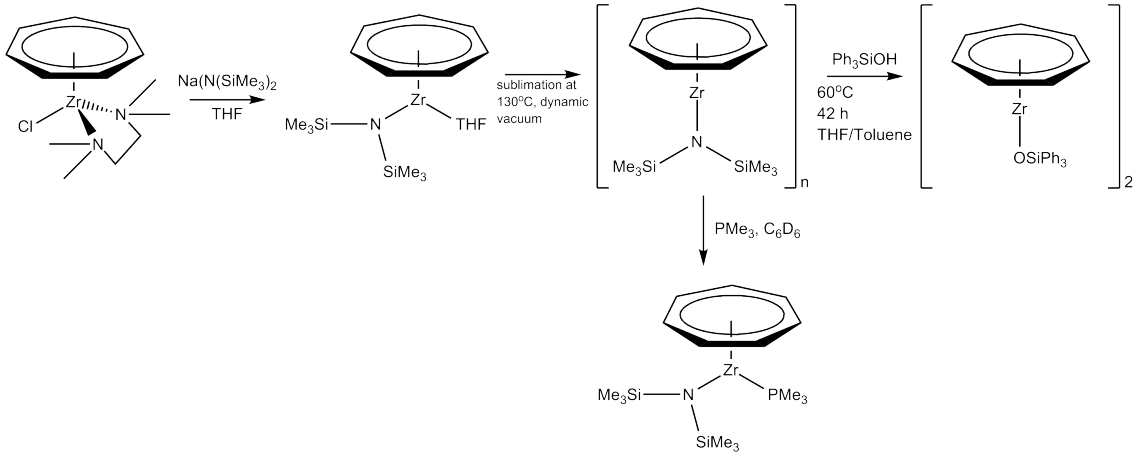

Scheme 1.27: Synthesis of the zirconium siloxide complex, $[(\eta^7-C_7H_7)Zr(OSiPh_3)]_2$

A second approach to synthesising zirconium derivates is to use an alkali metal siloxide. The dimeric structure, $[Zr_2(OSiPh_3)_6(OH)_2(H_2O)_2]\cdot C_7H_8$ was synthesised from Ph_3SiOLi in THF with NEt_3 and H_2O and is shown in Scheme 1.28. After work–up, X–ray quality crystals were grown from a solution of *n*–hexane. Analysis of the data showed the average Zr–O bond was 1.964(8) Å whilst the average Si–O bond is 1.618(1) Å, both well within the range of values found in similar complexes.[69]

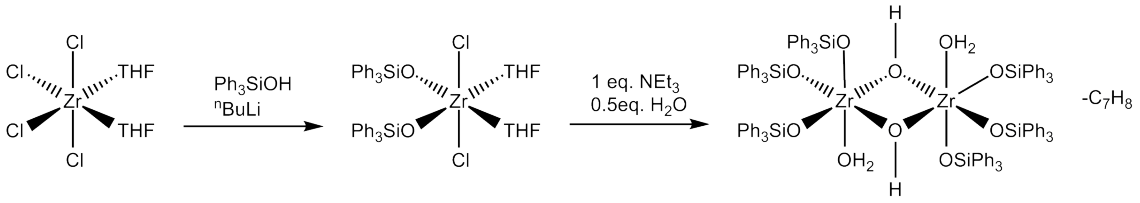

Scheme 1.28: Synthesis of the dimeric Zr^{IV} complex, $[Zr_2(OSiPh_3)_6(OH)_2(H_2O)_2]\cdot C_7H_8$

As shown in Scheme 1.23, the starting material $ZrCl_4(THF)_2$ was reacted with two equivalents of Ph_3SiOLi to give $[(Ph_3SiO)_2ZrCl_2(THF)_2](tol)_2$ and recrystallised from toluene. By omitting THF, the starting material $ZrCl_4$ reacted with two equivalents of Ph_3SiOLi, forming the highly toluene soluble product, $[(Ph_3SiO)_2ZrCl_2]_n$.

$[(Ph_3SiO)_2ZrCl_2(THF)_2](tol)_2$ reacted further with the chelate ligands, *N,N,N',N'* –tetra–methylethylenediamine (tmen), 2,2'–bipyridine (bpy) or 1,2–bis(diphenylphosphino)ethane

(diphos) in THF which led to ligand substitution and resulted in three different products, $[(Ph_3SiO)_2ZrCl_2(tmen)](tol)_n$, $[(Ph_3SiO)_2ZrCl_2(bpy)](tol)_n$ and $[(Ph_3SiO)_2ZrCl_2(diphos)](tol)_n$. The same starting material could also be reacted with MeLi in the presence of 2,2–bipyridine to form the complex, $[(Ph_3SiO)_2Zr(CH_3)_2(bpy)](tol)_2$. Finally, by varying the amount of Ph_3SiOLi in THF/toluene, $(Ph_3SiO)_3ZrCl_2(THF)](tol)_{0.5}$ and $[(Ph_3SiO)_2ZrCl_2(THF)]_2$ were synthesised respectively from $ZrCl_4(THF)_2$. Unfortunately aspects of the data were not reported but the data that was reported on is summarised in Table 1.2.[63]

Finally, $ZrCl_4$ was reacted with Ph_3SiONa in DME to synthesise $(DME)ZrCl_2(OSiPh_3)_2$ which was recrystallised from a solution of toluene. The X–ray diffraction analysis showed a Zr–O bond length of 1.911 Å and a Si–O bond length of 1.652 Å.[70]

Zirconium Compound	Oxidation State	Si–O Bond Length	Zr–O Bond Length
$[(\eta^7-C_7H_7)Zr(OSiPh_3)]_2$ [68]	III	—	2.215(3) Å
$[Zr_2(C_{18}H_{15}OSi)_6(OH)_2(H_2O)_2] \cdot C_7H_8$ [69]	IV	1.618(1) Å	1.964(8) Å
$Cp_2ZrCl(OSiPh_3)$ [58]	IV	—	1.961(6) Å
$Cp_2Zr(OSiPh_3)(\mu-H)_2BC_8H_{14})$ [58]	IV	1.614(3) Å	1.985(3) Å
$Cp^{"}(Ph_3SiO)_2ZrCl$ [60]	IV	—	1.925(5) Å
$Cp^{"}(Ph_3SiO)Zr(CH_2Ph)_2$ [60]	IV	—	—
$Cp^{"}(Ph_3SiO)_2Zr(CH_2Ph)$ [60]	IV	—	—
$[(Ph_3SiO)_2ZrCl_2(THF)_2](tol)_2$ [63]	IV	1.634(2) Å	1.928(2) Å
$[(Ph_3SiO)_2ZrCl_2]$ [63]	IV	—	—
$[(Ph_3SiO)_2ZrCl_2(tmen)](tol)_n$ [63]	IV	—	—
$[(Ph_3SiO)_2ZrCl_2(diphos)](tol)_n$ [63]	IV	—	—
$[(Ph_3SiO)_2ZrCl_2(bpy)](tol)_n$ [63]	IV	—	—
$[(Ph_3SiO)_2Zr(CH_3)_2(bpy)(tol)_2$ [63]	IV	1.626(3) Å	1.959(3) Å
$(Ph_3SiO)_3ZrCl_2(THF)](tol)_{0.5}$ [63]	IV	—	—
$[(Ph_3SiO)_2ZrCl_2(THF)]_2$ [63]	IV	1.646(2) Å	1.928(4) Å
$Cp_2Zr(OSiPh_3)_2$ [70]	IV	—	—
$(DME)ZrCl_2(OSiPh_3)_2$ [70]	IV	1.652 Å	1.911 Å
Average Bond Length	IV	—	2.215(3) Å
Average Bond Length	IV	1.631(8) Å	1.94(5) Å

Table 1.2: Summary of key bond lengths found in examples of zirconium triphenylsiloxides

1.3.5 Hafnium

As summarised in Table 1.3 the number of hafnium examples utilising triphenylsiloxide as a ligand is significantly less than the previous group 4 transition metals, titanium and zirconium.

Cyclopentadienyl derivatives as anchors

As shown in Scheme 1.18 the compound $Cp_2HfCl(OSiPh_3)$ was synthesised from the starting material $CpHfCl_2$ and one equivalent of Ph_3SiOH in the presence of piperidine. The Hf–O bond is 1.934(5) Å using X–ray diffraction analysis. Further reaction with $K[H_2BC_8H_{14}]$ afforded the metallocene $Cp_2Hf(OSiPh_3)(\mu-H)_2BC_8H_{14})$. The Hf–O bond length is 1.993(4) Å and the Si–O bond length is 1.608(4) Å.[58]

Other ligand systems

Similarly to the other group IV metals discussed and shown in Scheme 1.23, alkali metal siloxides can be used to synthesise hafnium triphenylsiloxide derivatives. The convenient starting material, $HfCl_4$ was reacted with Ph_3SiOLi at 0°C to synthesise the complex, $[(Ph_3SiO)_2HfCl_2(THF)_2](tol)_2$. The H–O bond length was observed by X–ray diffraction analysis at 1.929(2) Å whilst the Si–O bond length is 1.623(2) Å.[63]

Hafnium Compound	Oxidation State	Si–O Bond Length	Hf–O Bond Length
$Cp_2HfCl(OSiPh_3)$[58]	IV	—	1.934 Å
$Cp_2Hf(OSiPh_3)(\mu-H)_2BC_8H_{14})$[58]	IV	1.608(4) Å	1.993(4) Å
$[(Ph_3SiO)_2HfCl_2(THF)_2](tol)_2$[63]	IV	1.623(2) Å	1.929(2) Å
Average Bond Length	IV	1.615(8) Å	1.952(2) Å

Table 1.3: Summary of key bond lengths found in examples of hafnium triphenylsiloxides

1.3.6 Tris *tert*–butoxy siloxide as a molecular surface mimic

Tris *tert*–butoxy siloxides have long been used as surface models on transition metals and lanthanide systems, but until recently, actinide complexes of this nature were unknown.

The following analysis provides an insight into the usefulness of the ligand tris *tert*–butoxy siloxide as a model system for a variety of surface support materials.

1.3.7 Lanthanides

One of the first lanthanide *tert*–butoxy siloxide species was prepared specifically for the purpose of mimicking the surface material, MCM–48. [Ln(OSi(O^{t}Bu)$_3$)(AlMe$_4$)$_2$·(AlMe$_3$)] (Scheme 1.29) was characterised fully and revealed a 7 coordinate lanthanide cation with two asymmetrically η^2–coordinating tetramethylaluminium ligands, one asymmetrically η^2–coordinating siloxide ligands and one methyl group of a trimethylaluminate donor to give a distorted pentagonal bipyramidal geometry. The complex was prepared with both lanthanum and neodymium. The neodymium complex activated with Et$_2$AlCl produced *cis*–1,4–polyisopropene in variable yields. Importantly though, this work influenced research into several more lanthanide based siloxide complexes.[71]

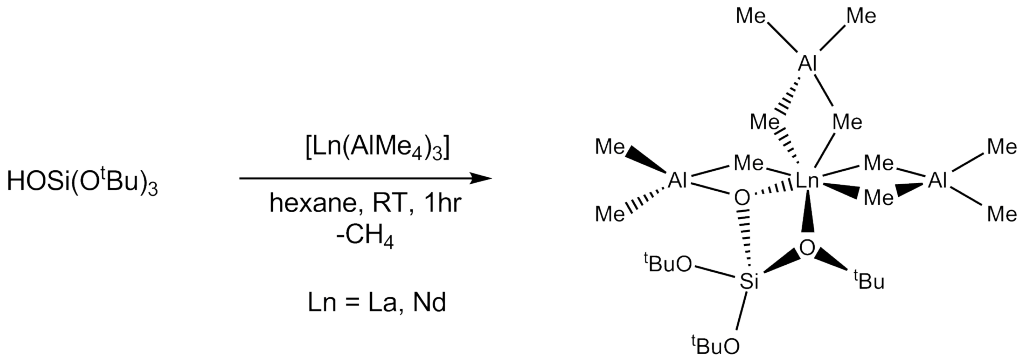

Scheme 1.29: Synthesis of [Ln(OSi(O^{t}Bu)$_3$)(AlMe$_4$)$_2$·(AlMe$_3$)]

A library of samarium complexes were reported using mixed ligand systems with cyclopentadienyl and siloxides and are shown in Figure 1.7. (Cp$*$)$_2$Sm(THF)$_2$ was reacted with 1.5 equivalents of (^{t}BuO)$_3$SiOH to form the unsymmetrical binuclear Sm(II) complex, [(Cp$\cdot$)Sm($\mu-$OSi(O^{t}Bu)$_3$)$_3$Sm. This was then treated with a variety of reagents to give a number of different samarium examples. One of the complexes synthesised,

$[(({}^t\mathrm{BuO})_3\mathrm{SiO})_3\mathrm{Sm}-(\mathrm{Cp}\cdot)\mathrm{Sm}(\mu-\mathrm{OSi}(\mathrm{O}{}^t\mathrm{Bu})_3)_3\mathrm{Sm}]$ is an inverse sandwich complex which is similar to a complex synthesised and characterised as part of this work and examined in section 4.2.[56]

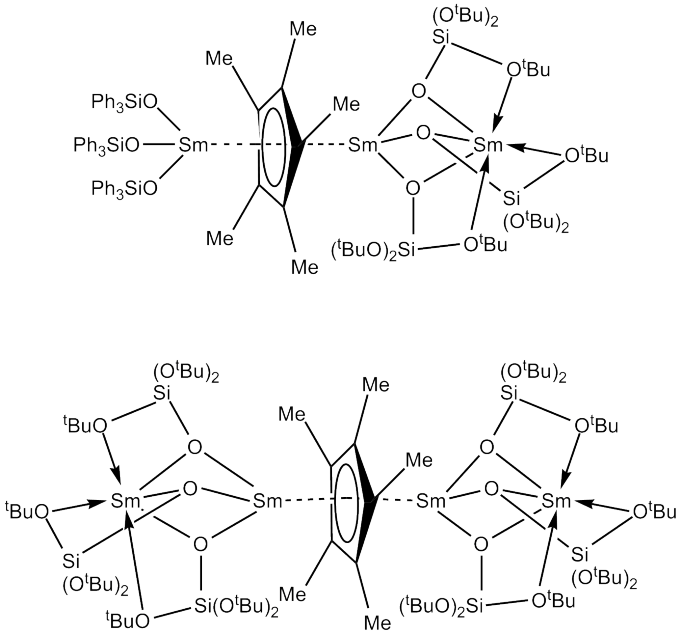

Figure 1.7: Binuclear samarium siloxide complexes synthesised from $(\mathrm{Cp}\cdot)_2\mathrm{Sm}(\mathrm{THF})_2$ and $({}^t\mathrm{BuO})_3\mathrm{SiOH}$

Protonolysis of the tris alkyl complex $[\mathrm{Ln}(\mathrm{CH_2SiMe_3})_3(\mathrm{THF})_2]$ (Ln = Y, Tb, Lu) with tris *tert*–butoxy silanol gave the complexes $[\mathrm{Ln}(\mu,\eta^2-\mathrm{OSi}(\mathrm{O}{}^t\mathrm{Bu})_3)(\mathrm{CH_2SiMe_3})_2]_2$ which were characterised by X–ray diffraction. Scheme 1.30 shows the subsequent reactions that were possible with these complexes.

Heteroleptic siloxide complexes $\mathrm{Ln}(\mathrm{OSi}(\mathrm{O}{}^t\mathrm{Bu})_3)(\mathrm{AlMe_3})(\mathrm{AlMe_4})_2]$ (Ln = Ce, Pr, Nd) were synthesised by methane elimination from $[\mathrm{Ln}(\mathrm{AlMe_4})_3]$ when reacted with one equivalent of tris *tert* butoxy silanol. They were then used further as precatalysts in isoprene polymerisation.[72] $(\eta^5-\mathrm{PC_4Me_2R_2})\mathrm{Nd}(\mathrm{AlMe_4})_2$ (R = Me, $\mathrm{SiMe_3}$) was also reacted with $({}^t\mathrm{BuO})_3\mathrm{SiOH}$ resulting in $(\eta^5-\mathrm{PC_4Me_2R_2})\mathrm{Nd}[\mathrm{OSi}(\mathrm{O}{}^t\mathrm{Bu})_3](\mathrm{AlMe_4})_2(\mathrm{AlMe_3})$ which was used as a model for surface experiments on mesoporous SBA–15 and methane elimination.[73]

$\mathrm{Ln}[(\mu-\mathrm{OSi}(\mathrm{O}{}^t\mathrm{Bu})_3(\mu-\mathrm{R})(\mathrm{AlR_2}]_2$ (Ln = Yb, Sm; R = Et; Ln = Yb; R = Me) have been de-

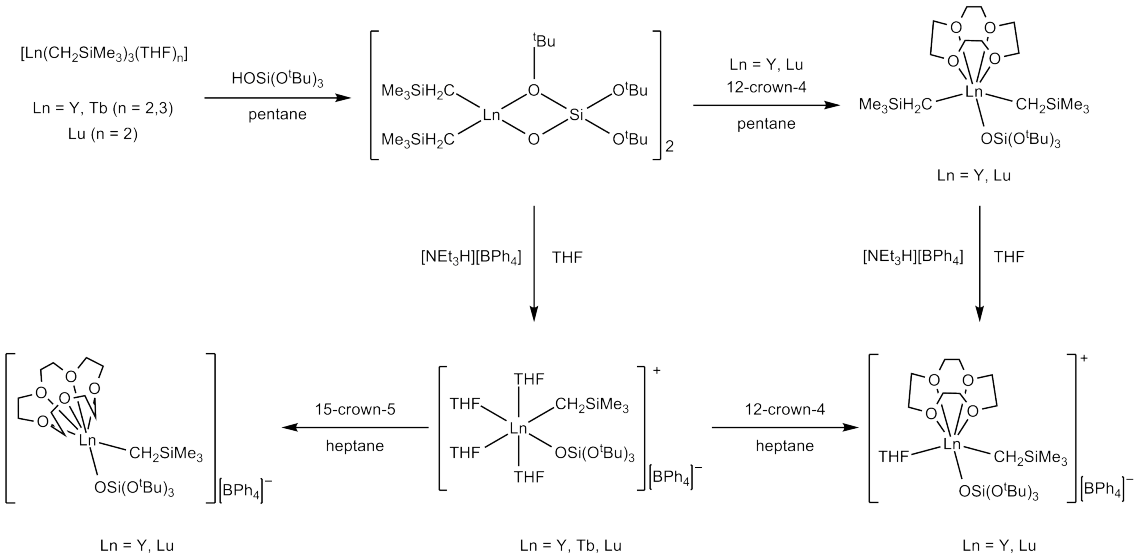

Scheme 1.30: Neutral and cationic lanthanide siloxide complexes synthesised using tris *tert* butoxy silanol

veloped by reacting $[Ln(AlEt_4)_2]_n$ (Ln = Sm, Yb) with one equivalent of $(^tBuO)_3SiOH$. The complexes were then used as molecular model complexes for the mesoporous silica KIT–6. The work introduced the concept of Surface OrganoLanthanide Chemistry (SOLnC) (see section 1.2.2 for analysis of SOMC) and the models synthesised provided evidence of alkane elimination, trialkylaluminium adduct formation and $Ln^{II}O$(siloxane) bonding.[74]

1.3.8 Transition metals

Transition metals furnished with $(^tBuO)_3SiO^-$ are widely known and Figure 1.8 shows one of the first titanium species, $(OPy)_2Ti(OSi(O^tBu)_3)$ (where Py = 2–pyridylcarbinol). By reacting $Ti(O^iPr)_4$ with PyOH the compound, $(OPy)_2Ti(O^iPr)_2$ was isolated and then further reacted with tris *tert*–butoxy silanol in order to synthesise the desired product. Structural characterisation data were published and the observed Ti–O bond was found to be 1.84 Å.[66]

A second titanium species, $[Cp \cdot 2\,Ti(OSi(O^tBu)_3)]$ shown in Scheme 1.31 was synthesised by protonolysis of the titanium–methylene bond in a singly tucked–in permethylti-

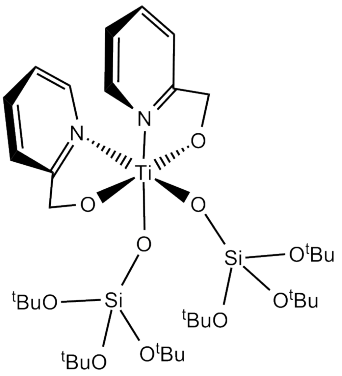

Figure 1.8: One of the first titanium species furnished with the tris *tert*–butoxy siloxide ligand, $(OPy)_2Ti(OSi(O^tBu)_3)$

tanocene [Cp · Ti(η^5:η^1- $C_5Me_4CH_2$)] with tris *tert*–butoxy silanol. Characterisation data were reported and the Ti–O bond lengths were found to be 1.9244(9) Å and TiO–Si bond lengths were observed at 1.6032(9) Å. In addition IR data showed an intense absorption band at 1025 cm^{-1}.[61]

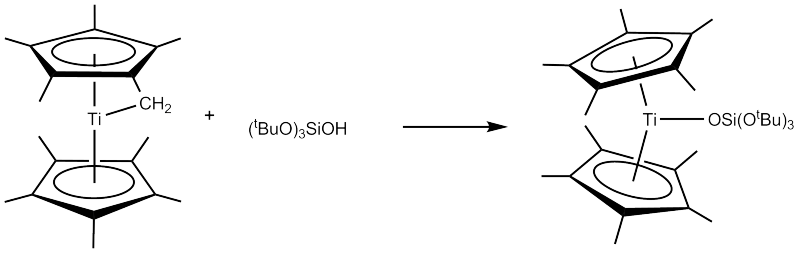

Scheme 1.31: [Cp · 2 Ti($OSi(O^tBu)_3$)], synthesised by protonolysis of the titanium–methylene bond in a singly tucked–in permethyltitanocene

Several zirconium species have also been developed using the tris *tert*–butoxy siloxide ligand and are shown in Scheme 1.32. $[Zr(OPr^i)_3(OSi(O^tBu)_3)]$ and $[Zr(OPr^i)_2(OSi(O^tBu)_3)_2]$ were first synthesised by adding one or two equivalents of tris *tert*–butoxy silanol to $[Zr(OPr^i)_4] \cdot Pr^iOH$. These complexes were further treated with 1.1 equivalents of ethane–1,2–diol to form $[Zr(O(CH_2)_2O)(OSi(O^tBu)_3)_2]$ and $[Zr(OPr^i)(O(CH_2)_2O)(OSi(O^tBu)_3)]$ respectively. The structural characterisation data of $[Ti(OPr^i)_2(OSi(O^tBu)_3)_2]$ were published which reported an observed Ti–O bond length of 1.734(2) Å to 1.810(2) Å. Unfortunately no other X–ray diffraction data were published.[75]

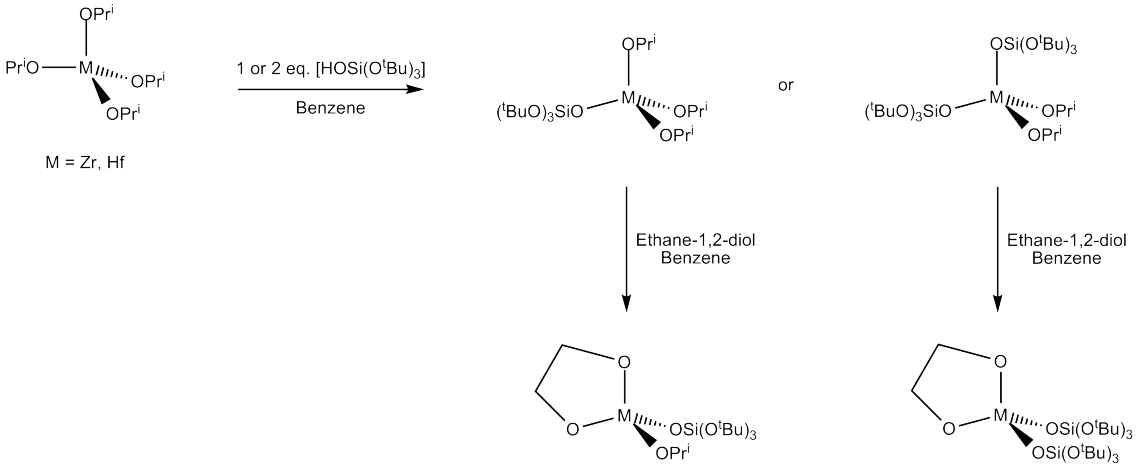

Scheme 1.32: Zirconia–silica mixed oxides developed as a possible catalytic support

Scheme 1.33 shows the synthesis of the complex M[OSi(O^{t}Bu)$_3$]$_4$ (M = Zr, Hf) using the addition of *tert*–butoxy silanol to a cold solution of M(NEt$_2$)$_4$. X–ray diffraction quality single crystals were grown and the data reported shows a Zr–O and Hf–O bond length of 1.979(2) Å and 1.961(8) Å respectively.[76] Hydrolysis of these complexes with careful addition of one or two equivalents of H_2O resulted in the products, M[OSi(O^{t}Bu)$_3$]$_4$(H_2O) and M[OSi(O^{t}Bu)$_3$]$_4$(H_2O)$_2$. Only X–ray diffraction data of Hf[OSi(O^{t}Bu)$_3$]$_4$(H_2O) were published and reported Hf–O bond distance of 1.941(4) Å and O–Si bond distances of 1.588(6) Å.[77]

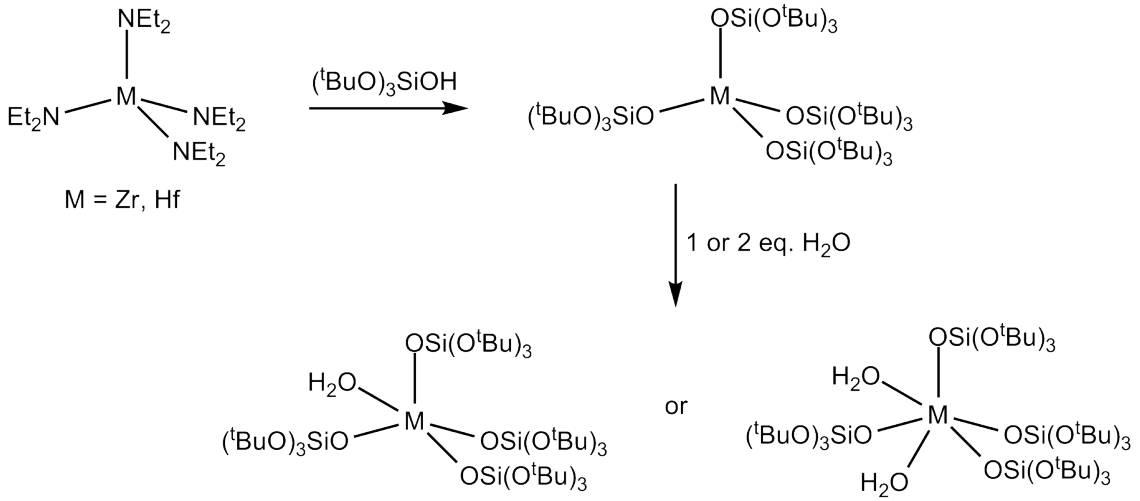

Scheme 1.33: Synthesis and hydrolysis of M[OSi(O^{t}Bu)$_3$]$_4$

Chapter 2

Synthesis and characterisation of $K[(Ph_3SiO)_5U]$ and its derivatives

An important factor in small molecule activation studies is the electronic and steric availability of the metal centre. Most small molecule activation takes place via coordination followed by some type of electronic change either through electron transfer from the metal to the small molecule or by a formally oxidative insertion of the metal centre into an available bond in the small molecule. Additionally, these steps may be sequential or concerted. The steric requirement can be set by using bulky ligands which provide steric protection to the metal centre. In order to achieve this, it is important that the ligands selected sterically saturate the metal centre whilst ensuring it remains coordinatively and electronically unsaturated. This can present problems if the ligands pack together so tightly they impede the path of a small molecule intended to react with the metal centre.

Steric bulk can be quantified in terms of Tolman cone angles or visualised using space filling models. Both systems provide useful information of how sterics can play a role in the reactivity of a system. For example, the Tolman cone angle of a methyl ligand (based

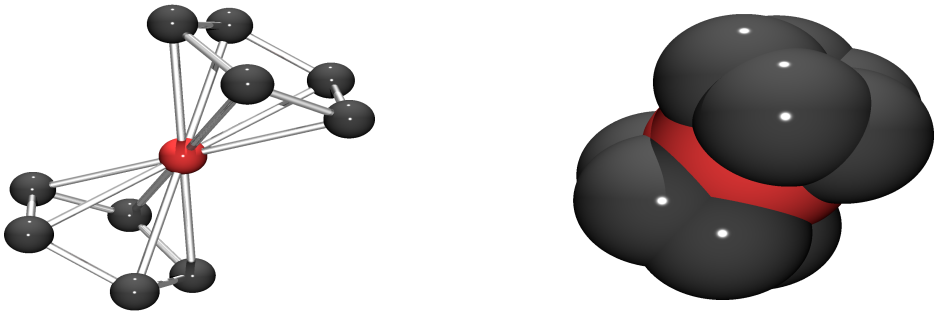

Figure 2.1: (left) Molecular structure of ferrocene using the ball and stick model; (right) Molecular structure of ferrocene using the space filling model; (Hydrogen atoms omitted from both for clarity)

on a metal covalent radius of 1.32 Å) is calculated to be 90° whilst the cone angles for ethyl, phenyl and *tert*–butyl are 102°, 105° and 126° respectively.[78] This information can be used to manipulate ligand systems in order to increase or decrease the protection provided to the metal centre.

Space filling models are three dimensional molecular models where atoms are represented by spheres. The individual spheres are proportional to the radii of the atoms which they represent. In addition the distances between the atoms are proportional to the distances between the atomic nuclei. The model provides a clear and concise method of assessing steric bulk which can otherwise be difficult. Figure 2.1 provides an example: ferrocene is a typical sandwich complex and the space filled model provides insight into the steric protection provided by the cyclopentadienyl rings and the available access to the iron atom in the equatorial region of the molecule.

The work reported here attempts to synthesise a sterically protected complex with the aim to catalytically transform small molecules, specifically carbon oxides. In this Chapter, investigations into different siloxide ligands are discussed along with the discovery and characterisation of $K[U(OSiPh_3)_5]$ and its derivatives.

2.1 Synthesis of siloxide transfer reagents

2.1.1 Synthesis of silanols

Due to the high cost of most siloxides, it was deemed appropriate to synthesise them rather than buy them. The literature provides little clue as to the best method to use with some methods too dangerous to consider, for example one method uses large amounts of ^{t}BuLi to be reacted with SiF_4 followed by base hydrolysis.[79] However, analysis of the desired products and the availability of low cost starting materials provided three main synthetic methods to trial, Grignard, metal–halogen exchange and ortho lithiation. Figure 2.2 shows the starting materials used for each R_3SiOH derivative attempted.

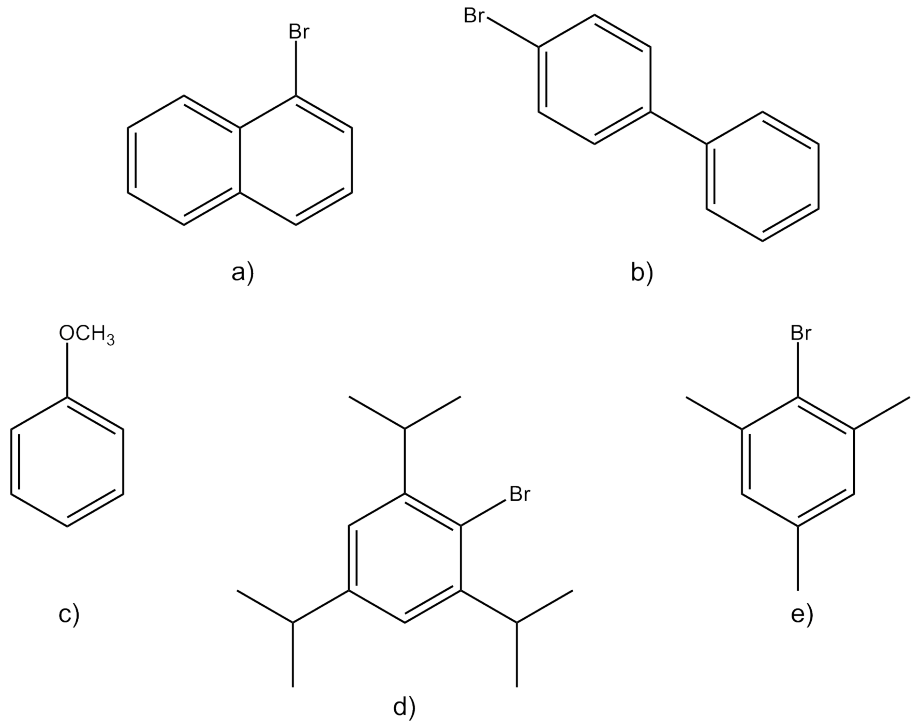

Figure 2.2: Starting materials for the synthesis of a variety of silanols a) 1–Bromonaphthalene b) 4–Bromobiphenyl c) Methoxybenzene (anisole) d) 1–Bromo–2,4,6–triisopropylbenzene e) 2–Bromomesitylene

The starting materials were used in an attempt to synthesise five different silanols, *tri*–(1–naphthyl) silanol, *tri*–(4–biphenyl) silanol, *tri*–(1–anisyl) silanol, *tri*–(2,4,6–triisopropylbenzene) silanol and *tri*–(2–mesitylene) silanol respectively. Of the three synthetic methods em-

ployed, metal–halogen exchange and ortho lithiation provided more satisfactory results. Despite some success, separation and purification of the products proved difficult with mass spectrometry analysis showing a mixture of *mono*, *bis*, *tris* and *tetra* products. Some of these experiments were conducted or repeated by students under the authors supervision as indicated in Table 2.1.

Starting Material	Synthetic Method	Identified Product(s)	Experimental
1–Bromonaphthalene	Grignard	tri(naphthyl)silanol	[80]
		binaphthalene	
	M–X exchange	intractable	[81]
4–Bromobiphenyl	Grignard	intractable	[81]
	M–X exchange	di(4–biphenyl)disilanol	[80]
Methoxybenzene (anisole)	Ortho lithiation	tri(anisyl)silanol	[80,81]
		di(1–anisole)disilanol	
1–Bromo–2,4,6–triisopropylbenzene	M–X exchange	intractable	author
2–Bromomesitylene	M–X exchange	intractable	author

Table 2.1: An overview of the experiments attempted in order to synthesise silanols with a summary of results

tri–(1–naphthyl)silanol

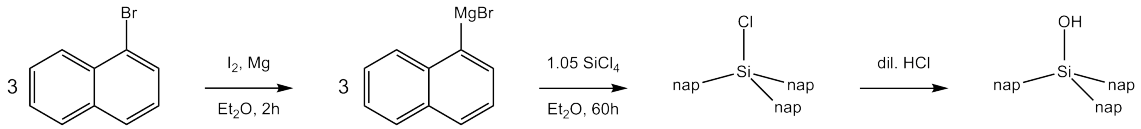

Scheme 2.1: Synthesis of *tri*–(1–naphthyl)silanol using Grignard methods

Some success was achieved in the synthesis of *tri*–(1–naphthyl)silanol by reacting the Grignard reagent $C_{10}H_7MgBr$ with the starting material and using $SiCl_4$ as the source of silicon. Mass spectrometry and ^1H NMR are used to analysise the resulting products and alongside the desired *tri*–(1–naphthyl)silanol (m/z = 426) the formation of binaphthalene

is found (m/z = 254). Concentration levels were then increased and the product *tetra*–(1–naphthyl)silane is observed (m/z = 536).[80]

tri–(4–biphenyl)silanol

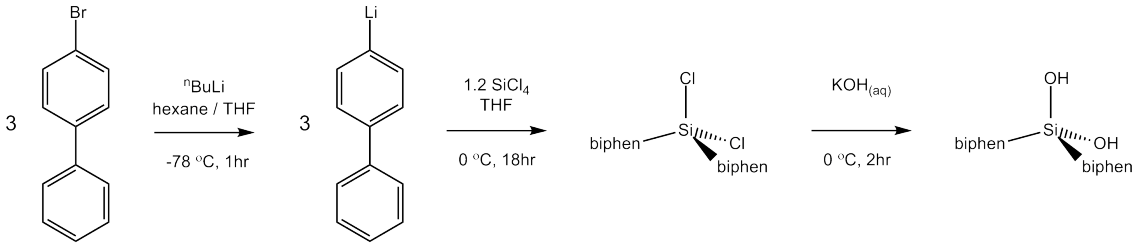

Scheme 2.2: Synthesis of *tri*–(4–biphenyl)silanol using metal–halogen exchange

Using metal–halogen exchange, the synthesis of *tri*–(4–biphenyl)silanol was attempted with little success. However the product, *di*–(4–biphenyl)disilanol is observed by ^{1}H NMR and mass spectrometry (m/z = 368). Unfortunately the NMR spectra showed overlapping signals and full assignment is not achieved. The starting material, 4–bromobiphenyl is identified in the spectrum and there is a clear shift towards the product. The reaction overall was unreliable and provided low yields and purity and therefore not pursued further.[80]

tri–(1–anisyl)silanol

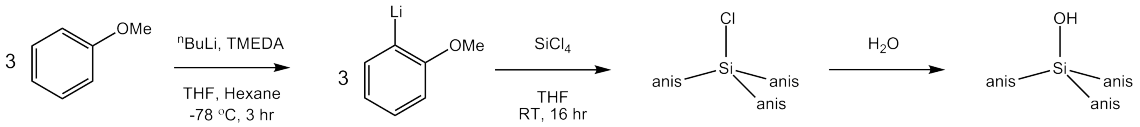

Scheme 2.3: Synthesis of *tri*–(1–anisole)silanol using ortho lithiation

In order to synthesise the desired product, anisole was reacted with ^{n}BuLi in the presence of TMEDA and then the resulting anisyl–lithium, was reacted in slight excess with $SiCl_4$. Mass spectrometry indicated the presence of the desired product (m/z = 349) alongside

di–(1–anisyl)disilanol (m/z = 276). The desired product is also observed by ^{1}H NMR. It is possible that the lithiation step did not go to completion, resulting in a mixture of final products.[80]

tri–(2,4,6–triisopropylbenzene)silanol and *tri*–(2–mesitylene)silanol

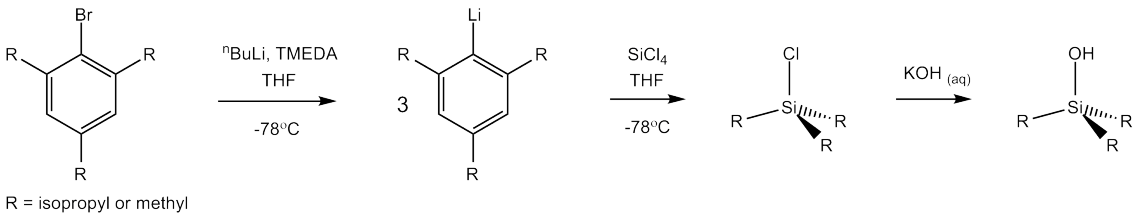

Scheme 2.4: Synthesis of *tri*–(2,4,6–triisopropylbenzene)silanol and *tri*–(2–mesitylene)silanol using ortho lithiation

The same ortho lithiation reaction was used to synthesise *tri*–(2,4,6–triisopropylbenzene) silanol and *tri*–(2–mesitylene) silanol. The experiment was conducted at -78 °C in order to slow the rate of the lithiation reaction. The lithiated product was then reacted slowly with $SiCl_4$ at -78 °C

In both cases the mass spectrometry results show a lack of *mono*, *bis*, *tris* or even *tetra* products with the ^{1}H NMR confirming the unsuccessful results. The silanes were also tested via mass spectrometry prior to reaction with KOH and the expected products are not identified at this stage suggesting either the lithiation process failed or as the lithiation synthesis has previously proved successful, it is possible the steric bulk of the ligand systems were to great to pack around the relatively small silicon atom.

2.1.2 Characterisation of silanols

Characterisation of Ph_3SiOH

Triphenylsilanol (98%) was purchased from Sigma Aldrich. Literature reports of spectroscopic data for this material are scarce and therefore, NMR spectroscopy analyses were undertaken.

For the parent silanol, the ^{1}H and $^{13}C\{H\}$ NMR spectra are unexceptional and show the standard splitting pattern associated with a mono–substituted phenyl group and are found to be in line with literature values that are available.[82]. The resonances for both nuclei are collated in Section 7.6.

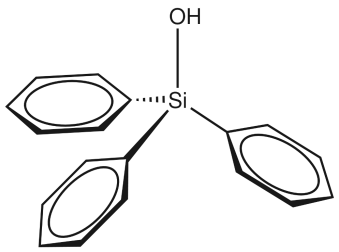

Figure 2.3: Triphenylsilanol

Four resonances are observed in the $^{13}C\{H\}$ NMR spectrum at δ 136.91, 134.76, 129.21 and 127.31 ppm and are assigned as *ipso*, *ortho*, *para* and *meta* respectively. In addition, three resonances are also observed in the ^{1}H NMR spectrum at δ 7.62–7.60, 7.37–7.29 (multiplet) and 6.02 ppm which, in conjunction with the HSQC and HMBC data (Appendices B.7 and B.8) and the proton integration values, are assigned as *ortho*, *meta/para* and Si−**OH** respectively. The resonance observed at δ 6.02 ppm is assigned to the proton bound to the oxygen as there are no resonances correlating to a ^{13}C environment in the HSQC spectrum. Finally the ^{29}Si NMR spectroscopy data shows the expected single silicon environment at δ -17 ppm.

In the solid state, triphenylsilanol has been reported as a tetrameric unit with the four oxygen atoms arranged in a slightly distorted (non planar) square with O–O distances on the edges of the square in the range of 2.637–2.684 Å which is suggestive of hydrogen bonding. The two diagonals across the square show O–O distances in the range of 3.42–3.61 Å. X–ray diffraction data of triphenylsilanol is consistent across the literature. The average Si–O bond is found to be 1.644 Å.[83] [84] The average Si–Ph bond is 1.875 Å and the average O–H bond is 0.852 Å, finally the average length from the silicon atom to the hydrogen atom is 2.121 Å.[85]

Solid state ^{29}Si CPMAS NMR spectroscopy data were reported and showed eight crystallographically inequivalent Si sites being observed and fully resolved at 363K. These eight silicon environments refer to the four sites shown in the 'clockwise' arrangement and another four silicon sites in a second, 'anticlockwise' arrangement both shown in Figure 2.4.[86]

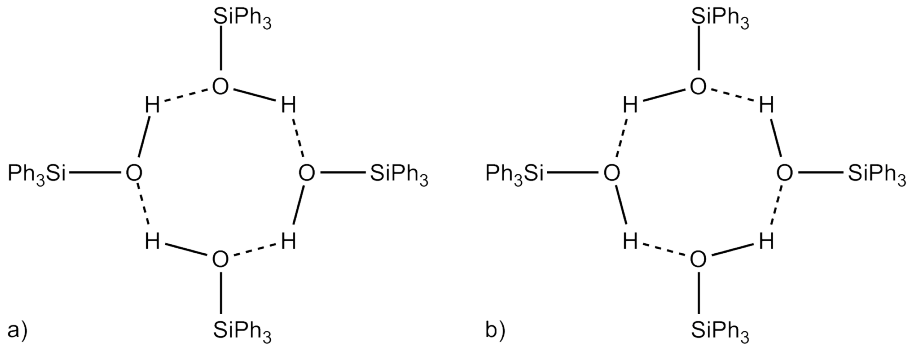

Figure 2.4: Solid State Triphenylsilanol Tetrameric Unit a) clockwise b) anticlockwise

The IR spectrum of triphenylsilanol in the solid state shows two distinct absorbances at 3068 cm^{-1} and 3270 cm^{-1}. Comparing these data with other silanols[27] the broad peak is likely to correlate with the hydrogen bonded Si–OH group, whilst the sharp peak is assigned to the free Si–OH group.

Characterisation of (^{t}BuO)$_3$SiOH

Tris *tert*–butoxy silanol (99.999%) was purchased from Sigma Aldrich and the structure is shown in Figure 2.5 . Literature reports of spectroscopic data for this material are much more widely available than of the previously discussed Ph_3SiOH. However, spectroscopic analysis was undertaken in order to ascertain the purchased material was clean and dry before use.

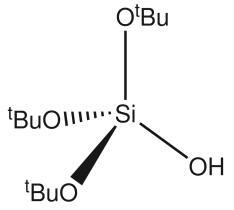

Figure 2.5: Tris *tert*–butoxy silanol

For the parent silanol, the ^{1}H and ^{13}C$\{$H$\}$ NMR spectra are unexceptional. The resonances for both nuclei are shown in Section 7.24 along with the respective assignments.

Two resonances are observed in the ^{13}C$\{$H$\}$ NMR spectrum at δ 72.77 and 31.99 ppm. This is in line with published data which reported two resonances in the ^{13}C$\{$H$\}$ spectrum at δ 73.0 and 31.2 ppm ($CDCl_3$) and are assigned to $((CH_3)_3\mathbf{C}O)_3SiOH$ and $((\mathbf{C}H_3)_3CO)_3SiOH$ respectively.[87]

Two resonances are also observed in the ^{1}H NMR spectrum at δ 5.25 and 1.30 ppm and in conjunction with HMBC NMR spectroscopy data (Appendix E.3), the resonances are assigned as $((CH_3)_3CO)_3SiO\mathbf{H}$ and $((C\mathbf{H}_3)_3CO)_3SiOH$ respectively. These data correlate well with the ^{1}H NMR spectroscopy literature values which reported the resonance at δ 1.32 ppm (in $CDCl_3$) to be $((C\mathbf{H}_3)_3CO)_3SiOH$.[87]

In the solid state the silicon atom in tris *tert*–butoxy silanol is observed to be in a distorted tetrahedral geometry and hydrogen bonding is found between two silanol units form-

ing a dimeric unit as shown in Figure 2.6. The Si–O distances range from 1.605(2) to 1.635(2)Å with the longest Si–O bond distance due to the hydrogen bonding interaction with the neighbouring tris *tert*–butoxy silanol unit. The hydrogen bonding is reportedly also responsible for the narrow O–Si–O bond angle of 114.9(1)°.[87]

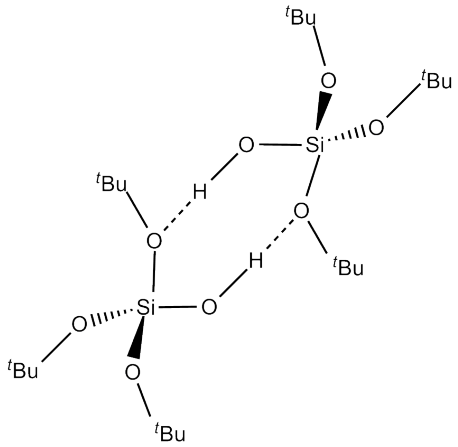

Figure 2.6: Solid State tris *tert*–butoxy silanol dimeric unit

2.1.3 Synthesis and characterisation of siloxides

Synthesis and characterisation of Ph_3SiOK

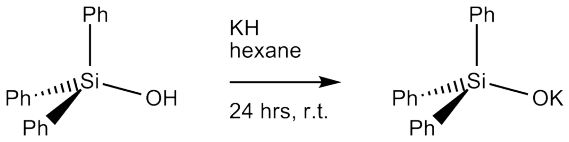

Scheme 2.5: Synthesis of PhSiOK

The elaboration of the uranium centre with siloxides required a siloxide transfer reagent. The most straight–forward route was salt metathesis given the acidity of the hydroxyl proton in triphenylsilanol (pKa 10.8),[88]. Variations of this method have been established in previous work on siloxides: $[Li(OSiPh_3)]_n$, $[K(THF)_{0.2}(OSiPh_3)]_n$ and $[K(OSiMe_2{}^tBu)]_n$ are prepared from the deprotonation of Ph_3SiOH or $^tBuMe_2SiOH$ with either ^nBuLi in hexane or KH in THF respectively which is the preferred method used in this work.[89] In

addition the siloxide, $NaOSi^tBu_3$ was prepared in 80–90% yields via reflux of $^tBu_3SiOH$ with sodium metal in hexanes.[34]

$^{13}C\{H\}$, ^1H, HSQC and HMBC NMR spectroscopy analysis of Ph_3SiOK was undertaken and resonances are in a similar pattern to the resonances observed previously for Ph_3SiOH (Section 2.1.2). The $^{13}C\{H\}$ resonances are observed at δ 145.77, 135.81, 128.54 and 128.27 ppm and assigned as *ipso*, *ortho*, *para* and *meta* respectively. The ^1H resonances are observed at δ 7.49 and 7.25–7.17 and are assigned as *ortho* and *meta/para* respectively. These data correlate well with the HSQC and HMBC data which are shown in Appendices B.11 and B.12.

Synthesis and characterisation of $(^tBuO)_3SiOK$

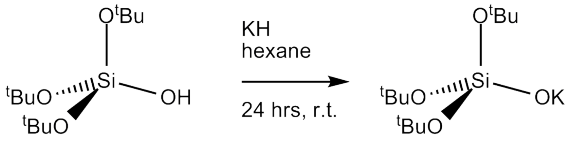

Scheme 2.6: Synthesis of $(^tBuO)_3SiOK$

In order to generate $(^tBuO)_3SiOK$, tris *tert*–butoxy silanol was treated in the same manner as the triphenylsilanol in section 2.1.3, from a modified literature procedure.[90] The product was analysed by $^{13}C\{H\}$, ^1H, HSQC and HMBC NMR spectroscopy. The $^{13}C\{H\}$ NMR spectrum showed two resonances at δ 71.07 and 32.83 ppm and are assigned in line with literature reports as $((CH_3)_3\mathbf{C}O)_3SiOK$ and $((\mathbf{C}H_3)_3CO)_3SiOK$ respectively. The ^1H spectrum showed the expected one resonance at δ 1.32 ppm and is assigned to $((C\mathbf{H}_3)_3CO)_3SiOH$. HSQC and HMBC data confirm this analysis and are shown in Appendices E.7 and E.8 respectively.

2.2 Synthesis and characterisation of $K[U(OSiPh_3)_5]$

There are only three known examples of triphenylsiloxides being used as a ligand system on a uranium metal centre, none of which were developed with the goal of mimicking surface supports.[91,92] Scheme 2.7 shows a U^{IV} complex synthesised by a protonolysis reaction between triphenylsilanol and $[Cp_3U(NEt_2)]$. X–ray diffraction analysis of the product, $[Cp_3U(OSiPh_3)]$, identified the U–O bond length as 2.135(8) Å, whilst the Si–O bond length is observed at 1.62(1) Å. The U–O–Si bond angle is observed as almost linear at 172.6(6)°.[91]

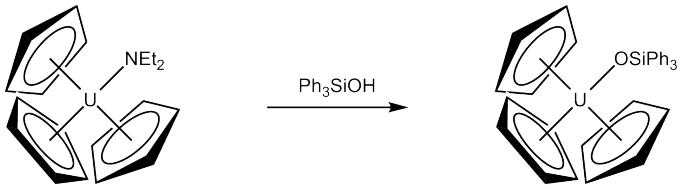

Scheme 2.7: Synthesis of $[Cp_3U(OSiPh_3)]$

Scheme 2.8 shows two further examples. The U^V complex is synthesised by adding one equivalent of $HSiPh_3$ to $(^{Ar}acnac)_2UO_2$ ($^{Ar}acnac$ = ArNC(Ph)CHC(Ph)O; Ar = 3,5-$^tBu_2C_6H_3$) in the presence of $B(C_6F_5)_3$. $U(OSiPh_3)(OB(C_6F_5)_3)(^{Ar}acnac)_2$ can then be reduced to U^{IV} by reacting it with Cp_2Co to form $[Cp_2Co][U(OSiPh_3)(OB(C_6F_5)_3)(^{Ar}acnac)_2$ in 78% yield. The U–O_{silox} bond length is observed at 2.034(9) Å for the U^V complex with the Si–O bond length observed at 1.666(9) Å. The reduced U^{IV} complex has a slightly longer U–O bond length of 2.173(8) Å and a Si–O bond length of 1.610(9) Å.[92]

The data summarised in Table 2.2 are consistent with each other. The U^{IV} complexes exhibit U–O bond distances of 2.16 Å average, whilst the Si–O bond length is 1.62 Å average. The U^V species possess shorter U–O bond lengths at 2.03 Å, whilst the Si–O bond length has marginally increased to 1.67 Å. The data implies a correlation between the oxidation state increasing and the U–O bond distance decreasing, however a much

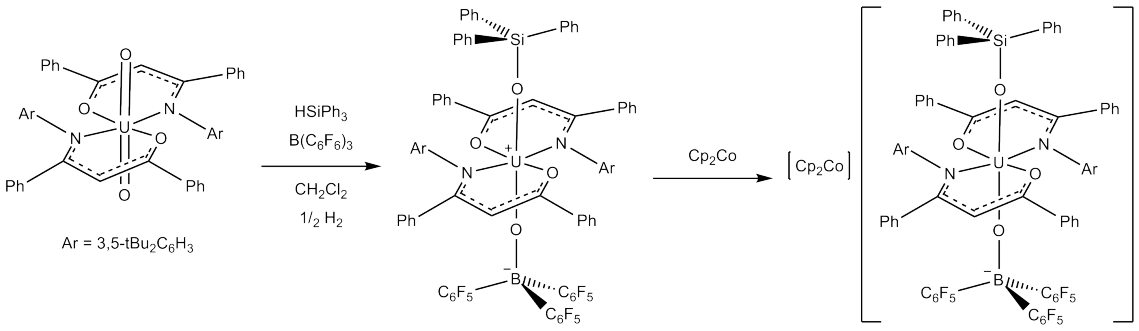

Scheme 2.8: Synthesis of $U(OSiPh_3)(OB(C_6F_5)_3)(^{Ar}acnac)_2$ and $[Cp_2Co][U(OSiPh_3)(OB(C_6F_5)_3)(^{Ar}acnac)_2]$

larger sample group is needed before this can be relied upon.

Compound	Oxidation State	U–O Bond Distance / Å	O–Si Bond Distance / Å
$[Cp_3U(OSiPh_3)]$[91]	IV	2.135(8)	1.62(1)
$[Cp_2Co][U(OSiPh_3)(OB(C_6F_5)_3)(^{Ar}acnac)_2$[92]	IV	2.173(8)	1.610(9)
$U(OSiPh_3)(OB(C_6F_5)_3)(^{Ar}acnac)_2$[92]	V	2.034(9)	1.666(9)

Table 2.2: Summary of key bond distances for uranium complexes with one or more triphenylsiloxy ligands

2.2.1 Synthesis of $K[U(OSiPh_3)_5]$

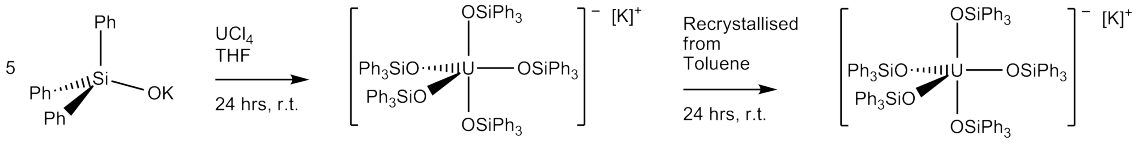

Scheme 2.9: Synthesis of $K[U(OSiPh_3)_5]$

In an attempt to synthesise $U(OSiPh_3)_3Cl$, uranium tetrachloride and three equivalents of Ph_3SiOK were added to THF at room temperature. The resulting products were intractable due to the formation of multiple produces *vide infra* in Section 2.4.2, however, when Ph_3SiOK was layered on UCl_4 in THF, a colour change was observed at the interface between the two layers. Other stoichiometries were therefore investigated which resulted in $K[U(OSiPh_3)_5]$ being synthesised by the following methods.

Treatment of a uranium tetrachloride in THF with five equivalents of Ph_3SiOK at room temperature with vigorous stirring resulted in a solution that quickly changed from dark green to turquoise to blue to lilac and pink. The product was extracted with toluene and the resulting product was recrystallised from toluene at room temperature. Large purple crystals, up to a centimetre across, of X–ray diffraction quality were prepared as shown in Figure 2.7.

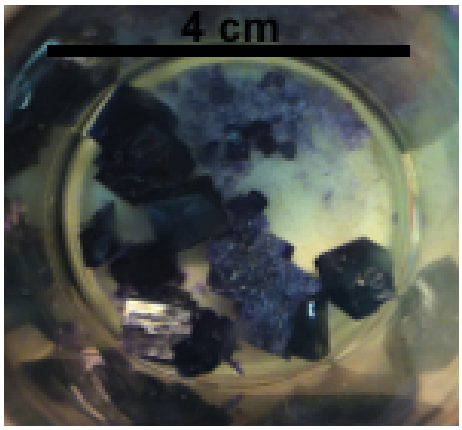

Figure 2.7: Photograph of crystallised $K[U(OSiPh_3)_5]$ measuring up to 1 cm in diameter

2.2.2 Characterisation of $K[U(OSiPh_3)_5]$: X–ray Diffraction

$K[U(OSiPh_3)_5]$ crystallises from toluene in the monoclinic space group P $2_1/n$ with an *R* factor of 4.51. The lattice parameters for this structure are *a* = 13.7420(2) Å, *b* = 26.867o(3) Å, *c* = 24.2270(2) Å, α = 90 °, β = 105.9140(10) °, γ = 90 °.

The molecular structure is shown in Figures 2.8 and 2.9. The uranium centre has a trigonal bipyramidal geometry consisting of five siloxy ligands with the potassium counterion, coordinated to three of the phenyl rings on three siloxy ligands in an η^3, η^3 and η^6 fashion and this distorts the geometry away from the standard trigonal bipyramidal. In addition, the potassium ion is coordinated to two of the oxygen atoms resulting in the lengthening of the respective U–O bonds, which are located *cis* to each other.

Comparing these experimental values to the complexes, $U(OSiPh_3)_xR_y$ in Table 2.2, it is clear that bond lengths for $K[U(OSiPh_3)_5]$ compare well to other U^{IV} $U(OSiPh_3)_xR_y$ species providing evidence of a U^{IV} complex.

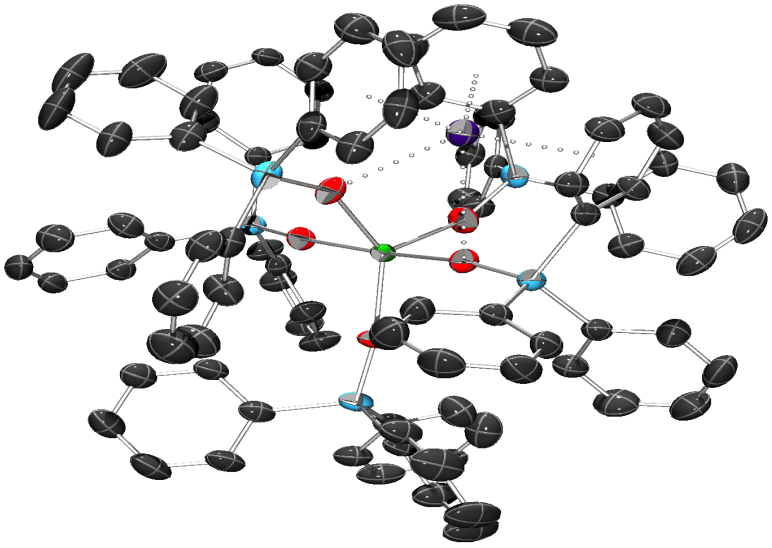

Figure 2.8: Molecular structure of $K[U(OSiPh_3)_5]$ (Hydrogen atoms omitted for clarity)

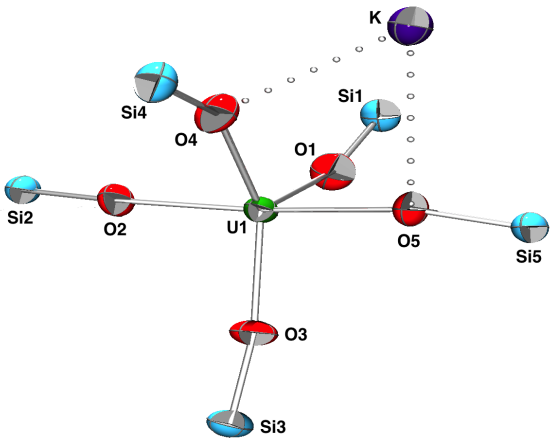

Figure 2.9: Core molecular structure of $K[U(OSiPh_3)_5]$ containing the Si, O U and K atoms (Hydrogen atoms and phenyl rings omitted for clarity)

Figures 2.10 and 2.11 show the full range of literature values for complexes of the general formula $U(OSiR_3)_xR'_y$(R, R' = alkyl, aryl) (blue) and experimental values for $K[U(OSiPh_3)_5]$ (red). The average literature bond length for **U–O**SiR_3 is 2.054 Å, the average bond length for U**O–Si**R_3 is 1.662 Å and the average bond length for UO**Si–R$_3$** is 1.858 Å.[85] Comparing these figures to the average experimental bond lengths for $K[U(OSiPh_3)_5]$ which

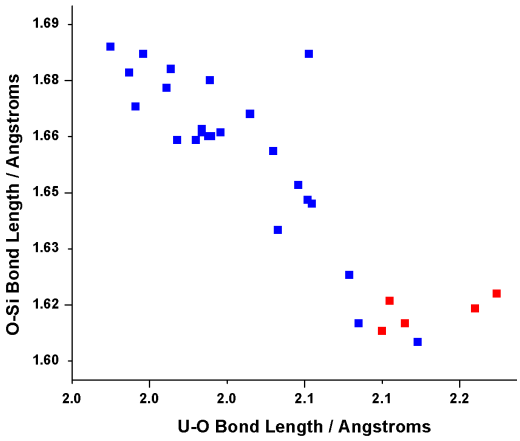

Figure 2.10: Correlation between U–O bond distances and O–Si for uranium compounds with the ligand R_3SiO. (Data points in red are the experimental values for $K[U(OSiPh_3)_5]$)

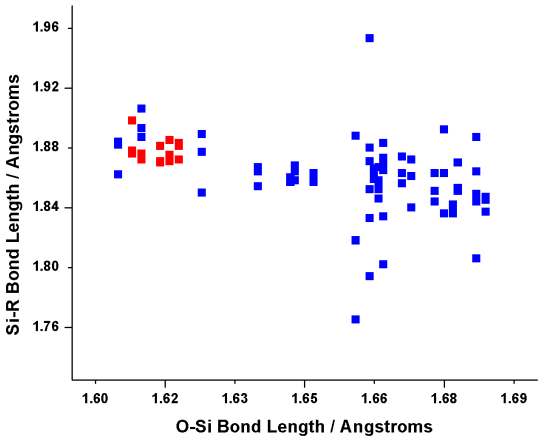

Figure 2.11: Correlation between O–Si bond distances and Si–R_3 for uranium compounds with the ligand R_3SiO. (Data points in red are the experimental values for $K[U(OSiPh_3)_5]$)

are observed at 2.181(2) Å for **U–O**$SiPh_3$, 1.617(2) Å for U**O–Si**Ph_3 and 1.879(3) Å for UO**Si–Ph$_3$** it is clear that the experimental values are within previously reported ranges.

Two of the U–O distances for $K[U(OSiPh_3)_5]$ shown in Figure 2.10 fall beyond the range of literature values in $U(OSiR_3)_xR'_y$ species. These two points refer to the two U–O bonds that are coordinated to the potassium counterion. In addition the two data points also relate to two of the shortest O–Si bonds with the molecule. The coordination with the electron deficient potassium counterion results in some of the oxygen's electron density being used in this coordination rather than the uranium or silicon bonding, weakening and lengthening the U–O bonds. In addition, by comparing these data directly against other $U(OSiPh_3)_xR_y$ compounds as shown in Table 2.2, it seems that longer U–O bond distances are expected when phenyl is used as the R group, presumably due to the large and rigid steric bulk.

In addition there is a distinct correlation between the lengthening of the U–O bond and the shortening of the O–Si bond. This same trend is observed in all group IV and early first

row transition metal siloxides.[85] However if the alkoxide group, M−−OCPh$_3$ is analysed, no correlation is observed between the M−−O bond and the O−−C bond suggesting that the pattern observed in the siloxides is driven by the sterics or electronics of the silicon atom.[85] An explanation for this observation lies with the fact that both uranium and silicon are oxophillic atoms. When the electronics or the sterics of the molecule change, weakening the U–O bond, the oxygen atom is more available to the silicon, thus reducing the O–Si bond length. Figures 2.12 and 2.13 also show a distinct correlation between the lengthening of the U–O bond and an overall lengthening of the intramolecular U–Si distance. The figure shows a correlation as the electron density on the oxygen atom is more available to the oxophillic silicon, the total distance between the uranium and silicon lengthens overall.

Inverse Trans Influence

The inverse *trans* effect was first introduced in 1992 by Denning[93] and describes the stabilisation of ligands *trans* to certain other ligands which are labelled '*trans* directing ligands'. Semi–core 6*p*–orbitals mix with valence *d*– or *f*–orbitals and this provides the basis for the inverse *trans* influence, however, the presence of both orbital types in the actinide valence shell complicates the description for actinide species and the semi–core 6*p*–orbitals are not the sole determining factor.[94]

The concept requires the comparison of bond lengths in six coordinated species of the type MZY$_5{}^{n-}$ where Z is either an oxo or nitrido group and Y is a halide. Where M is a transition metal of the type $d^{0,1,2}$ the the metal–halide *trans* bond is typically found to be 5–15% longer than the equivalent metal–halide *cis* bond. However, as alluded to above, the situation is more complex for actinide species and in similar complexes where M is either U or Pa the M–Y *trans* distances are found to be 4–8% shorter than

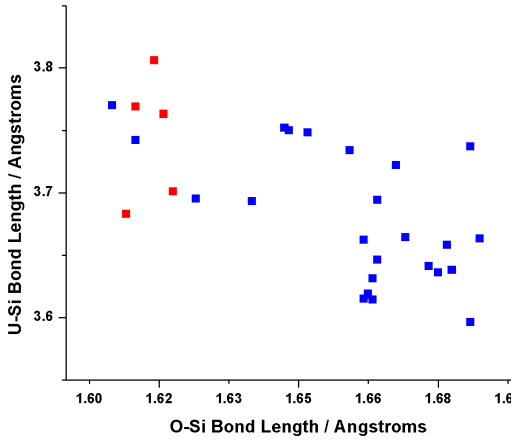

Figure 2.12: Correlation between O–Si bond length and U–Si distances for uranium compounds with the ligand R_3SiO. (Data points in red are the experimental values for $K[U(OSiPh_3)_5]$)

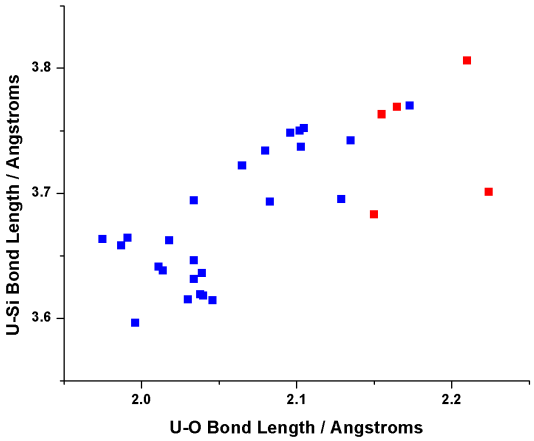

Figure 2.13: Correlation between U–O bond length and U–Si distances for uranium compounds with the ligand R_3SiO. (Data points in red are the experimental values for $K[U(OSiPh_3)_5]$)

the equivalent M–Y *cis* bonds.[95] Subsequent studies, using DFT, show this effect in a number of complexes, albeit the average shortening of the *trans* bond is closer to 2%.[94] [96]

This effect could be, at least partially, responsible for the lengthening and shortening of bonds observed within this complex. Only two ligands are *trans* to each other, O2–U1–O5 with an angle of 172.51° or 178.38° if measuring the Si2–U1–Si5 angle. The average bond length of the equatorial *cis* U–O bonds is 2.180 Å and 2.183 Å for the *trans* bonds. In addition the comparison between the O–Si bond lengths show a similar trend, with the equatorial O–Si observed at 1.617 Å average and the *trans* O–Si bonds are 1.620 Å average. Whilst initially unremarkable, when compared to each other, a different trend in observed. Instead of the U–O lengthening (or shortening) and corresponding O–Si bond shortening (or lengthening) in this case both the U–O and O–Si *trans* bonds are marginally greater in length than the *cis* U–O and O–Si bonds showing a small '*trans*' effect but no inverse *trans* effect.

Finally Figure 2.11 shows some correlation between the O–Si and Si–R bond distances. The Si–R bond lengths are typical of such complexes and are mostly unaffected by the uranium centre or the potassium counterion.

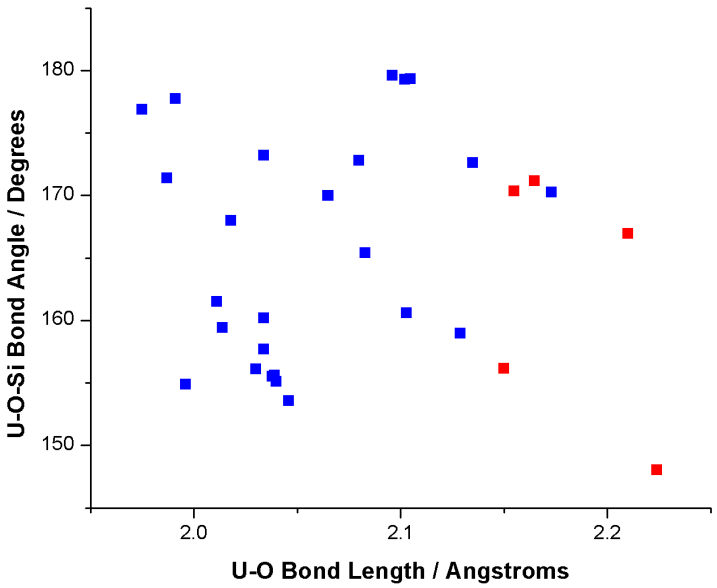

Figure 2.14: U–O–Si bond angles for uranium compounds with the ligand R_3SiO. (Data points in red are the experimental values for $K[U(OSiPh_3)_5]$)

Figure 2.14 shows the U–O–Si bond angles found in the literature and the U–O–Si bond angles found for $K[U(OSiPh_3)_5]$. Four of the five U–O–Si bond angles are within a range that has been observed before, however, one bond angle is lower than this literature range and two are considerably more bent than the other three. These two ligands also coordinate to the potassium counterion via the two oxygen atoms. The presence of the counterion coordinating to the two closest ligands reduces the angles to 148.0(8) ° and 167.0(8) °.

2.2.3 'Ate' complexes

'Ate complexes are defined as complexes where a salt has been formed by the coordination of an extra ligand to the metal centre. The central atom increases its coordination sphere by one, in addition to becoming negatively charged, but remains in the same formal oxidation state. In this case the uranium centre in UCl_4 which is neutral and has a coordination number of four, has become a negatively charge anion with a coordination number of five in $K[U(OSiPh_3)_5]$, therefore filling the criteria to be deemed an 'ate' complex. Examples of other uranium 'ate' complexes are shown in Figure 2.15.

Only Figure 2.15–f is a siloxide complex and therefore the closest to $K[U(OSiPh_3)_5]$ in terms of its electronics and structure. Figure 2.15–f was analysed by X–ray diffraction and shown to possess U–O bond distances of 2.228(17) Å. This bond length is longer than the average bond U–O bond distance for $K[U(OSiPh_3)_5]$ which is 2.18 Å. As $K[U(OSiPh_3)_5]$ is higher in oxidation state and coordination number (CN = 5, OS = 4 compared to CN = 4, OS = 3) it would be expected that the bond length would increase as the bond weakens. However as this is not the case and therefore the ligand structure should be considered. The O^{t}Bu groups are inductively more electron withdrawing than a Ph ring and it is the O^{t}Bu groups that are inductively removing electron density somewhat from the uranium centre, in turn weakening the bonds and increasing the bond lengths.

2.2.4 Characterisation of $K[U(OSiPh_3)_5]$: NMR

$^{13}C\{H\}$ and ^1H NMR spectra were obtained in d_8–toluene solution. The resonances observed display a similar pattern to the starting materials and the resonances were assigned accordingly as shown in Tables 2.3 and 2.4. Full spectra are shown in Appendices B.13 and B.14 along with HSQC and HMBC data shown in Appendices B.15 and B.16

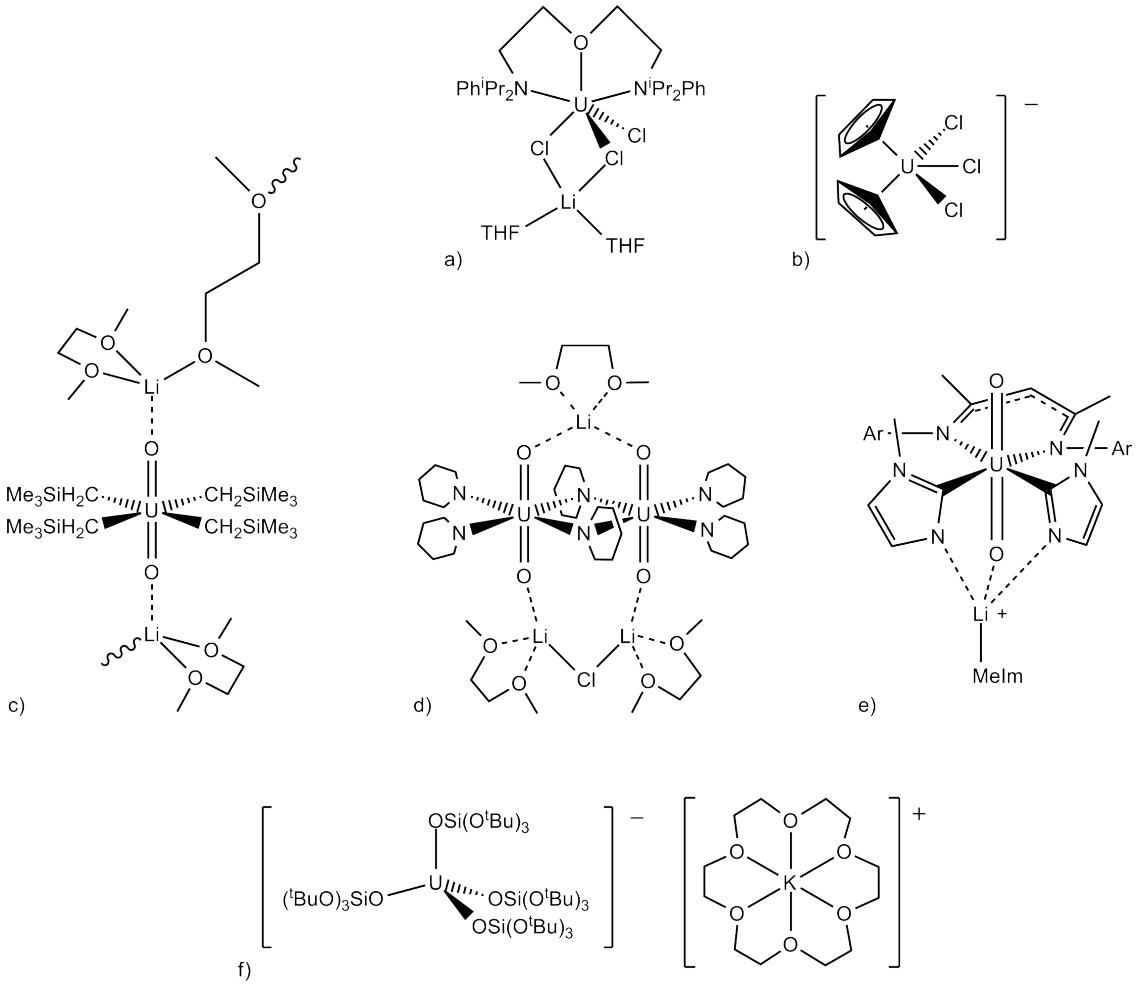

Figure 2.15: Examples of uranium 'ate' complexes
a) [^{DIPP}NCOCN]$UCl_3Li(THF)_2$ [97];
b) $[Cp^*UCl_3]^-$ [98];
c) $[Li(DME)_{1.5}]_2[UO_2(CH_2SiMe_3)_4]$ [99];
d) $[(Li(DME))_2Cl][Li(DME)][UO_2(NC_5H_{10})_3]_2$ [100];
e) [Li(MeIm)][UO($\eta-$O)(Ar_2nacnac)($\eta-C,N-C_4H_5N_2)_2$] [101];
f) [K(18*c*6)][U(OSi(O^{t}Bu)$_3$)$_4$] [102]

The $^{13}C\{H\}$ NMR spectrum clearly shows four carbon environments at δ 150.19, 128.45, 127.11 and 126.58 ppm. The weakest signal at δ 150.19 ppm is assigned to the *ipso* carbon and this correlates well with the HSQC spectrum which shows no proton correlation for this resonance. The other resonances are assigned as *ortho*, *para* and *meta* respectively and in accordance with the ^{1}H NMR spectroscopy integration values and the HSQC and HMBC data.

The ^{1}H NMR spectrum shows three proton environments at δ 6.54, 5.61 and 4.91 ppm in a 1:2:2 ratio which is as expected with a plane of symmetry passing from the siloxide

substituent, through the phenyl ring to the *para* proton. With an integration of 1H, the resonance at δ 6.54 ppm is assigned to the proton in the*para* position. The resonance at δ 4.91 ppm is broadened (FWHH = 84.6 Hz) due to the proximity to the uranium centre and is therefore assigned to the proton closest to the uranium centre in the *ortho* position. This leaves the resonance at δ 5.61 ppm assigned to the proton in the *meta* position.

Carbon Assignment	δ/ppm
ipso	150.19
ortho	128.45
para	127.11
meta	126.58

Table 2.3: NMR Spectroscopy Resonances for the $^{13}C\{H\}$ spectrum of K[U(OSiPh$_3$)$_5$] in d_8–toluene

Proton Assignment	δ/ppm (multiplicity, coupling constant)
para	6.54 (s, 1H)
meta	5.61 (s, 2H)
ortho	4.91 (s, broad, 2H)

Table 2.4: NMR Spectroscopy Resonances for the ^{1}H spectrum of K[U(OSiPh$_3$)$_5$] in d_8–toluene

It is commonly found that in investigating paramagnetic complexes, the NMR resonances broaden which can make signals of low intensity all but impossible to detect. This is due to the presence of unpaired electrons, resulting in large isotropic shifts and the broadening of the resonances making accurate integrations difficult to obtain and usually obscures any nuclear spin–spin coupling. The magnitude of these effects can vary, depending on the number of unpaired electrons in a system and the electron spin relaxation time, both of which vary with the metal, oxidation state and coordination environment. This means there is no single rule which applies to all compounds and the relationship between chemical shift and chemical environment varies greatly.[103] However, by increasing the spectral window and decreasing the relaxation delay, the NMR spectra of paramagnetic complexes

can easily be acquired.

The NMR data presented here, has sharp resonances which are normally seen within diamagnetic complexes, the sample was analysed by elemental analysis and proved to be analytically pure and within C, 0.8% and H, 0.6% of calculated values. In addition, the ^{1}H spectrum window was broadened to +200 to -200 ppm and the relaxation delay was decreased, in order to search for any broadened peaks that might indicate a paramagnetic species, but none were found as shown in Figure 2.16. Whilst sharp resonances with low FWHH measurements are unusual, it has been observed with previously published 'ate' complexes.[97]

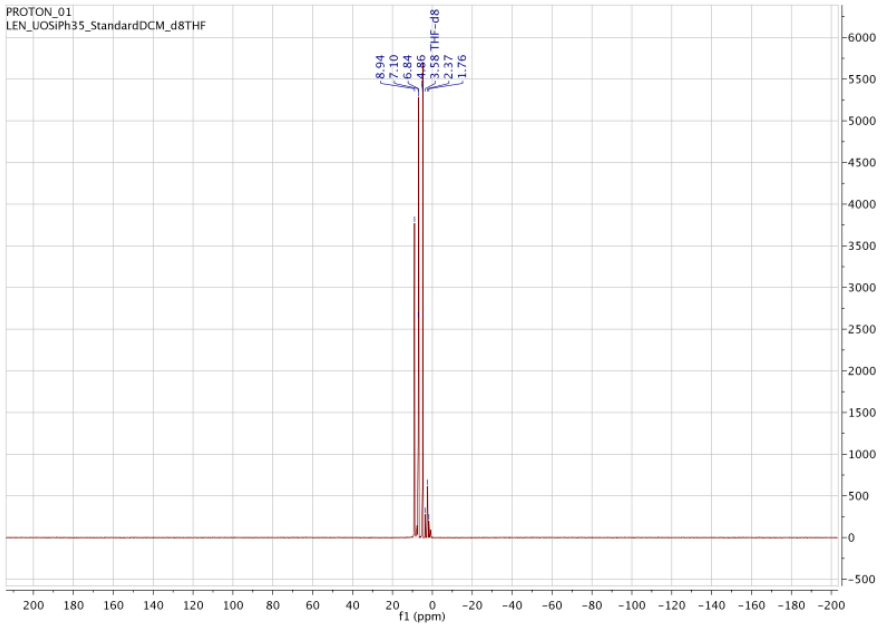

Figure 2.16: ^{1}H NMR spectrum of K[U(OSiPh$_3$)$_5$] with broadened window of +200 to -200 ppm

2.3 Synthesis and characterisation of ([K(py)$_6$][U(OSiPh$_3$)$_5$(py)])$_2$

([K(py)$_6$][U(OSiPh$_3$)$_5$(py)])$_2$ was prepared by reacting UCl$_4$ with six equivalents of Ph$_3$SiOK in THF. The crude product was extracted with a toluene/hexane mix before recrystallisation from pyridine at -40°C.

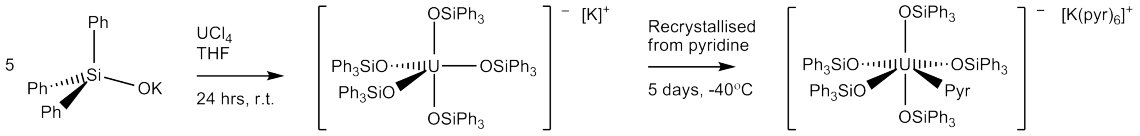

Scheme 2.10: Synthesis of $([K(py)_6][U(OSiPh_3)_5(py)])_2$

2.3.1 Characterisation of $([K(py)_6][U(OSiPh_3)_5(py)])_2$: X–ray Diffraction

$([K(py)_6][U(OSiPh_3)_5(py)])_2$ crystallises as the pyridine trisolvate in triclinic space group P-1 with an *R* factor of 4.79. The lattice parameters for this structure are *a* = 15.2760(2) Å, *c* = 17.6573(3) Å, *c* = 23.5609(4) Å, α = 94.8100(10) °, β = 108.0410(10) °, γ = 90.2700(10) °.

The structure is highly complex, with two formula units per unit cell, a total of 541 atoms. From the molecular structure shown in Figure 2.17 the uranium centre has a square bipyramidal geometry consisting of five siloxy ligands with the sixth site occupied by a pyridine molecule. The counterion, potassium, is also co–ordinated to six pyridine molecules and a further three pyridine molecules are found in the crystal cell. It should be noted that for clarity Figure 2.17 only shows half the crystal cell, with the other half consisting of another formula unit.

The average experimental bond length for $([K(py)_6][U(OSiPh_3)_5(py)])_2$ for **U–O**SiR_3 is 2.215(5) Å, 1.606(5) Å for U**O–Si**R_3 and 1.886(2) Å for UO**Si–R$_3$**. Figures 2.19 and 2.20 show the full range of U–O and O–Si literature values for the general formula $U(OSiR_3)_xR'_y$ (blue) and the experimental bond lengths for $[K(py)_6][(Ph_3SiO)_5U(py)]$ (red).

Comparing the literature average bond lengths to the average experimental bond lengths for $([K(py)_6][U(OSiPh_3)_5(py)])_2$ the U–O bonds are found to be slightly longer than expected. Based on the hypothesis described in the previous section (Section 2.2.2), these elongated U–O bonds suggest the O–Si bonds should be amongst the shortest found

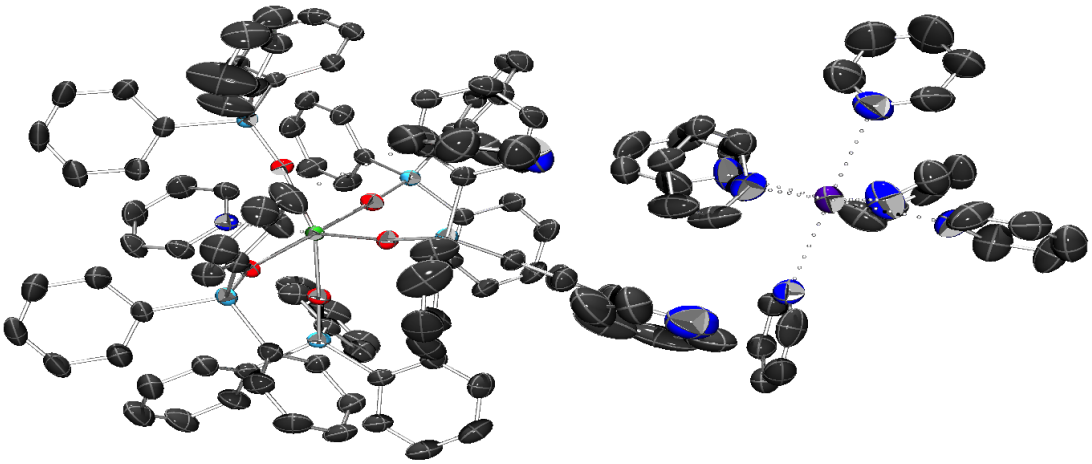

Figure 2.17: Molecular structure of $([K(py)_6][U(OSiPh_3)_5(py)])_2$ (Only half the cell is shown; hydrogen atoms omitted for clarity)

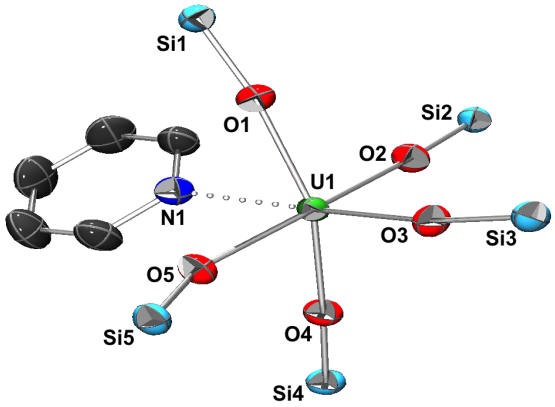

Figure 2.18: Core molecular structure of $[K(py)_6][(Ph_3SiO)_5U(py)]$ containing the Si, O U and K atoms and coordinated pyridine (Hydrogen atoms, phenyl rings, potassium counterion and solvate molecules have been omitted for clarity)

which is shown to be the case in Figure 2.20. This correlation is again highlighted by comparing the total U–O–Si distance to the U–O or O–Si bond length and is shown in Figures 2.21 and 2.22.

To explain the lengthening of the U–O bond the coordinating solvent molecule should also be considered. The lone pair on pyridine acts as a σ–donor to the uranium centre, in contrast to the homoleptic starting material. In the latter, the five oxygen atoms compete as π–donors to both the uranium centre and as discussed in section 1.2.1, to a lesser ex-

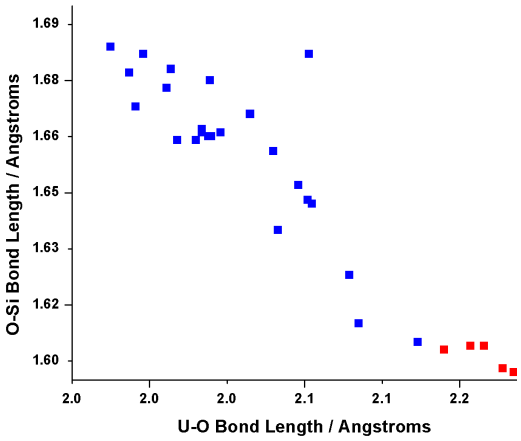

Figure 2.19: Correlation between U–O bond distances and O–Si for uranium compounds with the ligand R_3SiO. (Data points in red are the experimental values for $([K(py)_6][U(OSiPh_3)_5(py)])_2$)

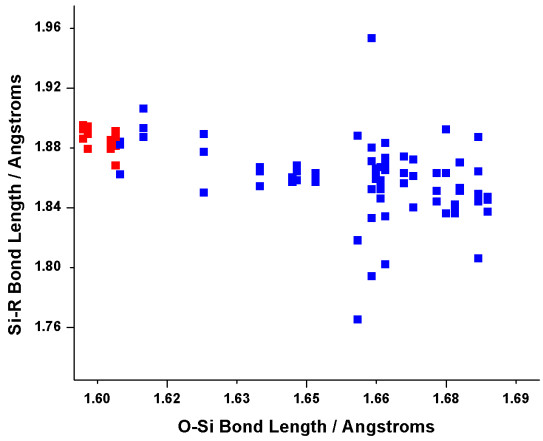

Figure 2.20: Correlation between O–Si bond distances and Si–R_3 for uranium compounds with the ligand R_3SiO. (Data points in red are the experimental values for $([K(py)_6][U(OSiPh_3)_5(py)])_2$)

tent to the silicon atom. With greater electron density present in the heteroleptic pyridine complex, the donation from the oxygen atoms is lessened and consequentially, the bond is marginally longer. In addition, if the inverse trans effect (Section 2.2.2) is considered, the ligand (U1–Si3), which is trans to the pyridine ligand, is shown have the shortest U–O bond found within this compound, although still longer than the ligands on $K[U(OSiPh_3)_5]$. A similar, non halide, inverse trans effect has been observed previously within a uranium (V) imide complex.[104]

Figure 2.20 indicates there is little correlation between the O–Si and Si–R bond distances with only a slight trend in favour of shorter Si–R bonds in the presence of longer O–Si bonds with the observed Si–R bonds well within the precedent set in the literature. Figure 2.23 shows the average U–O–Si bond angles for complexes $U(OSiR_3)_n$ (blue) and the experimental values for $([K(py)_6][U(OSiPh_3)_5(py)])_2$ (red) which, whilst spread across the literature range are still within the limits of published data.

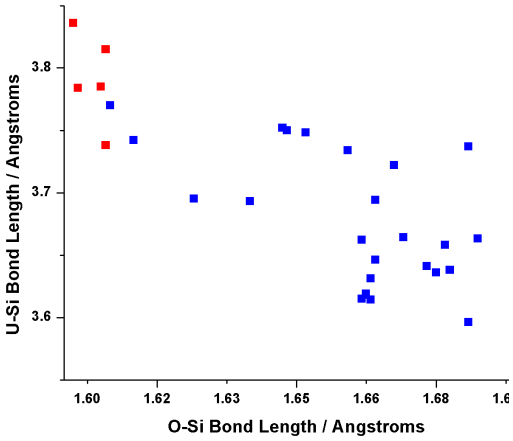

Figure 2.21: Correlation between O–Si bond length and U–Si distances for uranium compounds with the ligand R_3SiO. (Data points in red are the experimental values for $([K(py)_6][U(OSiPh_3)_5(py)])_2$)

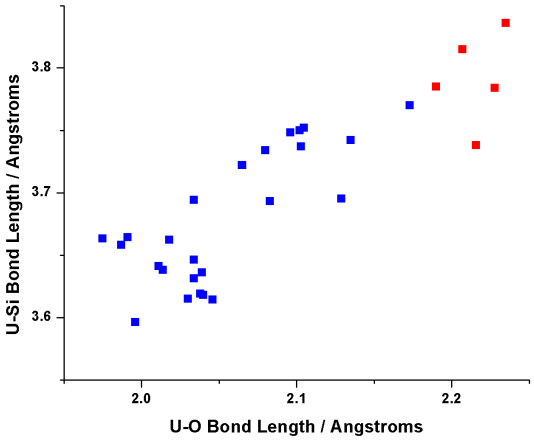

Figure 2.22: Correlation between U–O bond length and U–Si distances for uranium compounds with the ligand R_3SiO. (Data points in red are the experimental values for $([K(py)_6][U(OSiPh_3)_5(py)])_2$)

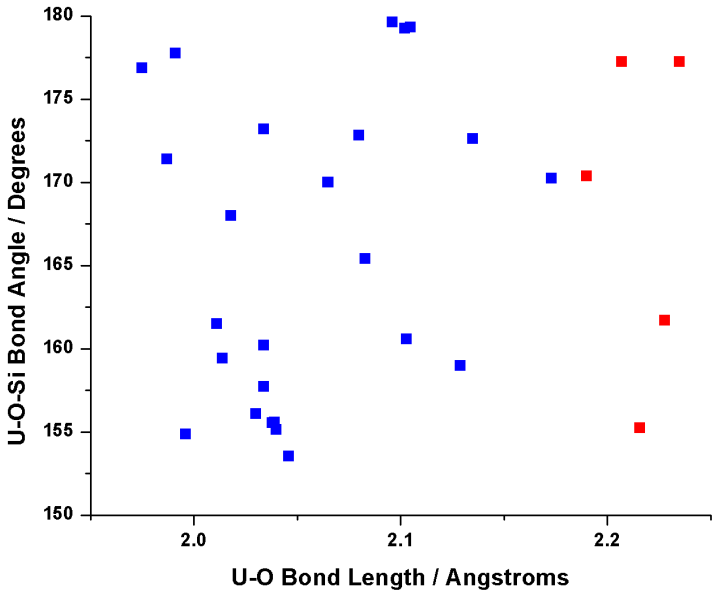

Figure 2.23: U–O–Si bond angles for uranium compounds with the ligand R_3SiO. (Data points in red are the experimental values for $([K(py)_6][U(OSiPh_3)_5(py)])_2$)

2.3.2 Characterisation of $([K(py)_6][U(OSiPh_3)_5(py)])_2$: NMR

^{1}H and $^{13}C\{H\}$ NMR spectra were collected from solutions in d_5–pyridine, the resonances and assignments are shown in Tables 2.5 and 2.6. The $^{13}C\{H\}$ NMR spectroscopy data

show a number of resonances. Once the resonances for pyridine and trace toluene are assigned, the three resonances left at δ 137.43, 128.12 and 127.71 ppm are assigned to the carbons in the *ortho*, *para* and *meta* positions respectively based on comparisons with the starting materials and analysis of the ^{1}H and HSQC NMR spectroscopy data (Appendix B.19).

The ^{1}H NMR spectroscopy data show three resonances in the familiar pattern at δ 9.22, 7.30 and 7.08 ppm. The integration values show the resonances to be in a 2:1:2 ratio suggestive of *ortho*, *para* and *meta* respective assignments. The resonance at δ 9.22 ppm is relatively broad compared to the other resonances (FWHH = 518.1 Hz). Broadening of the peak is evidence that this resonance should be assigned to the *ortho* protons as they are the closest to the uranium centre.

Carbon Assignment	δ/ppm
ortho	137.43
para	128.12
meta	127.71

Table 2.5: NMR Resonances for the $^{13}C\{H\}$ spectrum of $([K(py)_6][U(OSiPh_3)_5(py)])_2$ in d_5–pyridine

Proton Assignment	δ/ppm (multiplicity, coupling constant)
ortho	9.22 (s, broad, 6H)
para	7.29 (q, J = 11.5 Hz, 3H)
meta	7.08 (s, 6H)

Table 2.6: NMR Resonances for the ^{1}H spectrum of $([K(py)_6][U(OSiPh_3)_5(py)])_2$ in d_5–pyridine

2.4 Synthesis and characterisation of K[$(Ph_3SiO)_5U(THF)$]

Uranium tetrachloride and five equivalents of Ph_3SiOK were stirred together vigorously in THF at room temperature. Within minutes the solution had changed from green to lilac to

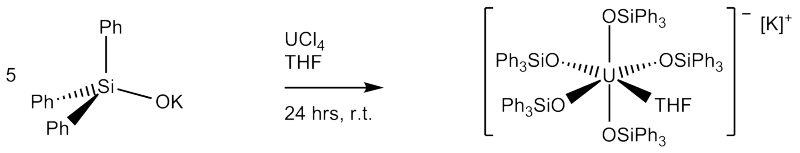

Scheme 2.11: Synthesis of $K[(Ph_3SiO)_5U(THF)]$

pink. After work up, the resulting pale pink solid was dissolved in THF which resulted in a deep pink solution. Recrystallisation was difficult due to the high solubility of the product in THF. Other non–coordinating solvents (benzene, pentane and hexane) were trialled, with a minimum amount of THF added in order to ensure the complex recrystallised with THF coordinated, but without success. Despite these difficulties, NMR spectroscopy data complimented the data collected for $K[U(OSiPh_3)_5]$ and $([K(py)_6][U(OSiPh_3)_5(py)])_2$ well.

2.4.1 Characterisation of $K[(Ph_3SiO)_5U(THF)]$: NMR

$^{13}C\{H\}$ and ^{1}H NMR spectroscopy data were obtained and compared to the starting materials of Ph_3SiOH and Ph_3SiOK. The resonances observed display a similar pattern to the starting materials and with this information, along with the proton integration values and HSQC data shown in Appendix B.23, the resonances are assigned as shown in Tables 2.7 and 2.8.

Carbon Assignment	δ/ppm
ipso	143.94
ortho	138.04
para	128.41
meta	128.11

Table 2.7: NMR Resonances for the $^{13}C\{H\}$ spectrum of $K[(Ph_3SiO)_5U(THF)]$ in d_8–THF

Similarly to the $K[U(OSiPh_3)_5]$ the mono–substituted phenyl ring was expected to have

Proton Assignment	δ/ppm (multiplicity, coupling constant)
ortho	8.96 (s, 2H)
para	7.12 (t, *J* = 7.3 Hz, 1H)
meta	6.87(t, *J* = 7.1 Hz, 2H)

Table 2.8: NMR Resonances for the ^{1}H spectrum of K[$(Ph_3SiO)_5U(THF)$] in d_8–THF

four carbon environments. The $^{13}C\{H\}$ NMR spectrum supports this hypothesis with four carbon environments observed in approximately the correct ratios at δ 143.94, 138.04, 128.41 and 128.11 ppm and are assigned to the *ipso*, *ortho*, *para* and *meta* carbons respectively.

The ^{1}H NMR spectrum was expected to have three proton environments in a 1:2:2 ratio (*para*, *meta*, *ortho*). This is observed in the spectrum with the *ortho* resonance slightly broadening (FWHH = 18.8 Hz). In order to further confirm the proposed $^{13}C\{H\}$ and ^{1}H assignments, both HSQC and HMBC spectra were collected and analysed which can be seen in Appendix B.23 and B.24.

The isotope ^{29}Si has a low natural abundance of only 4.68% and low receptivity of 2.09[105] compared to ^{13}C and for this reason it is very difficult to observe directly by NMR spectroscopy. 2D NMR spectroscopy methods provide an alternative by indirectly observing the silicon atoms and reconstructing the silicon dimension. An example of this is found in the ^{29}Si HMBC spectrum of K[$(Ph_3SiO)_5U(THF)$] in Figure 2.24 and clearly shows one observed silicon environment at δ -29ppm indicating the molecule either has identical ligand environments or it is fluxional in solution. By repeating the ^{29}Si HMBC NMR spectroscopy at a -38$\circ$, two silicon environments are observed, shown in Figure 2.25. By considering the structure of ([$K(py)_6$] [$U(OSiPh_3)_5(py)$])$_2$ which also has a coordinated solvent molecule, two ligand environments are predicted, *cis* and *trans* to a coordinated THF molecule and therefore explaining the two silicon environments seen in Figure 2.25.

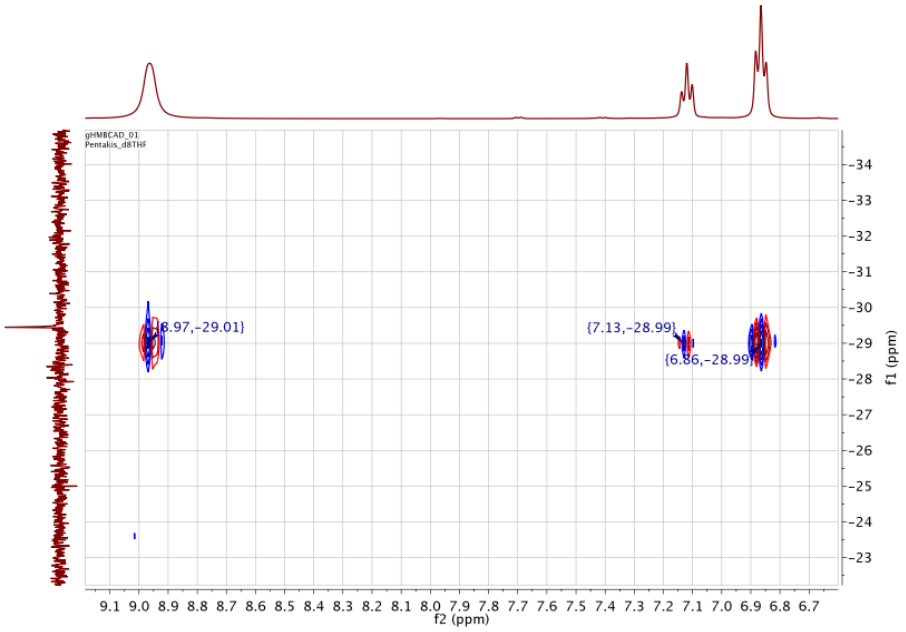

Figure 2.24: ^{29}Si NMR HMBC spectrum of K[$(Ph_3SiO)_5U(THF)$] in d_8–THF

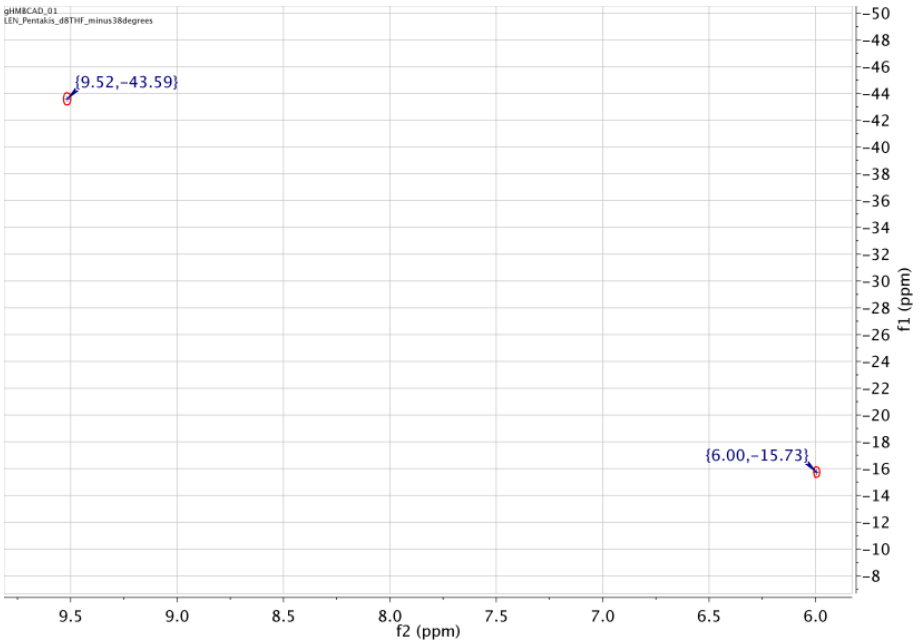

Figure 2.25: ^{29}Si NMR HMBC spectrum of K[$(Ph_3SiO)_5U(THF)$] at -38 °C in d_8–THF

2.4.2 Characterisation of K[$(Ph_3SiO)_5U(THF)$] : Negative ion ESI HRMS

Due to the 'rainbow' of colour changes observed during the synthesis of all the above uranium siloxides, investigations into the nature of the intermediates present were undertaken, specifically focused towards stepwise substitution, in order to afford well–defined

and hopefully isolable intermediates.[106]

The possibility of stepwise complex formation during the synthesis meant ESI HRMS characterisation techniques could be used to identify species on the addition of each individual ligand. In a typical ESI HRMS experiment, a suspension of UCl_4 was prepared in THF as well as a solution of Ph_3SiOK in the same solvent volumetrically. Aliquots equal to one equivalent of the ligand were added to the UCl_4 and reacted for 20 minutes before ESI HRMS injection, using a gas–tight Hamilton syringe and data collection were undertaken, the results of which are summarised in Table 2.9.

Ph_3SiOK	HRMS m/z	Relative Intensity	Anion Assignment
1 eq.	358.9515	0.39	—
	414.8908	0.28	UCl_5
	655.0104	0.33	$Ph_3SiOUCl_4$
2 eq.	358.9517	0.22	—
	655.0105	0.18	$Ph_3SiOUCl_4$
	895.1304	0.33	$(Ph_3SiO)_2UCl_3$
	1170.2239	0.15	$(Ph_3SiO)_3UCl_3$
	1410.3450	0.12	$(Ph_3SiO)_4UCl_2$
3 eq.	1133.2587	0.22	$(Ph_3SiO)_3UCl_2$
	1410.3479	0.22	$(Ph_3SiO)_4UCl_2$
	1614.4872	0.57	$[(Ph_3SiO)_5U]$
4 eq.	1614.4781	1.0	$K[U(OSiPh_3)_5]$
5 eq.	1614.4781	1.0	$K[U(OSiPh_3)_5]$
6 eq.	275.0889	0.17	Ph_3SiO
	589.1415	0.31	$(Ph_3SiO)_2K$
	1156.3733	0.35	$K_2[OU(OSiPh_3)_3]$
	1401.4449	0.17	—

Table 2.9: Negative ion ESI HRMS data for the synthesis of $K[(Ph_3SiO)_5U(THF)]$ in THF

The data highlights that multiple ions are present up until 3 equivalents of Ph_3SiOK were added. At this stage, the primary negative ion is the $K[U(OSiPh_3)_5]$ species at m/z 1614.4781, with two other species at m/z 1133.2587 and 1410.3479. On addition of the fourth and fifth equivalent of Ph_3SiOK the only negative ion observed is the desired

$K[U(OSiPh_3)_5]$ at m/z 1614.4781 suggesting uranium has a predisposition to large coordination numbers, which is expected based on the electronics and sterics of uranium. In addition, 'ate' complexes (Section 2.2.3), generally exhibit greater kinetic stability than the equivalent neutral counterpart. This stability is achieved by saturating the uranyl coordination sphere which suggests the addition of a sixth ligand would not react or result in the dissociation of the molecule.[100,101]

Considering this theory further, the reported bond dissociation energies of U−−O are 761(17) kJ/mol, OU−−O at 678(59) kJ/mol and O_2U−−O at 644 kJ/mol. It is clear that the greater the number of oxygen ligands, the weaker the bonds become. Assuming the same theory applies to $K[U(OSiPh_3)_5]$, it could be deduced that if a sixth ligand binds to the uranium centre, the molecule becomes unstable and dissociates. In addition, if a sixth siloxide ligand binds to the uranium centre, the molecule will possess a 2- charge which is high for uranium and mostly unstable.

As predicted, on addition of the sixth equivalent, $K[U(OSiPh_3)_5]$ completely disappears and multiple ions are observed. Five coordinating ligands leaves the uranium centre sterically saturated with space left only for smaller ligands such as a coordinating solvent making the addition of a sixth bulky ligand destabilising.

In addition the ESI HRMS data show the generation of $[(Ph_3SiO)K(OSiPh_3)]^-$ which is seen in literature within larger structures or as a fragment of a larger tetramer structure similar to that shown in Figure 2.4 and has been previously characterised by X–ray diffraction crystallography.[89] It is possible that the generation of this species is more stable than a $K_2[U(OSiPh_3)_6]$ derivative. In addition to the siloxide species two other peaks are observed at m/z 1156.3733 and 1401.4449 which are tentatively assigned to uranium based derivatives, thermodynamically more stable than $K_2[U(OSiPh_3)_6]$ and potentially some form of 'ate' complex, known to be kinetically more stable due to an increase in

coordination number.[100]

With the analysis confirming that the K[U(OSiPh$_3$)$_5$] species is by far the most stable, the aim of synthesising U(Ph$_3$SiO)$_3$Cl is therefore unlikely via a metathesis reaction between three equivalents of the ligand and the UCl$_4$ starting material. A different approach was therefore required. A logical solution to the problem would be to substitute the Ph$_3$SiO$^-$ ligands with another more sterically bulky species, stabilising a uranium complex with a lower coordination number. A second solution would be to remove a Ph$_3$SiO$^-$ ligand from the already formed K[U(OSiPh$_3$)$_5$] complex via a second metathesis reaction resulting in a leaving group or functional group on the uranium centre. The second option is investigated further in section 2.5.

2.5 Chemistry of the [U(OSiPh$_3$)$_5$] fragment

Given the steric encumbrance of the uranium centre in K[U(OSiPh$_3$)$_5$], and given the resistance of K[U(OSiPh$_3$)$_5$] to reduction in a tractable manner, other methods to open the coordination sphere to form a heteroleptic complex of the general form [U(OSiPh$_3$)$_3$X] were explored. The anionic nature of K[U(OSiPh$_3$)$_5$] implies that an electrophilic modification should be possible. As such, treatment of K[U(OSiPh$_3$)$_5$] with TMSOTf aimed to degrade the K[U(OSiPh$_3$)$_5$] complex by removal of Ph$_3$SiO$^-$ to form (R$_3$SiO)$_{5-x}$U(OTf)$_x$ with TfO$^-$ representing the required leaving group.

Me$_3$SiOTf and TMSOTf have been widely used in substitution reactions with the ligand R$_3$SiO$^-$.[107] An example of such a substitution reaction is shown in Scheme 2.12 which uses a germanium siloxide compound.[108] Further examples of such reactions have been documented using *d*–block metal centres and one such reaction is shown in Scheme 2.13 which substitutes the Me$_3$SiO$^-$ group on a rhenium compound with the desired TfO$^-$

leaving group.[109]

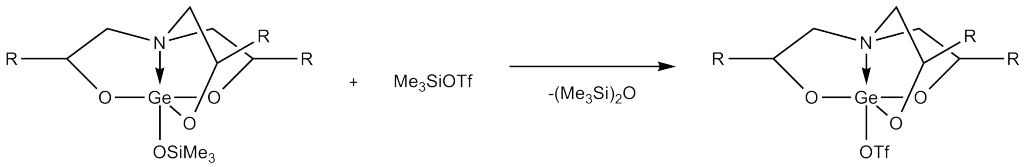

Scheme 2.12: The substitution reaction between Me_3SiO^- and TfO^- (A *p*–block example)

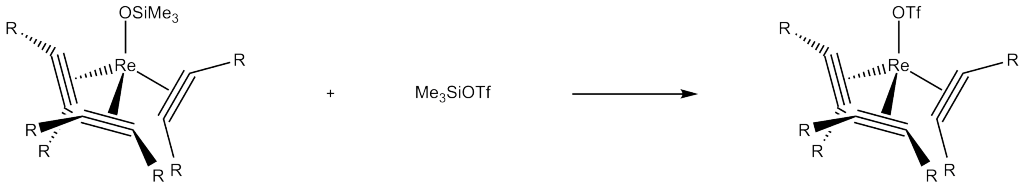

Scheme 2.13: The substitution reaction between Me_3SiO^- and TfO^- (A *d*–block example)

Another good example of this type of substitution reaction being employed for a uranium complex is shown in Scheme 2.14.[110]

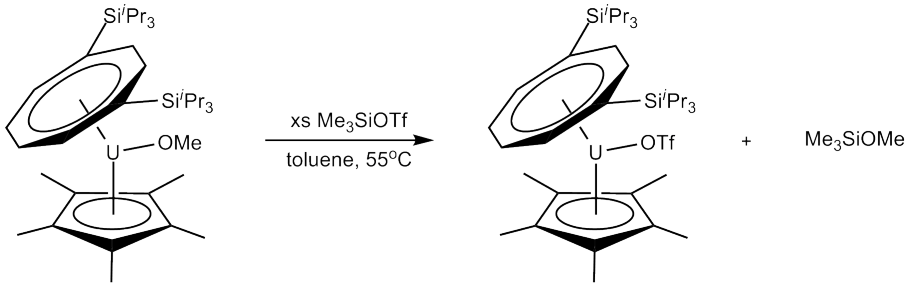

Scheme 2.14: The substitution reaction between Me_3O^- and TfO^- (An *f*–block example)

In order to substitute a single Ph_3SiO^- ligand from the already formed $K[U(OSiPh_3)_5]$ with the pseudo halogen and convenient leaving group, TfO^- (Scheme 2.16) investigative reactions were undertaken, starting with a thorough analysis of how the starting materials, Ph_3SiOH and Ph_3SiOK react with TMSOTf and to identify if $Ph_3SiO-TMS$ was formed.

2.5.1 Characterisation of $Ph_3SiOTMS$, HOTf and KOTf : NMR

Ph_3SiOH and Ph_3SiOK, were reacted TMSOTf in line with literature methods[111]. In addition, both d_8–THF and d_2–*dcm* were used as solvents and the products were then

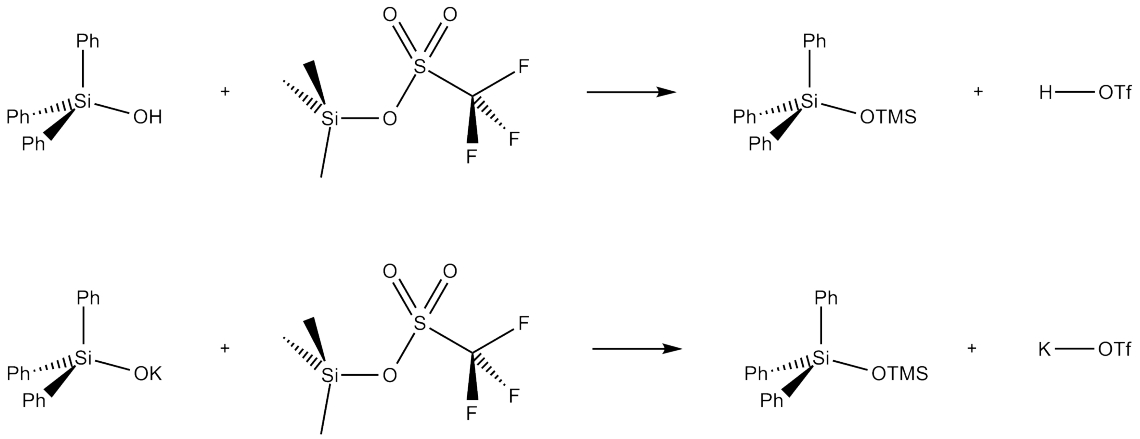

Scheme 2.15: Synthesis of $Ph_3SiOTMS$, HOTf and KOTf

characterised using NMR spectroscopy.

Initially TMSOTf was characterised by NMR spectroscopy and the $^{13}C\{H\}$ NMR spectrum clearly shows the distinct quartet resonance at δ 119.76 ppm which is assigned to TMS**OTf** in accordance with literature values.[82]

The reaction between TMSOTf and Ph_3SiOH or Ph_3SiOK was then characterised by ^{1}H, $^{13}C\{H\}$ and ^{19}F NMR. The quartet resonance observed in the TMSOTf spectrum is subsequently not observed after reaction with Ph_3SiOH or Ph_3SiOK. The **TMS**OTf resonance is observed at δ 0.30 ppm. After reaction with Ph_3SiOH or Ph_3SiOK the **TMS**O$SiPh_3$ resonance is observed at δ 2.23 and 2.28 ppm respectively. In addition four new resonances are observed which are assigned to the phenyl groups. The two siloxide products differ slightly but not to any great extent.

The ^{1}H NMR spectrum also shows a clear and consistent pattern of the **TMS**O$SiPh_3$ product from both the protonated and potassiated starting materials with resonances observed at δ 0.09 and 0.10 ppm respectively and the TMSOSi**Ph_3** resonances observed between δ 7.57 and 7.34 ppm. These data correlate well with literature values.[82] In addition, the compounds were analysed using ^{19}F NMR spectroscopy which confirmed the expected single fluorine environment, observed at δ -76 ppm for TMSOTf and δ -79

ppm for HOTf and KOTf.

2.5.2 Characterisation of the reaction between $K[U(OSiPh_3)_5]$ and TMSOTf : NMR

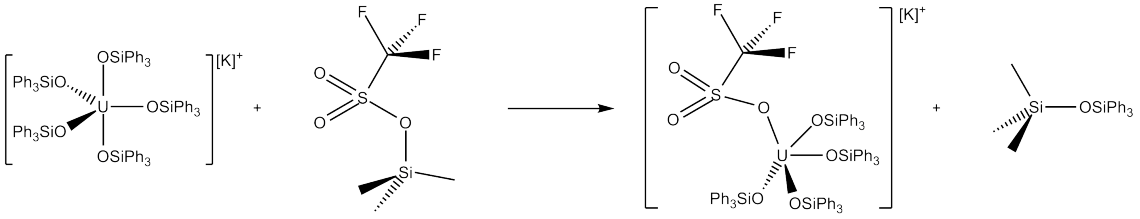

Scheme 2.16: Hypothetical reaction scheme of $K[U(OSiPh_3)_5]$ and TMSOTf

With $TMSOSiPh_3$ well characterised and understood by NMR spectroscopy, the complex $K[(Ph_3SiO)_5U(THF)]$ was reacted with one and two equivalents of TMSOTf in a solution of THF. As shown in Figures 2.26 and 2.27 the resulting products were characterised by $^{13}C\{H\}$ and ^{1}H NMR spectroscopy. Adding a third equivalent of TMSOTf was also carried out but this resulted in an intractable solid which proved difficult to extract from the NMR tube and impossible to purify. The cause of this is likely due to a polymerisation reaction between THF and TMSOTf.[112] In order to overcome this problem, DCM was used, which gave similar NMR spectroscopy results on addition of one and two equivalents of TMSOTf and an intractable solid on addition of the third equivalent.

The $^{13}C\{H\}$ and ^{1}H NMR spectra are shown in Figures 2.26 and 2.27. In both cases the red spectrum is the $K[(Ph_3SiO)_5U(THF)]$ in THF, the green spectrum shows the reaction between $K[(Ph_3SiO)_5U(THF)]$ and one equivalent of TMSOTf and the third, blue spectrum shows the reaction between $K[(Ph_3SiO)_5U(THF)]$ and two equivalents of TMSOTf. In both the $^{13}C\{H\}$ and ^{1}H NMR spectra the $K[(Ph_3SiO)_5U(THF)]$ signals completely disappear on addition of just one equivalent of TMSOTf showing that $K[(Ph_3SiO)_5U(THF)]$ has completely reacted. On addition of both one and two equivalents of TMSOTf the

product TMS−−OSiPh$_3$ is observed as indicated by the resonances at δ 137.31, 135.96, 130.72 and 128.69 ppm, providing evidence that at least one ligand has been removed from the K[(Ph$_3$SiO)$_5$U(THF)] species.

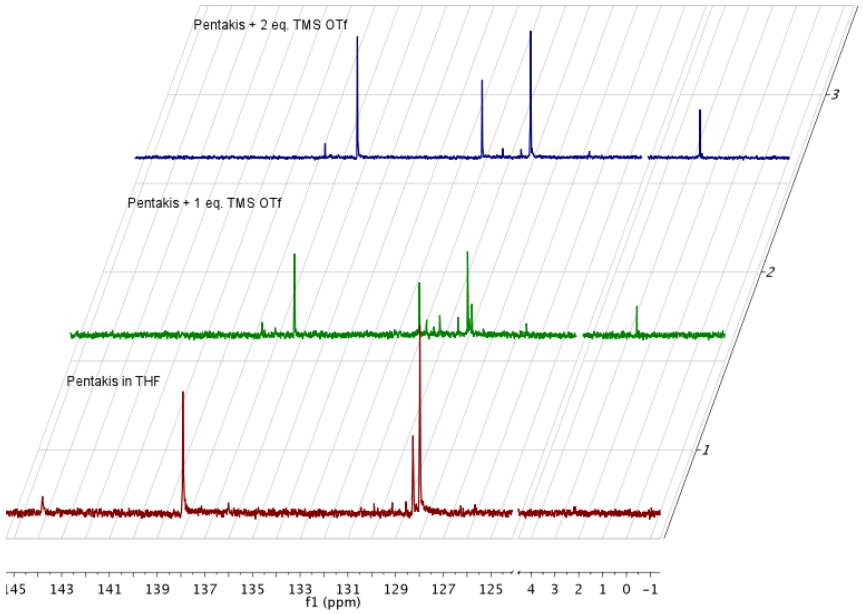

Figure 2.26: NMR Resonances for the $^{13}C\{H\}$ spectrum of the reaction between K[(Ph$_3$SiO)$_5$U(THF)] (red) and one (green) and two (blue) equivalents of TMSOTf in d_8−THF

The $^{13}C\{H\}$ spectrum in Figure 2.26 shows the resonances assigned to K[(Ph$_3$SiO)$_5$U(THF)] (red) completely disappear on addition of TMSOTf (green spectrum = 1 eq. and blue spectrum = 2 eq.). The spectra showing the products of the reaction between one and two equivalents of TMSOTf and K[(Ph$_3$SiO)$_5$U(THF)] show four major resonances in a similar pattern to the familiar arrangement previously seen for K[(Ph$_3$SiO)$_5$U(THF)]. This is likely the result of a uranium complex, possibly the desired [U(OSiPh$_3$)$_{5-x}$OTf$_x$] but further analysis was difficult due to the intractable nature of the products. Further evidence for the hypothesised reaction (Scheme 2.16) can be gathered from the clear indication that TMSOSiPh$_3$ is synthesised. The resonances at δ 2.27 and 2.35 ppm are assigned to TMSOSiPh$_3$ and compare well with the previously assigned resonances from the reaction of Ph$_3$SiOH or Ph$_3$SiOK with TMSOTf in which the chemical shifts for TMSOSiPh$_3$

is assigned as δ 2.23 and 2.28 ppm respectively.

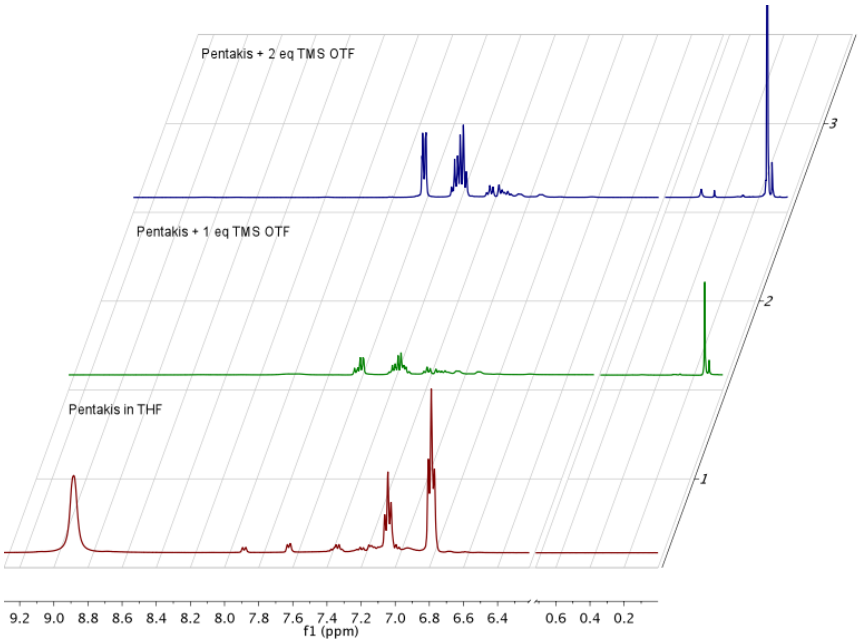

Figure 2.27: NMR Resonances for the ^{1}H spectrum of the reaction between K[$(Ph_3SiO)_5U(THF)$] (red) and one (green) and two (blue) equivalents of TMSOTf in d_8–THF

Figure 2.27 shows the ^{1}H NMR spectrum of the reaction between K[$(Ph_3SiO)_5U(THF)$] and TMSOTf and further supports the hypothesis in Scheme 2.16. The resonance at δ 0.11 ppm is assigned to **TMS**O$SiPh_3$ and was also observed from the reaction between Ph_3SiOH or Ph_3SiOK with TMSOTf. The intensity of the resonance increases as TMSOTf is added providing evidence that the addition of a second equivalent of TMSOTf removes more than one ligand from the uranium species K[$(Ph_3SiO)_5U(THF)$], which again is shown to completely react on the addition of just one equivalent on TMSOTf. Whilst the complex, K[$(Ph_3SiO)_5U(THF)$] is no longer observed, a new species with resonances in the aromatic region is identified and the resonances increase in intensity as TMSOTf is added. This is assigned tentatively to the desired complex, [$U(OSiPh_3)_{5-x}OTf_x$].

2.5.3 Characterisation of the reaction between K[$(Ph_3SiO)_5U(THF)$] and TMSOTf : Negative ion ESI HRMS

In addition to the NMR spectroscopy characterisation, negative ion ESI HRMS analysis was employed in order to establish whether the desired product [$U(OSiPh_3)_{5-x}OTf_x$] could be synthesised by removing a ligand from the uranium species K[$(Ph_3SiO)_5U(THF)$]. Each NMR spectroscopy sample as described above was also subjected to positive and negative ion ESI HRMS in order to identify products synthesised during the reaction, the results are shown in Table 2.10.

K[$(Ph_3SiO)_5U(THF)$] was first analysed by negative ESI HRMS without the addition of TMSOTf and the primary ion observed is at m/z 1614.48, as expected. A secondary ion is also observed at m/z 1370.44 which is assigned as [$U(OSiPh_3)_4O_2$]. This was likely formed on exposure to air during the ESI HRMS process.

On addition of one equivalent of TMSOTf to K[$(Ph_3SiO)_5U(THF)$], the primary ion observed at m/z 1488.34 is identified as the desired product, [$U(OSiPh_3)_4OTf$]. In addition, [$U(OSiPh_3)_3OTf_2$] is observed as a secondary product, indicating the ligand exchange is a favourable reaction. On addition of a second equivalent of TMSOTf a single ion peak at m/z 1235.06 is observed which is assigned as [$U(OSiPh_3)_2OTf_3$].

TMSOTf	HRMS m/z	Relative Intensity	Anion Assignment
0 eq.	1614.4829	0.74	[$U(Ph_3SiO)_5$]
	1370.4401	0.26	[$U(OSiPh_3)_4O_2$]
1 eq.	1488.3454	0.69	[$U(OSiPh_3)_4(OTf)$]
	1361.2143	0.31	[$U(OSiPh_3)_3(OTf)_2$]
2 eq.	1235.0673	1.00	[$U(OSiPh_3)_2(OTf)_3$]

Table 2.10: Negative ion ESI HRMS data of the reaction between K[$(Ph_3SiO)_5U(THF)$] and TMSOTf

The negative ion ESI HRMS data show that even when two equivalents of TMSOTf were added to K[$(Ph_3SiO)_5U(THF)$] the only negative ion observed is [$U(OSiPh_3)_2(OTf)_3$]. In order to balance the equation, other ions must be formed during the reaction and therefore positive ion ESI HRMS was employed.

2.5.4 Characterisation of the reaction between K[$(Ph_3SiO)_5U(THF)$] and TMSOTf : Positive ion ESI HRMS

To further investigate the reaction, positive ion ESI HRMS analysis was undertaken, the results of which are shown in Table 2.11. On addition of one or two equivalents of TMSOTf to K[$(Ph_3SiO)_5U(THF)$] the primary ion observed in both cases is K[$TMSOSiPh_3$] which shows the TfO^- exchanged with Ph_3SiO^-, providing further evidence of the proposed reaction scheme.

Similarly to the negative ion ESI HRMS results, the procedures in place to excluded air from the system were not rigorous enough and the air sensitive complex, K[$(Ph_3SiO)_5U(THF)$] reacted with oxygen to form $K_2[U(OSiPh_3)_4O_2]$. Due to this, oxygen based derivatives were observed as minor products throughout the experiment.

Analysis of the results unaffected by oxygen, showed K[$(Ph_3SiO)_5U(THF)$] reacted with one equivalent of TMSOTf to form [$U(OSiPh_3)_3(OTf)_3$] and [$U(OSiPh_3)_2(OTf)_4$] on addition of the second equivalent, highlighting the excellent substitution potential of TMSOTf. These negative and positive ion ESI HRMS lead to a chemical equation of;

$$10K[U(Ph_3SiO)_5]+13TMSOTf \rightarrow 7[U(OSiPh_3)_4(OTf)]+3[U(OSiPh_3)_3(OTf)_2]+13K[TMSOSiPh_3] \quad (2.5.1)$$

TMSOTf	HRMS m/z	Relative Intensity	Cation Assignment
O eq.	1465.3680	0.12	—
	1692.4103	0.88	$K_2[U(OSiPh_3)_5]$
1 eq.	387.0987	0.2	$K[TMSOSiPh_3]$
	1323.2942	0.27	$K_2[U(OSiPh_3)_3(OTf)O_2]$
	1395.3547	0.13	$K[U(OSiPh_3)_4O]$
	1450.4253	0.17	$K_2[U(OSiPh_3)_4O_2]$
	1511.1901	0.05	$[U(OSiPh_3)_3(OTf)_3]$
	1930.3151	0.17	—
2 eq.	387.0990	0.56	$K[TMSOSiPh_3]$
	1269.2176	0.10	$K[U(OSiPh_3)_3(OTf)O]$
	1385.0786	0.18	$[U(OSiPh_3)_2(OTf)_4]$
	2168.4412	0.16	—

Table 2.11: Positive ion ESI HRMS data of the reaction between $K[(Ph_3SiO)_5U(THF)]$ and TMSOTf

2.6 UV–Vis spectroscopy $K[U(OSiPh_3)_5]$ and $K[(Ph_3SiO)_5U(THF)]$

The nature of actinide complexes, especially the early actinides, makes interpreting the electronic absorption spectra more difficult than those of the *d*–block metals or the lanthanides. This is due to several effects, including relativistic effects on the energy, the presence of spin–orbit coupling that is substantial and the greater degree to which the 5*f* orbitals interact with the ligands.

There are two descriptions of spin–orbit coupling that reflect the possible extremal interactions between the orbital motion of the electron, denoted by *l*, the orbital quantum number, and the intrinsic angular momentum of the electron, denoted by *s*.

In the case when the orbital motion of the electron is such that the magnetic field, due to motion of the nucleus in the rest–frame of the electron, is so large that the interaction of

the individual spin with the individual motion is so strong that it is best described by an individual vector sum of these momenta, denoted as *j*. These individual *j*–momenta then sum together to give the total angular momentum of the system, *J*. This is the *jj* coupling scheme. Under this scheme, the inter–electron repulsions are much smaller than the spin–orbit coupling scheme.

The other case occurs when the electron–electron momenta dominate and the field, due to the motion of the nucleus, is small. In this case, the momenta due to the orbital motions couple to give a resultant *L* and the spin–spin interation couple to yield *S*; these two momenta then form the resultant total angular momentum of the state, denoted by *J*. This is the Russell–Saunders or *LS* coupling scheme. The Russell–Saunders coupling scheme treats spin–orbit coupling as much weaker than inter–electronic repulsions

In either case, the energy due to the spin–orbit interaction is the same and is given by

$$E_{SO} = \frac{\lambda}{2}\left(J\left(J+1\right) - L\left(L+1\right) - S\left(S+1\right)\right) \tag{2.6.1}$$

where λ represents the spin–orbit coupling constant, which is the average of the variation of the radial potential for the electron concerned and therefore represents the radial portion of the energy term. As $\lambda \propto Z^4$, then the magnitude of the splitting is very sensitive to the atomic number Z.[113]

The 'intermediate coupling scheme'[114] lies between these two schemes and applies when the interelectron repulsions are of a similar magnitude to the spin–orbit coupling. Actinide chemistry is therefore complex as, in general, actinides in fact lie somewhere between the two models. In practice this results in significantly altered absorption spectra from the smallest change in ligand set for any given actinide in any given oxidation

state.[2,115]

Due to the relatively large size of the 5*f* orbitals of the actinides, the electrons overlap much more significantly with the orbitals of the ligand systems than the 4*f* orbitals of the lanthanide species. This in turn causes much higher extinction coefficients and in addition, the overlapping with the ligand orbitals forming a covalent bond, increases the orbital size. This is due to the resulting molecular orbital formed from the two atomic orbitals (nephelauxetic effect). These effects cause a much greater variation (position and intensity) in the resulting electronic absorption spectra for actinide species.[2] In addition the electronic dipole transitions are normally forbidden but in the presence of an asymmetric ligand field, the transition can be allowed. This can occur by a permanent distortion in the dipole or by a temporary coupling with an asymmetric metal–ligand vibration also referred to as vibronic coupling.[2]

Other transitions, apart from the *f*–*f* transitions, which are formally not allowed (Laporte rule) can occur. Firstly, *f*–*d* transitions, which are formally allowed, occur above 20000 cm^{-1} (500 nm) and are normally broad and intense. This is due to the large energy gap between the 5*f* orbitals and the energetically higher, 6*d* orbitals (albeit smaller than 4*f* to 5*d* transitions). Finally, metal–ligand charge–transfer (MLCT) transitions are observed in the actinides and are normally found in the UV region. The peaks are again normally broad and intense and the tails of such peaks are commonly seen in the visible region. It is normally the MLCT transitions that are responsible for the intense colours frequently observed in the actinides.

Despite the difficulty of assigning the electronic absorption spectra for actinides, work has been carried out to assign the bands observed for simple complexes such as f^2 systems. Figure 2.28 is reproduced from literature sources[2,116] and shows the calculated ground state of such a system to be $^3H_4$. Due to the relatively large nature of the 5*f* orbitals,

the energy levels are more sensitive to the coordination number of the complexes. For example, differences can be observed between the spectra of the 6 coordinate, $[UCl_6]^{2-}$ and that of aqueous U^{IV}.[2] As a result, the interpretation of actinide electronic absorption spectra should be carried out individually on each compound.[115]

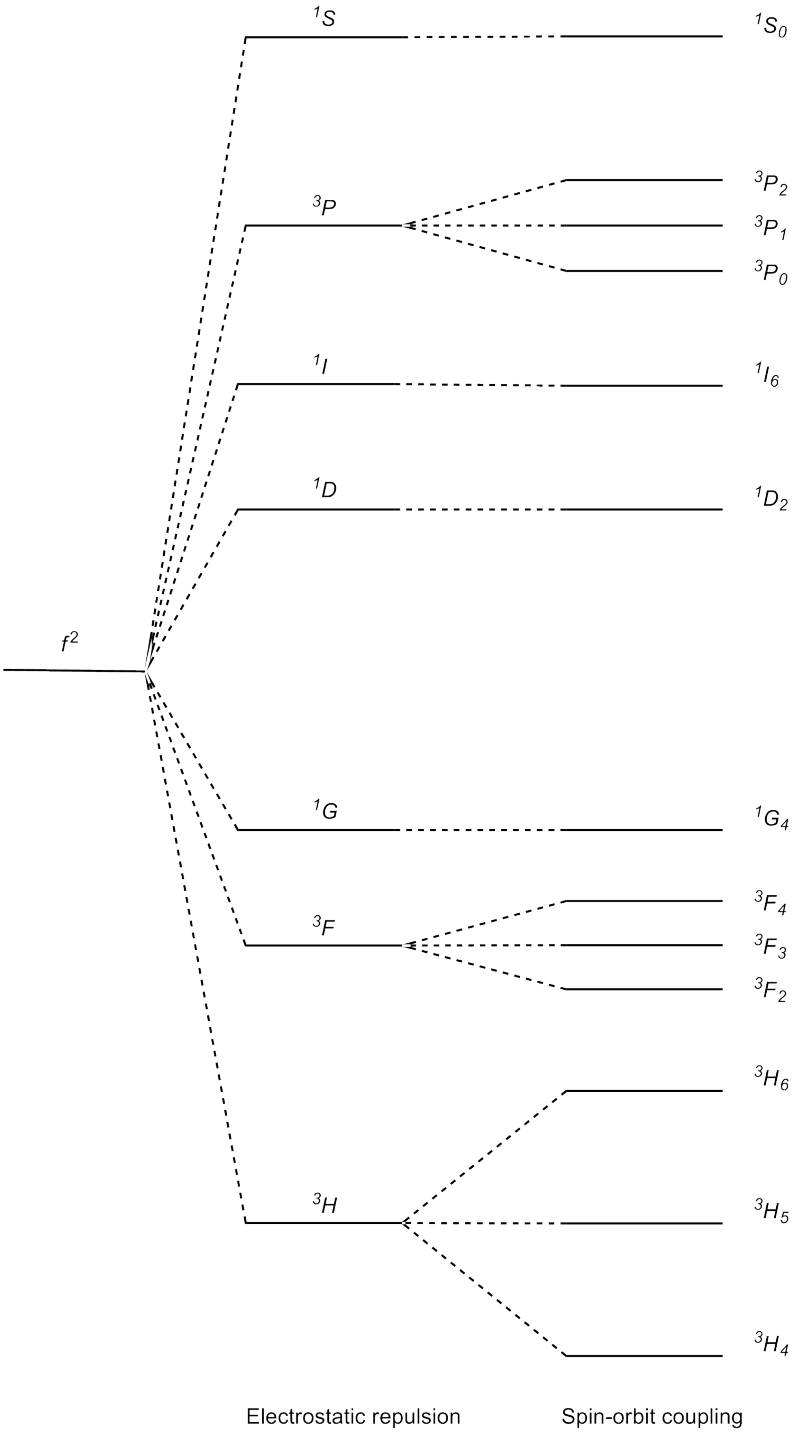

Figure 2.28: Qualitative energy level diagram for an f^2 system such as UCl_4 showing the effects of electrostatic repulsion and spin–orbit coupling

The electronic absorption spectra of UCl_4 in THF is shown in Appendix K.1 and clearly shows nine absorption bands which are also shown in Chapter 7. These bands correlate well with literature sources and are assigned accordingly.[117–119] Analysis further into the UV region (below 400 nm) proved problematic due to the high levels of 'noise' in this region and the LMCT bands that are likely the source of the intense green colour of UCl_4 were not clearly observed. UCl_4 was also analysed in toluene, shown in Appendix K.2 and clearly shows seven absorption bands which are also assigned accordingly in Table 7.3.

All the complexes synthesised as part of this work so far are U^{IV} and therefore f^2 systems, however, they do possess different coordination numbers. The $K[U(OSiPh_3)_5]$ complex has a coordination number of five, whilst the $K[(Ph_3SiO)_5U(THF)]$ complex has a coordination number of six, which should result in different electronic absorption spectra. In addition, the $K[U(OSiPh_3)_5]$ complex does not possess perfect symmetry and the crystal structure of $K[(Ph_3SiO)_5U(THF)]$ was not obtained, but for the purposes of assigning electronic absorption spectra, the symmetry groups D_{3h} for ($K[U(OSiPh_3)_5]$) and C_{4v} for ($K[(Ph_3SiO)_5U(THF)]$ is investigated.

The electronic absorption spectra of $K[U(OSiPh_3)_5]$ in THF and toluene both exhibit moderate absorptions in the visible region with extinction coefficients in the region of 3–25 M^{-1} cm^{-1}. These extinction coefficients are indicative of *f*–*f* transitions.[120] Figure 2.29 shows the absorptions observed in THF and Table 2.12 assigns these peaks based on previously reported cases of six coordinate f^2 uranium complexes.[119] Appendix K.10 shows the same complex but dissolved in toluene and is also reported in Table 2.12 with tentative assignments based on previously reported five coordinate f^2 uranium compounds.[119] In general terms the more polar the solvent the broader the bands are likely to be, with the less polar solvents showing far greater resolution. The polar solvents can

interact with the solute through intermolecular bonding which is seen in the molecular structure of $[K(py)_6][(Ph_3SiO)_5U(py)]$ and presumed to be true in the $K[(Ph_3SiO)_5U(THF)]$ structure. If the solvent aligns its dipole moment with that of the solute the ground state and the excited states of the solute can increase or decrease and change the frequency of the absorbed photon causing the different transition energies which then become 'averaged', causing peak broadening. Non polar solvents however, can interact through polarizability via London interactions (induced–dipole–induced–dipole interactions between molecules).

Comparing $K[(Ph_3SiO)_5U(THF)]$ to $K[U(OSiPh_3)_5]$ the data in Table 2.12 shows several bands of the same or similar wavelengths. In addition, there are four peaks in the spectrum of $K[(Ph_3SiO)_5U(THF)]$, not observed in the $K[U(OSiPh_3)_5]$ spectrum at 397.5, 525.5, 652.6 and 716.0 nm and the $K[U(OSiPh_3)_5]$ spectrum shows two peaks at 607.5 and 735.5 nm. These transitions must therefore be assigned to transitions effected by the change in symmetry. It must be noted that due to the reasons outlined above these conclusions and assignments are tentative.

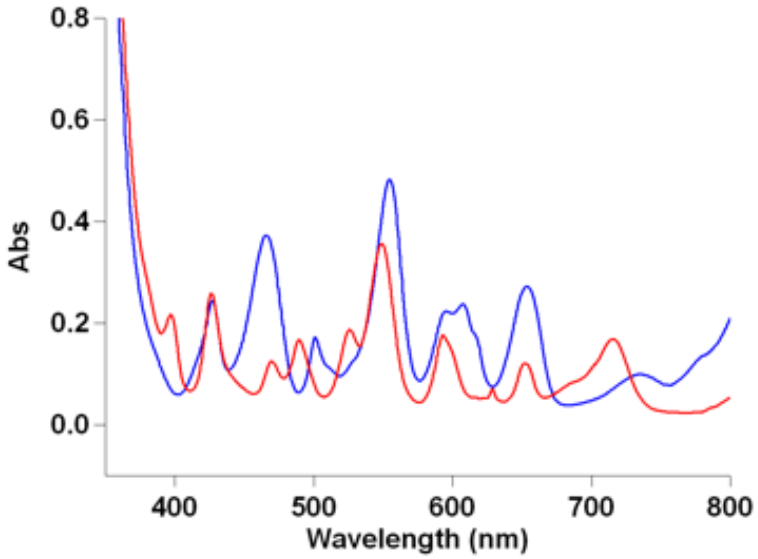

Figure 2.29: UV–Vis spectrum for $K[(Ph_3SiO)_5U(THF)]$ in THF (Red) and $K[U(OSiPh_3)_5]$ in Toluene (Blue)

Compound	λ / nm	ϵ / L mol^{-1} cm^{-1}	A	Assignment
K[$(Ph_3SiO)_5U(THF)$]	397.5	11.42	0.216	$^3P,^1D$[119]
	426.5	13.69	0.259	—
	469.5	6.61	0.125	—
	489.5	8.83	0.167	—
	525.5	9.89	0.187	^3P[119]
	549.0	18.87	0.357	^3P[119]
	593.1	9.31	0.176	$^1D,^3P$[119]
	628.5	3.75	0.071	—
	652.6	6.40	0.121	—
	716.0	8.94	0.169	—
K[$U(OSiPh_3)_5$]	427.5	12.37	0.245	—
	466.0	18.84	0.373	—
	501.0	8.74	0.173	^3P[119]
	554.6	24.39	0.483	^3P[119]
	595.4	11.31	0.224	$^1D,^3P$[119]
	607.5	11.97	0.237	—
	654.0	13.74	0.272	—
	735.5	5.05	0.100	—

Table 2.12: Molar absorptivity (ϵ) of K[$U(OSiPh_3)_5$] and K[$(Ph_3SiO)_5U(THF)$] with tentative assignments

2.6.1 Formation of K[$(Ph_3SiO)_5U(THF)$] : UV–Vis spectroscopy

Analysis of each step of the K[$(Ph_3SiO)_5U(THF)$] synthesis by UV–Vis spectroscopy were conducted. Accurate concentrations were recorded of UCl_4 in THF and 5 x 1 eq. of Ph_3SiOK. Each single ligand equivalent was added to the UCl_4 in turn and analysed by UV–Vis spectroscopy of which the full spectra are shown in Appendices K.1, K.3, K.4, K.5, K.6 and K.7. The results of the experiments were hindered by the production of

the side product, KCl suspended in the solution. Attempts were made to remove KCl by filtration but this affected concentrations making the identification of isosbestic points challenging. The results here were obtained by reacting Ph_3SiOK with UCl_4 and waiting for the KCl to settle prior to UV–vis analysis.

The graphs in the appendices and Figure 2.30 clearly show the reaction progression. The data indicates that UCl_4 (black line) reacts immediately with just one equivalent of the ligand, Ph_3SiOK. With the UCl_4 completely reacted, the changes observed are suggestive of the production of a new species. Despite the issues surrounding the production of KCl, three isosbestic points were observed and highlighted by the red boxes in Figure 2.30.

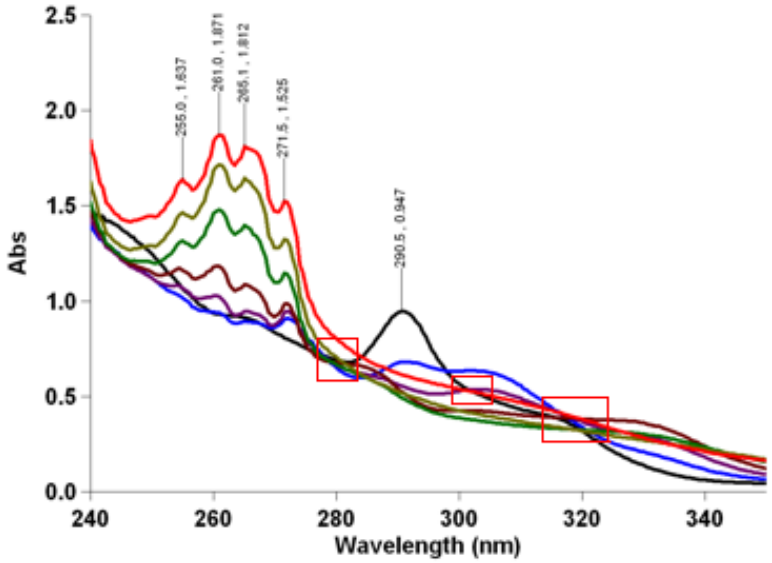

Figure 2.30: UV–Vis spectrum of UCl_4 and the addition of Ph_3SiOH in one equivalent aliquots (Black=UCl_4; Blue=1eq; Purple=2eq; Brown=3eq; Green=4eq; Olive=5eq; Red=6eq) with isosbestic points

Isosbestic points are indicative of only two dominant species present in the reaction solution. If two species have equal values for the molar absorption coefficients at the same wavelength, the likelihood of a third species also possessing the same molar absorption coefficient is so remote, the information is generally considered to be confirmation of two dominant species. The first isosbestic point at 280 nm highlighted in Figure 2.30

seems to indicate that up to five equivalents, there are two dominant species. On the addition of the sixth equivalent (red line), the isosbestic point is no longer observed and therefore more than two dominant species are likely to be present which is also seen in Section 2.4.2. The second isosbestic point is clearer at 300 nm with the UCl4, second and sixth equivalent lines all crossing. Finally at 320 nm, up to two isosbestic points can be determined.

Chapter 3

Reactivity Studies of $K[(Ph_3SiO)_5U]$

As $K[(Ph_3SiO)_5U]$ proved to be a viable and stable siloxide complex, it was prudent to investigate it in terms of its reactivity, especially as the two complexes, $K[(Ph_3SiO)_5U(THF)]$ and $([K(py)_6][U(OSiPh_3)_5(py)])_2$ formed six coordinate complexes whilst the $K[(Ph_3SiO)_5U]$ was only a five coordinate. It seemed probable that the five coordinate complex could, sterically at least, sustain a further bonded species and therefore a variety of small molecules were reacted with the complex as shown in Scheme 3.1.

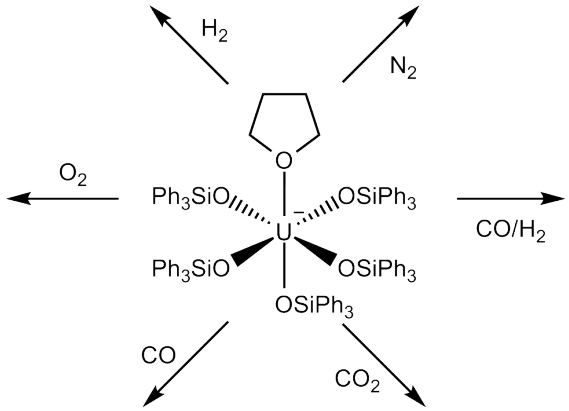

Scheme 3.1: Reactivities of $K[(Ph_3SiO)_5U(THF)]$ that were investigated, $K[(Ph_3SiO)_5U]$ was investigated with the same small molecules

Both the complexes $K[(Ph_3SiO)_5U]$ and $K[(Ph_3SiO)_5U(THF)]$ were investigated in terms of their reactivity with small molecules and the reaction with O_2 showed promising results.

As uranium has a predisposition to form the dioxo species with the two oxygen atoms located in the *trans* positions, work was also carried out to identify this species and if a monooxo species could be synthesised. Monooxo species by comparison, are rare, with only 18 publications containing 24 monooxo examples found in the literature. Of these, five are RN=U=O species, which are isolobal with O=U=O. From the remaining monooxo examples, most are synthesised via an oxygen atom donor reaction and only one is synthesised by reacting with carbon dioxide.

3.1 Uranium dioxo species

The uranyl group, UO_2^{2+} is the most common uranium oxide species and is normally linear rather than bent as is found in transition metals and earlier actinides such as thorium. This is thought to be due to the large energy gap between the 5*f* orbitals and the energetically higher 6*d* orbitals. Whilst thorium is able to use its 6*d* orbitals to overlap with the *p* orbitals on the ligand, uranium can bond with an *f*–*p* overlap as shown in Figure 3.1.[2]

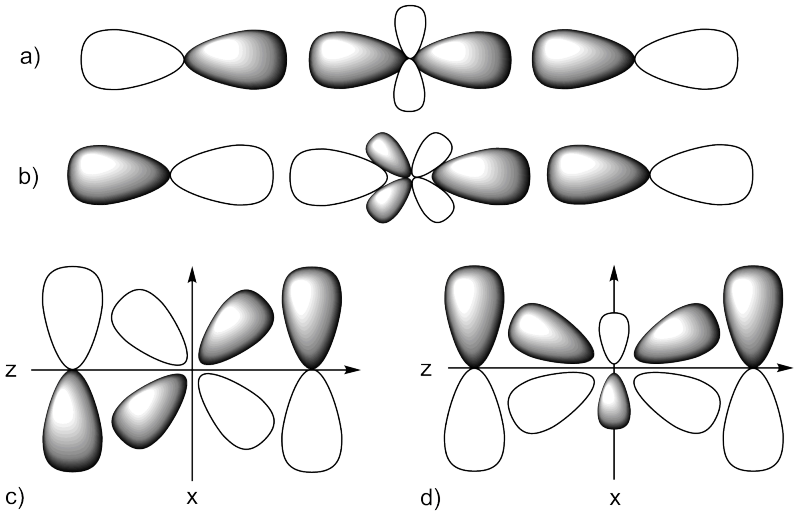

Figure 3.1: σ and π–bonding in the uranyl ion $[UO_2]^{2+}$: a) σ_g–bonding in the uranyl ion; b) σ_u–bonding in the uranyl ion; c) π_u–bonding – d_{xz}–p_x overlap; d) π_g–bonding – f_{xz^2}–p_x overlap[2]

A literature search for all uranyl species gave an average U–O bond length of 1.767 Å

and a range of 1.359 Å to 1.961 Å.[85] The UO_2^{2+} uranyl group can be easily detected by IR spectroscopy with a strong band in the region of 920–980 cm^{-1}, caused by the asymmetric O–U–O stretching vibration and a band around 860 cm^{-1} in the Raman spectrum caused by the symmetric O–U–O stretching vibration.[2] In the electronic absorption spectra fine structure can be observed due to the symmetric uranyl stretching vibrations in uranyl complexes, normally around 450 nm.[2] The UO_2^{+} species also exists but is less common due to its relative instability, compared to the UO_2^{2+} uranyl group.

Table 3.1 summarises calculated U–O bond lengths and compares these with calculated U–N species.[121] From this information a pattern can be observed in the bond lengths, as the UO_2^{n+} species changes from U^{VI} to U^{IV} the bond length increases. Finally, by comparing the $[UO_2]$ and $[UN_2]$ moiety by calculation, it was observed that the bond lengths are relatively similar.[121]

Species	Bond Length / Å
UO_2^{2+}	1.6718
UO_2^{+}	1.7410
UO_2	1.8305
UN_2	1.8645

Table 3.1: Calculated Relativistic U–O Bond Lengths

3.1.1 Uranyl halides, UO_2^{2+}

The majority of known U^{VI} complexes contain the UO_2 group with a few exceptions and uranyl halides are well studied and provide a convenient entry into dioxo structures.[122,123] UO_2F_2 derivative is synthesised by reacting UO_3 with gaseous anhydrous HF at temperatures which can range from 350 to 500 °C in a nickel reactor.[124] The dichloride derivative $UO_2Cl_2(THF)_3$[125] is prepared utilising a simple one pot dehydration of

$UO_2Cl_2 \cdot x(H_2O)$ and the diiodide derivative, UO_2I_2[126] is synthesised by reacting uranyl triflate with iodotrimethyl silane and recrystallisation from pyridine gives $UO_2I_2(py)_3$.[126] Key characterisation data are summarised in Table 3.2 for these compounds along with a sample of other uranyl halide species.

Compound	U=O_{uranyl} bond length / Å	Stretching frequency / cm^{-1}
UO_2F_2[124,127]	1.74	900–985
$UO_2Cl_2(THF)_3$[125]	1.766(6), 1.765(6)	875, 841
$[UO_2Cl_4]^{2-}$[128,129]	1.76	908[a]
$UO_2Br_2.3\,H_2O$[130]	1.73(1)	—
UO_2I_2[126]	—	988, 982
$UO_2I_2(py)_3$[126]	1.757(6), 1.754(6)	927
$UO_2I_2(OPPh_3)_2$[130]	1.760(4)	—

Table 3.2: O**U=O**$_{uranyl}$ bond lengths and stretching frequencies for selected uranyl compounds
a = Computational data

The bond distances observed in the uranyl halides derivatives give an average U=O_{uranyl} bond length of 1.753(7) Å which is slightly longer than that predicted in Table 3.1 (1.6718 Å). In addition this analysis gives an IR range of 841cm^{-1} to 988cm^{-1}. These data will provide a good basis for comparison with the dioxo and monooxo examples discussed in the following sections.

3.2 Uranium monooxo species

3.2.1 Reactions with uranium oxide halides

Reported in the 1970's, the first monooxos were UOF_4[131,132] and $[UOCl_5][Ph_4P]$[128,133] and these became versatile and valuable precursors for a number of monooxo com-

pounds. Characterising data are summarised in Table 3.3.[128,132] The compounds listed are all U^{VI} compounds and together give an average U–O_{oxo} bond length of 1.77(1) Å. Further data on these monooxo compounds are unfortunately lacking, with only the U–O_{oxo} stretching frequencies reported. The data indicate that a strong peak indicative of a U–O_{oxo} stretch is commonly found in the region of 900 cm^{-1} with weaker bands possible in the same region. Specific values for these starting materials are shown in Table 3.3

Compound	U–O_{oxo} bond length / Å	Stretching frequency / cm^{-1}
UOF_4[132]	1.77(3)–1.79(2)	891
$[UOCl_5][Ph_4P]$[128,133]	1.76(1)	838, 928

Table 3.3: U–O_{oxo} bond lengths and stretching frequencies for selected U^{VI} monooxo starting materials

These starting materials are precursors for the development of other U^{VI} monooxos. $UOCl_4(NP(m-Tol)_3)$[134], $[Ph_4P][UOCl_4(NSPh_2)]$[135], $[Ph_4P][UOCl(NS(p-ClC_6H_4)_2)]$[135] and $[Ph_4P][UOCl_4(NPPh_3)]$[135] are all examples of this and the characterisation data that are available are summarised in Table 3.4. Analysis shows the average U–O_{oxo} bond length in these complexes is 1.77(4) Å. This value is almost identical to the previously discussed average for the monooxo starting materials and is therefore a good approximation of monooxo U–O_{oxo} bond lengths in U^{VI} compounds.

Of these U^{VI}complexes only two have had the U–O_{oxo} stretching frequencies, reported as 850 cm^{-1} and 845 cm^{-1} for $UOCl_4(NP(m-Tol)_3)$[134] and $[Ph_4P][UOCl_4(NSPh_2)]$[135] respectively. Comparing these values to the previously discussed IR frequencies it shows that U^{VI} monooxo complexes generally have an observed U–O_{oxo} stretching frequency within the range of 800–900 cm^{-1} with weaker bands falling outside of this range. Unfortunately no further data regarding this type of compound in different oxidation states are available, therefore comparisons must be made to a second class of monooxo com-

pounds which are synthesised from oxygen atom donor reactions and are discussed in section 3.2.2.

Compound	U–O_{oxo} bond length / Å	Stretching frequency / cm^{-1}
$UOCl_4(NP(m-Tol)_3)$ [134]	1.759(13)	850
$[Ph_4P][UOCl_4(NSPh_2)]$ [135]	1.786(3)	845
$[Ph_4P][UOCl(NS(p-ClC_6H_4)_2)]$ [135]	—	—
$[Ph_4P][UOCl_4(NPPh_3)]$ [135]	1.777(3)	—

Table 3.4: U–O_{oxo} bond lengths and stretching frequencies for selected U^{VI} monooxo compounds

$[K(18-crown-6)(Et_2O)]\,[UO(\mu_2-NCH_2CH_2N(CH_2CH_2NSiBu^tMe_2)_2)]_2$ [136], shown in Figure 3.2 is particularly interesting as it is currently the only known dimer and is synthesised from the uranyl starting material $[K(18-crown-6)]_2[UO_2Cl_4]$. It is reported to have a mixed valency of $U^{V/VI}$ and the U–O_{oxo} bond length is observed at 1.838(5) Å. The compound is structurally equivalent between the two monomeric units (indicated by an inversion centre at the midpoint of the compound). This means there is no way of accurately assigning separate oxidation states to either uranium centre crystallographically, giving a possible valence average of $U^{5.5}$ via delocalisation or rapid intramolecular electron transfer of the unpaired electron. The U–O_{oxo} stretching frequency of this complex is observed and reported at 827 cm^{-1} which is as expected if the electron density on the metal centre is considered. As the oxidation state decreases from U^{VI} to U^{V}, the electron density will increase. Therefore the bond length will increase proportionately, weakening the bond and reducing the IR stretching frequency.

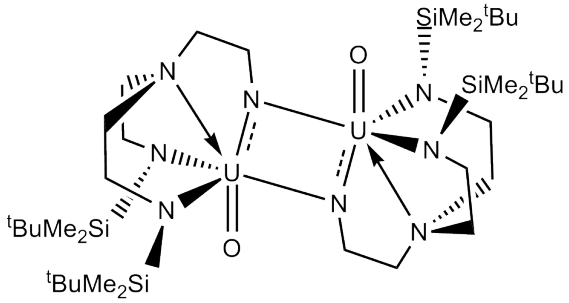

Figure 3.2: The mixed valent ($U^{V/VI}$) dimeric monooxo complex, $[K(18-crown-6)(Et_2O)][UO(\mu_2-NCH_2CH_2N(CH_2CH_2NSiBu^tMe_2)_2)]_2$

3.2.2 Oxygen atom donor reactions

Terminal monooxo compounds resulting from oxygen atom transfer reactions are more commonly found in literature and include a fair number of examples of U^{V} and U^{VI} oxidation states. There are also a few examples of U^{IV} monooxo complexes, but these are rare and, of the few that have been reported, not all have been fully characterised.

Uranium IV compounds

Due to the greater electron density on U^{IV} metal centres, it is expected that the U–O_{oxo} bond lengths of these species would be greater than those of U^{V} or U^{VI} compounds.

$Tp^*_2U(O)$[137] and $Cp^{'}_2U(O)$[138] are synthesised using the oxygen atom donor pyridine–*N*–oxide, but unfortunately suitable X–ray quality single crystals of the latter complex were not able to be grown and therefore X–ray data on the complex are lacking. A third monooxo compound synthesised via serendipitous oxygen was $Cp^*_2U(O)[C(NMeCMe)_2]$ and provides an interesting insight into U^{IV} monooxo compounds.[139]

The available characterisation data for these structures are shown in Table 3.5. The information gives an average U^{IV}-O_{oxo} bond length of 1.890(5) Å and this fits the hypothesis that U^{IV} complexes have longer terminal oxo bonds when compared to the previously dis-

cussed U^{VI} monooxo starting materials and their direct products (section 3.2.1). No IR data have been reported to date on U^{IV} complexes.

Compound	Oxygen atom donor	U–O_{oxo} bond length / Å
$Tp^*_2U(O)$[137]	pyridine–*N*–oxide	1.863(4)
$Cp^{'}2U(O)$[138]	pyridine–*N*–oxide	—
$Cp^*_2U(O)[C(NMeCMe)_2]$[139]	—	1.917(6)

Table 3.5: U–O_{oxo} bond lengths for selected U^{IV} monooxo compounds synthesised from oxygen atom donor reactions

Uranium V compounds

U^V monooxo complexes resulting from oxygen atom donor reactions are more commonly found in literature. Pyridine–*N*–oxide, is commonly used as the oxygen atom transfer reagent in the synthesis of monooxo compounds and $(Cp^*)_2U(O-dipp)(O)$[140] (dipp = 2,6–diisopropylphenyl) is an example. Also, $(1,2,4-(Me_3C)_3C_5H_2)_2U(O)(py)$ is synthesised and the addition of $Me_2NC_5H_4N$ (dmap) displaced the pyridine to give the complex, $(1,2,4-(Me_3C)_3C_5H_2)_2U(O)(dmap)$ as a second U^V complex.[138] The pyridine derivative proved unstable but the dmap derivative gave quality single crystals for X–ray characterisation.

Another commonly found oxygen atom donor is trimethylamine–*N*–oxide. When reacted with $[U(NN'_3)(CH_3PMe_3)]$ (NN'_3 = $N(CH_2CH_2NSiMe_2{}^tBu)_3$), $[U(NN'_3)(O)]$[141] was synthesised. Unfortunately, full characterisation could not be achieved as the purification steps proved difficult and X–ray quality single crystals could not be grown.

Water is not a compound frequently used as an oxygen atom donor in uranium chemistry, but the uranium imido complex, $[U(N^tBu)(O)I_2(THF)(NH_2Ph)_2]$[142] was initially discovered

by accident due to traces of H_2O on glassware reacting with $[U(N^tBu)_2I_2(THF)_2]$. The complex was fully characterised but in order to develop a more rational synthesis for the discovery, further reactions with one equivalent of H_2O were carried out with little success. However, the use of $B(C_5F_5)_3{\cdot}H_2O$ proved fruitful, providing two characterised U^{VI} monooxo examples which will be discussed further in the section 3.2.2.

The product, $[Ph_3PCH_3][U(O)(CH_2SiMe_2N{-}SiMe_3)(NR_2)_2]$ was synthesised by reacting the previously discussed U^{IV} carbene with the widely used oxygen atom donor, TEMPO (TEMPO = 2,2,3,3–tetramethyl–piperidine–1–oxyl).[143] The product was then treated further to synthesise a U^{VI} complex which is discussed later.

Although the U^V complexes are in fact more commonly reported, the characterisation of such species has proved difficult and data are therefore limited. The data that are available are collated in Table 3.6 and this gives an average U^V-O_{oxo} bond length of 1.837(1) Å, which is as expected.

Compound	Oxygen atom donor	U–O_{oxo} bond length / Å
$(Cp^*)_2U(O{-}2,6{-}dipp)(O)$[140]	pyridine–*N*–oxide	1.859(6)
$(1,2,4{-}(Me_3C)_3C_5H_2)_2U(O)(py)$[138]	pyridine–*N*–oxide	—
$(1,2,4{-}(Me_3C)_3C_5H_2)_2U(O)(dmap)$[138]	pyridine–*N*–oxide	1.860(3)
$[U(NN'_3)(O)]$[141]	trimethylamine–*N*–oxide	—
$[U(N^tBu)(O)I_2(THF)(NH_2Ph)_2]$[142]	H_2O	1.781(4)
$[Ph_3PCH_3][U(O)(CH_2SiMe_2NSiMe_3)(NR_2)_2]$[143]	TEMPO	1.847(2)

Table 3.6: U–O_{oxo} bond lengths for selected U^V monooxo compounds synthesised from oxygen atom donor reactions

$(1,2,4{-}(Me_3C)_3C_5H_2)_2U(O)(dmap)$ and $(1,2,4{-}(Me_3C)_3C_5H_2)_2U(O)(py)$ have IR stretching frequencies reported at 765 cm^{-1} and 760 cm^{-1} respectively.[138] These two U^V complexes are unfortunately the only reported IR frequencies and whilst data on the other

complexes would have been desirable, these observed frequencies are lower than the previously discussed U^{VI} IR frequency range (section 3.2.1), which is as expected.

Regardless of synthetic methods or oxidation state, only two complexes have magnetic moment data reported. $[Ph_3PCH_3][U(O)(CH_2SiMe_2NSiMe_3)(NR_2)_2]$ exhibited an effective magnetic moment of 1.97 μ_B at 300 K and 1.47 μ_B at 4 K using SQUID magnetometry. This is comparable to the data reported for t[$U(NN'_3)(O)$] which exhibited an effective magnetic moment of 1.47 μ_B at 225–295 K which was analysed using the Evans method.

Uranium VI compounds

U^{VI} complexes are by far the most commonly found uranium monooxo compounds, although most of them are synthesised from U^{VI} starting materials and have therefore been discussed previously in section 3.2.1. The following examples are all synthesised from oxygen atom donor reactions.

$(Cp^*)_2U(dipp)(O)$[140] (dipp = 2,6–diisopropylphenyl) was synthesised from the addition of pyridine–*N*–oxide to a solution of $(Cp^*)_2U(dipp)(THF)$. A second example is the complex, $[Ph_3PCH_3][U(O)(CH_2SiMe_2NSiMe_3)(NR_2)_2$ which can undergo a one electron oxidation reaction resulting in the U^{VI} complex $U(O)(CH_2SiMe_2NSiMe_3)(NR_2)_2$.[143] Finally, the last U^{VI} complex to be discussed here is $[(BIPM)UOCl_2]$[144] (BIPM = $C(PPh_2NSiMe_3)_2$). The U^{VI} carbene was synthesised by treating $[(BIPM)UCl_3Li(THF)_2]$ with the oxygen atom donor 4–morpholine *N*–oxide. Once again the production of X–ray quality crystals was difficult, but disordered crystals were obtained and the data are quoted along with the other examples in Table 3.7. These data give an average U^{VI}–O_{oxo} bond length of 1.828(6) Å which gives a good approximation of the expected monooxo bond lengths to be found in a newly synthesised U^{VI} complex. More information can be gathered if the

isolobal nature of nitrogen and oxygen is considered.

Compound	Oxygen atom donor	U–O_{oxo} bond length / Å
$(Cp^*)_2U(N-2,6-diisopropylphenyl)(O)$ [140]	pyridine–*N*–oxide	1.844(4)
$U(O)(CH_2SiMe_2NSiMe_3)(NR_2)_2$ [143]	TEMPO	1.800(2)
$[(BIPM)UOCl_2]$ [144]	4–morpholine *N*–oxide	1.841(4)

Table 3.7: U–O_{oxo} bond lengths for selected U^{VI} monooxo compounds synthesised from oxygen atom donor reactions

3.2.3 Isolobal nitrogen species

Using the MLX electron counting system, an oxygen heteroatom is bonded in an X_2 fashion. The nitrene moiety, RN-, can be considered isolobal with oxygen, if bonded to the uranium centre in an X_2 manner. Ligands of the general formula RN=U are X_2 ligands with a lone pair also found on the nitrogen. On this basis, RN=U=O can be considered electronically equivalent to the uranyl species, O=U=O. The following reported U^{VI} monooxo complexes all have a nitrogen atom bonded to the uranium, which is considered isolobal to an oxygen atom and therefore can be thought of as a uranyl type species but they should not be dismissed completely as they are still technically monooxo species.

Of these complexes, three were synthesised from the starting material with the general formula, $(Cp^*)U(NAr)(L)$ (Ar = $(2,4,6-Me_3C_5H_2)$, $(2,6-iPr_2C_5H_3)$ or $(2,6-{}^tBu_2C_5H_3)$ and L = pyridine or THF).

Pyridine–*N*–oxide was used to donate an oxygen atom and formed $(Cp^*)_2U(O)(Ar)$ [145] (Ar = $(2,4,6-Me_3C_5H_2)$ or $(2,6-iPr_2C_5H_3)$) whilst $(Cp^*)_2U(O)(N-2,6-{}^tBu_2C_5H_3)$ [145] was synthesised from nitrous oxide (N_2O). In addition, following on from the previously discussed U^V complex and in search of a rational synthesis for the compound

$[U(N^tBu)(O)I_2(THF)(NH_2Ph)_2]$, two new U^{VI} complexes were synthesised using the oxygen atom donor, $B(C_6F_5)_3 \cdot H_2O$. Of the two products, $U(N^tBu)(O)I_2(THF)_2$[142] and $U(N^tBu)(O)I_2(Ph_3PO)_2$[142], only the latter could be fully characterised as the former complex was too badly disordered.

This analysis gives an average U–O_{oxo} bond length for U^{VI} complexes of the formula RN=U=O of 1.764(5) Å and combined with the previously discussed U^{VI} complexes, an average of 1.812(6) Å. As expected, this is shorter than the average U^{IV} and U^{V} monooxo bond lengths showing that the uranium centre is more contracted as the oxidation state increases.

Terminal U–O_{oxo} stretching frequency data are more extensively reported on U^{VI} complexes. The IR stretching frequencies of $U(N^tBu)(O)I_2(THF)_2$ and $U(N^tBu)(O)I_2(Ph_3PO)_2$ are observed at 883 cm^{-1} (KBr pellet) and 903 cm^{-1} respectively shown in Table 3.8.[142] $[(BIPM)UOCl_2]$ is observed to have an IR stretching frequency of 917 cm^{-1} shown in Table 3.7.[144] These complexes all fall within the expected range of IR stretching frequencies, higher than the previously discussed U^{V} values. $(Cp^*)_2U(O)(N{-}2,4,6{-}Me_3C_5H_2)$ and $(Cp^*)_2U(O)(N{-}2,6{-}{}^tBu_2C_5H_3)$ had reported IR stretching frequencies of 757 cm^{-1} and 755 cm^{-1} respectively.[145] These are lower than expected for U^{VI} complexes. The ligands on these complexes are far greater in size than the previously discussed ligand systems and will therefore effect the asymmetric stretching of the molecule and consequently the stretching frequencies.

3.3 Small molecule activation

Perhaps most relevant to this work, due to its reactivity with a small molecule, is the monooxo complex synthesised by reacting the U^{III} aryl oxide substituted triazacyclonon-

Compound	Oxygen atom donor	U–O_{oxo} bond length / Å	Stretching frequency / cm^{-1}
$(Cp^*)_2U(O)(N{-}2,4,6{-}Me_3C_5H_2)$ [145]	pyridine–*N*–oxide	—	757
$(Cp^*)_2U(O)(N{-}2,6{-}iPr_2C_5H_3)$ [145]	pyridine–*N*–oxide	—	—
$(Cp^*)_2U(O)(N{-}2,6{-}{}^tBu_2C_5H_3)$ [145]	N_2O	—	755
$U(N{}^tBu)(O)I_2(THF)_2$ [142]	$B(C_6F_5)_3 \cdot H_2O$	—	883
$U(N{}^tBu)(O)I_2(Ph_3PO)_2$ [142]	$B(C_6F_5)_3 \cdot H_2O$	1.764(5)	903

Table 3.8: RN=**U–O_{oxo}** bond lengths and stretching frequencies for selected U^{VI} monooxo compounds synthesised from oxygen atom donor reactions

ane complex, $[((^RArO)_3tacn)U(NMes)]$ (R = ^{t}Bu or Ad) with CO_2 as shown in Scheme 3.2.[146] The U^V products, $[((^RArO)_3tacn)U(O)]$ are fully characterised and U–O_{oxo} bonds are observed to be 1.848(8) Å where R = ^{t}Bu and 1.848(4) Å where R = Ad. These data are comparable to the previously discussed U^V monooxo species which have an average U–O_{oxo} bond length of 1.837(1) Å. The side product from this reaction is R−NCO and it is hypothesised that it is the generation of this isocyanate that provides the driving force for the reaction.

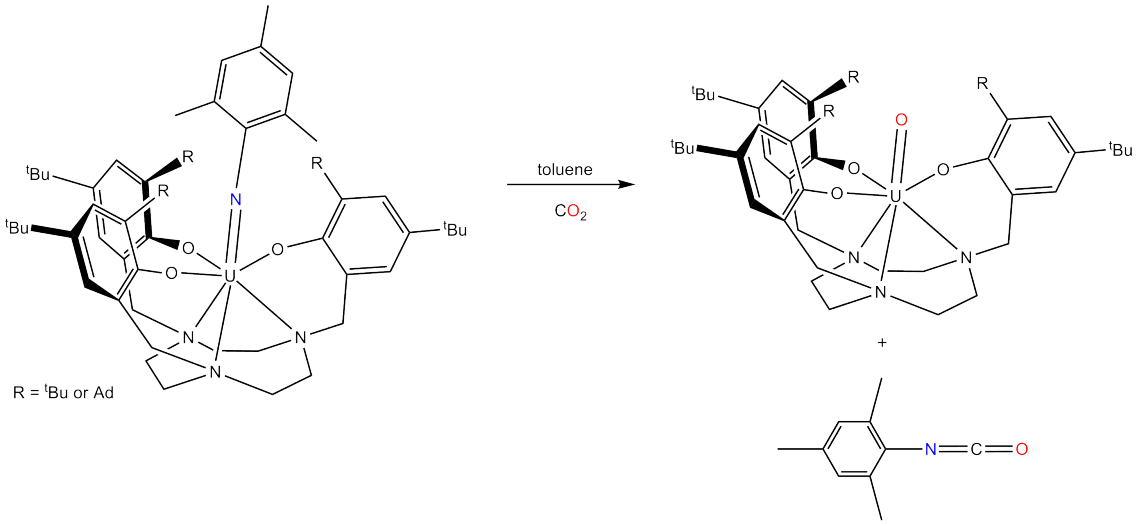

Scheme 3.2: Synthesis of U^V imido and U^V oxo complexes

Electronic absorption spectra were studied in the range of 300 to 2100 nm. Both the U^V complexes lack the strong ligand to metal charge transfer bands which were observed

for the respective starting materials. Instead the complexes possess a different set of absorption bands. Four, sharp and low intensity bands were observed at λ_{max} = 1770 nm, 1480 nm, 1205 nm and 850 nm. In addition a shoulder was observed at 585 nm. The distinct absorption bands were attributed to *f*–*f* transitions but were unable to be compared to other U^V oxo species, because none have been fully characterised in this way.

SQUID data were also collected on the two U^V species. [((^{tBu}ArO)$_3$tacn)U(O)] had an effective magnetic moment ranging from 1.61 to 1.98 μ_B with a temperature range of 5–300K. For [((^{Ad}ArO)$_3$tacn)U(O)], the effective magnetic moment value ranged from 1.49 to 1.92 μ_B over the same temperature range. Calculated values at 0 K were 1.19 and 1.36 μ_B respectively.

Whilst these terminal monooxo complexes provide interesting and much needed information about the reactivity of uranium and its compounds, none provide conclusive evidence of a uranium terminal monooxo species which has been synthesised from O_2 alone.

3.4 Synthesis and characterisation of $K_2[(Ph_3SiO)_4UO_2]$

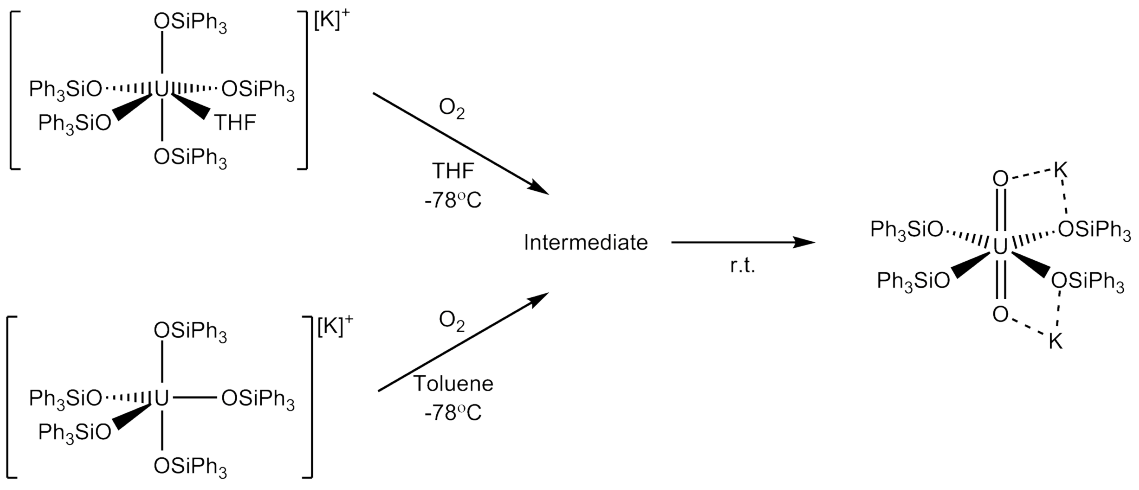

Scheme 3.3: Synthesis of $K_2[(Ph_3SiO)_4UO_2]$

In order to understand the reactivity of K[$(Ph_3SiO)_5U(THF)$] and K[$U(OSiPh_3)_5$], they were separately exposed to one equivalent of oxygen at -78 °C in THF and toluene respectively.

K[$U(OSiPh_3)_5$] in toluene was reacted with one equivalent of O_2 at -78 °C. The solution turned from purple to brown and remained so whilst kept at low temperature. When the solution was warmed to room temperature it became yellow. The experiment was also run at room temperature alone and the brown intermediate colour was observed very briefly before turning yellow.

The reaction at -78 °C was repeated using K[$(Ph_3SiO)_5U(THF)$] in THF and the same observations were recorded. When the reaction was repeated at room temperature in THF, the brown intermediate colouration was not observed and the solution turned from pink to yellow in two hours indicating a faster reaction in a coordinating solvent. From the resulting yellow solution, at room temperature, one crystal was isolated from a solvent system of benzene/pentane. X–ray and react IR analysis showed the product to be $K_2[(Ph_3SiO)_4UO_2]$ and are discussed below.

3.4.1 Characterisation of $K_2[(Ph_3SiO)_4UO_2]$: X–ray Diffraction

The complex crystallises in space group P-1 with an *R* factor of 3.55. The lattice parameters for this structure are *a* = 13.7729(3) Å, *b* = 14.3688(3) Å, *c* = 19.3087(3) Å, α = 101.0470(10) °, β = 90.5910(10) °, γ = 91.9460(10) °.

From the molecular structure shown in Figures 3.3 and 3.4 the molecule is observed to have a square bipyramidal geometry consisting of four equatorial siloxide ligands and two oxygen atoms in a *trans* arrangement. It has two potassium counter–ions which co–ordinate to the oxygen atoms and three phenyl rings each (K_1 = η^3, η^1, η^1; K_2 = η^6, η^6, η^1).

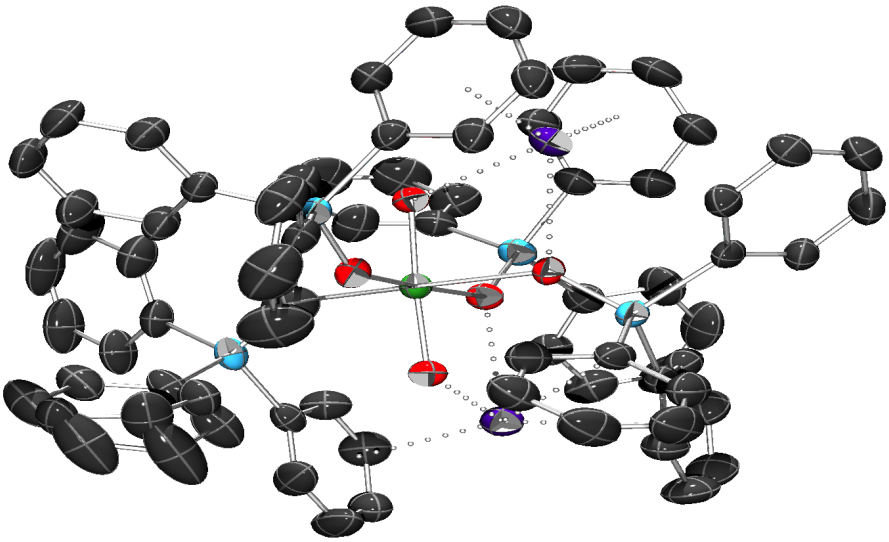

Figure 3.3: Molecular structure of $K_2[(Ph_3SiO)_4UO_2]$ (Hydrogen atoms omitted for clarity)

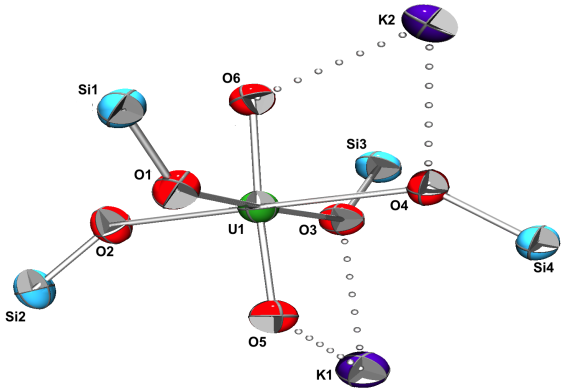

Figure 3.4: Core molecular structure of $K_2[(Ph_3SiO)_4UO_2]$ containing the Si, O U and K atoms (Hydrogen atoms and phenyl rings omitted for clarity)

The four equatorial siloxide ligands have an average U–O_{silox} bond length of 2.247(7) Å with a small range of 2.210(2) Å to 2.286(2) Å giving the complex a good level of symmetry. Comparing these data to the $K[U(OSiPh_3)_5]$ complex shows the U–O_{silox} bond has lengthened slightly in the dioxo species (0.066 Å).

The two U–O_{uranyl} bonds are observed at 1.824(2) Å and 1.819(2) Å and are closest to the $U^{IV}O_2$ species when compared to the data in Table 3.1. Electron counting the molecule suggests it is a U^{VI} species and therefore in order to ascertain if this discrepancy is consistent with other published material, a survey of six coordinate linear O=U=O uranium

complexes was undertaken, the results of which are shown in Figure 3.5. This analysis gave an average of 1.767 Å.[85] A wider analysis of experimental values showed the range of bond distances to be varied, whilst the data in Table 3.1 relates to the calculated average bond distances only. The bond lengths of the uranium species presented here are well within experimental range.

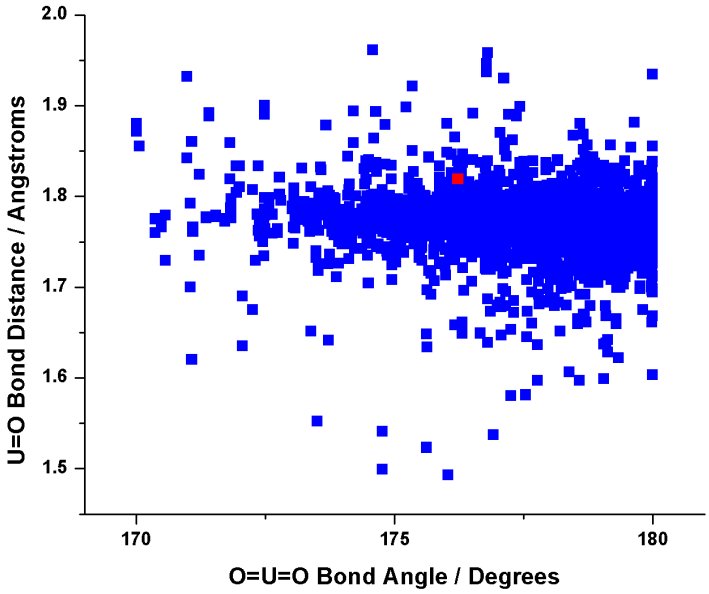

Figure 3.5: Comparison of U=O bond distances uranyl compounds. (Data points in red are the experimental values for $K_2[(Ph_3SiO)_4UO_2]$

3.4.2 Characterisation of $K_2[(Ph_3SiO)_4UO_2]$: React IR

Due to the difficulty in gathering NMR spectroscopy data, variable temperature IR spectroscopy was conducted on a React IR Toepler line. One equivalent of O_2 was reacted with $K[(Ph_3SiO)_5U(THF)]$ in THF at -78 °C, warming slowly to room temperature. THF was also analysed and the subsequent data were subtracted from the reaction with O_2 to ensure any activity in the spectra was solely due to the uranium species and subsequent reaction rather than a change in THF as the temperature varied. The data are shown in Figure 3.6 with the relevant peaks expanded in Figure 3.7.

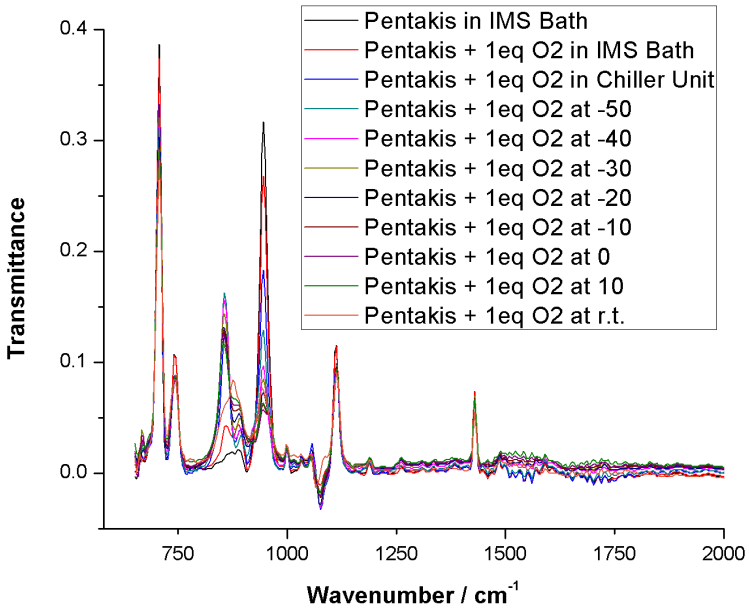

Figure 3.6: React IR Data of $(Ph_3SiO)_5UK + O_2$

As shown in Figure 3.7, a peak at 945.9 cm^{-1} starts to decrease as soon as O_2 is added to the system and continues to reduce as the reaction progresses to room temperature. A second peak at 893.8 cm^{-1} increases marginally as the reaction progresses and warms to room temperature, eventually becoming a shoulder on a more defined peak at 875.1 cm^{-1}. The peak at 875.1 cm^{-1} starts to appear at -10°C and is well defined as the temperature reaches room temperature. A third peak at 856.5 cm^{-1} immediately appears as soon as O_2 is added to the reaction. The peak increases in intensity slowly as the solution is warmed, but at -50 °C the peak reaches maximum intensity and starts decreasing in size as the reaction continues to warm. The peak remains until room temperature is reached and then the peak drops significantly and becomes a shoulder on a larger peak at 875.1 cm^{-1}.

The linear $[UO_2]^{2+}$ stretch is commonly found between 920 and 980 cm^{-1}.[2,147] However, analysis undertaken in Section 3.1 and summarised in Table 3.2 shows that dioxo stretching frequencies can be found in a wider range from 841 to 988 cm^{-1}. For ex-

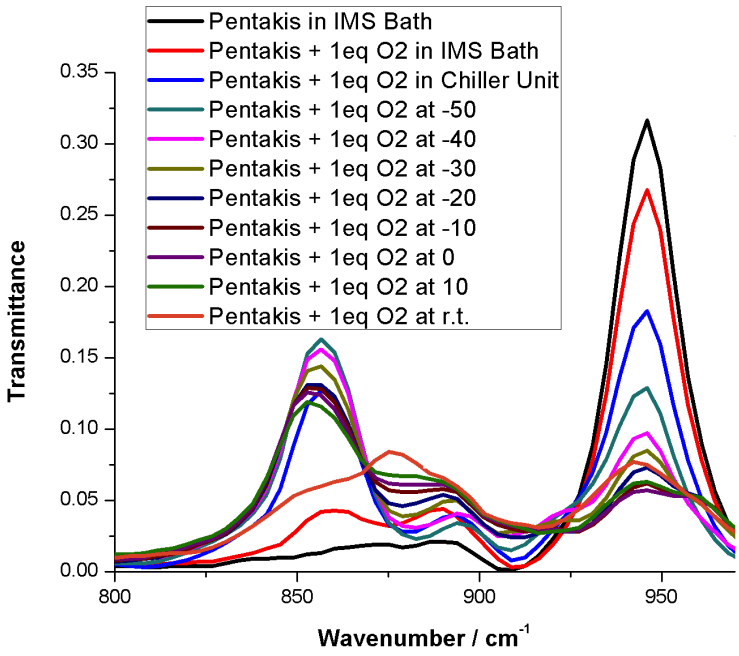

Figure 3.7: Zoomed in Section of the React IR Data of $(Ph_3SiO)_5UK + O_2$

ample the complex $UO_2Cl_2(THF)_3$ [125] has a stretching frequency of 841 and 875 cm^{-1}. The monooxo species reviewed indicate a slightly different range of values, from 838 to 928 cm^{-1}, however further analysis of IR studies currently published shows that the UO region can be located within a much wider range, from 800 to 950 cm^{-1}.[148–150]. Comparing this data to the experimental data gathered here, the peak observed at 945.9 cm^{-1} which is shown to decrease as O_2 is added is assigned to the U–O_{silox} stretch whilst the peak at 856.5 cm^{-1} which increases until the temperature reaches -50°C and then decreases is a, currently unidentified, intermediate species which was initially hypothesised based on colour changes observed in solution as the reaction warmed to room temperature. The two remaining peaks at 893.8 and 875.1 cm^{-1} are both well within the defined range for dioxo species and monooxo species. Monooxo complexes are normally found at lower frequencies than UO_2 or uranyl stretches and therefore the peak at 875.1 cm^{-1} is assigned as a monooxo species and the peak at 893.8 cm^{-1} is assigned as the UO_2 stretch.

3.5 Synthesis and characterisation of $[K(THF)_2][(Ph_3SiO)_4UO(THF)]$

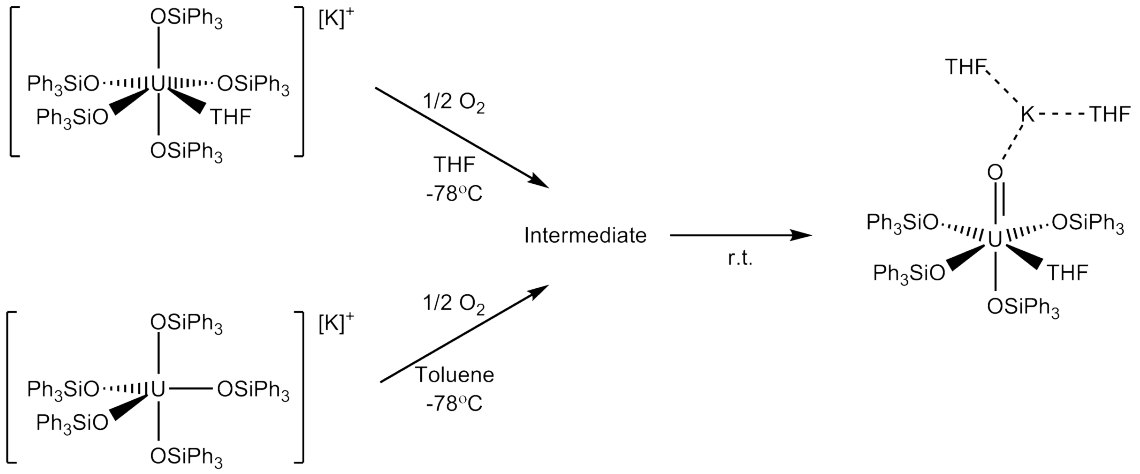

Scheme 3.4: Synthesis of $[K(THF)_2][(Ph_3SiO)_4UO(THF)]$

As previously shown, uranium monooxo species are relatively rare compared to the uranyl species and therefore work was undertaken to investigate the reactivity of $K[U(OSiPh_3)_5]$ and $K[(Ph_3SiO)_5U(THF)]$ in terms of controlled and accurate addition of oxygen.

$K[(Ph_3SiO)_5U(THF)]$ in THF was exposed to half an equivalent of O_2 at -78 °C. The solution turned brown quickly and remained so at -78 °C. When warmed to room temperature the solution turned orange. The reaction proceeded with the same outcome at room temperature without the brown solution being observed.

The experiment was repeated using $K[U(OSiPh_3)_5]$ in toluene at -78 °C and room temperature with similar results. The exception being that the brown colour was observed briefly at room temperature before the orange solution was formed within seconds. The brown solution indicates the presence of an intermediate species which was stable at temperatures of -78 °C and unstable at room temperature. In both cases the final orange solution was worked up and X–ray diffraction quality single crystals were recrystallised from THF/pentane at -40 °C. Analysis showed the product to be a rare monooxo species, $[K(THF)_2][(Ph_3SiO)_4UO(THF)]$.

3.5.1 Characterisation of $[K(THF)_2][(Ph_3SiO)_4UO(THF)]$: X–ray Diffraction

$[K(THF)_2][(Ph_3SiO)_4UO(THF)]$ crystallised in space group P2 1/c with an *R* factor of 5.68. The lattice parameters for this structure were *a* = 13.6745(5) Å, *b* = 17.1515(6) Å, *c* = 36.6721(13) Å, α = 90 °, β = 90.6740(10) °, γ = 90 °.

From the molecular structures shown in Figures 3.8 and 3.9 the molecule consists of four siloxy ligands with a fifth site coordinating to a THF molecule and a sixth site bound to an oxygen atom which is coordinated to a potassium counterion and two further THF molecules. The molecule has a reflection in the σ plane and therefore has a C_s point group.

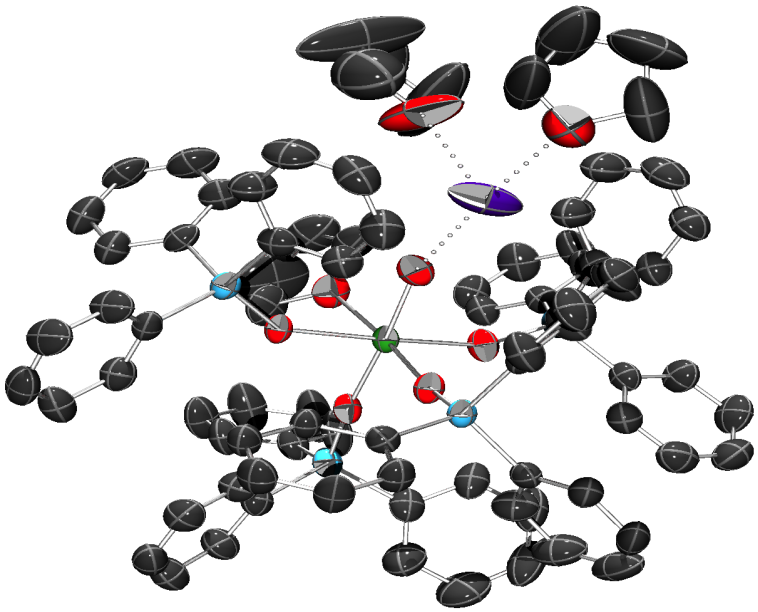

Figure 3.8: Molecular structure of $[K(THF)_2][(Ph_3SiO)_4UO(THF)]$ (Hydrogen atoms omitted for clarity)

The three equatorial siloxide ligands have an average U–O_{silox} bond length of 2.200(7) Å, marginally shorter than the dioxo complex (2.243 Å). The siloxide ligand *trans* to the monooxo is shorter than the equatorial ligands at 2.126(5) Å, possibly due to an inverse *trans* influence.[151–153]

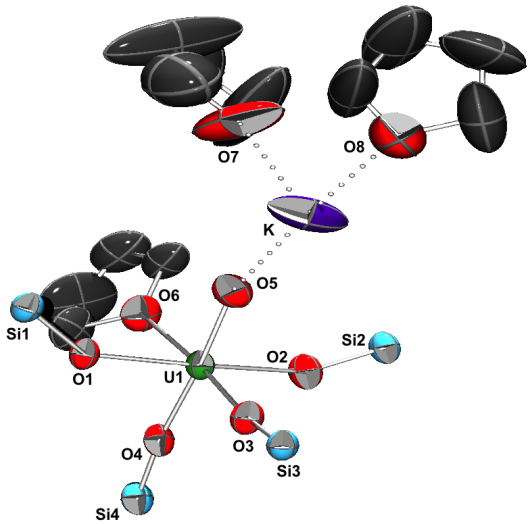

Figure 3.9: Core molecular structure of $[K(THF)_2][(Ph_3SiO)_4UO(THF)]$ containing the Si, O U and K atoms and coordinated THF (Hydrogen atoms and phenyl rings omitted for clarity)

The U–O_{oxo} bond length is observed as 1.865(5) Å which is inbetween the previously discussed U^{IV} and U^{V} monooxo complexes. In addition the U–O_{oxo} bond length of the monooxo complex is longer than the U–O_{uranyl} bond length of 1.821(7) Å which is expected based in the previous analysis of uranium dioxo and monooxo species. This analysis is also depicted in Figure 3.10.

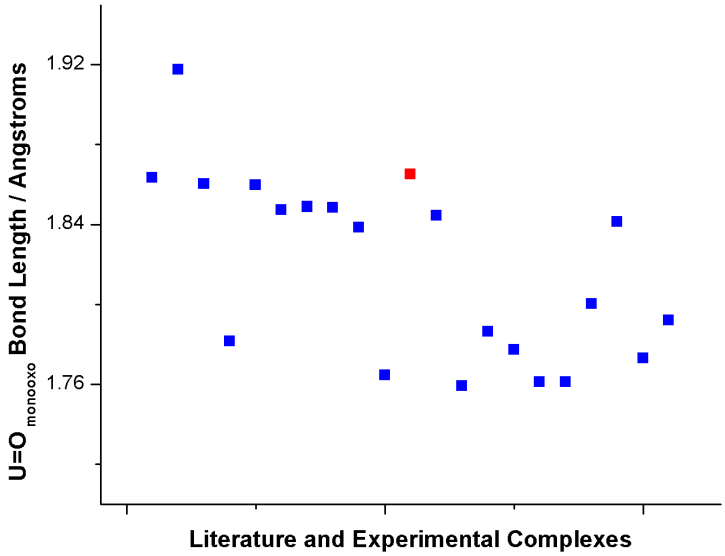

Figure 3.10: U–O_{oxo} bond lengths of the monooxo complexes. (Data point in red is the experimental value for $[K(THF)_2][(Ph_3SiO)_4UO(THF)]$

3.5.2 Characterisation of $[K(THF)_2][(Ph_3SiO)_4UO(THF)]$: NMR

$^{13}C\{H\}$ and ^{1}H NMR spectra of the crude monooxo product are shown in Figures 3.11 and 3.12 over layered by the spectrum of $K[(Ph_3SiO)_5U(THF)]$ in green. It is clear that the reaction leaves little or no starting material, and in addition the presence of Ph_3SiOH is observed with the OH resonance clearly observed at δ 6.01 ppm in the ^{1}H NMR spectrum. The formation of Ph_3SiOH is observed in a 1:1 ratio with the proposed $[K(THF)_2][(Ph_3SiO)_4UO(THF)]$. Analysing the $^{13}C\{H\}$ spectrum it seems likely that more than two species are present and as purification via recrystallisation was unreliable with low yields, further methods were employed to investigate this species.

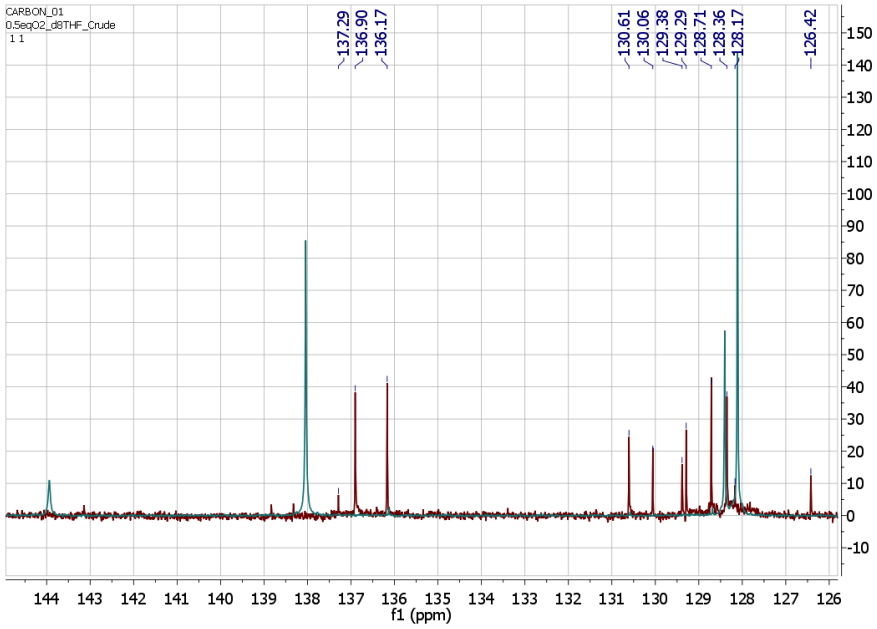

Figure 3.11: NMR Resonances for the $^{13}C\{H\}$ spectrum of $[K(THF)_2][(Ph_3SiO)_4UO(THF)]$ (red) and $K[(Ph_3SiO)_5U(THF)]$ (green) in d_8–THF

As the previous experiment has shown, even with attempted purification, the NMR spectra were complex, with multiple chemical environments identified and silanol seemingly ubiquitous. A second experiment was undertaken in which the $K[(Ph_3SiO)_5U(THF)]$ was exposed to half an equivalent of oxygen in an NMR tube at -78 °C. ^{1}H NMR spectroscopy analysis was then undertaken at -78 °C and at 10 °C intervals thereafter until the sample

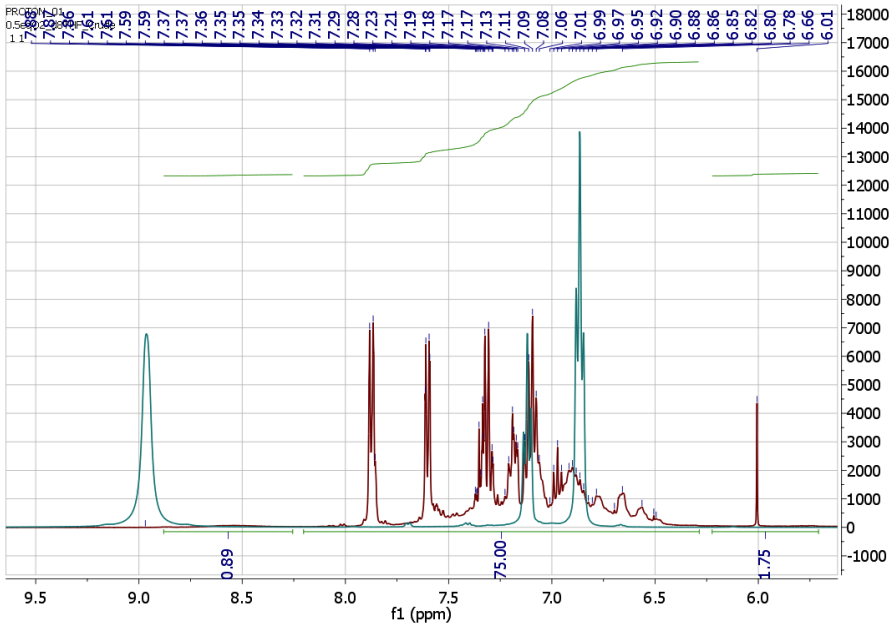

Figure 3.12: NMR Resonances for the ^{1}H spectrum of $[K(THF)_2][(Ph_3SiO)_4UO(THF)]$ (red) and $K[(Ph_3SiO)_5U(THF)]$ (green) in d_8–THF

had reached room temperature. The resulting spectra are shown in Figure 3.13 with the $K[(Ph_3SiO)_5U(THF)]$ at room temperature and at -78 °C assigned. The addition of O_2 to the sample at -78 °C is shown with the remaining spectra showing the sample at 10 °C intervals from -78 °C to 30 °C.

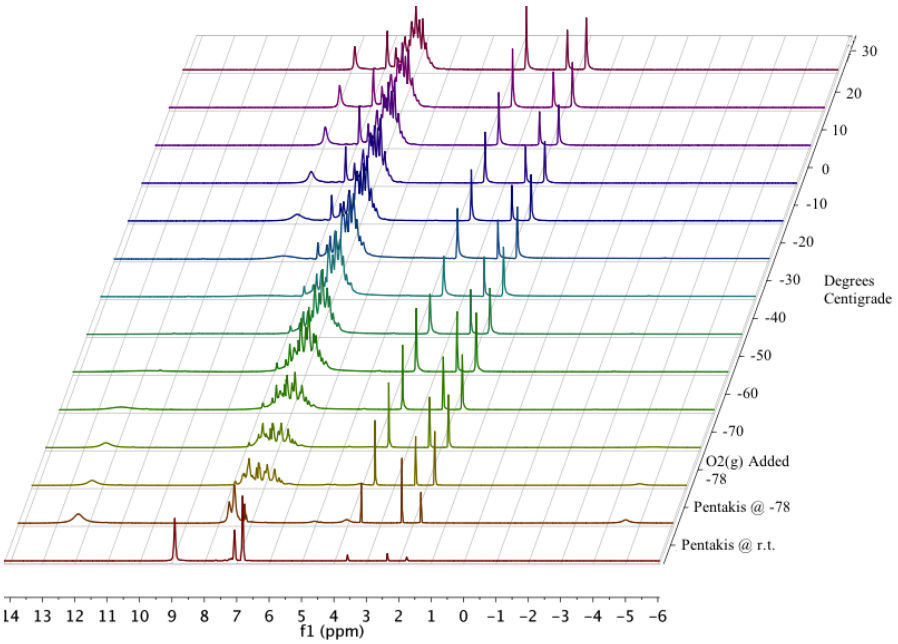

Figure 3.13: NMR Resonances for the ^{1}H spectra of $K[(Ph_3SiO)_5U(THF)]$ reacting with 0.5 eq. O_2 from -78 °C to 30 °C in 10 °C intervals in d_8–THF

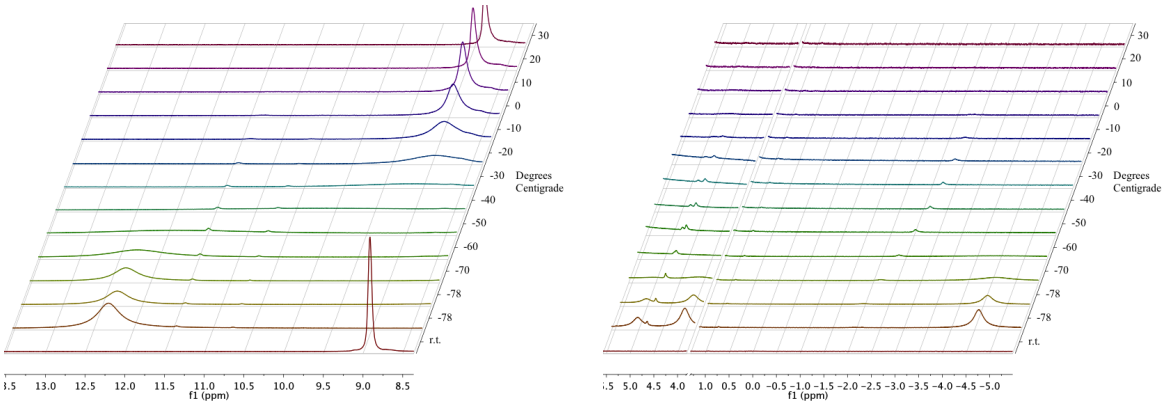

(a) (b)

Figure 3.14: Zoomed in sections of Figure 3.13 a) δ 13.5 to 8.5 ppm; b) δ 5.5 to -5.5 ppm in d_8–THF (omitted for clarity)

The data show the changes that occur to the K[$(Ph_3SiO)_5U(THF)$] species when the temperature is reduced to -78 °C. Based on the integration values of the resonances in the spectrum of K[$(Ph_3SiO)_5U(THF)$] at -78 °C, the broad resonance at δ 12.32 ppm is assigned as the *para* protons on the phenyl rings. This resonance broadens as the temperature increases and at -50 °C the resonance is so broad it is difficult to identify. Additionally the resonance shifts upfield until the temperature reaches -20 °C when the resonance starts to sharpen at δ 8.97 ppm. This is previously assigned to the *para* protons of the starting material K[$(Ph_3SiO)_5U(THF)$], suggesting that in the timescales of the NMR spectroscopy experiment the reaction did not go to completion. Secondly the two resonances at δ 7.66 and 7.50 ppm at -78 °C are assigned as the *meta* and *ortho* protons on the phenyl ring. Four new resonances also occur, the first is a doublet of triplets at δ 7.20 ppm, the other three are broad singlets at δ 5.02, 4.03 and -4.59 ppm and each of these new resonances integrate as 0.5 to each phenyl group.

By adding half an equivalent of O_2 to the solution at -78 °C, the resonances assigned to the K[$(Ph_3SiO)_5U(THF)$] immediately reduce by a factor of four and multiple new resonances appear in the region of δ 6–8 ppm, which are assigned to the phenyl rings on the monooxo complex. In addition, it is noted that other uranium based complexes are synthesised including the previously discussed dioxo species and the resonances between

δ 6–8 ppm are indicative of multiple species and discussed further in Section 3.6. In addition the resonances observed at δ 5.02, 4.03 and -4.59 ppm also reduce by a factor of four and disappear by the time the temperature reaches -70 °C.

New resonances between δ 7.02–6.84 ppm and δ 6.70–6.54 ppm occur but they overlap and are difficult to define further. In comparison to the simple separation of the *meta*–,*para* and *ortho*–protons seen in Ph_3SiOH, Ph_3SiOK and $K[U(OSiPh_3)_5]$, the aromatic region of the product is complex and highly coupled, with no clear and identifiable (*ortho*,*meta*,*para*) splitting pattern, indicative of one or more new species.

3.5.3 Characterisation of $[K(THF)_2][(Ph_3SiO)_4UO(THF)]$: Negative ion ESI

In addition to the NMR spectroscopy data, negative ion ESI HRMS was also employed to identify other products formed during the reaction with oxygen. $K[(Ph_3SiO)_5U(THF)]$ in THF was exposed to 0.5 eq. oxygen and once reacted, the resulting orange solution was analysed. The negative ion ESI HRMS results are shown in Table 3.9.

HRMS m/z	Relative Intensity	Anion Assignment
1354.3904	0.23	$[(Ph_3SiO)_4UO]$
1400.4260	0.23	—
1443.4801	0.25	$[(Ph_3SiO)_4UO_2(THF)]$
1615.00	0.03	$[(Ph_3SiO)_5U]$
1630.00	0.07	$[(Ph_3SiO)_5UO]$
1645.5173	0.12	$K[(Ph_3SiO)_4UO_2(THF_3)]$
1701.35	0.08	$K[(Ph_3SiO)_5UO_2]$

Table 3.9: Negative ion ESI HRMS data of the reaction between $K[(Ph_3SiO)_5U(THF)]$ and 0.5 eq. O_2

The peaks at m/z 1354.3904 and 1400.4260 have identical isotope distribution patterns the first of which is identified as $[(Ph_3SiO)_4UO]$ with the second peak as yet, unidentified.

The peaks at m/z 1615, 1630 and 1645.5173 also have identical isotope distribution patterns and are assigned as $[(Ph_3SiO)_5U]$, $[(Ph_3SiO)_5UO]$ and $K[(Ph_3SiO)_4UO_2(THF_3)]$ respectively. These data show the multiple species suspected from the NMR spectroscopy data are present in solution under ESI HRMS conditions. Additionally the data confirms that the starting material, $K[(Ph_3SiO)_5U(THF)]$ reacts almost completely with oxygen with only trace amounts observed in the ESI HRMS analysis.

From these data, $[(Ph_3SiO)_4UO]$ and $[(Ph_3SiO)_4UO_2(THF)]$ are the major products with an unidentified peak at m/z 1400.4260. It is likely that the solution was exposed to oxygen during the ESI HRMS process which would account for the discrepancy in the stoichiometric sum, however it seems apparent when analysing the NMR and ESI HRMS data that the monooxo and dioxo are both formed on addition of oxygen. This provides an understanding as to why the two species are difficult to isolate.

3.6 Intermediate species and mechanistic hypothesis

Dioxygen can bind to a single metal centre to give a MO_2 moiety in which the oxidation state is uncertain. Figure 3.15 illustrates these possibilities. With no electron transfer, the hypothetical, neutral species is formed, shown in Figure 3.15(a) while one electron transferred results in a superoxide complex shown in Figure 3.15(b). The transfer of two electrons results in the formation of the peroxo complex shown in Figure 3.15(c). Using these species, previously published examples, the ESI HRMS data and the NMR spectroscopy data, a tentative mechanistic hypothesis can be proposed.

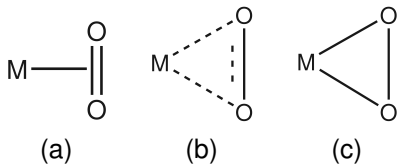

Figure 3.15: Active oxygen species: (a) dioxygen, bound side–on; (b) superoxide and (c) peroxide

3.6.1 Mechanistic pathways

Previous examples of dioxygen coordination and subsequent cleavage are reported in the literature[154] and a generic cleavage reaction is shown in Equation 3.6.1;

$$2M + O_2 \rightarrow MO_2 + M \rightarrow MOOM \rightarrow 2M = O \qquad (3.6.1)$$

One such example used magnesium reduction of the readily available cobalt halide, Tp'CoX (Tp' = hydridotris(3–*tert*–butyl–5–methylpyrazolyl)borate, X = Cl, I) in a nitrogen atmosphere resulting in the dinitrogen complex Tp'Co(N_2). This product was then reacted further with an excess of dioxygen resulting in the superoxo product, Tp'Co(O_2) as shown in Figure 3.16. Tp'Co(O_2) and Tp'Co(N_2) were then reacted together which resulted in the product Tp'CoOH in high yields. The authors hypothesised the dinitrogen was released and the two cobalt complexes formed a dinuclear peroxo–bridged cobalt complex which, via hydrogen abstraction from the ligand system, produced the Tp'CoOH species.[155] Further characterisation data and reactivities were published later.[156–158]

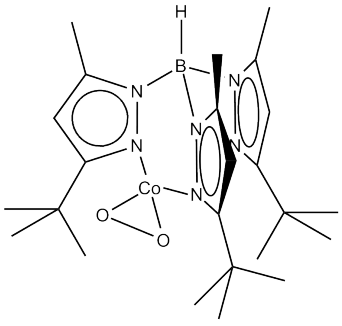

Figure 3.16: Side–on superoxo complex of cobalt

Similarly, [Ni(tmc)][OTf], shown in Scheme 3.5 was used and in order to access a nickel peroxo species with the activation of dioxygen, tmc was chosen as the ligand because it eliminates the vacant coordination sites around the nickel in *cis* positions. The available coordination sites, *trans* to each other, were surrounded by the bulky ligand system therefore forcing the binding of oxygen in an 'end–on' manner rather than 'side–on'. Scheme 3.5[159] shows the resulting species found from this reaction with dioxygen. The authors, whilst sure of the resulting products, are unsure of the mechanism and how the bridged dinickel species or the 'end–on' bound dioxygen species can form [Ni(tmc)(OH)][OTf] and based this hypothesis on DFT calculations.[159]

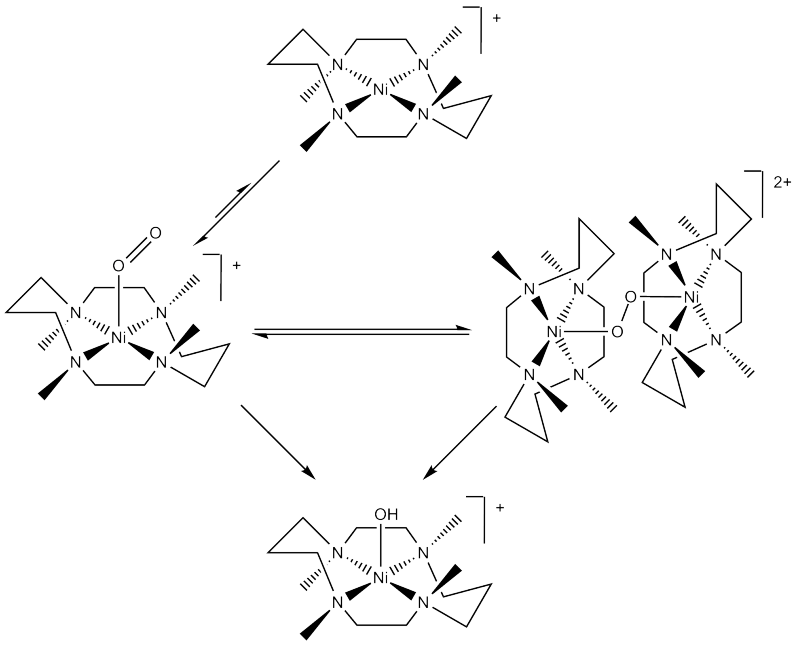

Scheme 3.5: Dioxygen activation at monovalent nickel

The mechanism for the formation of the monooxo complex must account for the observed formation of one molar equivalent of Ph_3SiOH in high spectroscopic yield, despite the repeatedly low isolated yield of $[K(THF)_2][(Ph_3SiO)_4UO(THF)]$. In the variable temperature reaction between dioxygen and $K[U(OSiPh_3)_5]$, an intermediate, corresponding to the brown intermediate in low temperature preparative reactions, was observed, which displayed an IR band consistent with either a bridging dioxo species or a side–bound dioxo

species. In other work in this laboratory, U(η^2-O_2)(OSi(O^{t}Bu)$_3$)$_4$(THF)) was prepared serendipitously[80] shown in Figure 3.17 and discussed further in Section 5.4.

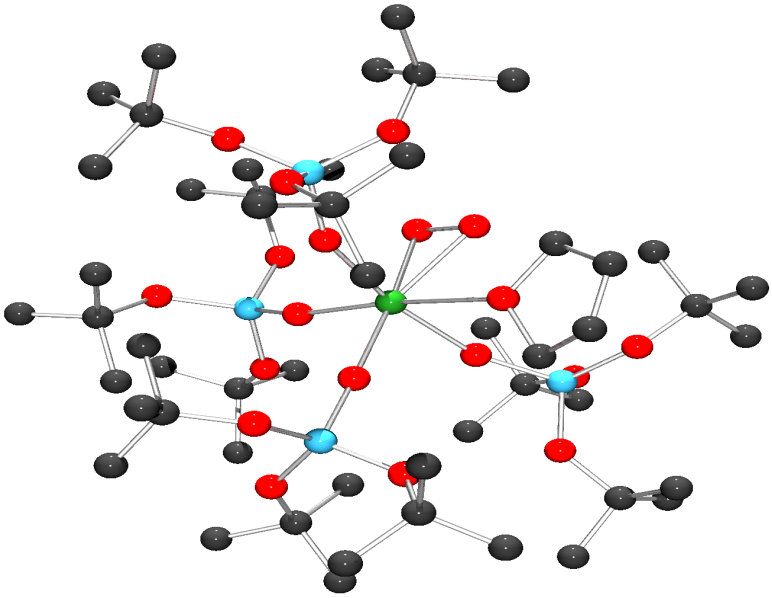

Figure 3.17: Peroxo species U(η^2-O_2)(OSi(O^{t}Bu)$_3$)$_4$(THF))[80]

The O–O bond length in this complex is 1.374(4) Å, which lies between the bond lengths in gas phase hydrogen peroxide (1.474 Å) and superoxide ion (1.33 Å).[155]

Scheme 3.6 shows a tentative mechanism that accounts for all of the observed properties of the reaction and the spectroscopic data, including the NMR integration analysis which indicated the silanol and monooxo were formed in a 1:1 ratio. Dioxygen binds to the uranium centre in K[U(OSiPh$_3$)$_5$] and forms eventually a side–bound peroxide species. The *in situ* peroxide complex then reacts with a second equivalent of K[U(OSiPh$_3$)$_5$], forming the mixed–valent dimer [(Ph$_3$SiO)UOOU(OSiPh$_3$)$_5$]$^{2-}$ shown below. Either this di-uranium complex or the earlier $\eta^2 - O2$ complex is responsible for the new band observed at low temperature in the variable temperature infra–red spectrum and the temperature–sensitive brown species observed during the course of the reaction.

The [(Ph$_3$SiO)UOOU(OSiPh$_3$)$_5$]$^{2-}$ complex is unstable: electron transfer into the peroxide

moiety then cleaves the O-O linkage with a formal one electron oxidation from a siloxide ligand, which leaves as a siloxyl radical.

The bond strength for the oxygen–hydrogen bond in R_3SiO-H is found to be 494 kJ mol^{-1}, which is stronger than a C–H bond.[160] From these data, abstraction of a hydrogen atom from the ligand (which would lead to a disruption of the splitting pattern in the NMR spectrum), or from the solvent, (which will result in the formation of an NMR–silent Ph_3SiOD bond) accounts for the observation of the charge and coordination sphere of the isolated product and the appearance of one mole–equivalent of Ph_3SiOH.

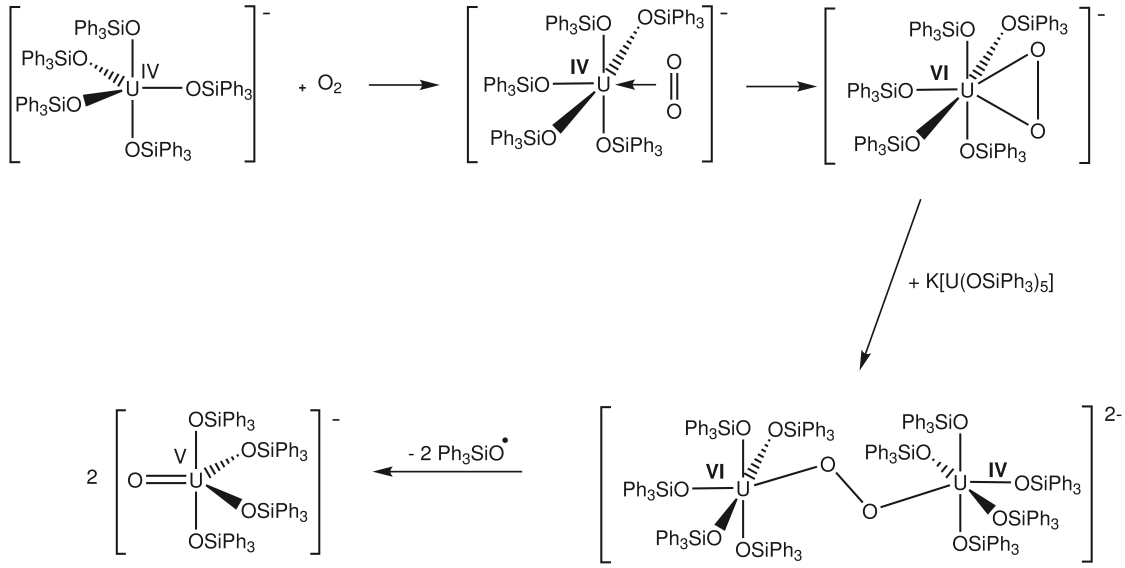

Scheme 3.6: Proposed uranium superoxide and peroxide mechanism of formation for the monooxo species

3.7 Reaction of $K[(Ph_3SiO)_5U(THF)]$ and CO_2

In order to test the nucleophilicity of coordinated Ph_3SiO, $K[(Ph_3SiO)_5U(THF)]$ was dissolved in d_8–THF and exposed to three equivalents of CO_2 at -78 °C using Toepler line techniques. The solution showed no obvious signs of reaction whilst the temperature remained at -78 °C, but once warmed to room temperature the solution became yel-

low/brown in colour. A small number of X–ray diffraction quality crystals were grown from THF.

3.7.1 Characterisation of $(Ph_3SiO)_5U(THF)$: X–ray Diffraction

$(Ph_3SiO)_5U(THF)$ crystallises in space group P2 1/n with an *R* factor of 7.83. The lattice parameters for this structure are *a* = 13.1098(5) Å, *b* = 25.5252(6) Å, *c* = 25.7502(10) Å, α = 90 °, β = 92.0610(10) °, γ = 90 °.

From the molecular structure shown in Figures 3.18 and 3.19 the molecule is observed to have a square bipyramidal geometry consisting of five siloxy ligands with a sixth site coordinating to a THF molecule. There is no counterion observed within the crystal structure which suggests the molecule is in an oxidation state of U^V and clearly must be the result of a one electron oxidation, the nature of which is unknown.

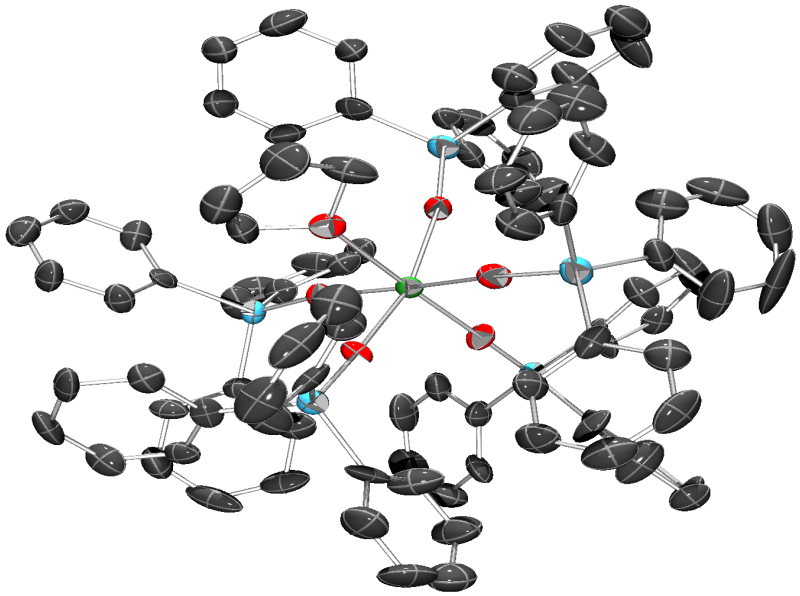

Figure 3.18: Molecular structure of $(Ph_3SiO)_5U(THF)$ (Hydrogen atoms omitted for clarity)

Figures 3.20 and 3.21 show the full range of U–O and O–Si literature values for $U(OSiR_3)_xR'_y$ (blue) and the average U–O and O–Si bond lengths for $(Ph_3SiO)_5U(THF)$ (red).

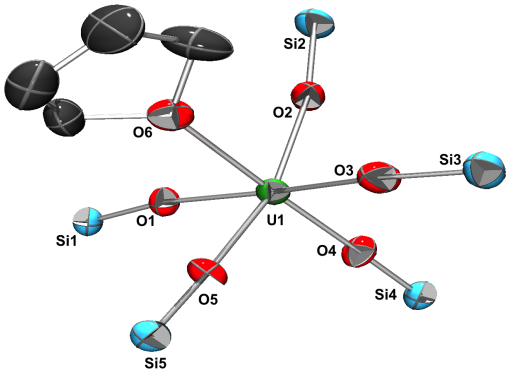

Figure 3.19: Core molecular structure of $(Ph_3SiO)_5U(THF)$ containing the Si, O U and K atoms and coordinated THF (Hydrogen atoms and phenyl rings omitted for clarity)

$(Ph_3SiO)_5U(THF)$ has an average experimental bond length for **U–O**$SiPh_3$ of 2.111(5) Å, U**O–Si**Ph_3 of 1.63(9) Å and UO**Si–Ph$_3$** of 1.87(7) Å. Overall, the data for $(Ph_3SiO)_5U(THF)$ was much closer to the mean literature values than the previously discussed $K[U(OSiPh_3)_5]$ and $([K(py)_6][U(OSiPh_3)_5(py)])_2$ complexes which both had structural data which were found at the extreme end of the ranges. The U–O bond in the $(Ph_3SiO)_5U(THF)$ species is much shorter than in $([K(py)_6][U(OSiPh_3)_5(py)])_2$ and $K[U(OSiPh_3)_5]$ however this is expected as the U^V oxidation state would normally present shorter bond lengths with the reduced electron density on the uranium centre. In addition, THF is typically a weak σ–donor and therefore less electron density is pushed onto the uranium metal centre from the coordinated solvent. The electron deficient uranium centre gains its electron density from the other ligands, shortening the U–O_{silox} bonds.

The average bond angles are typical of a square bipyramidal geometry. The cis O–U–O average bond angle is 89.2(4) °. The slight deviation from the expected 90 ° is explained by the steric bulk of the ligands around the uranium. The siloxy ligands are sterically bulky and therefore distort away from an otherwise square bipyramidal geometry and occupy the otherwise empty space surrounding the much smaller THF molecule. This is also highlighted by considering the trans O–U–O bond angles which are experimentally

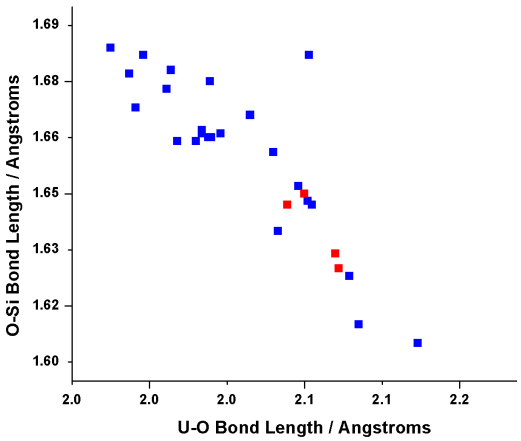

Figure 3.20: Correlation between U–O bond distances and O–Si for uranium compounds with the ligand R_3SiO. (Data points in red are the experimental values for $(Ph_3SiO)_5U(THF)$)

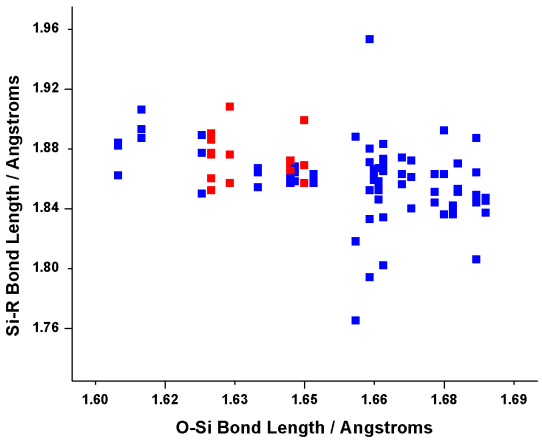

Figure 3.21: Correlation between O–Si bond distances and Si–R_3 for uranium compounds with the ligand R_3SiO. (Data points in red are the experimental values for $(Ph_3SiO)_5U(THF)$)

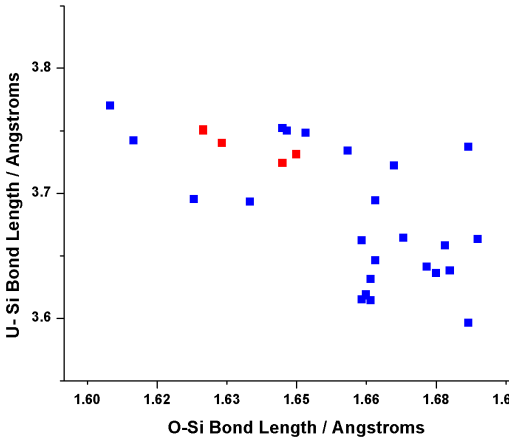

Figure 3.22: Correlation between O–Si bond length and U–Si distances for uranium compounds with the ligand R_3SiO. (Data points in red are the experimental values for $(Ph_3SiO)_5U(THF)$)

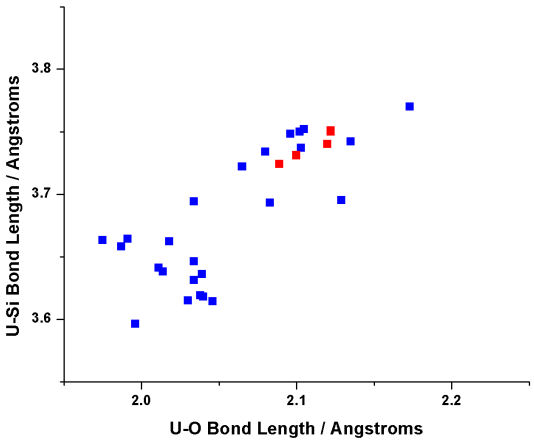

Figure 3.23: Correlation between U–O bond length and U–Si distances for uranium compounds with the ligand R_3SiO. (Data points in red are the experimental values for $(Ph_3SiO)_5U(THF)$)

shown to be 178.05 ° on average, not the expected 180 °, the ligands are bent towards the small THF molecule.

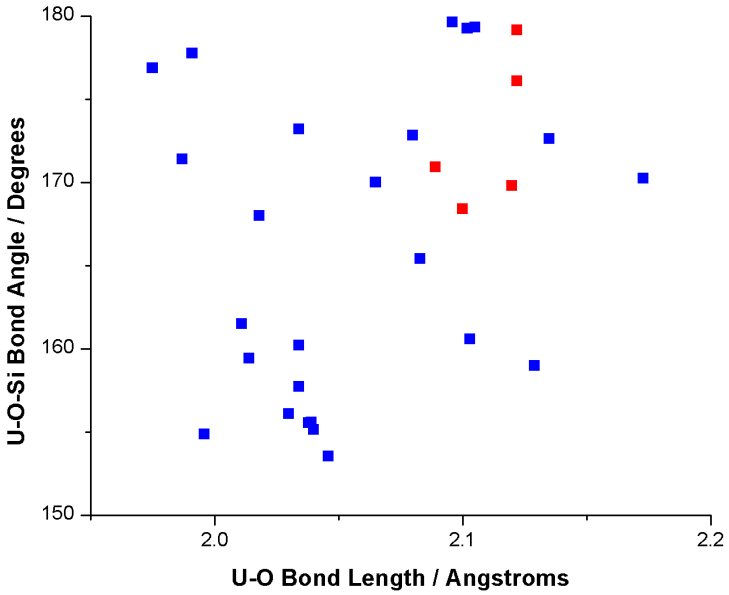

Figure 3.24: U–O–Si bond angles for uranium compounds with the ligand R_3SiO. (Data points in red are the experimental values for $(Ph_3SiO)_5U(THF)$)

3.7.2 Characterisation of $(Ph_3SiO)_5U(THF)$: NMR

$^{13}C\{H\}$, ^{1}H and HSQC NMR spectroscopy data were all obtained on the reaction mixture, the results of which are shown in Appendices D.3, D.4 and D.5 and discussed further here. Both the ^{1}H and ^{13}C spectra clearly show the vast majority of the species found in the solution is the initial starting material, $K[(Ph_3SiO)_5U(THF)]$. In addition there is a clear indication that Ph_3SiOH is present by the observation of the distinct OH resonance in the ^{1}H spectrum and previously discussed in section 2.1.2. This would suggest that the addition of CO_2 is initiating a reaction in which the displacement of at least one of the ligands occur, however the reaction does not go to completion resulting in large amounts of starting material remaining. The only isolated product from the reaction mixture was the U^{V} species observed by X–ray diffraction.

3.7.3 Synthesis and characterisation of Ph_3SiO-A where A = Li, Na, Rb, Cs or Tl

Initially, the X–ray diffraction data on these reactions with oxygen were difficult to solve and side bound dioxygen was identified instead of the disordered potassium ion that was actually present. It seemed appropriate to ascertain if the compounds could be synthesised with different counter ions possessing greater electron density. Scheme 3.7 shows an overview of the alkali metal based starting materials that were investigated and Table 3.10 shows some of the various reactions and experimental conditions that were trialled.

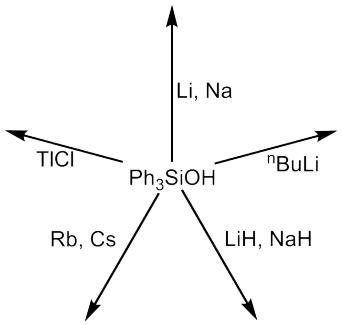

Scheme 3.7: Attempted synthesise of Ph_3SiO-A where A = Li, Na, Rb, Cs or Tl

In addition to the above reactions, literature methods were used to synthesise, $[Li(OSiPh_3)]n$, $K_8(OSiPh_3)_8(DME)_3$ and $[K(THF)_x(OSiPh_3)]$.[89] These products were reacted further with UCl_4 but the final products were not easily extracted and therefore pure samples were difficult to obtain and analyse.

Two of the tabulated reactions proved the most successful and could be reliably repeated. These reactions, between the silanol and either KH or ^{n}BuLi, became the favoured methods of siloxide production, specifically using KH due to ease of use under inert glove box conditions and has been discussed fully in Section 2.1.3. Unfortunately the reactions with rubidium and caesium proved completely unsuccessful with the reactions mixture

Silanol/ Siloxide	Alkali Metal Sources	Solvent system system	timeframes	temperature
Ph_3SiOH	LiH	hexane	24 hrs	r.t.
			24 hrs	80°C
		toluene	48 hrs	r.t.[161]
Ph_3SiOH	^{n}BuLi	hexane	30 mins	r.t.
Ph_3SiOH	KH	hexane	30 mins	r.t.
			24 hrs	r.t.
			24 hrs	80°C
Ph_3SiOH	NaH	hexane	24 hrs	r.t.
			24 hrs	80°C
		pentane	12 hrs	r.t.
		THF	12 hrs	r.t.
Ph_3SiOH	Cs	THF	6 hrs	r.t.
Ph_3SiOH	Rb	THF	24 hrs	r.t.
		d_8–THF	1 hr	r.t.
		pentane	24 hrs	-78°C
Ph_3SiOK	TlCl	THF	24 hrs	r.t.

Table 3.10: Summary of experiments conducted in order to vary the alkali metal bonded to the siloxide

resembling black sludge and any products, completely intractable.

As this avenue proved unsuccessful, attempts were made to change the counter ion on the uranium complex directly. Excess RbI and CsI were both reacted with $K[U(OSiPh_3)_5]$ and analysed by ^{1}H and $^{13}C\{H\}$ NMR. The results for the caesium iodide reaction are shown in Figures 3.25 and 3.26.

Analysis of the $^{13}C\{H\}$ NMR spectrum clearly shows multiple species have been formed. The ^{1}H NMR data show the same pattern of resonances observed for $K[(Ph_3SiO)_5U(THF)]$

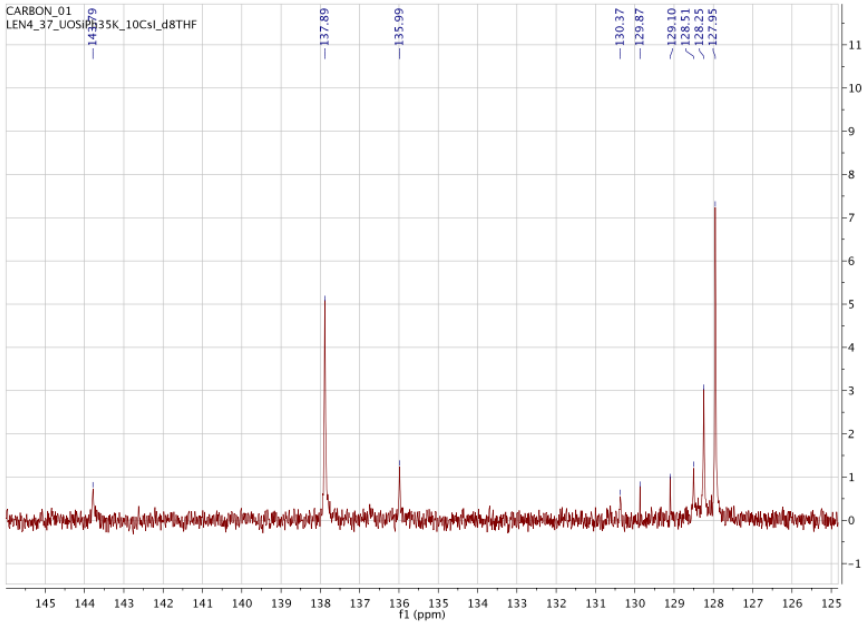

Figure 3.25: NMR Resonances for the $^{13}C\{H\}$ spectrum of the reaction between $K[(Ph_3SiO)_5U(THF)]$ and excess CsI in d_8–THF

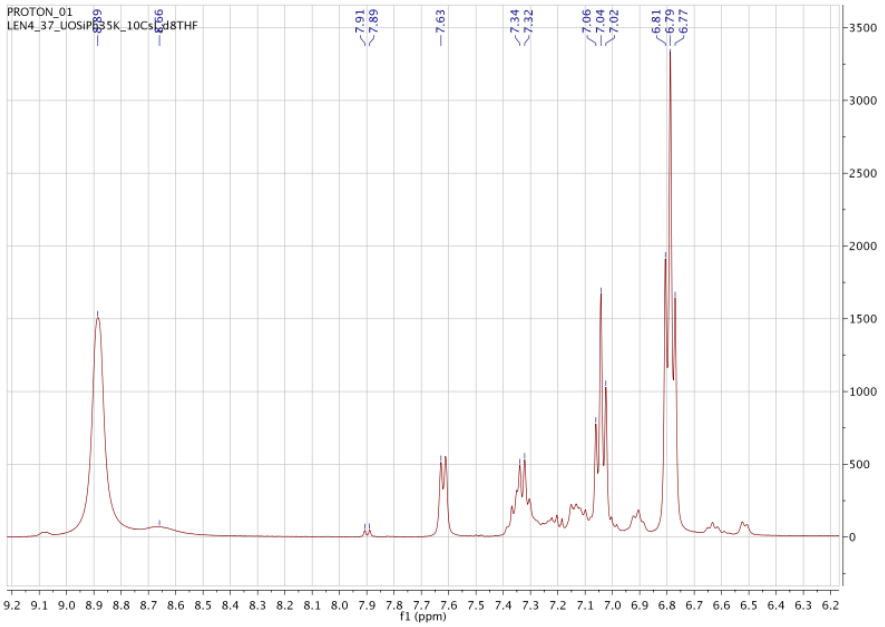

Figure 3.26: NMR Resonances for the ^{1}H spectrum of the reaction between $K[(Ph_3SiO)_5U(THF)]$ excess CsI in d_8–THF

but slightly shifted to δ 8.89, 7.06–7.02 and 6.81–6.77 ppm. This suggests that RbI has reacted with $K[(Ph_3SiO)_5U(THF)]$ forming $Rb[(Ph_3SiO)_5U(THF)]$ with the ^{29}Si NMR spectrum indicating one silicon environment at δ -69.42 ppm. Recrystallisation was attempted in a variety of solvent systems, THF, toluene, and toluene/hexane, at room temperature

and -40°C but unsuccessful.

Chapter 4

Studies of

[(U(OSi(O^{t}Bu)$_3$)$_3$)$_2$($\mu-\eta^6$:η^6-tol))]

Between November 2012 and April 2014, most of the compounds synthesised as part of this work were published by Mazzanti et al. of the Institut Nanonsciences et Cryogénie, CEA, Grenoble.[90,162–164]

Investigations into other ligand systems that retain the primary Si–O–U linkage were undertaken, using *tert*–butoxy siloxide to more accurately mimic the electronic nature of a mesoporous silica surface, while retaining significant steric encumbrance.

The ligand is commonly found on transition metals and occasionally lanthanide species both of which are discussed in section 1.3.6. The use of tris *tert*–butoxy siloxide has long been identified as a possible mimic for surface materials (section 1.2.2).[165,166] At the start of this work (summer 2012) tris *tert*–butoxy siloxides had not been successfully used as supporting ligands on actinide based complexes.

4.1 Uranium tris *tert*–butoxy siloxides

The Mazzanti group used siloxides as supporting ligands in U^{III} mediated small molecule activation. A homoleptic siloxide complex, $[(U(OSi(O^tBu)_3)_2(\mu-OSi(O^tBu)_3))_2]$ was synthesised. This was achieved by treating $[U(N(SiMe_3)_2)_3]$ with three equivalents of $(^tBuO)_3SiOH$ in hexane at -40 °C and recrystallised from hexane in yields of 82%.[162] X–ray analysis of the single crystals showed the complex was a centrosymmetric dinuclear structure. The geometry of the two uranium ions were observed as a distorted pentagonal bipyramid with the oxygen atoms of two terminal siloxide ligands bonding to each uranium centre, two bridging bidentate siloxide ligands and a neutral *tert*–butoxy group of a bridging siloxide ligand. Despite the reducing nature of the complex, the coordination of the siloxide ligands provided enough electron donating character that it was stable at room temperature for a few hours. The U–U distance was determined to be 3.9862(2) Å and the U–O distances for the terminal siloxides was 2.193(4) Å on average which was determined to be within the range of other typical uranium(III) alkoxide complexes. The bridging siloxides were observed to have longer U–O bond distances of 2.396(3) Å and 2.549(3) Å and the neutral *tert*–butoxy group had a U–O bond distance of 2.540(2) Å which were all comparable to other similar lanthanide complexes.[162] Scheme 4.1 shows the reaction between $[(U(OSi(O^tBu)_3)_2(\mu-OSi(O^tBu)_3))_2]$ and CO_2, CS_2 and toluene.

In the case of CS_2, a stoichiometric amount was added to the uranium complex which resulted in an immediate change in colour from brown to yellow forming the two electron reduction product, $[(U(OSi(O^tBu)_3)_3)_2(\mu-\eta^2(C,S):\eta^2(S,S)-CS_2)]$. The highly soluble product could be extracted in an analytically pure form, from hexane, in yields of 53%. X–ray quality crystals were crystallised from toluene and the analysis showed a U^{IV} dimer with the two uranium centres bridged by a CS_2^{2-} group, which binds the two uranium

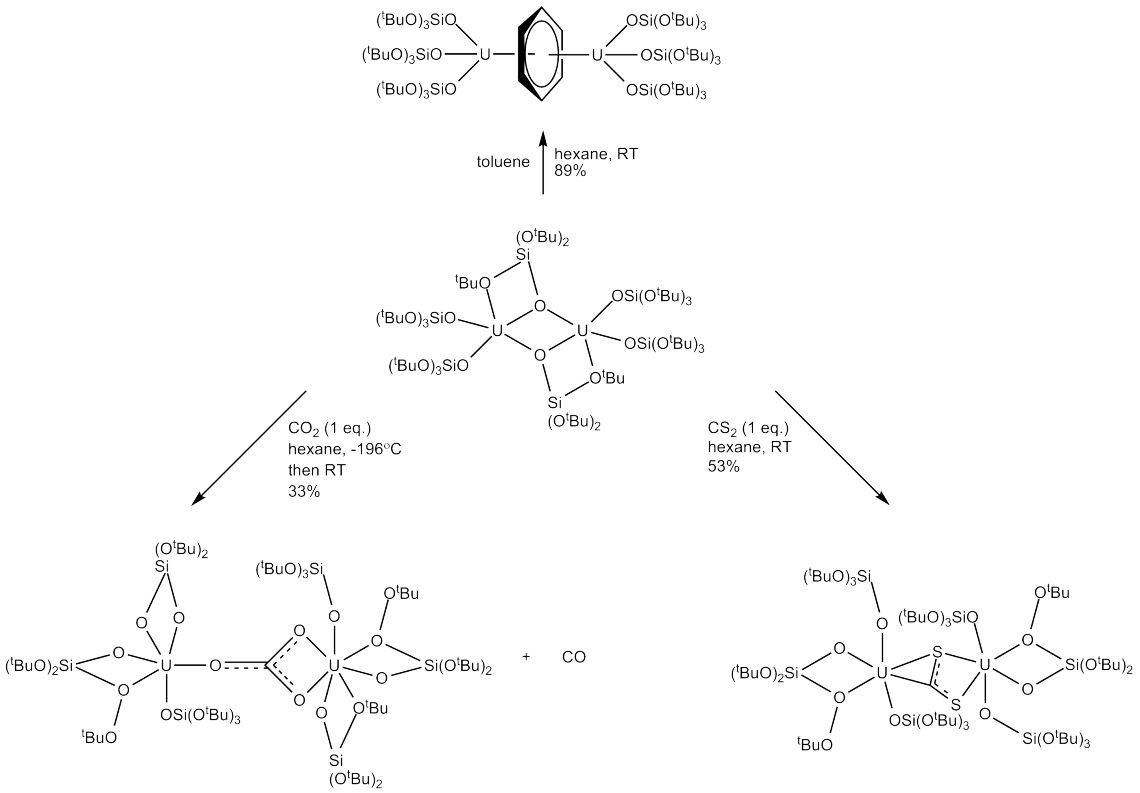

Scheme 4.1: Mazzanti's reduction of CO_2, CS_2 and toluene by $[(U(OSi(O^tBu)_3)_2(\eta-OSi(O^tBu)_3))_2]$ (November 2012)[162]

centres in a rare $\mu-\eta^2(CS_1):\eta^2(S_1S_2)$ binding mode. The two uranium centres are six–coordinate with an average siloxide U–O distance of 2.11(5) Å and a U–O^{t}Bu bond distance of 2.642(3) Å. The central CS_2^{2-} unit is unlike free CS_2 in that it is asymmetrical, with each C–S bond observed at 1.748(11) Å and 1.594(12) Å (C–S bond distance 1.560(3) Å in free CS_2). In addition the S–C–S bond angle also deviates from the linear free CS_2 to 131.6(8)°. These data compare well to other transition metals complexes with similar bonding patterns.[162]

$[(U(OSi(O^tBu)_3)_2(\mu-OSi(O^tBu)_3))_2]$ was then investigated in terms of its reactivity with CO_2. The uranium complex was suspended in hexane and reacted with one equivalent of CO_2 for six hours which resulted in a slow change in colour to form a light green solution. In addition the evolution of CO was observed which was identified by NMR spectroscopy. After work–up the resulting green residue was recrystallised from toluene

at -40°C and analysis showed the product to be the dimeric U^{IV}/U^{IV} carbonate complex, $[(U(OSi(O^tBu)_3)_3)_2(\mu\eta^1{:}\eta^2CO_3)]$, in yields of 33%. The reaction was monitored by ^{1}H NMR spectroscopy over a period of six hours, showing $[(U(OSi(O^tBu)_3)_2(\mu{-}OSi(O^tBu)_3))_2]$ was converted into $[(U(OSi(O^tBu)_3)_3)_2(\mu\eta^1{:}\eta^2CO_3)]$ and $[U(OSi(O^tBu)_3)_4]$ in a 2:5:1 ratio respectively. In addition it was noted that the carbonate complex decomposed in the presence or absence of CO_2 to yield $[U(OSi(O^tBu)_3)_4]$ indicating a slow ligand redistribution process and an unidentified U^{IV} carbonate complex.[162]

$[(U(OSi(O^tBu)_3)_3)_2(\mu\eta^1{:}\eta^2CO_3)]$ was observed to possess a dimeric structure with the carbonate complex bridging between the two uranium centres in a $\mu\eta^1{:}\eta^2$ fashion. Each uranium centre is coordinated by a terminal siloxide ligand with a U–O distance of 2.09(1) Å in addition to two siloxide ligands with an average U–O bond distance of 2.18(1) Å. Finally two siloxide ligands bond in a bidentate fashion so each uranium atom is bonded to two oxygen atoms from ^{t}BuO groups with an average U–O bond distance of 2.67(6) Å. The bridging carbonate group binds to the two uranium centres in a $\mu\eta^1{:}\eta^2$ fashion with one shorter U–O bond length (2.25(2) Å) compared to the other two (2.404(2) Å). The carbonate C–O distances are 1.28(1) Å.[162]

Finally, $[(U(OSi(O^tBu)_3)_2(\mu{-}OSi(O^tBu)_3))_2]$ was reacted with excess toluene in hexane to synthesise the diuranium inverted sandwich complex, $[(U(OSi(O^tBu)_3)_3(\mu{-}\eta^6{:}\,\eta^6\text{-tol}))_2]$. The X–ray analysis showed the presence of two identical $U(OSi(O^tBu)_3)_3$ units bridged by a toluene molecule in a $\mu\eta^6{:}\eta^6$ symmetrical fashion. The C–C bond distance in the bridging toluene molecule is 1.432(3) Å which is found to be marginally longer than free toluene but similar to other systems containing reduced arenes. The average U–C bond distance is 2.692(3) Å and this was found to be shorter than other U^{III} complexes with neutral arenes. The siloxide ligands were found to have U–O bond distances of 2.117(2) Å which are much shorter than those of $[(U(OSi(O^tBu)_3)_2(\mu{-}OSi(O^tBu)_3))_2]$ and suggest

the presence of a U^{IV} ion. The author therefore describes this complex as "a U^{IV} complex of a dianionic toluene ligand resulting from the reduction of toluene by a U^{III} siloxide complex." However it is noted that a U^{V} complex with a tetraanionic arene is also a possibility. Table 4.1 shows a comparison between the complexes reported by Mazzanti.[162]

Complex	U–$O_{terminal}$ / Å	U–O_{tBu} / Å	U–O_{silox} / Å	Date reported
$[(U(OSi(O^tBu)_3)_2(\mu OSi(O^tBu)_3))_2]$	2.193(4)	2.540(2)	2.472(8) (bridging)	Nov 2012
$[(U(OSi(O^tBu)_3)_3(\mu-\eta^6:\eta^6\text{-tol}))_2]$	2.117(2)	—	—	Nov 2012
$[(U(OSi(O^tBu)_3)_3)_2(\mu-\eta^1:\eta^2CO_3)]$	2.09(1)	2.67(6)	2.18(1)	Nov 2012
$[(U(OSi(O^tBu)_3)_3)_2(\mu-\eta^2(CS).\eta^2(SS)-CS_2)]$	2.08(0)	2.642(3)	2.16(7)	Nov 2012

Table 4.1: Comparison of key bond distances and angles for Mazzanti's uranium siloxide complexes

In July 2013 Mazzanti published work highlighting the some reactivity studies undertaken. $[(U(OSi(O^tBu)_3)_4]$ was reacted with KC_8 and 18-crown-6 to form the monomeric 'ate' complex, $[K(18C6][U(OSi(^tBu)_3)_4]$ in yields of 69%. The work also investigated the reactivities with trimethylsilyl and adamantyl azides which are summarised in Schemes 4.2 and 4.3.[90]

In November 2013, Mazzanti published further results, investigating the reactivities of the inverted sandwich complex, $[(U(OSi(O^tBu)_3)_3(\mu-\eta^6:\eta^6\text{-tol}))_2]$. Two new complexes were synthesised by the reduction of the parent arene bridged complex with stoichiometric amounts of KC_8 resulting in the products $[K(U(OSi(O^tBu)_3)_3)_2(\mu\eta^6:\eta^6-C_7H_8)]$ and $[K_2(U(OSi(O^tBu)_3)_3)_2(\mu\eta^6:\eta^6-C_7H_8)]$ resulting in three complexes which possess three different states of charge and were investigated in terms of the structure and electronics.[163]

Finally in April 2014, Mazzanti published work highlighting the sterically demanding silox-

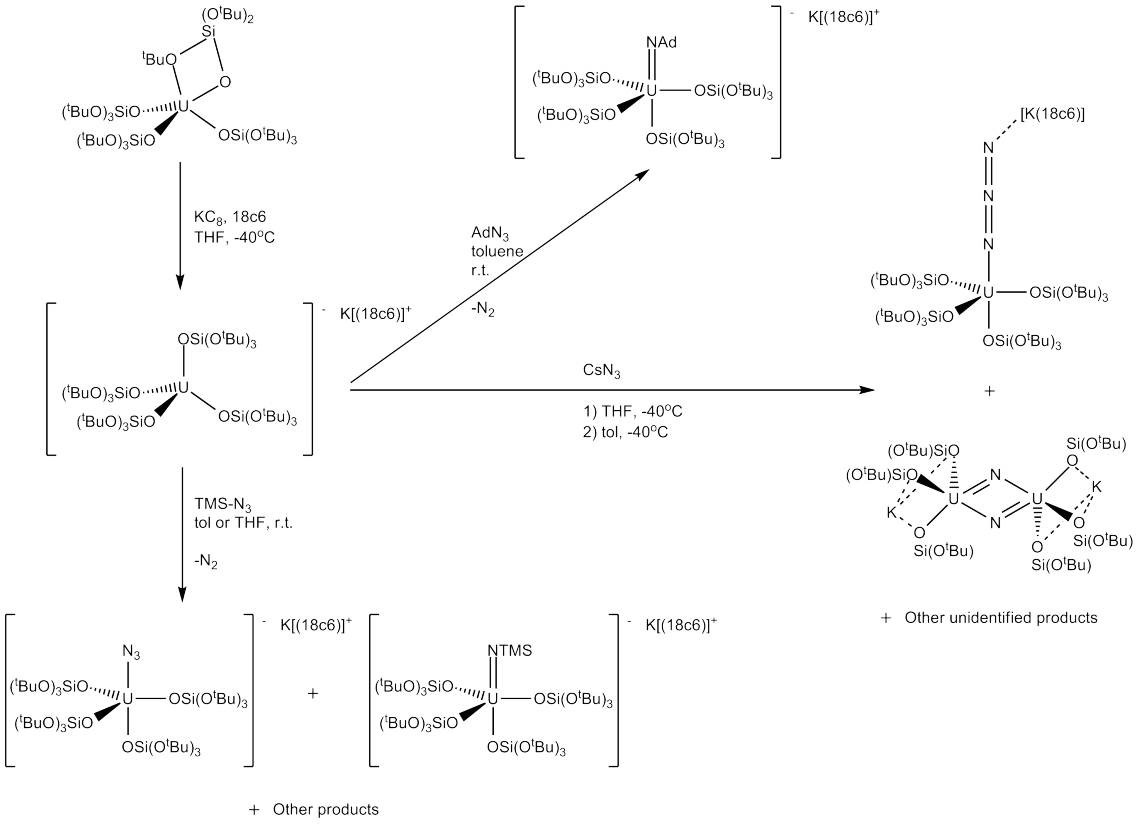

Scheme 4.2: Synthesis of [K(18*C*6][U(OSi(^{t}Bu)$_3$)$_4$] and subsequent reactions with AdN_3, $TMSN_3$ and CsN_3, July 2013[90]

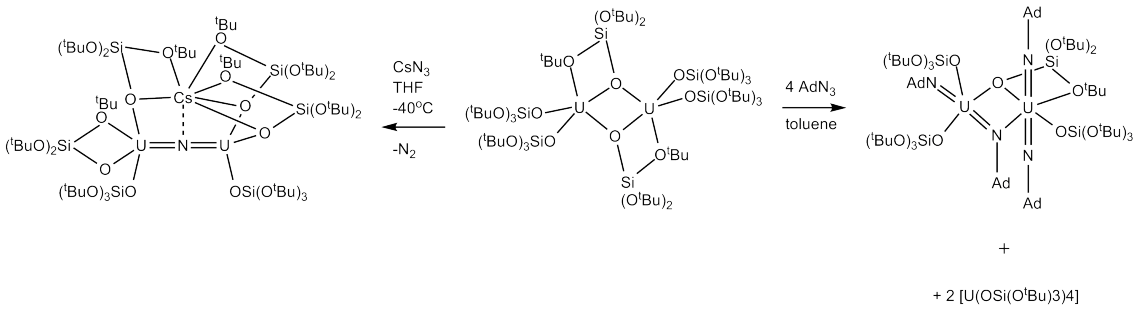

Scheme 4.3: Reaction of [U(OSi(O^{t}Bu)$_3$)$_2$(μ−OSi(O^{t}Bu)$_3$)]$_2$ with AdN_3 and CsN_3, July 2013[90]

ide ligands inducing a large cooperative effect in the reduction of CO_2 shown in Scheme 4.4. The previously reported [K(18c6][U(OSi(^{t}Bu)$_3$)$_4$] was found to promote the selective reductive disproportionation of CO_2, yielding CO and the mononuclear U^{IV} carbonate complex, [U(OSi(O^{t}Bu)$_3$)$_4$($\mu-\kappa^2$:κ^1-CO_3)K$_2$(18c6)].[164]

The reaction of [U(OSi(O^{t}Bu)$_3$)$_4$K] with 1 atm of CO_2, in toluene, at room temperature resulted in the analytically pure terminal oxo pentavalent uranium complex [UO(OSi(O^{t}Bu)$_3$)$_4$K]

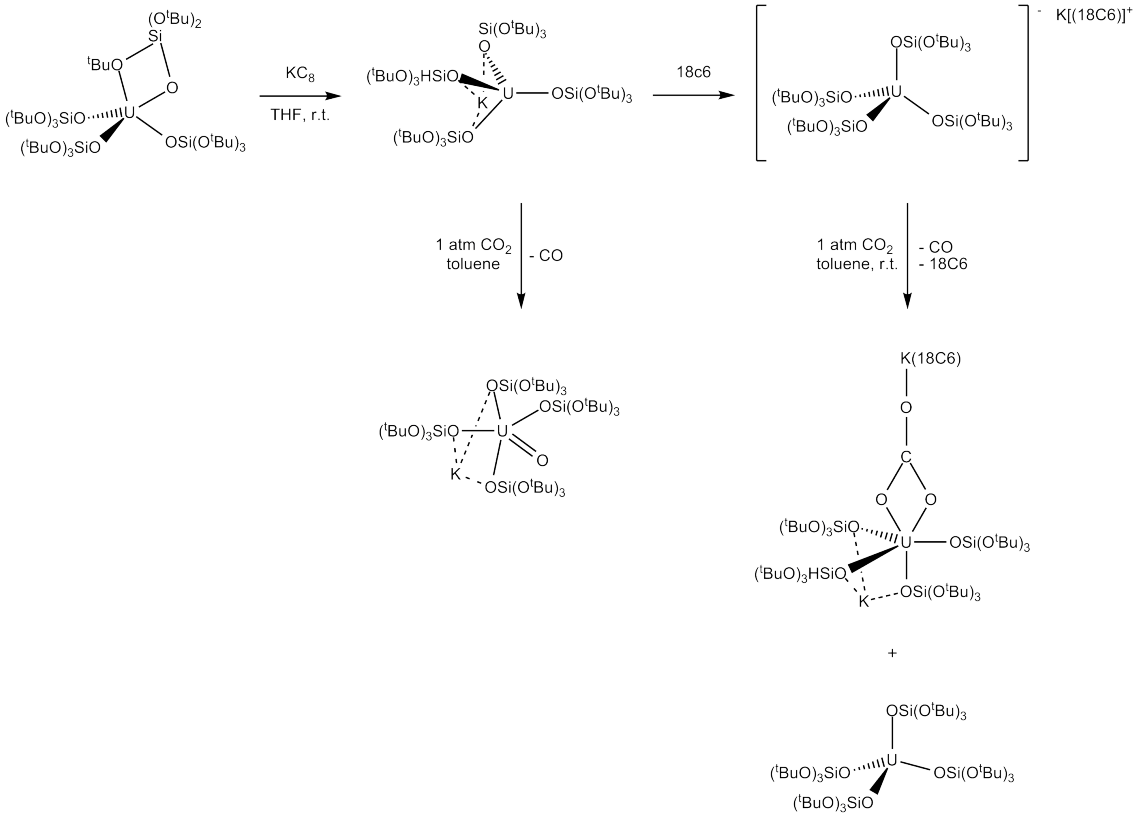

Scheme 4.4: Synthesis and reactions of $[U(OSi(O^tBu)_3)_4K]$ and $[K(_{18}c_6)][U(OSi(O^tBu)_3)_4]$ with CO_2, (April 2014)[164]

in yields of 77%. $^{13}C\{H\}$ NMR studies showed the presence of CO and X–ray diffraction showed the uranium centre in a distorted octahedral geometry, coordinated by two oxygen atoms from a siloxide ligand bound in a bidentate fashion, three monodentate siloxide ligands, also coordinated to a potassium ion and one terminal oxo ligand with a U=O distance of 1.825(2) Å which is comparable to other U^V monooxo complexes discussed in Section 3.2. The U–O_{silox} bond distance, *trans* to the oxo is 2.142(2) Å which was also found to be the shortest, possibly indicative of an inverse trans influence (see Section 2.2.2). The average U–O bond for the terminal siloxide ligands was 2.211(7) Å and the final bidentate ligand had a U–O bond distance of 2.257(2) Å.[164]

$[K(18c6)][U(OSi(O^tBu)_3)_4]$ was also investigated in terms of its reactivity with 1 atm of CO_2. The reaction was instantaneous at room temperature with the evolution of CO observed (confirmed by $^{13}C\{H\}$ NMR). ^1H NMR analysis was used to analyse the two

products that were synthesised in a 1:1 ratio which were identified as [U(OSi(O^{t}Bu)$_3$)$_4$] and [K($_{18}$c$_6$)][U(OSi(O^{t}Bu)$_3$)$_4$]. Pale pink single crystals of the later, of X–ray diffraction quality, were recrystallised from toluene. The data showed the uranium centre to be hexacoordinated in a distorted octahedral geometry. Four siloxide ligands are bound to the uranium centre along with a terminally bound carbonate ligand and a potassium counter ion bound to three of the oxygen atoms on the siloxide ligands. The U–O bond distances of the bridging siloxide ligands were found to be slightly longer at 2.23(1) Å than the non–bridging siloxide ligands at 2.205(5) Å.[164]

4.2 Synthesis of K[(U(OSi(O^{t}Bu)$_3$)$_3$)$_2$($\mu-\eta^6$:η^6-tol))]

As previously discussed in Section 1.3.6 tris *tert*–butoxy siloxides have long been used as surface models on transition metals and lanthanide systems. Until recently however, actinide complexes were unknown. Simple analysis of the uranium and siloxide starting materials available generated two potential targets for synthesis, U(OSi(O^{t}Bu)$_3$)$_3$ and UCl(OSi(O^{t}Bu)$_3$)$_2$. Therefore, in a number of experiments, (^{t}BuO)$_3$SiOK was reacted with either UI$_3$ or UCl$_4$.

By reacting three equivalents of (^{t}BuO)$_3$SiOK in THF with UI$_3$, which was also suspended in THF and added dropwise, the product K[(U(OSi(O^{t}Bu)$_3$)$_3$)$_2$($\mu-\eta^6$:η^6-tol))] was synthesised. The reaction was stirred vigorously and colour changes were observed within a few minutes, from royal blue to chocolate brown. Once the reaction was complete the resulting brown solid was dissolved in toluene and X–ray quality crystals were grown at -40 °C in yields of 16%.

In comparison, Mazzanti's inverted sandwich complex, [(U(OSi(O^{t}Bu)$_3$)$_3$($\mu-\eta^6$:η^6-tol))$_2$] was synthesised by reacting an orange suspension of [(U(OSi(O^{t}Bu)$_3$)$_2$($\mu-$OSi(O^{t}Bu)$_3$))$_2$]

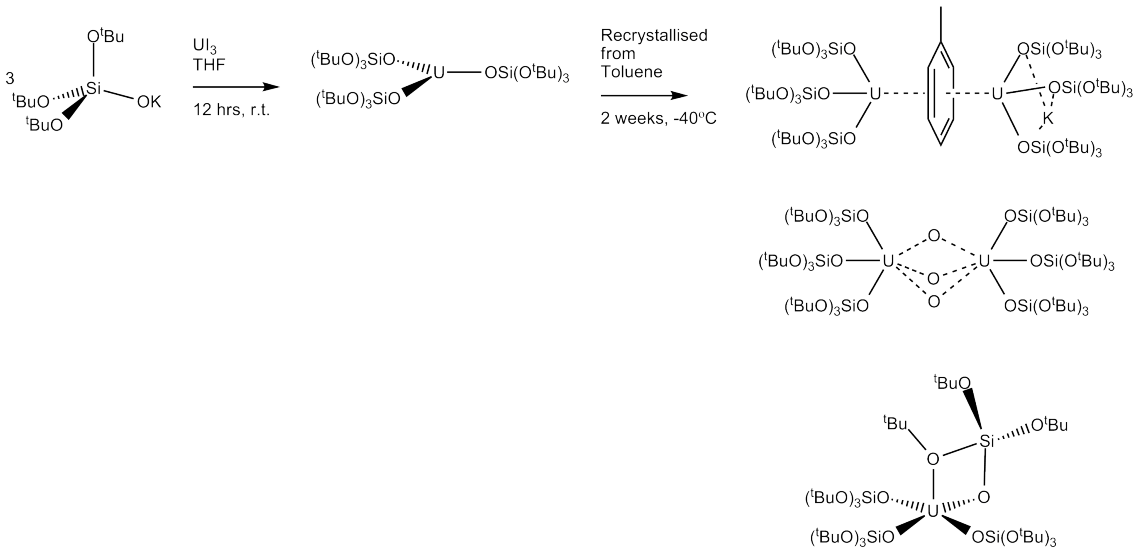

Scheme 4.5: Synthesis of K[(U(OSi(O^{t}Bu)$_3$)$_3$)$_2$($\mu-\eta^6$:η^6-tol))]

in hexane with a few drops of toluene over a period of two days. The reaction resulted in the formation of large dark brown crystals which were filtered and rinsed in toluene and dried *in vacuo* in yields of 89%.

4.2.1 Characterisation of K[(U(OSi(O^{t}Bu)$_3$)$_3$)$_2$($\mu-\eta^6$:η^6-tol))] : X–ray Diffraction

The compound K[(U(OSi(O^{t}Bu)$_3$)$_3$)$_2$($\mu-\eta^6$:η^6-tol))] crystallises in P 2$_1$ space group. The lattice parameters for this structure are *a* = 14.3524(3) Å, *b* = 23.5604(5) Å, *c* = 18.3105(4) Å, α = 90 °, β = 103.258(1) °, γ = 90 °.

In comparison, Mazzanti's [(U(OSi(O^{t}Bu)$_3$)$_3$($\mu-\eta^6$:η^6-tol))$_2$] complex crystallises in R-3 space group with an *R* factor of 3.33. The lattice parameters for Mazzanti's structure are *a* = 23.5027(5) Å, *b* = 23.5027(5) Å, *c* = 16.1715(4) Å, α = 90 °, β = 90 °, γ = 120 °

The X–ray diffraction image of K[(U(OSi(O^{t}Bu)$_3$)$_3$)$_2$($\mu-\eta^6$:η^6-tol))] is shown in Figures 4.1 and 4.2. Each uranium atom has a distorted trigonal pyramidal geometry and can be assigned a C$_{3v}$ point group. Alternatively, the whole molecule is assigned a D$_{3d}$

point group. Each uranium atom has three *tert*–butoxy ligands bonded to it and the two uranium centres (U1 and U2) are coordinated to a central toluene molecule in an inverted sandwich type orientation, the two sets of *tert*–butoxy ligands are in a staggered conformation due to the steric bulk of the ligands. There is also one counterion present which is coordinated to all three ligands on U1 atom, via the oxygen atoms.

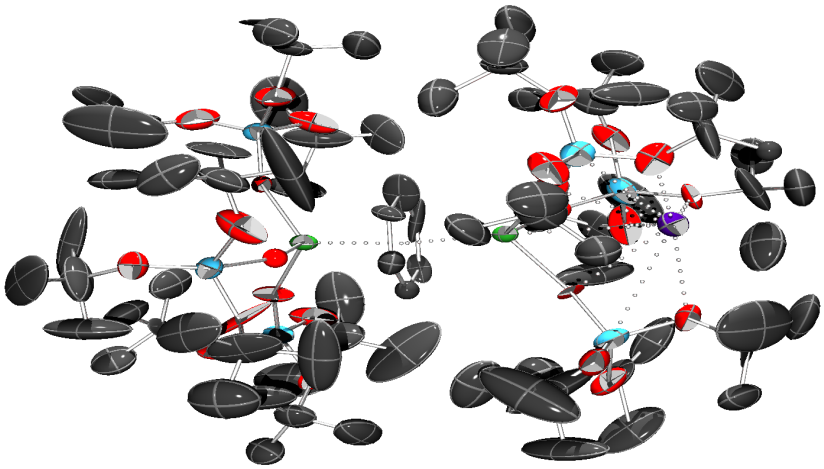

Figure 4.1: Molecular structure of K[(U(OSi(O^{t}Bu)$_3$)$_3$)$_2$($\mu-\eta^6$:η^6-tol))] (Hydrogen atoms omitted for clarity)

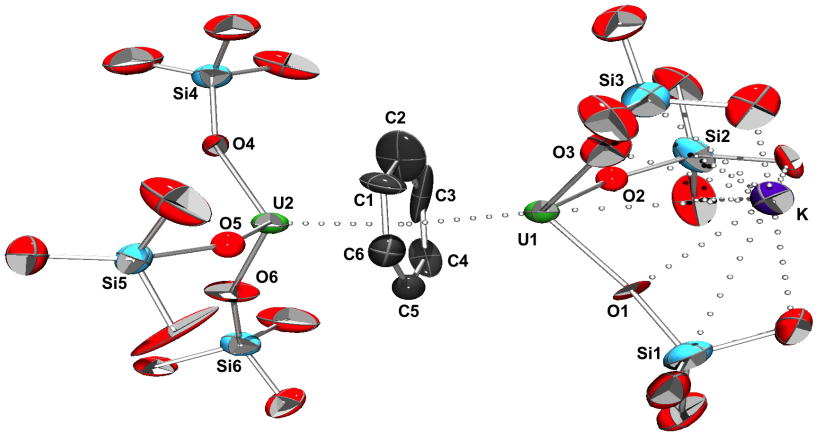

Figure 4.2: Core molecular structure of K[(U(OSi(O^{t}Bu)$_3$)$_3$)$_2$($\mu-\eta^6$:η^6-tol))] containing the Si, O U and K atoms and bridging toluene (Hydrogen atoms and *tert*–butoxy groups omitted for clarity)

Similarly, Mazzanti's structure possesses three siloxide ligands on each of the two uranium centres (U1 and U1L) which are also in a staggered conformation due to sterics. The two uranium atoms are coordinated to a central toluene molecules in an inverted sandwich orientation. Mazzanti's structure does not possess a coordinated potassium counter ion unlike the complex presented as part of this work.

Table 4.2 shows the key bond distances of both structures. Mazzanti's complex has an average U–O bond distance of 2.117 Å which is slightly shorter (*ca.* 0.009 Å) than the U–O bond distance of the complex presented here. In addition Mazzanti's complex has slightly shorter O–Si bond lengths (*ca.* 0.39 Å) but longer U–C_{tol} (*ca.* 0.084 Å) than K[(U(OSi(O^{t}Bu)$_3$)$_3$)$_2$($\mu-\eta^6$:η^6-tol))] which is discussed further in Section 4.2.2.

The U–O bond distances for K[(U(OSi(O^{t}Bu)$_3$)$_3$)$_2$($\mu-\eta^6$:η^6-tol))] range from 1.9681 Å to 2.2467 Å with the average across both uranium centres found to be 2.126 Å. The O–Si bond distances range from 1.5366 Å to 1.8077 Å with an average of 1.653 Å. Figures 4.5 and 4.6 compare these values to other actinide based complexes furnished with a tris *tert*–butoxy ligand system. This comparison clearly shows the U–O bond distances are within previously identified limits for similar systems. Analysis of the O–Si bonds however, show there are two bonds (1.7574 Å and 1.8077 Å) that exceed previously identified O–Si bond distances. These lengthened bonds correspond with the shortest of the U–O bonds within the molecule. In addition, one elongated O–Si bond is located on each of the uranium centres which indicates that the potassium counterion, which is coordinated to one of the uranium centres, is not responsible for the lengthening of these bonds.

The U–O distances for each uranium centre are shown schematically in Figure 4.3, showing the difference between the U1 close to the potassium ion in (a) and the uncoordinated U2 centre in (b).

Complex	U–O_{silox} / Å	O–$Si_{siloxide}$ / Å	U–C_{tol} / Å	C_{tol}–C_{tol} / Å
K[(U(OSi(O^{t}Bu)$_3$)$_3$)$_2$(μ–η^6:η^6-tol))]				
tol–U1–O1–Si1	2.0713	1.7574	2.6014	1.3900
tol–U1–O2–Si2	2.1965	1.5969	2.5840	1.3900
tol–U1–O3–Si3	2.2467	1.5366	2.5993(1)	1.3900
tol–U1			2.6318	1.3900
tol–U1			2.6489	1.3900
tol–U1			2.6338	1.3900
Average	**2.172**	**1.630**	**2.617**	**1.390**
tol–U2–O4–Si4	2.1221	1.6216	2.5193	
tol–U2–O5–Si5	1.9681	1.8077	2.5452	
tol–U2–O6–Si6	2.1457	1.5987	2.6249	
tol–U2			2.6778	
tol–U2			2.6531	
tol–U2			2.5743	
Average	**2.079**	**1.676**	**2.599**	
Total average	**2.126**	**1.653**	**2.608**	
[(U(OSi(O^{t}Bu)$_3$)$_3$(μ–η^6:η^6-tol))$_2$] [162]				
tol–U1–O1–Si1	2.118	1.614(3)	2.695	1.432(5)
tol–U1–O1A–Si1A	2.117	1.614(2)	2.695	1.432(6)
tol–U1–O1B–Si1B	2.116	1.614(4)	2.694	1.432(6)
tol–U1			2.689	1.432(5)
tol–U1			2.689	1.432(5)
tol–U1			2.690	1.432(5)
tol–U1L–O1L–Si1	2.118	1.614(3)	2.689	
tol–U1L–O1M–Si1	2.117	1.614(2)	2.689	
tol–U1L–O1N–Si1	2.116	1.614(4)	2.690	
tol–U1L			2.695	
tol–U1L			2.695	
tol–U1L			2.694	
Total average	**2.117**	**1.614**	**2.692**	**1.432**

Table 4.2: Key bond lengths: A comparison between K[(U(OSi(O^{t}Bu)$_3$)$_3$)$_2$(μ–η^6:η^6-tol))] and Mazzanti's [(U(OSi(O^{t}Bu)$_3$)$_3$(μ–η^6:η^6-tol))$_2$] structure [162]

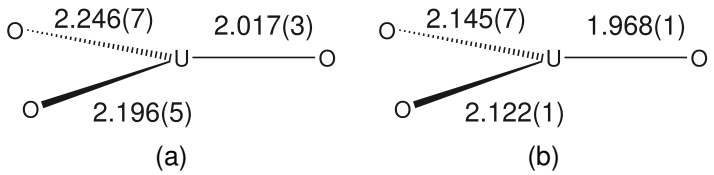

Figure 4.3: Uranium–oxygen distances in K[(U(OSi(O^{t}Bu)$_3$)$_3$)$_2$(μ–η^6:η^6-tol))] at the U centre close to K (a) and distant from K (b)

The presence of one short and two long bonds around each uranium is reminiscent of the second order Jahn–Teller distortion, often seen in trigonal metal systems. [167–169] Second order Jahn–Teller distortions have been discussed in detail with respect to pyramidalisa-

tion of trigonal *d*–metal transition metal complexes in detail, where a C_{3v} pyramidal geometry can be preferred if the interaction of the d_{xz} and d_{yz} is more favourable than the interaction of the ligand system i.e. p_x, $d_{x^2-y^2}$ and p_y, d_{xy}.[170,171]

In the plane of the molecule, a similar effect is possible, as the *a* electronic ground state will always mix with the LUMO symmetry and will distort, in principle, if the LUMO has *e* symmetry. The effect of the 5*f* orbitals can be ignored for two reasons, the level of covalency associated with these orbitals is very small and the irreducible representations of the 5*f* span all of those present in any C_3–derived group. This means that any direct product is possible when using the 5*f*–orbitals as a basis. If, however, there is a small degree of covalency due to the 6*d* orbitals, then a similar mechanism may be present in this system, though it is notable that the structure published by Mazzanti of $[(U(OSi(O^tBu)_3)_3)_2(\mu-\eta^6:\eta^6\text{-tol}))]$ was in space group R-3 with the U1 and U1L atoms positioned directly along the C_3 as shown in Figure 4.4. The location of the C_3 axis through the pair of uranium centres shows that any electronic distortion is extremely small.

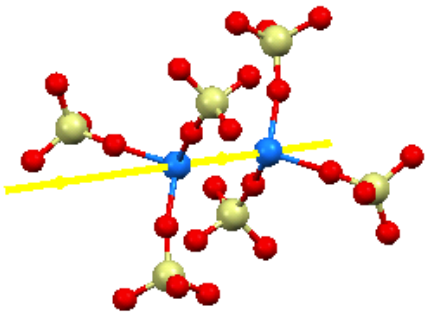

Figure 4.4: Mazzanti's inverted sandwich complex with the C_{3v} axis highlighted, Blue = uranium; Red = oxygen; Yellow = silicon (Carbon and hydrogen atoms are omitted for clarity)

In addition, the lattice packing is also considered as an explanation as to why one U–O bond is shorter on each uranium centre. However, when the lattice is investigated, it is observed that each of the short U–O bonds are parallel to each other, both directed along the same *z*–axis and therefore it is concluded that the lattice packing is not responsible

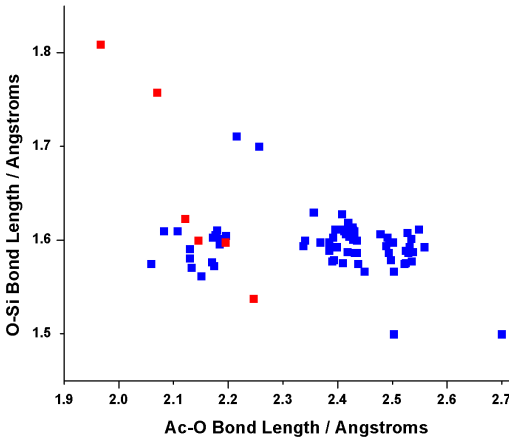

Figure 4.5: Correlation between Ac–O bond distances and O–Si for actinide compounds with the ligand $(^{t}BuO)_3SiO$. (Data points in red are the experimental values for $K[(U(OSi(O^{t}Bu)_3)_3)_2(\mu-\eta^6:\eta^6\text{-tol}))]$

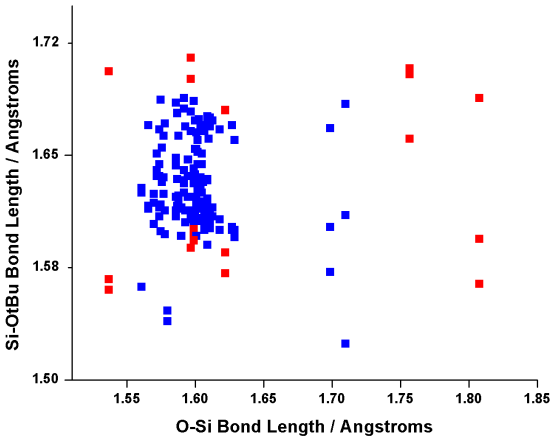

Figure 4.6: Correlation between O–Si bond distances and $Si-O^{t}Bu$ for actinide compounds with the ligand $(^{t}BuO)_3SiO$. (Data points in red are the experimental values for $K[(U(OSi(O^{t}Bu)_3)_3)_2(\mu-\eta^6:\eta^6\text{-tol}))])$

for the shortening of these two bonds.

On average, U1 is found to have shorter than average O–Si bonds at 1.630 Å and longer than average U–O bonds 2.172 Å. This lengthening and contracting across the U–O–Si bonds was also seen in the $K[U(OSiPh_3)_5]$ complex and analysed in Chapter 2.

The U–O–Si bond angles range from 149.65° to 175.58° with an average of 161.99 °. Figure 4.7 shows that this is within the range of published data. The U1–O–Si angles are more linear (average 169.6 °) to due the coordination of the potassium counterion compared to the non potassiated side, U2–O–Si (154.3 ° average).

4.2.2 Bridging arenes

Bridging arenes or 'inverted sandwich' complexes are those which have the general structure, $L_nM–ArR–ML_n$ where ArR is an arene. The arene featured could be benzene,[172,173] toluene,[162,172,174,175] naphthalene,[176,177] biphenyl,[172] cycloheptatrienyl[178]

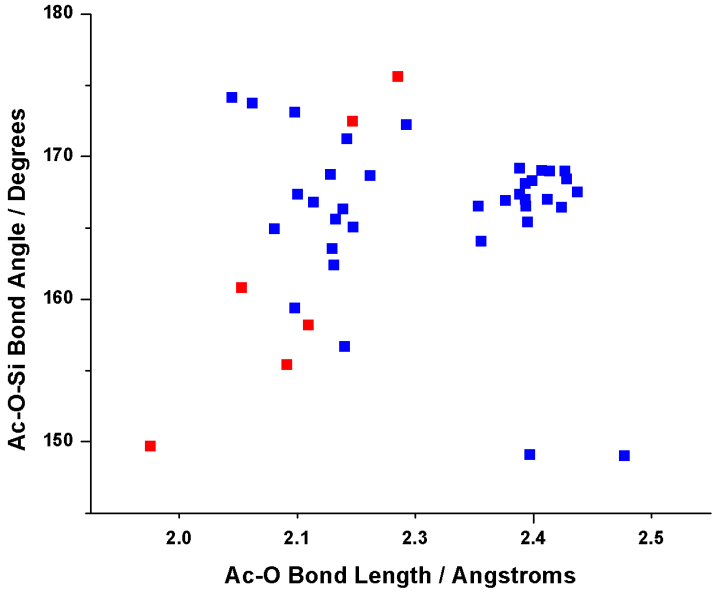

Figure 4.7: U–O–Si bond angles for actinide compounds with the ligand $(^{t}BuO)_3SiO$. (Data points in red are the experimental values for $K[(U(OSi(O^{t}Bu)_3)_3)_2(\mu-\eta^6:\eta^6\text{-tol}))]$)

or cyclooctatetraene[176] bonded as the bridging ligand. Bridging arenes on actinides are relatively rare[179] but the general structure is mainly observed in low valent uranium chemistry. The first example of an arene bridged uranium was $(\mu-C_7H_8)[U(N[R]Ar)_2]_2$ as shown in Figure 4.8.[174] It is generally accepted that δ bonding play an important role between both the *d* and *f*–orbitals of the uranium (*d*–*f* mixing) and the LUMO of the appropriate symmetry of the ligand in actinocene complexes[177] but development in this area is required and investigating the nature of bonding in inverted sandwich complexes could provide further insight into this area.[162,163,175]

In this work, the toluene molecule is coordinated to both uranium centres in an inverted sandwich motif with a U–Centroid–U angle of 174.8° and an average U–C bond distance of 2.599 Å on the non potassiated side and 2.617 Å on the potassiated side as highlighted in Table 4.2. These bond lengths are marginally shorter than Mazzanti's structure which has an average U–C bond length of 2.692 Å. Both complexes have much shorter U–C bond lengths than those found in uranium complexes of neutral arenes (average

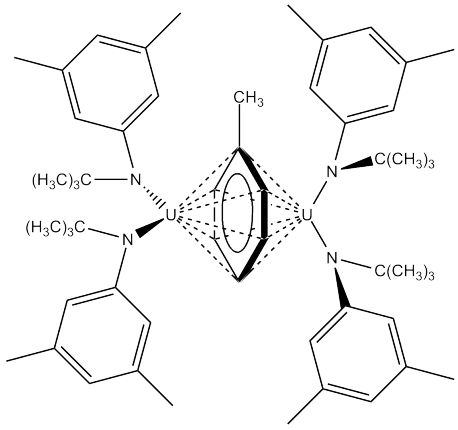

Figure 4.8: An early example of an arene bridged diuranium complex

2.93 Å).[162] In both cases the bridging toluene molecule is bound in a η^6:η^6 symmetrical fashion to the two uranium centres.

Table 4.2 shows the average C–C bond distance within the toluene molecule is 1.39 Å which is slightly longer than free toluene (1.379 Å[85]). This is suggestive that the toluene has been reduced slightly. Mazzanti's structure has an observed C–C bond distance of 1.432 Å in the toluene bridge[162] which is much longer and suggestive of a greater reduction of the toluene than observed in K[(U(OSi(O^{t}Bu)$_3$)$_3$)$_2$($\mu-\eta^6$:η^6-tol))].

Covalent Bond Classification

Whilst the covalent bond classification (CBC) method is applicable only in the case of very significant covalency, and therefore is not applicable to the actinides as a general description of the bonding situation, the notation is useful to describe electron assignments within a molecule.

According to the C.B.C method[180,181], any metal or ligand can be organised into one of four classifications, M, L, X or Z. The central metal is classified as M whilst ligands can be separated into L, X or Z based on their bonding electronics. X and L ligands simply contribute either one or two electrons respectively to the bond with the metal centre. Z

ligands possess empty orbitals which require donation of two electrons from the metal in order to form a bond. Additionally the method provides an outline of how to treat cations and anions and according to the C.B.C method, anions are treated as X^- and this converts to L as illustrated by the following example for $[MoX_6]^{3-}$;

$$[MoX_6]^{3-} = [MoX_3(X^-)_3] \text{ and if } X^- = L \text{ then } [MoL_3X_3]$$

Therefore, by implementing all the rules to the uranium complex reported here, the following can be concluded;

$$[U_2L_3X_6]^- = [U_2L_3X_5(X^-)] = [U_2L_4X_5]$$

The above analysis assumes the arene is neutral which gives the molecule an oxidation state for each uranium centre as $U^{2.5}$ ($U_2L_4X_5$) which is unlikely. If the arene acts as a dianion (L_2X_2) then the molecule would formally be counted as $U_2L_3X_7$ which gives an oxidation state for each uranium as $U^{3.5}$.

Mazzanti's complex, $[(U(OSi(O^tBu)_3)_2(\mu-OSi(O^tBu)_3))_2]$[162] was described as a U^{IV} ion centre with a dianionic toluene bridged ligand resulting from the reduction of toluene by the U^{III} siloxide complex. The average U–O bond length of the complex described here is 2.126 Å which is slightly longer than Mazzanti's inverted sandwich complex (U–O 2.117 Å), but shorter than the non bridged U^{III} derivative, $[(U(OSi(O^tBu)_3)_2(\mu-OSi(O^tBu)_3))_2]$ supporting the hypothesis that the uranium centres described here are in a $U^{3.5}$ state.

4.2.3 Characterisation of K[(U(OSi(O^{t}Bu)$_3$)$_3$)$_2$($\mu-\eta^6$:η^6-tol))] : NMR

The NMR spectroscopy data correlate well with the observed X–ray diffraction data. The X–ray diffraction data suggest two uranium centres in an inverted sandwich conformation

and the two uranium centres differing only with proximity to the coordinated potassium counterion. Analysis of the $^{13}C\{H\}$ and ^{1}H NMR spectrum also show two different chemical environments in solution with equal integration values as shown in Appendices E.9 and E.10.

The $^{13}C\{H\}$ NMR spectroscopy data are tabulated in Table 4.3 and clearly show two chemical environments. The electro–positive nature of the potassium counterion changes the magnetic environment of the uranium atom and the coordinated *tert*–butoxy groups and are assigned to the resonance at δ 28.78 ppm whilst the *tert*–butoxy groups that are not coordinated to the potassium counterion are assigned to the second resonance at δ 33.27 ppm.

This structure is further supported by the ^{1}H NMR spectrum. The resonance observed at δ -0.54 ppm (FWHH = 8.4 Hz) is assigned to the *tert*–butoxy groups coordinated to the potassium counter ion, whilst the other non–coordinated *tert*–butoxy groups are assigned to the resonance at δ 2.38 ppm (FWHH = 1.72 Hz). This hypothesis is additionally supported by the integrals which are of equal value and HSQC data which are shown in Appendix E.12.

Carbon Assignment	δ/ppm
U((^{t}**Bu**O)$_3$SiO)$_3$ (U2)	33.27
K[((^{t}**Bu**O)$_3$SiO)$_3$U] (U1)	28.78

Table 4.3: NMR Resonances for the $^{13}C\{H\}$ spectrum of K[(U(OSi(O^{t}Bu)$_3$)$_3$)$_2$(μ–η^6:η^6-tol))] in d_6–benzene

Proton Assignment	δ/ppm (multiplicity, coupling constant)
U((^{t}**Bu**O)$_3$SiO)$_3$ (U2)	2.38 (s, 1H)
K[((^{t}**Bu**O)$_3$SiO)$_3$U] (U1)	-0.54 (s, 1H)

Table 4.4: NMR Resonances for the ^{1}H spectrum of K[(U(OSi(O^{t}Bu)$_3$)$_3$)$_2$(μ–η^6:η^6-tol))] in d_6–benzene

NMR spectroscopy techniques were used to investigate the reaction pathway and Figure 4.9 shows the results of these experiments. The ^{1}H NMR spectrum clearly show two resonances at δ 2.38 and 0.07 ppm increasing in intensity as $(tBuO)_3SiOK$) is added. Comparing this to the ^{1}H NMR spectrum observed for the inverted sandwich complex and the $(tBuO)_3SiOK$) starting material, these resonances are assigned to U2 and U1 respectively. Interestingly, other species are also observed during the synthesis. A resonance appears at δ 12.95 ppm as one equivalent of the ligand is added and slowly decreases as further equivalents of ligand are added providing evidence of a possible intermediate. In addition resonances at δ 5.88 and 1.54 ppm are observed which increase in intensity as ligand is added, providing evidence of a second product being synthesised which could provide a reason why the product was difficult to recrystallise reliably.

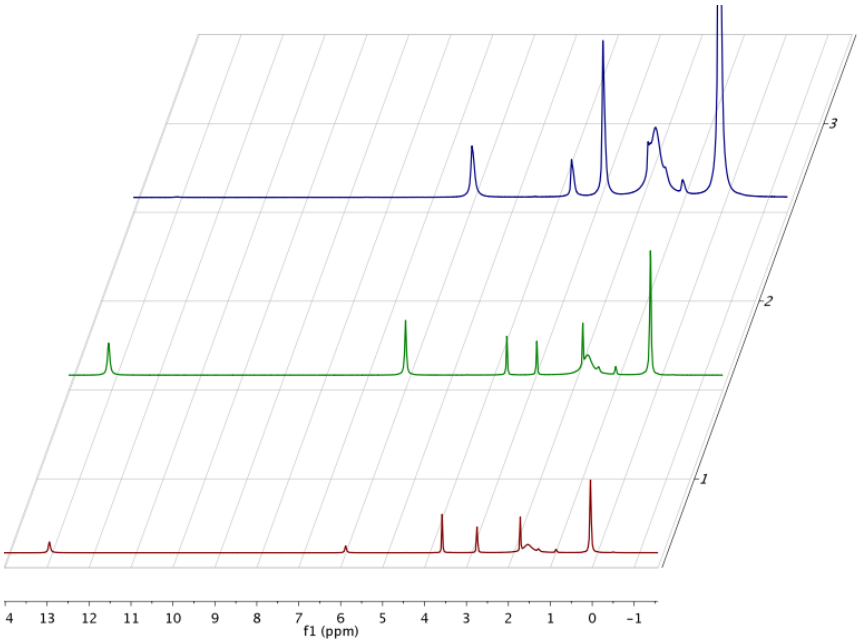

Figure 4.9: Stacked ^{1}H NMR spectra for the reaction between UI_3 and 1 eq. of $(tBuO)_3SiOK$) (red), 2 eq. of $(tBuO)_3SiOK$) (green) and 3 eq. of $(tBuO)_3SiOK$) (blue) in d_8–THF

Robin–Day classification

The Robin–Day classification separates mixed valence systems into three classes simply referred to as class I, class II and class III depending on the strength of the electronic interactions between the oxidised and reduced sites. Class I refers to complexes where the electrons are localised and completely trapped on the separate sites. Class III refers to complexes were the electrons are completely delocalised and their position indistinguishable. Class II lies between the two extreme positions and the electrons are partially delocalised. Considering the NMR spectroscopy and X–ray diffraction evidence it is logical to assign this complex as a class I complex where the electrons are localised on the two separate uranium sites and therefore can be observed both in the solution and solid state.[182–184]

4.2.4 Synthesis of K[(U(OSi(O^{t}Bu)$_3$)$_3$)$_2$($\mu-\eta^6$:η^6-tol))] : Negative ion ESI

In order to ascertain the products that were synthesised during the reaction, negative ion ESI HRMS was employed as a further analysis technique. The starting material UI_3 was suspended in THF and the ligand species, (^{t}BuO)$_3$SiOK was dissolved in THF. Aliquots equal to one equivalent of the ligand were added to the UI_3. Each equivalent was analysed and recorded by negative ion ESI HRMS and shown in Table 4.5.

On addition of both one and two equivalents of (^{t}BuO)$_3$SiOK, only two major fragments are observed, neither being the desired product, U(OSi(O^{t}Bu)$_3$)$_3$. The uranium species observed has two siloxide ligands and three iodides. However, as soon as three equivalents of the ligand were added to the solution the desired *tris* product is observed along with the *tetra* side product, both of which are stable over a three hour period. The synthesis of more than one product, also observed by NMR spectroscopy, presented prob-

$(^t$BuO$)_3$SiOK	HRMS m/z	Relative Intensity	Anion Assignment
1 eq.	745.6644	0.37	UI_4
	961.1200	0.06	—
	1145.0823	0.56	$[((^t$BuO$)_3$SiO$)_2UI_3]$
2 eq.	745.6689	0.04	UI_4
	961.1241	0.08	—
	1145.0914	0.89	$[((^t$BuO$)_3$SiO$)_2UI_3]$
3 eq.	1059.5356	0.32	$[((^t$BuO$)_3$SiO$)_3UO_2]$
	1154.4550	0.23	$[((^t$BuO$)_3$SiO$)_3$UI]
	1290.7186	0.45	$[((^t$BuO$)_3$SiO$)_4$U]
3 eq. (3 hours)	1059.5356	0.38	$[((^t$BuO$)_3$SiO$)_3UO_2]$
	1154.4550	0.22	$[((^t$BuO$)_3$SiO$)_3$UI]
	1290.7182	0.41	$[((^t$BuO$)_3$SiO$)_4$U]

Table 4.5: Negative ion ESI HRMS data of the synthesis of K[(U(OSi(O^{t}Bu)$_3$)$_3$)$_2$($\mu-\eta^6$:η^6-tol))]

lems regarding the crystallisation of the products, but co–crystallisation was achieved, the results of which are discussed in Section 4.3. In addition, and as previously seen in Section 2.5, unavoidable oxygen impurities reacted with the products and are seen in the ESI HRMS results.

4.3 Co–crystallisation products

Alongside the orange/brown crystals of K[(U(OSi(O^{t}Bu)$_3$)$_3$)$_2$($\mu-\eta^6$:η^6-tol))] discussed in Section 4.2, two other products co–crystallised which were visually very different and all three were isolated. The two co–crystallised products were black block crystals and green block crystals. The black blocks were analysed by X–ray diffraction and found to be an oxo bridged compound, $[((^t$BuO$)_3$SiO$)_3$U$]_2(\mu^2$-O$)_3$, whilst the green block crystals

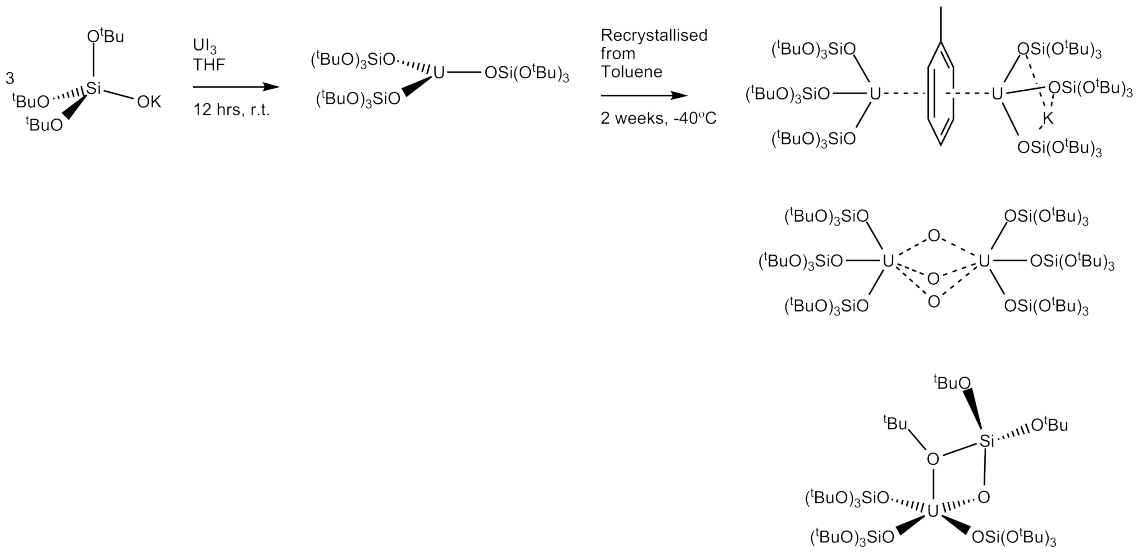

Scheme 4.6: Synthesis of K[(U(OSi(O^{t}Bu)$_3$)$_3$)$_2$($\mu-\eta^6$:η^6-tol))] and two cocrystallisation products, [((^{t}BuO)$_3$SiO)$_3$U]$_2$(μ^2-O)$_3$ and [(U(OSi(O^{t}Bu)$_3$)$_4$)]

were identified as the tetrakis unit, ((^{t}BuO)$_3$SiO)$_4$U which had also been synthesised directly from UCl_4 by J. Pankhurst, a Masters student under the authors supervision. The crystallised products, K[(U(OSi(O^{t}Bu)$_3$)$_3$)$_2$($\mu-\eta^6$:η^6-tol))], [((^{t}BuO)$_3$SiO)$_3$U]$_2$(μ^2-O)$_3$ and ((^{t}BuO)$_3$SiO)$_4$U crystallised in approximately a 5:2:3 ratio but the X–ray diffraction data were not of publishable quality.

4.3.1 Characterisation of [((^{t}BuO)$_3$SiO)$_3$U]$_2$(μ^2-O)$_3$: X–ray Diffraction

The compound crystallises in space group R3. The lattice parameters for this structure are *a* = 23.4821(2) Å, *b* = 23.4821(2) Å, *c* = 16.2502(3) Å, α = 90°, β = 90°, γ = 120°.

The X–ray diffraction data shown in Figure 4.10 shows two tris *tert* butoxy uranium units to be bridged by three oxygen atoms. It can therefore be surmised that each uranium unit has a distorted trigonal pyramidal geometry with a C_{3v} point group. The entire molecule however has a point group of D_{3d}. The two sets of *tert* butoxy ligands on each uranium centre are in a staggered conformation due to the steric bulk of the ligands.

The U–O_{silox} bond distances range from 2.08(1) Å to 2.16(2) Å with an average of 2.11 Å. The O–Si bond distances range from 1.57(1) Å to 1.64(2) Å with an average distance of 1.60 Å.[85] Comparing these distances to the K[(U(OSi(O^tBu)$_3$)$_3$)$_2$($\mu-\eta^6$:η^6-tol))] complex the U–O_{silox} bond distance have decreased slightly whilst the O–Si bond distance have also decreased suggesting that the three oxygen bridging atoms are withdrawing electron density from the uranium centres. The U–O–Si bond angles range from 163.7(8)° to 167.0(9) ° with an average angle of 165.3°. The O–U–O bond angles range from 85.7(4)° to 146.5(4)° with an average angle of 115.7°.

In addition, the U–$O_{bridged}$ bond distances range from 2.679(4) Å to 2.689(4) Å with an average of 2.684 Å, slightly longer than the U–O_{silox} bond distances and longer than the average U–O–U bond distances previously reported (average 2.32 Å).[85] Analysis of other U–(μ^2-O)3)–U complexes were undertaken but none found. Analysis of other U–(μ^2-O)2)–U was conducted with the average U–O found to be 2.127 Å[85] which is shorter than the U–(μ^2-O)3)–U bond distance reported here, however this is to be expected as the bridging trioxo requires more electron density and weaken the bonds. In addition the average U–(μ^2-O)2)–U bond angle found in the literature was 107.38°[85], whilst the average U–(μ^2-O)3)–U angle for [((^{t}BuO)$_3$SiO)$_3$U]$_2$(μ^2-O)$_3$ is 155.8(2)°. Again this is expected with the shorter U–O_{oxo} bonds, sterics will increase the bond angles to increase the intramolecular distance between the oxygen atoms.

Delocalised bonding in bridged diuranium species

Representing the cluster core as shown in Figure 4.11, it is possible to assemble a bonding picture between the bridging trioxo species and the bridging arene systems in the limit of full delocalisation and ignoring relative orbital contributions.

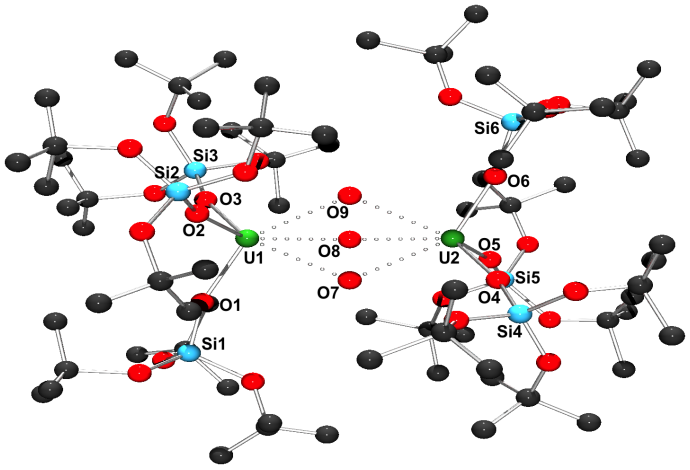

Figure 4.10: Molecular structure of $[((^{t}BuO)_3SiO)_3U]_2(\mu^2\text{-}O)_3$ (Hydrogen atoms omitted for clarity)

With [U] = $U(OSi^{t}Bu_3)_3$ and assuming that each $U-OSi^{t}Bu_3$ linkage represents a two–centre two–electron bond, then U will contribute three electrons to the core cluster. In the case of the core of the arene–bridged dimers, each carbon atom contributes three electrons to the framework of the cluster, excluding the exohedral C–H from the count. Of these, then two electrons per carbon will be involved with C–C σ–bonding, leaving one electron per carbon atom available to the cluster. Six electrons are therefore available, making a total of twelve electrons in the bonding model of the core.

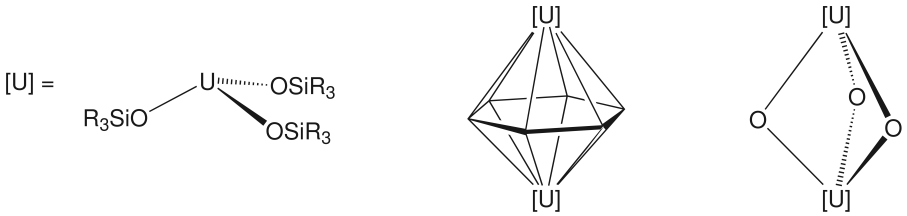

Figure 4.11: The core structure for U_2X_6 (X = CH) and U_2X_3 (X = O) cores for diuranium 'inverted sandwiches'

In the case of the trioxo–bridged system, the count for the neutral uranium centres are identical; each oxygen atom then carries two non–bonding electron pairs and a pair of electrons that are available to the cluster core. In this sense, the bridge yields exactly the same number of electrons as the arene bridged system, that is six electrons in both cases. Both bridge clusters therefore contain twelve electrons each.

For [((^{t}BuO)$_3$SiO)$_3$U]$_2$(μ^2-O)$_3$, the oxidation state of uranium is clearly six on both cases, with the electrons being localised on the formally bridging oxide ligands. For arene–bridged systems, the oxidation states are discussed above.

4.4 Synthesis and characterisation of U(OSi(O^{t}Bu)$_3$)$_4$

The complex U(OSi(O^{t}Bu)$_3$)$_4$ which was co–crystallised alongside the inverted sandwich complex [(U(OSi(O^{t}Bu)$_3$)$_3$)$_2$($\mu-\eta^6$:η^6-tol))] was also synthesised by the following method by a Masters student under the authors supervision.[80]

4.4.1 Synthesis of U(OSi(O^{t}Bu)$_3$)$_4$

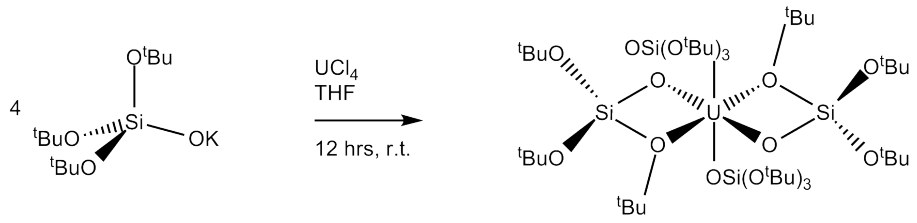

Scheme 4.7: Synthesis of U(OSi(O^{t}Bu)$_3$)$_4$

Treatment of uranium tetrachloride in THF with four equivalents of (^{t}BuO)$_3$SiOK at room temperature, with stirring, resulted in a blue solution. A blue solid was extracted from the solution in 60% yields when the solvent was removed *in vacuo*. The blue crude product turned light purple when subjected to extended periods of vacuum. In solution the product also turns green when cooled to -40°C. The product was then recrystallised from a toluene solution at -40°C resulting in purple crystals.[80]

4.4.2 Characterisation of [(U(OSi(O^{t}Bu)$_3$)$_4$)] : X–ray Diffraction

U(OSi(O^{t}Bu)$_3$)$_4$ crystallises from toluene in temperatures of -40°C in the space group C 2/c with an *R* factor of 4.64. The lattice parameters are *a* = 24.2415(5) Å, *b* = 13.5626(3) Å, *c* = 41.0629(9) Å, α = 90°, β = 96.6880(10)° and γ = 90°.

The molecular structure is shown in Figures 4.12 and 4.13. The structure shows the uranium centre is five coordinate with three siloxide ligands bonded monodentate and one of the ligands bonding in a bidentate fashion to give a distorted square pyramid geometry of C_{4v} symmetry. In this conformation the uranium centre has an oxidation state of U^{IV} as the internally solvating ^{t}BuO group coordinates through a dative bond. The bond length of the dative bond is lengthened from an average of 2.141 Å to 2.562 Å, an increase of 0.42 Å.

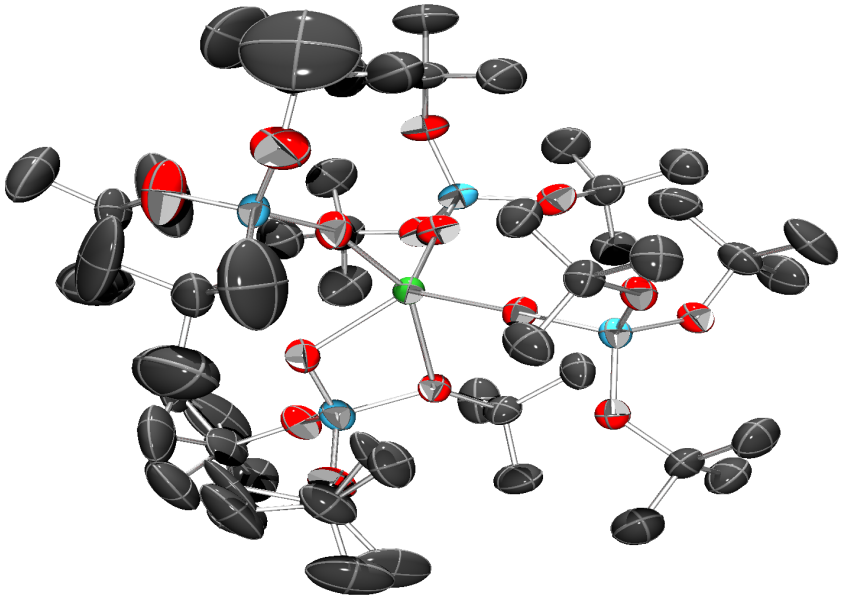

Figure 4.12: Molecular structure of U(OSi(O^{t}Bu)$_3$)$_4$ (Hydrogen atoms omitted for clarity)[80]

The U–O_{silox} bond distance range from 2.111(3) Å to 2.135(3) Å with an average of 2.12(3) Å, very similar to the $U^{3.5}$ complex, K[(U(OSi(O^{t}Bu)$_3$)$_3$)$_2$($\mu-\eta^6$:η^6-tol))] (2.125 Å) and shorter than Mazzanti's U^{III} inverted sandwich, [(U(OSi(O^{t}Bu)$_3$)$_2$(ηOSi(O^{t}Bu)$_3$))$_2$][162]

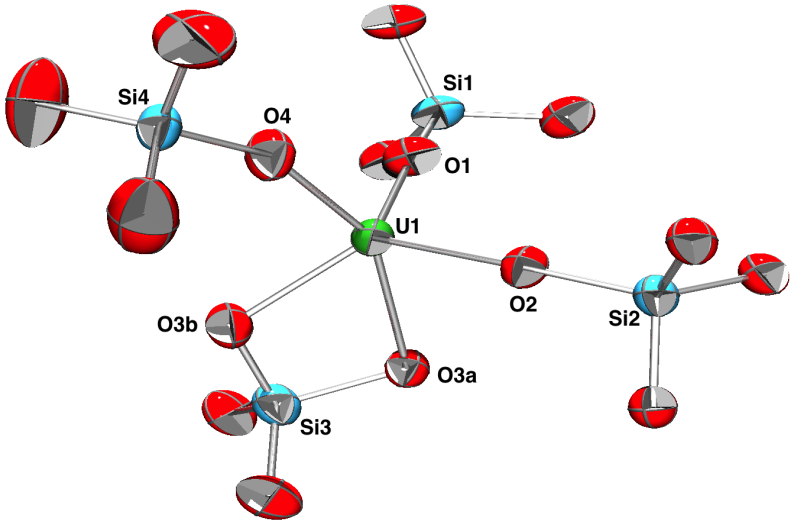

Figure 4.13: Core molecular structure of U(OSi(O^{t}Bu)$_3$)$_4$ containing the Si, O and U atoms (Hydrogen atoms and tert–butyl carbon atoms omitted for clarity) [80]

(2.193(4) Å), providing support to the formal oxidation state calculated to be U^{IV}. The bidentate tris *tert* butoxy siloxide ligand is bound via one siloxide oxygen (2.195 Å) and via the *tert* butoxy oxygen (2.563 Å) in a dative bonding fashion. The O–Si bond lengths range from 1.596(3) Å to 1.618(3) Å with an average of 1.607(3) Å. This average is shorter than the U$^{3.5}$ complex, K[(U(OSi(O^{t}Bu)$_3$)$_3$)$_2$($\mu-\eta^6$:η^6-tol))] but this is expected as the U–O bond lengths are slightly longer.

In addition to the above structures, crystals were also grown from THF at -40°C. Analysis showed the turquoise crystals to be the *bis*–THF derivative, U(OSi(O^{t}Bu)$_3$)$_4$(THF)$_2$ has shown in Figure 4.14, however the data was not of publishable quality and further evidence of this structure was obtained by NMR spectroscopy.

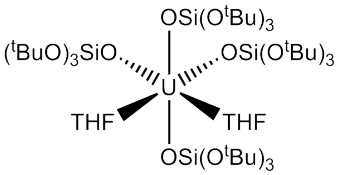

Figure 4.14: Structure of U(OSi(O^{t}Bu)$_3$)$_4$(THF)$_2$ [80]

4.4.3 Characterisation of U(OSi(O^{t}Bu)$_3$)$_4$: NMR

Analysis of the complex was conducted via $^{13}C\{H\}$ and ^{1}H NMR in both coordinating and non–coordinating solvents. Toluene was used as the non–coordinating solvent and two resonances are observed in the ^{1}H NMR spectrum in a 1:1 ratio, indicating two distinct chemical environments. These are assigned as a terminal siloxide unit and an internally solvating siloxide unit. The $^{13}C\{H\}$ NMR spectrum showed four resonances at δ 69.14, 67.61, 29.73 and 28.07 ppm. Each ^{t}BuO unit has two predicted carbon chemical environments and in conjunction with the ^{1}H NMR analysis, the resonances are assigned as shown in Table 4.6. ^{29}Si NMR analysis showed two resonances at δ -21.17 and -55.28 ppm which further confirms only two siloxide environments.

Carbon Assignment	δ/ppm	Solvent
1a	69.14	Toluene
1b, 1c	67.61	
2a	29.73	
2b, 2c	28.07	
1a, 1b, 1c	72.64	THF
2a	37.96	
2b, 2c	31.86	

Table 4.6: NMR Spectroscopy Resonances for the $^{13}C\{H\}$ spectrum of U(OSi(O^{t}Bu)$_3$)$_4$ in d_8–toluene and in d_8–THF[80]

In addition to these results, NMR analysis was undertaken in the coordinating solvent, THF and it was found that the ligand chemical environments are better defined. ^{1}H NMR analysis shows three resonances at δ 6.05, 5.28 and 1.02 ppm in a 3:1:5 ratio which fits with the structure proposed in Figure 4.15 and assigned as shown in Table 4.7. Further to these results, $^{13}C\{H\}$ NMR analysis was undertaken and the spectrum showed three resonances at δ 72.64, 37.96 and 31.86 ppm which are in line with the proposed structure

Proton Assignment	δ/ppm (multiplicity, coupling constant)	Solvent
A	1.10 (s, 1H)	Toluene
B, C	1.06 (s, 1H)	
C	6.05 (s, 3H)	THF
B	5.28 (s, 1H)	
A	1.02 (s, 5H)	

Table 4.7: NMR Spectroscopy Resonances for the ^{1}H spectrum of U(OSi(O^{t}Bu)$_3$)$_4$ in d_8–toluene and in d_8–THF [80]

shown in Figure 4.15 and are therefore assigned as shown in Table 4.6.

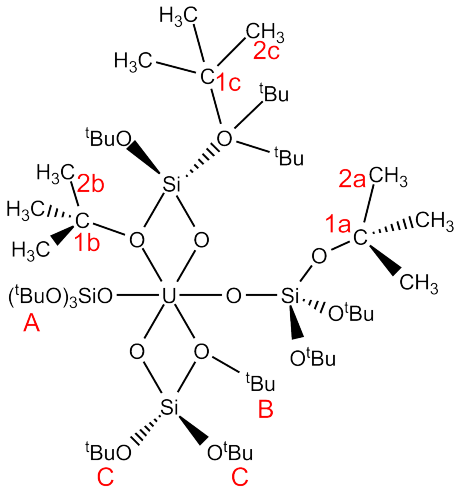

Figure 4.15: Solution state structure and NMR assignments for U(OSi(O^{t}Bu)$_3$)$_4$ in d_8–toluene and d_8–THF

Mazzanti also published ^{13}C{H} and ^{1}H NMR data in d_{14}–hexane of the decomposition product, [U(OSi(O^{t}Bu)$_3$)$_4$]. This analysis only showed one resonance in the ^{1}H NMR spectra at δ 0.982 ppm and two resonances in the ^{13}C{H} NMR spectra at δ 68.127 and 28.778 ppm. Assuming each ^{t}Bu unit has two carbon chemical environments (**C**(CH$_3$)$_3$ and C(**C**H$_3$)$_3$) then, in solution at least, the structure has equal siloxide chemical environments. NMR analysis in other solvents were not available in detail so direct comparisons cannot be made at this time, however, Mazzanti's solid state, X–ray analysis showed the complex to possess three terminal siloxide ligands and one internally solvating ligand,

similar to the analysis described above and shown in Figure 4.13.

4.4.4 Characterisation of U(OSi(O^{t}Bu)$_3$)$_4$: Mass Spectrometry

The expected molecular ion peak is observed at m/z = 1290 with another peak observed at m/z = 1027 which corresponds to the molecule with one ligand removed.

4.5 Synthesis and characterisation of UCl(OSi(O^{t}Bu)$_3$)$_3$

As previously discussed in Section 4.2, the complex UCl(OSi(O^{t}Bu)$_3$)$_2$ was a synthetic target for the puroposes of siloxide based surface mimics and therefore, under instruction from the author, (^{t}BuO)$_3$SiOK was reacted with UCl_4 in the following synthesis.

4.5.1 Synthesis of UCl(OSi(O^{t}Bu)$_3$)$_3$

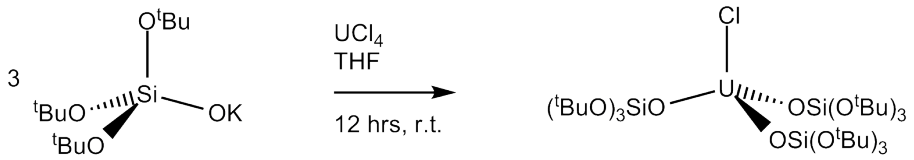

Scheme 4.8: Synthesis of UCl(OSi(O^{t}Bu)$_3$)$_3$

Treatment of UCl_4 in THF with three equivalents of (^{t}BuO)$_3$SiOK at room temperature, with stirring, resulted in a blue/green solution. A blue solid remained when the solvent was removed *in vacuo*. The product was then recrystallised from a THF solution at -40°C resulting in turquoise blue crystals.[80]

4.5.2 Characterisation of $UCl(OSi(O^tBu)_3)_3$: X–ray Diffraction

$UCl(OSi(O^tBu)_3)_3$ crystallises from THF in temperatures of -40°C in the space group C with an *R* factor of 6.6. The lattice parameters are *a* = 24.724 Å, *b* = 14.208 Å, *c* = 38.674 Å, α = 90°, β = 107.478° and γ = 90°.

The molecular structure is shown in Figures 4.16 and 4.17. It should be noted that these figures show half the unit cell. The full unit cell comprised of two asymmetric molecules and one THF solvent molecule. The structure shows each uranium centre is six coordinate in a distorted octahedron geometry with no counter ion, confirming the predicted U^{IV} hypothesis. On each uranium centre, three $(^tBuO)_3SiO^-$ ligands are located on one single face of the octahedron with the opposite face being occupied by the two THF molecules and the chloride. There is no symmetry associated with this molecule and therefore point group C_1 is assigned.

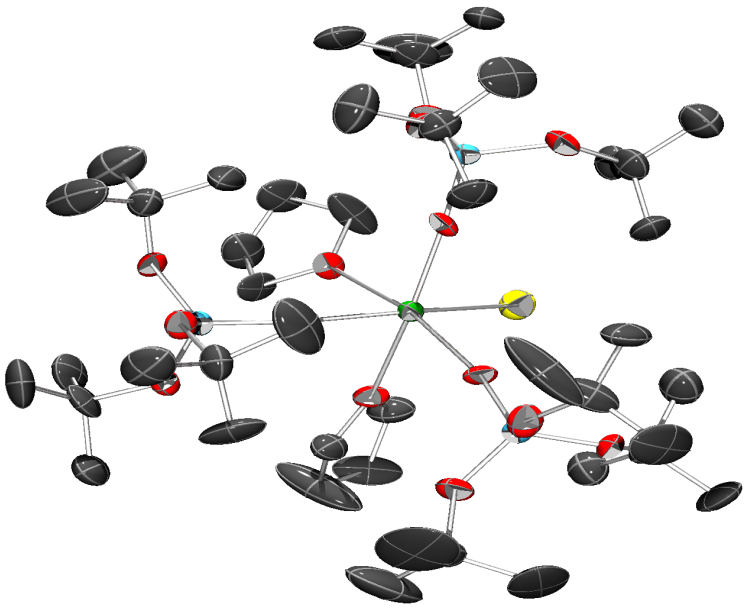

Figure 4.16: Molecular structure of $UCl(OSi(O^tBu)_3)_3$ (Hydrogen atoms omitted for clarity and yellow = Cl atom)[80]

The X–ray diffraction analysis shows an average U–O_{silox} bond distance of 2.152 Å and average O–Si bond distance of 1.599 Å. Comparing these data with the inverted sand-

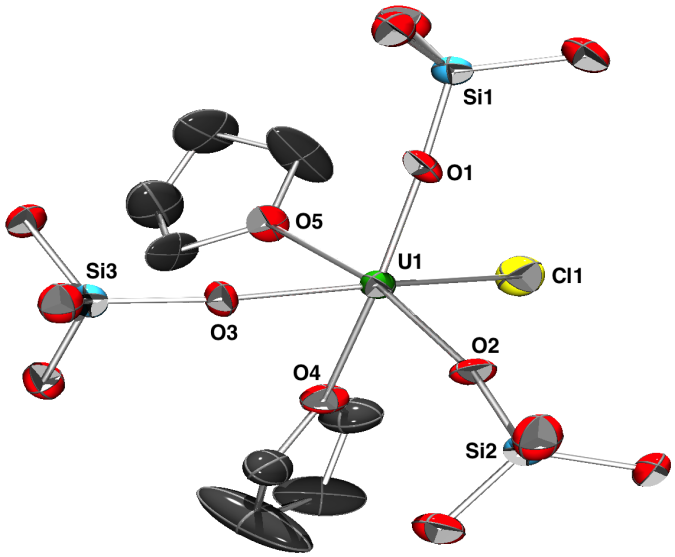

Figure 4.17: Core molecular structure of $UCl(OSi(O^tBu)_3)_3$ containing the Si, O and U atoms (Hydrogen atoms and tert–butyl carbon atoms omitted for clarity and yellow = Cl atom)[80]

wich complex, $K[(U(OSi(O^tBu)_3)_3)_2(\mu{-}\eta^6{:}\eta^6\text{-tol}))]$ discussed in Section 4.2, the U–O distance is expected to be marginally longer in the U^{IV} chloride complex than the $U^{3.5}$ inverted sandwich complex and this is found to be accurate. In addition and as expected, as the U–O bond distance is longer than the $U^{3.5}$ inverted sandwich complex and the $U(OSi(O^tBu)_3)_4$ reported above, it also has the shortest O–Si bond distances. In addition the average U–O_{THF} bond is observed at 2.4952 Å and the average U–Cl bond is 2.687 Å, both within typical ranges found in the literature (U–O_{THF} = 2.497 Å average; U–Cl = 2.655 Å average[85]).

4.5.3 Characterisation of $UCl(OSi(O^tBu)_3)_3$: NMR

$^{13}C\{H\}$, ^1H and ^{29}Si NMR spectra were obtained in d_8–toluene solution. The resonances observed are summarised in Tables 4.8 and 4.9. Despite the X–ray diffraction analysis showing the complex crystallises as the *bis*–THF adduct, once the product was washed thoroughly and exposed to vacuum, NMR analysis showed all the ligands to be in an

equivalent chemical environment in solution.

Carbon Assignment	δ/ppm
1a	76.14
2a	35.50

Table 4.8: NMR Spectroscopy Resonances for the $^{13}C\{H\}$ spectrum of $UCl(OSi(O^tBu)_3)_3$ in d_8–toluene at room temperature[80]

Proton Assignment	δ/ppm (multiplicity, coupling constant)	Temperature °C
B	8.68	-80
C	4.58	
D	1.21	
A	5.96 (s, 27H)	20
A	4.83 (s, 27H)	70

Table 4.9: NMR Spectroscopy Resonances for the ^1H spectrum of $UCl(OSi(O^tBu)_3)_3$ in d_8–toluene at variable temperatures[80]

A variable temperature ^1H NMR experiment was conducted in order to assess the solution state structure further. The ^{t}Bu signal identified at δ 5.96 ppm at room temperature moves from δ 8.68 ppm at -80°C to δ 4.83 ppm at 70°C. This signal is broad at extremely low or high temperatures (FWHH = 0.65 ppm and 0.25 ppm) but sharpens around -20°C (FWHH = 0.09 ppm). In addition, at -20°C two further resonances are observed at δ 4.79 and 1.06 ppm that shift to 4.58 and 1.21 when cooled to -80°C. The ratio of these signals are 1:1:1 with the broad resonance previously assigned to ^{t}Bu. This indicates that at temperatures of -20°C or below the siloxide ligands are in different chemical environments, whilst at temperatures above -10°C the siloxide ligands are in equivalent chemical environments as shown in Figure 4.18 and confirmed by ^{29}Si NMR which shows a single resonance at δ -61.91 ppm.

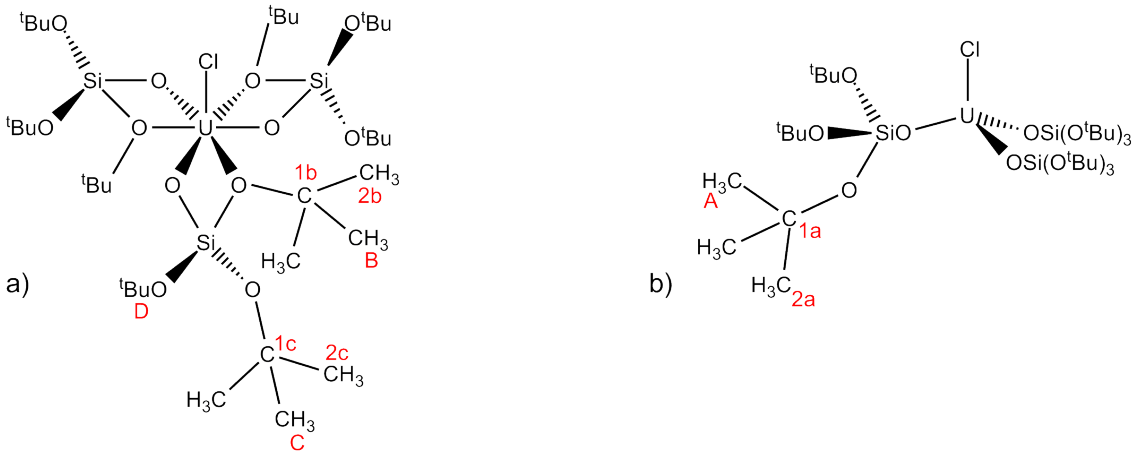

Figure 4.18: Solution state structure and NMR assignments for $UCl(OSi(O^tBu)_3)_3$ in d_8–toluene at a) -80°C to -20°C and b) -10°C to 70°C

Chapter 5

Reactivity studies of uranium *tris*–tertbutoxy complexes

Between November 2012 and April 2014, most of the compounds synthesised as part of this work were published by Mazzanti et al. of the Institut Nanonsciences et Cryogénie, CEA, Grenoble.[90,162–164]

Reductive functionalisation of carbon oxides is proving to be of vital importance and looks to provide huge potential applications with regards to solving the issues surrounding the global energy crisis.[185,186] The chemistry of the 5*f* elements already contains reductive functionalisation of carbon oxides, albeit in homogeneous phase and further research in this area looks promising. Some interesting reviews on this subject have been published and discussed in section 1.1.1.[1,5,187]

5.1 Reactivity studies of K[(U(OSi(O^{t}Bu)$_3$)$_3$)$_2$($\mu-\eta^6$:η^6-tol))]

5.1.1 Small molecule activation

In order to investigate the reactivity of K[(U(OSi(O^{t}Bu)$_3$)$_3$)$_2$($\mu-\eta^6$:η^6-tol))], NMR spectroscopy studies were undertaken with carbon oxides and other small molecules as illustrated in Scheme 5.1.

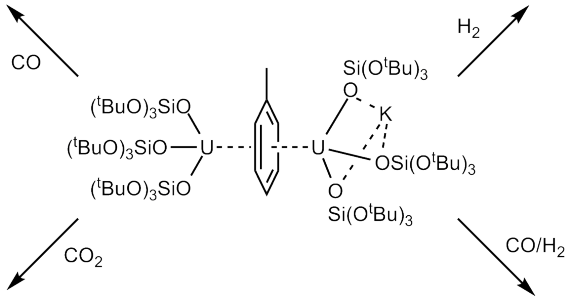

Scheme 5.1: Reactivities of K[(U(OSi(O^{t}Bu)$_3$)$_3$)$_2$($\mu-\eta^6$:η^6-tol))] which were investigated

Each of these experiments were undertaken by adding one equivalent of the relevant gas using a Toepler line, to the NMR spectroscopy sample which was dissolved in d_8–THF and were carried out at -78°C, room temperature and over varying timescales. Unfortunately, K[(U(OSi(O^{t}Bu)$_3$)$_3$)$_2$($\mu-\eta^6$:η^6-tol))] was found to decompose at low temperatures and over short time frames (days) to U(OSi(O^{t}Bu)$_3$)$_4$ and with the liberation of (^{t}BuO)$_3$SiOH and isobutylene. This made the analysis of data from the reactivity studies problematic.

Due to the difficulties in obtaining data on any reactivities with small molecules, decomposition analysis was undertaken on K[(U(OSi(O^{t}Bu)$_3$)$_3$)$_2$($\mu-\eta^6$:η^6-tol))] over a period of one month. A control sample was treated identically to the reactivity studies described above (minus the gas addition) and NMR spectroscopy data was collected at low temperatures. Changes in the resonances were clearly identified even after a few days.

The results of these experiments are shown in Appendix F. However, ultimately the de-

composition of K[(U(OSi(O^{t}Bu)$_3$)$_3$)$_2$($\mu-\eta^6$:η^6-tol))] interfered with any accurate analysis of data and resonance assignments. Further isolation of any decomposition products or products from the gas reaction were attempted but unsuccessful, probably due to the mixture of products and reactants that were present in the reaction solution.

In November 2012, Mazzanti published NMR spectrum that showed the decomposition of [(U(OSi(O^{t}Bu)$_3$)$_3$)$_2$($\mu-\eta^1$:η^2CO$_3$)] to U(OSi(O^{t}Bu)$_3$)$_4$ over a period of 1 to 6 days as shown in Scheme 5.2.[162].

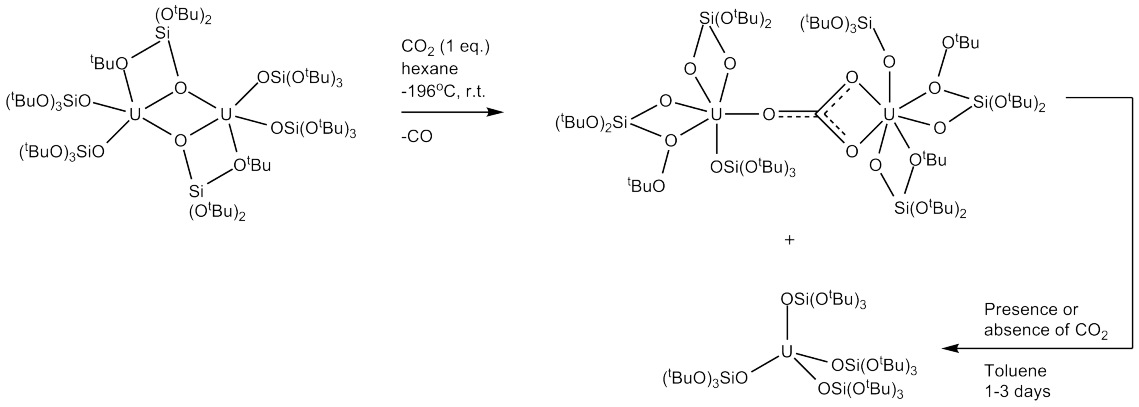

Scheme 5.2: Decomposition of [(U(OSi(O^{t}Bu)$_3$)$_3$)$_2$($\mu-\eta^1$:η^2CO$_3$)] to U(OSi(O^{t}Bu)$_3$)$_4$ (November 2012)[162]

Initially, on addition of CO_2 to [(U(OSi(O^{t}Bu)$_3$)$_2$($\eta-$OSi(O^{t}Bu)$_3$))$_2$], two further products were formed, [(U(OSi(O^{t}Bu)$_3$)$_3$)$_2$($\mu-\eta^1$:η^2CO$_3$)] and U(OSi(O^{t}Bu)$_3$)$_4$ in a 2.5:1 ratio respectively. However, leaving a solution of [(U(OSi(O^{t}Bu)$_3$)$_3$)$_2$($\mu-\eta^1$:η^2CO$_3$)] in toluene for up to three days showed that the decomposition continued whether CO_2 was present or not. This suggests that the complex underwent a slow ligand rearrangement resulting in the formation of U(OSi(O^{t}Bu)$_3$)$_4$ and an unidentified U^{IV} carbonate complex. Analysis of any decomposition of [(U(OSi(O^{t}Bu)$_3$)$_3$($\mu-\eta^6$:η^6-tol))$_2$] was not published by Mazzanti, however some analysis was carried out as part of this work on the decomposition of K[(U(OSi(O^{t}Bu)$_3$)$_3$)$_2$($\mu-\eta^6$:η^6-tol))].

In this work, the $^{13}C\{H\}$ NMR spectrum for the reaction of K[(U(OSi(O^{t}Bu)$_3$)$_3$)$_2$($\mu-\eta^6$:η^6-tol))]

with CO, CO_2 and CO/H_2 all show the same resonance at approximately δ 31 ppm after a few days, suggesting any reaction that had occurred with the gases does not effect the decomposition product. The same resonance was also observed in the control sample which did not have any gas added to the sample. This evidence, coupled with the co–crystallisation of $U(OSi(O^tBu)_3)_4$ with $K[(U(OSi(O^tBu)_3)_3)_2(\mu{-}\eta^6{:}\eta^6\text{-tol}))]$ in an inert atmosphere suggests the decomposition occurs via an intramolecular pathway not related to any reaction with a gaseous small molecule.

In addition to Mazzanti's work, analysis on the thermal stability of $U(OSi(O^tBu)_3)_4$ was carried out within this group.[80] The results showed the complex decomposed via an intramolecular process, liberating $(^tBuO)_3SiOH$ and isobutylene steadily over a period of a few days. A solution of $U(OSi(O^tBu)_3)_4$ in d_8–toluene was sealed in a Young's NMR tube and pressurised with argon gas. ^1H NMR analysis was carried out over 16 days, the results of which are shown in Figure 5.1. The silanol resonances at δ 1.36 ppm which are assigned to ^{t}Bu and δ 1.84 ppm, assigned to Si–OH, increase in intensity over time. At five days, two new alkene resonances appeared at δ 4.71 and 4.76 ppm along with a new methyl resonance at δ 1.46 ppm, all of which increased with time in a linear fashion. Due to the *bi*–dentate coordination observed in $U(OSi(O^tBu)_3)_4$ and shown in Figure 4.13, the ^{t}Bu group on the internally solvating ligand becomes an excellent leaving group. The NMR data suggests that the decomposition proceeds *via* proton abstraction from the ^{t}Bu group by a neighbouring siloxide ligand, resulting in the elimination of $(^tBuO)_3SiOH$ and *iso*–butylene which would account for the alkene resonances observed.

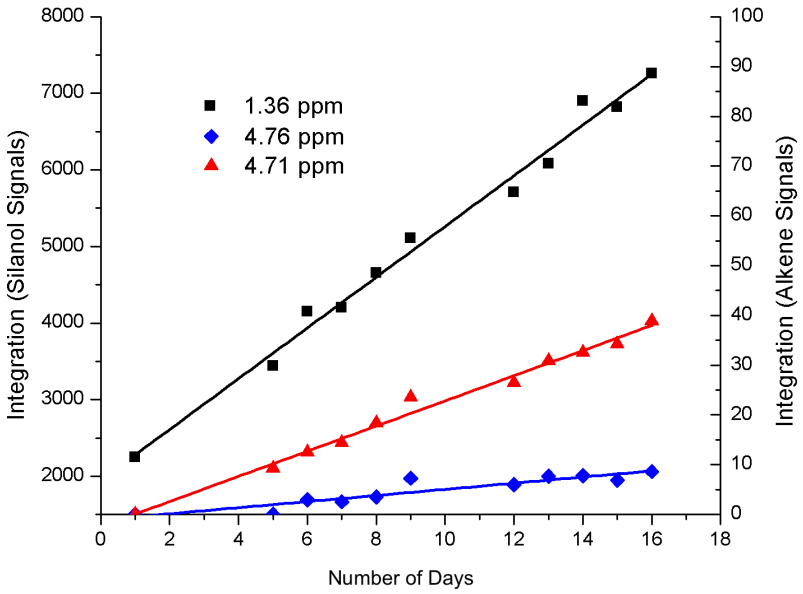

Figure 5.1: Thermal decomposition analysis of $U(OSi(O^tBu)_3)_4$.[80]

5.2 Reactivity studies of $UCl(OSi(O^tBu)_3)_3$

Further to the work described in Sections 4.4 and 4.5, the students also carried out a number of reactivity studies in collaboration with the author, the results of which are described below.[80,81]

5.2.1 Alkylation by metathesis

In order to provide a general starting material for the exploration of insertion reactions of carbon oxides at uranium centres, an alkylated uranium species was required, which could then undergo hydrogenation to a metal hydride, as shown in Equation 5.2.1.

$$U(R)(OSi(O^tBu)_3)_3 + H_2 \rightarrow U(H)(OSi(O^tBu)_3)_3 + RH \qquad (5.2.1)$$

or direct insertion to form the alkyl carboxylate complex as shown in Equation 5.2.2.

$$U(R)(OSi(O^tBu)_3)_3 + CO_2 \rightarrow U(O_2CR)(OSi(O^tBu)_3)_3 \quad (5.2.2)$$

Accordingly, $UCl(OSi(O^tBu)_3)_3$ was treated with equimolar amounts of KCH_2Ph forming a viscous orange/brown oil. Recrystallisation of the oil from hexane at -40°C forms cubic crystals which were analysed as the *bis* benzyl product, $K[U(CH_2Ph)_2(OSi(O^tBu)_3)_3]$.

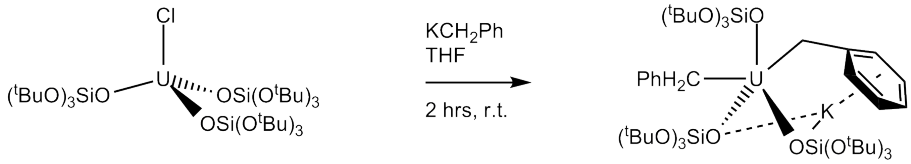

Scheme 5.3: Synthesis of $[U(CH_2Ph)_2(OSi(O^tBu)_3)_3]K$

5.2.2 Characterisation of $K[U(CH_2Ph)_2(OSi(O^tBu)_3)_3]$: X–ray Diffraction

$K[U(CH_2Ph)_2(OSi(O^tBu)_3)_3]$ crystallises in the 21/n space group. The lattice parameters for this structure are a = 13.787 Å, b = 21.080 Å, c = 21.756 Å, $\alpha = 90°$, $\beta = 97.197°$, $\gamma = 90°$.

The molecular structure is shown in Figures 5.2 and 5.3. The uranium centre has a trigonal bipyramidal geometry with a C_{2v} symmetry. Three siloxide ligands are bonded in a monodentate fashion and two benzyl ligands are bonded *cis* to each other. The potassium counter ion is coordinated to one of the benzyl ligands and two of the siloxide ligands via four oxygens and two silicon atoms.

This U^{IV} complex is observed with average U–O bond distances and O–Si bond distances of 2.181(3) Å and 1.604(4) Å, respectively. Of all the U^{IV} complexes reported here, $K[U(CH_2Ph)_2(OSi(O^tBu)_3)_3]$ has the longest average U–O bonds distance and one of the

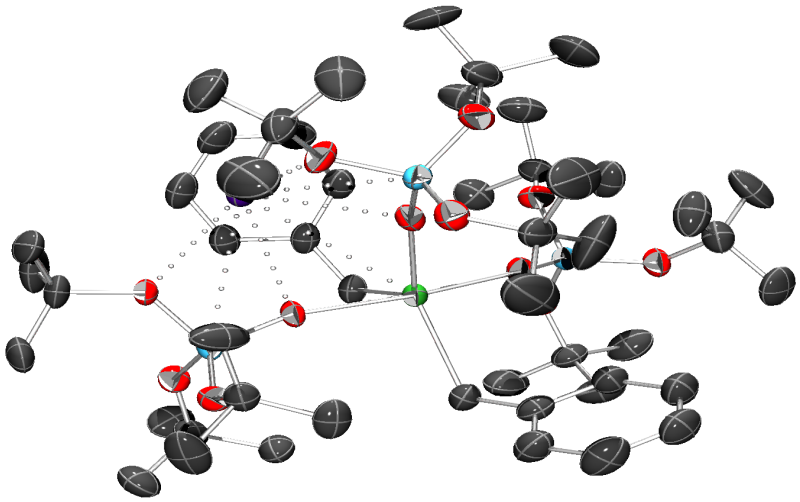

Figure 5.2: Molecular structure of $K[U(CH_2Ph)_2(OSi(O^tBu)_3)_3]$ (Hydrogen atoms omitted for clarity)[80]

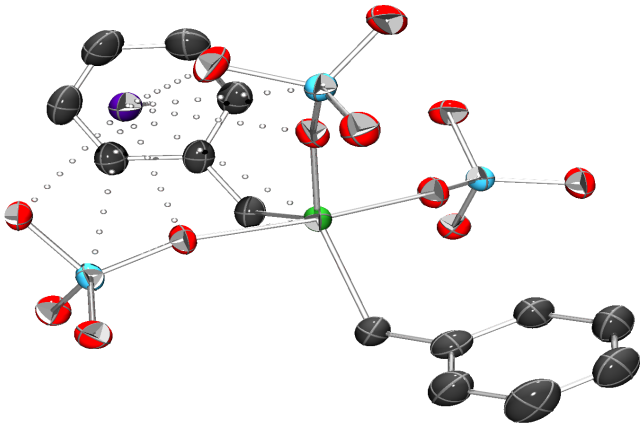

Figure 5.3: Core molecular structure of $K[U(CH_2Ph)_2(OSi(O^tBu)_3)_3]$ containing the benzyl carbons, Si, O and U atoms (Hydrogen atoms and tert–butyl carbon atoms omitted for clarity)[80]

shortest average O–Si bond distance (only $UCl(OSi(O^tBu)_3)_3$ being shorter by 0.005 Å). This is likely due to the electronics of the benzyl ligands being more donating than either chlorides or butoxy groups. The U–C_{benzyl} bond distances are 2.405(5) Å and 2.480(5) Å which are slightly shorter than average literature values (2.615 Å.[188]) and this is due to the electronics of the siloxide ligands drawing electron density away from the uranium

centre. The potassium counter ion reduces the U–C–C bond angle to 105.6(3)° of the benzyl ligand it is coordinated to, compared to the non–coordinating benzyl–potassium ligand which has a U–C–C bond angle of 120.6(4) °.

5.2.3 Characterisation of $K[U(CH_2Ph)_2(OSi(O^tBu)_3)_3]$: NMR

$^{13}C\{H\}$ and ^1H NMR spectrum of the $K[U(CH_2Ph)_2(OSi(O^tBu)_3)_3]$ are shown in Tables 5.1 and 5.2. The benzyl signals are difficult to assign accurately in the $^{13}C\{H\}$ NMR spectrum. The data indicate that there is only one benzyl environment whereas the ^1H NMR spectrum indicates two distinct benzyl environments. This discrepancy is likely due to overlapping signals in the $^{13}C\{H\}$ NMR spectrum and the presence of a broad signal underlying the aromatic region.

The ^1H NMR spectrum shows two distinct siloxide chemical environments with resonances observed at δ 1.97 and 0.92 ppm in a 1:2 ratio which are assigned to the single non–coordinating siloxide ligand and the two siloxide ligands coordinating to the potassium counter ion respectively. ^{29}Si NMR analysis confirms the presence of two siloxide environments with resonances observed at δ 95.2 and -25.0 ppm.

Carbon Assignment	δ/ppm
Ph *ipso*	129.72
Ph *ortho*	128.81
Ph *meta*	128.61
Ph *para*	162.22
$OSi(OC(\mathbf{C}H_3)_3)$	72.80
$OSi(O\mathbf{C}(CH_3)_3)$	38.21
Benzyl CH_2	1.43

Table 5.1: NMR Spectroscopy Resonances for the $^{13}C\{H\}$ spectrum of $K[U(CH_2Ph)_2(OSi(O^tBu)_3)_3]$ in d_6–benzene

Proton Assignment	δ/ppm (multiplicity, coupling constant)
Ph *meta*	7.13 (d, 6H)
Ph *para*	7.07 (d, 5H)
Ph *ortho*	6.99 (d, 7H)
Benzyl CH_2	1.49 (s, 4H)
^{t}Bu$_{noncoordinating}$	1.97 (s, 27H)
^{t}Bu$_{Kcoordinating}$	0.92 (s, 54H)

Table 5.2: NMR Spectroscopy Resonances for the ^{1}H spectrum of K[U(CH$_2$Ph)$_2$(OSi(O^{t}Bu)$_3$)$_3$] in d_6–benzene

5.3 Reactivity studies of U(OSi(O^{t}Bu)$_3$)$_4$

In order to ascertain if the U(OSi(O^{t}Bu)$_3$)$_4$ complex would reaction and activate small molecules, reactivity studies were undertaken with a number of small molecules, the results of which are presented here.

5.3.1 Reaction between U(OSi(O^{t}Bu)$_3$)$_4$ and CO_2

U(OSi(O^{t}Bu)$_3$)$_4$ was dissolved in THF and reacted with 1 eq. of CO_2 gas. After 24 hours the resulting green solution was then cooled to -40°C producing large green cubic crystals suitable for X–ray diffraction analysis which was determined to be the *bis*–THF derivative of the starting material U(OSi(O^{t}Bu)$_3$)$_4$(THF)$_2$ showing the U–O bond is inert towards CO_2 in this instance.

5.3.2 Reaction between U(OSi(O^{t}Bu)$_3$)$_4$ and O_2

U(OSi(O^{t}Bu)$_3$)$_4$ was dissolved in THF and reacted with a one molar equivalent of O_2 gas. After a few hours, the resulting yellow solution was worked up and recrystallisation was

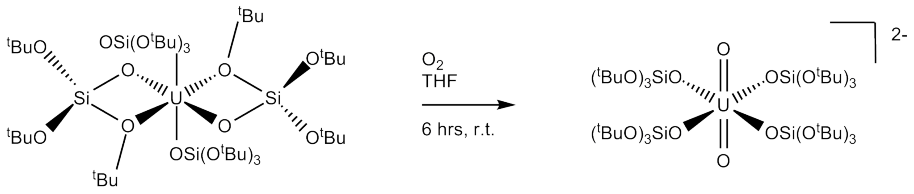

Scheme 5.4: Proposed synthesis and structure of the product from the reaction between $U(OSi(O^tBu)_3)_4$ and O_2

attempted but unsuccessful.

^{1}H NMR analysis shows a sharp resonance at δ 2.43 ppm indicating a single siloxide environment and no internal ligand solvation. Unfortunately mass spectrometry analysis was difficult to assign and therefore IR analysis was attempted. The IR spectrum shows a strong band at 904 cm^{-1} which is normally found to be a uranyl stretch in line with the literature analysis in Chapter 3. In addition the visible spectrum shows no indication of *f*–*f* transitions indicating the species is a 5*f*^{0} complex (U^{VI}). A broad peak is observed at 428 nm which is potentially the uranyl LMCT band.

5.4 Synthesis of $U(\mu^2-O_2)(OSi(O^tBu)_3)_4(THF)$

In order to attempt an oxidation without addition of oxygen atoms to the uranium centre, $U(OSi(O^tBu)_3)_4$ was treated with an excess of iodine. $U(OSi(O^tBu)_3)_4$ was dissolved in hexane and excess I_2 was sublimed onto the solution.

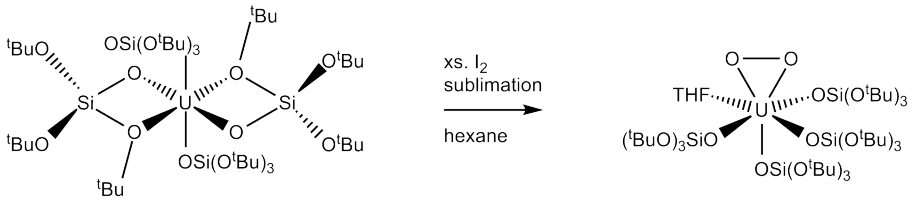

Scheme 5.5: Synthesis of $U(\mu^2-O_2)(OSi(O^tBu)_3)_4(THF)$

The blue solution quickly turned indigo and was left exposed to I_2 for a further 20 minutes.

After work–up the black residue was recrystallised from THF at -40°C resulting in black plate crystals suitable for X–ray diffraction.

5.4.1 Characterisation of U(μ^2-O_2)(OSi(O^{t}Bu)$_3$)$_4$(THF): X–ray Diffraction

U(μ^2-O_2)(OSi(O^{t}Bu)$_3$)$_4$(THF) crystallises in the P 21/n space group with an *R* factor of 4.41. The lattice parameters for this structure are *a* = 24.3626(4) Å, *b* = 13.9506(3) Å, *c* = 25.3050(3) Å, α = 90°, β = 118.5590(10)°, γ = 90°.

The molecular structure is shown in Figures 5.4 and 5.5. The uranium centre is *pseudo*–octahedral with the O_2 ligand occupying one vertex along on of the axes. The complex also has three equatorial siloxide ligands, one axial siloxide ligand *trans* to a side–on bound diatomic oxygen and an equatorial THF molecule. The peroxo group was assigned as such with Q–peak analysis as it showed 17 electrons across the two sites. As iodine has 53 electrons it was ruled out as a disordered iodine atom. The only explanation is air leaked into the system during the reaction and oxygen reacted with the uranium complex.

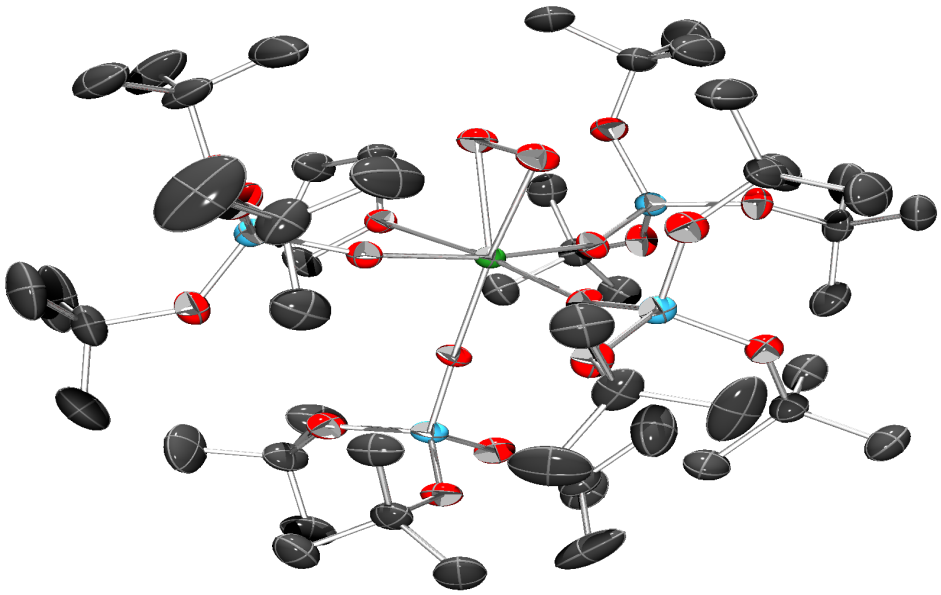

Figure 5.4: Molecular structure of the peroxo species U(η^2-O_2)(OSi(O^{t}Bu)$_3$)$_4$(THF)) (Hydrogen atoms omitted for clarity)[80]

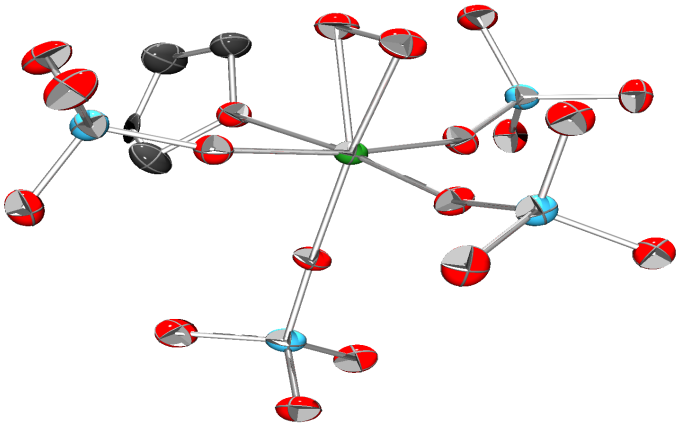

Figure 5.5: Core molecular structure of the peroxo species U(η^2-O_2)(OSi(O^{t}Bu)$_3$)$_4$(THF)) containing the Si, O and U atoms and THF molecule (Hydrogen atoms and tert–butyl carbon atoms omitted for clarity)[80]

The O_2 ligand is bound to the uranium asymmetrically. The U–O distances are 2.200(2) Å and 2.187(3) Å whilst the O–O distance is observed at 1.374(4) Å which is a significant change from free O_2 at 1.21 Å[189] but within normal O–O bond distances for this type of complex as previously discussed in Section 3.6.1.

The average U–O bond distance is observed at 2.091 Å which, unsurprisingly due to the peroxo ligand, is the shortest so far within the complexes reported here. This means the O–Si bond distance is one of the longest at 1.629 Å average with only the inverted sandwich complex showing longer O–Si bond distances (0.023 Å). The U–O_{THF} bond distance is 2.4804 Å.

5.4.2 Characterisation of U(μ^2-O_2)(OSi(O^{t}Bu)$_3$)$_4$(THF): NMR

$^{13}C\{H\}$ and ^1H NMR spectrum of the peroxo are shown in Tables 5.3 and 5.4.

The NMR data confirms the structure observed in the solid state is also stable in solution as the number of proton and carbon environments observed equate to those of the THF

adduct. The $^{13}C\{H\}$ NMR spectrum data are shown in Table 5.3 and are assigned accordingly, three clear O**C**$(CH_3)_3$ carbon environments along with three further OC(**C**$H_3)_3$ carbon environments.

Carbon Assignment	δ/ppm
OSi(OC(**C**$H_3)_3$) (*cis* to THF)	72.82
OSi(OC(**C**$H_3)_3$) (*trans* to peroxo)	72.52
OSi(OC(**C**$H_3)_3$) (*trans* to THF)	71.51
OSi(O**C**$(CH_3)_3$) (*cis* to THF)	32.47
OSi(O**C**$(CH_3)_3$) (*trans* to peroxo)	32.11
OSi(O**C**$(CH_3)_3$) (*trans* to THF)	31.79

Table 5.3: NMR Spectroscopy Resonances for the $^{13}C\{H\}$ spectrum of U(μ^2-O_2)(OSi(O^{t}Bu)$_3$)$_4$(THF) in d_6–benzene

The ^{1}H NMR data are shown in Table 5.4 and support the hypothesis that the THF adduct is stable in solution. Four clear proton environments are identified with one clearly assigned to THF and the other three assigned to the siloxide ligands, using the multiplicities to identify individual resonances.

Proton Assignment	δ/ppm (multiplicity, coupling constant)
OSi(OC(C**H**$_3)_3$) (*trans* to O_2)	2.23 (s, 29H)
THF	2.05 (s, 8H)
OSi(OC(C**H**$_3)_3$) (*cis* to THF)	1.73 (s, 54H)
OSi(OC(C**H**$_3)_3$) (*trans* to THF)	1.66 (s, 27H)

Table 5.4: NMR Spectroscopy Resonances for the ^{1}H spectrum of U(μ^2-O_2)(OSi(O^{t}Bu)$_3$)$_4$(THF) in d_6–benzene

The reaction was repeated with little success. I_2 was repeatedly diffused over a solution of U(OSi(O^{t}Bu)$_3$)$_4$ dissolved in hexane but resulted in a green solution instead of the desired black solution described above. In an attempt to recreate an oxygen 'impurity', one molar equivalent on O_2 was added to the solution during the reaction, but resulted in

intractable orange and brown solids.

Chapter 6

Conclusions

Siloxides have been used as molecular mimics for silica surfaces for a number of years. Despite this, research into using uranium in these systems has been lacking as most of the work concentrates on transition metals and to a lesser extent, the lanthanides. In addition, the type of siloxide previously investigated is also limited, with tris *tert*–butoxy siloxide forming a significant proportion of examples.

During the course of this work a number of previously unreported complexes have been synthesised and characterised using Ph_3SiO^- as the ligand. The complexes, $K[U(OSiPh_3)_5]$, $([K(py)_6]\,[U(OSiPh_3)_5(py)])_2$ and $K[(Ph_3SiO)_5U(THF)]$ are all presented here with full characterisation data, including ESI HRMS analysis of the formation. In addition, investigations into the UV–Vis spectra of these complexes were attempted, with interesting results which can aid a better understanding of these complex systems and provides a valuable insight into the *f*–elements and the role *f*–orbitals have on the chemistry and geometry of such systems.

In order to open the coordination sphere to form a heteroleptic complex of the general form $U(OSiPh_3)_3X$ where X represents a good leaving group, attempts where made to

use TMSOTf in a metathesis type reaction in order to remove a siloxide ligand in favour of the excellent leaving group, TfO^{-}. ESI HRMS and NMR spectroscopy techniques were employed to analyse these reactions at each step and to identify the products synthesised.

Reactivity studies were undertaken on the uranium siloxides using a number of gaseous small molecules such as oxygen and carbon oxides. As a result of these studies, a rare and novel U^{V} monooxo complex, $[K(THF)_2][(Ph_3SiO)_4UO(THF)]$ was synthesised, successfully isolated and characterised. The discussion includes observations of an intermediate species and a possible mechanism of formation. In addition, a uranyl derivative, $K_2[(Ph_3SiO)_4UO_2]$ was also synthesised and characterised.

Finally, a second ligand system which could be used to mimic a silica surface is investigated and the complexes, $K[(U(OSi(O^tBu)_3)_3)_2(\mu{-}\eta^6{:}\,\eta^6\text{-tol}))]$, $[((^tBuO)_3SiO)_3U]_2(\mu^2\text{-}O)_3$ and $U(OSi(O^tBu)_3)_4$ are presented here along with reactivity studies on the complexes. During the course of this work, similar complexes were published by Mazzanti[90,102,162–164] and the complexes are analysed and compared to the published structures.

Chapter 7

Experimental

All solvents used in synthetic procedures were pre-dried over 4 Å (1.6mm) molecular sieves before reflux over the appropriate drying agent, which are collated in Table 7.1.

Solvent	Drying agent	Solvent	Drying agent
Diethyl ether	NaK_3	Benzene	K
Tetrahydrofuran	K	Toluene	Na
Dimethoxyethane	K	Pentanes	NaK_3
Dioxane	Na	Hexanes	K
Methanol	$Mg(OMe)_2$	Pyridine	K or CaH_2

Table 7.1: Drying agents for solvents

Anhydrous solvent was then collected in an ampoule containing a potassium mirror (for hydrocarbons) or 4 Å molecular sieves (for ethers). Solvents used for NMR spectroscopy were dried over CaH_2 or K prior to reflux for approximately one week, before being vacuum transferred into an ampoule containing a potassium mirror or NaK. These solvents were then freeze, pump, thaw, degassed at least three times before use.

Air or moisture sensitive samples for NMR spectroscopy were prepared by vacuum transfer on the high-vacuum line of the appropriate NMR solvent into an NMR tube sealed with a Young's tap.

All air or moisture sensitive solids and solutions were handled using standard Schlenk techniques under argon or nitrogen, or in an argon-filled glove box, with concentrations of H_2O and O_2 less than 0.1 ppm. Glassware was dried in a 170°C oven after being cleaned thoroughly in a base and acid bath. Recrystallizations were performed in a glove box freezer (-40°C), in a chest freezer (-30°C) or in a -80°C freezer. Reactions were conducted in standard Schlenk ware, vials or high-vacuum ampoules.

NMR spectra were recorded on either a 400 MHz or 500 MHz Varian spectrometer, with resonant frequencies for different nuclei given in Table 7.2. ^{29}Si NMR spectra were run with a relaxation delay of 1 second or 0.1 second for weak samples, all others were run with the default settings.

B_0 / T	9.3778	11.74
Nucleus	Frequency / MHz	Frequency / MHz
^{13}C	100.5801	125
^{1}H	400	500
^{19}F	376.3760	—
^{29}Si	79.4	—

Table 7.2: NMR frequencies

Alkali metals and alkali metal hydrides were freed of hydrocarbon oil by extensive washing with hexane. ^{t}BuLi was received as a nominal 1.6 M solution in hexane. The solution was filtered through a fine frit and then evaporated in the glove box to yield a white crystalline solid that was stored at -40°C. All other reagents were used as received unless specified

in the preparation.

All negative and positive electrospray ionisation ESI were conducted by Dr. A. Abdul-Sada, University of Sussex. A 4.7 Tesla Bruker Daltonics APEX III Fourier Transform Mass Spectrometer (FTMS) with electrospray ionisation (ESI) was used to carry out all the experiments in this work. Due to the low volatility and thermal liability of the ionic uranium complexes, the electron impact EI was not suitable. In order to monitor the reaction and characterise the final product at different stages, both negative and positive electrospray ionisation ESI was used. The complexes were prepared in the glove box and loaded in a 250 μL Hamilton gas-liquid-tight syringe. Samples were dissolved in dry THF which was the solvent used for spraying the complexes. The concentration of the sample for ESI was 1ng/μL. The Fourier transformer mass spectrometry APX III 4.7 Tess high resolution with Apolo ESI source was used. The negative sources conditions included; capillary voltage 4400 V, spray shield 3800 V, capillary exit - 187, dry temperature 150 C, skimmer 1-24.5 v, skimmer 2-7.8. These were optimised to help in using THF as a spray solvent.

All single crystal X-ray data were collected and solved by Dr. M. Roe at the University of Sussex. Data were collected at 173 K with an Enraf-Nonius FR590 diffractometer, using graphite-monochromated Mo K α radiation (λ - 0.71073 Å). Data collection was made with a 95 mm CCD camera on a κ-goniostat, handled using KappaCCD software. Final cell parameter calculations were performed using the WinGX package. The data were corrected for absorption using MULTISCAN program. Refinement was performed using SHELXL-97. ORTEP representations were generated using ORTEP-3 and POV-Ray software.

UV-vis data were collected using a Varian Cary-50 spectrophotometer, using a 1 cm quatrz cell sealed with a Young's tap for air and / or moisture sensitive samples. All samples were dissolved in THF, was the masses of analyte and solvent accurately known.

Background absorption was subtracted manually from each data set, using absorption data previously collected of anhydrous THF in a matched quartz cell, using OriginPro 8 software.

Elemental analysis were carried out by E. M. Pascher at Mikroanalytisches Labor Pascher, Germany. Samples were flame sealed under vacuum.

IR data was collected using *in situ* ReactIR^{TM} equipment with a diamond probe, with samples prepared as THF solutions before transfer to an IR cell fitted with gas-tight O-rings and a Rotaflo® stopcock, connected to a high vacuum argon line with a Swagelok® connection to a gas tight line and Toepler pump.

7.1 *tri*-(naphthyl)silanol

Activated Mg turnings (1.51 g, 62.1 mmol, excess) were added to enough Et_2O to cover the turnings. The Grignard reaction was then initiated with a single crystal of I_2 and a few drops of 1-bromonaphthalene with no stirring. Once an exothermic reaction had begun a 0.1 M solution of 1-bromonaphthalene (3.5 mL, 25mmol) in Et_2O (220 mL) was added dropwise and stirring commenced.The reaction mixture started turning cloudy before turning clear and then orange/brown. After 2 hours of stirring, the Mg turnings appeared black. This solution was then added dropwise to a 0.1 M solution of $SiCl_4$ (1 mL, 8.7 mmol, 0.35 eq.) in Et_2O (85 mL) over a period of one hour with no immediate changes observed. The reaction was left stirring for 60 hours which resulted in a tan/beige precipitate. $HCl_{aq.}$ was then added causing a vigorous exothermic reaction and a yellow precipitate which was suspended at the interface between a yellow organic fraction and a colourless aqueous fraction. The organic fraction was collected and washed with water and separated from the aqueous fraction. It was then dried using Na_2SO_4 which was

removed with filtration. The solvent was then removed *in vacuo* resulted in a yellow solid which was recrystallised from hot ethanol.[80]

Yield: 2.06 g / 58%

^{1}H NMR (d_6-benzene): δ / ppm: 7.74 (d, J = 5 Hz, 1H, 9-position), 7.72 (d, J = 5 Hz, 1H, 6-position), 7.50 (d, J = 10 Hz, 1H, 2-position), 7.36 (t, J = 5 Hz, 1H, 8-position), 7.32 (d, J = 5 Hz, 1H, 4-position), 7.22 (t, J = 7.5 Hz, 1H, 7-position), 7.02 (t, J = 10 Hz, 1H, 3-position), 7.00 (s, Si−OH)

Mass Spectroscopy (EI): m/z = 426 ($(C_{10}H_7)_3Si-OH$)

7.2 Synthesis of *tri*-(4-biphenyl)silanol

A 0.17 M solution of 4-bromobiphenyl (1.00 g, 4.29 mmol) in THF (25 mL) was cooled to -78°C. ^{n}BuLi (3 mL, 4.29 mmol, 1 eq.) in hexane (1.37 M solution) was added dropwise, with stirring. The clear solution turned yellow and a white precipitated was observed. The reaction was left stirring at -78°C for one hour. A 0.2 M solution of $SiCl_4$ (0.23 mL, 2 mmol, 0.4 eq.) in THF (10 mL) was then added dropwise with stirring. The reaction turned clear and colourless and was left stirring for 18 hours, slowly warming to room temperature. The reaction was then cooled to 0°C before a 0.78 M solution of KOH (0.33 g, 5.89 mmol) in H_2O (7.5 mL) was added. A white precipitate was observed upon addition which was filtered and washed with cold Et_2O. The white solid was analysed and assigned as $(C_{12}H_9)_2Si(OH)_2$ and not the desired *tri*-(4-biphenyl)silanol.[80]

Yield: 0.36 g / 45.6%

^{1}H NMR (d_2-CD_2Cl_2): δ / ppm: 7.81 (d, J = 10 Hz, 1H, 8-position), 7.78 (d, J = 10 Hz, 2H, 2-position), 7.68 (d, J = 5 Hz, 2H, 6-position), 7.60-7.64 (m, 3.5H, 3,7-positions)

Mass Spectroscopy (EI): m/z = 368 ($(C_{12}H_9)_2Si(OH)_2$)

7.3 *tri*-(1-anisyl)silanol

Anisole (2.17 mL, 20 mmol, 1 eq.) was diluted in hexane (34.4 mL) and THF (5.6 mL). TMEDA (3.00 mL, 20 mmol, 1 eq.) was added to the reaction and the solution was then cooled to -78°C. A 1.6 M solution of ^{n}BuLi (20 mmol, 1 eq.) in hexane was then added dropwise to the reaction, with stirring over a period of one hour. The clear solution rapidly turned yellow and then cloudy towards the end of the addition. The reaction was left stirring and warming to room temperature for three hours. The solution was then added dropwise to a 0.33 M solution of $SiCl_4$ (0.76 mL, 6.7 mmol, 0.33 eq.) in THF (20 mL) at room temperature. The clear solution turned pale yellow and white vapour was observed. The reaction was left to stir for 16 hours and then cooled to 0°C. H_2O was then added slowly which resulted in a white precipitate which was collected by filtration and washed with cold Et_2O.[80]

Yield: 0.80 g / 34.2%

^{1}H NMR (d_2-CD_2Cl_2): δ / ppm: 7.48 (d of d, J = 5,10 Hz, 1H, 3-position), 7.42 (t of d, J = 0,7.5 Hz, 1H, 4-position), 6.97 (t, J = 10 Hz, 1H, 5-position), 6.88 (d, J = 10 Hz, 1H, 6-position)

Mass Spectroscopy (EI): m/z = 349 ($(C_7H_7O)_3Si$), 276 ($(C_7H_7O)_2Si(OH)_2$)

7.4 Synthesis of *tri*-(2,4,6-triisopropylbenzene)silanol

2-Bromo 1,3,5-triisopropylbenzene (0.447 mL, 1.765 mmol, 1 eq.) was diluted in THF and cooled to -78°C. A 1.6 M solution of ^{n}BuLi (0.30 mL, 1 eq.) in hexane was added dropwise to the solution of 2-bromo 1,3,5-triisopropylbenzene over a period of one hour resulting in a dense white vapour. The solution was left stirring for three hours. The solution was then added dropwise to a 0.33 M solution of $SiCl_4$ (0.0675 mL, 0.5884 mmol, 0.33 eq.) in

THF at -78°C resulting in the formation of a white vapour. After one hour the solution had turned yellow and was left stirring and warmed to room temperature over a period of 12 hours. The predicted product $(C_{15}H_{23})_3SiCl$ was then extracted by filtration to remove the side product KCl (0.1072 g recovered) and solvent removed *in vacuo* leaving a yellow oil.

Mass Spectroscopy (EI): m/z = 260

7.5 Synthesis of *tri*-(2-mesitylene)silanol

2-Bromomesitylene (0.384 mL, 2.511 mmol, 1 eq.) was diluted in THF and cooled to -78°C. A 1.6 M solution of ^{n}BuLi (0.43 mL, 1 eq.) in hexane was also cooled to -78°C and added dropwise to the solution of 2-Bromomesitylene over a period of one hour resulting. The solution initially turned bright yellow with a white vapour and then turned beige. The solution was left stirring for one hour at -78°C and a white precipitate was observed. The solution was then added dropwise to a 0.33 M solution of $SiCl_4$ (0.0961 mL, 0.837 mmol, 0.33 eq.) in THF at -78°C resulting in the formation of a white vapour and the solution turned yellow. The reaction was left stirring at -78°C for one hour and warmed to room temperature over a period of 3 hours and the solution turned brown/red. The solution was filtered with no obvious solid extracted, the side product, KCl (0.1322 g recovered) was extracted from hexane and the solvent removed from the filtrate *in vacuo* and analysis undertaken.

Mass Spectroscopy (EI): m/z = 120

7.6 Characterisation of Ph_3SiOH

Tiphenylsilanol (98%) was purchased from Sigma Aldrich and used as received.

$^{13}C\{H\}$ NMR	(d_8-THF):	δ / ppm: 136.91 (*ipso*), 134.76 (*ortho*), 129.21 (*para*), 127.31 (*meta*)
^{1}H NMR	(d_8-THF):	δ / ppm: 7.61 (d, J = 6.8 Hz, 6H, *ortho*), 7.33 (m, 9H, *meta / para*), 6.02 (s, 1H, OH)
^{29}Si NMR	(d_8-THF):	δ / ppm: -17.02
HSQC NMR	(d_8-THF):	δ / ppm: 7.62, 134.87 (*ortho*); 7.36, 129.31 (*para*); 7.32, 127.39 (*meta*); 3.59, 66.94 (THF); 1.73, 24.77 (THF)
HMBC NMR	(d_8-THF):	δ / ppm: 7.61, 129.15; 7.60, 136.83; 7.30, 136.85; 6.01, 136.85; 3.58, 66.33 (THF); 3.58, 24.43 (THF); 1.72, 66.36 (THF); 1.72, 24.45 (THF)

7.7 Synthesis of Ph_3SiOK

Synthetic methods were found in the literature for the synthesis of Ph_3SiONa, however the methods used multiple solvents and heating up to 115°C which seemed overly complex.[190] The following methods were adapted from a synthesis published by Caulton.[89]

Triphenylsilanol (4.3948g, 0.0159 mol, 1 eq.) was added to hexane and stirred. Potassium hydride (0.6377g, 0.0159 mol, 1 eq.) was added and no immediate changes were observed. After a few minutes a milky white precipitate was observed along with the evolution of a gas (presumed to be H_2). The solution left to stir for 24 hours before it was filtered, washed three times with hexane and dried *in vacuo* for four to six hours.

Yield: 4.8038 g / 96.08 %

$^{13}C\{H\}$ NMR	(d_8-THF):	δ / ppm: 145.77 (*ipso*), 135.81 (*ortho*), 128.54 (*para*), 128.27 (*meta*), 67.57 (THF), 25.51 (THF)
^{1}H NMR	(d_8-THF):	δ / ppm: 7.49 (d, J = 6.9 Hz, 2H, *ortho*), 7.25-7.17 (m, 3H, *meta/para*), 3.58 (THF), 1.73 (THF)
HSQC NMR	(d_8-THF):	δ / ppm: 7.47, 135.53; 7.18, 128.11; 3.58, 67.57; 1.73, 25.58
HMBC NMR	(d_8-THF):	δ / ppm: 7.46, 145.75; 7.46, 135.80; 7.46, 128.45; 7.19, 135.81; 7.16, 128.27; 7.15, 145.74; 3.58, 67.57; 3.58, 25.47; 1.73, 67.59; 1.73, 25.56

7.8 Synthesis of UCl_4

The method used to synthesise UCl_4 was taken from the literature[191] and modified by Ibers[192] in 2007. It should also be noted that the method used here presents an explosion risk and an improved synthesis has been published by Kiplinger.[193]

UO_3 (3.7800g, 0.0132 mol, 1 eq.) was added to a large three necked round bottomed flask fitted with a reflux condenser, a thermometer and a glass stopper. A glass stirrer bar was also added to the flask. Hexachloropropene (9.5mL, 0.0674 mol, 5 eq.) was then carefully added and the solution was stirred. The solution was gradually heated, at approximately 40°C reflux was observed. At 140°C no reaction had occurred and it was switched off overnight. At 163°C a slight colour change was observed and at 166°C an exothermic reaction occurred followed by a colour change to a deep red. Following the initial reaction a green line was observed on the edge of the flask followed by growth of large single crystals. The solution was left at reflux for 1 hour before being switched off overnight. Reflux was restarted at 168°C and left for eight hours, this was repeated three times, before being left to cool and stir for 48 hours.

Carbon tetrachloride (20mL) was added to the reaction to wash out any unreacted hexachloropropene and filter canulated out, this was repeated three times. Carbon tetrachloride was then added again and the green solid was canulated out into a clean round bottomed flask. The carbon tetrachloride was then filter canulated out and the resulting green solid was dried *in vacuo*.

Yield: 4.0522g / 81%

Compound	λ / nm	ϵ / L mol^{-1} cm^{-1}	A	Assignment
UCl_4	408.0	1.87	0.123	$^3P,^1D$[119]
in THF	438.0	4.79	0.315	—
	453.9	6.55	0.431	^1I[119]
	470.0	4.35	0.286	—
	489.9	4.57	0.301	—
	508.0	3.42	0.225	^3P[119]
	556.0	3.47	0.228	^3P[119]
	645.9	11.58	0.762	—
	666.1	10.78	0.709	—
UCl_4	437.5	18.83	0.098	—
in Toluene	453.5	23.25	0.121	^1I[119]
	491.0	15.95	0.083	—
	549.5	10.95	0.057	^3P[119]
	587.5	8.84	0.046	$^1D,^3P$[119]
	648.0	16.91	0.088	—
	664.0	18.83	0.098	—

Table 7.3: Molar absorptivity (ϵ) of the compound UCl_4 in THF and toluene with assignments

7.9 K[U(Ph$_3$SiO)$_5$]

Uranium tetrachloride (0.500g, 1.3165 mmol, 1 eq.) was suspended in THF and stirred vigorously. Triphenylsiloxide (2.0700g, 6.5824 mmol, 5 eq.) was dissolved in THF and then added to the UCl_4 dropwise over a period of five minutes. A colour change from dark green to bright green to dark blue to dark purple was observed. After two hours the solution was dark pink and the reaction was stirred for 24 hours. The solution was filtered through a frit and the solvent removed *in vacuo*. The resulting sticky pink product was washed in pentane until a loose pale pink powder. The solid was dissolve in toluene and

filtered to remove the side product, KCl and left to recrystallise at room temperature.

Yield: 1.6406g / 75.33%

$^{13}C\{H\}$ NMR	(d_8-Toluene):	δ / ppm: 150.19 (*ipso*), 137.47 (Toluene), 129.09-128.61 (Toluene), 128.45 (*ortho*), 128.18-127.70 (Toluene), 127.11 (*para*), 126.58 (*meta*), 125.35-124.87 (Toluene), 20.78-19.83 (Toluene)
^{1}H NMR	(d_8-Toluene):	δ / ppm: 7.05 (d, J = 7.2 Hz, 1H, Toluene), 6.97 (d, J = 10.4 Hz, 2H, Toluene), 6.54 (s, 7H, *para*), 5.61 (s, 12H, *meta*), 4.91 (s, 10H, *ortho*), 2.15-2.10 (m, 2H, Toluene)
HSQC NMR	(d_8-Toluene):	δ / ppm: 7.07, 127.52 (Toluene); 6.96, 128.25 (Toluene); 6.55, 127.49 (*para*); 5.62, 126.28 *meta*; 2.09, 20.40 (Toluene)
HMBC NMR	(d_8-Toluene):	δ / ppm: 7.08, 137.50; 7.08, 128.53; 7.00, 128.63; 6.75, 128.71; 6.54, 126.77; 6.33, 128.28; 2.09, 137.86; 2.09, 129.32

Anal Calcd: C, 65.37; H, 4.57; O, 4.84; K, 2.36; Si, 8.46; U, 14.39; Found: C, 64.84, H, 4.54: O, 4.0

UV-Vis (Toluene) nm / A : 427.5, 0.245; 466.0, 0.373; 501.0, 0.173; 554.6, 0.483; 595.4, 0.224; 607.5, 0.237; 654.0, 0.272; 735.5, 0.100

7.10 $([K(py)_6][(Ph_3SiO)_5U(py)])_2$

Uranium tetrachloride (0.0201g, 0.0529 mmol, 1 eq.) was added to THF at room temperature and stirred vigorously until dissolved. Ph_3SiOK (0.1g, 0.3179 mmol, 6 eq.) was added to THF and then added dropwise to the UCl_4 solution, stirring vigorously. Within minutes the solution had changed from green to lilac to pink. The solution was filtered through a grade 3 frit and the solvent was removed *in vacuo*. The pale pink precipitate was washed in pentane four times and then dried *in vacuo* for 30 minutes. The solid was then dissolved in a minimum amount of toluene and an excess of hexane was added. A pink solid precipitated out which was filtered and dried *in vacuo* (0.0681g). The pink solid turned bright orange when dissolved in a minimum amount of pyridine. The orange solution was filtered and left to cool to -40°C for three days which resulted in orange crystals

approximately 1mm in size. The crystals were then filtered and washed in cold pyridine over a pre-cooled frit.

Yield: 0.0545g / 55%

$^{13}C\{H\}$ NMR	(d_5-Pyridine):	δ / ppm: 149.80 (pyridine), 138.15, 137.43 *ortho*, 135.81 (pyridine), 129.52, 128.72, 128.12 *para*, 127.71 *meta*, 125.87, 123.83 (pyridine), 21.44
^{1}H NMR	(d_5-Pyridine):	δ / ppm: 9.22 (s, broad, 6H, *ortho*), 8.74 (m, 1H, pyridine), 8.05 (m, 1H), 7.62 (m, 1H, pyridine), 7.50 (m, 1H, pyridine), 7.29 (q, J = 11.5 Hz, 3H, *para*), 7.08 (s, 6H, *meta*), 2.29 (s, 1H)
HSQC	(d_5-Pyridine):	δ / ppm: 8.34, 136.83 (*ortho*); 8.28, 136.40; 8.01, 135.82; 7.58 (pyridine), 135.91; 7.47, 130.24; 7.47 (pyridine), 128.47; 7.26, 128.24 (*para*); 7.25, 126.57; 7.06, 129.45; 7.04, 127.85 (*meta*); 2.26, 21.81

7.11 K[$(Ph_3SiO)_5U(THF)$]

Uranium tetrachloride (0.5000g, 1.3165 mmol, 1 eq.) was added to THF at room temperature and stirred vigorously until suspended. Ph_3SiOK (2.0700g, 6.5824 mmol, 5 eq.) was added to THF and then added dropwise to the UCl_4 solution, stirring vigorously. Within minutes the solution had changed from dark green to turquoise to blue to lilac. After four hours the solution was filtered through a grade 3 frit and the solvent was removed *in vacuo*. The pink solid from the filtrate was washed in pentane five times and then dried *in vacuo* for 30 minutes.

Yield: 2.1327g / 82.98%

^{13}C{H} NMR	(d_8-THF):	δ / ppm: 143.94 (*ipso*), 138.04 (*ortho*, 130.58, 128.41 (*para*, 128.11 (*meta*, 67.57 (THF), 25.61 (THF)
^{1}H NMR	(d_8-THF):	δ / ppm: 8.96 (s, 2H, *ortho*), 7.12 (t, J = 7.3 Hz, 1H, *para*), 6.87, (t, J = 7.1 Hz, 2H, *meta*), 3.58 (s, 1H, THF), 1.77 (1H, THF)
^{29}Si HMBC	(d_8-THF):	δ / ppm: 8.97, -29.01; 7.13, -28.99; 6.86, -28.99
^{29}Si HMBC -38 °C	(d_8-THF):	δ / ppm: 9.52, -43.59; 6.00, -15.73
HSQC	(d_8-THF):	δ / ppm: 8.95, 138.31 (*ortho*); 7.11, 128.69 (*para*); 6.85, 128.42 (*meta*); 3.58, 67.42 (THF); 1.76, 25.37 (THF)
HMBC	(d_8-THF):	δ / ppm: 8.97, 137.91; 8.97, 128.08; 7.54, 137.91; 7.27, 143.79; 7.27, 127.60; 7.13, 137.90; 6.86, 143.79; 6.86, 127.99; 6.71, 138.02; 6.44, 143.79; 6.44, 127.98; 3.58, 67.29; 3.58, 25.37; 1.77, 67.20; 1.77, 25.34

Mass Spectroscopy (HRMS Negative ESI):
1 eq. Ph_3SiOK m/z = 358.9515 (5.4x10^6), 414.8908 (3.8x10^6), 655.0104 (4.7x10^6), 895.1304 (0.9x10^6), 1275.05 (0.6x10^6)
2 eq. Ph_3SiOK m/z = 275 (0.4x10^6), 358.9517 (1.1x10^6), 655.0105 (1.0x10^6), 895.1304 (1.7x10^6), 1170.2239 (0.7x10^6), 1410.3450 (0.6x10^6)
3 eq. Ph_3SiOK m/z = 1133.2587 (0.2x10^7), 1410.3479 (0.2x10^7), 1614.4872 (0.8x10^7)
4 eq. Ph_3SiOK m/z = 1614.4781 (2.0x10^6)
5 eq. Ph_3SiOK m/z = 1614.4781 (2.0x10^6)
6 eq. Ph_3SiOK m/z = 275.0889 (0.6x10^7), 589.1415 (0.9x10^7), 912.30 (0.2x10^7), 1156.3733 (1.0x10^7), 1401.4449 (0.6x10^7)

UV-Vis (THF) nm / A : 397.5, 0.216; 426.5, 0.259; 469.5, 0.125; 489.5, 0.167; 525.5, 0.187; 549.0, 0.357; 593.1, 0.176; 628.5, 0.071; 652.6, 0.121; 716.0, 0.169

7.12 Experiments with TMSOTf

7.12.1 TMSOTf

TMSOTf (99%) was purchased from Sigma Aldrich and used as received.

^{13}C{H} NMR	(d_8-THF):	δ / ppm: 119.76 (q, $^1J_{CF}$ = 316.8 Hz, TMS-**OTf**), 0.30 (**TMS**-OTf)
^{1}H NMR	(d_8-THF):	δ / ppm: 0.45 (**TMS** OTf)
^{19}F NMR	(d_8-THF):	δ / ppm: 74.40, 76.53, 76.72

7.12.2 Reaction between TMSOTf + Ph_3SiOH

Ph_3SiOH (*ca.* 0.001 g, 0.0036 mmol, 1 eq.) was added to an NMR tube and dissolved in a minimum amount of d_8-THF. TMSOTf (*ca.* 0.65 μL, 0.0036 mmol, 1 eq.) was the added to the sample and analysis undertaken.

$^{13}C\{H\}$ NMR	(d_8-THF):	δ / ppm: 137.22 (TMS OSi**Ph$_3$** *ipso*), 135.87 (TMS OSi**Ph$_3$** *ortho*), 130.65 (TMS OSi**Ph$_3$** *para*), 128.62 (TMS OSi**Ph$_3$** *meta*), 67.57 (THF), 25.44 (THF), 2.23 (**TMS** OSiPh_3)
^{1}H NMR	(d_8-THF):	δ / ppm: 7.56 (dd, *J* = 7.9, 1.3 Hz, 2H, TMS OSi**Ph$_3$** *ortho*), 7.37 (d, *J* = 7.3 Hz, 1H, TMS OSi**Ph$_3$** *para*), 7.33 (d, *J* = 7.2 Hz, 2H, TMS OSi**Ph$_3$** *meta*), 3.58 (THF), 1.72 (THF), 0.09 (**TMS** OSiPh_3)
^{19}F NMR	(d_8-THF):	δ / ppm: 76.24, 79.11

7.12.3 Reaction between TMSOTf + Ph_3SiOK

Ph_3SiOK (*ca.* 0.001 g, 0.0032 mmol, 1 eq.) was added to an NMR tube and dissolved in a minimum amount of d_8-THF. TMSOTf (*ca.* 0.575 μL, 0.0032 mmol, 1 eq.) was the added to the sample and analysis undertaken.

$^{13}C\{H\}$ NMR	(d_8-THF):	δ / ppm: 137.28 (TMS OSi**Ph$_3$** *ipso*), 135.93 (TMS OSi**Ph$_3$** *ortho*), 130.70 (TMS OSi**Ph$_3$** *para*), 128.67 (TMS OSi**Ph$_3$** *meta*), 67.57 (THF), 25.83 (THF), 2.28
^{1}H NMR	(d_8-THF):	δ / ppm: 7.57 (d, *J* = 7.1 Hz, 2H, TMS OSi**Ph$_3$** *ortho*), 7.37 (d, *J* = 7.1 Hz, 1H, TMS OSi**Ph$_3$** *para*), 7.34 (d, *J* = 7.1 Hz, 2H, TMS OSi**Ph$_3$** *meta*), 0.10 (s, 5H)
^{19}F NMR	(d_8-THF):	δ / ppm: 76.23, 79.10

7.12.4 Reaction between TMSOTf + K[$(Ph_3SiO)_5U(THF)$]

K[$(Ph_3SiO)_5U(THF)$] (0.0200g, 0.0121 mmol, 1 eq) was dissolved in THF. Trimethylsilyltriflate (2.2 μL, 0.0121 mmol, 1 eq.) was injected into the solution and analysis undertaken. The second equivalent of TMSOTf (2.2 μL, 0.0121 mmol, 1 eq.) was then added to the

reaction mixture and analysis was repeated. The reaction turned the pink solution pale in colour and resulted in an intractable mixture.

1eq. TMSOTf

$^{13}C\{H\}$ NMR	(d_8-THF):	δ / ppm: 137.31, 135.96, 130.72, 130.41, 129.86, 129.10, 128.69, 128.63, 128.52, 126.23, 67.57, 25.51, 2.28
^{1}H NMR	(d_8-THF):	δ / ppm: 7.96 (s, 1H), 7.59 (m, 4H), 7.35 (m, 6H), 7.19 (t, J = 7.4 Hz, 2H), 7.11 (m 2H), 7.00 (s, 1H), 6.88 (s, 1H), 3.58 (s, 7H), 2.31 (s, 1H), 1.73 (s, 3H), 1.10 (s, 3H)

2eq. TMSOTf

$^{13}C\{H\}$ NMR	(d_8-THF):	δ / ppm: 137.38, 136.02, 130.79, 129.93, 129.16, 128.76, 126.30, 67.57, 25.54, 2.35
^{1}H NMR	(d_8-THF):	δ / ppm: 15.35 (s, 4H), 13.45 (s, 2H), 13.27 (s, 3H), 12.03 (t, J = 7.2 Hz, 1H), 7.59 (d, J = 7.9 Hz, 17H), 7.38 (dt, J = 13.8, 6.8 Hz, 30H), 7.25-6.99 (m, 12H), 6.89 (s, 2H), 3.66-3.50 (m, 19H), 2.32 (s, 4H), 1.73 (s, 16H), 0.51 (s, 1H), 0.12 (s, 25H)

Mass Spectroscopy (HRMS Negative ESI) :
0 eq. TMSOTf m/z = 1370.4401 (0.5x10^7), 1614.4829 (1.4x10^7)
1 eq. TMSOTf m/z = 1361.2143 (1.8x10^5), 1488.3454 (4.0x10^5)
2 eq. TMSOTf m/z = 1235.0673 (1.1x10^6)

Mass Spectroscopy (HRMS Positive ESI) :
0 eq. TMSOTf m/z = 1465.3680 (0.5x10^6), 1692.4103 (7.0x10^6)
1 eq. TMSOTf m/z = 387.0987 (3.0x10^6), 1323.2942 (4.0x10^6), 1395.3547 (1.8x10^6), 1450.4253 (2.6x10^6), 1511.1901 (0.8x10^6), 1930.3151 (2.6x10^6)
2 eq. TMSOTf m/z = 387.0990 (7.0x10^6), 1269.2176 (1.5x10^6), 1385.0786 (2.0x10^6), 2168.4412 (2.0x10^6)

7.13 K[$(Ph_3SiO)_4U(O_2)$]

Potassium pentakissiloxy uranium (0.0502g, 0.0303 mmol, 1 eq.) was dissolved in approximately 0.6mL of THF in an ampoule. Using a toepler line, oxygen (4.2 mmHg, 0.0302 mmol, 1 eq.) was added at -78°C. The solution turned brown very quickly and remained brown at -78°C. The solution was removed from the acetone / CO_2 cold bath and warmed slowly to room temperature. On warming the solution turned yellow. The solution was then dried *in vacuo* and dissolved in a minimum amount of benzene. Pentane was added to the solution until a precipitate was momentarily observed. The solution was then left

at room temperature to recrystallise.

Yield: 0.015g / 29.88%

Wavenumber / cm-1	IMS Bath	IMS Bath O_2 added	Chiller Unit	-50	-40	-30	-20	-10	0	10	Room Temp
1485.9	0.013	0.013	0.014	0.015	0.017	0.018	0.017	0.017	0.018	0.019	0.010
1113.5	0.115	0.114	0.099	0.097	0.097	0.098	0.096	0.095	0.094	0.094	0.091
945.9	0.317	0.268	0.183	0.129	0.097	0.085	0.073	0.062	0.057	0.063	0.075
890.0	0.021	0.044	0.038	0.030	0.037	0.049	0.054	0.058	0.061	0.063	0.066
741.1	0.107	0.106	0.087	0.082	0.084	0.085	0.083	0.081	0.080	0.085	0.084
707.6	0.387	0.374	0.333	0.321	0.313	0.310	0.303	0.294	0.290	0.292	0.282

Table 7.4: React IR data for the reaction between $K[(Ph_3SiO)_5U(THF)]$ and O_2 at various temperatures

7.14 $K[(Ph_3SiO)_4UO$

$K[(Ph_3SiO)_5U(THF)]$ (0.4151g, 0.2510 mmol, 1 eq.) was added to an ampoule in the glove box and dissolved in a minimum amount of THF. The ampoule was evacuated on a high vacuum line (*ca.* 10^{-6} bar). A second ampoule was also evacuated on the high vacuum line which had a volume of 81 cm^3. 37 mbar of O_2 was expanded into the line and into a second ampoule which was then sealed. The high vacuum line was then evacuated and the two ampoules were sealed from the rest of the line leaving a connection between the two. Whilst the $K[(Ph_3SiO)_5U(THF)]$, THF solution was stirring, the O_2 was released into the ampoule and left to stir for two hours. The resulting orange solution was then pumped down to a minimum amount of THF and removing any unreacted O_2 before being taken back into the glove box. Pentane was then added to the THF solution and left at -40 °C to recrystallise. The crystals were then filtered, washed in cold THF and dried *in vacuo*.

Yield: 0.0377g / 9.33%

$^{13}C\{H\}$ NMR	(d_8-THF):	δ / ppm: 137.29, 136.90, 136.17, 130.61, 130.06, 129.39, 129.29, 128.71, 128.36, 128.17, 126.42
^{1}H NMR	(d_8-THF):	δ / ppm: 8.53 (s, 1H), 7.87 (d, J = 6.9 Hz, 7H), 7.60 (d, J = 6.6 Hz, 5H), 7.35 (d, J = 3.2 Hz, 1H), 7.36-7.28 (m, 6H), 7.23-7.14 (m, 6H), 7.09 (p, J = 7.1, 6.4 Hz, 11H), 6.97 (t, J = 7.4 Hz, 2H), 6.89 (qd, J = 16.0, 12.8, 5.9 Hz, 7H), 6.78 (q, J = 6.3, 4.4 Hz, 2H), 6.66 (dd J = 7.5, 3.7 Hz, 2H), 6.56 (t, J = 7.4 Hz, 1H), 6.01 (s, 1H), 3.58 (s, 4H), 2.30 (s, 3H), 1.73 (s, 3H)

Mass Spectroscopy (HRMS Negative ESI) :
m/z = 1354.3904 (1.5x10^6), 1400.4260 (1.6x10^6), 1443.4801 (1.7x10^6), 1615.00 (0.2x10^6), 1630.00 (0.5x10^6), 1645.5173 (0.8x10^6), 1701.35 (0.5x10^6)

7.15 $(THF)(Ph_3SiO)_5U$

K[$(Ph_3SiO)_5U(THF)$] (0.0212g, 0.0128 mmol, 1 eq.) was dissolved in d_8-THF at -78 °C. Using a Toepler line, 3 equivalents of CO_2 were added to the solution. No change was observed initially. When warmed to room temperature the solution turned yellow in colour. A small number of crystals were grown from THF at room temperature.

Yield: 0.0071g / 33.49%

$^{13}C\{H\}$ NMR	(d_8-THF):	δ / ppm: 143.84, 137.93, 137.15, 136.27, 136.03, 130.47, 129.92, 129.15, 128.74, 128.67, 128.57, 128.29, 128.00, 126.28, 126.13, 67.57, 25.95, 21.74
^{1}H NMR	(d_8-THF):	δ / ppm: 8.91 (s, 8H), 7.90 (m, 1H), 7.64 (dd, J = 7.7, 1.6 Hz, 2H), 7.51 (d, J = 6.5 Hz, 1H), 7.41-6.97 (m, 18H), 6.92 (s, 3H), 6.81 (t, J = 7.3 Hz, 12H), 3.58 (s, 2H), 2.34 (s, 1H), 1.74 (s, 1H)
HSQC	(d_8-THF):	δ / ppm: 8.91, 136.56; 8.85, 136.54; 7.08, 126.80; 6.83, 126.56; 6.77, 126.71

7.16 Reaction between Ph_3SiOH and LiH

Ph_3SiOH (0.05 g, 0.1809 mmol, 1 eq.) was dissolved in hexane and stirred. LiH (0.0015 g, 0.1887 mmol, 1.eq.) was then added as a solid with no immediate changes observed.

After 24 hours the solution had turned cloudy with a thin layer of precipitate observed. The solution was filtered and solvent removed *in vacuo* resulting in a white solid. Variations of this reaction were attempted by refluxing the solution in an oil bath which was heated to 80°C and changing the solvent system to toluene.

Yield: 0.0260 g / 50.58 %

$^{13}C\{H\}$ NMR	(d_6-benzene):	δ / ppm: 136.11, 135.47, 130.21, 128.17, 128.30-127.82 (benzene)
^{1}H NMR	(d_6-benzene):	δ / ppm: 7.81-7.78 (m, 5H), 7.33-7.32 (m, 9H), 2.00 (s, 1H)

7.17 Reaction between Ph_3SiOH and $^{n}BuLi$

Ph_3SiOH (4.8950 g, 17.71 mmol, 1 eq.) was dissolved in hexane and stirred. A 4.60 M solution of $^{n}BuLi$ (3.825 mL, 17.7 mmol, 1 eq.) was added slowly and left to stir. After 30 minutes the solution had turned milky white and the solution was filtered and solvent removed *in vacuo* resulting in a white solid.

Yield: 5.1819 / 103.64 %

$^{13}C\{H\}$ NMR	(d_8-THF):	δ / ppm: 145.37, 136.30, 128.42, 127.59, 67.57 (THF), 25.49 (THF)
^{1}H NMR	(d_8-THF):	δ / ppm: 7.63 (s, 2H), 7.20 (s, 3H), 3.58 (THF), 1.75 (THF), 1.29 (hexane), 0.89 (hexane)
^{7}Li NMR	(d_8-THF):	δ / ppm: 1.45

7.18 Reaction between Ph_3SiOH and NaH

Ph_3SiOH (0.05 g, 0.1809 mmol, 1 eq.) was added to hexane and stirred. NaH (0.0044 g, 0.1834 mmol, 1 eq.) was added as a solid and stirred for 48 hours. The solution had

turned cloudy and was filtered and the solvent removed *in vacuo* resulting in a white solid. Variations of this method were trialled, refluxing the solution in an oil bath heated to 80°C.

Yield: 0.0149 g / 27.74 %

$^{13}C\{H\}$ NMR	(d_6-benzene):	δ / ppm: 135.47, 130.21, 128.35, 129.17, 128.25-127.87 (benzene)
^{1}H NMR	(d_6-benzene):	δ / ppm: 7.66-7.64 (m, 2H), 7.19-7.16 (m, 4H), 1.86, 1.36, 0.92

7.19 Reaction between Ph_3SiOH and Cs

Ph_3SiOH (0.0204 g, 0.0738 mmol, 1 eq.) was dissolved in THF. Separately Cs metal (0.0094 g, 0.0707 mmol, 1 eq.) was added to a vial. The solution of Ph_3SiOH was then added slowly to the Cs and stirred vigourously. The Cs metal turned black almost immediately. After a few minutes the solution turned orange/yellow and then brown. After one hour the solution had turned orange/red. Within six hours the solution was clear and colourless. The solution was filtered to remove any unreacted Cs and a sample was extracted for analysis. The remaining solution was used in a further reaction.

$^{13}C\{H\}$ NMR	(d_8-THF):	δ / ppm: 146.16, 136.01, 129.82, 129.06, 128.45, 128.18, 126.19, 67.57 (THF), 25.49 (THF)
^{1}H NMR	(d_8-THF):	δ / ppm: 11.69, 9.26, 8.89, 7.63, 7.61, 7.34, 7.32, 7.31, 7.04, 6.81, 6.79, 6.78, 6.02, 3.58 (THF), 1.78 (THF), 1.31, 0.89

7.20 Reaction between Ph_3SiOH and Rb

Ph_3SiOH (0.05 g, 0.1809 mmol, 1 eq.) was dissolved in THF. Separately Rb metal (0.0155 g, 0.1809 mmol, 1 eq.) was added to a vial. The solution of Ph_3SiOH was then added slowly to the Rb and stirred vigourously with no immediate changes observed.

After a 30 minutes the solution turned orange. After 12 hours the solution had turned yellow. Within six hours the solution was clear and colourless. The solution was filtered to remove any unreacted Rb and a sample was extracted for analysis. The remaining solution was used in a further reaction. The reaction was repeated at -78°C.

$^{13}C\{H\}$ NMR (d_8-THF): δ / ppm: 232.77, 135.81, 128.42, 128.20, 67.57 (THF), 25.50 (THF)
^{1}H NMR (d_8-THF): δ / ppm: 7.47, 7.19, 5.95, 3.58 (THF), 1.73 (THF)

7.21 Reaction between Ph_3SiOK and TlCl

Ph_3SiOK (0.0208 g, 0.0661 mmol, 1 eq.) was added to THF. TlCl (0.0156 g, 0.0650, 1 eq.) was added to the solution slowly. No changes were observed and the solution was filtered and solvent removed *in vacuo*. The reaction was repeated using toluene.

Yield: 0.0278 g / 78.97 % crude

7.22 Reaction between $K[(Ph_3SiO)_5U(THF)]$ and CsI

$K[(Ph_3SiO)_5U]$ (0.0105 g, 0.0063 mmol, 1 eq.) was added to THF forming $K[(Ph_3SiO)_5U(THF)]$ and stirred vigorously. Excess CsI (0.0105 g, 0.0404 mmol, 6.5 eq.) was added slowly with no immediate changes observed. After 12 hours the solution was pale pink with some solids observed. The reaction was filtered to remove unreacted solids and solvent removed *in vacuo* leaving an off white solid.

Yield: 0.0078 g / 74.29 % crude

$^{13}C\{H\}$ NMR	(d_8-THF):	δ / ppm: 143.79, 137.89, 135.99, 130.37, 129.87, 129.01, 128.51, 128.25, 127.95, 67.57 (THF), 25.51 (THF)
^{1}H NMR	(d_8-THF):	δ / ppm: 8.89, 7.91-7.89, 7.63, 7.34-7.32, 7.06-7.02, 6.81-6.77, 3.58 (THF), 2.32, 1.74 (THF)
^{29}Si NMR	(d_8-THF):	δ / ppm: 69.42

7.23 Reaction between K[$(Ph_3SiO)_5U$(THF)] and RbI

K[$(Ph_3SiO)_5U$] (0.0105 g, 0.0063 mmol, 1 eq.) was added to THF forming K[$(Ph_3SiO)_5U$(THF)] and stirred vigorously. Excess RbI (0.0135 g, 0.0636 mmol, 10 eq.) was added slowly with no immediate changes observed. After 12 hours the solution was pale pink with some solids observed. The reaction was filtered to remove unreacted solids and solvent removed *in vacuo* leaving a beige/yellow solid.

Yield: 0.0064 g / 60.95 % crude

^{1}H NMR	(d_8-THF):	δ / ppm: 7.59 (s, 5H), 7.32-7.30 (d, 7H), 7.18, 7.16, 7.13, 7.07, 6.00 (s, 1H), 3.58 (THF), 2.42, 2.30, 1.77, 1.73 (THF)

7.24 Characterisation of ($^{t}BuO)_3SiOH$

Tris *tert*-butoxy silanol (99.999%) was purchased from Sigma Aldrich and used as received.

$^{13}C\{H\}$ NMR	(d_8-THF):	δ / ppm: 72.77 ($((CH_3)_3\mathbf{C}O)_3SiOH$), 31.99 ($((\mathbf{C}H_3)_3CO)_3SiOH$)
^{1}H NMR	(d_8-THF):	δ / ppm: 5.25 ($((CH_3)_3CO)_3SiO\mathbf{H}$), 1.30 ($((C\mathbf{H}_3)_3CO)_3SiOH$)
HMBC NMR	(d_8-THF):	δ / ppm: 1.31, 72.92; 1.43, 32.14; 1.30, 32.27; 1.14, 32.21

7.25 Synthesis of (^{t}BuO)$_3$SiOK

Synthesised in an identical manner to Ph_3SiOK and modified from literature preparations.[90] Tris *tert*-butoxy silanol (4.00g, 0.0151 mol, 1eq.) was dissolved in hexane and stirred vigorously. Potassium hydride (0.6058g, 1.0515 mol, 1 eq.) was added slowly as a solid. Bubbles were observed in the reaction vessel, assumed to be H_2 and a white precipitate formed during the exothermic reaction. After a few minutes the reaction turned clear and was left to stir for 24 hours. The resulting solution was filtered through a frit and the solvent removed *in vacuo*. The white solid was washed in three times with hexane and dried *in vacuo*.

Yield: 3.8625 g / 84.55 %

^{13}C{H} NMR	(d_8-THF):	δ / ppm: 71.07 (((CH$_3$)$_3$**C**O)$_3$SiOK), 67.57 (THF), 32.83 (((**C**H$_3$)$_3$CO)$_3$SiOK), 25.70 (THF)
^{1}H NMR	(d_8-THF):	δ / ppm: 3.58 (THF), 1.73 (THF), 1.32 (s, 7H, ((C**H**$_3$)$_3$CO)$_3$SiOK)
^{29}Si NMR	(d_8-THF):	δ / ppm: -88.38, -110.90
HSQC NMR	(d_8-THF):	δ / ppm: 1.32, 32.83
HMBC NMR	(d_8-THF):	δ / ppm: 1.32, 32.83; 1.32, 71.07

7.26 K[(U(OSi(O^{t}Bu)$_3$)$_3$)$_2$($\mu-\eta^6$:η^6-tol))]

Uranium iodide (0.1320 g, 0.2133 mmol, 1 eq.) was dissolved in THF. Tris *tert*-butoxy siloxide (0.1936 g, 0.6400 mmol, 3 eq.) was dissolved in THF and added to the UI_3 dropwise over a period of 5 minutes. A colour change from royal blue to chocolate brown was observed within minutes. The solution was left to stir overnight and then filtered to remove the side product, KI and dried *in vacuo*. The resulting brown solid was dissolved in toluene, filtered and left to recrystallise at -40 °C for two weeks resulting in orange/brown plate crystals.

Yield: 0.0186 g / 8.5%

$^{13}C\{H\}$ NMR	(d_6-benzene):	δ / ppm: 128.08, 33.27 (U((^{t}**Bu**O)$_3$SiO)$_3$ (U1)), 28.78 (K[((^{t}**Bu**O)$_3$SiO)$_3$U] (U2))
^{1}H NMR	(d_6-benzene):	δ / ppm: 7.16 (m, 3H), 2.42 (s, 1H), 2.38 (s, 9H, U((^{t}**Bu**O)$_3$SiO)$_3$ (U1)), 1.38 (s, 1H), -0.54 (s, 9H, K[((^{t}**Bu**O)$_3$SiO)$_3$U] (U2))
^{29}Si HMBC	(d_6-benzene):	δ / ppm: -25.00
HSQC	(d_6-benzene):	δ / ppm: 7.16, 128.06; 2.36, 32.87; 2.37, 32.82; -0.57, 28.26

Mass Spectroscopy (HRMS Negative ESI) :
1 eq. Ph_3SiOK m/z = 745.6644 (0.90 x 10^7), 961.1200 (0.15 x 10^7), 1145.0823 (1.30 x 10^7)
2 eq. Ph_3SiOK m/z = 745.6689 (0.1 x 10^5), 961.1241 (0.5 x 10^5), 1145.0914 (6.8 x 10^5)
3 eq. Ph_3SiOK m/z = 1059.5356 (2.5 x 10^6), 1154.4550 (1.8 x 10^6), 1290.7186 (3.5 x 10^6)
3 eq. (+ 3 hours) Ph_3SiOK m/z = 1059.53 (6.0 x 10^5), 1154.45 (3.0 x 10^5), 1290.71 (2.2 x 10^5)

7.27 Co-crystallisation products - [((^{t}BuO)$_3$SiO)$_3$U]$_2$(μ^2-O)$_3$

Uranium iodide (0.0222 g, 0.0359 mmol, 1 eq.) was dissolved in THF. Tris *tert*-butoxy siloxide (0.0332 g, 0.1097 mmol, 3 eq.) was dissolved in THF and added to the UI_3 dropwise over a period of 5 minutes. A colour change from royal blue to chocolate brown was observed within minutes. The solution was left to stir overnight and then filtered to remove the side product, KI and dried *in vacuo*. The resulting brown solid was dissolved in toluene, filtered and left to recrystallise at -40 °C for two weeks resulting in black block crystals.

Yield: 0.0072 g / 3.3%

7.28 Co-crystallisation products - [(U(OSi(O^{t}Bu)$_3$)$_4$)]

Uranium iodide (0.0222 g, 0.0359 mmol, 1 eq.) was dissolved in THF. Tris *tert*-butoxy siloxide (0.0332 g, 0.1097 mmol, 3 eq.) was dissolved in THF and added to the UI_3 dropwise over a period of 5 minutes. A colour change from royal blue to chocolate brown was observed within minutes. The solution was left to stir overnight and then filtered to remove the side product, KI and dried *in vacuo*. The resulting brown solid was dissolved in toluene, filtered and left to recrystallise at -40 °C for two weeks resulting in green block crystals.

Yield: 0.0114 g / 5.2%

7.29 UCl(OSi(O^{t}Bu)$_3$)$_3$

Uranium tetrachloride (0.0246g, 0.0648 mmol, 1 eq.) was suspended in THF. (^{t}BuO)$_3$SiOK (0.0588g, 0.1943 mmol, 3 eq.) was also dissolved in THF and added dropwise to the UCl_4. The green suspension quickly turned light blue and then a cloudy turquoise after four hours. The reaction was left to stir for 24 hours. The solvent was removed *in vacuo* and the remaining solid was washed in pentane and filtered repeatedly removing the side product KCl and any unreacted (^{t}BuO)$_3$SiOK. The pentane was removed from the blue filtrate *in vacuo* and the remaining blue and white solids were washed in pentane repeatedly. Extraction of one of the solids proved difficult, as the solubility's of both were identical. Crude separation was achieved by dissolving both solids in toluene and under vacuum the white solid precipitated first, sticking to the glassware. As soon as the blue solid started to precipitate, it was decanted using a pipette. The blue solid was crystallised from a saturated solution of THF at -40°C.

Yield: 0.0404g / 58.7% crude

^{13}C{H} NMR	(d_8-toluene):	δ / ppm: 76.14, 35.50
^{1}H NMR	(d_8-toluene):	δ / ppm: 5.96 (s, FWHH = 0.19 ppm, ^{t}Bu)
^{29}Si HMBC	(d_8-toluene):	δ / ppm: -61.91

7.30 U(OSi(O^{t}Bu)$_3$)$_4$

Uranium tetrachloride (0.03g, 0.0789 mmol, 1 eq.) was suspended in THF. (^{t}BuO)$_3$SiOK (0.0954g, 0.00032 mmol, 4 eq.) was also dissolved in THF and added dropwise to the UCl_4. The green suspension quickly turned light blue and then a cloudy turquoise after four hours. The reaction was left to stir for 24 hours. The solvent was removed *in vacuo* and the remaining solid was washed in pentane and filtered repeatedly to remove the side product, KCl and any unreacted (^{t}BuO)$_3$SiOK. The pentane was removed from the blue filtrate *in vacuo* and the remaining blue and white solids were washed in pentane repeatedly. The product turned purple on exposure to vacuum. Extraction of one of the solids proved difficult, as the solubility's of both were identical. Crude separation was achieved by dissolving both solids in toluene and under vacuum the white solid precipitated first, sticking to the glassware. As soon as the blue solid started to precipitate, it was decanted using a pipette. The blue solid was crystallised from a saturated solution of toluene at -40°C.

Yield: 0.053g / 52.1%

^{13}C{H} NMR	(d_8-toluene):	δ / ppm: 28.07, 29.73, 67.61, 69.14
^{1}H NMR	(d_8-toluene):	δ / ppm: 1.06 (s, 1H), 1.10 (s, 1H)
^{29}Si	(d_8-toluene):	δ / ppm: -55.28, -21.17
HSQC	(d_8-toluene):	δ / ppm: 1.06, 28.07; 1.10, 29.73
^{13}C{H} NMR	(d_8-THF):	δ / ppm: 31.86, 37.96, 72.64, 89.26
^{1}H NMR	(d_8-THF):	δ / ppm: 1.02 (s, 4H), 5.28 (s, 1H), 6.05 (s, 3H)

Mass Spectrometry : m/z = 1290 (M+ U(OSi(O^{t}Bu)$_3$)$_4$), 1027 (M+ OSi(O^{t}Bu)$_3$)

7.31 Reaction between K[(U(OSi(O^{t}Bu)$_3$)$_3$)$_2$($\mu-\eta^6$:η^6-tol))] and CO

UI_3 (0.02 g, 0.0323 mmol, 1 eq.) was added to a Young's NMR tube with Ph_3SiOK (0.0293 g, 0.0970 mmol, 3 eq.) and dissolved in d_8-THF at room temperature and left to react for one hour. The reaction was then cooled to -78°C and ^{13}CO (5.1 cm/Hg, 1 eq.) was added *via* the Toepler line. The solution showed no immediate changes. After six days the solution started to look darker in colour, probably due to decomposition. The NMR analysis was conducted at -78°C.

Day 1	$^{13}C\{H\}$ NMR	(d_8-THF):	δ / ppm: 72.47, 67.57 (THF), 32.81, 25.53 (THF), 2.32
Day 2	$^{13}C\{H\}$ NMR	(d_8-THF):	δ / ppm: 71.40, 67.57 (THF), 33.02, 25.79 (THF), 1.13
Day 8	$^{13}C\{H\}$ NMR	(d_8-THF):	δ / ppm: 185.51, 67.57 (THF), 60.59, 25.48 (THF)
Day 9	$^{13}C\{H\}$ NMR	(d_8-THF):	δ / ppm: 185.49, 90.80, 67.57 (THF), 45.10, 25.49 (THF), 1.39, -25.48
Day 23	$^{13}C\{H\}$ NMR	(d_8-THF):	δ / ppm: 185.49, 90.77, 67.57 (THF), 60.74, 45.05, 25.49 (THF)
Day 23 @ 30°C	$^{13}C\{H\}$ NMR	(d_8-THF):	δ / ppm: 185.41, 67.57 (THF), 31.79, 25.58 (THF)
Day 1	^{1}H NMR	(d_8-THF):	δ / ppm: 3.58 (THF), 1.72 (THF), 1.32, 0.02, 0.51
Day 2	^{1}H NMR	(d_8-THF):	δ / ppm: 11.91, 11.12, 3.58 (THF), 1.73 (THF), 1.30, 0.25, -4.00
Day 8	^{1}H NMR	(d_8-THF):	δ / ppm: 38.12, 26.30, 24.25, 14.09, 12.81, 11.99, 11.20, 10.66, 3.58 (THF), 2.23, 1.74 (THF), 0.89, 0.51, 0.41, -3.96
Day 9	^{1}H NMR	(d_8-THF):	δ / ppm: 38.22, 26.27, 11.99, 10.67, 3.58 (THF), 2.24, 1.75 (THF), 0.43, -3.95, -9.71, -11.49, -12.77
Day 23	^{1}H NMR	(d_8-THF):	δ / ppm: 37.64, 29.01, 26.63, 26.07, 11.98, 10.66, 3.58 (THF),2.24, 1.75 (THF),1.47, 1.27, 0.44, -3.94, -7.85, -9.63, -10.40, -11.42, -12.75
Day 23 @ 30°C	^{1}H NMR	(d_8-THF):	δ / ppm: 22.06, 7.88, 3.58 (THF), 3.44, 2.89, 2.79, 1.70 (THF), 1.53, -0.14 – -0.53

7.32 Reaction between K[(U(OSi(O^{t}Bu)$_3$)$_3$)$_2$($\mu-\eta^6$:η^6-tol))] and CO_2

UI_3 (0.02 g, 0.0323 mmol, 1 eq.) was added to a Young's NMR tube with Ph_3SiOK (0.0293 g, 0.0970 mmol, 3 eq.) and dissolved in d_8-THF at room temperature and left to react for one hour. The reaction was then cooled to -78°C and $^{13}CO_2$ (5.2 cm/Hg, 1 eq.) was added *via* the Toepler line. The solution showed no immediate changes. The NMR analysis was conducted at -78°C.

Day 1 $^{13}C\{H\}$ NMR (d_8-THF): δ / ppm: 67.57 (THF), 33.24, 32.77, 32.48, 31.96, 25.48 (THF)
Day 2 $^{13}C\{H\}$ NMR (d_8-THF): δ / ppm: 67.57 (THF), 33.24, 32.77, 32.48, 31.96, 25.48 (THF)
Day 7 $^{13}C\{H\}$ NMR (d_8-THF): δ / ppm: 72.77, 67.57 (THF), 32.48, 31.96, 25.48 (THF)

7.33 Reaction between K[(U(OSi(O^{t}Bu)$_3$)$_3$)$_2$($\mu-\eta^6$:η^6-tol))] and CO/H_2

UI_3 (0.02 g, 0.0323 mmol, 1 eq.) was added to a Young's NMR tube with Ph_3SiOK (0.0293 g, 0.0970 mmol, 3 eq.) and dissolved in d_8-THF at room temperature and left to react for one hour. The reaction was then cooled to -78°C and ^{13}CO

ceH2 (5.2 cm/Hg, 1 eq.) was added *via* the Toepler line. The solution showed no immediate changes. After six days the solution started to look darker in colour, probably due to decomposition. The NMR analysis was conducted at -78°C.

Day 1	$^{13}C\{H\}$ NMR	(d_8-THF):	δ / ppm: 71.28 – 71.14, 67.57 (THF), 63.61, 32.88, 28.83, 25.68 (THF), -1.60, -66.98
Day 10	$^{13}C\{H\}$ NMR	(d_8-THF):	δ / ppm: 186.41, 91.59, 68.33 (THF), 61.49, 45.84, 26.27 (THF)
Day 11	$^{13}C\{H\}$ NMR	(d_8-THF):	δ / ppm: 185.45, 72.82, 72.77, 67.57 (THF), 31.79, 25.60 (THF), 85.15
Day 1	^{1}H NMR	(d_8-THF):	δ / ppm: 11.97, 3.58 (THF), 1.74 (THF), 1.31, -0.23, -4.01
Day 10	^{1}H NMR	(d_8-THF):	δ / ppm: 11.95, 3.58 (THF), 1.74 (THF), 1.04, -0.05, -3.97

7.34 K[U(CH$_2$Ph)$_2$(OSi(O^{t}Bu)$_3$)$_3$]

UCl(OSi(O^{t}Bu)$_3$)$_3$ (0.2g, 0.188 μ mol, 1 eq.) was added to THF. A solution of $C_6H_5CH_2K$ (0.0448g, 0.376 μ mol, 2 eq.) in THF was added to the solution of UCl(OSi(O^{t}Bu)$_3$)$_3$ and the colour changed to green and then yellow. After two hours the solution was orange/brown. The solvent was removed *in vacuo* leaving a sticky orange residue. The residue was washed repeatedly in pentane and filtered to remove a white solid. The orange brown residue was then crystallised from hexane at -40°C.

Yield: 0.1498g / 61.2%

$^{13}C\{H\}$ NMR	(d_6-benzene):	δ / ppm: 129.72 (*ipso* Ph), 128.81 (*ortho* Ph), 128.61 (*meta* Ph), 162.22 (*para* Ph), 72.80 (^{t}Bu), 38.21 (^{t}Bu), 1.43 (benzyl CH_2)
^{1}H NMR	(d_6-benzene):	δ / ppm: 7.13 (d, 6H, $^3J_{HH}$ = 10 Hz, *meta* Ph), 7.07 (d, 5H, $^3J_{HH}$ = 10 Hz, *para* Ph), 6.99 (d, 7H, $^3J_{HH}$ = 5 Hz, *ortho* Ph), 1.49 (s, 4H, benzyl-CH_2), 1.97 (s, 27H, ^{t}Bu), 0.92 (s, 54H, ^{t}Bu)

7.35 U(OSi(O^{t}Bu)$_3$)$_4$ with CO$_2$

U(OSi(O^{t}Bu)$_3$)$_4$ (0.2361g, 0.183 mmol, 1 eq.) was dissolved in a minimum amount of THF. The solution was freeze, pump, thaw, degassed three times on a high vac line before

it was exposed to CO_2 (148.45 mbar in 3.054 x 10^{-5} m^3, 1 eq.). The solution turned green within 24 hours. The solution was then cooled to -40°C and large green cubic crystals crystallised. X-ray diffraction showed the product to be $U(OSi(O^tBu)_3)_4(THF)$.

7.36 $U(OSi(O^tBu)_3)_4$ and O_2

$U(OSi(O^tBu)_3)_4$ (18.3mg, 14.2 μ mol, 1 eq.) was dissolved in a minimum amount of THF. The solution was freeze, pump, thaw, degassed three times and then exposed to O_2 (14 mbar in 3.054x$10^{-5}m^3$, 1.2 eq.). The solution slowly turned grey then yellow over 3 hours. The solvent was removed *in vacuo* resulted in a yellow residue that was then washed in pentane five times. Attempts to recrystallise failed.

Yield: 0.0222g / 118.2%

^{1}H NMR (d_8-THF): δ / ppm: 2.43 (s, ^{t}Bu)

7.37 $U(\mu^2-O_2)(OSi(O^tBu)_3)_4(THF)$

$U(OSi(O^tBu)_3)_4$ (0.123g, 95.3 μ mol, 1 eq.) was dissolved in hexane. The schlenk flask was then attached to another schlenk flask *via* a fly-over bridge under a positive flow of argon. Excess I_2 crystals were added to the second schlenk and the whole systems was freeze, pump, thaw, degassed. The I_2 was then heated until it started to sublime over to the stirring blue solution of $U(OSi(O^tBu)_3)_4$. The solution turned indigo and was left for a further 20 minutes to ensure the reaction had gone to completion. The solvent and excess I_2 were removed *in vacuo* resulting in a black residue. Recrystallisation was achieved from THF at -40°C to give black plate like crystals suitable for X-ray diffraction.

$^{13}C\{H\}$ NMR	(d_6-benzene):	δ / ppm: 72.82 (^{t}Bu *cis* to THF), 72.52 (^{t}Bu *trans* to peroxo), 72.51 (^{t}Bu *trans* to THF), 72.41 ((^{t}BuO)$_3$SiOK), 32.47 (^{t}Bu *cis* to THF), 32.11 (^{t}Bu *trans* to peroxo), 31.79 (^{t}Bu *trans* to THF), 31.61 ((^{t}BuO)$_3$SiOK)
^{1}H NMR	(d_6-benzene):	δ / ppm: 2.23 (s, broad, 29H, O^{t}Bu *trans* to peroxo), 2.05 (s, 8H, bound THF), 1.73 (s, 54H, O^{t}Bu *cis* to THF), 1.66 (s, 27H, O^{t}Bu *trans* to THF), 1.39 (^{t}BuOSiOK)
^{29}Si	(d_6-benzene):	δ / ppm: -90.61 (*cis* to THF), -95.00 (*trans* to peroxo), -95.17 (*trans* to THF)

Bibliography

[1] A. R. Fox, S. C. Bart, K. Meyer and C. C. Cummins, *Nature*, 2008, **455**, 341–349.

[2] S. Cotton, *Lanthanide and Actinide Chemistry*, John Wiley and Sons, Ltd, 1st edn., 2006.

[3] A. F. Holleman and E. Wiberg, *Inorganic Chemistry*, Academic Press, 34th edn., 1995.

[4] E. Hashem, G. Lorusso, M. Evangelisto, T. McCabe, C. Schulzke, J. A. Platts and R. J. Baker, *Dalton Trans.*, 2013, 14677–14680.

[5] P. L. Arnold, *Chem. Commun.*, 2011, 9005–9010.

[6] R. R. Schrock, *PNAS*, 2006, 17087.

[7] B. A. MacKay and M. D. Fryzuk, *Chem. Rev.*, 2004, 385–401.

[8] A. Mittasch, *Friedrich Nietzsches Naturbefkissenheit*, 1950, **2**, 7–56.

[9] P. Roussel and P. Scott, *J. Am. Chem. Soc.*, 1998, **120**, 1070–1071.

[10] A. L. Odom, P. L. Arnold and C. C. Cummins, *J. Am. Chem. Soc.*, 1998, **120**, 5836–5837.

[11] I. Korobkov, S. Gambarotta and G. P. A. Yap, *Angew. Chem. Int. Ed.*, 2002, **41**, 3433–3436.

[12] F. G. N. Cloke and P. B. Hitchcock, *J. Am. Chem. Soc.*, 2002, **124**, 9352–9353.

[13] W. J. Evans, S. A. Kozimor and J. W. Ziller, *J. Am. Chem. Soc.*, 2003, **125**, 14264–14265.

[14] R. J. Martinie, J. J. Bultema, M. N. V. Wal, B. J. Burkhart, D. A. V. Griend and R. L. DeKock, *J. Chem. Educ.*, 2011, 1094–1097.

[15] S. S. Sung and R. Hoffmann, *J. Am. Chem. Soc.*, 1985, 578–584.

[16] E. J. Kuhlmann and J. J. Alexander, *Coord. Chem. Revs.*, 1980, 195–225.

[17] P. L. Arnold, Z. R. Turner, A. I. Germeroth, I. J. Casely, G. S. Nichol, R. Bellabarbad and R. P. Tooze, *Dalton Trans.*, 2013, 1333–1337.

[18] J. G. Brennan, R. A. Andersen and J. L. Robbins, *J. Am. Chem. Soc.*, 1986, **108**, 335–336.

[19] I. Castro-Rodriguez and K. Meyer, *J. Am. Chem. Soc.*, 2005, **127**, 11242–11243.

[20] O. T. Summerscales, F. G. N. Cloke and P. B. Hitchcock, *Science*, 2006, 829–831.

[21] O. T. Summerscales, F. G. N. Cloke, P. B. Hitchcock, J. C. Green and N. Hazari, *J. Am. Chem. Soc.*, 2006, 9602–9603.

[22] R. E. Cramer, R. B. Maynard, J. C. Paw and J. W. Gilje, *Organometallics*, 1982, 869–871.

[23] I. Castro-Rodriguez, H. Nakai, L. N. Z. amd A. L. Rheingold and K. Meyer, *Science*, 2004, **305**, 1757–1759.

[24] S. M. Mansell, N. Kaltsoyannis and P. L. Arnold, *J. Am. Chem. Soc.*, 2011, 9036–9051.

[25] N. Tsoureas, L. Castro, A. F. R. Kilpatrick and F. G. N. Cloke, *Chem. Sci.*, 2014, 3777–3788.

[26] C. Coperet, M. Chabanas, R. P. Saint-Arroman and J. M. Basset, *Angew. Chem. Int. Ed.*, 2003, 156–181.

[27] V. Chandrasekhar, R. Boomishankar and S. Nagendran, *Chem. Rev.*, 2004, 5847–5910.

[28] R. T. Sanderson, *J. Inorg. Nucl. Chem.*, 1968, 375–393.

[29] *Michigan State University, Department of Chemistry*, 2014.

[30] A. E. Reed and P. R. Schleyer, *J. Am. Chem. Soc.*, 1990, 1434–1445.

[31] F. Weinhold and R. West, *Organometallics*, 2011, 5815–5824.

[32] D. W. J. Cruickshank, *J. Chem. Soc. (Resumed)*, 1961, 5486–5504.

[33] H. Oberhammer and J. E. Boggs, *J. Am. Chem. Soc.*, 1980, 7241–7244.

[34] P. T. Wolczanski, *Polyhedron*, 1995, 3335–3362.

[35] F. G. A. Stone and D. Seyferth, *J. Inorg. Nuc. Chem.*, 1955, 112–118.

[36] R. West and R. H. Baney, *J. Am. Chem. Soc.*, 1959, 6145–6148.

[37] H. A. Bent, *Chem. Rev.*, 1960, 275–311.

[38] V. Vidal, A. Theolier, J. Thivolle-Cazat and J. M. Basset, *Science*, 1997, **276**, 99–102.

[39] J. M. Basset, C. Coperet, L. Lefort, B. M. Maunders, O. Maury, E. LeRoux, G. Saggio, S. Soignier, D. Soulivong, G. J. Sunley, M. Taoufik and J. Thivolle-Cazat, *J. Am. Chem. Soc.*, 2005, **127**, 8604–8605.

[40] J. M. Basset, C. Coperet, D. Soulivong, M. Taoufik and J. Thivolle-Cazat, *Acc. Chem. Res.*, 2010, **43**, 323–334.

[41] R. R. Schrock and J. D. Fellmann, *J. Am. Chem. Soc.*, 1978, **100**, 3359–3370.

[42] V. Dufaud, G. P. Niccolai, J. Thivolle-Cazat and J. M. Basset, *J. Am. Chem. Soc.*, 1995, **117**, 4288–4294.

[43] V. Vidal, A. Theolier, J. Thivolle-Cazat, J. M. Basset and J. Corker, *J. Am. Chem. Soc.*, 1996, **118**, 4595–4602.

[44] F. Quignard, A. Choplin and J. M. Basset, *Chem. Commun.*, 1991, 1589–1590.

[45] C. Thieuleux, E. A. Quadrelli, J. M. Basset, J. Dobler and J. Sauer, *Chem. Commun.*, 2004, 1729–1731.

[46] F. J. Feher and T. A. Budzichowski, *Polyhedron*, 1995, **14**, 3239–3253.

[47] F. J. Feher, *J. Am. Chem. Soc.*, 1986, **108**, 3850–3852.

[48] F. J. Feher and J. F. Walzer, *Inorg. Chem.*, 1991, **30**, 1689–1694.

[49] F. J. Feher, J. F. Walzer and R. L. Blanski, *J. Am. Chem. Soc.*, 1991, **113**, 3618–3619.

[50] F. J. Feher and R. L. Blanski, *J. Am. Chem. Soc.*, 1992, **114**, 5886–5887.

[51] M. J. McGeary, P. S. Coan, K. Folting, W. E. Strieb and K. G. Caulton, *Inorg. Chem.*, 1991, 1723–1735.

[52] W. J. Evans, R. E. Golden and J. W. Ziller, *Inorg. Chem.*, 1991, 4963–4968.

[53] P. S. Gradeff and K. Yunlu, *Polyhedron*, 1989, 1001–1005.

[54] P. S. Gradeff, K. Yunlu, T. J. D. anf J. M. Olofson, R. J. Doedens and W. J. Evans, *Inorg. Chem.*, 1990, 420–424.

[55] Z. Xie, K. Chui, Q. Yang, T. C. W. Mak and J. Sun, *Organometallics*, 1998, 3937–3944.

[56] M. Nishiura, Z. Hou and Y. Watatsuki, *Organometallics*, 2004, 1359–1368.

[57] T. J. Boyle, S. D. Bunge, P. G. Clem, J. Richardson, J. T. Dawley, L. A. M. Ottley, M. A. Rodriguez, B. A. Tuttle, G. R. Avilucea and R. G. Tissot, *Inorg. Chem.*, 2005, 1588–1600.

[58] F. Lacroix, C. E. Plecnik, S. Liu, F. C. Liu, E. A. Meyers and S. G. Shore, *J. Organomet. Chem.*, 2003, 69–77.

[59] J. J. Carbo, O. G. del Moral, A. Martin, M. Mena, J. M. Poblet and C. Santamaria, *Chem. Eur. J.*, 2008, 7930–7938.

[60] R. Duchateau, U. Cremer, R. J. Harmsen, S. I. Mohamud, H. C. L. Abbenhuis, R. A. V. Santen, A. Meetsma, S. K. H. Thiele, M. F. H. VanTol and M. Kranenburg, *Organometallics*, 1999, 5447–5459.

[61] V. Varga, I. Cisarova, R. Gyepes, M. Horacek, J. Kubista and K. Mach, *Organometallics*, 2009, 1748–1757.

[62] P. Sobota, S. Przybylak, J. Ejfler, M. Kobylka and L. B. Jerzykiewicz, *Inorg. Chim. Acta*, 2002, 159–164.

[63] B. Schweder, H. Gorls and D. Walther, *Inorg. Chim. Acta*, 1999, 14–23.

[64] B. F. G. Johnson, M. C. Klunduk, C. M. Martin, G. Sankar, S. J. Teate and J. M. Thomas, *J. Organomet. Chem.*, 2000, 221–225.

[65] W. Darwish, S. Schlecht, A. Schaper, M. Froba, K. Harms, W. Massa and J. Sundermeyer, *Z. Anorg. Allg. Chem.*, 2009, 1215–1224.

[66] T. J. Boyle, R. M. Sewell, L. A. M. Ottley, H. D. Pratt, C. J. Quintana and S. D. Bunge, *Inorg. Chem.*, 2007, 1825–1835.

[67] W. M. P. B. Menge and J. G. Verkade, *Inorg. Chem.*, 1991, 4628–4631.

[68] A. Glöckner, C. G. Daniliuc, M. Freytag, P. G. Jones and M. Tamm, *Chem. Commun.*, 2012, 6598–6600.

[69] B. Schweder, D. Walther and W. Imhof, *Acta. Cryst.*, 2006, m465–m468.

[70] E. A. Babaian, D. C. Hrncir, S. G. Bolt and J. L. Atwood, *Inorg. Chem.*, 1986, 4818–4821.

[71] A. Fischbach, M. G. Klimpel, M. Widenmeyer, E. Herdtweck, W. Scherer and R. Andwander, *Angew. Chem. Int. Ed.*, 2004, 2234–2239.

[72] M. Zimmermann, N. A. Froystein, A. Fischbach, P. Sirsch, H. M. Dietrich, K. W. Tornroos, E. Herdtweck and R. Anwander, *Chem. Eur. J.*, 2007, 8784–8800.

[73] E. LeRoux, Y. Liang, K. W. Tornroos, F. Nief and R. Anwander, *Organometallics*, 2012, 6526–6537.

[74] E. LeRoux, O. Michel, H. M. Sommerfeldt, Y. Liang, C. Maichle-Mossmer, K. W. Tornroos and R. Anwander, *Dalton Trans.*, 2010, 8552–8559.

[75] V. Dhayal, A. Chaudhary, B. L. Choudhary, M. Nagar, R. Bohra, S. M. Mobin and P. Mathur, *Dalton Trans.*, 2012, 9439–9450.

[76] K. W. Terry, C. G. Lugmair and T. D. Tilley, *J. Am. Chem. Soc.*, 1997, 9745–9756.

[77] C. G. Lugmair and T. D. Tilley, *Inorg. Chem.*, 1998, 764–769.

[78] C. A. Tolman, *Chem. Rev.*, 1977, 313–348.

[79] E. M. Dexheimer, L. Spialter and L. D. Smithson, *J. Organomet. Chem.*, 1975, 21–27.

[80] J. Pankhurst, *Model compounds of uranium and the activation of small molecules*, M.Chem. Thesis, University of Sussex, 2013.

[81] M. Ansell, *Summer Student, Project Work*, University of Sussex, 2011.

[82] *Spectral Database for Organic Compounds*, 2013, `http://sdbs.riodb.aist.go.jp/sdbs/cgi-bin/cre_index.cgi`.

[83] H. Puff, K. Braun and H. Reuter, *J. Organomet. Chem.*, 1991, 119–129.

[84] K. F. Bowes, C. Glidewella and J. N. Low, *Acta Cryst.*, 2002, 409–415.

[85] I. R. Thomas, I. J. Bruno, J. C. Cole, C. F. Macrae, E. Pidcock and P. A. Wood, *J. Appl. Cryst.,*, 2010, **43**, 362–366.

[86] A. E. Aliev, C. E. Atkinson and K. D. M. Harris, *J. Phys. Chem. B*, 2002, **106**, 9013–9018.

[87] J. Beckmann, D. Dakternieks, A. Duthie, M. Larchin and E. R. T. Tiekink, *Appl. Organomet. Chem.*, 2003, 52–62.

[88] M. M. Amini, G. Mohammadnezhada, M. Mirzaeeb and H. R. Khavasi, *Appl. Organometal. Chem.*, 2010, **24**, 431–438.

[89] M. J. McGeary, K. Folting, W. E. Streib, J. C. Huffman and K. G. Caulton, *Polyhedron*, 1991, 2699–2709.

[90] C. Camp, J. Pecaut and M. Mazzanti, *J. Am. Chem. Soc.*, 2013, 12101–12111.

[91] M. Porchia, N. Brianese, U. Casellato, F. Ossola, G. Rossetto, P. Zanella and R. Graziani, *J. Chem. Soc. Dalton Trans.*, 1989, 677–682.

[92] D. D. Schnaars, G. Wu and T. W. Hayton, *Inorg. Chem.*, 2011, 4695–4697.

[93] R. G. Denning, *Electronic structure and bonding in actinyl ions*, Springer Berlin Heidelberg, 2012, pp. 215–276.

[94] E. O'Grady and N. Kaltsoyannis, *J. Chem. Soc., Dalton Trans.*, 2002, 1233–1239.

[95] R. G. Denning, *J. Phs. Chem. A*, 2007, 4125–4143.

[96] H. Chermette, K. Rachedi and F. Volatron, *J. Molecular Structure*, 2006, 109–121.

[97] K. C. Jantunen, F. Haftbaradaran, M. J. Katz, R. J. Batchelor, G. Schatte and D. B. Leznoff, *Dalton Trans.*, 2005, 3083–3091.

[98] M. Sharma, M. Botoshansky, T. Bannenberg, M. Tamm and M. S. Eisen, *C. R. Chimie*, 2010, 767–774.

[99] L. A. Seaman, P. Hrobarik, M. F. Schettini, S. Fortier, M. Kaupp and T. W. Hayton, *Angew. Chem. Int. Ed.*, 2013, 3259–3263.

[100] L. A. Seaman, D. D. Schnaars, G. Wu and T. W. Hayton, *Dalton Trans.*, 2010, 6635–6637.

[101] M. F. Schettini, G. Wu and T. W. Hayton, *Chem. Commun.*, 2012, 1484–1486.

[102] C. Camp, O. Cooper, J. Andrez, J. Pecaut and M. Mazzanti, *Dalton Trans.*, 2015, 2650–2656.

[103] C. Pariya and K. H. Theopold, *Current Science*, 2000, 1345–1351.

[104] O. P. Lam, S. M. Franke, H. Nakai, F. W. Heinemann, W. Hieringer and K. Meyer, *Inorg. Chem.*, 2012, 6190–6199.

[105] R. Krentz and R. K. Pomeroy, *Inorg. Chem.*, 1985, 2976–2980.

[106] J. Blixt, B. Gyori and J. Glaser, *J. Am. Chem. Soc.*, 1989, 7784–7791.

[107] E. V. Gauchenova, S. S. Karlov, A. A. Selina, E. S. Chernyshova, A. V. Churakov, J. A. K. Howard, N. A. Troitsky, S. N. Tandura, J. Lorberth and G. S. Zaitseva, *J. Organomet. Chem.*, 2003, 8–21.

[108] S. S. Karlov, P. L. Shutov, N. G. Akhmedov, M. A. Seip, J. Lorberth and G. S. Zaitseva, *J. Organomet. Chem.*, 2000, 387–394.

[109] R. R. Conry and J. M. Mayer, *Organometallics*, 1993, 3179–3186.

[110] A. S. P. Frey, F. G. N. Cloke, M. P. Coles, L. Maron and T. Davin, *Angew. Chem. Int. Ed.*, 2011, 6881–6883.

[111] K. R. Reddy, M. C. Matelich, B. G. Ugarkar, J. E. Gomez-Galeno, J. DaRe, K. Ollis, Z. Sun, W. Craigo, T. J. Colby, J. M. Fujitaki, S. H. Boyer, P. D. vanPoelje and M. D. Erion, *J. Med. Chem.*, 2008, 666–676.

[112] J. S. Hrkach and K. Matyjaszewski, *Macromolecules*, 1990, 4042–4046.

[113] J. F. C. Turner, *F1024: Chemistry of the Non-transition elements*, 2013.

[114] K. T. Moore and G. van der Laan, *Rev. Mod. Phys.*, 2009, **81**, 235–298.

[115] N. Kaltsoyannis and P. Scott, *The f Elements*, Oxford Science Publications, 1st edn., 2007.

[116] M. Hirose and C. Miyake, *Inorg. Chim. Acta*, 1988, 293–296.

[117] M. Karbowiak, A. Mech and J. Drozdzynski, *Chem. Phys.*, 2005, 135–145.

[118] E. Hashem, A. N. Swinburne, C. Schulzke, R. C. Evans, J. A. Platts, A. Kerridge, L. S. Natrajan and R. J. Baker, *RSC Adv.*, 2013, 4350–4361.

[119] Z. Barandiaran and L. Seijo, *J. Chem. Phys.*, 2003, 7439–7456.

[120] D. E. Morris, R. E. DaRe, K. C. Jantunen, I. Castro-Rodriguez and J. L. Kiplinger, *Organometallics*, 2004, 5142–5133.

[121] P. Pyykko and Y. Zhao, *Inorg. Chem.*, 1991, 3787–3788.

[122] M. Pepper and B. E. Bursten, *Chem. Rev.*, 1991, 719–741.

[123] F. Ruiperez and U. Wahlgren, *J. Phys. Chem.*, 2010, 3615–3621.

[124] M. Atoji and M. J. McDermott, *Acta. Cryst.*, 1970, **B26**, 1540–1544.

[125] M. P. Wilkerson, C. J. Burns, R. T. Paine and B. L. Scott, *Inorg. Chem.*, 1999, **38**, 4156–4158.

[126] J. C. Berthet, M. Nierlich and M. Ephritikhine, *Chem. Commun.*, 2004, 870–871.

[127] D. P. Armstrong, W. D. Bostick and W. H. Fletcher, *Appl. Spectrosc.*, 1991, 1008–1016.

[128] J. F. deWet and J. G. H. duPreez, *J. Chem. Soc., Dalton Trans.*, 1978, 592–597.

[129] G. Liu, N. P. Deifel, C. L. Cahill, V. V. Zhurov and A. A. Pinkerton, *J. Phys. Chem.*, 2012, 855–864.

[130] M. J. Crawford, A. Ellern, K. Karaghiosoff, P. Mayer, H. Noth and M. Suter, *Inorg. Chem.*, 2004, 7120–7126.

[131] P. W. Wilson, *J. Chem. Soc., Chem. Commun.*, 1972, 1241.

[132] R. T. Paine, R. R. Ryan and L. B. Asprey, *Inorg. Chem.*, 1975, **14**, year.

[133] K. W. Bagnall and J. G. H. duPreez, *J. Chem. Soc., Chem. Commun.*, 1973, **0**, 820–821.

[134] D. R. Brown, R. G. Denning and R. H. Jones, *J. Chem. Soc., Chem. Commun.*, 1994, **22**, 2601.

[135] V. C. Williams, M. Muller, M. A. Leech, R. G. Denning and M. L. H. Green, *Inorg. Chem.*, 2000, **39**, 2538–2541.

[136] P. B. Duval, C. J. Burns, W. E. Buschmann, D. L. Clark, D. E. Morris and B. L. Scott, *Inorg. Chem.*, 2001, **40**, 5491–5496.

[137] S. J. Kraft, J. Walensky, P. E. Fanwick, M. B. Hall and S. C. Bart, *Inorg. Chem.*, 2010, **49**, 7620–7622.

[138] G. Zi, L. Jia, E. L. Werkema, M. D. Walter, J. P. Gottfriedsen and R. A. Andersen, *Organometallics*, 2005, **24**, 4251–4264.

[139] W. J. Evans, S. A. Kozimor and J. W. Ziller, *Polyhedron*, 2004, **23**, 2689–2694.

[140] D. S. Arney and C. J. Burns, *J. Am. Chem. Soc.*, 1993, **115**, 9840–9841.

[141] P. Roussel, R. Boaretto, A. J. Kingsley, N. W. Alcock and P. Scott, *J. Chem. Soc., Dalton. Trans.*, 2002, **7**, 1423–1428.

[142] T. W. Hayton, J. M. Boncella, B. L. Scott and E. R. Batista, *J. Am. Chem Soc.*, 2006, **128**, 12622–12623.

[143] S. Fortier, N. Kaltsoyannis, G. Wu and T. W. Hayton, *J. Am. Chem. Soc.*, 2011, **133**, 14224–14228.

[144] D. P. Mills, O. J. Cooper, F. Tuna, E. J. L. McInnes, E. S. Davies, J. McMaster, F. Moro, W. Lewis, A. J. Blake and S. T. Liddle, *J. Am. Chem. Soc.*, 2012, **134**, 10047–10057.

[145] D. S. Arney and C. J. Burns, *J. Am. Chem. Soc.*, 1995, **117**, 9448–9460.

[146] S. C. Bart, C. Anthon, F. W. Heinemann, E. Bill, N. M. Edelstein and K. Meyer, *J. Am. Chem. Soc.*, 2008, **130**, 12536–12546.

[147] K. Nakamoto, *Infrared spectra of inorganic and coordination compounds*, Wiley Interscience, 2nd edn., 1970.

[148] J. G. Kim, Y. S. Park, Y. K. Ha and K. Song, *J. Nuclear Science and Technology*, 2009, 1188–1192.

[149] G. S. Groenwold, A. K. Gianotto, M. E. McIlwain, M. J. V. Stipdonk, M. Kullman, D. T. Moore, N. Polfer, J. Oomens, I. Infante, L. Visscher, B. Siboulet and W. A. DeJong, *J. Phys. Chem.*, 2008, 508–521.

[150] D. W. Green, G. T. Reedy and S. D. Gabelnick, *J. Chem. Phys.*, 1980, 4207–4216.

[151] B. Kosog, H. S. LaPierre, F. W. Heinemann, S. T. Liddle and K. Meyer, *J. Am. Chem. Soc.*, 2012, 5284–5289.

[152] H. S. LaPierre and K. Meyer, *Inorg. Chem.*, 2013, 529–539.

[153] A. J. Lewis, K. C. Mullane, E. Nakamaru-Ogiso, P. J. Carroll and E. J. Schelter, *Inorg. Chem.*, 2014, 6944–6953.

[154] W. B. Tolman, *Acc. Chem. Res.*, 1997, 227–237.

[155] J. W. Egan, B. S. Haggerty, A. L. Rheingold, S. C. Sendlinger and K. H. Theopold, *J. Am. Chem. Soc.*, 1990, 2445–2446.

[156] O. M. Reinaud, G. P. A. Yap, A. L. Rheingold and K. H. Theopold, *Angew. Chem. Int. Ed. Engl.*, 1995, 2051–2052.

[157] A. Hess, M. R. Horz, L. M. Liable-Sands, D. C. Lindner, A. L. Rheingold and K. H. Theopold, *Angew. Chem. Int. Ed.*, 1999, 166–168.

[158] K. Qin, C. D. Incarvito, A. L. Rheingold and K. H. Theopold, *Angew. Chem. Int. Ed.*, 2002, 2439–2441.

[159] M. T. Kieber-Emmons and C. G. Riordan, *Acc. Chem. Res.*, 2007, 618–625.

[160] S. J. Blanksby and G. B. Ellison, *Acc.Chem. Res.*, 2003, **36**, 255–263.

[161] V. A. Zeitler and C. A. Brown, *J. Am. Chem. Soc.*, 1957, 4618–4621.

[162] V. Mougel, C. Camp, J. Pecaut, C. Coperet, L. Maron, C. E. Kefalidis and M. Mazzanti, *Angew. Chem. Int. Ed.*, 2012, 1–6.

[163] C. Camp, V. Mougel, J. Pecaut, L. Maron and M. Mazzanti, *Chem. Eur. J.*, 2013, 17528–17540.

[164] O. Cooper, C. Camp, J. Pecaut, C. E. Kefalidis, L. Maron, S. Gambarelli and M. Mazzanti, *J. Am. Chem. Soc.*, 2014, 6716–6723.

[165] B. Marciniec and H. Maciejewski, *Coord. Chem. Rev.*, 2001, 301–335.

[166] C. Krempner, *Microreview*, 2011, 1689–1698.

[167] M. A. Halcrow, *Chem. Soc. Rev.*, 2013, 1784–1795.

[168] K. M. Keller, *Ph.D. thesis*, University of Sussex, 2012.

[169] P. J. C. Green, *Personal communication to Dr. J.F.C. Turner*, 2012.

[170] L. Perrin, L. Maron and O. Eisenstein, *Faraday Discuss.*, 2003, 25–39.

[171] L. Perrin, L. Maron, O. Eisenstein and M. Lappert, *New J. Chem.*, 2003, 121–127.

[172] P. L. Arnold and S. M. Mansell, *Nature Chemistry*, 2012, 668–674.

[173] W. J. Evans, S. A. Kozimor, J. W. Ziller and N. Kaltsoyannis, *J. Am. Chem. Soc.*, 2004, 14533–14547.

[174] P. L. Diaconescu, P. L. Arnold, T. A. Baker, D. J. Mindiola and C. C. Cummins, *J. Am. Chem. Soc.*, 2000, 6108–6109.

[175] B. Vlaisavljevich, P. L. Diaconescu, W. Lukens, L. Gagliardi and C. Cummins, *Organometallics*, 2013, 1341–1352.

[176] P. L. Diaconescu and C. C. Cummins, *J. Am. Chem. Soc.*, 2002, 7660–7661.

[177] P. L. Diaconescu and C. C. Cummins, *Inorg. Chem.*, 2012, 2902–2916.

[178] T. Arliguie, M. Lance, M. Nierlich and M. Ephritikhine, *J. Chem. Soc., Dalton Trans.*, 1997, 2501–2504.

[179] S. T. Liddle, *Coord. Chem. Revs.*, 2015, 211–227.

[180] M. L. H. Green, *J. Organomet. Chem.*, 1995, 127–148.

[181] M. L. H. Green and G. Parkin, *J. Chem. Educ.*, 2014, 807–816.

[182] P. Day, N. Hush and R. Clark, *Phil. Trans. R. Soc. A*, 2008, 5–14.

[183] B. Brunschwig, C. Creutz and N. Sutin, *Chem. Soc. Rev.*, 2002, 168–184.

[184] M. Parthey, J. B. G. Gluyas, M. A. Fox, P. J. Low and M. Kaupp, *Chem. Eur. J.*, 2014, 6895–6908.

[185] G. A. Olah, A. Goeppert and G. K. S. Prakash, *J. Org. Chem.*, 2009, 487–498.

[186] W. Sattler and G. Parkin, *J. Am. Chem. Soc.*, 2012, 17462–17465.

[187] M. Ephritikhine, *Dalton Trans.*, 2006, 2501–2516.

[188] S. A. Johnson, J. J. Kiernicki, P. E. Fanwick and S. C. Bart, *Organometallics*, 2015, 2889–2895.

[189] N. N. Greenwood and A. Earnshaw, *Chemistry of the Elements*, Elsevier Butterworth Heinemann, 2nd edn., 2010.

[190] J. F. Hyde, O. K. Johannson, W. H. Daudt, R. F. Fleming, H. B. Laudenslager and M. P. Roche, *J. Am. Chem. Soc.*, 1953, 5615–5618.

[191] J. A. Hermann and J. F. Suttle, *Inorg. Synthesis*, 1957, **5**, 143–145.

[192] D. L. Gray, L. A. Backus, H. Hans-Albrecht, S. Skanthakumar, A. Loidl, L. Soderholm and J. A. Ibers, *Inorg. Chem.*, 2007, **46**, 6992–6996.

[193] M. J. Monreal, R. K. Thomson, T. Cantat, N. E. Travia, B. L. Scott and J. L. Kiplinger, *Organometallics*, 2011, 2031–2038.

[194] *ASTM G173 - 03 "Standard Tables for Reference Solar Spectral Irradiances: Direct Normal and Hemispherical on 37° Tilted Surface"*, ASTM international, West Conshohocken, PA, USA technical report, 2012.

[195] G. Myhre, E. J. Highwood, K. P. Shine and F. Stordal, *Geophys. Res. Lett.*, 1998, **25**, 2715–2718.

[196] M. J. Elrod, *J Chem. Educ.*, 1999, **76**, 1702.

[197] A. C. Hong, C. J. Young, M. D. Hurley, T. J. Wallington and S. A. Mabury, *Geophys. Res. Lett.*, 2013, **40**, 6010–6015.

[198] IPCC, *Climate Change 2013 - The Physical Science Basis: Working Group I Contribution to the Fifth Assessment Report of the Intergovernmental Panel on Climate Change*, Cambridge University Press, 2014.

[199] IPCC, *Climate Change 2007 - The Physical Science Basis: Working Group I Contribution to the Fourth Assessment Report of the IPCC*, Cambridge University Press, 2007.

[200] *Overview of Greenhouse Gases*, 2014, `http:/www.epa.gov/climatechange/ghgemissions/gases.html`.

[201] *Carbon Dioxide Information Analysis Centre*, 2013, `http://cdiac.ornl.gov`.

[202] P. T. (NOAA/ESRL) and R. K. S. I. on Oceanography), *Mauna Loa CO2 Annual Mean Data*, 2013, www.esrl.noaa.gov/gmd/ccgg/trends.

[203] G. Marland and R. M. Rotty, *Tellus Series B-Chemical and Physical Meteorology*, 1984, **36**, 232–261.

[204] J. Tollefson, *Nature*, 2013, 321–322.

[205] J. E. Hansen, R. Ruedy, M. Sato, K. and Lo, *Global Annual Temperature Anomalies (Land + Ocean) 1880-2010*, CDIAC, 2011, www.cdiac.ornl.gov.

[206] *The New Climate Dice: Public Perception of Climate Change*, 2012, http://www.giss.nasa.gov/research/briefs/hansen_17/.

[207] R. L. Hirsch, R. Bezdek and R. Wendling, *Peaking of World Oil Production: Impacts, Mitigation and Risk Management*, Nova Science Publishers Inc, 2006.

[208] *International Energy Statistics*, 2013, http://www.eia.gov/cfapps/ipdbproject/IEDIndex3.cfm?tid=44&pid=44&aid=2.

[209] R. W. Bentley, *Energy Policy*, 2002, **30**, 189–205.

[210] R. W. Bentley, S. A. Mannan and S. J. Wheeler, *Energy Policy*, 2007, **35**, 6364–6382.

[211] N. A. Owen, O. R. Inderwildi and D. A. King, *Energy Policy*, 2010, **38**, 4743–4749.

[212] G. C. Watkins, *Energy Policy*, 2006, **34**, 508–514.

[213] D. S. Jenkinson, *Plant and Soil*, 2001, **228**, 3–15.

Appendix A

The Global Picture

A.1 The nature of greenhouse gases

An upward trend in global temperatures is now generally accepted as fact and is the current position of the scientific consensus. A major factor in this is the alteration of the atmospheric composition through the unrestrained release of CO_2 and other small molecules, which, when coupled with the incident solar radiation and terrestrial radiation from reflection, causes a change in the radiation balance of the Earth and therefore heating of the atmosphere. Such gases are known as 'greenhouse gases' (GHG).

The term 'greenhouse gas' covers a number of industrially and agriculturally important small molecules that include CO_2, CH_4, N_2O and fluorinated gases. The effect of each gas on the climate is determined by three main factors:

- The concentration of the gas
- The kinetics of gas formation and destruction of the gas resulting in an atmospheric residence time

· The fundamental interaction of the molecule with radiation

A.2 The atmospheric radiation field

The sun has a surface temperature of approximately 5800 K. Although the sun is not a black body, as it is thermodynamically open, its spectrum approximates to a black body or Planck radiator. The theoretical frequency spectrum for a Planck radiator is given by:

$$I_\nu(T) = \frac{2h\nu^3}{c^2\left[\exp\left(\frac{h\nu}{k_B T}\right) - 1\right]} \tag{A.2.1}$$

where k_B is Boltzmann's constant, T is the absolute temperature, c is the speed of light and ν is the frequency. An alternative expression in terms of the wavelength of the radiation is given by:

$$I_\lambda(T) = \frac{2hc^2}{\lambda^5\left[\exp\left(\frac{hc}{\lambda k_B T}\right) - 1\right]} \tag{A.2.2}$$

Equation A.2.2 is plotted in Figure A.1 together with the ASTM standard solar spectrum.[194]

Absorbtion by atmospheric components substantially alters the radiation incident on the surface, as shown in Figure A.2. The upper trace shows the spectrum incident at the top of the atmosphere (I. I.), the middle trace shows the solar spectrum incident at the earth's surface (S. I.) after modification by passage through the atmosphere and the lower trace (ΔI) shows the difference between the two and therefore the modification of the solar incident spectrum, primarily by near infrared absorbtions by H_2O and CO_2.

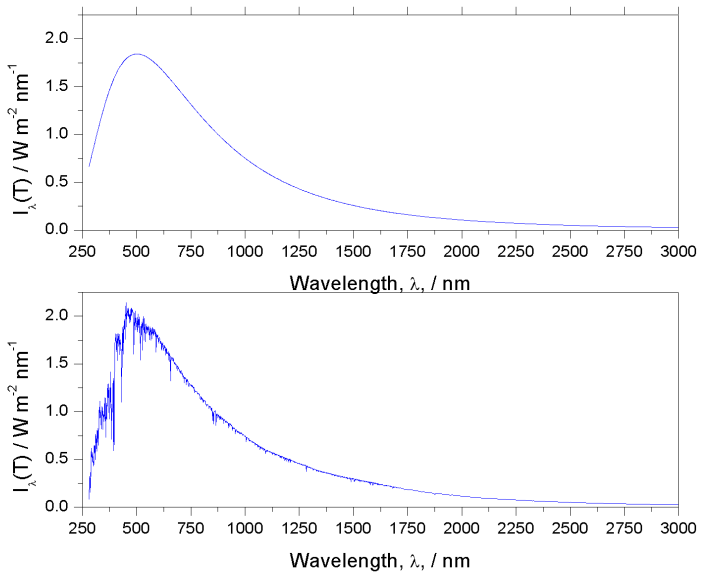

Figure A.1: A comparison between the ASTM solar spectrum (bottom) and Equation A.2.2 with $T = 5,777$ K (top); values for Equation A.2.2 have been scaled to match the the ASTM G173 normalisation.

Coupling of GHG's to the incoming radiation is the first part of energy transfer into the atmosphere and is broadly governed by the vibrational selection rule in infrared spectroscopy: that the vibration must have the same character as the dipole operators in the point group of the molecule. Thus it is important to note that no homodiatomic molecule can couple to electromagnetic radiation and there is no relaxation via photon emission available for compounds such as N_2 or O_2.

At the surface of the earth, the incident solar radiation is largely absorbed, with some being scattered. The absorbed fraction is then dissipated as heat, which is reradiated at the characteristic temperature of the earth's surface. On average over the whole surface, this temperature is 288 K. There is also a substantial quantity of heat from radioactive decay. The shift in wavelength incident solar spectrum and the reradiated spectrum is shown in Figure A.3, which does not reproduce absolute integrated intensities of the fluxes involved and are calculated from idealised Planck radiators.

Given that 10,000 nm = 1,000 cm^{-1}, then the reradiation of the solar spectrum occurs in

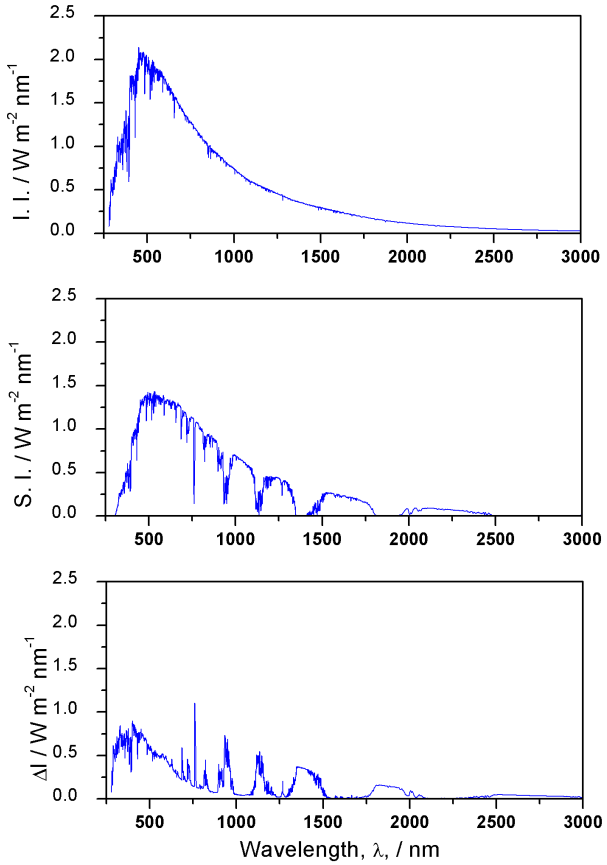

Figure A.2: Atmospheric absorbtion and its effect on the solar spectrum incident at the surface: the upper trace shows the incident solar spectrum, the middle trace, the incident solar spectrum at the surface and the lower trace, the difference ΔI = I. I. − S. I.

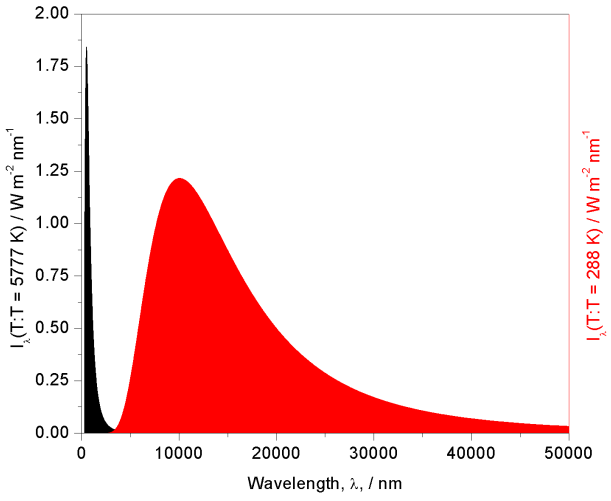

Figure A.3: Calculated Planck radiator spectrum that represent the incident radiation (black, T = 5777 K) and the reradiated thermal radiation from the earth's surface (red, T = 288 K). Absolute integrated intensities are not reproduced.

the infrared region, making the infrared properties of a GHG critical in the photophysics of global warming.

A.3 The Global Warming Potential

For practical purposes, a measure of the effect on the global temperature for each GHG, and particularly its concentration, is desirable. This is termed the 'Global Warming Potential' (GWP) and contains each these three main factors. The potential is also a relative measure and values are quoted referenced to CO_2, given the importance and dominance of the greenhouse gas burden of CO_2. Using kinetic data for the removal of GHG, a time-dependance can also be determined and the GWP is normally quoted over a given period of time.[195,196]

For any single gas, the energy absorbed per molecule, which is the integrated intensity of its infrared spectrum and is the absorbtion cross–section for the molecule, yields an equation for the radiative forcing, ρ, of the form:

$$\rho = \Sigma_i \sigma_i f_i \tag{A.3.1}$$

where *i* represents the frequency band, σ_i the absorption cross–section in that band and f_i the natural reradiated spectrum within that band.

The radiative forcing for a greenhouse gas, γ, is then given by:

$$\gamma = N\rho \cdot \int \exp\left(-\frac{t}{\tau}\right) dt \tag{A.3.2}$$

where N is a measure of concentration and τ is the average life time of the gas in the atmosphere. The quoted values for the GWP, Γ, are given in ratio to that for CO_2 and therefore the GWP for a greenhouse gas is given by:

$$\Gamma\,(\mathrm{GHG}) = \frac{\int_0^t \gamma\,(\mathrm{GHG}\,)\;dt}{\int_0^t \gamma\,(\mathrm{CO_2})\;dt} \tag{A.3.3}$$

Several issues arise with this expression. It depends both on the cross–section of the gas and of that of CO_2; it also depends on the life–time of the gas in the atmosphere as well and if this is longer than that of CO_2, such as for $N(C_4F_9)_3$[197], then the GWP can be very significant over a long period of time. Standard values for Γ are quoted for 1 kg of gas in comparison to 1 kg of CO_2 and data are widely available; all data quoted here are taken from the International Panel on Climate Change (IPCC) reports for 2013 and 2007.[198,199] Table A.1 presents constants from the IPCC 2007 report for use in GWP calculations. Given the dominance of CO_2 by mole fraction in the total atmospheric greenhouse gas burden, its lifetime is parametrised as shown in Table A.1 with $a_0 = 0.217$, $a_1 = 0.259$, $a_2 = 0.338$, $a_3 = 0.186$, $\tau_1 = 172.9$ years, $\tau_2 = 18.51$ years, and $\tau_3 = 1.186$ years.

Compound	τ / years	ρ / W m^{-2} ppb^{-1}
CO_2	$\tau\,(CO_2) = a_0 + \sum_{i=1}^{3} a_i \exp\left(-\frac{t}{\tau_i}\right)$	1.4×10^{-5}
CH_4	12	3.7×10^{-4}
N_2O	114	3.03×10^{-3}
CCl_2F_2	100	0.32
CCl_4	26	0.13
CH_3Br	0.7	0.01
CHF_3	270	0.19
SF_6	3,200	0.52

Table A.1: Values of τ and ρ for selected greenhouse gases for γ calculations[199]

Graphs of γ illustrate the impact of each gas on the atmosphere. The most important greenhouse gases that have an anthropogenic source are CO_2, CH_4 and N_2O. The individual γ-graphs are shown in Figure A.4

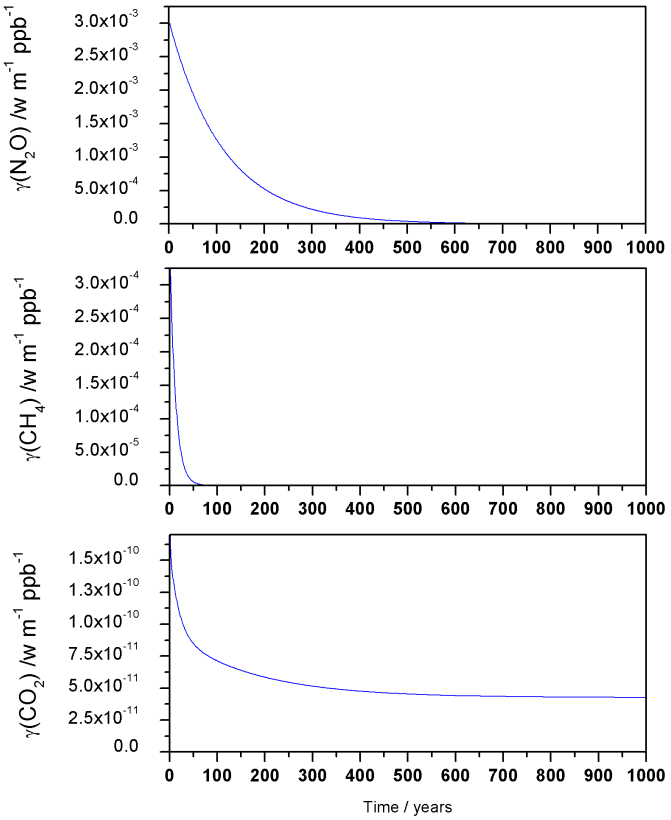

Figure A.4: Radiative forcing values for CO_2, CH_4 and N_2O over 1000 year timescale. Note that $\gamma(CO_2)$ does not reach zero due to its natural occurrence

Figure A.5 illustrates the GWP as a factor of time and it becomes clear that whilst CO_2 is not the most potent greenhouse gas on an absolute, molecular level, in terms of timescales CO_2 is a major contributor to the greenhouse gas atmospheric burden.[200]

Figure A.6 shows the hydrooxygenate greenhouse gases and their relative strengths versus their most commonly found oxidation state and clearly shows the inert nature of CO_2. The energy of formation is much more negative than any of the other hydrooxygenates indicating the molecule is incredibly stable and therefore unlikely to be amenable to further reactions.

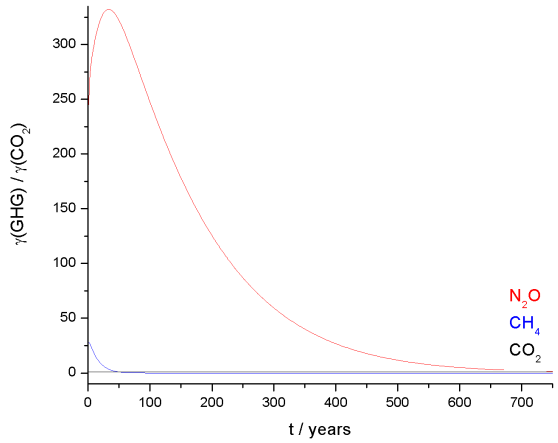

Figure A.5: Relative global warming potentials for N_2O and CH_4, with CO_2 also shown, to emphasise the relative nature of the measure

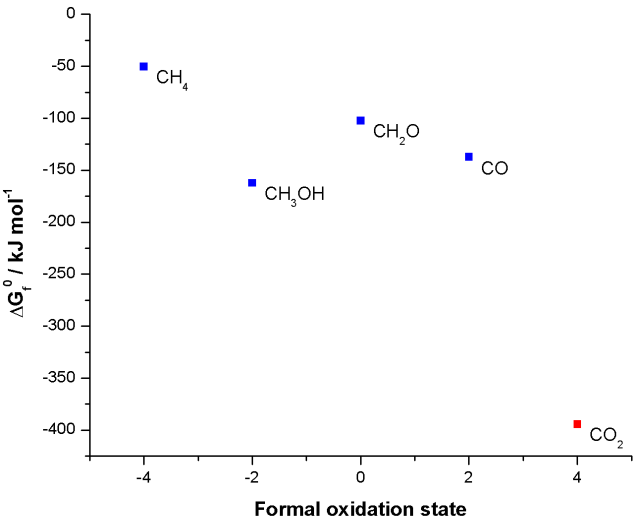

Figure A.6: Relative strengths of hydrooxygenates

Furthermore and of critical importance, the emissions of CO_2 are directly correlated with human activity, primarily due to the dependance on fossilised energy in the form of fossil fuels. Fossil fuel combustion leads directly to the uncontrolled release of CO_2 and current estimates from combustion are shown in Figure A.7. Therefore, given the dominance of hydrocarbons on the GEB and the correlated effects on the global radiation balance, a terminal solution to this dependant pair of globally important problems is urgent.

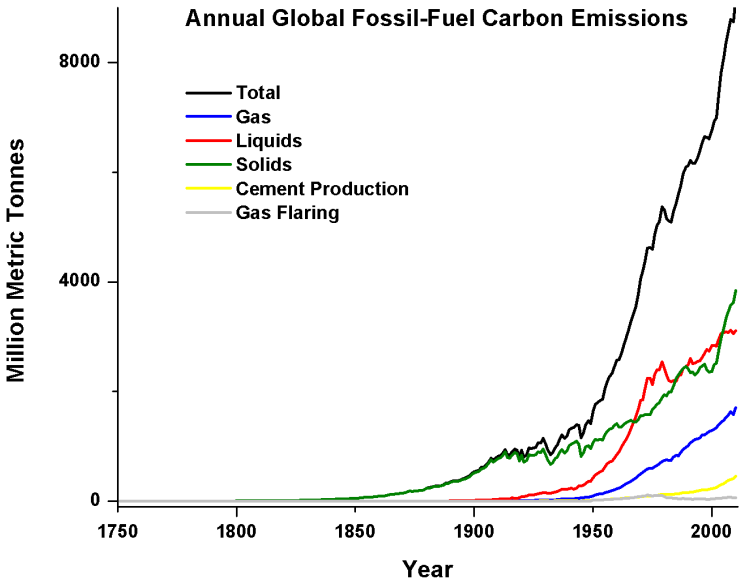

Figure A.7: Global fossil fuel emissions 1751 - 2010

A minimum set of qualities exist that any technical solution must possess. They must be driven by a renewable source such as light, wave or wind, in order to decouple from the generation of CO_2 by combustion. Secondly such a process must be reductive and either remove CO_2 from the atmosphere, converting it into a reduced product or by using the reduction of CO_2 as a thermodynamic working fluid for energy production. The reductive nature of the solution is driven by the thermodynamics of C_x species as previously discussed. A wider set of technical solutions also exist, derived from this approach: 'depowering' current thermally driven industrial processes through development of photocatalytic approaches can have a very large effect on industrial energy consumption.

A.4 Historical variations in CO_2

The first two graphs in Figure A.8 show recorded CO_2 concentrations from ice cores at two different stations. The graph in Figure A.8(a) clearly shows natural variations of CO_2

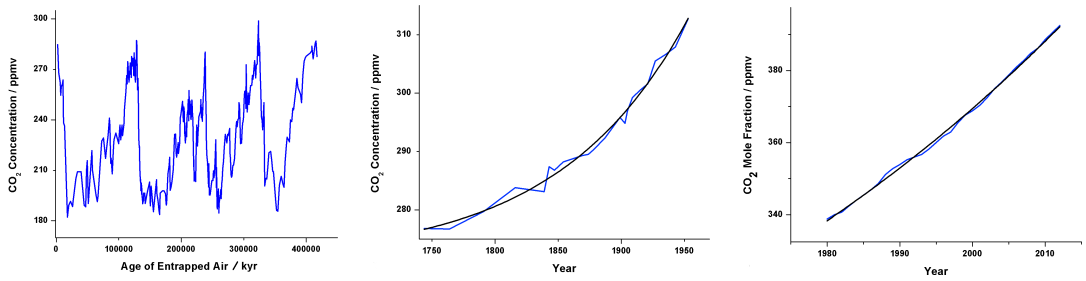

Figure A.8: Historical atmospheric CO_2 concentrations, derived from ice core data: (a) CO_2 concentration from the Ice Core Record, Vostock, Antarctic, (b) CO_2 concentration from the Ice Core Record, Siple Station, Antarctica, in comparison with (c) atmospheric measurements from the Mauna Loa observatory

levels over a 400000 year period before human activities began. It is clear that Earth undergoes a natural cycle of warming and cooling with the highest CO_2 levels recorded at approximately 300 ppmv.[201] The graph in Figure A.8(b) uses ice core data to show the rise in CO_2 levels since 1750 for a two hundred year period. The approximate exponential nature of the graph indicates the rate at which CO_2 is entering the Earth's atmosphere. The key point to note is that in the early 1900's the CO_2 concentration levels rapidly exceed all previous concentration levels from the ice core data.[201]

Finally, the third graph in Figure A.8(c) shows the level of atmospheric CO_2 since the 1980's according to measurements and experiments conducted at the Mauna Loa observatory, which is the oldest site used for the direct measurement of CO_2 in the atmosphere. The graph shows a steady increase in the CO_2 levels in the Earth's atmosphere with the CO_2 concentrations far exceeding all previous measurements.[202] Considering these data alongside the previous discussion regarding the inert nature of CO_2 and the timescales associated with the removal of CO_2 from the atmosphere it seems apparent that, although the levels of CO_2 are rising by relatively small amounts, it is the timescales required to reverse the process that presents the largest problem.

In addition, by comparing these atmospheric composition data with CO_2 emissions from burning fossil fuels since 1751, as shown in Figure A.7, a similar upward trend is ob-

served.[203] Figure A.7 shows that the total fossil fuel carbon emissions started to rise in the 1850's which correlates well with expansion of the industrial revolution. Much improved systematic data became available in the early 1950's with the development of the Mauna Loa Observatory, which began direct measurement of atmospheric CO_2 concentrations. As well as being a direct and current measure of CO_2, these data lower the reliance on ice core data.[204]

With one exception in the 1970's which corresponds with the 1973 oil crisis caused by members of OAPEC proclaiming an oil embargo, the rate of increase of CO_2 emissions from fossil fuels has not slowed. It is now generally accepted by the scientific community that the industrial use of fossil fuels and the increase in atmospheric CO_2 levels are directly linked.

Figure A.9[205] highlights the differences in global temperature since 1850 using the average global temperature as a baseline. From 1880 to 1930 there was a consistent trend of colder than average temperature anomalies. However, from the late 1930's to the 1970's the trend begins to shift and, whilst the temperature anomalies are still cooler than the average temperature, the extreme has shifted from -0.6 °C to -0.4 °C.

From 1978 onwards, the trend shifts even further to warmer than average temperature anomalies and shows no signs of slowing or decreasing. Whilst Figure A.9 shows temperature anomalies, Figure A.10[206] highlights the effects of the global average temperature increasing by just 1 °C, the effect at the extreme ends of the temperature range becomes more pronounced.

The bell curve in Figure A.10 shows the increase in temperature anomalies shifting the bell curve to the right and therefore increasing the mean temperature. The diagram also shows a change in the variance of the temperature anomalies which has the impact of

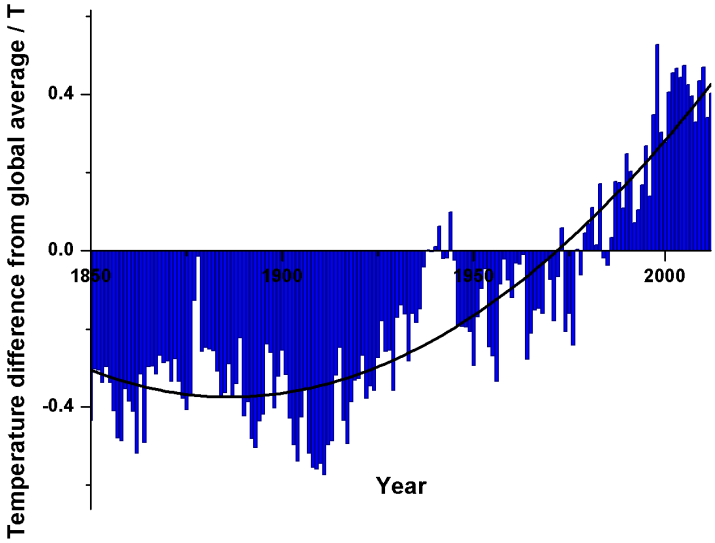

Figure A.9: Global temperature anomalies 1850 - 2012

flattening the bell curve and a rise in the number of occurrences of extreme temperatures at both ends of the scale.

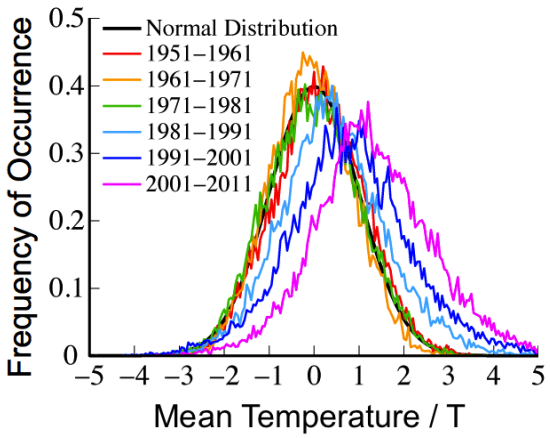

Figure A.10: Temperature anomaly distribution highlighting the impact of changes in the frequency of occurrence and an increase in mean temperature

This evidence suggests that the burning of fossil fuels is causing changes to our atmosphere and in all likelihood, the climate as well. Ultimately it becomes a question of timescales. The Global Energy Balance GEB is a delicate system that takes millions of years to convert carbon into fossil fuels and store as oil and coal. As millions of tonnes of

hydrocarbons are extracted and burnt every year, the carbon is rapidly released into the atmosphere and the reverse process of storage cannot compete, shifting the GEB. The burning of fossil fuels for energy is a practice that cannot continue indefinitely, not only because of the impact CO_2 is having on the atmosphere, but also because fossil fuels are a finite resource that will eventually deplete.

A.5 Peak oil crisis

A report published in 2005 entitled, 'Peaking of World Production: Impacts, Mitigation, and Risk Management'[207] was commissioned by the US Department of Energy. The report, also known as the 'Hirsch Report', examines the timescales for when the peak in oil production is likely to occur, any mitigating actions necessary and the impacts of such actions. In a summary of the report, Hirsch states;

> *The peaking of world oil production presents the U.S. and the world with an unprecedented risk management problem. As peaking is approached, liquid fuel prices and price volatility will increase dramatically, and, without timely mitigation, the economic, social, and political costs will be unprecedented. Viable mitigation options exist on both the supply and demand sides, but to have substantial impact, they must be initiated more than a decade in advance of peaking.*[207]

Humans have developed an ever increasing reliance on fossil fuels to power homes, businesses and transport. This is illustrated by comparing Figure A.7 to Figure A.11.[208] The world total energy consumption in 2010 was 11,943 million tonnes (oil equivalent), whilst the total fossil fuel carbon emissions equated to 9,167 million metric tonnes of

carbon in 2010. On these figures alone, the human population relies on carbon based fuels for 77% of energy requirements.

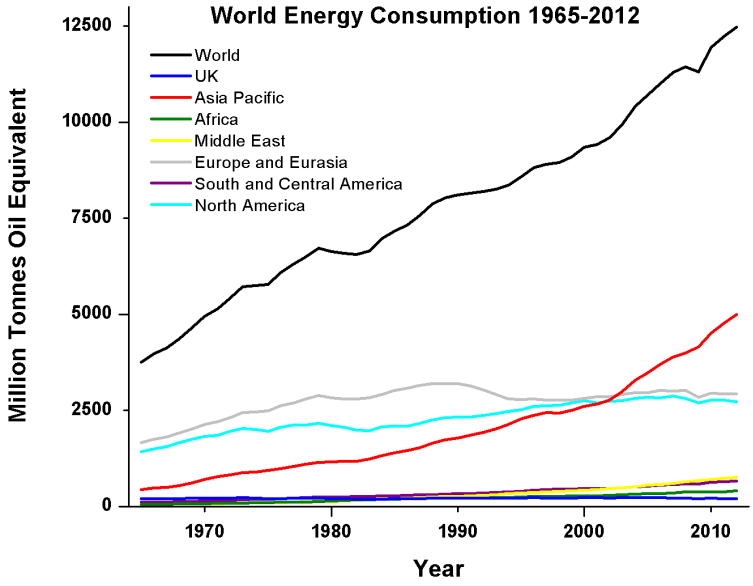

Figure A.11: World Energy Consumption 1965 - 2012

When global hydrocarbon stores will run out is a matter of debate and a method using '2P data' has been developed to estimate when this will occur. '2P data' refers to the oil reserves proved to be in existence plus the probable reserves yet to be discovered and it is estimated that in 2002 all regions had depleted at least half their oil reserves, except the Middle Eastern countries. This would effectively give the Middle Eastern countries control over the worlds oil supply in the future. In addition, the data suggests that in 2002 North America had depleted about three quarters of its oil reserves having reached its peak in 1971. The data also implies that Asia-Pacific and Europe were about to peak and therefore start declining. Overall, the global peak for oil reserves was estimated to be between 2007 and 2012 with a more optimistic estimate of between 2012 and 2017.[209] Alternative sources of '2P data' indicates a global oil peak between the years 2005 to 2015[210] or between 2010 and 2015.[211] Whilst the data vary, they still suggest that a

global oil peak is imminent.

Figure A.12 shows the proved oil reserves only and from the data it can be deduced that whilst the global oil reserves are increasing it is mainly due to new oil reserves being identified in Central and South America since 2010. All other individual areas are reaching a plateau, especially, North America, Asia, Oceania and Europe. Africa and the Middle East are increasing their reserves but at a slow rate.

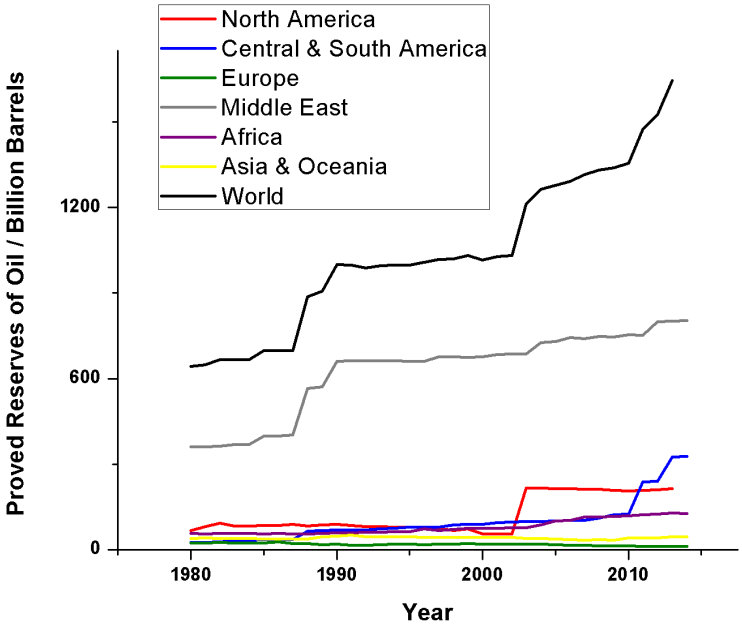

Figure A.12: Proved oil reserves 1980 - 2014

Hydrocarbons are a finite resource and even with improving technology, oil resources will decline. As this happens basic economics of supply and demand dictate that prices will increase, consequently making alternative energy sources more attractive and potentially reducing the demand for oil.[212] It seems unwise to rely on sources of oil that have yet to be discovered despite a reasonable certainty that extraction technology will improve in the future. However, it also seems unwise to rely on other hydrocarbon sources being available as oil becomes more scarce.

A.6 Technical solutions to climate change

Given the structure of the GEB, the future constraints of supply and the waste products from combustion, new approaches to a sustainable energy balance need to be developed as a matter of urgency. As discussed above in section A.3, the process, or more likely the array of processes, that can offer a technical solution must be driven sustainably, ideally by solar energy, and will also ideally reduce CO_2 to more useful materials. These processes must also be catalytic and run as close to ambient temperature as possible, to ensure that the process itself is not a major consumer of natural resources.[213]

Appendix B

NMR spectra - triphenysiloxide ligands

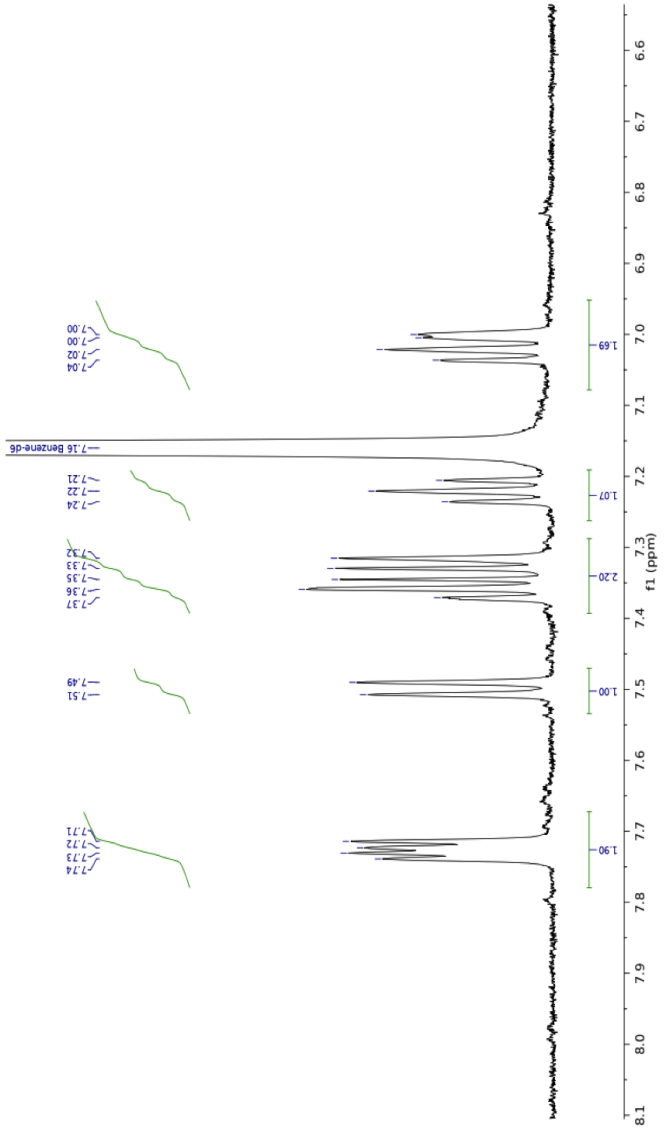

Figure B.1: ^{1}H NMR for (1-napthyl)$_3$silanol in d_6-Benzene[80]

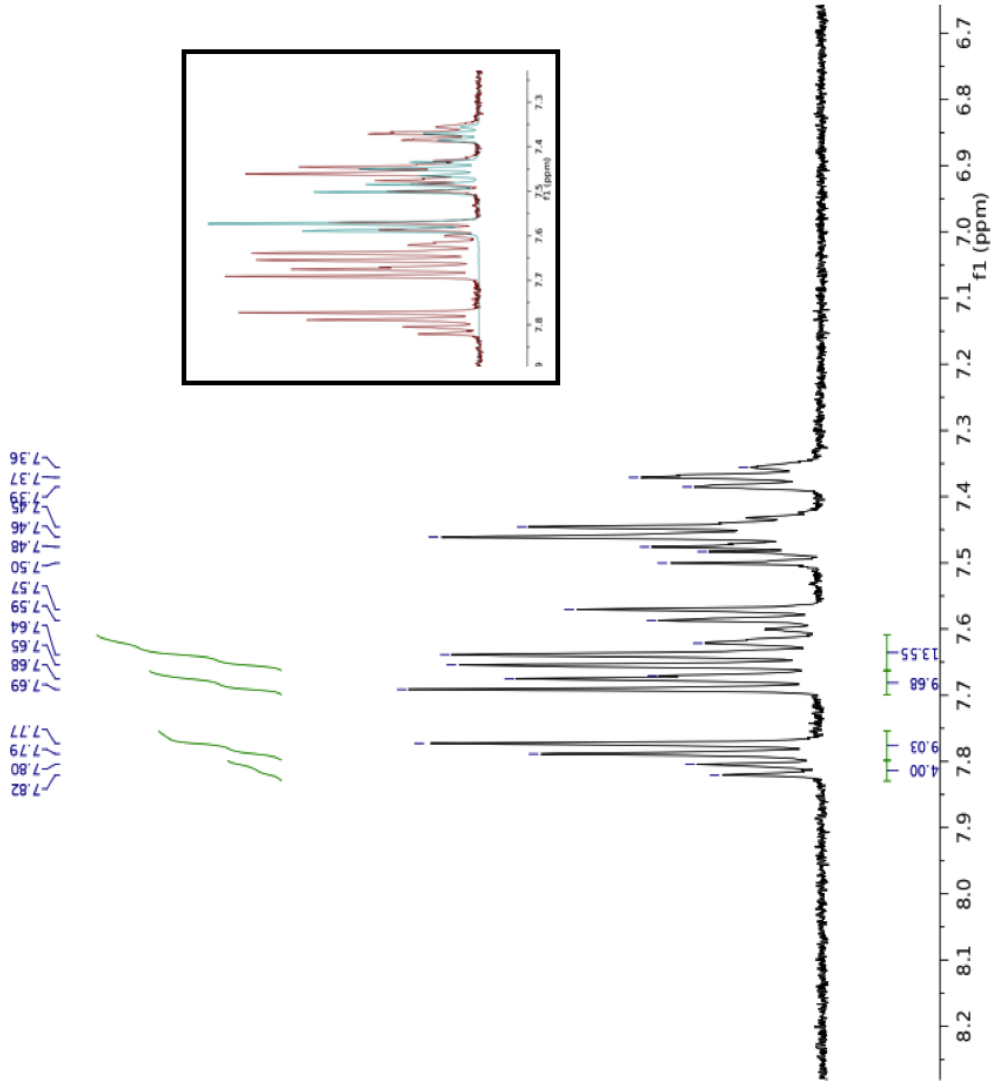

Figure B.2: ^{1}H NMR for (4-biphenyl)$_3$silanol in d_2-CD_2Cl_2 [80]

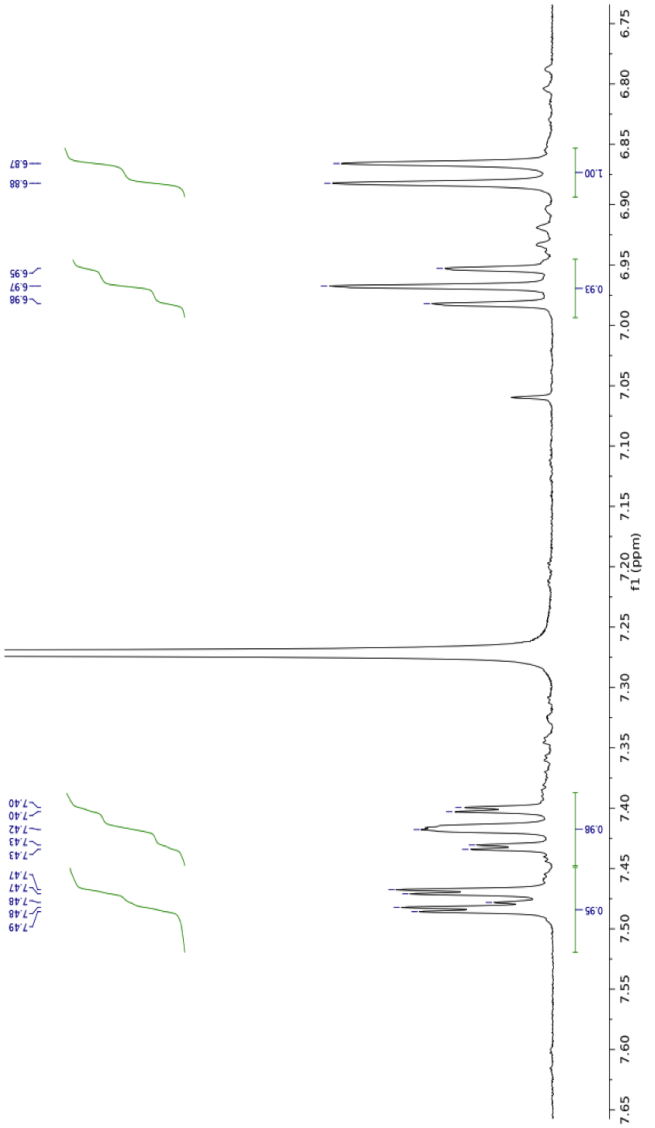

Figure B.3: ^{1}H NMR for (1-anisyl)$_3$silanol in d_2-CD_2Cl_2 [80]

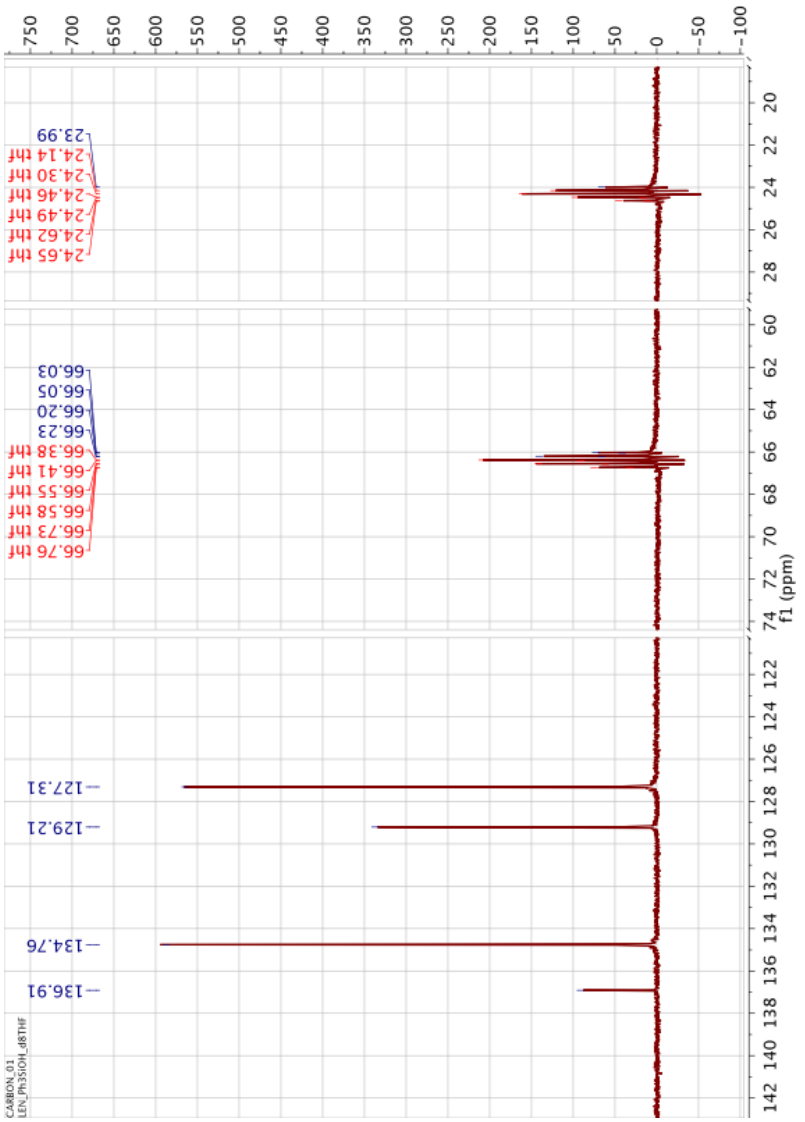

Figure B.4: $^{13}C\{H\}$ NMR for Triphenylsilanol in d_8-THF

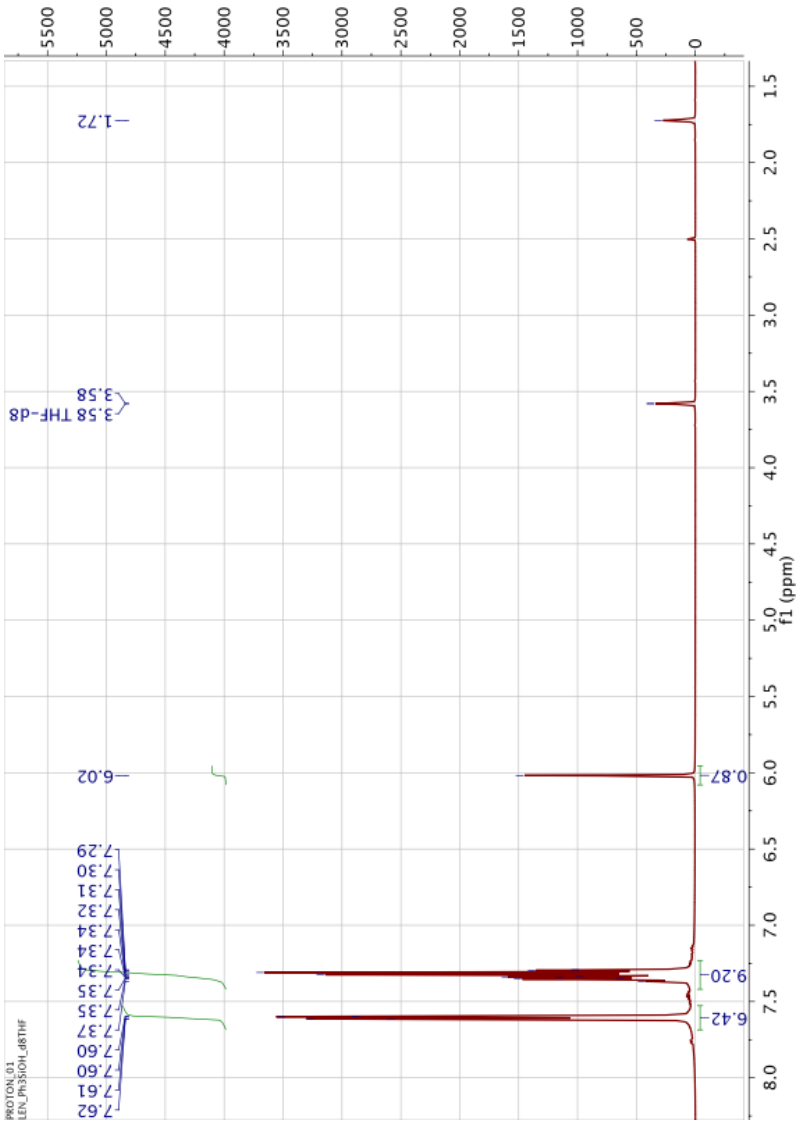

Figure B.5: ^{1}H NMR for Triphenylsilanol in d_8-THF

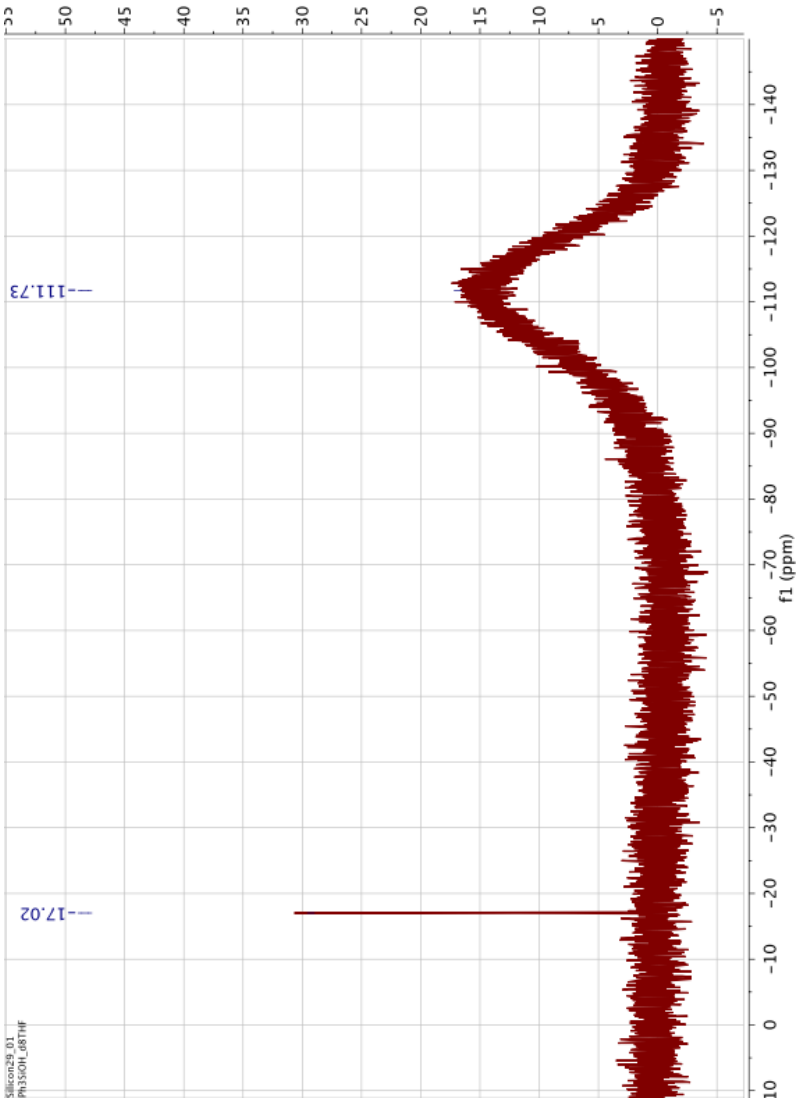

Figure B.6: ^{29}Si NMR for Triphenylsilanol in d_8-THF

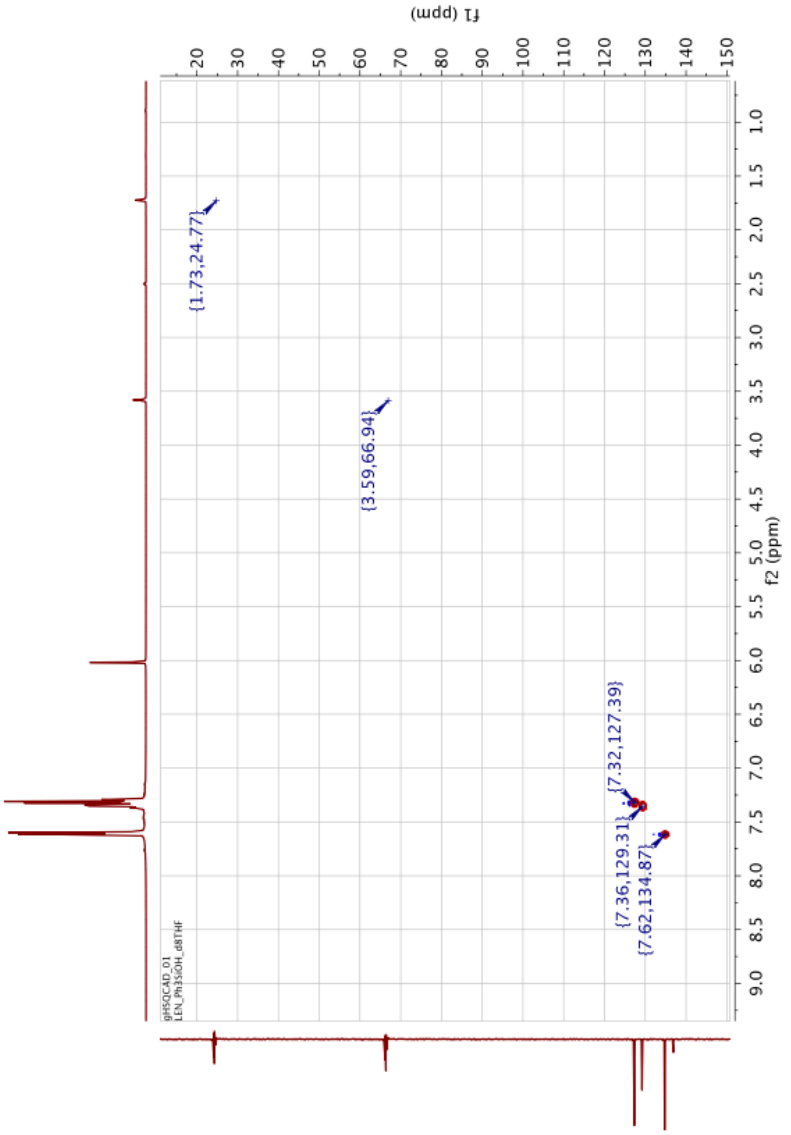

Figure B.7: HSQC NMR for Triphenylsilanol in d_8-THF

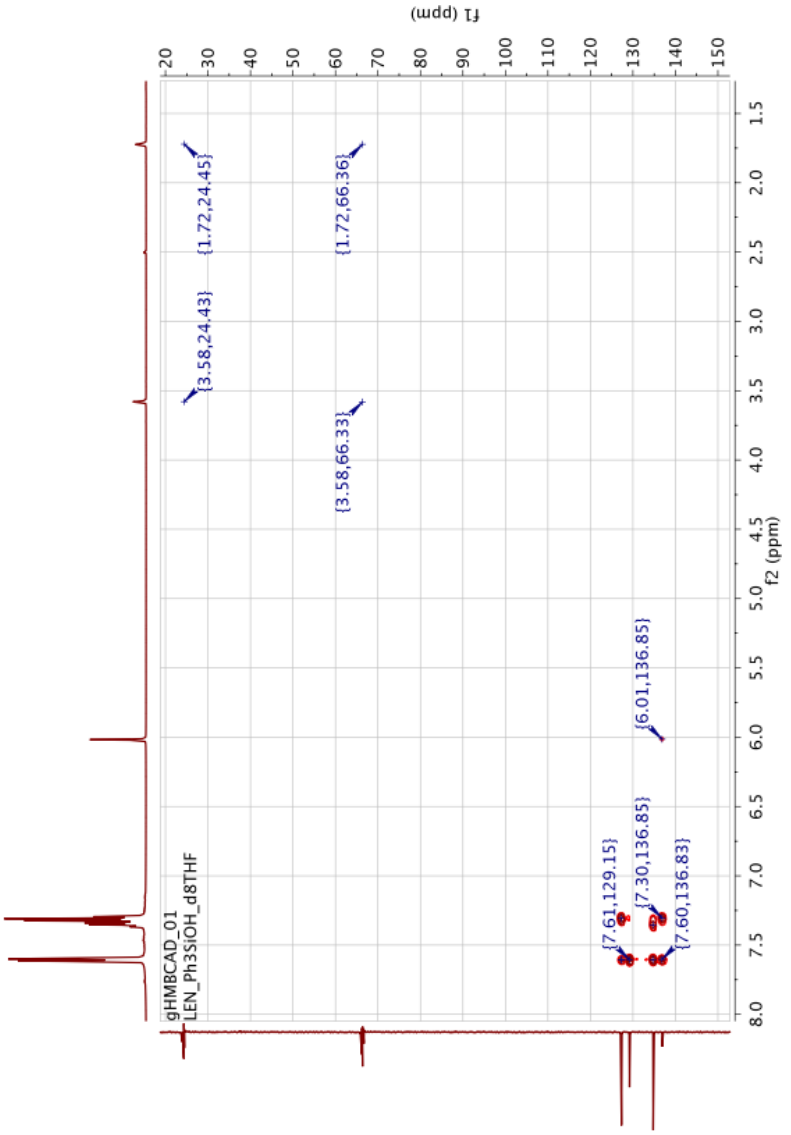

Figure B.8: HMBC NMR for Triphenylsilanol in d_8-THF

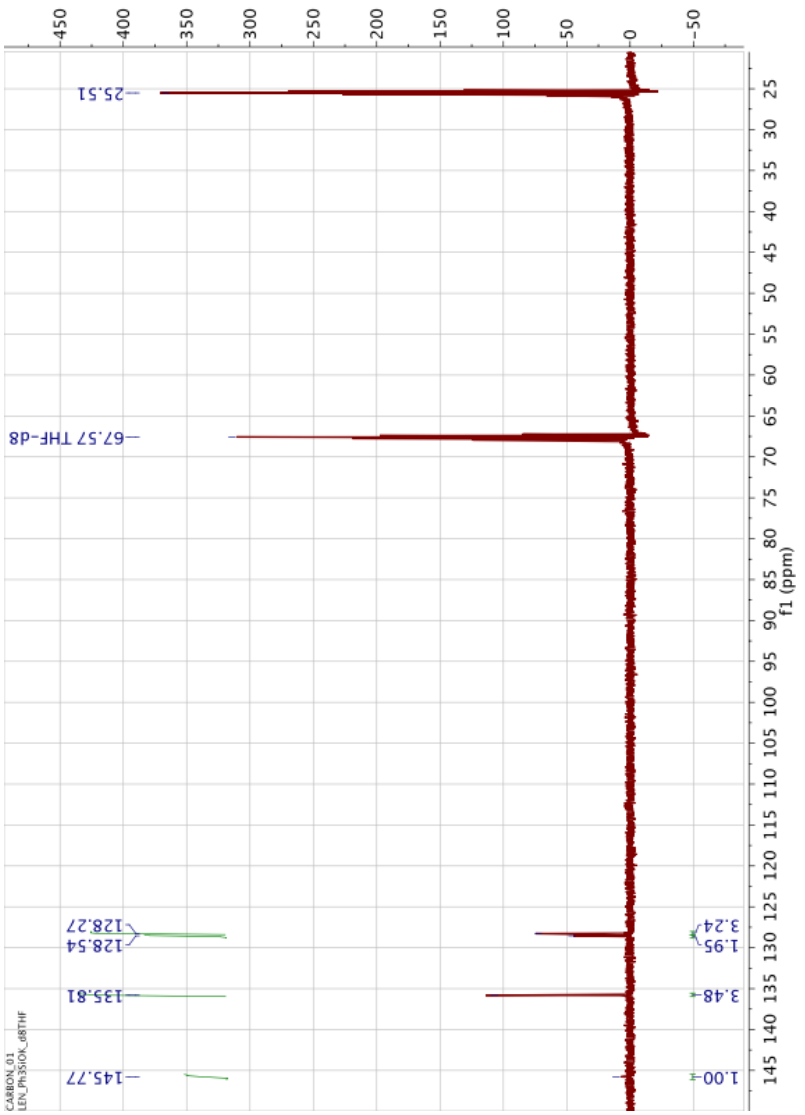

Figure B.9: $^{13}C\{H\}$ NMR for Triphenylsiloxide in d_8-THF

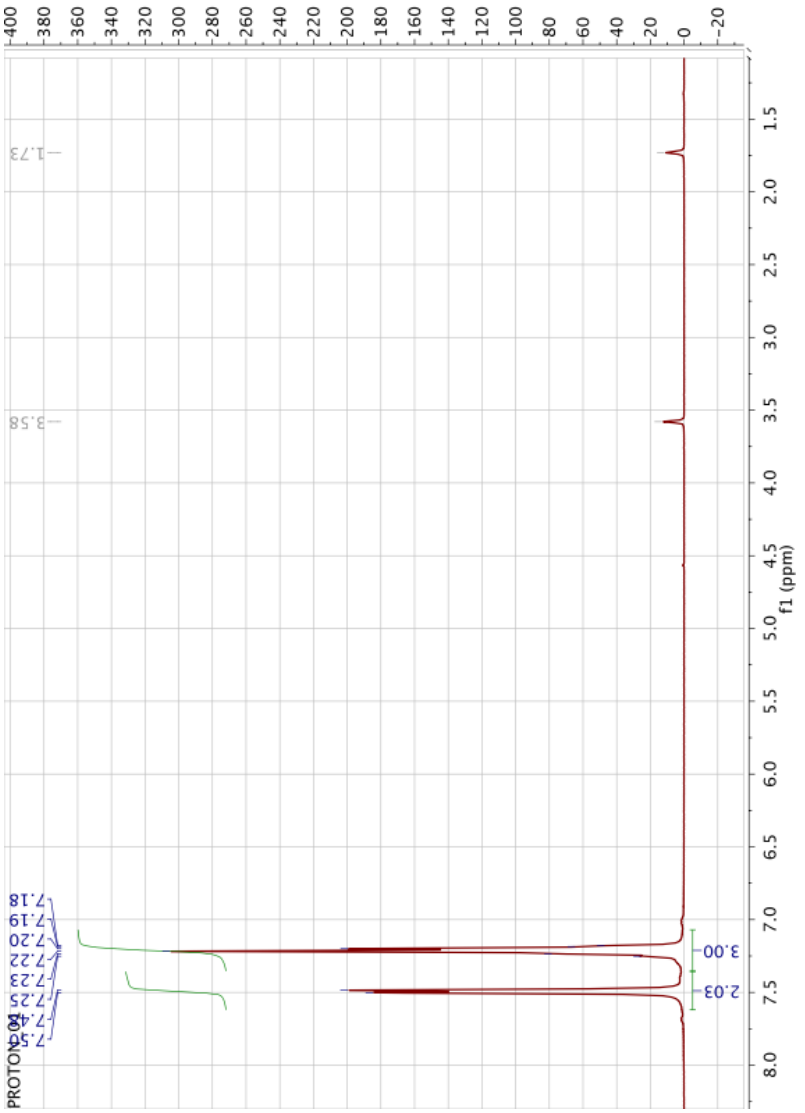

Figure B.10: ^{1}H NMR for Triphenylsiloxide in d_8-THF

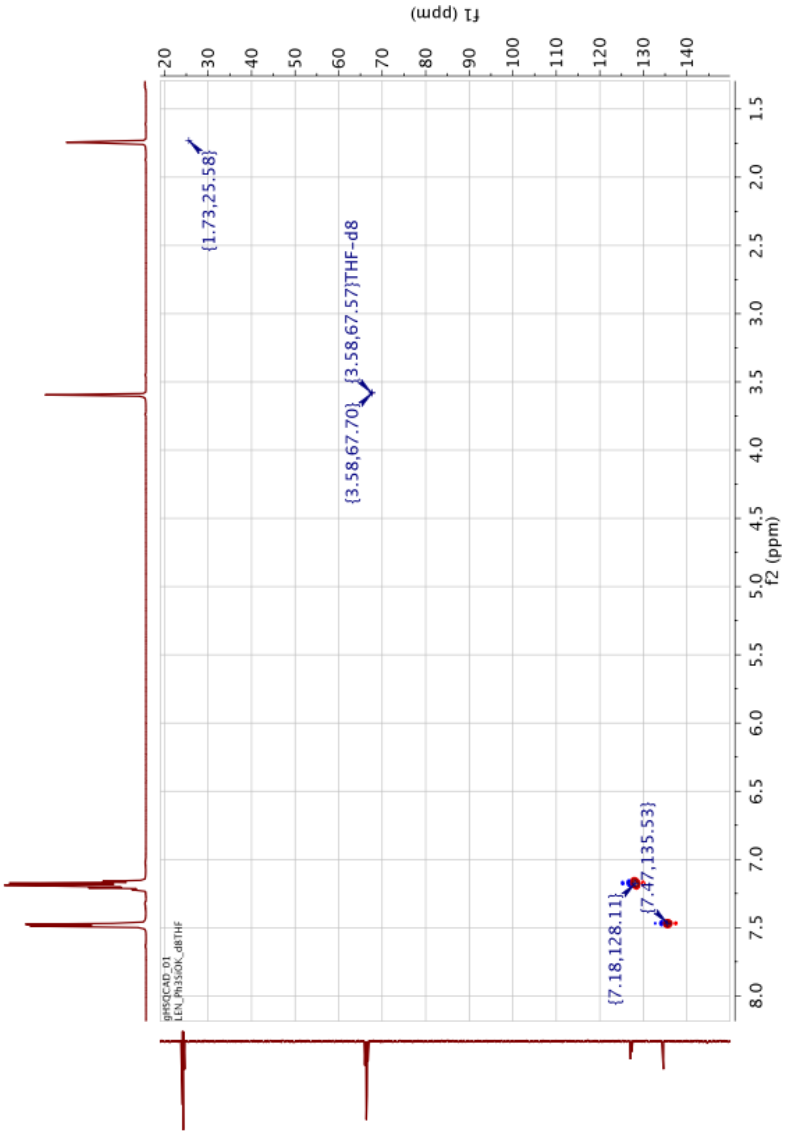

Figure B.11: HSQC NMR for Triphenylsiloxide in d_8-THF

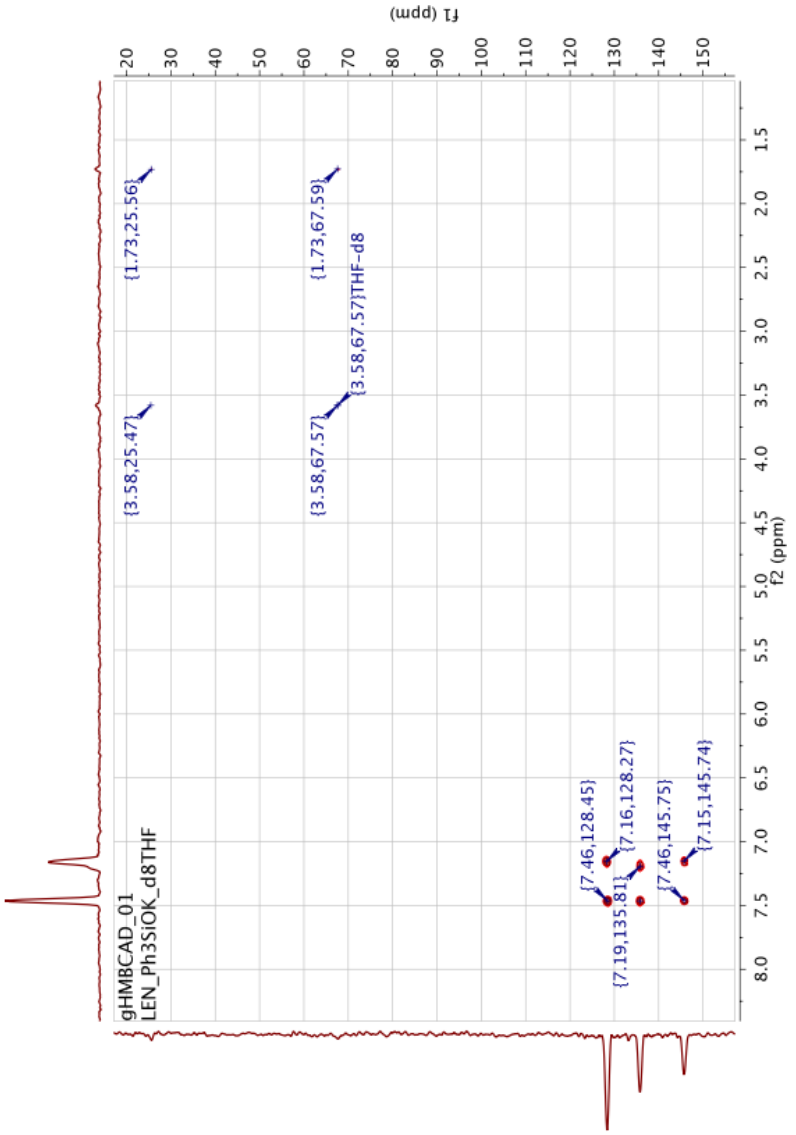

Figure B.12: HMBC NMR for Triphenylsiloxide in d_8-THF

Figure B.13: $^{13}C\{H\}$ NMR for K[U(OSiPh$_3$)$_5$] in d_8-Toluene

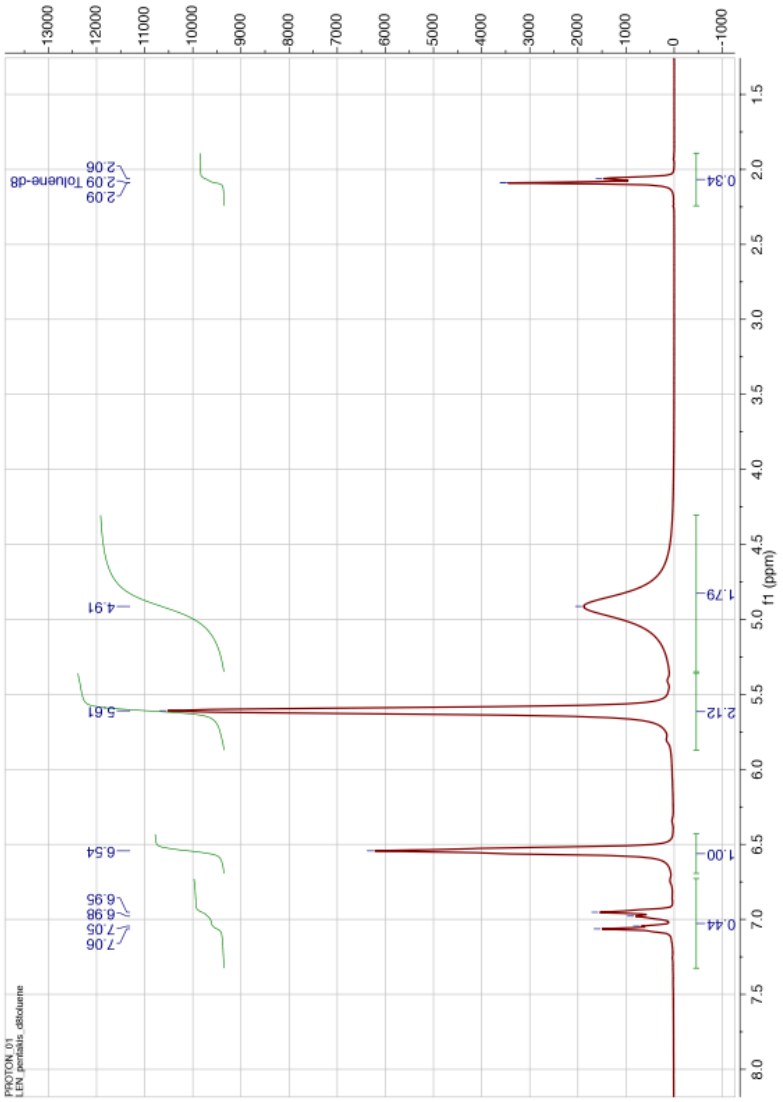

Figure B.14: ^{1}H NMR for K[U(OSiPh$_3$)$_5$] in d_8-Toluene

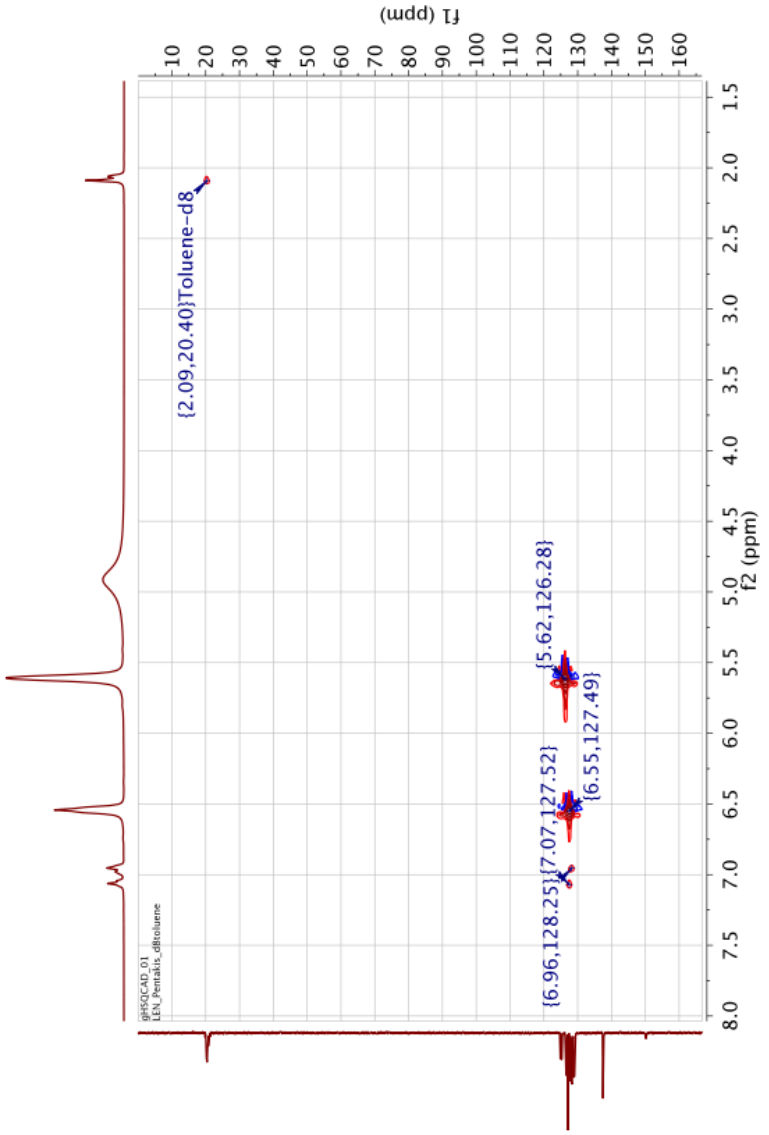

Figure B.15: HSQC NMR for K[U(OSiPh$_3$)$_5$] in d_8-Toluene

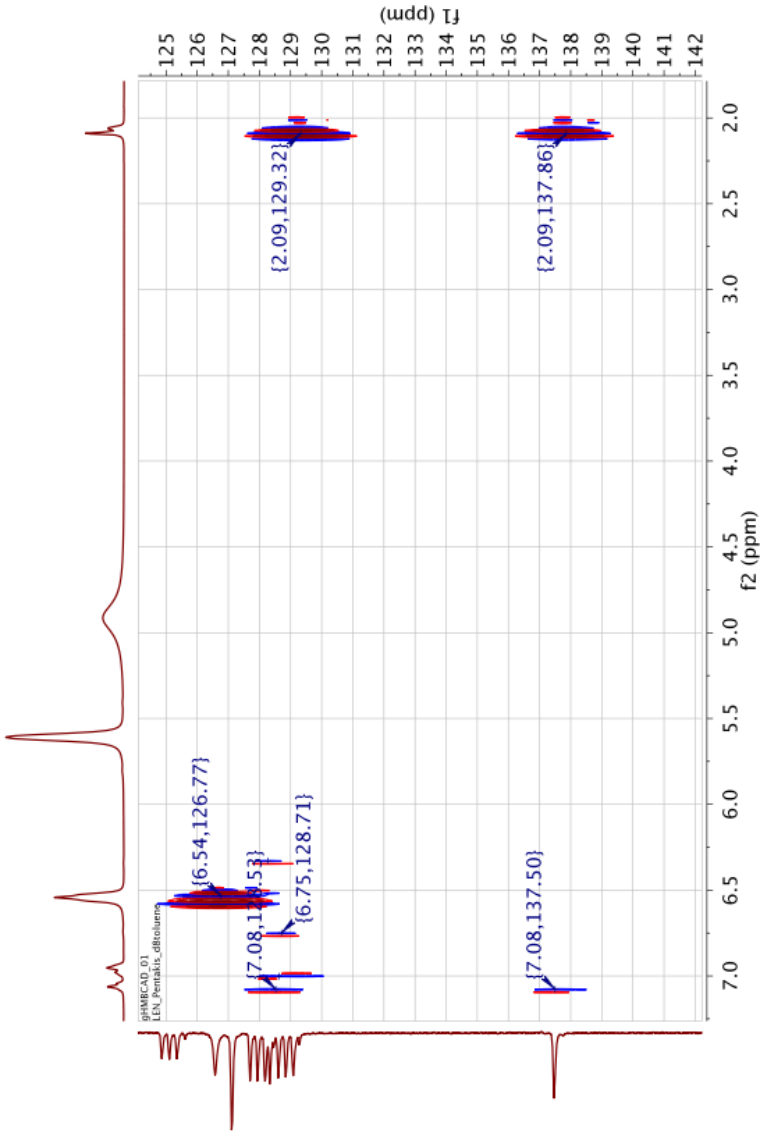

Figure B.16: HMBC NMR for K[U(OSiPh$_3$)$_5$] in d_8-Toluene

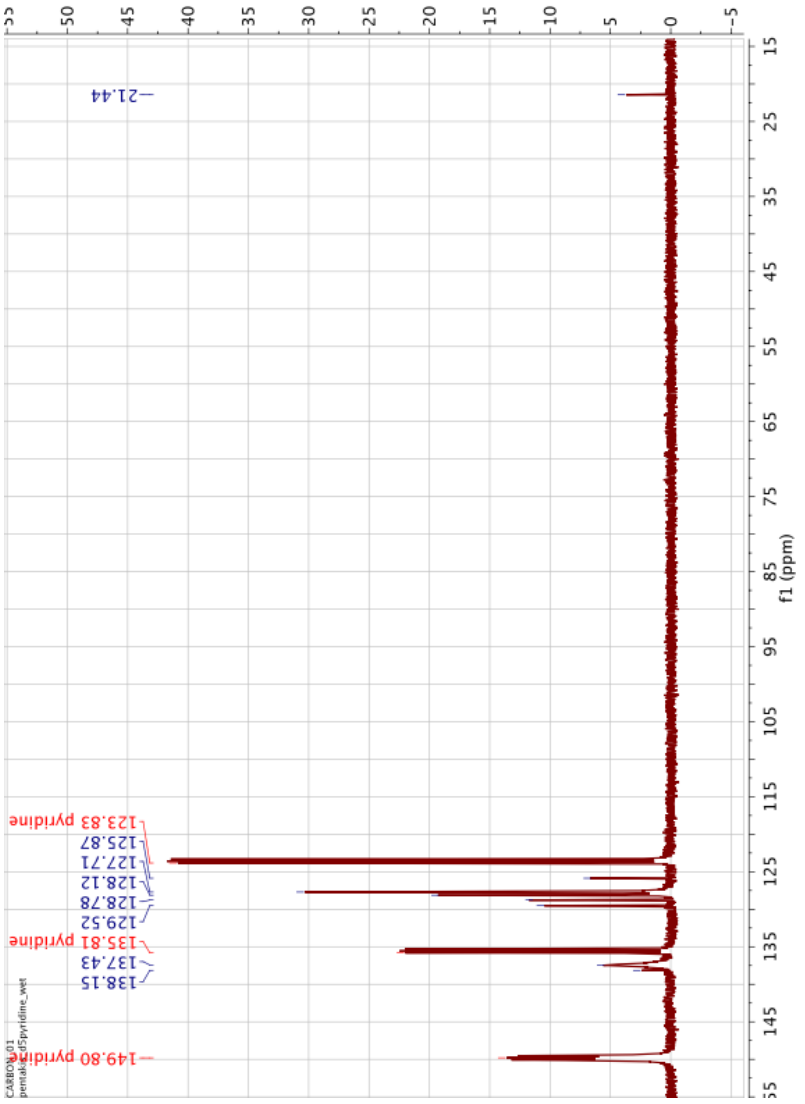

Figure B.17: $^{13}C\{H\}$ NMR for ($[K(py)_6]$ $[(Ph_3SiO)_5U(py)]$)$_2$ in d_5-Pyridine

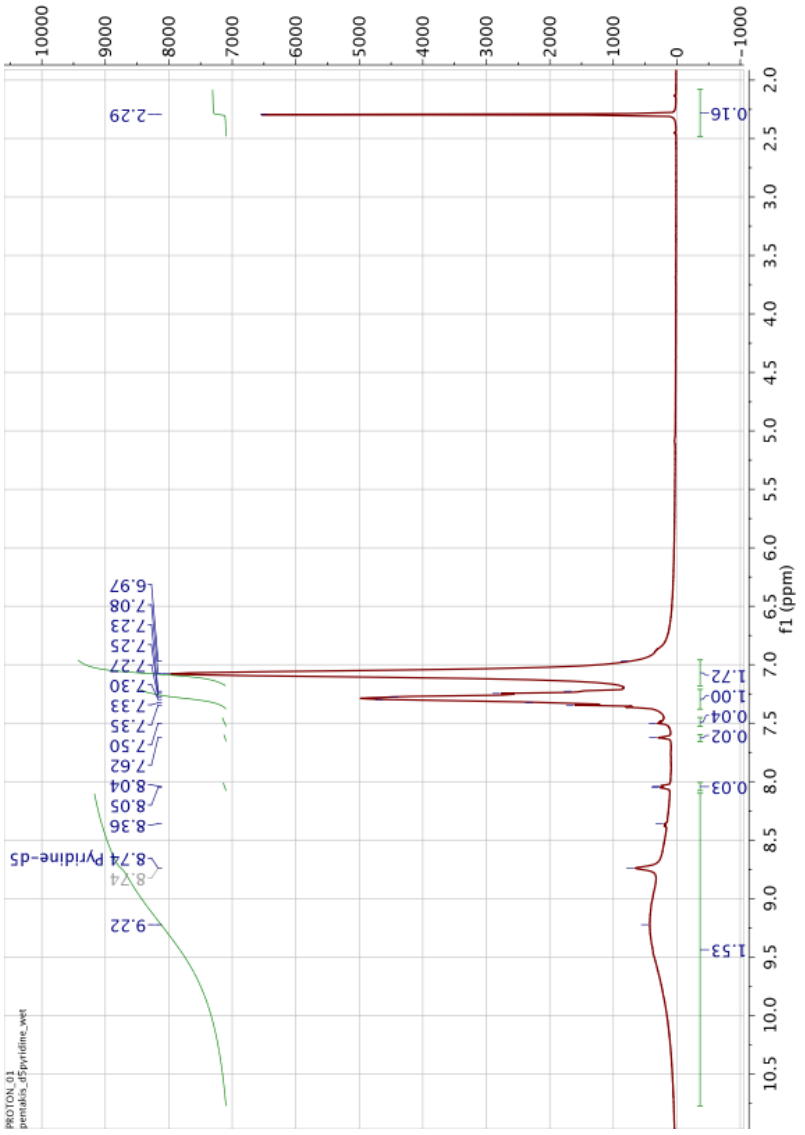

Figure B.18: ^{1}H NMR for ([K(py)$_6$] [(Ph$_3$SiO)$_5$U(py)])$_2$ in d_5-Pyridine

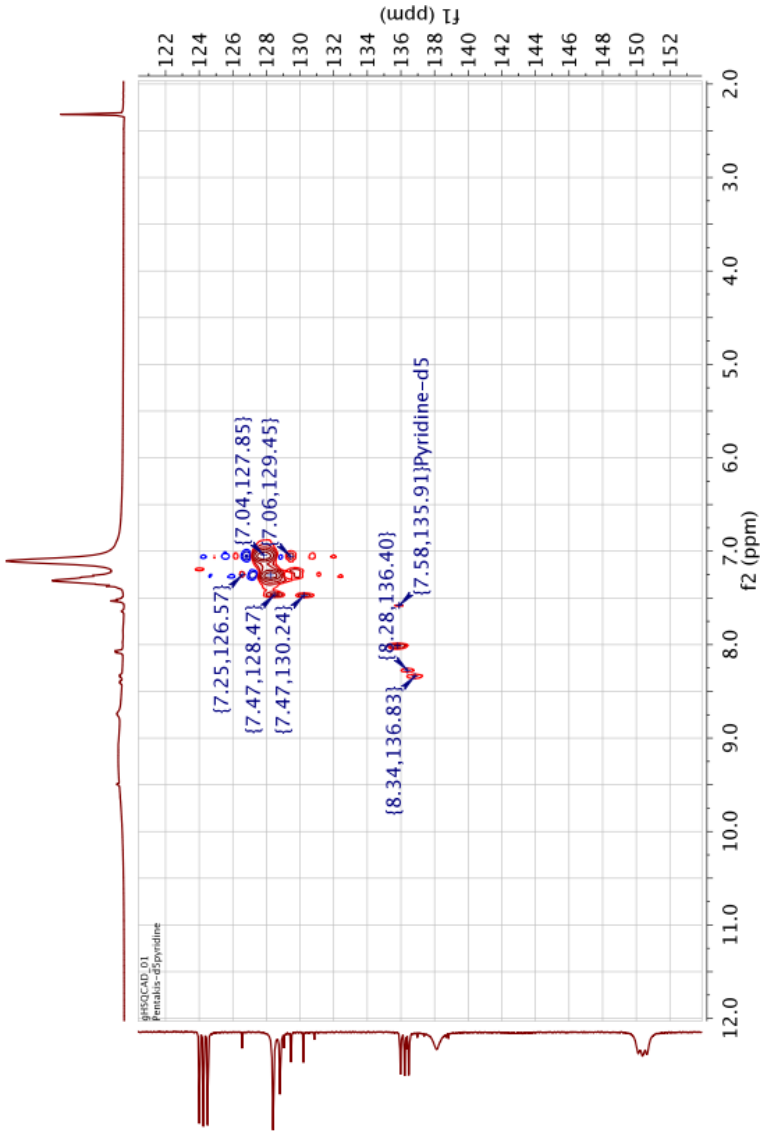

Figure B.19: HSQC NMR for $([K(py)_6]\ [(Ph_3SiO)_5U(py)])_2$ in d_5-Pyridine

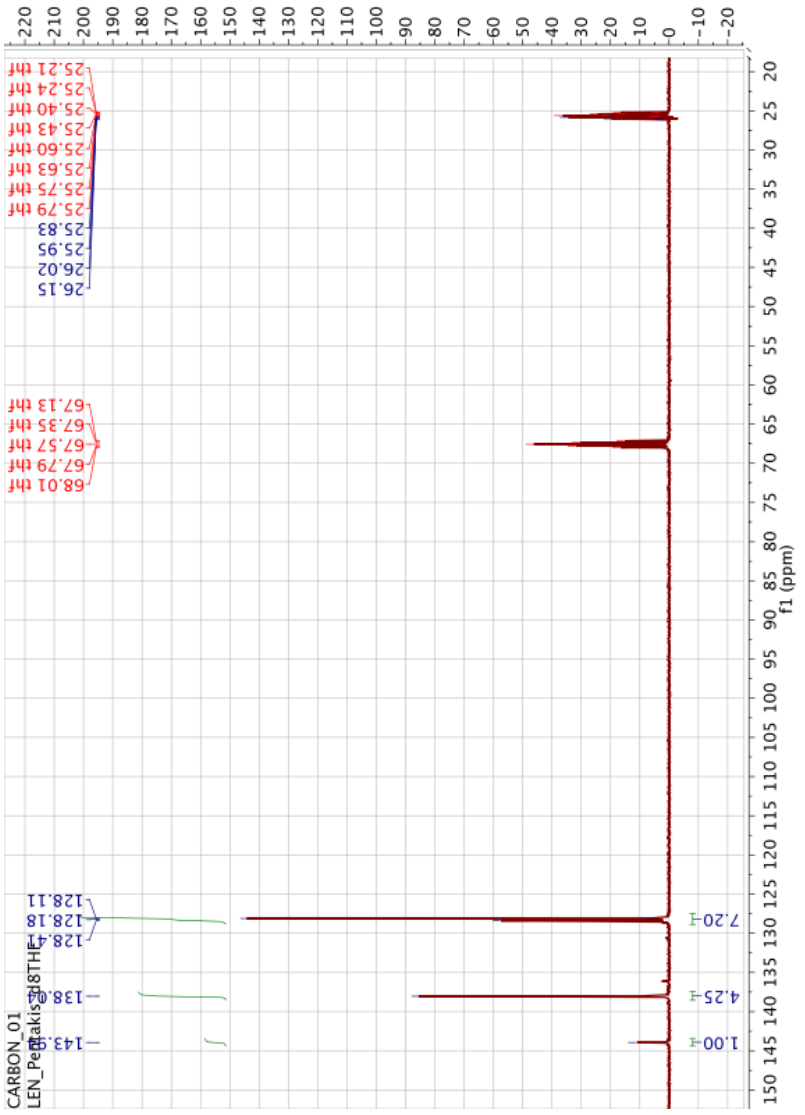

Figure B.20: $^{13}C\{H\}$ NMR for $K[(Ph_3SiO)_5U(THF)]$ in d_8-THF

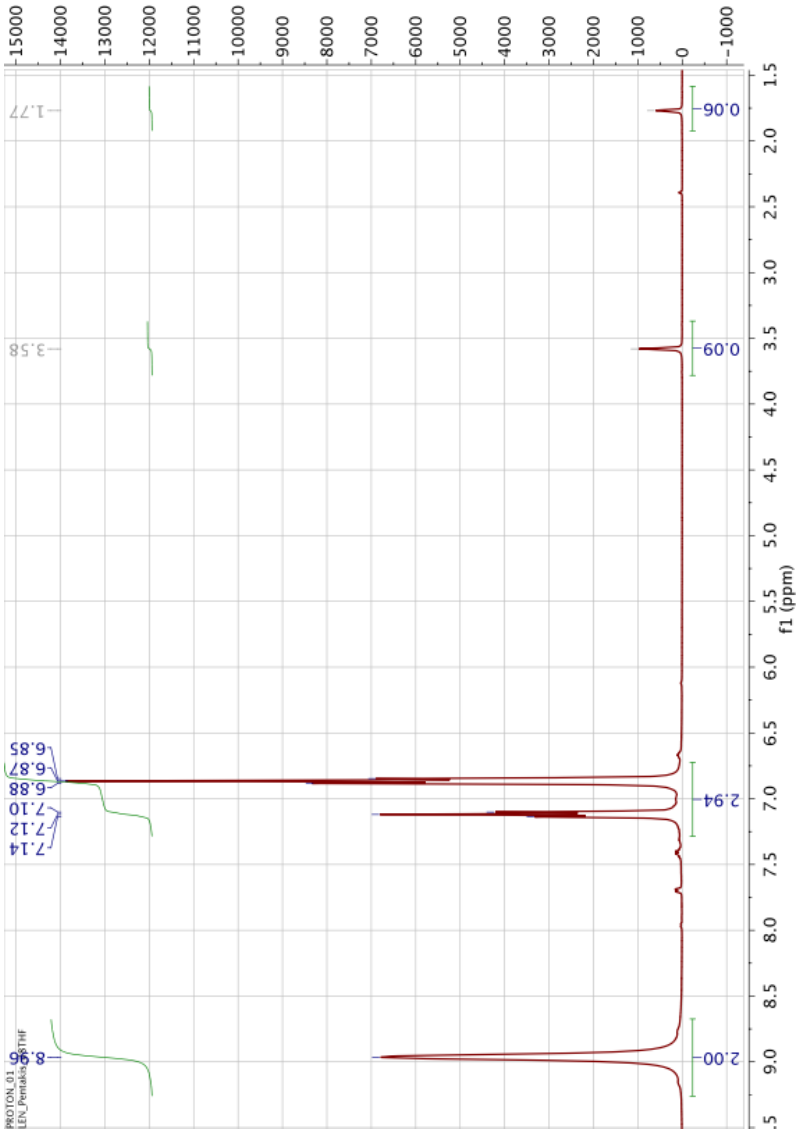

Figure B.21: ^{1}H NMR for K[$(Ph_3SiO)_5U(THF)$] in d_8-THF

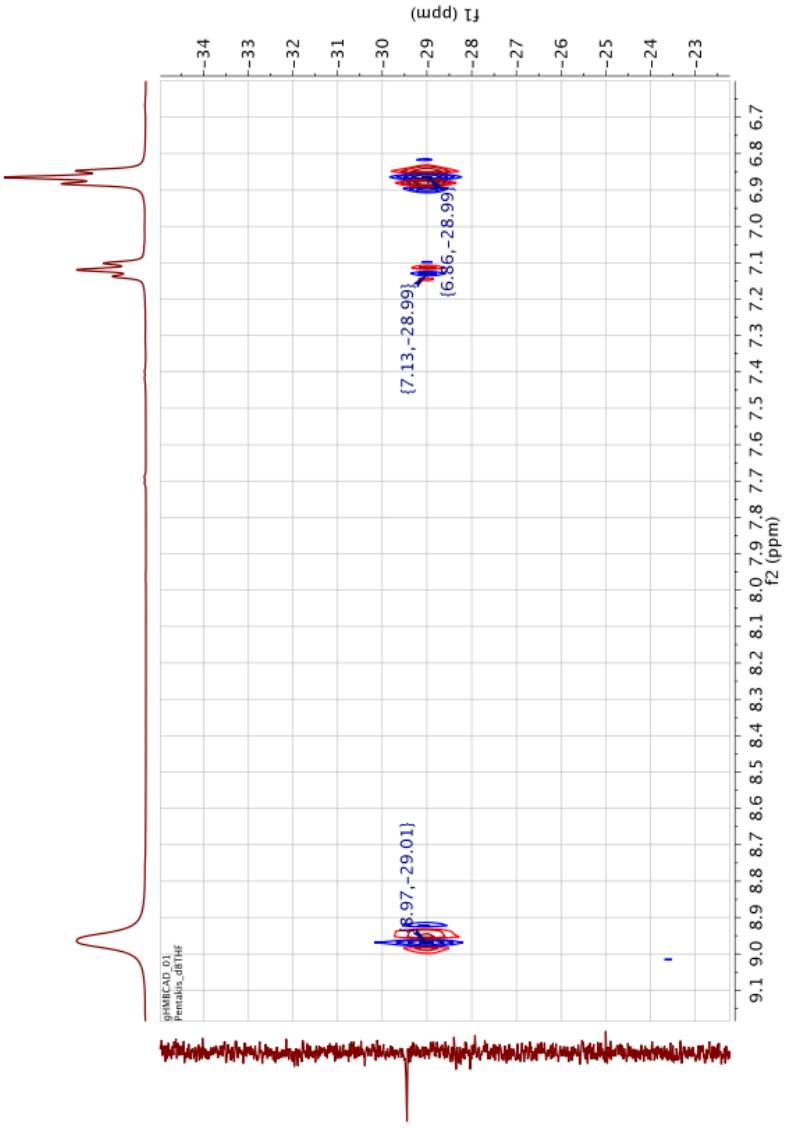

Figure B.22: ^{29}Si HMBC NMR for K[$(Ph_3SiO)_5U(THF)$] in d_8-THF

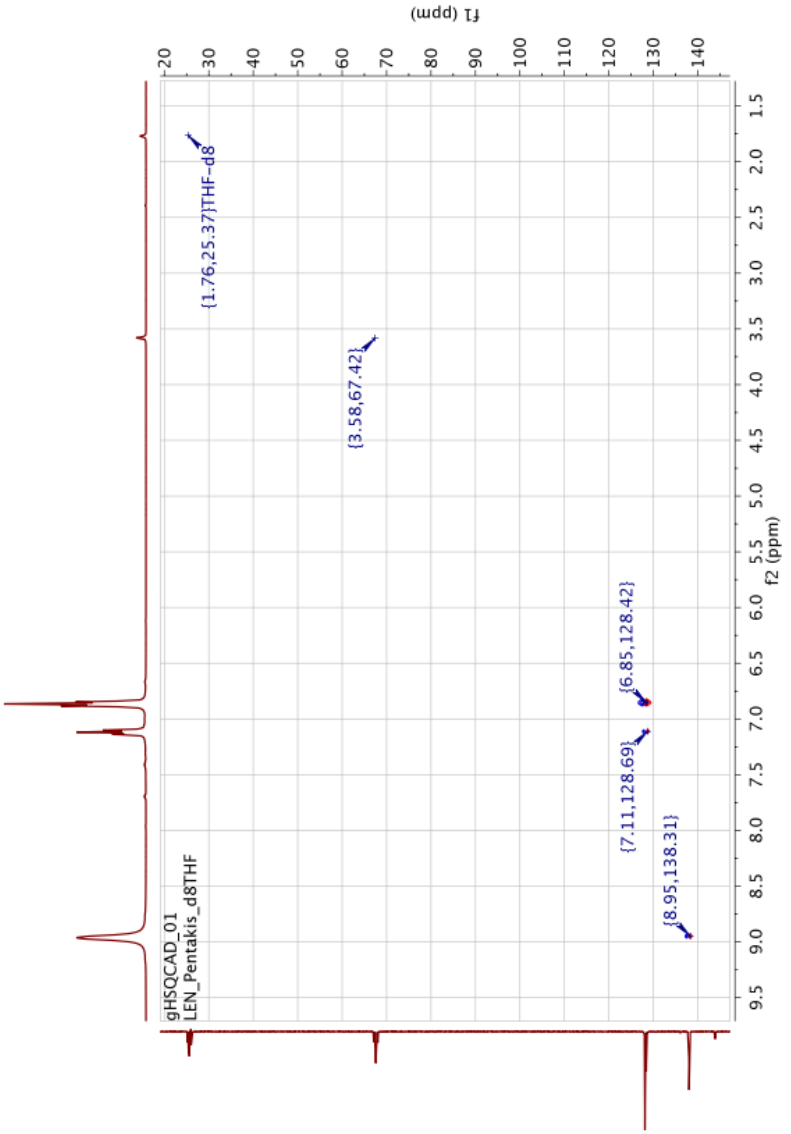

Figure B.23: HSQC NMR for K[$(Ph_3SiO)_5U(THF)$] in d_8-THF

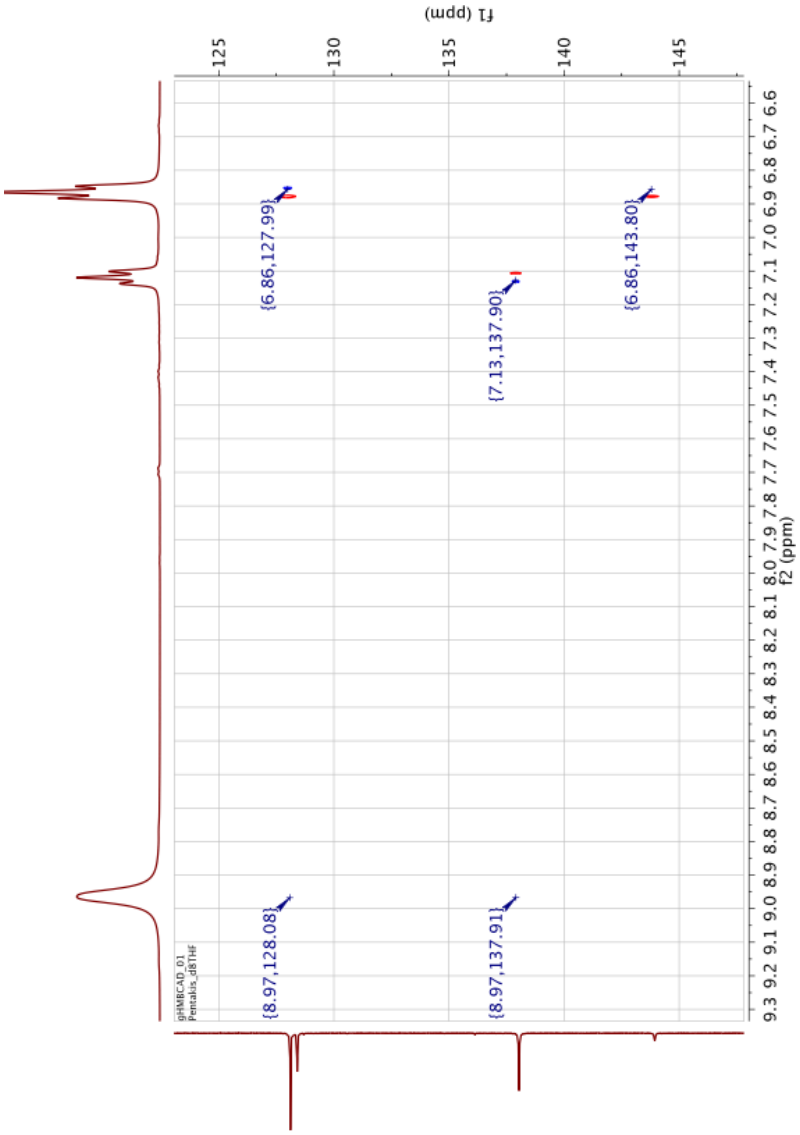

Figure B.24: HMBC NMR for K[$(Ph_3SiO)_5U(THF)$] in d_8-THF

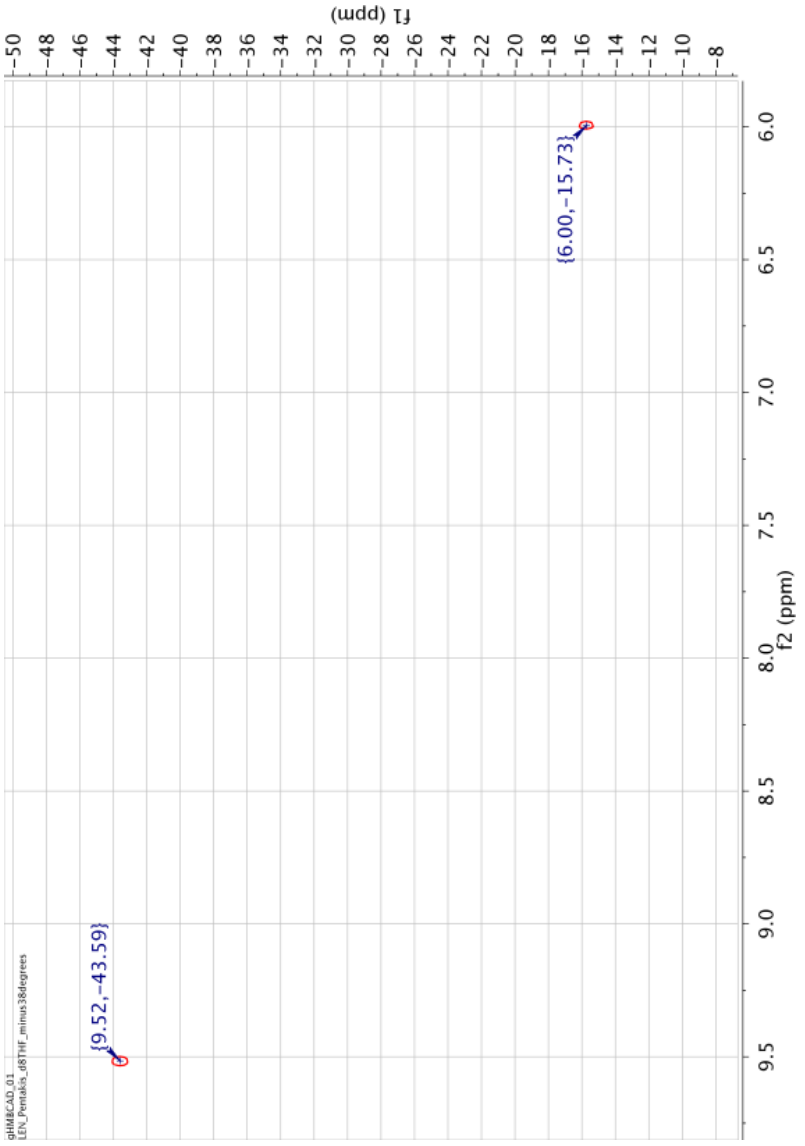

Figure B.25: ^{29}Si HMBC NMR for K[$(Ph_3SiO)_5U(THF)$] in d_8-THF

Appendix C

NMR spectra - reactions with TMSOTf

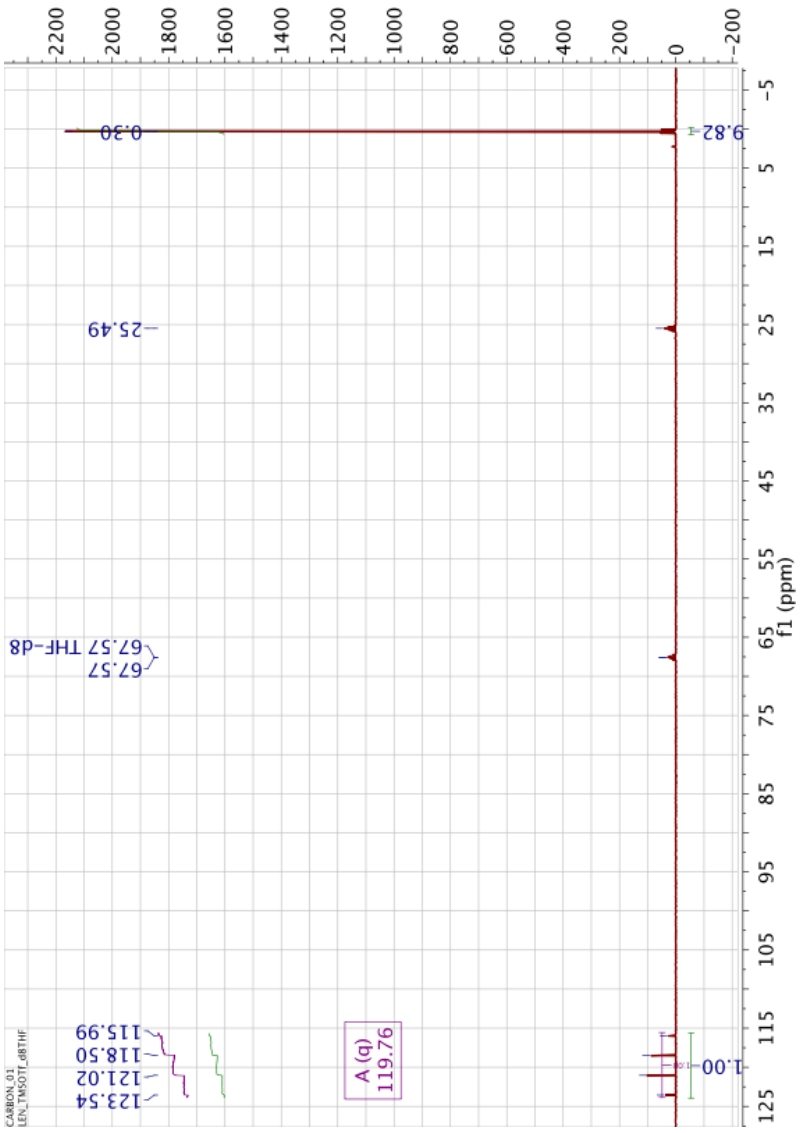

Figure C.1: $^{13}C\{H\}$ NMR for TMSOTf in d_8-THF

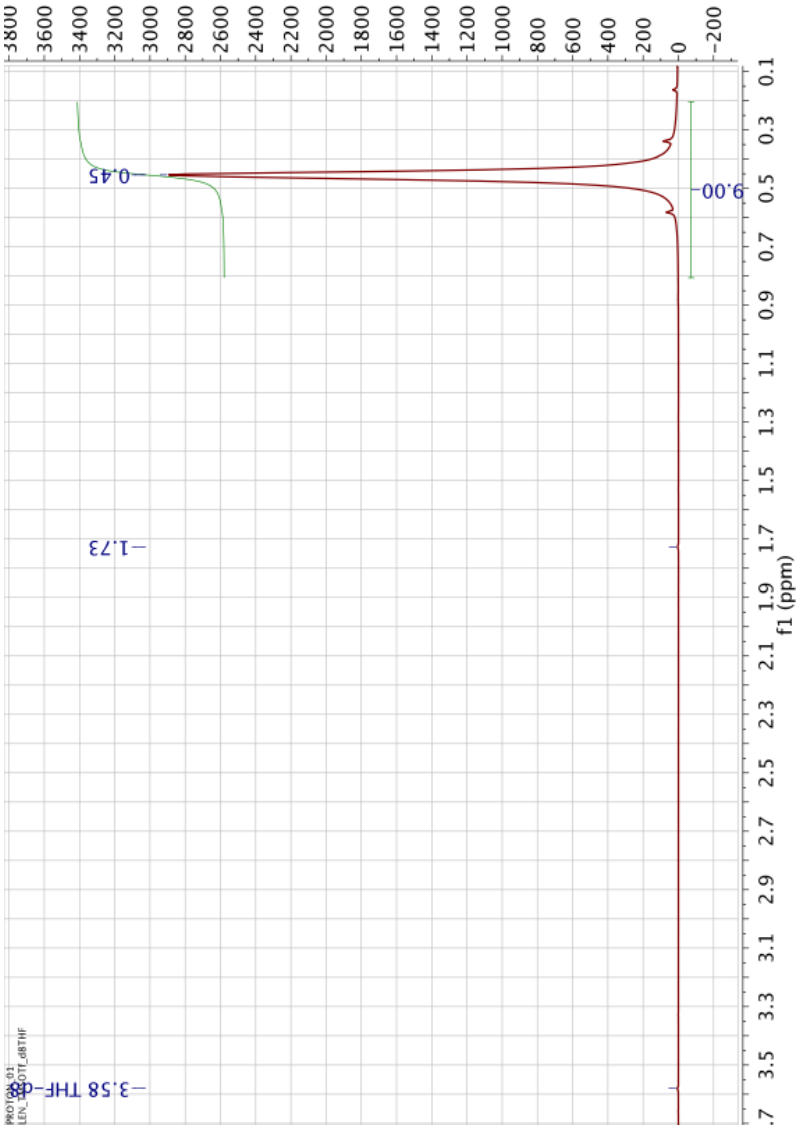

Figure C.2: ^{1}H NMR for TMSOTf in d_8-THF

Figure C.3: ^{19}F NMR for TMSOTf in d_8-THF

Figure C.4: $^{13}C\{H\}$ NMR for TMS−OSiPh$_3$ and H−OTf in d_8-THF

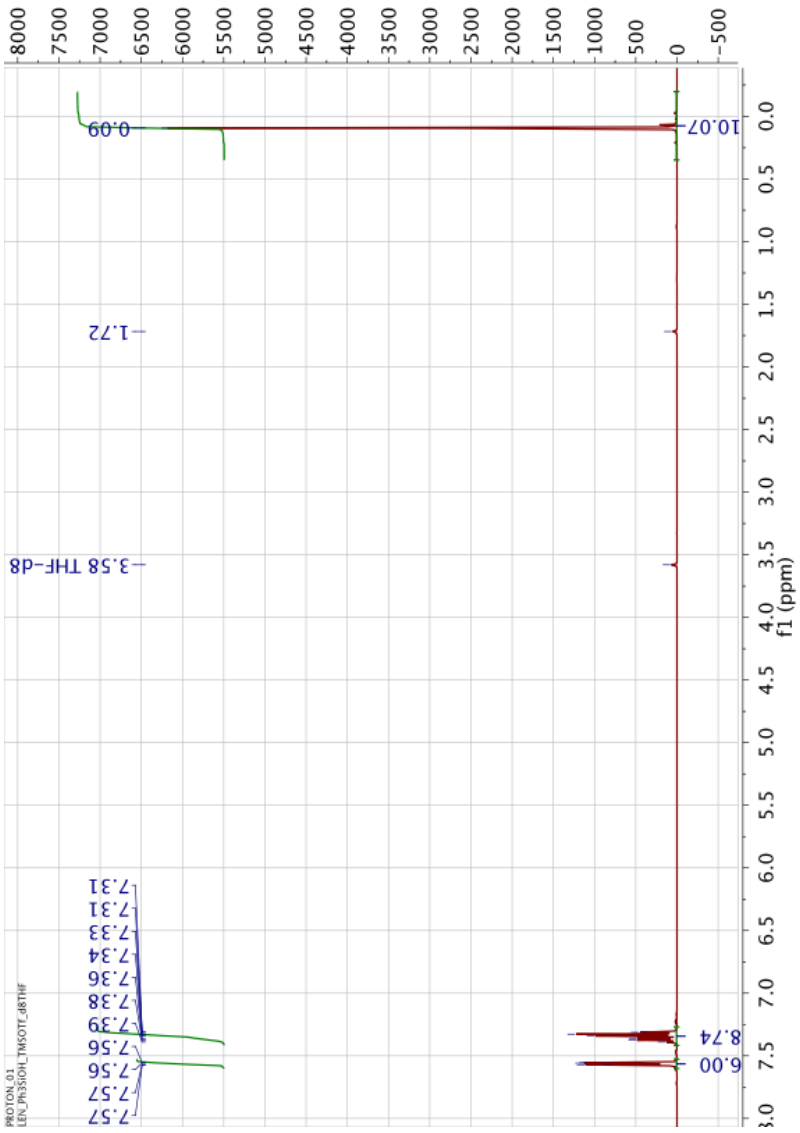

Figure C.5: ^{1}H NMR for TMS−OSiPh$_3$ and H−OTf in d_8-THF

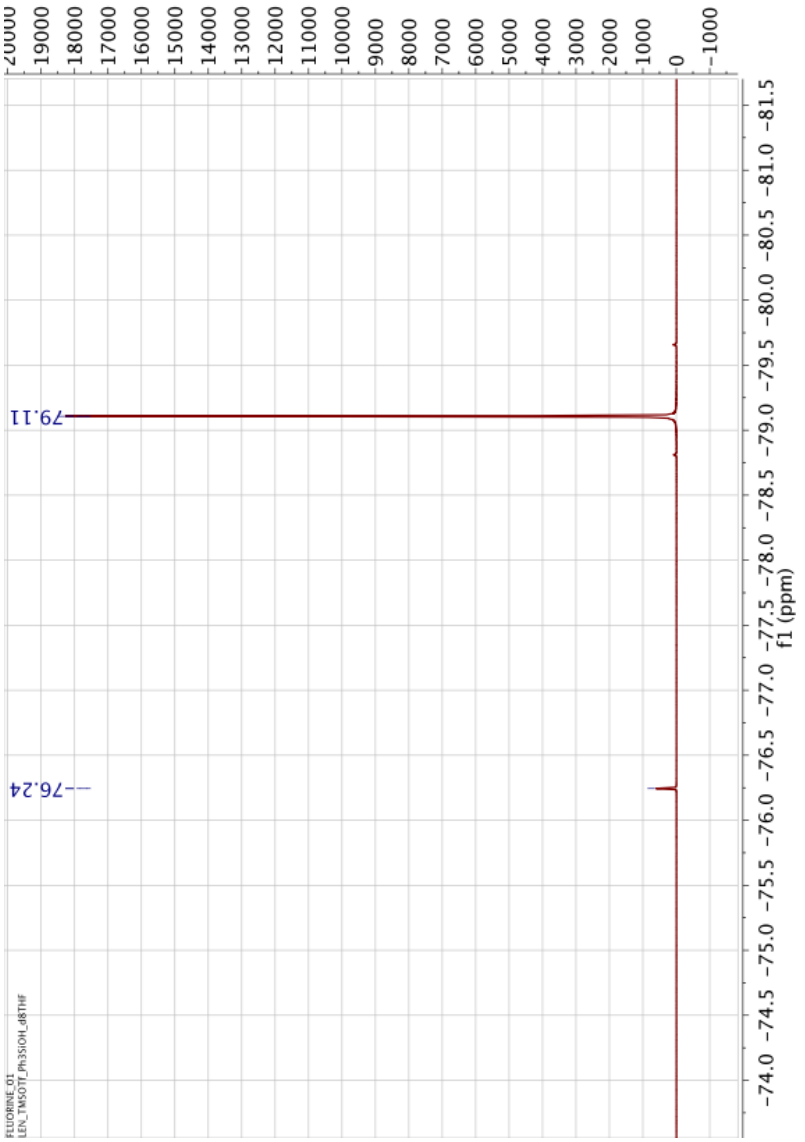

Figure C.6: ^{19}F NMR for H−OTf in d_8-THF

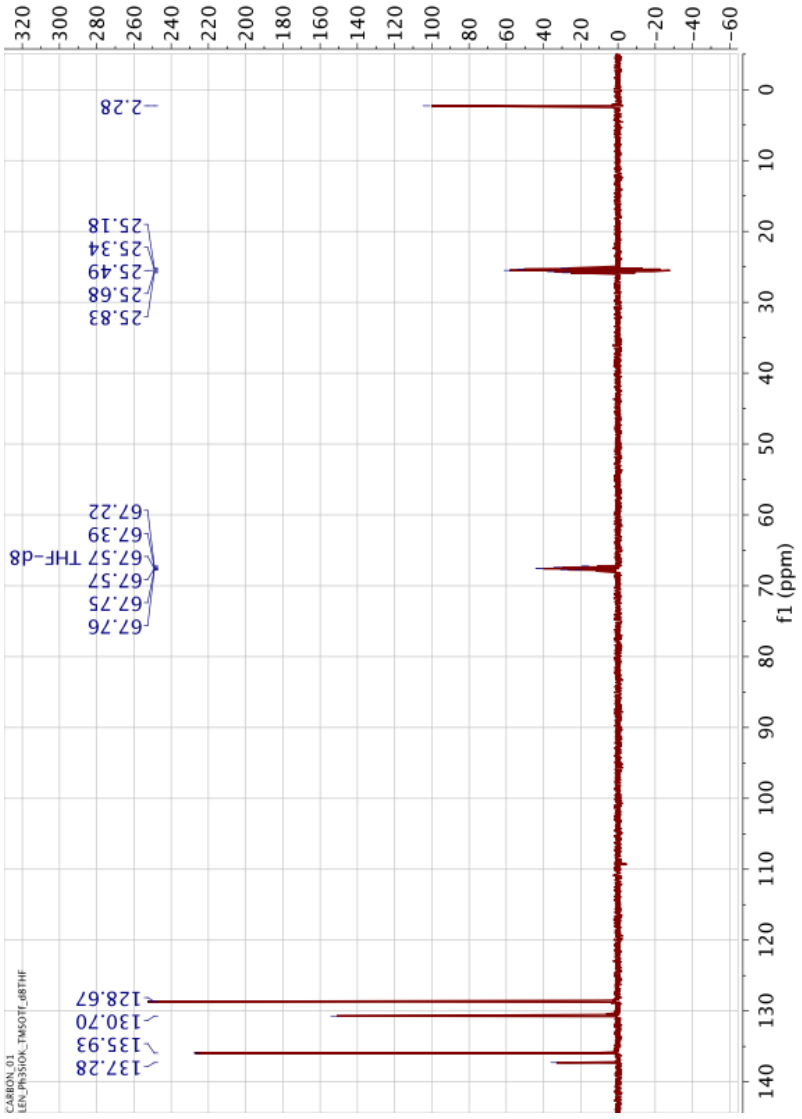

Figure C.7: $^{13}C\{H\}$ NMR for TMS−OSiPh$_3$ and K−OTf in d_8-THF

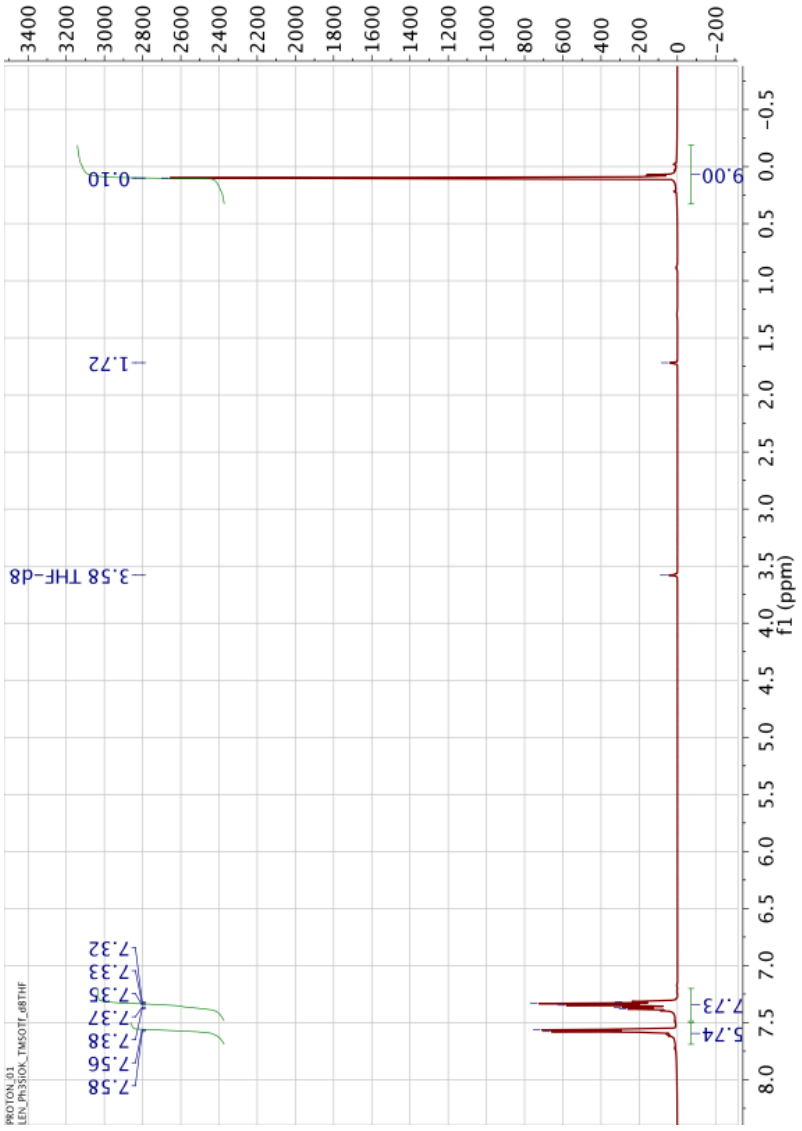

Figure C.8: ^{1}H NMR for TMS−OSiPh$_3$ and K−OTf in d_8-THF

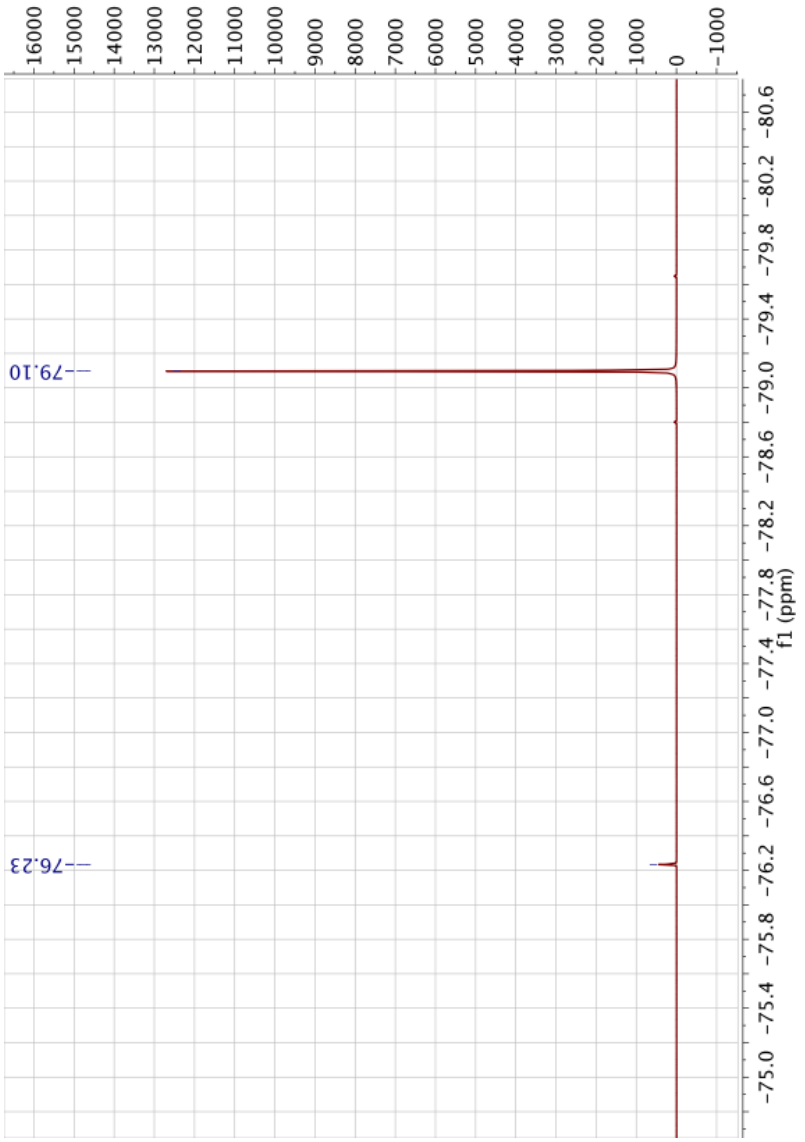

Figure C.9: ^{19}F NMR for K−OTf in d_8-THF

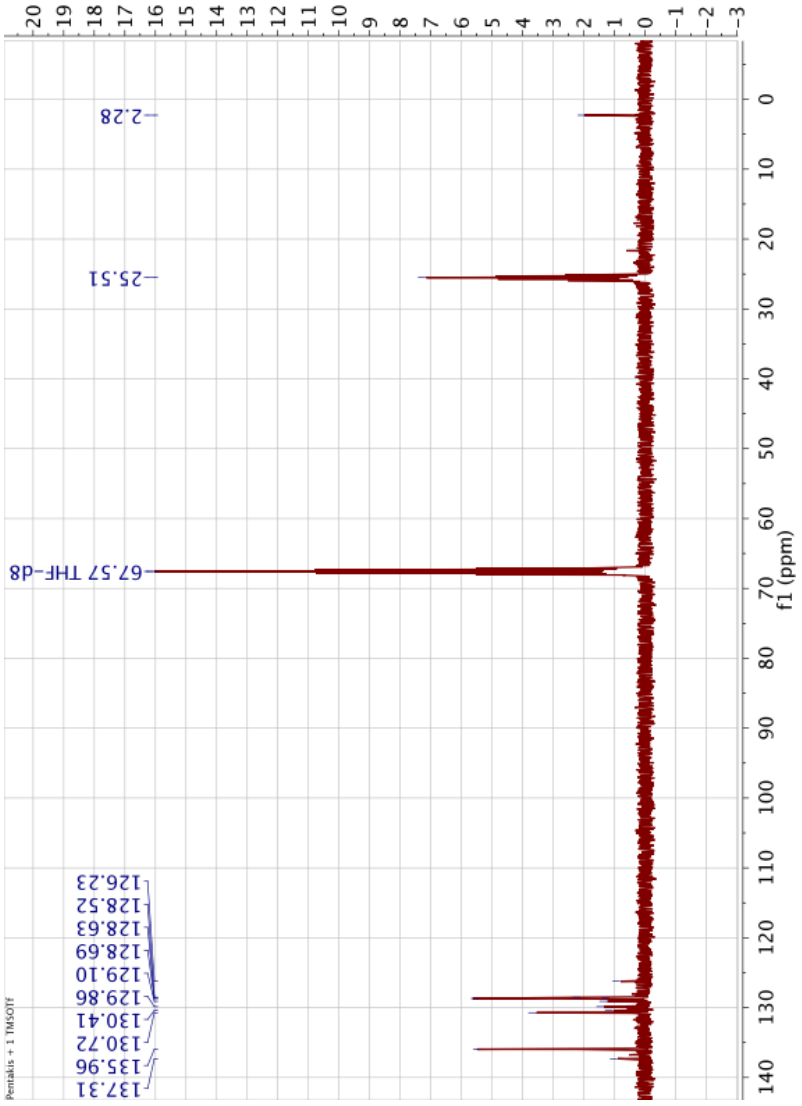

Figure C.10: $^{13}C\{H\}$ NMR for the reaction between $K[(Ph_3SiO)_5U(THF)]$ and 1 eq. TMSOTf in d_8-THF

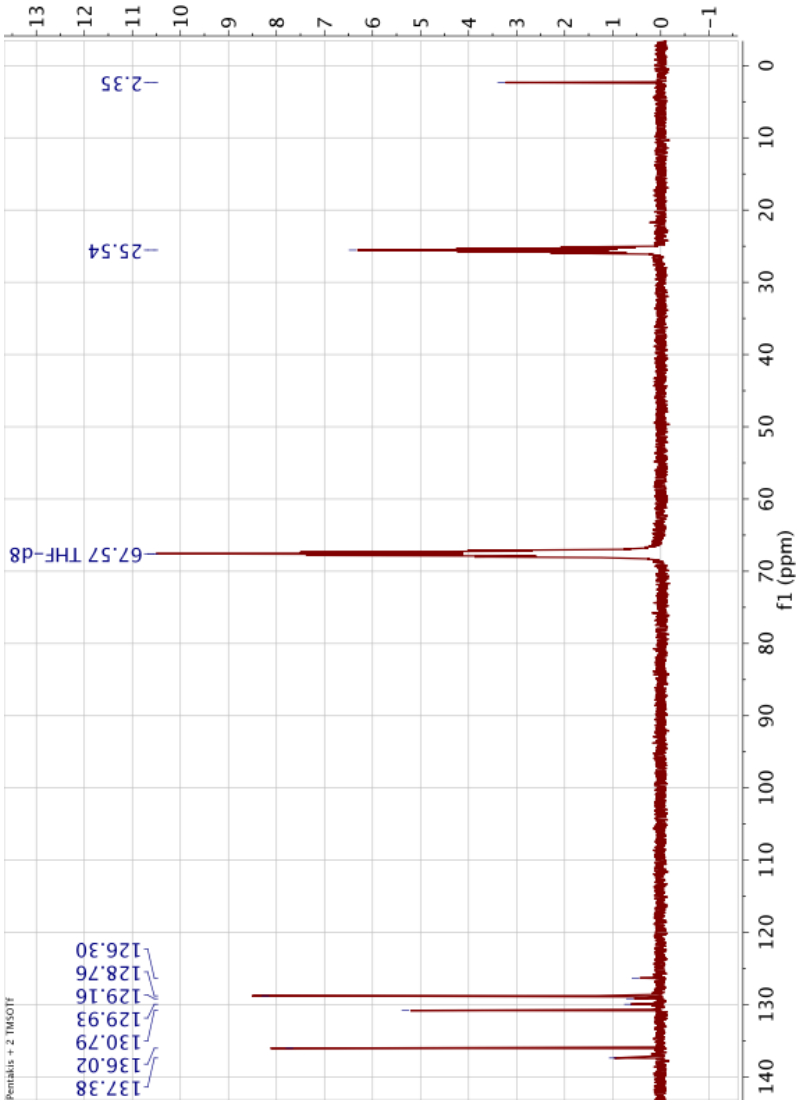

Figure C.11: $^{13}C\{H\}$ NMR for the reaction between $K[(Ph_3SiO)_5U(THF)]$ and 2 eq. TMSOTf in d_8-THF

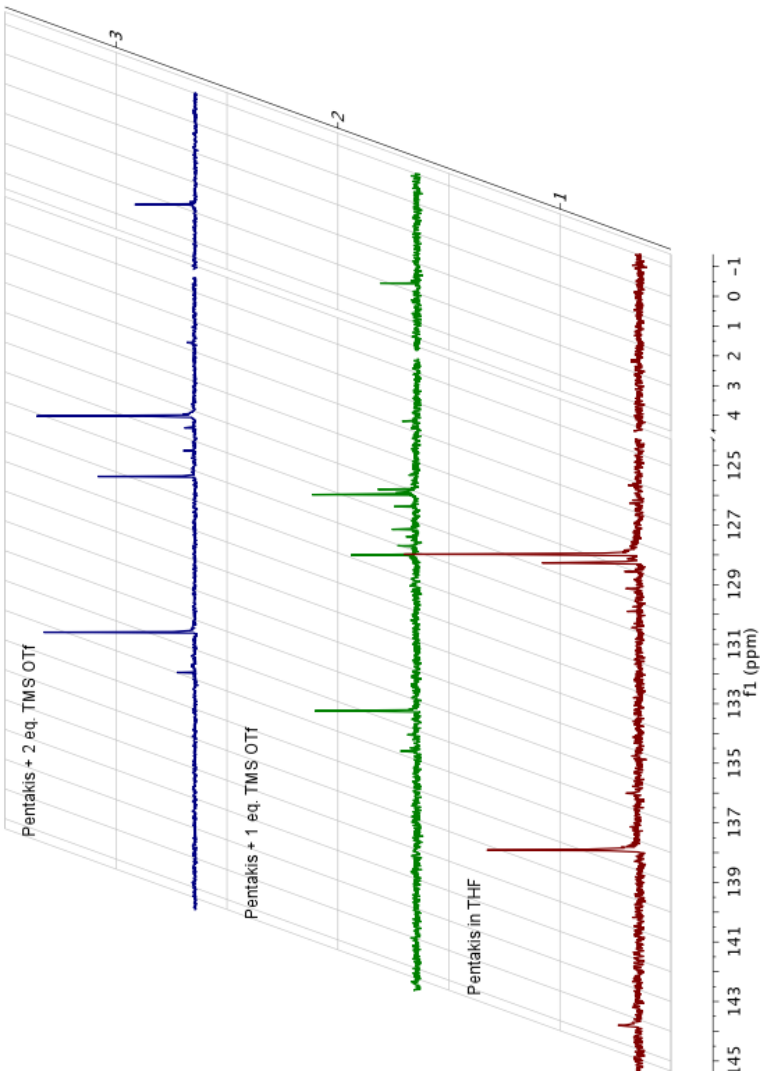

Figure C.12: $^{13}C\{H\}$ NMR of the reaction between $K[(Ph_3SiO)_5U(THF)]$ and 1 and 2 equivalents of TMSOTf

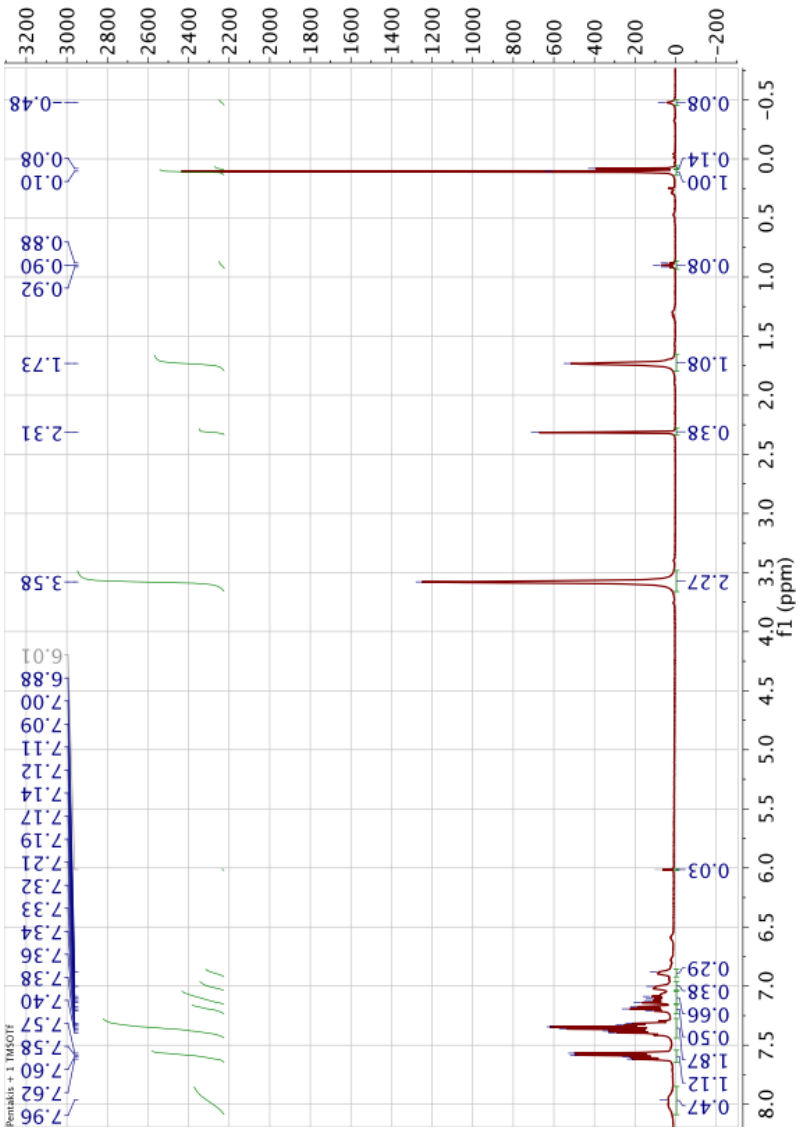

Figure C.13: ^{1}H NMR for the reaction between K[$(Ph_3SiO)_5U(THF)$] and 1 eq. TMSOTf in d_8-THF

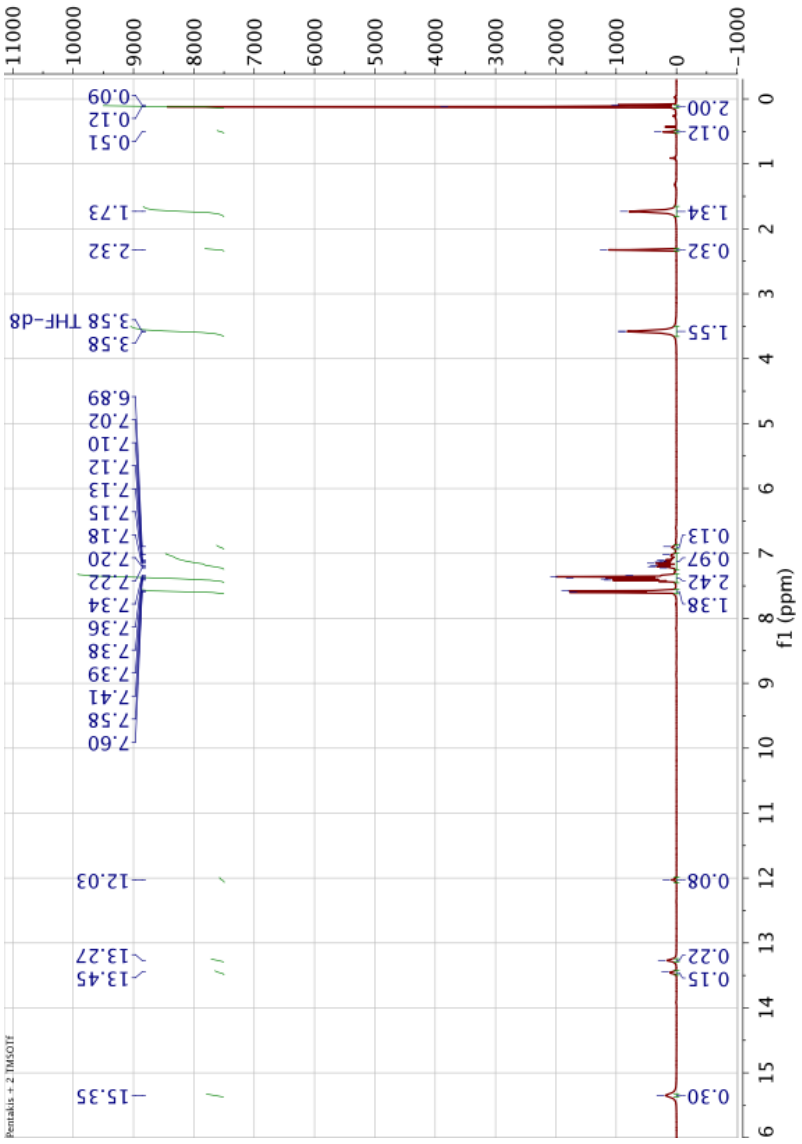

Figure C.14: ^{1}H NMR for the reaction between K[$(Ph_3SiO)_5U(THF)$] and 2 eq. TMSOTf in d_8-THF

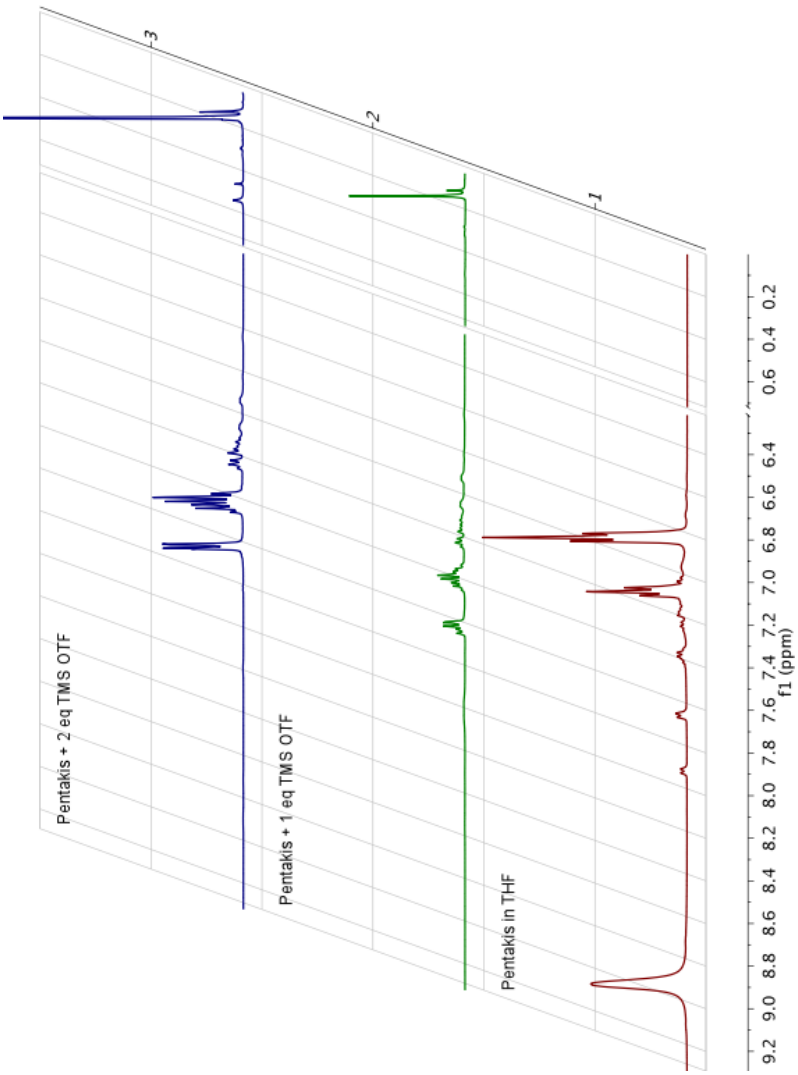

Figure C.15: ^{1}H NMR spectrum of the reaction between K[$(Ph_3SiO)_5U(THF)$] and 1 and 2 equivalents of TMSOTf

Appendix D

NMR spectra - triphenysiloxide ligands reactivity studies

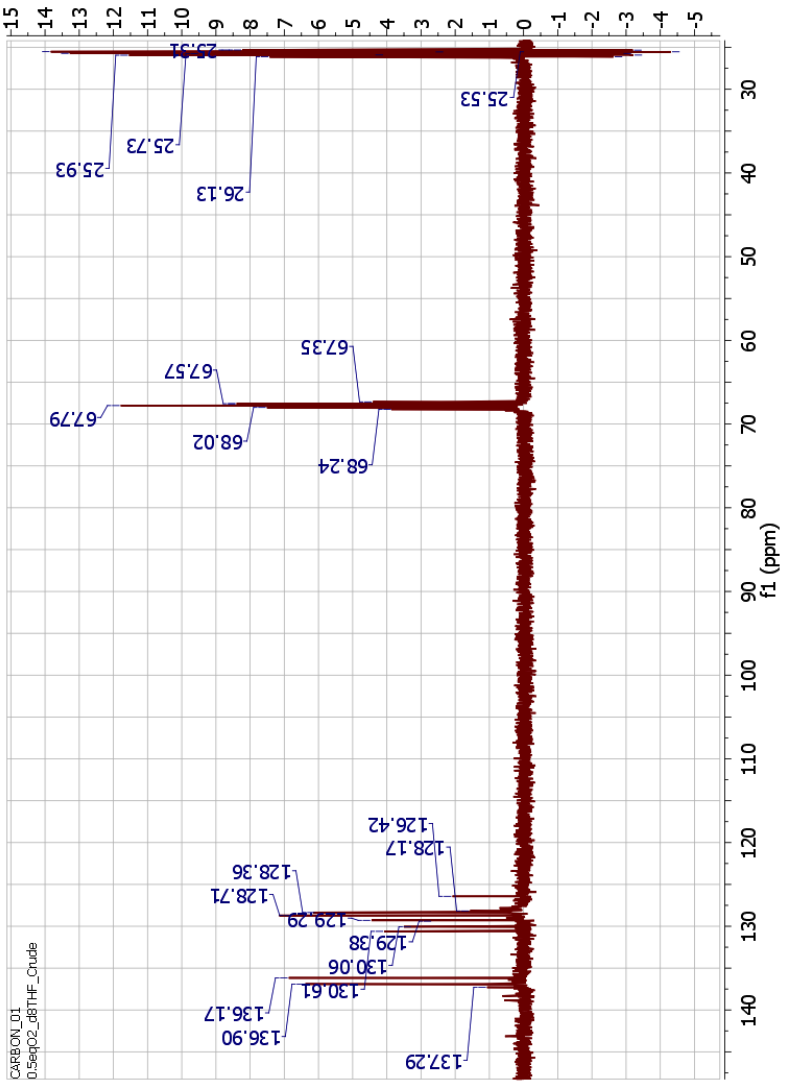

Figure D.1: $^{13}C\{H\}$ NMR for $[K(THF)_2][(Ph_3SiO)_4UO(THF)]$ in d_8-THF

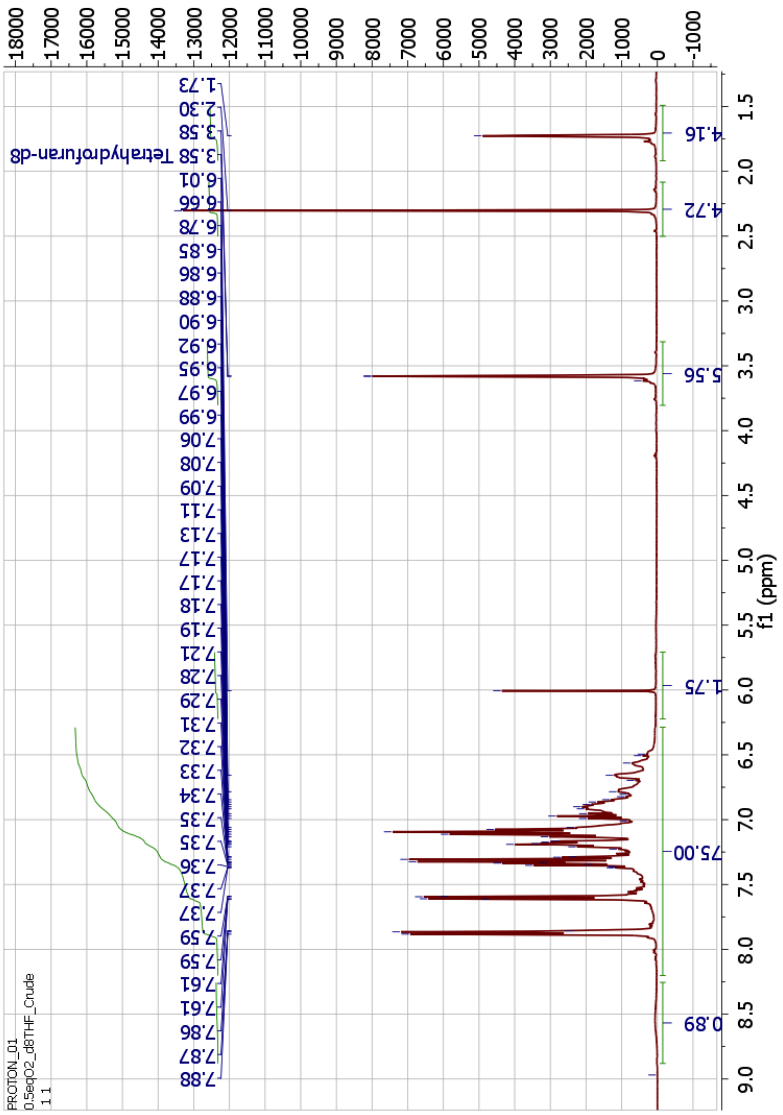

Figure D.2: ^{1}H NMR for $[K(THF)_2][(Ph_3SiO)_4UO(THF)]$ in d_8-THF

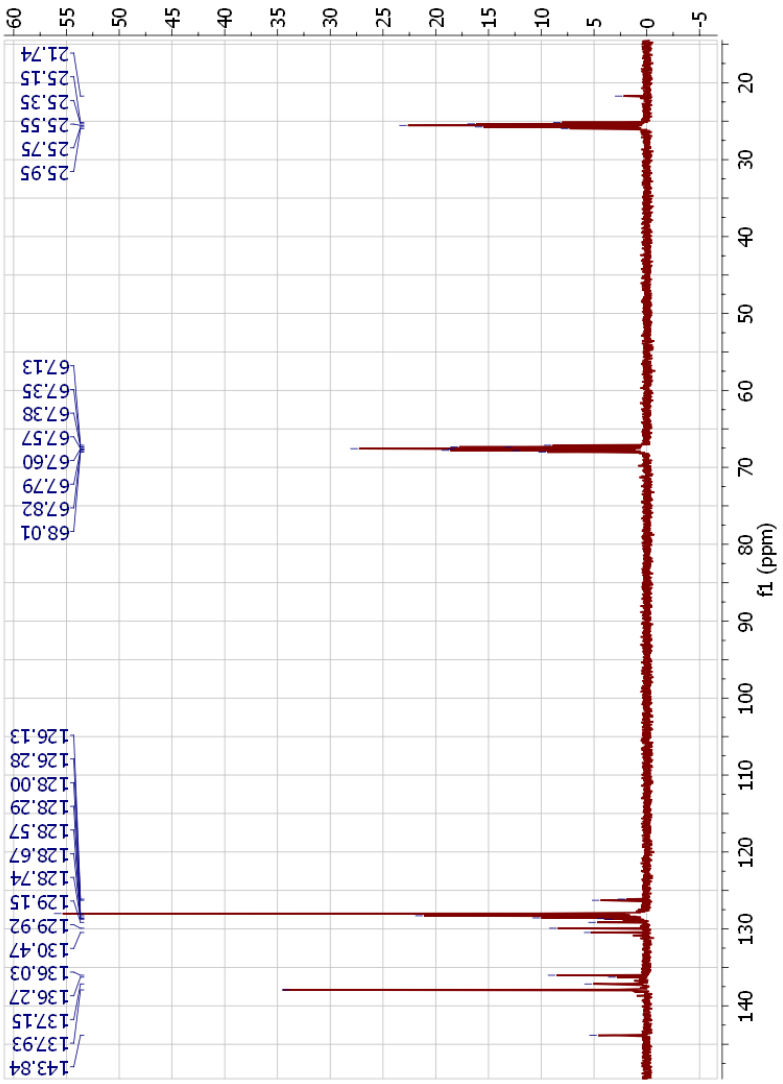

Figure D.3: $^{13}C\{H\}$ NMR for the reaction between K[$(Ph_3SiO)_5U(THF)$] and CO_2 in d_8-THF

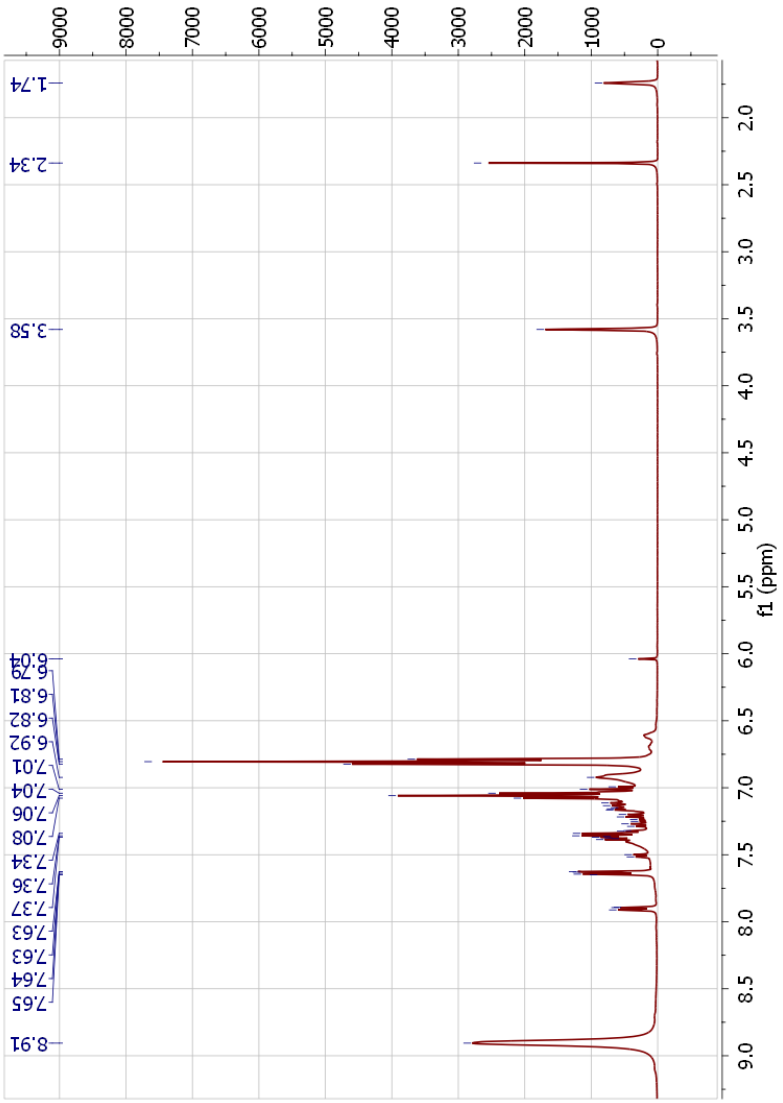

Figure D.4: ^{1}H NMR for for the reaction between K[$(Ph_3SiO)_5U(THF)$] and CO_2 in d_8-THF

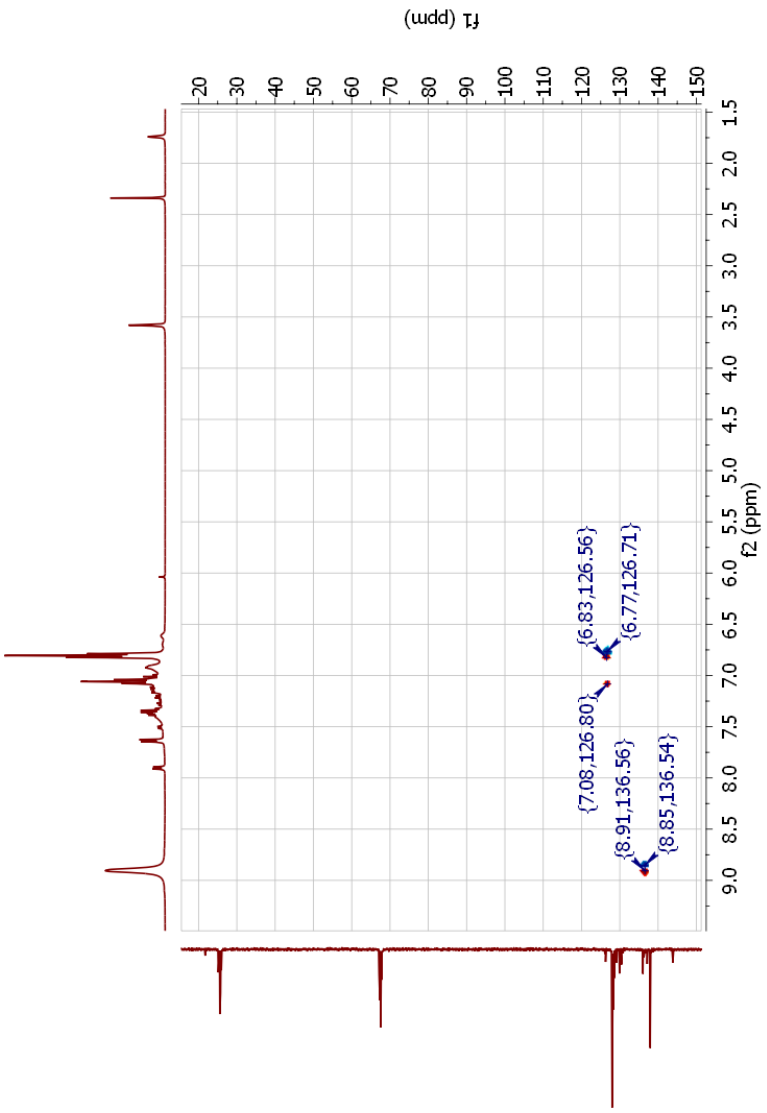

Figure D.5: HSQC NMR for for the reaction between K[$(Ph_3SiO)_5U(THF)$] and CO_2 in d_8-THF

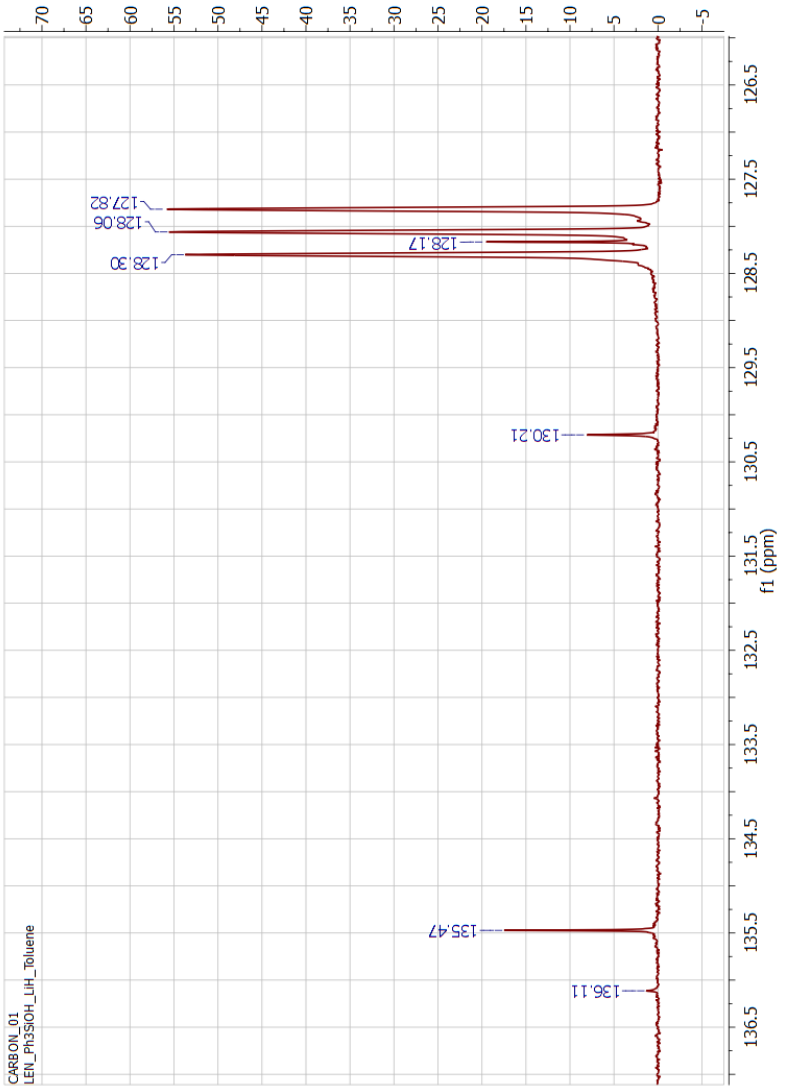

Figure D.6: $^{13}C\{H\}$ NMR for the reaction between Ph_3SiOH and LiH in d_6-benzene

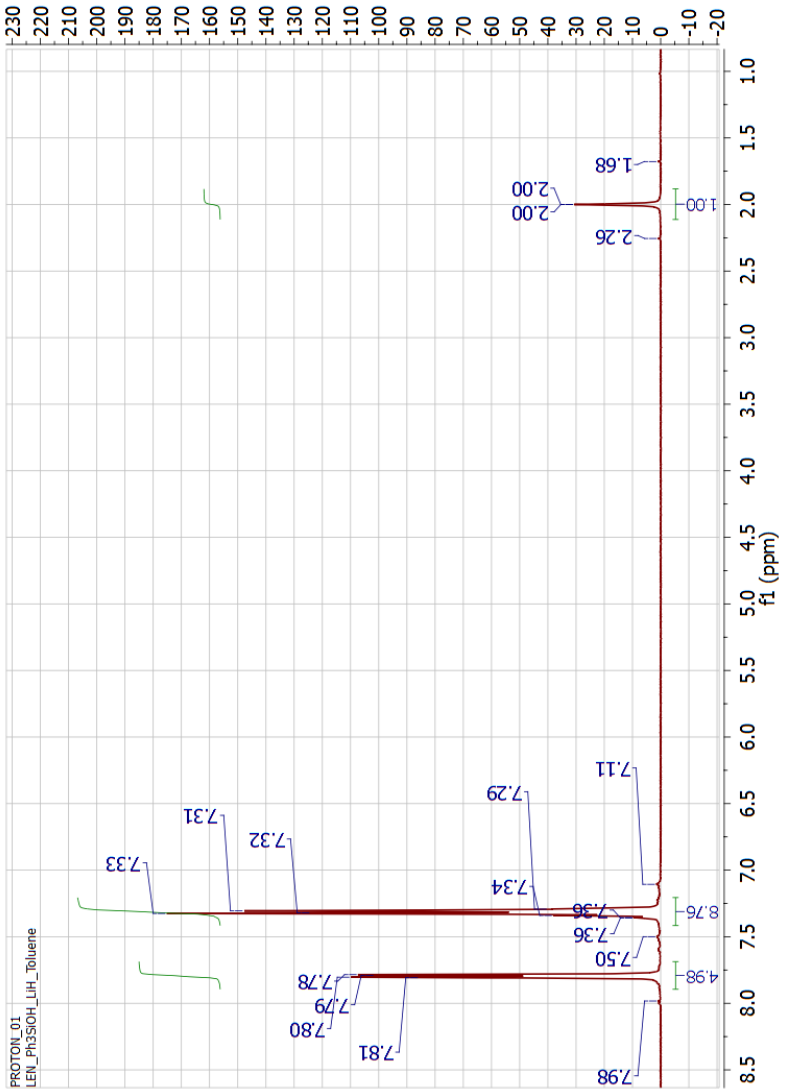

Figure D.7: ^{1}H NMR for the reaction between Ph_3SiOH and LiH in d_6-benzene

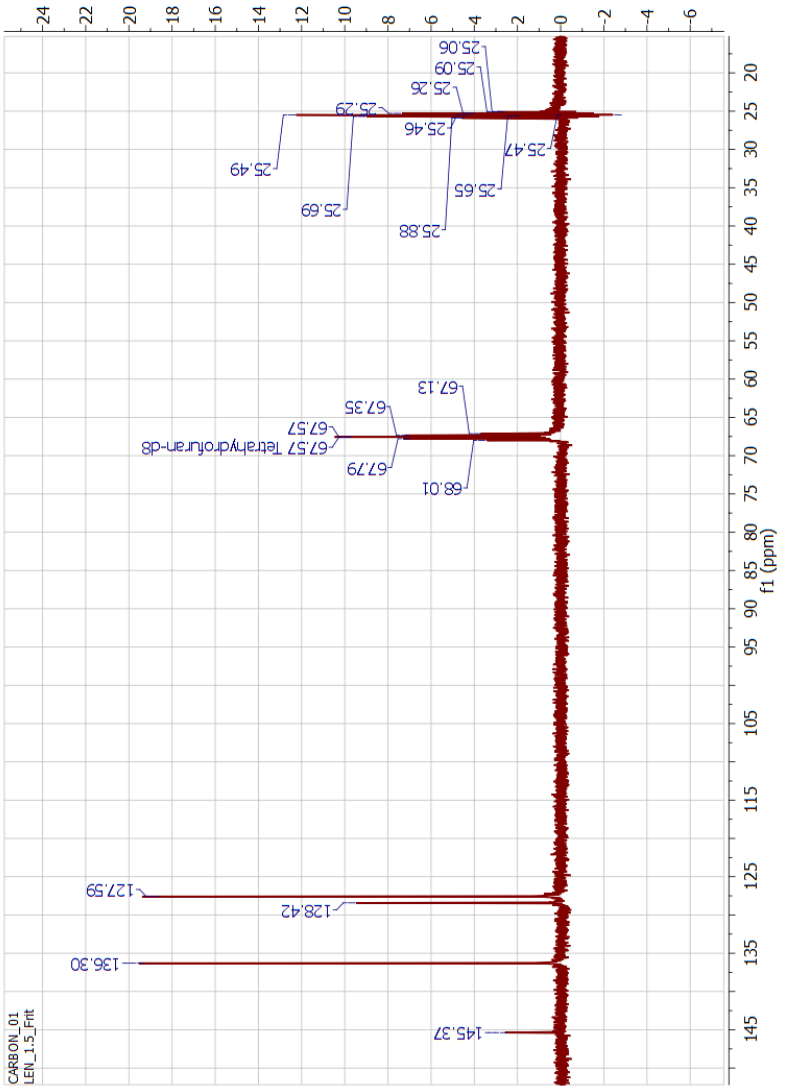

Figure D.8: $^{13}C\{H\}$ NMR for the reaction between Ph_3SiOH and $^{n}BuLi$ in d_8-THF

Figure D.9: ^{1}H NMR for the reaction between Ph_3SiOH and ^{n}BuLi in d_8-THF

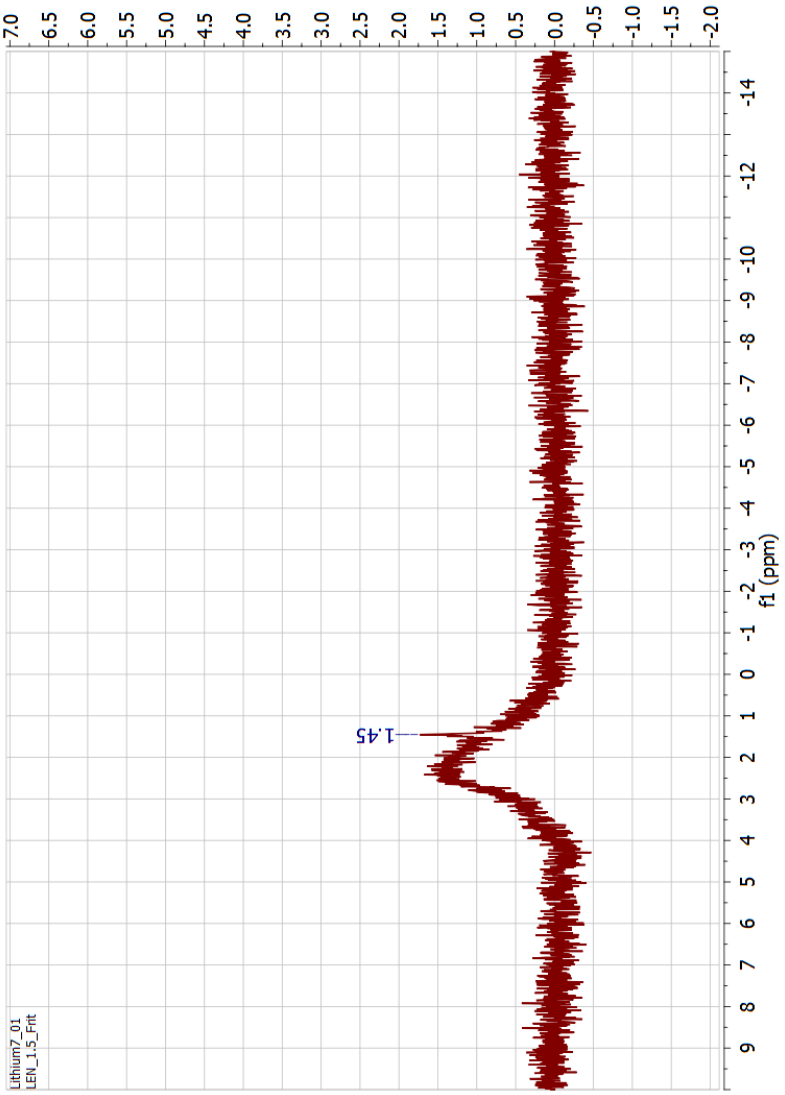

Figure D.10: ^{7}Li NMR for the reaction between Ph_3SiOH and ^{n}BuLi in d_8-THF

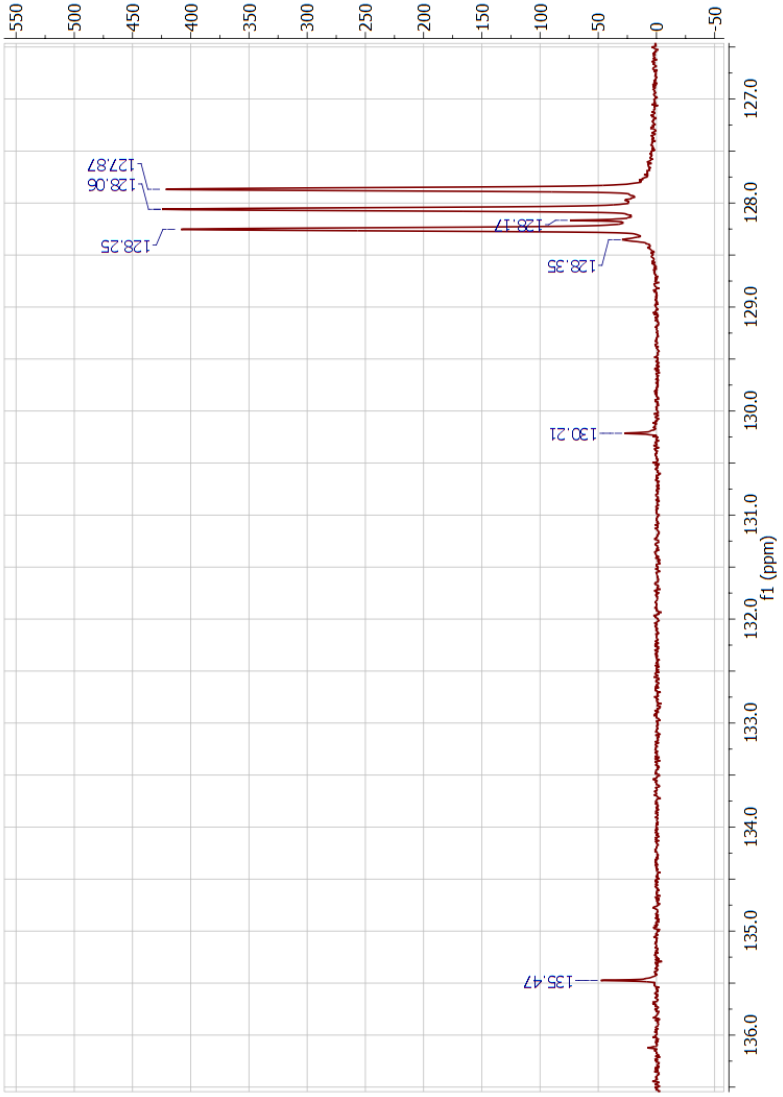

Figure D.11: $^{13}C\{H\}$ NMR for the reaction between Ph_3SiOH and NaH in d_6-benzene

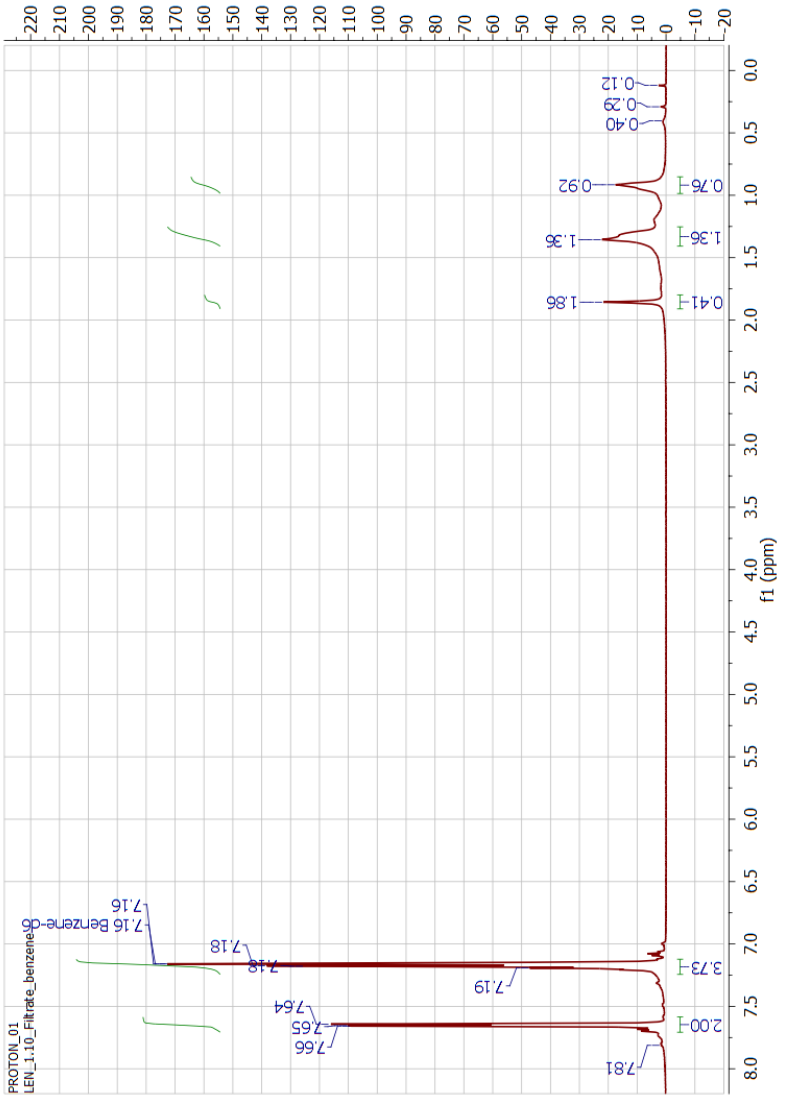

Figure D.12: ^{1}H NMR for the reaction between Ph_3SiOH and NaH in d_6-benzene

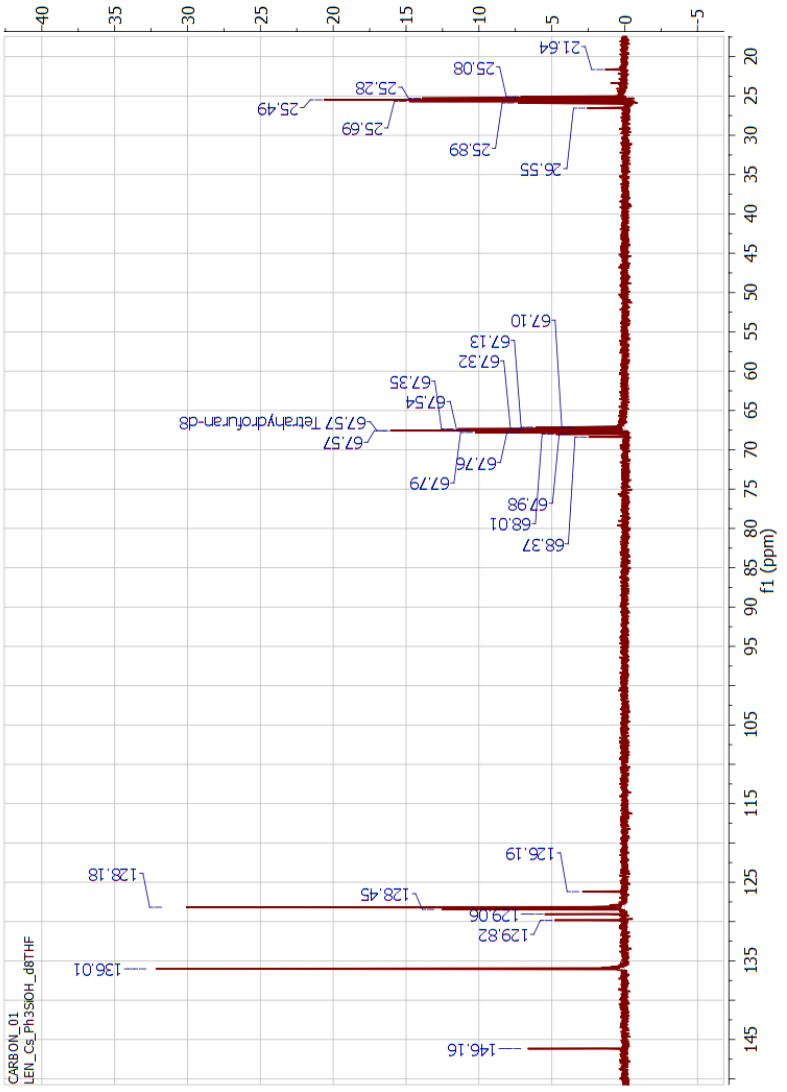

Figure D.13: $^{13}C\{H\}$ NMR for the reaction between Ph_3SiOH and Cs in d_8-THF

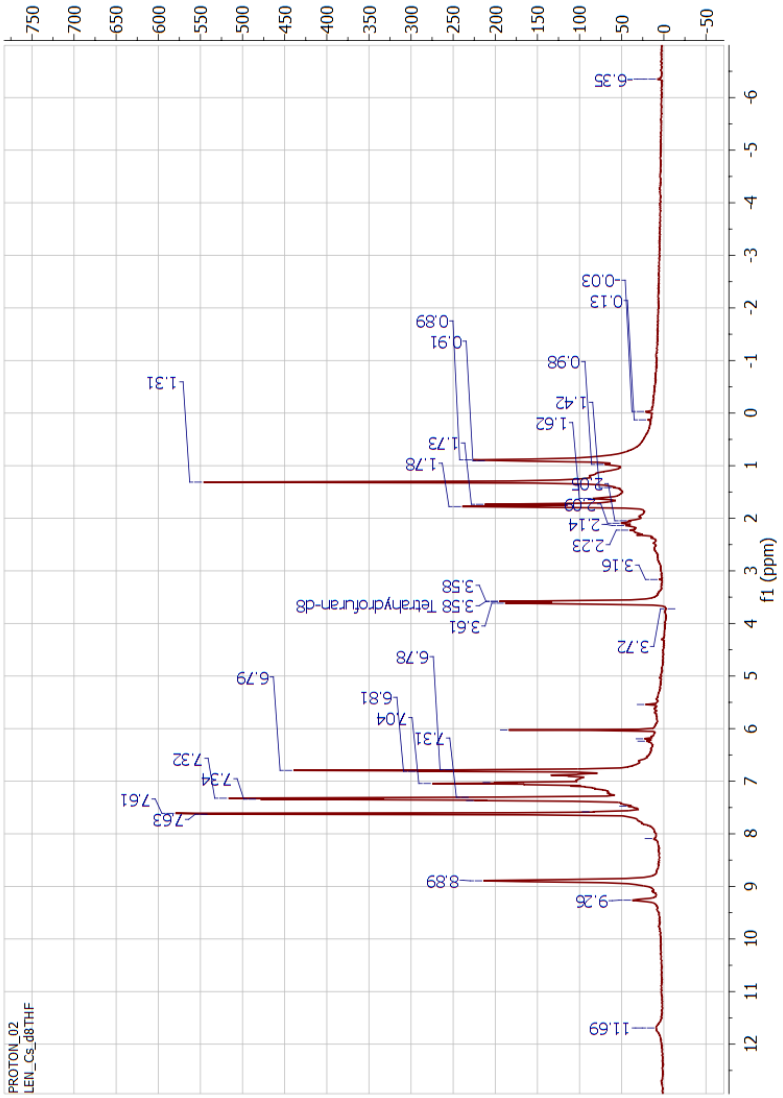

Figure D.14: ^{1}H NMR for the reaction between Ph_3SiOH and Cs in d_8-THF

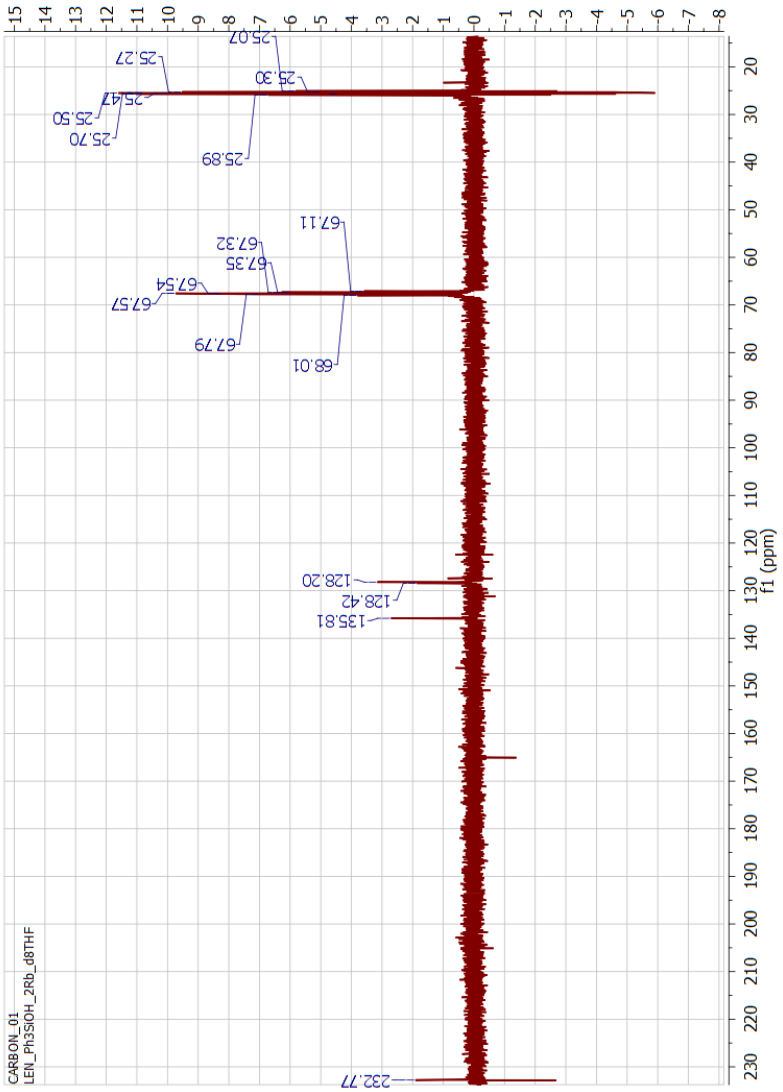

Figure D.15: $^{13}C\{H\}$ NMR for the reaction between Ph_3SiOH and Rb in d_8-THF

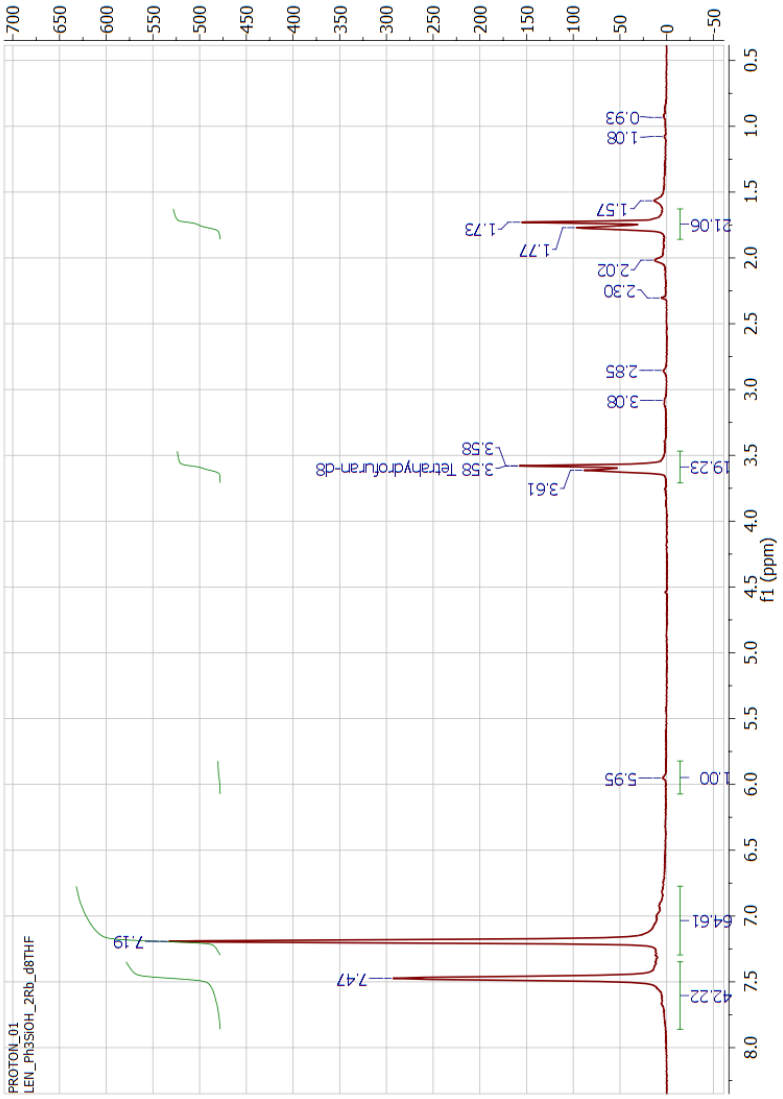

Figure D.16: ^{1}H NMR for the reaction between Ph_3SiOH and Rb in d_8-THF

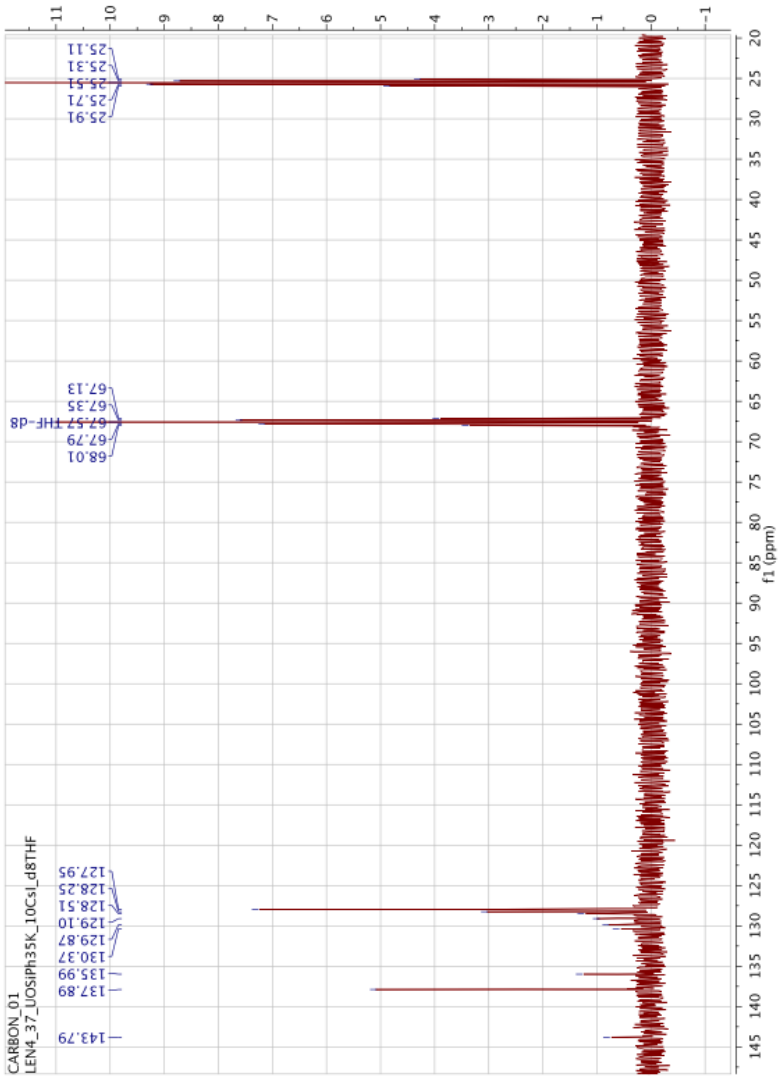

Figure D.17: $^{13}C\{H\}$ NMR for the reaction between K[$(Ph_3SiO)_5U(THF)$] and CsI in d_8-THF

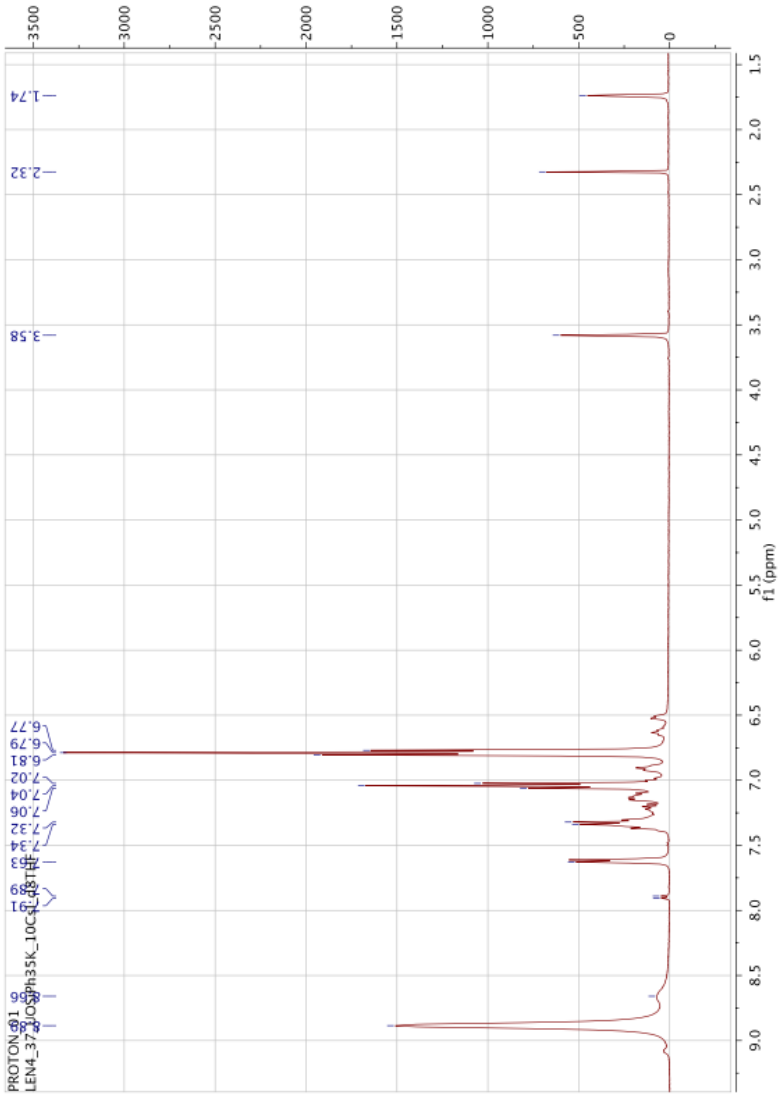

Figure D.18: ^{1}H NMR for for the reaction between K[$(Ph_3SiO)_5U(THF)$] and CsI in d_8-THF

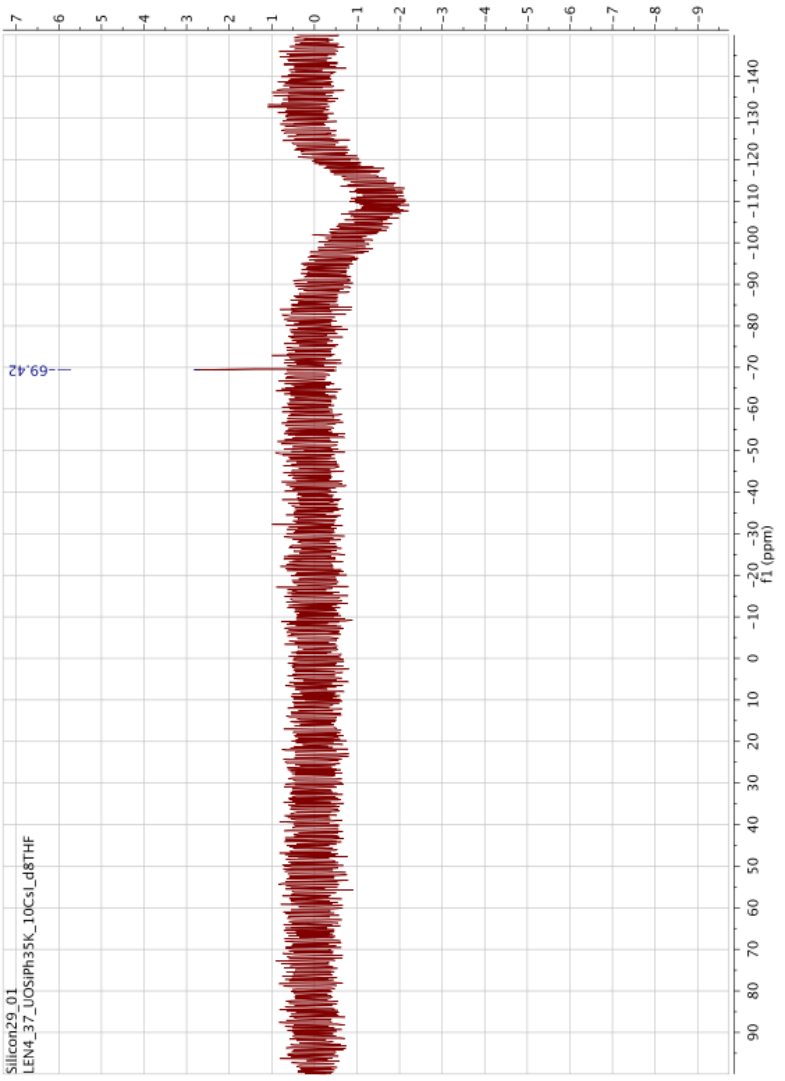

Figure D.19: ^{29}Si NMR for for the reaction between K[$(Ph_3SiO)_5U(THF)$] and CsI in d_8-THF

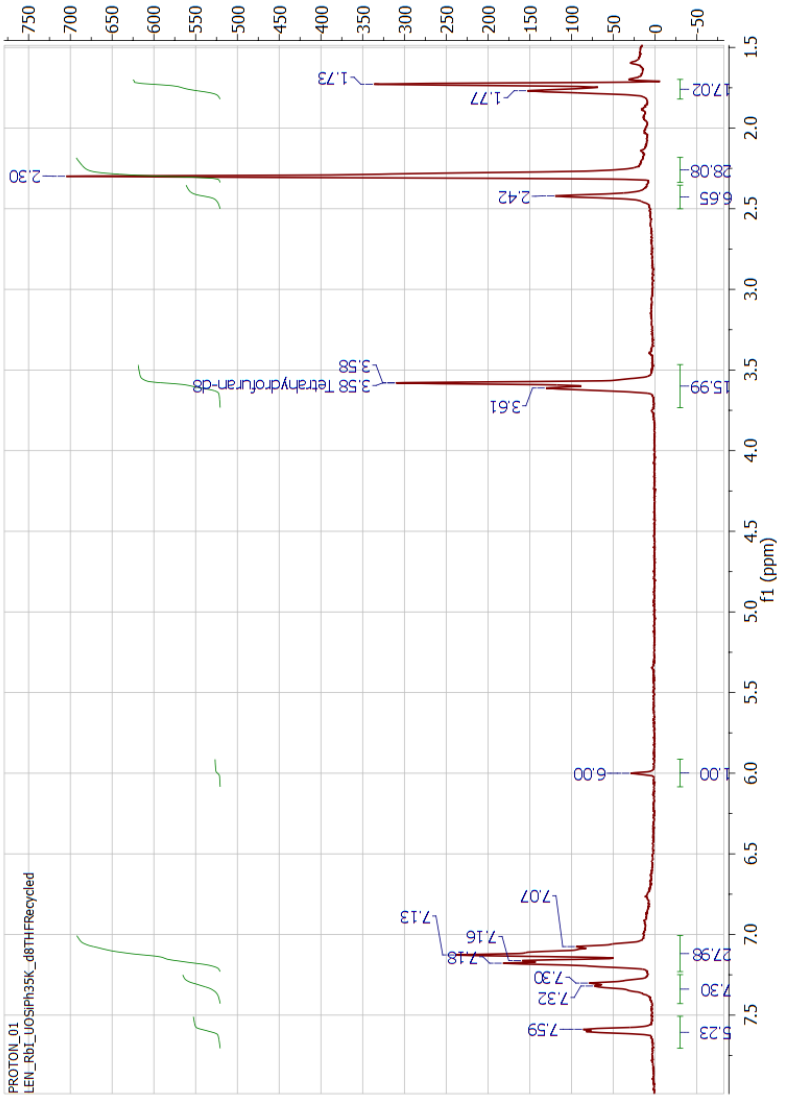

Figure D.20: ^{1}H NMR for the reaction between K[$(Ph_3SiO)_5U(THF)$] and RbI in d_8-THF

Appendix E

NMR spectra - tris *(tert)*-butoxide ligands

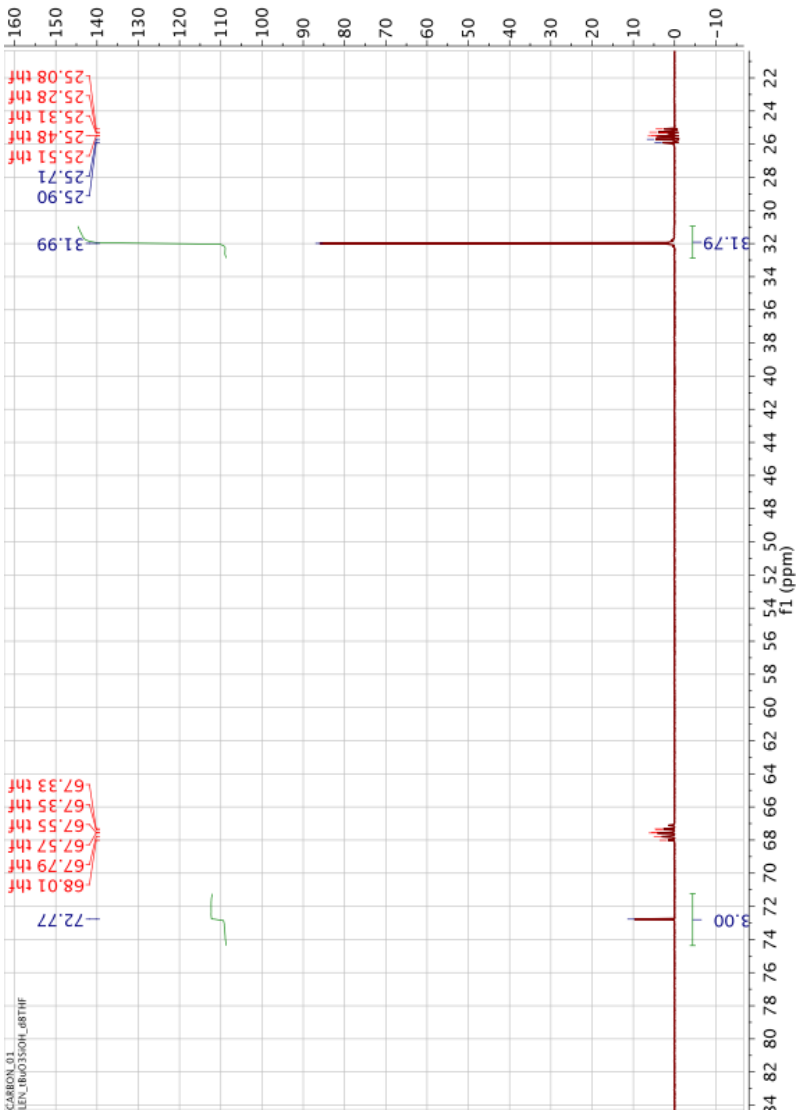

Figure E.1: $^{13}C\{H\}$ NMR for Tris *tert*-butoxy silanol in d_8-THF

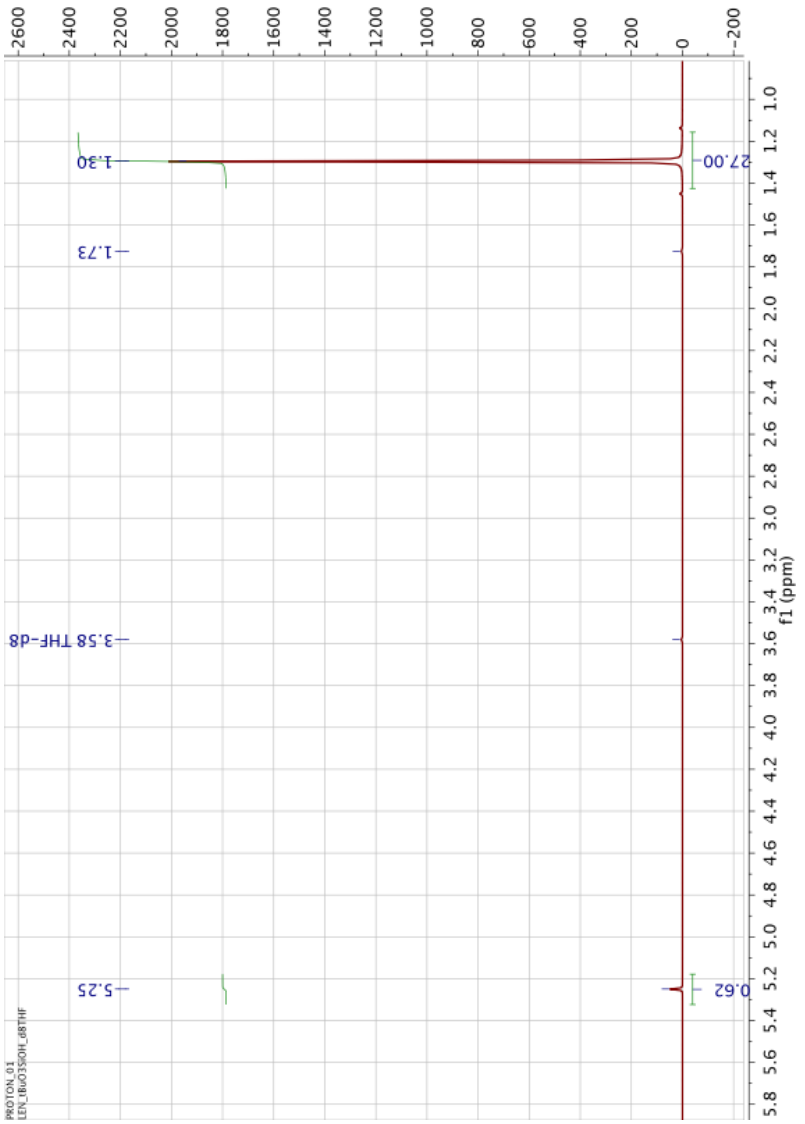

Figure E.2: ^{1}H NMR for Tris *tert*-butoxy silanol in d_8-THF

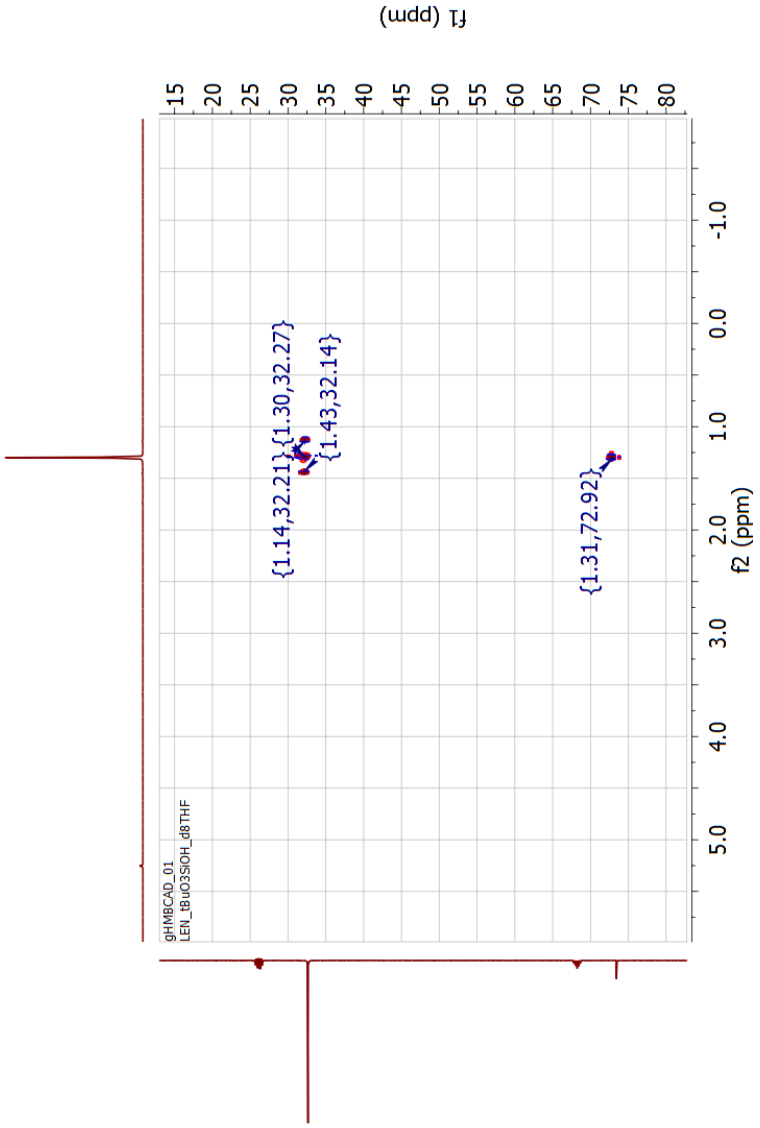

Figure E.3: HMBC NMR for Tris *tert*-butoxy silanol in d_8-THF

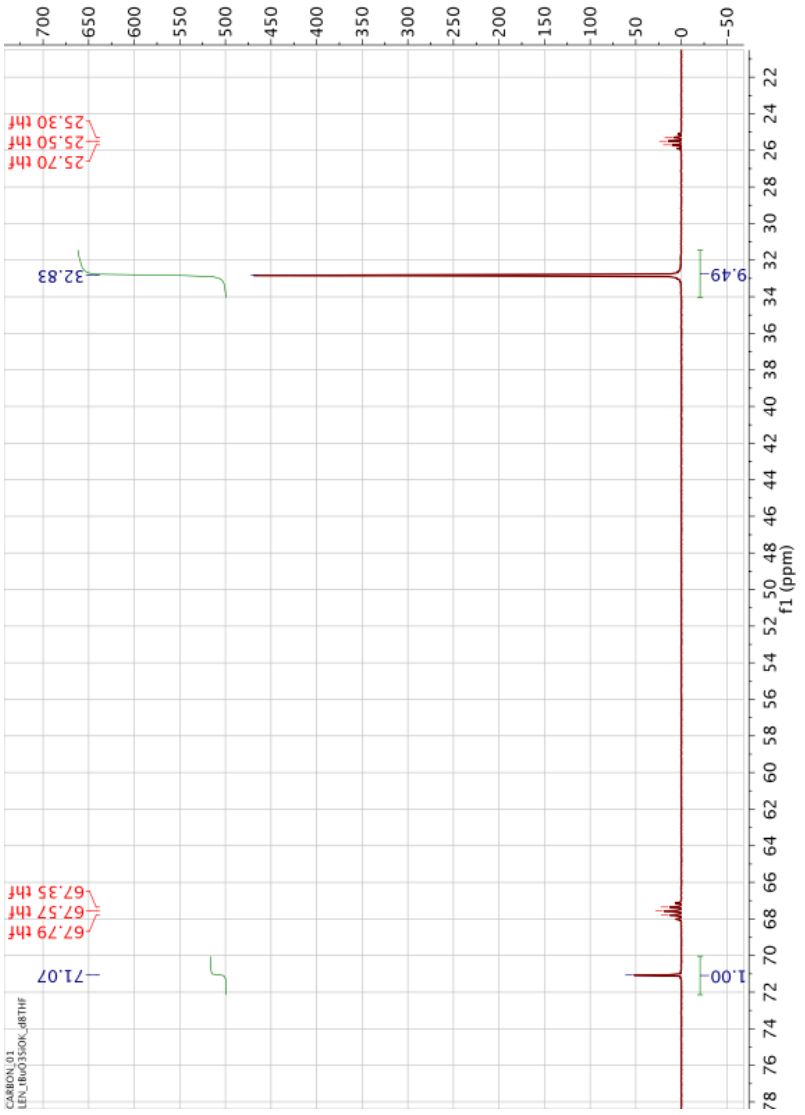

Figure E.4: $^{13}C\{H\}$ NMR for Tris *tert*-butoxy siloxide in d_8-THF

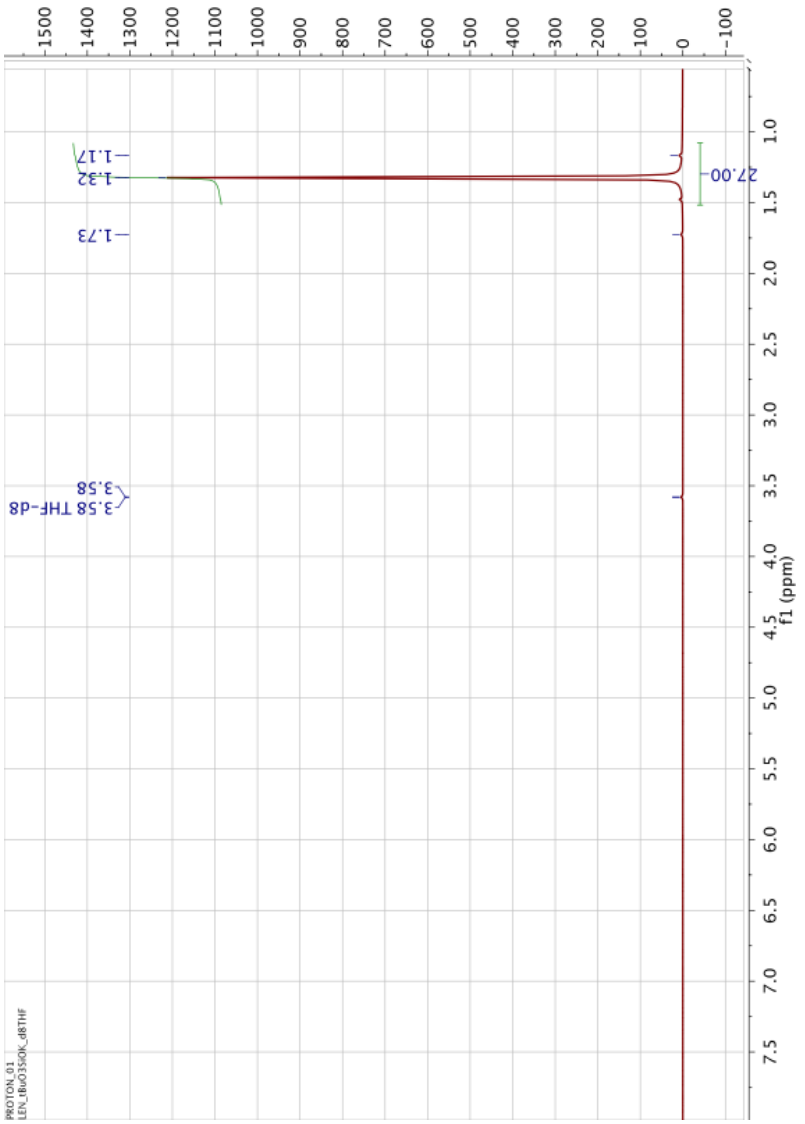

Figure E.5: ^{1}H NMR for Tris *tert*-butoxy siloxide in d_8-THF

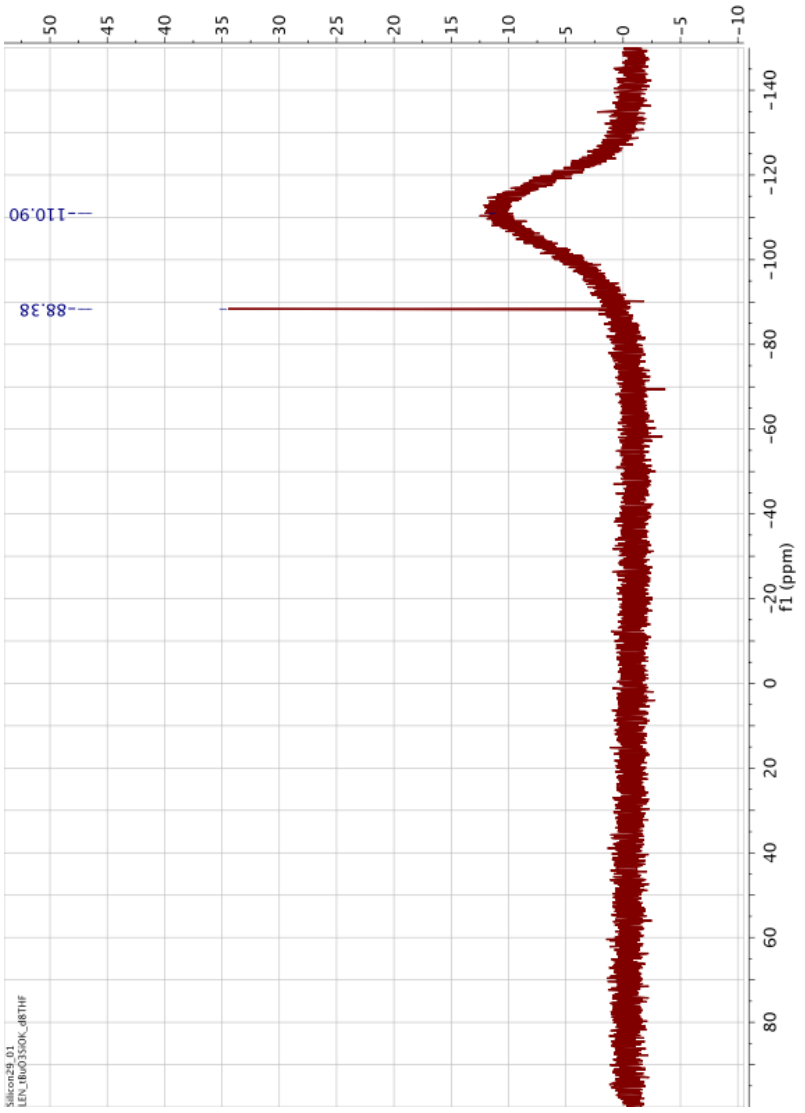

Figure E.6: ^{29}Si NMR for Tris *tert*-butoxy siloxide in d_8-THF

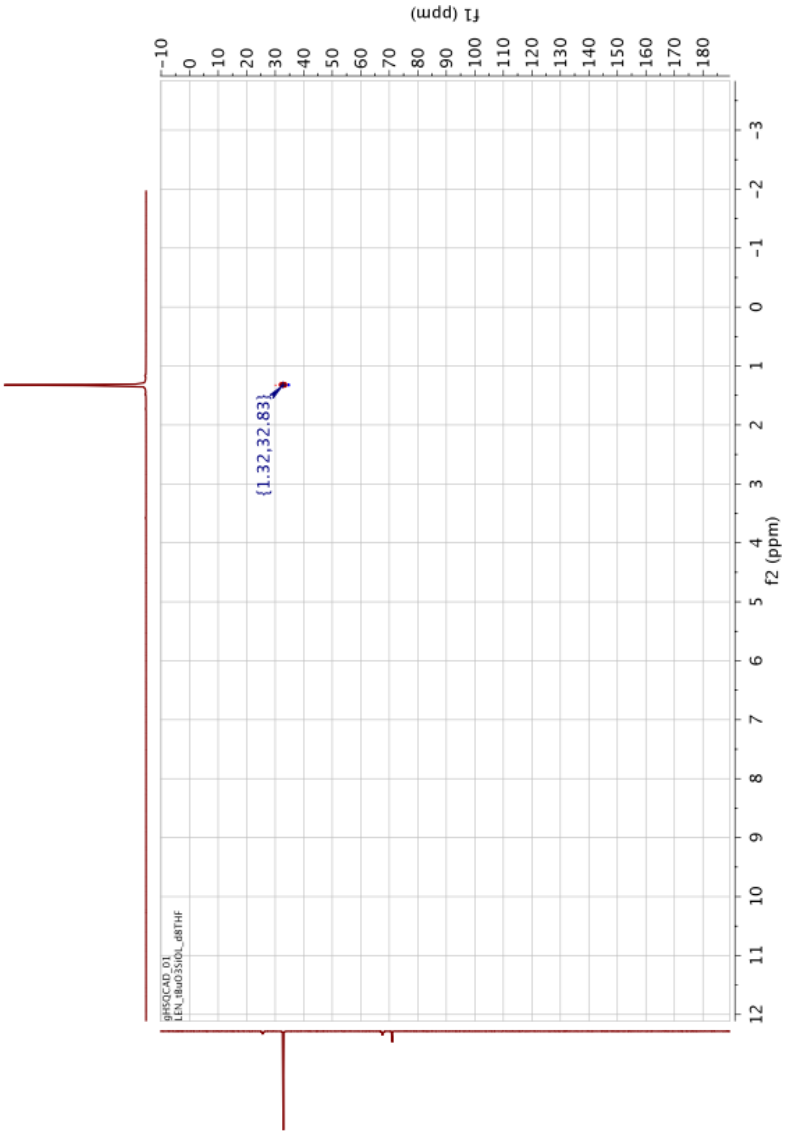

Figure E.7: HSQC NMR for Tris *tert*-butoxy siloxide in d_8-THF

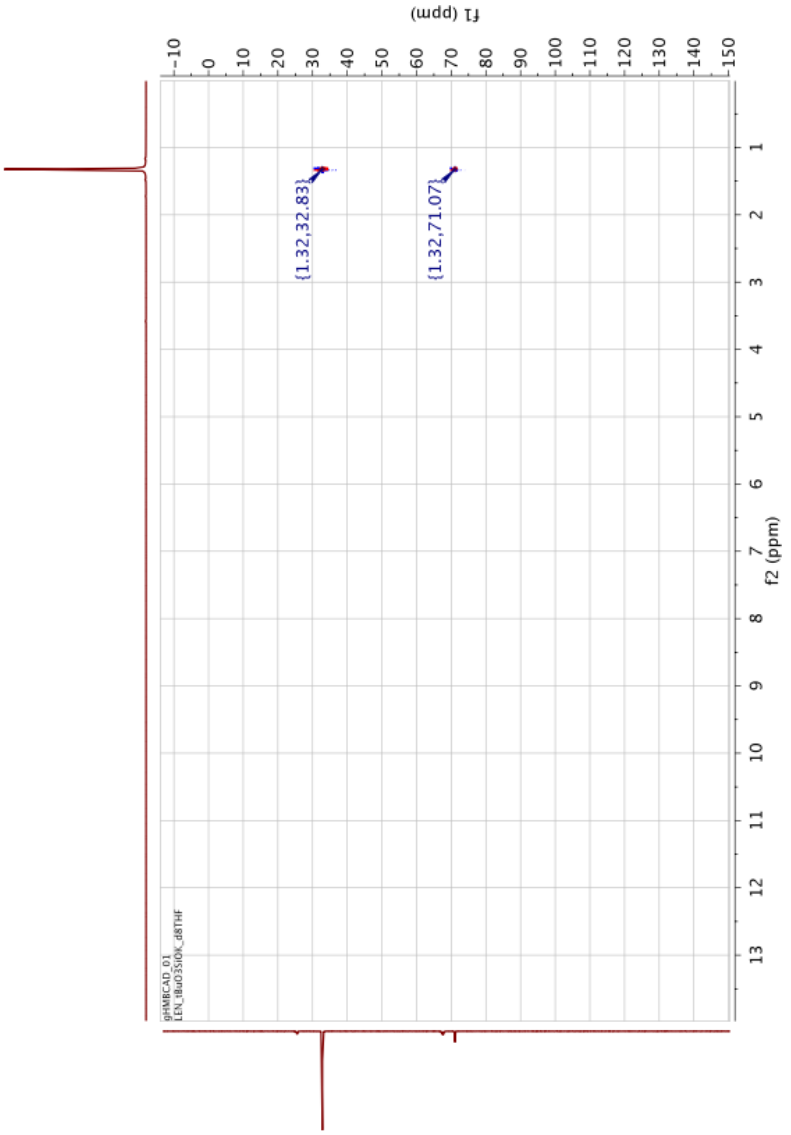

Figure E.8: HMBC NMR for Tris *tert*-butoxy siloxide in d_8-THF

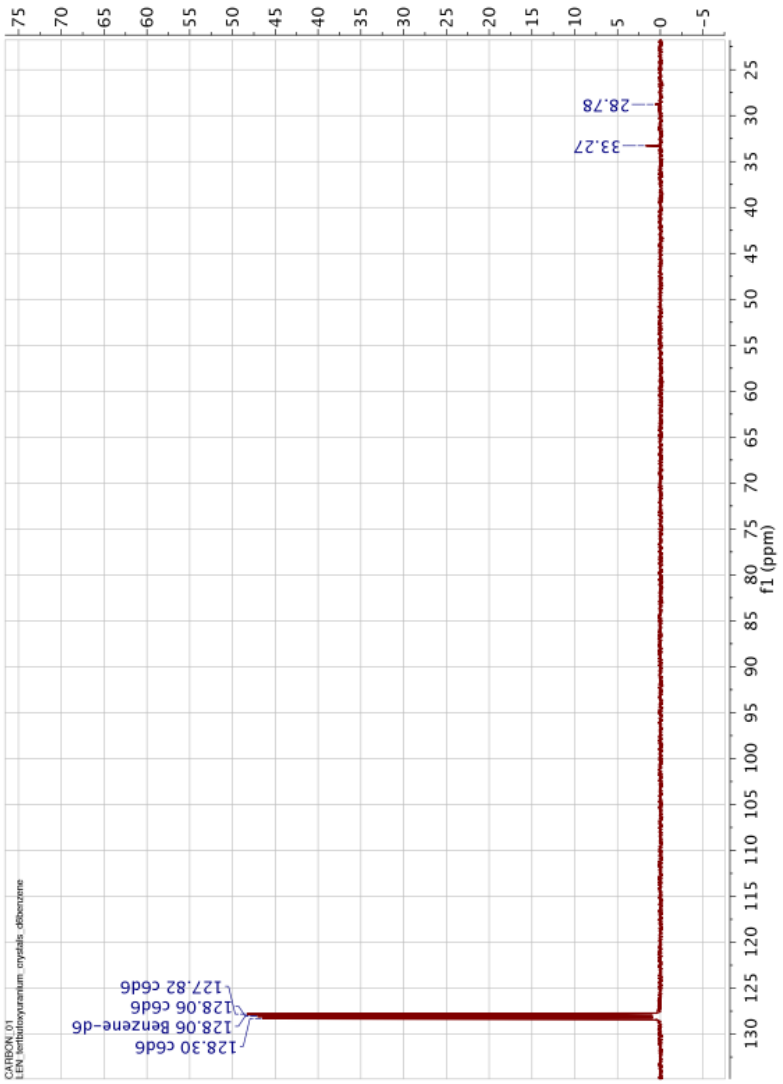

Figure E.9: $^{13}C\{H\}$ NMR for the inverted sandwich complex K[(U(OSi(O^{t}Bu)$_3$)$_3$)$_2$($\mu-\eta^6$:η^6-tol))] in d_6-Benzene

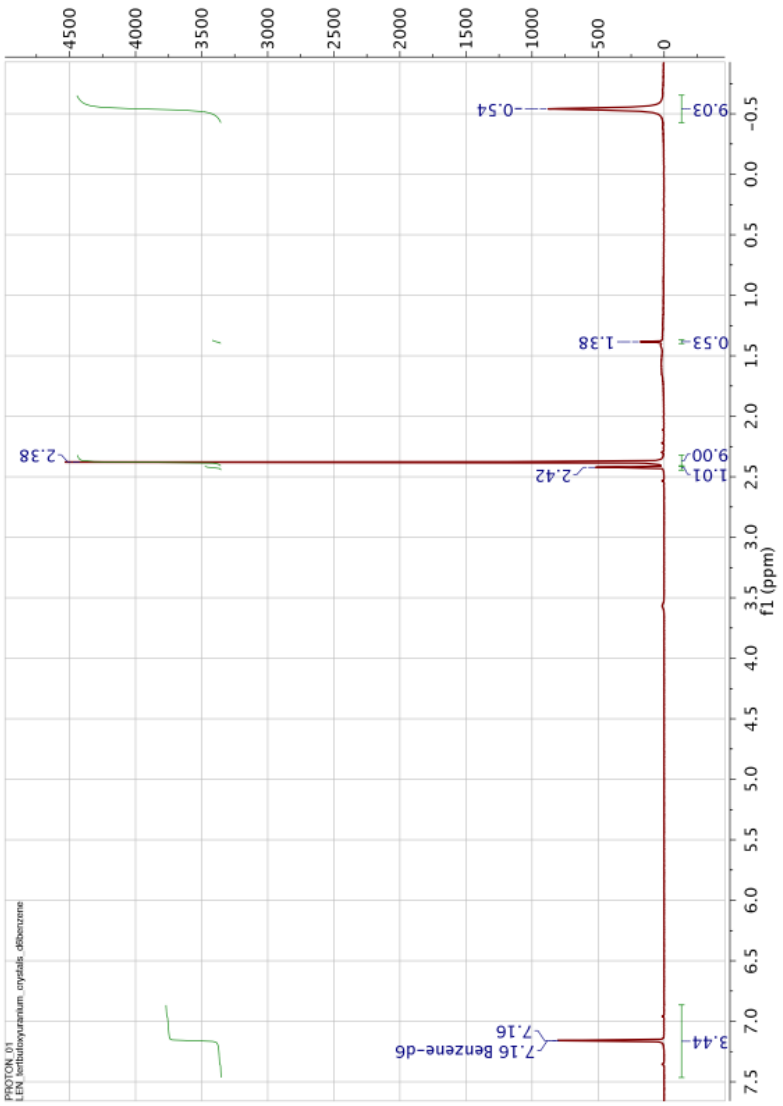

Figure E.10: ^{1}H NMR for the inverted sandwich complex K[(U(OSi(O^{t}Bu)$_3$)$_3$)$_2$($\mu-\eta^6$:η^6-tol))] in d_6-Benzene

Figure E.11: ^{29}Si NMR for the inverted sandwich complex K[(U(OSi(O^{t}Bu)$_3$)$_3$)$_2$(μ–η^6:η^6-tol))] in d_6-Benzene

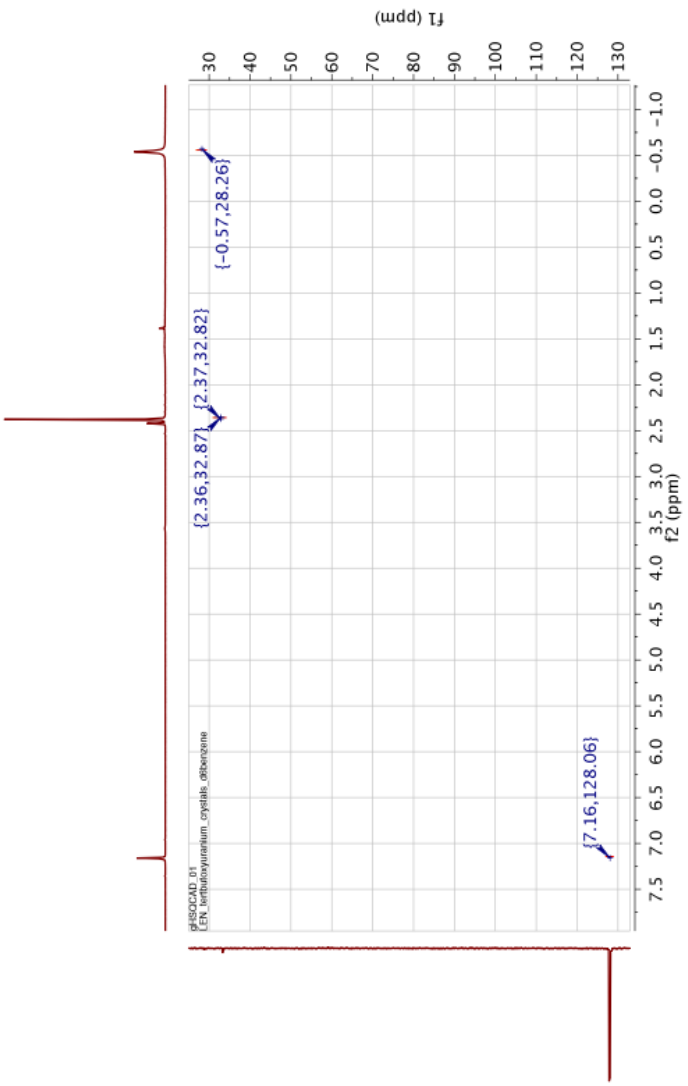

Figure E.12: HSQC NMR for the inverted sandwich complex K[(U(OSi(O^{t}Bu)$_3$)$_3$)$_2$($\mu-\eta^6:\eta^6$-tol))] in d_6-Benzene

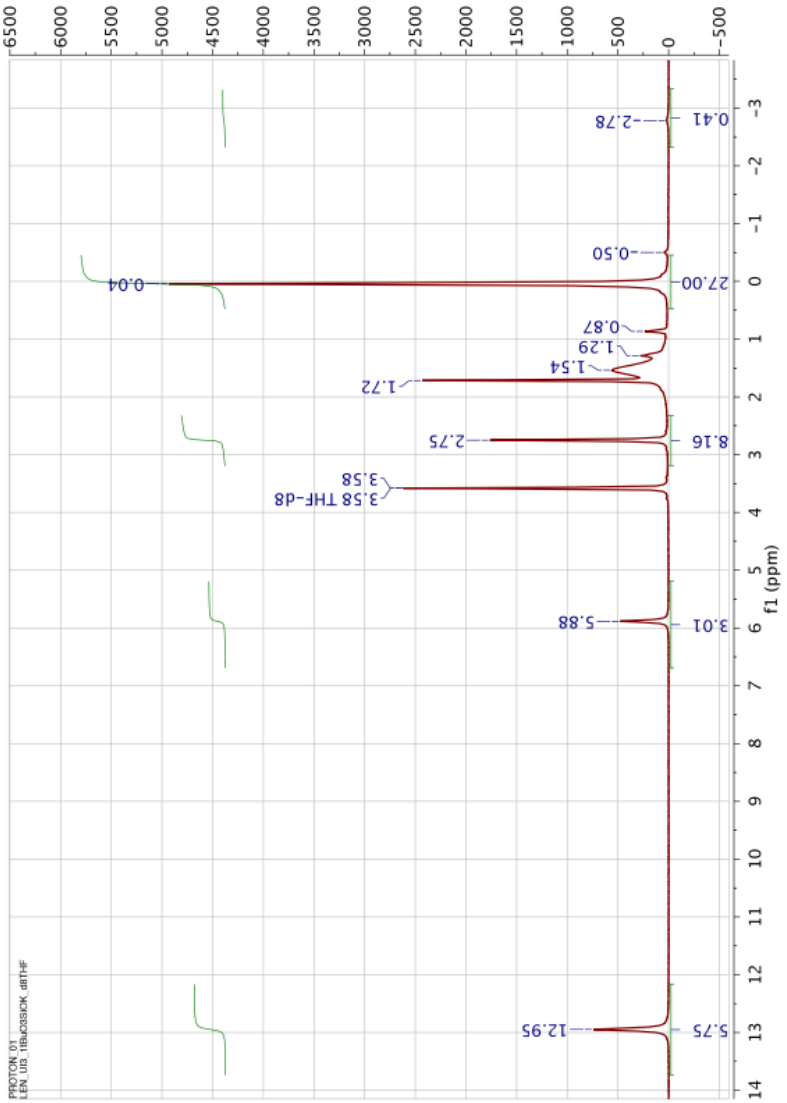

Figure E.13: ^{1}H NMR for the reaction between 1 eq. $(O^{t}Bu)_3SiOK$ and UI_3 in d_8-THF

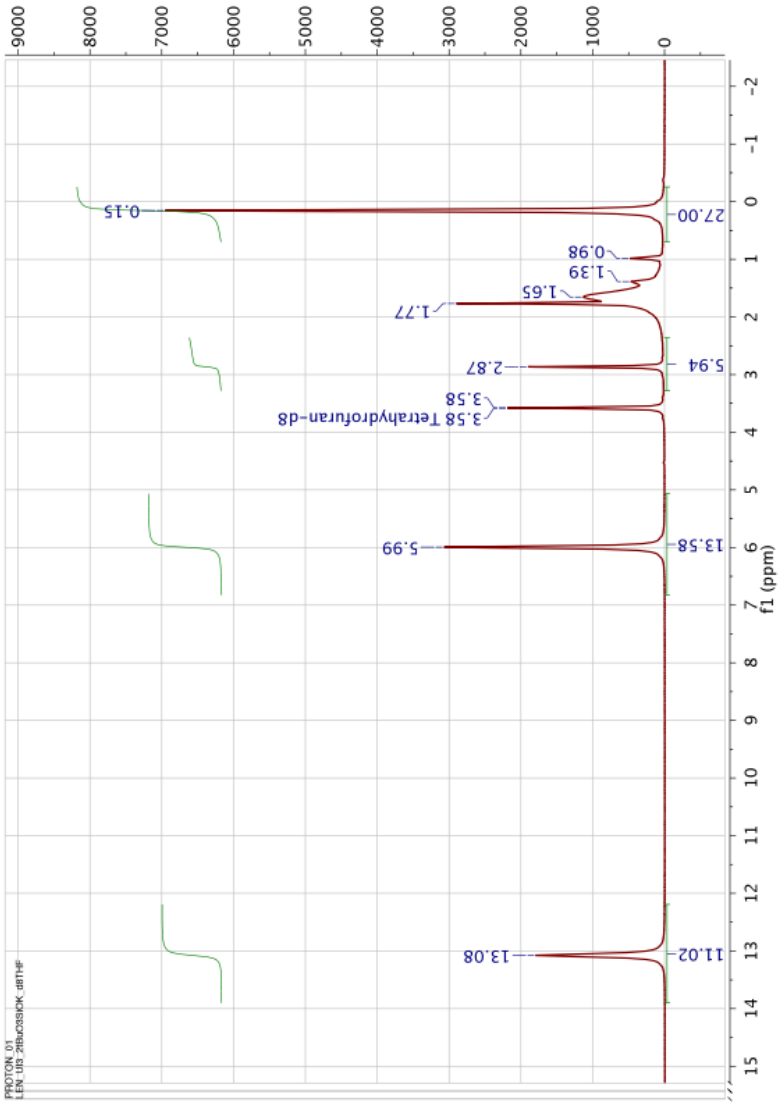

Figure E.14: ^{1}H NMR for the reaction between 2 eq. $(O^{t}Bu)_3SiOK$ and UI_3 in d_8-THF

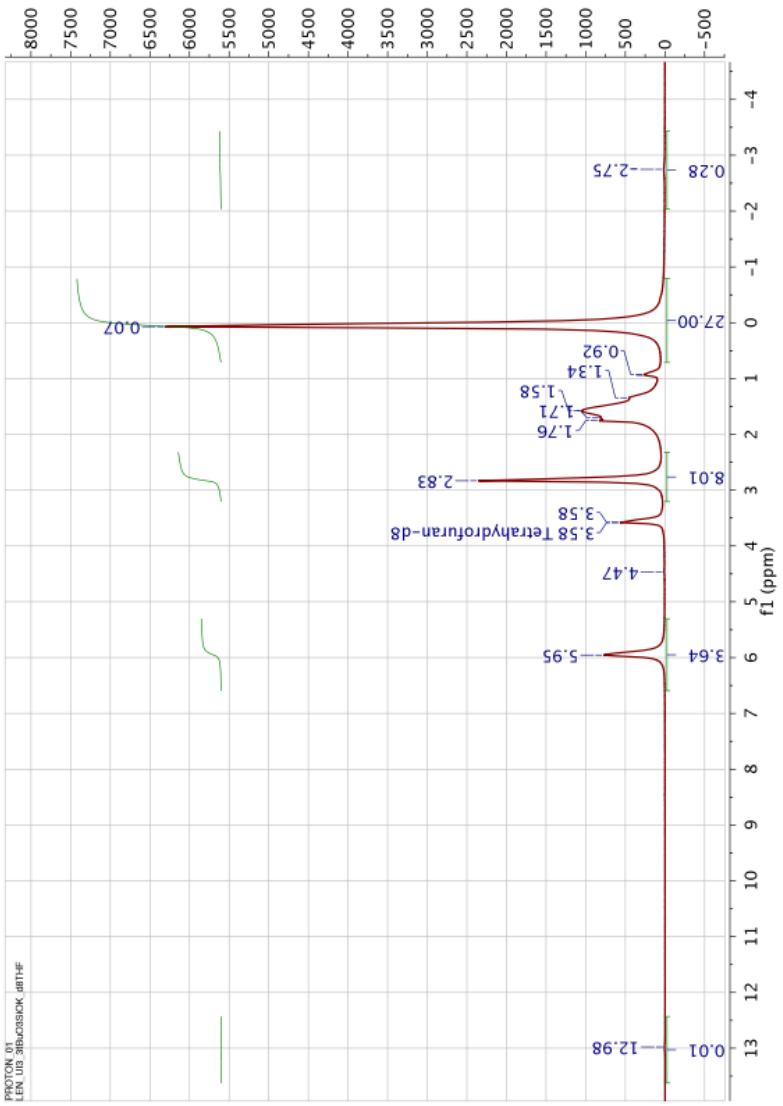

Figure E.15: ^{1}H NMR for the reaction between 3 eq. $(O^{t}Bu)_3SiOK$ and UI_3 in d_8-THF

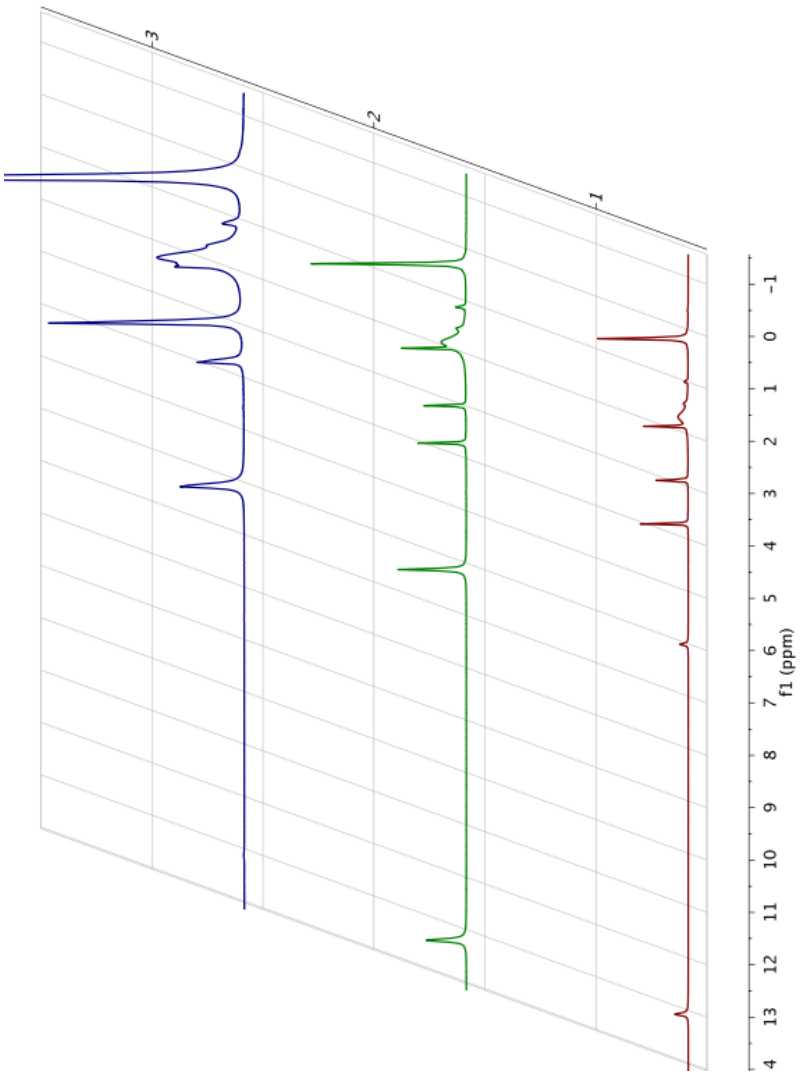

Figure E.16: Stacked ^{1}H NMR for the reaction between $(O^{t}Bu)_3SiOK$ and UI_3 in d_8-THF

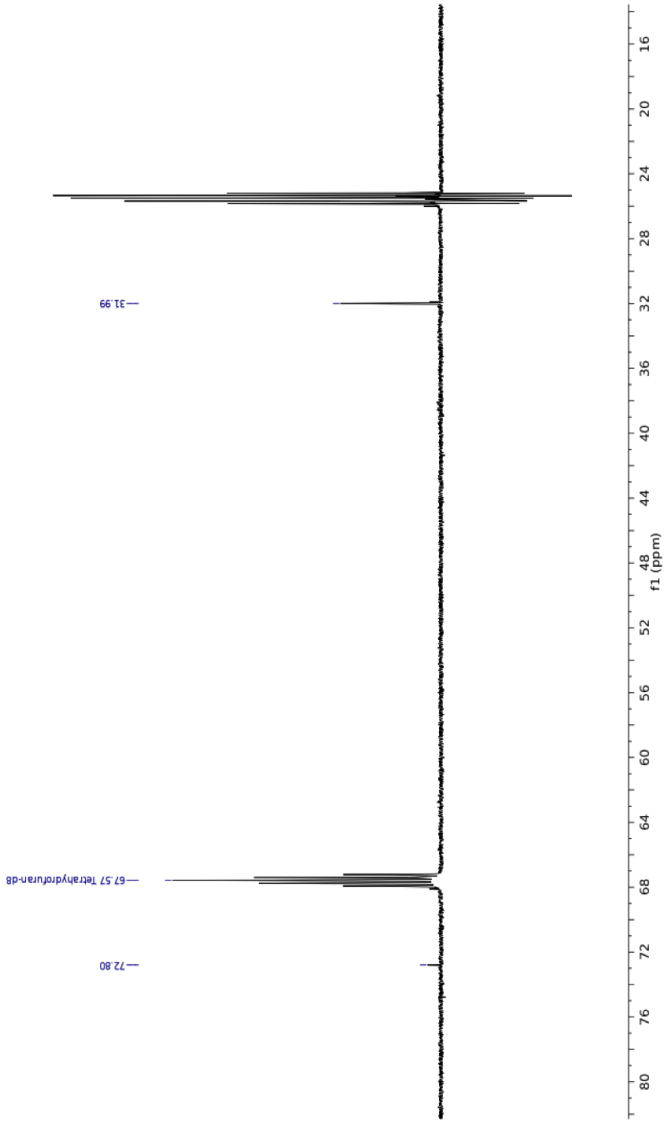

Figure E.17: $^{13}C\{H\}$ NMR for $U(OSi(O^tBu)_3)_4$ in d_8-THF

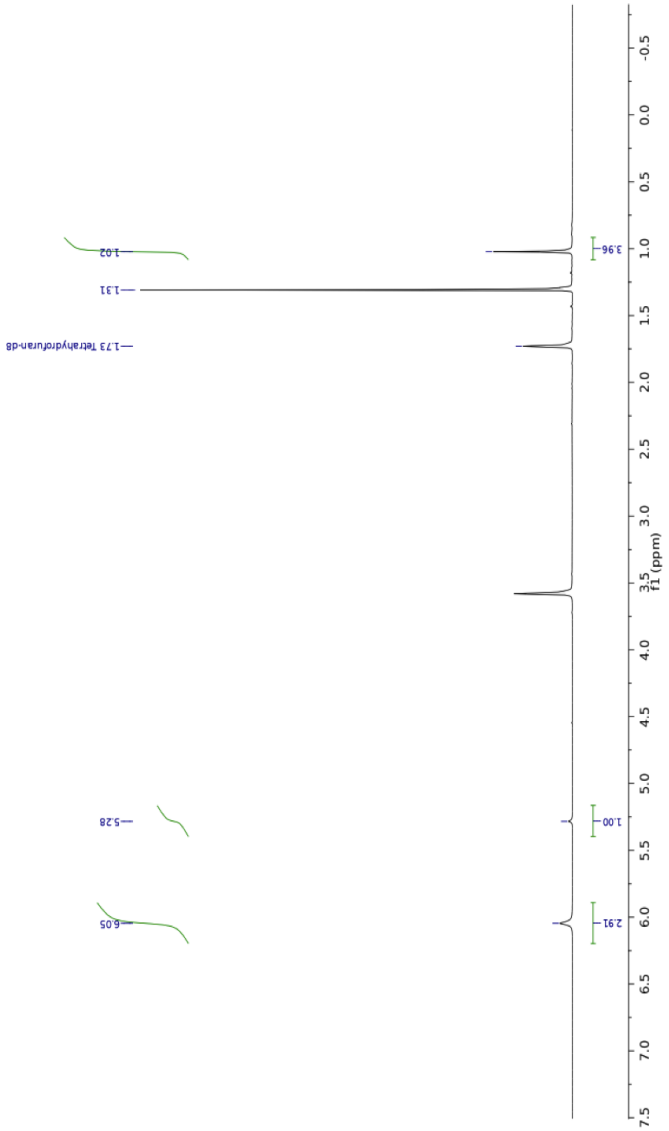

Figure E.18: ^{1}H NMR for U(OSi(O^{t}Bu)$_3$)$_4$ in d_8-THF

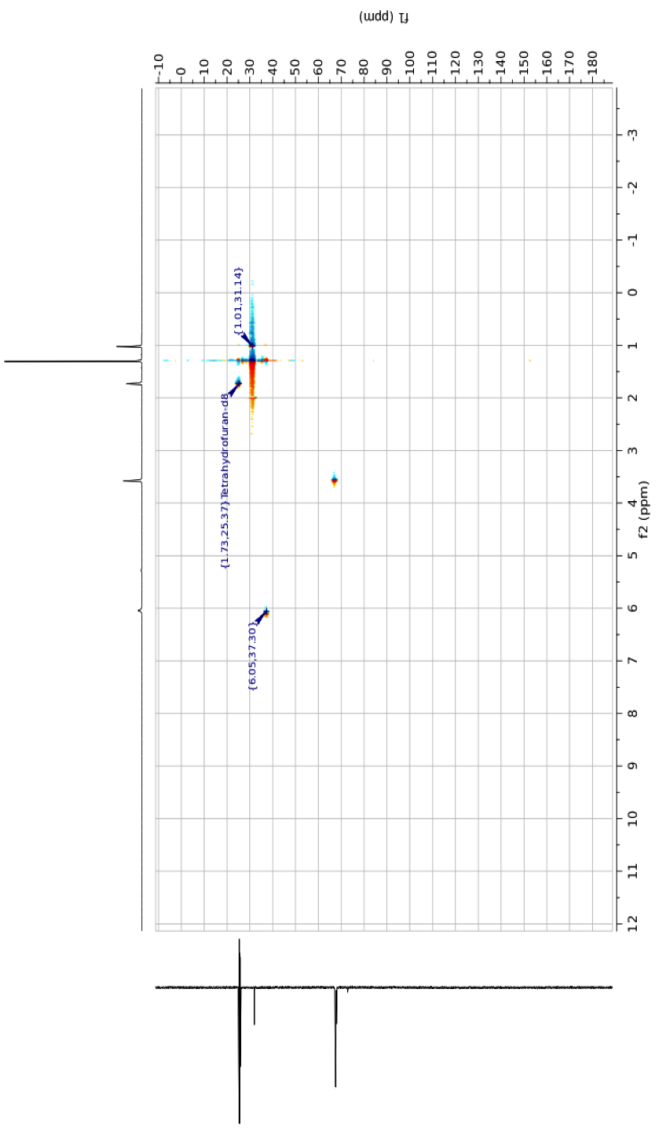

Figure E.19: HMBC NMR for $U(OSi(O^tBu)_3)_4$ in d_8-THF

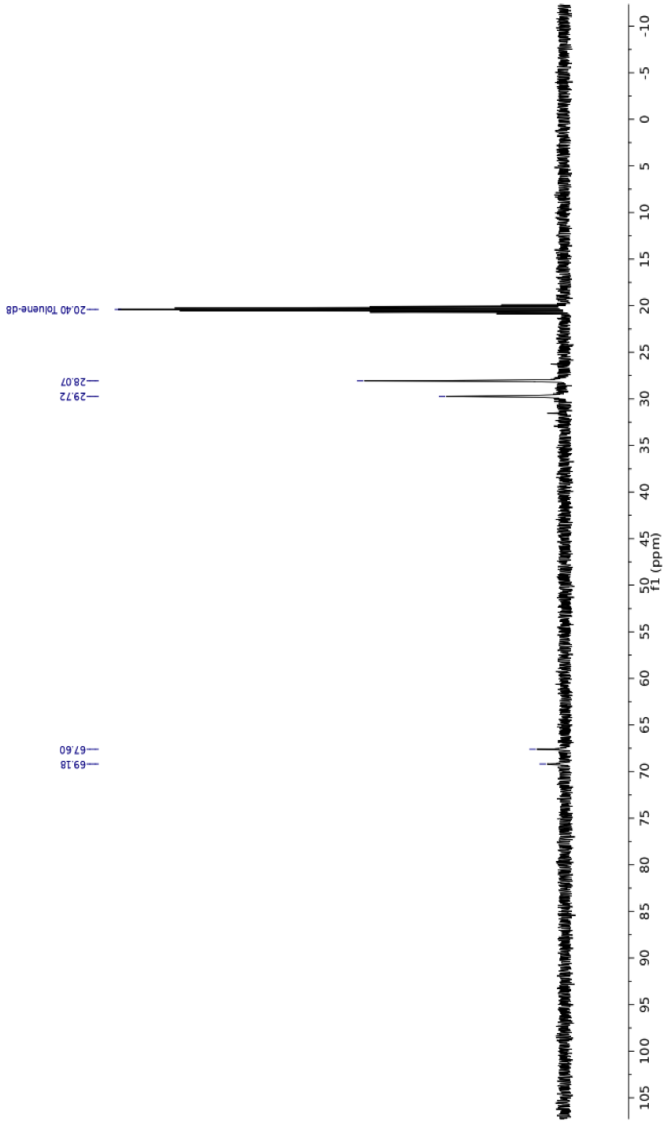

Figure E.20: $^{13}C\{H\}$ NMR for $U(OSi(O^tBu)_3)_4$ in d_8-toluene

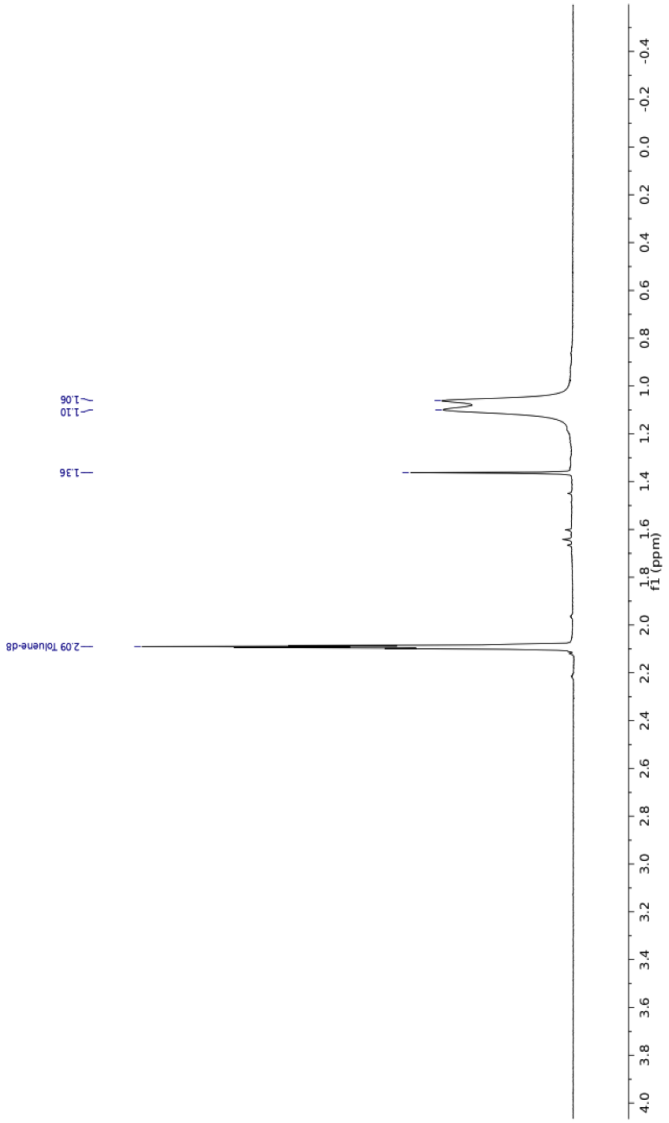

Figure E.21: ^{1}H NMR for U(OSi(O^{t}Bu)$_3$)$_4$ in d_8-toluene

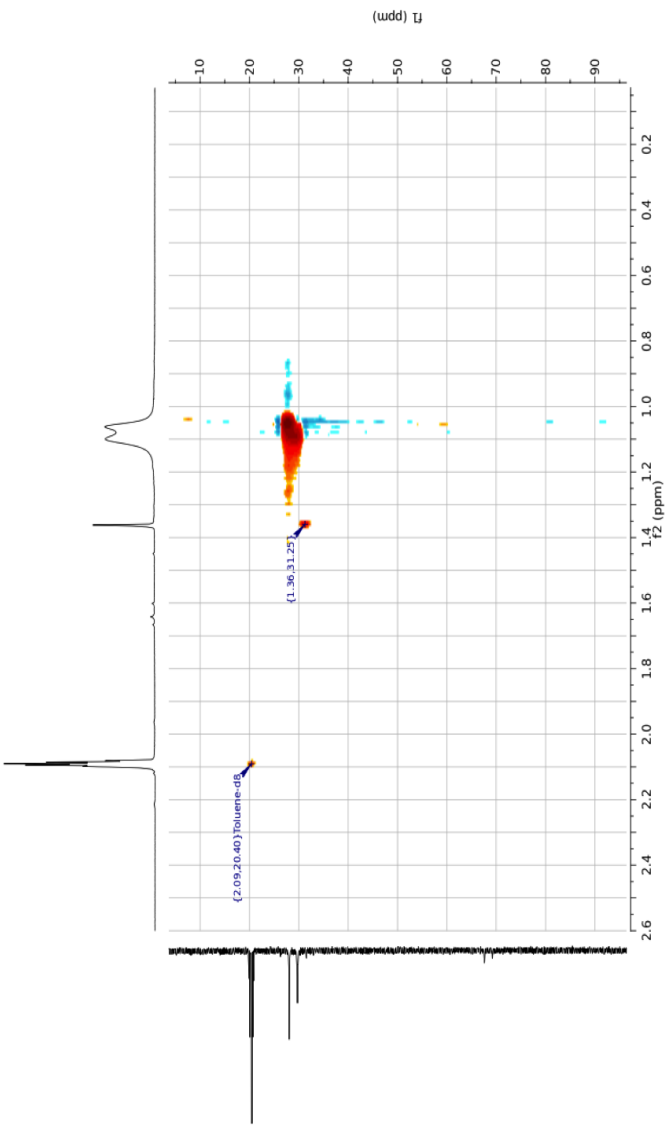

Figure E.22: HMBC NMR for $U(OSi(O^tBu)_3)_4$ in d_8-toluene

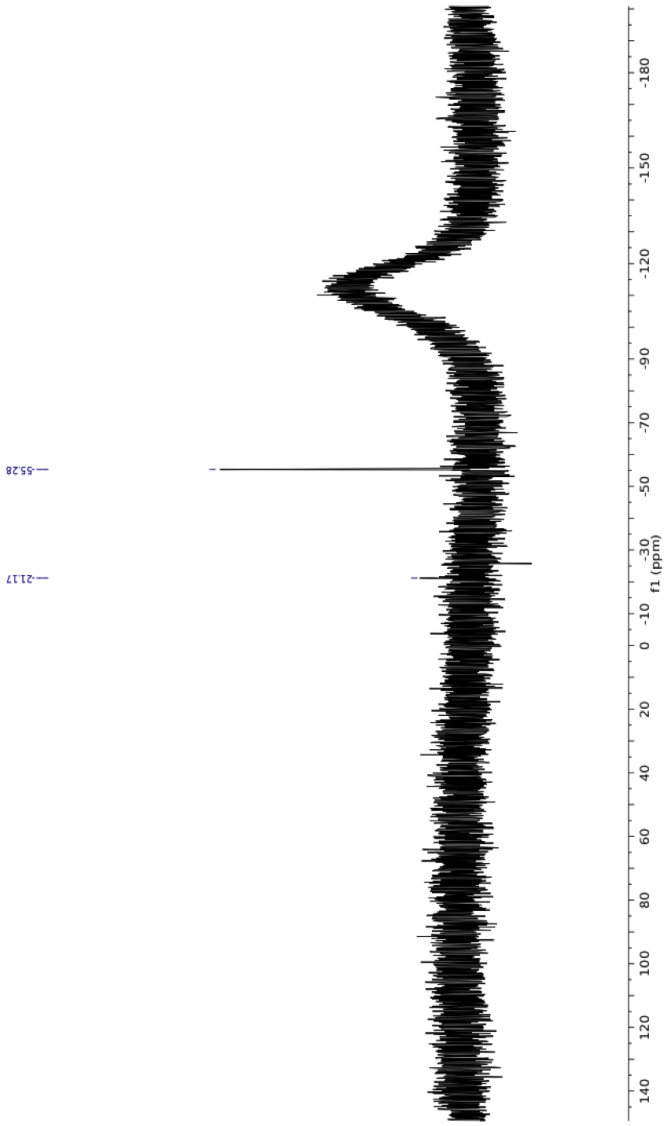

Figure E.23: ^{29}Si NMR for U(OSi(O^{t}Bu)$_3$)$_4$ in d_8-toluene

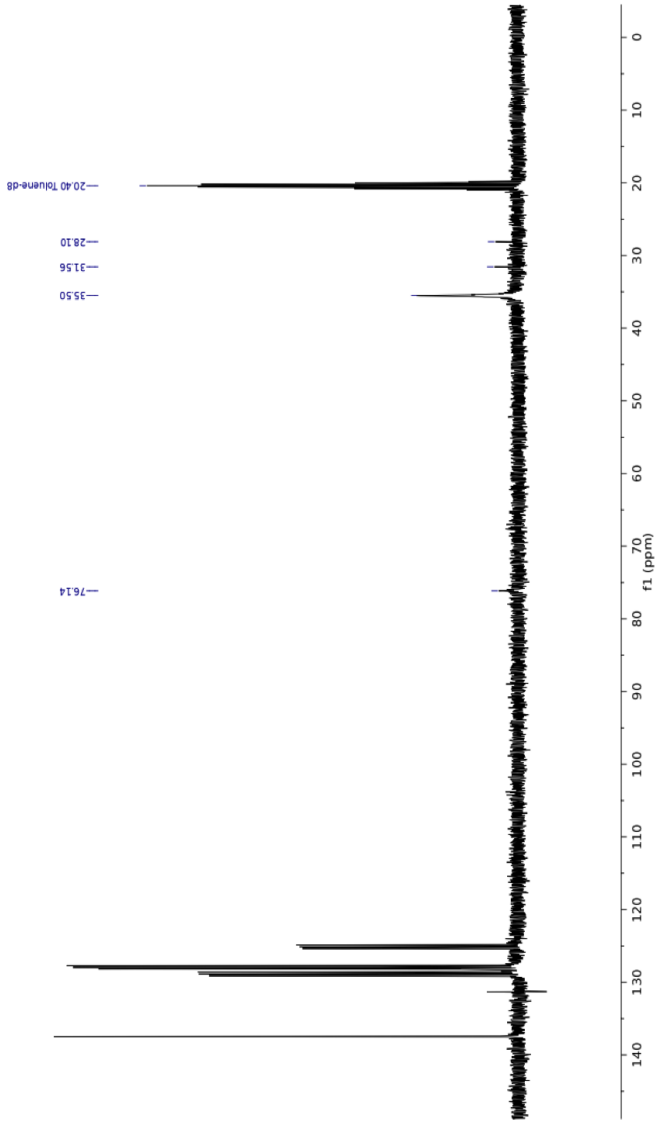

Figure E.24: $^{13}C\{H\}$ NMR for $UCl(OSi(O^tBu)_3)_3$ in d_8-toluene

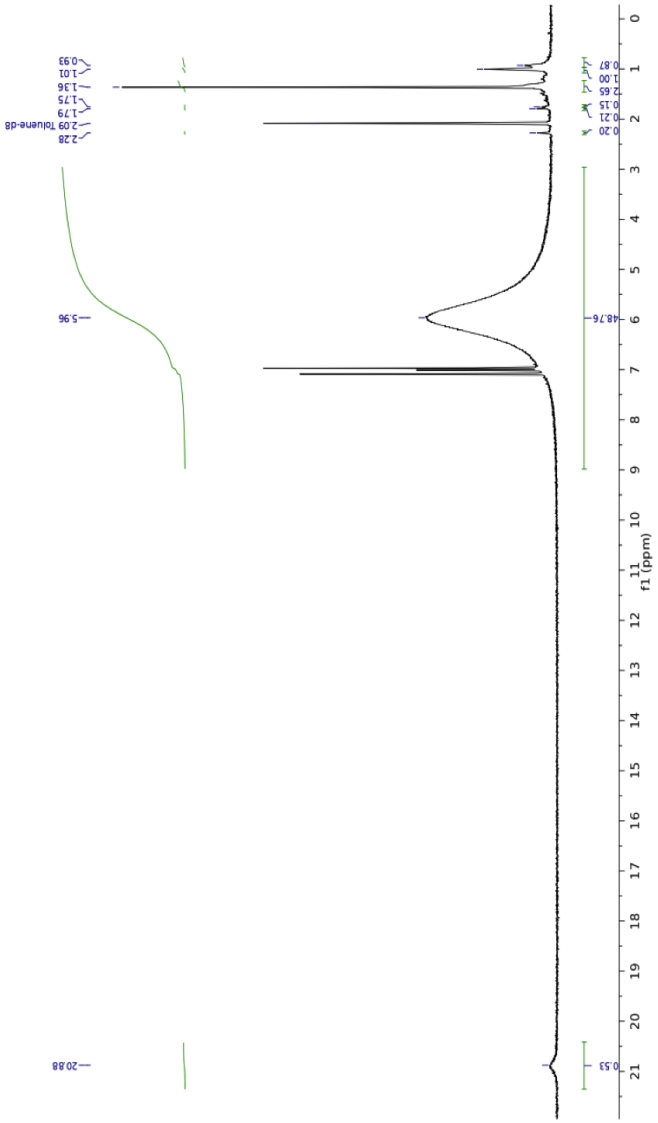

Figure E.25: ^{1}H NMR for UCl(OSi(O^{t}Bu)$_3$)$_3$ in d_8-toluene

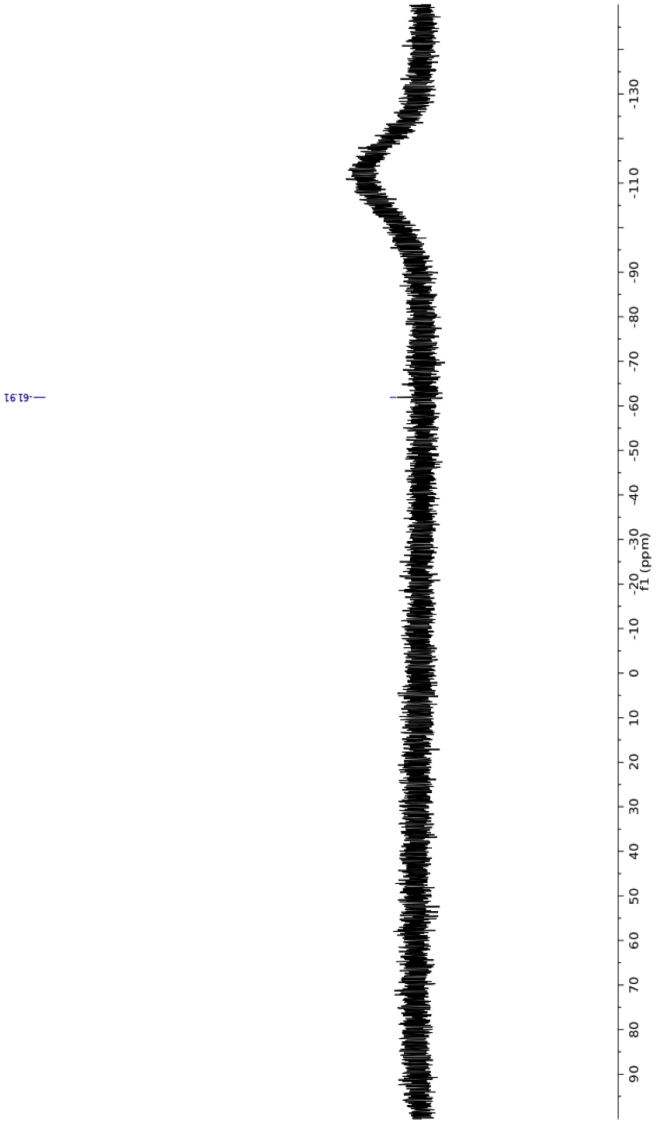

Figure E.26: ^{29}Si NMR for UCl(OSi(O^{t}Bu)$_3$)$_3$ in d_8-toluene

Appendix F

NMR spectra - tris *(tert)*-butoxide ligands reactivity studies

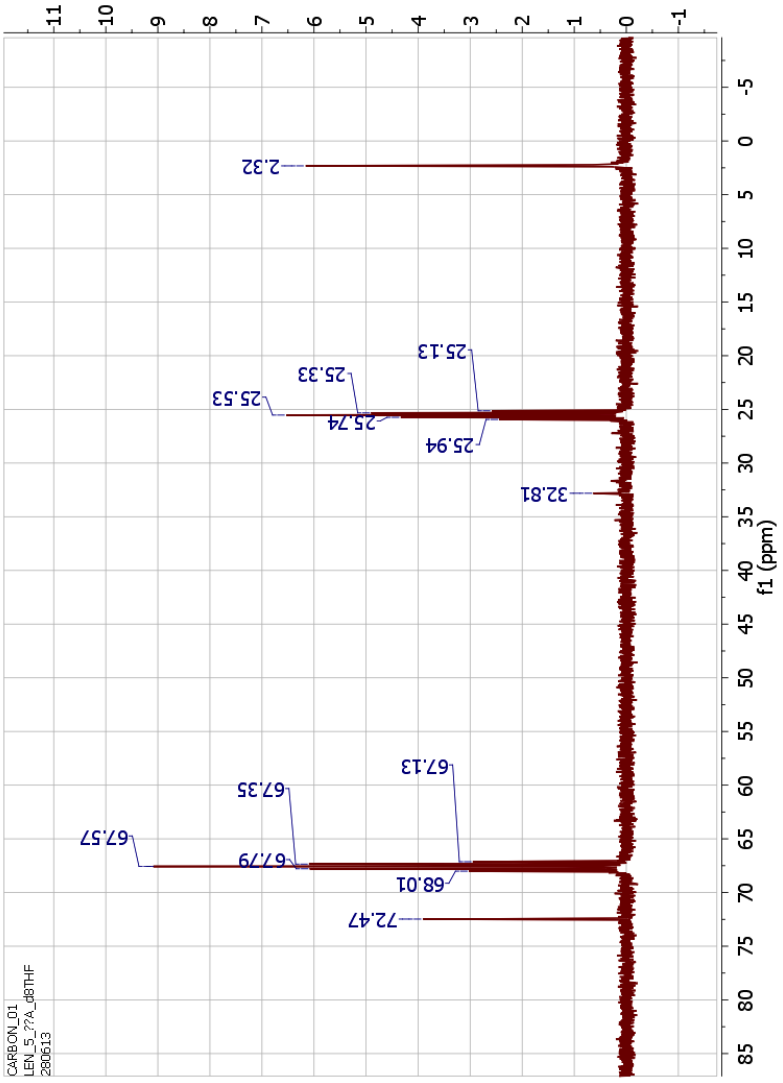

Figure F.1: $^{13}C\{H\}$ NMR for the reaction between K[(U(OSi(O^{t}Bu)$_3$)$_3$)$_2$($\mu-\eta^6$:η^6- tol))] and ^{13}CO at -78 °C Day 1 in d_8-THF

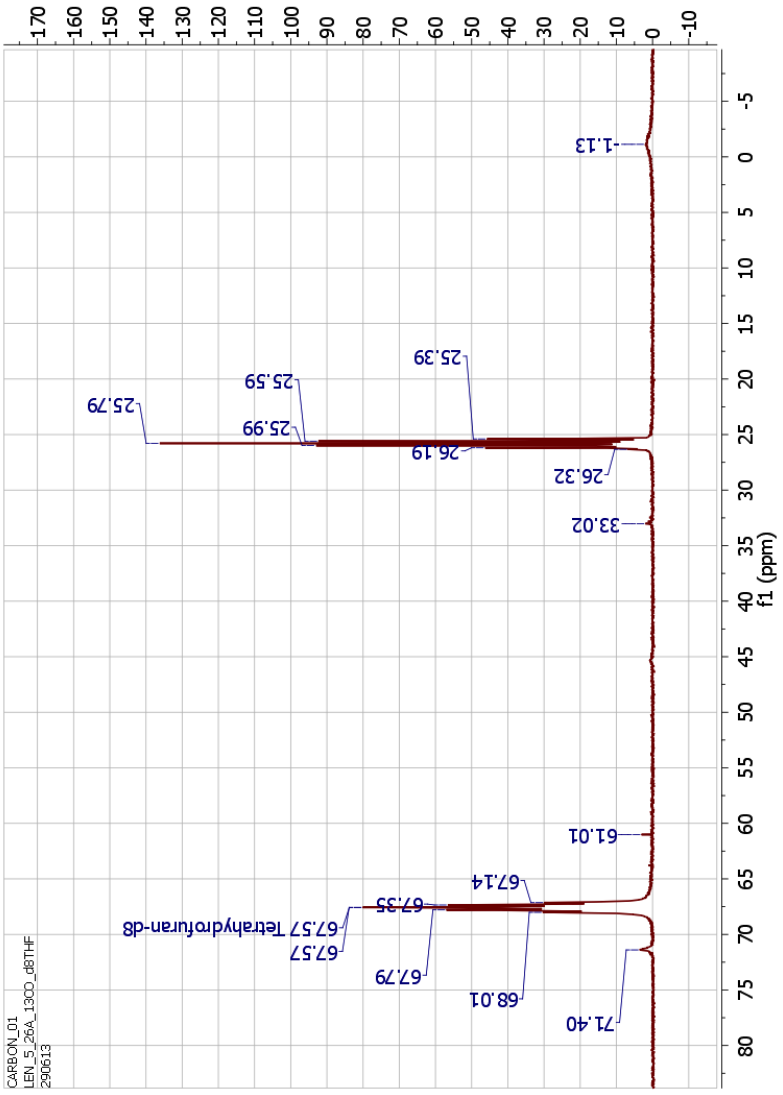

Figure F.2: $^{13}C\{H\}$ NMR for the reaction between K[(U(OSi(O^{t}Bu)$_3$)$_3$)$_2$($\mu-\eta^6$:η^6-tol))] and ^{13}CO at -78 °C Day 2 in d_8-THF

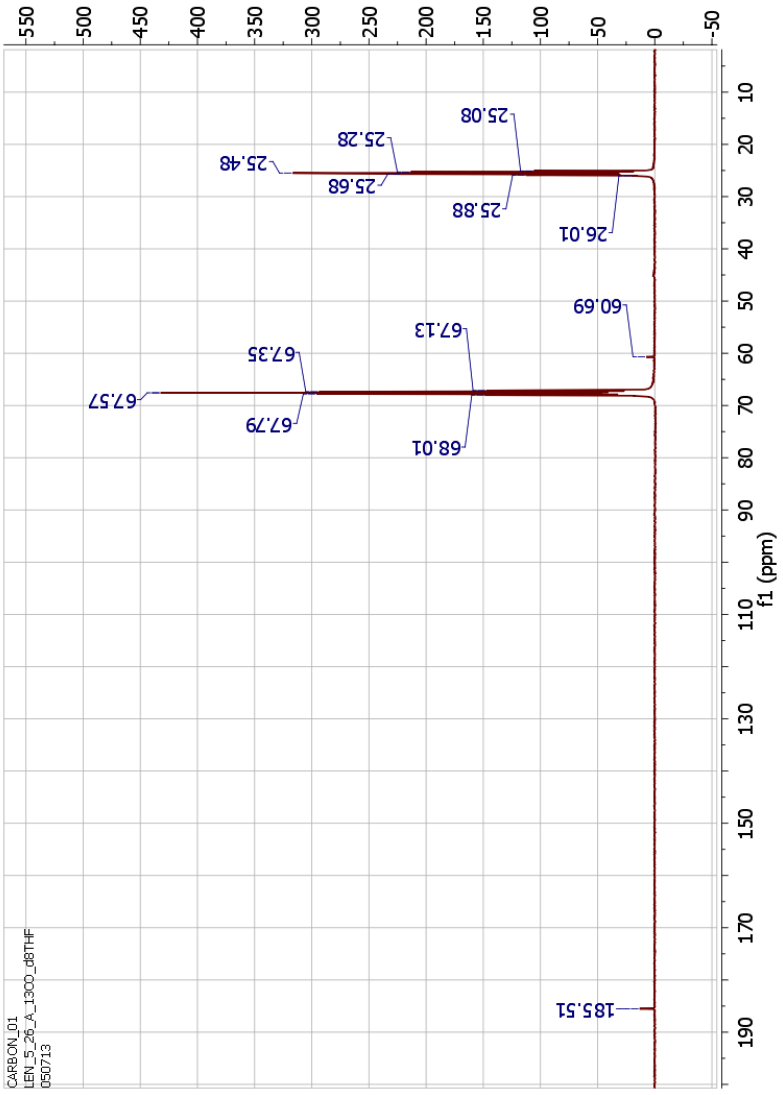

Figure F.3: $^{13}C\{H\}$ NMR for the reaction between K[(U(OSi(O^{t}Bu)$_3$)$_3$)$_2$($\mu-\eta^6$:η^6- tol))] and ^{13}CO at -78 °C Day 8 in d_8-THF

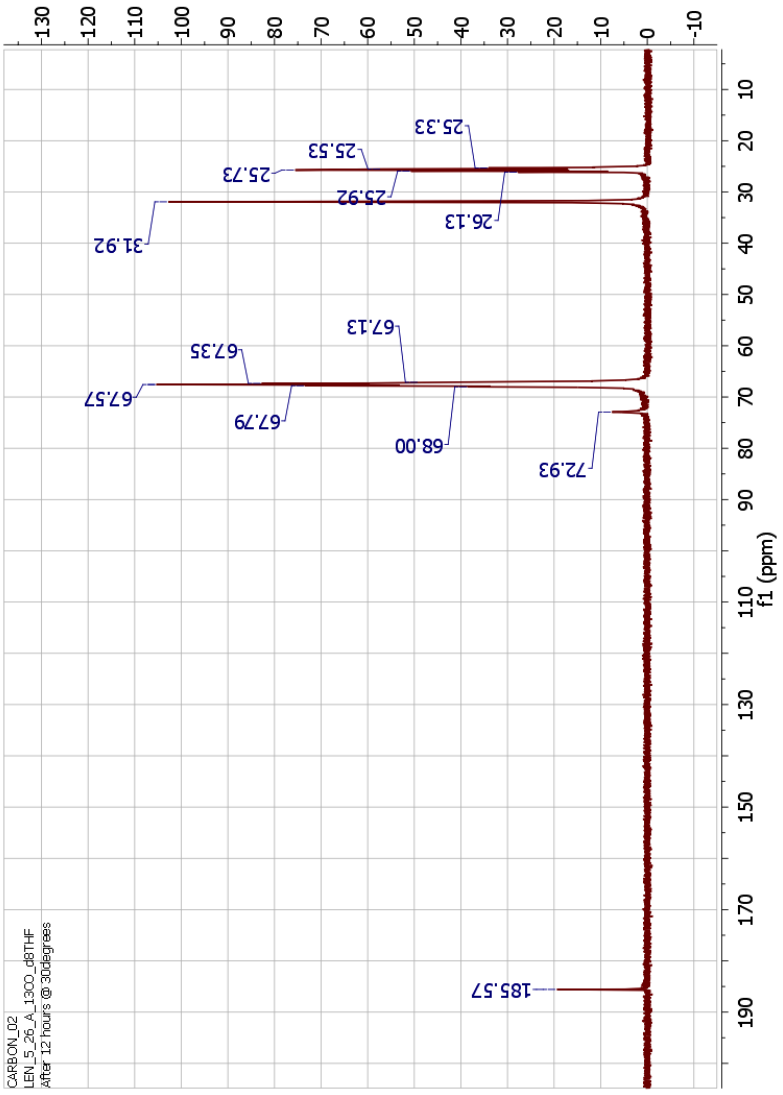

Figure F.4: $^{13}C\{H\}$ NMR for the reaction between K[(U(OSi(O^{t}Bu)$_3$)$_3$)$_2$($\mu-\eta^6$:η^6- tol))] and ^{13}CO at 30 °C Day 9 in d_8-THF

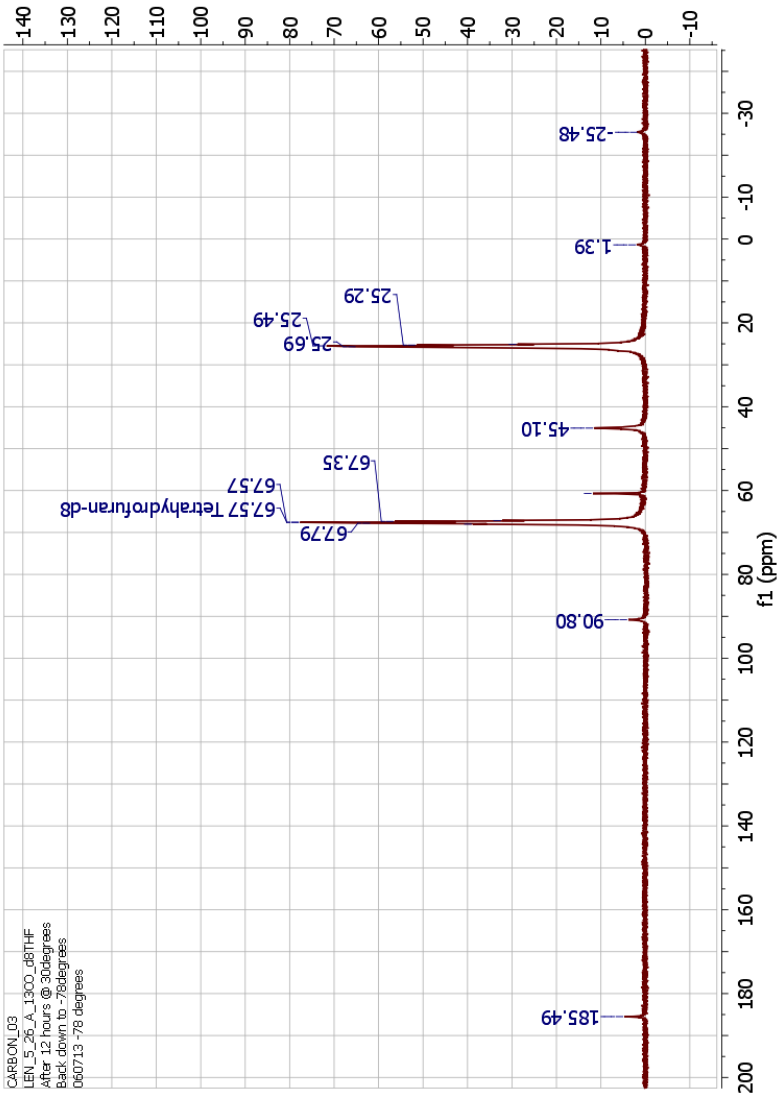

Figure F.5: $^{13}C\{H\}$ NMR for the reaction between K[(U(OSi(O^{t}Bu)$_3$)$_3$)$_2$($\mu-\eta^6$:η^6- tol))] and ^{13}CO at -78 °C Day 9 in d_8-THF

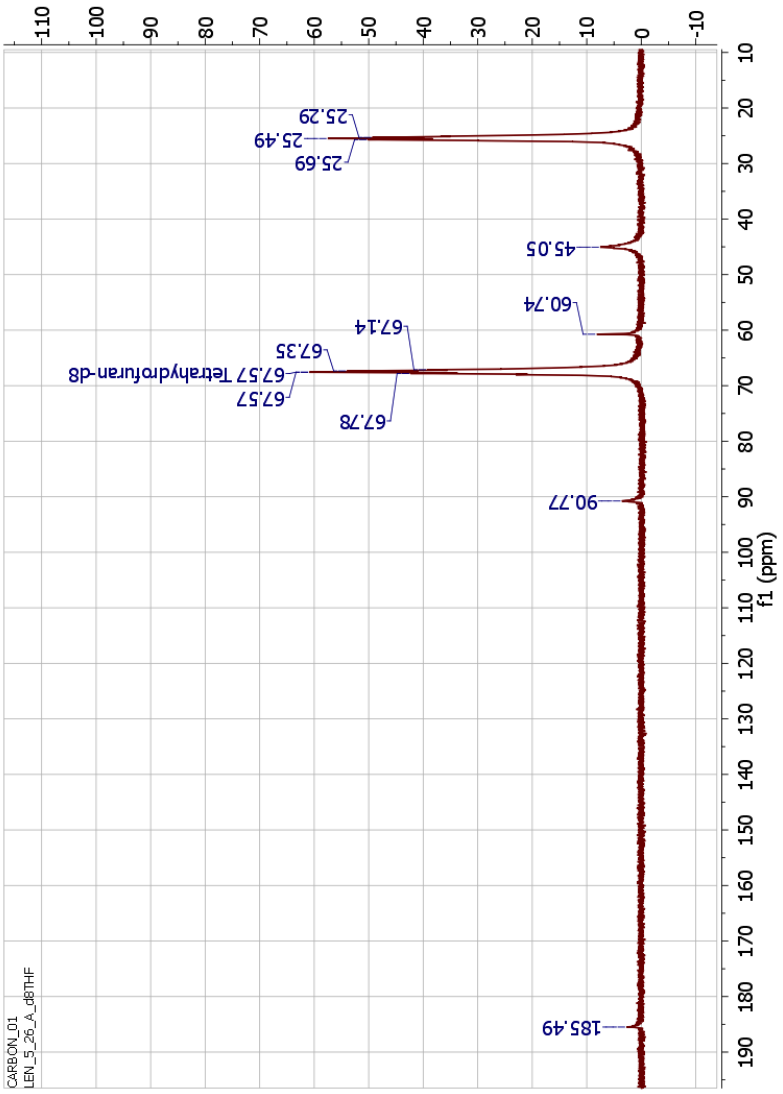

Figure F.6: $^{13}C\{H\}$ NMR for the reaction between K[(U(OSi(O^{t}Bu)$_3$)$_3$)$_2$($\mu-\eta^6$:η^6- tol))] and ^{13}CO at -78 °C Day 23 in d_8-THF

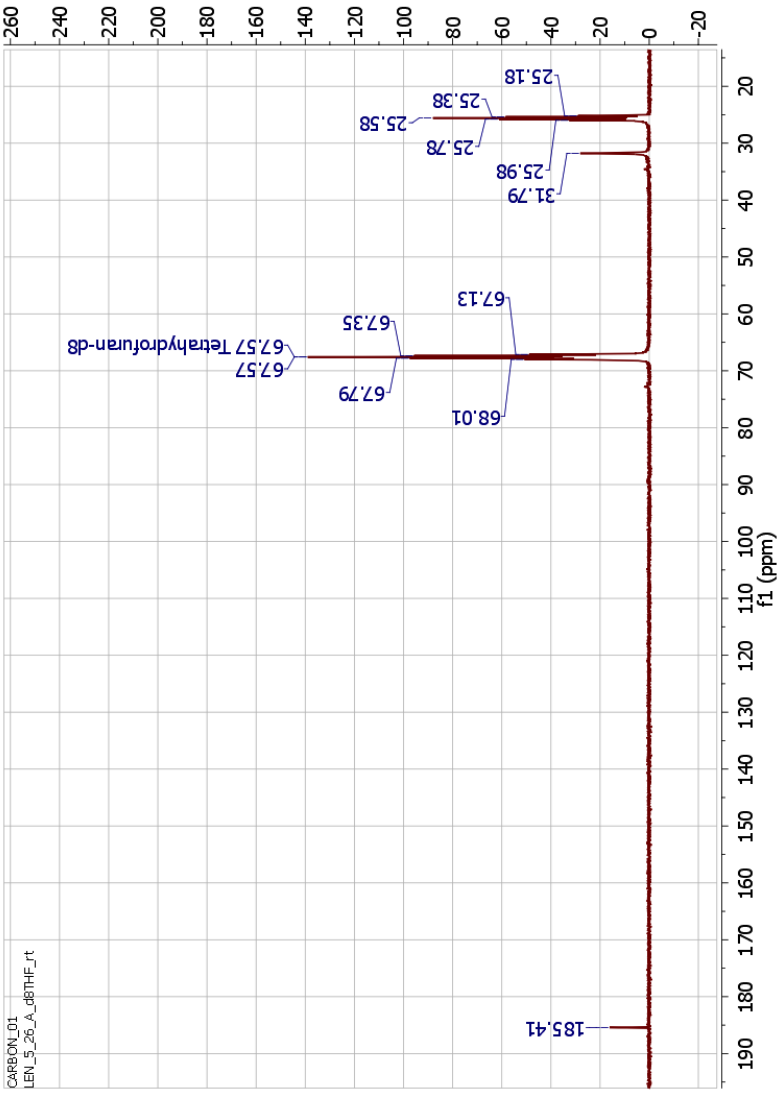

Figure F.7: $^{13}C\{H\}$ NMR for the reaction between K[(U(OSi(O^{t}Bu)$_3$)$_3$)$_2$($\mu-\eta^6$:η^6-tol))] and ^{13}CO at 30 °C Day 23 in d_8-THF

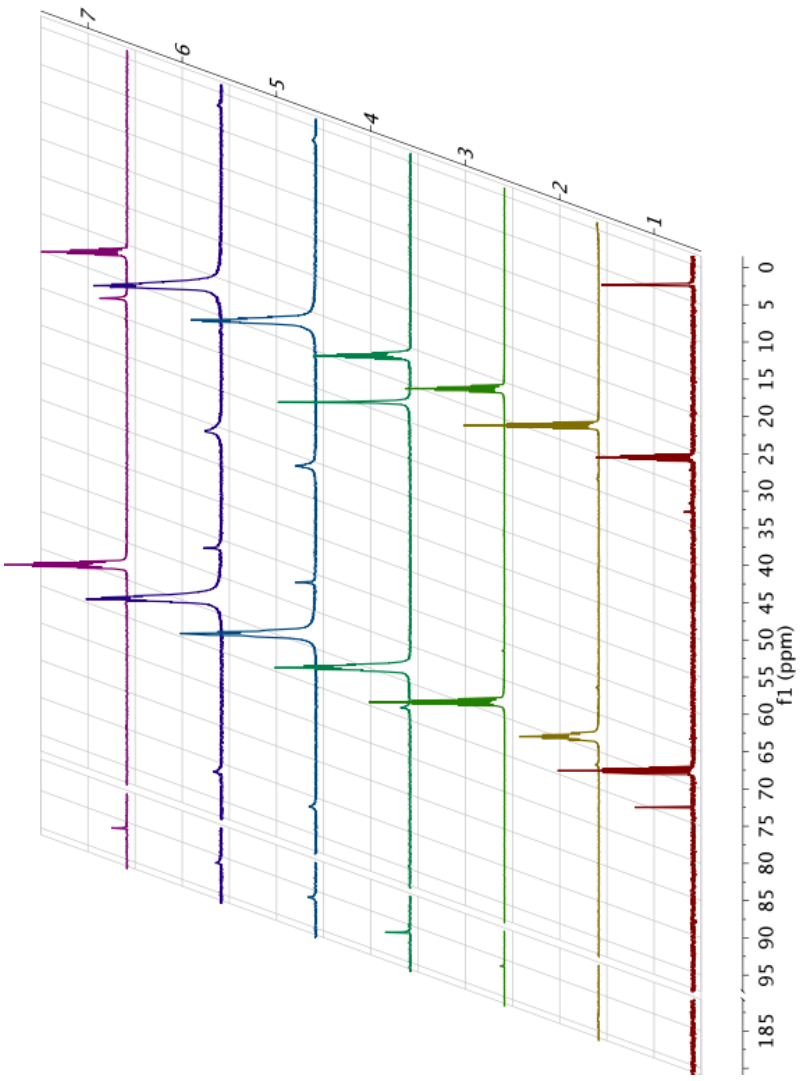

Figure F.8: Stacked $^{13}C\{H\}$ NMR for the reaction between K[(U(OSi(O^{t}Bu)$_3$)$_3$)$_2$($\mu-\eta^6$:η^6-tol))] and ^{13}CO in d_8-THF

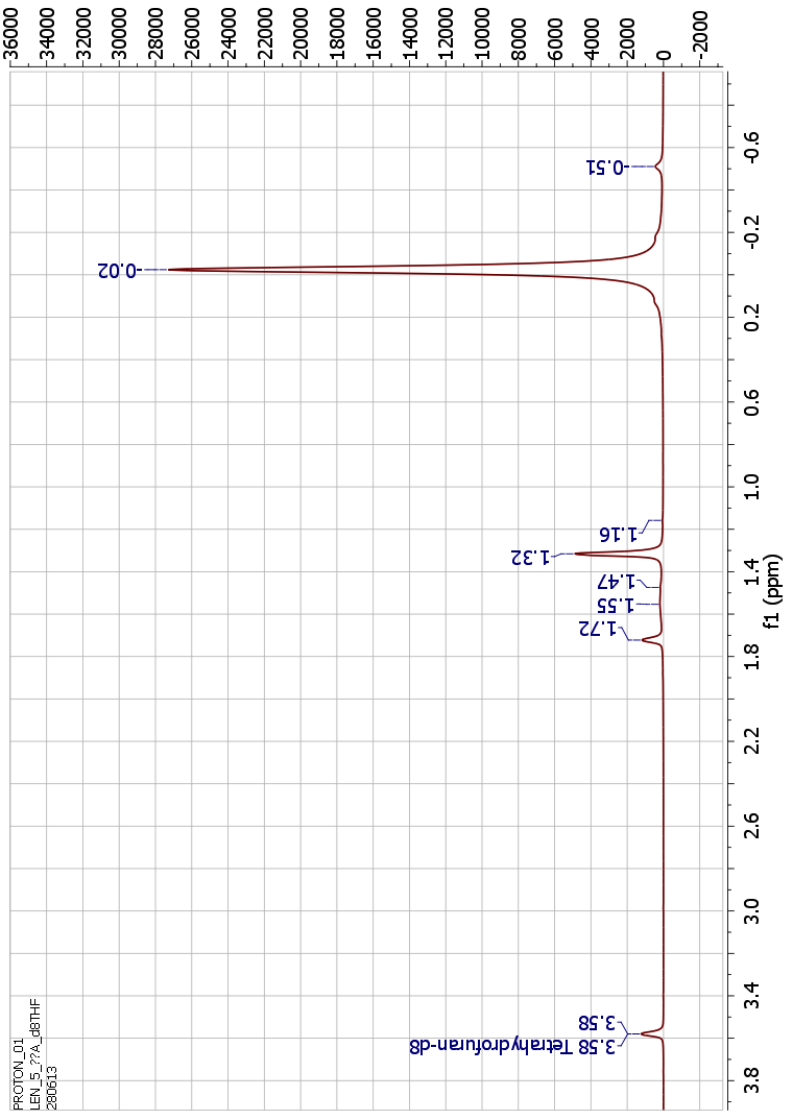

Figure F.9: ^{1}H NMR for the reaction between K[(U(OSi(O^{t}Bu)$_3$)$_3$)$_2$($\mu-\eta^6$:η^6-tol))] and ^{13}CO at -78 °C Day 1 in d_8-THF

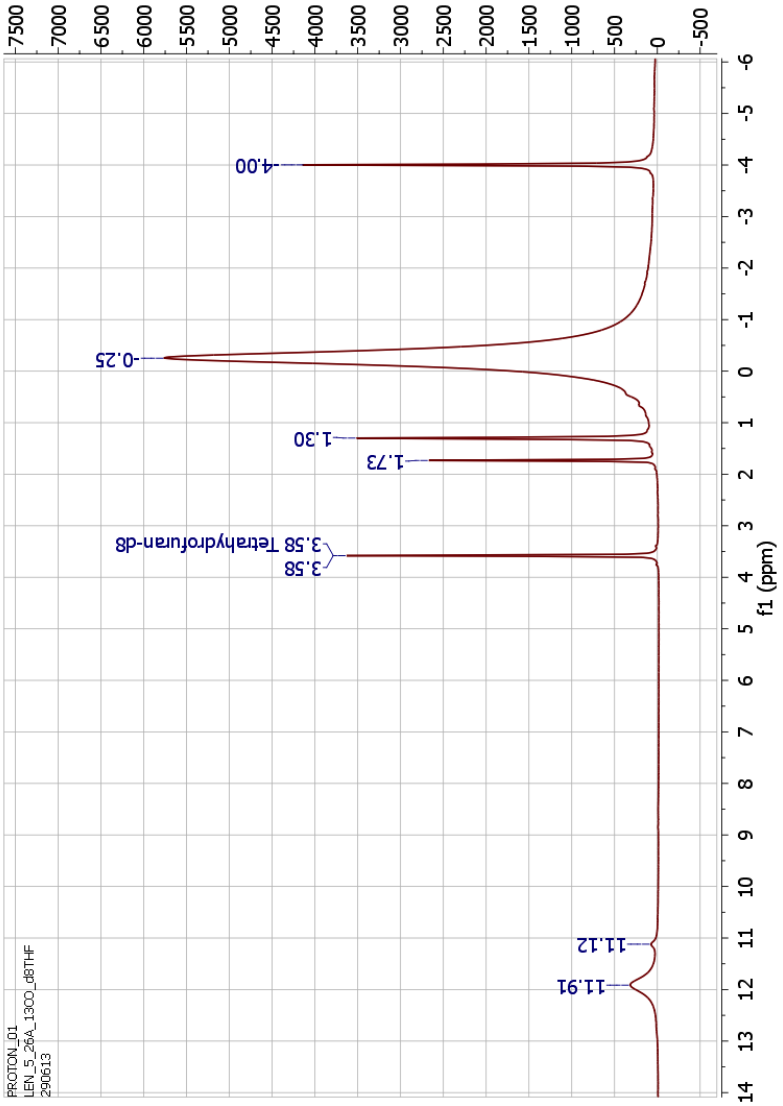

Figure F.10: ^{1}H NMR for the reaction between K[(U(OSi(O^{t}Bu)$_3$)$_3$)$_2$($\mu-\eta^6$:η^6-tol))] and ^{13}CO at -78 °C Day 2 in d_8-THF

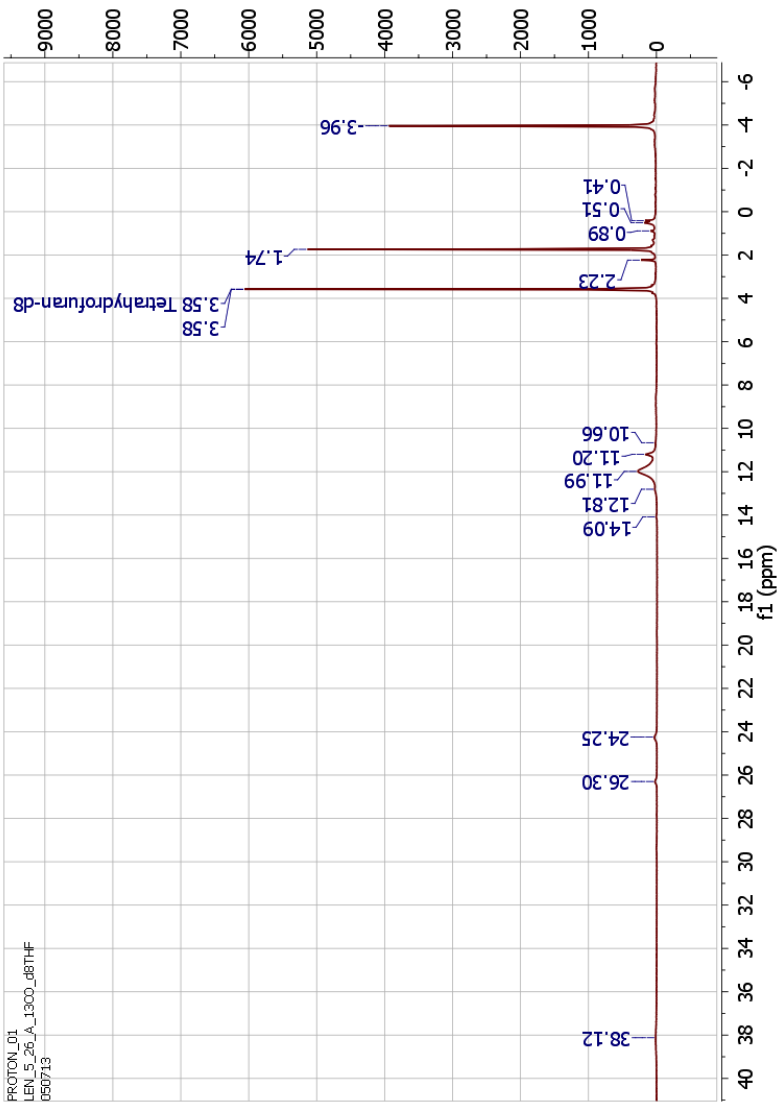

Figure F.11: ^{1}H NMR for the reaction between K[(U(OSi(O^{t}Bu)$_3$)$_3$)$_2$($\mu-\eta^6$:η^6-tol))] and ^{13}CO at -78 °C Day 8 in d_8-THF

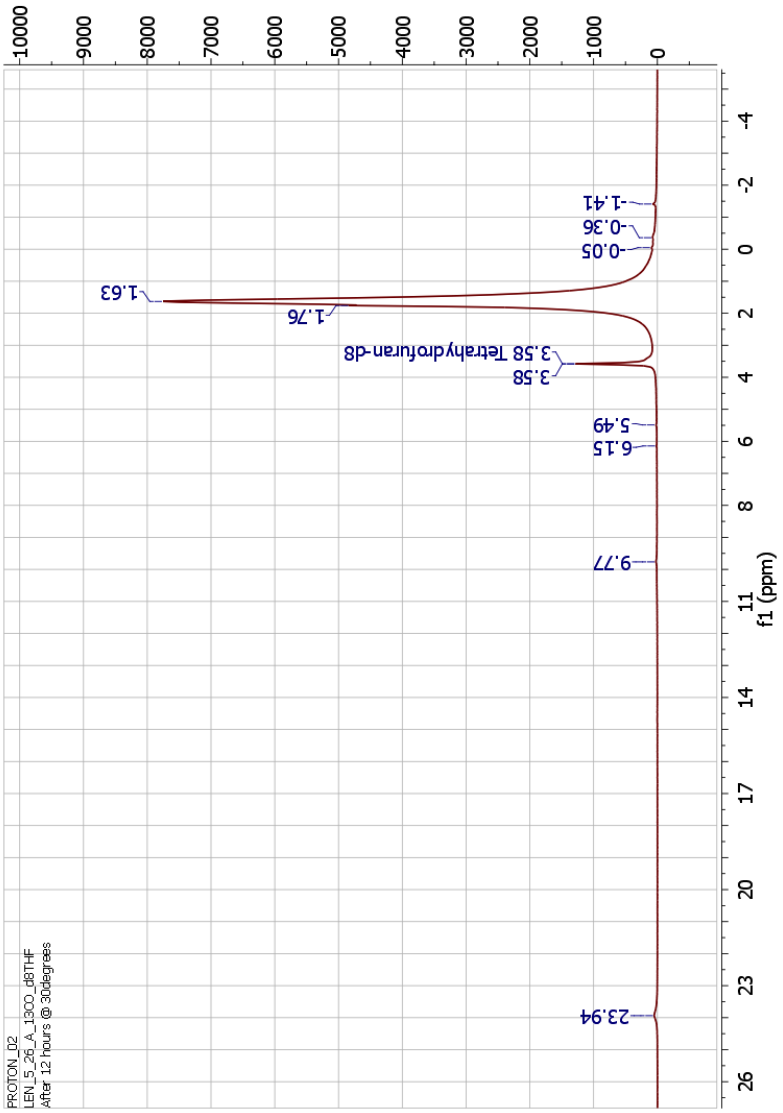

Figure F.12: ^{1}H NMR for the reaction between K[(U(OSi(O^{t}Bu)$_3$)$_3$)$_2$($\mu-\eta^6$:η^6-tol))] and ^{13}CO at 30 °C Day 9 in d_8-THF

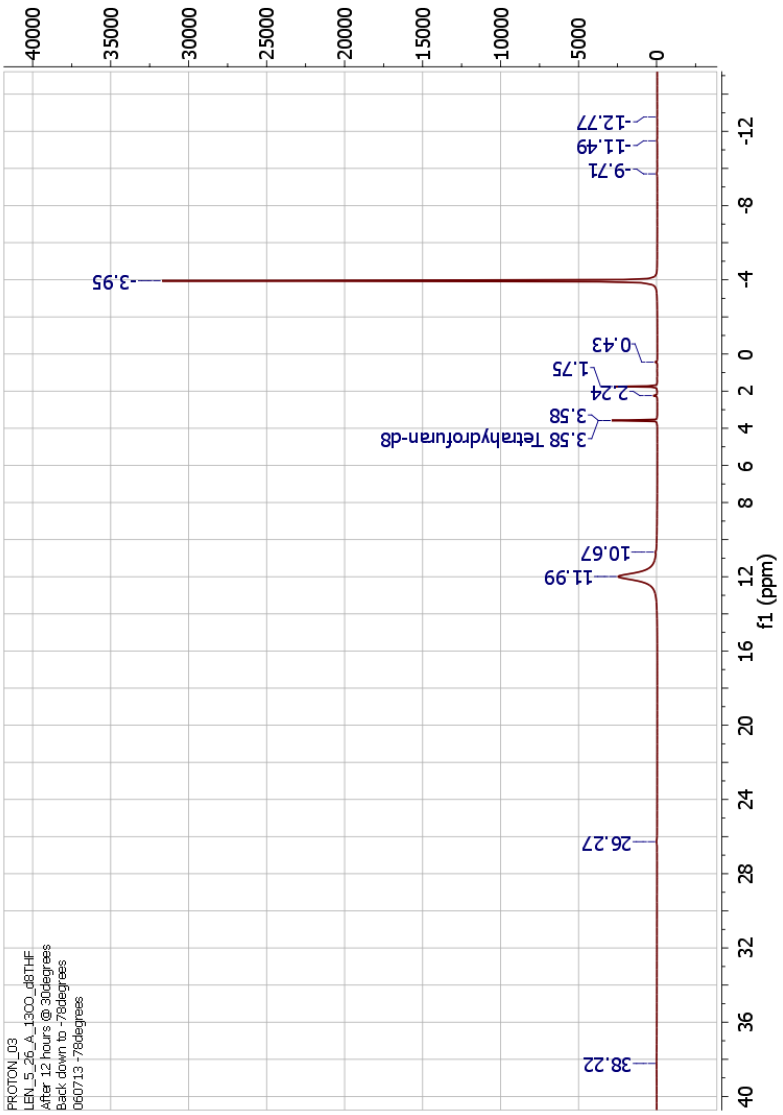

Figure F.13: ^{1}H NMR for the reaction between K[(U(OSi(O^{t}Bu)$_3$)$_3$)$_2$($\mu-\eta^6$:η^6-tol))] and ^{13}CO at -78 °C Day 9 in d_8-THF

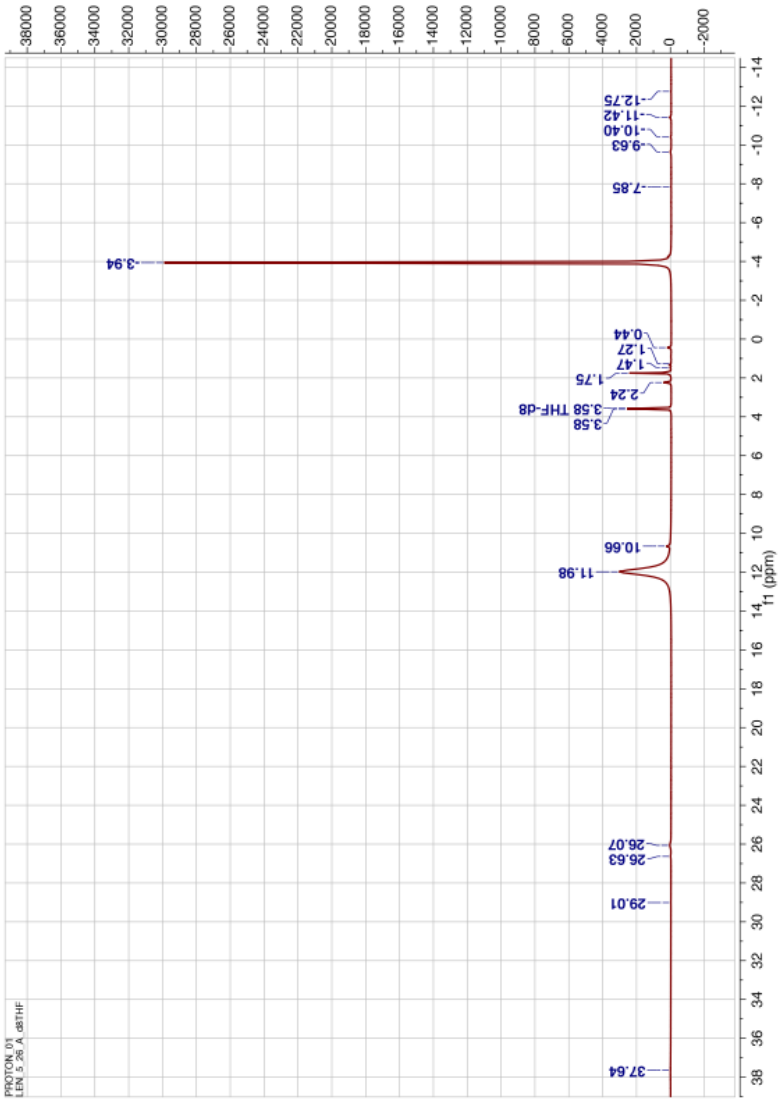

Figure F.14: ^{1}H NMR for the reaction between K[(U(OSi(O^{t}Bu)$_3$)$_3$)$_2$(μ–η^6:η^6-tol))] and ^{13}CO at -78 °C Day 23 in d_8-THF

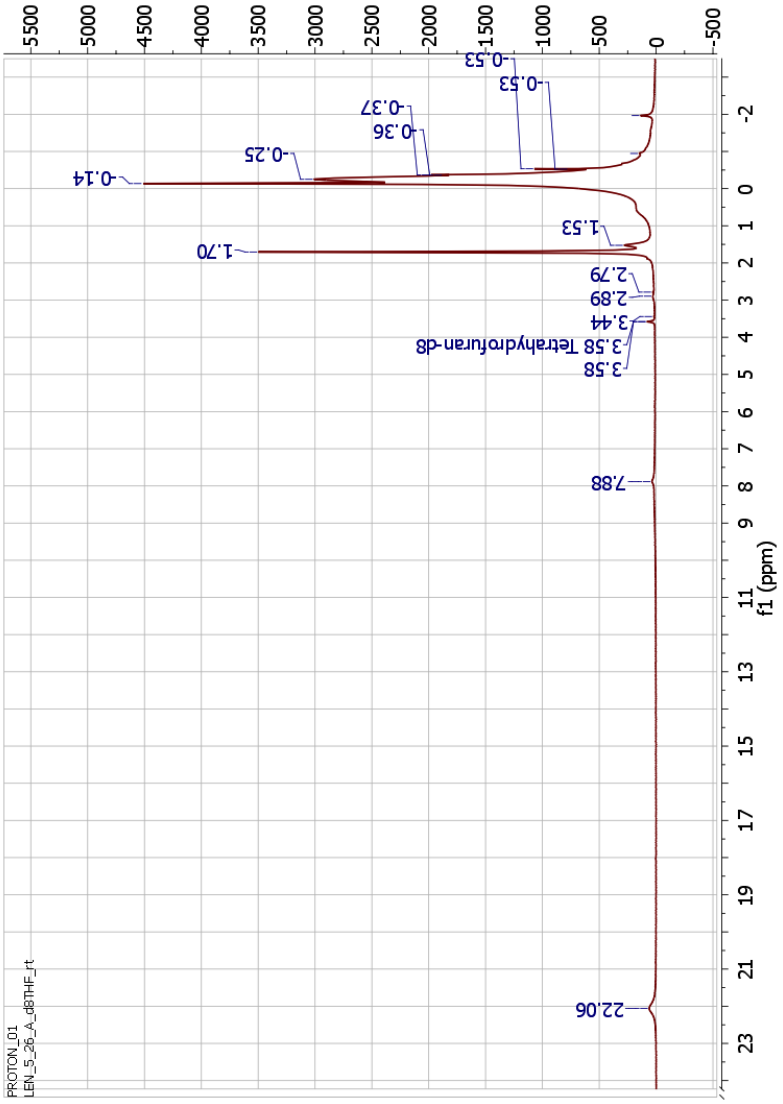

Figure F.15: ^{1}H NMR for the reaction between K[(U(OSi(O^{t}Bu)$_3$)$_3$)$_2$($\mu-\eta^6$:η^6-tol))] and ^{13}CO at 30 °C Day 23 in d_8-THF

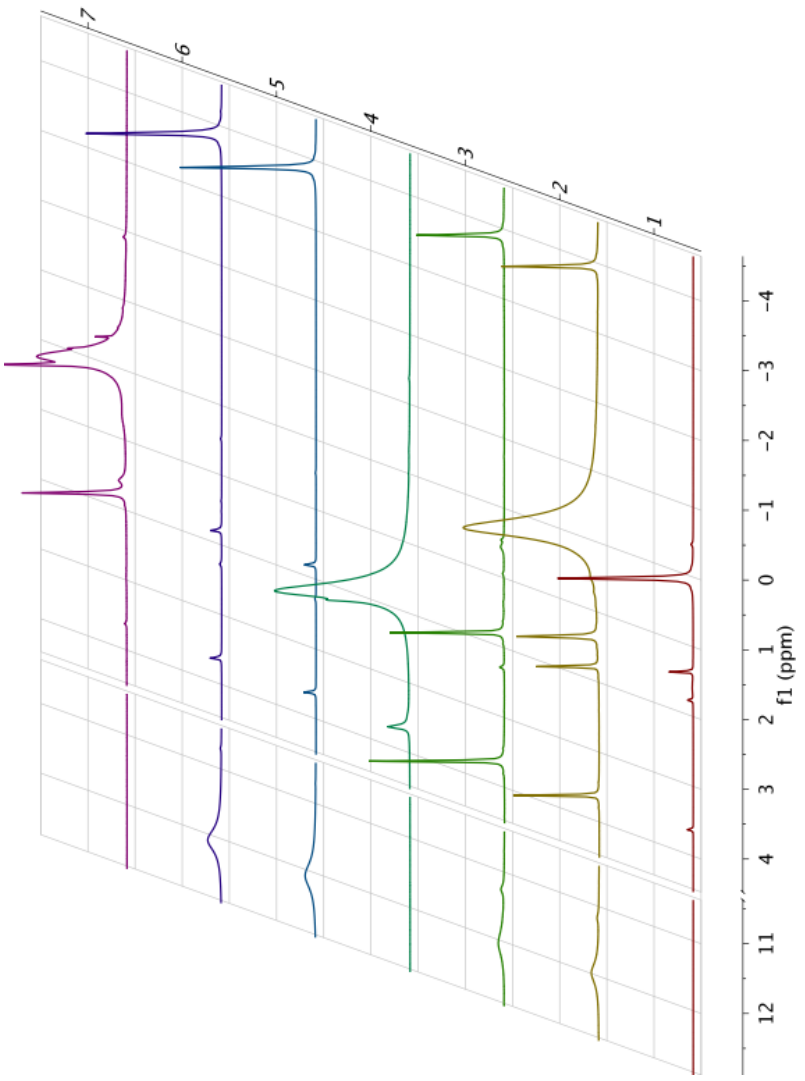

Figure F.16: Stacked ^{1}H NMR for the reaction between K[(U(OSi(O^{t}Bu)$_3$)$_3$)$_2$($\mu-\eta^6$:η^6-tol))] and ^{13}CO in d_8-THF

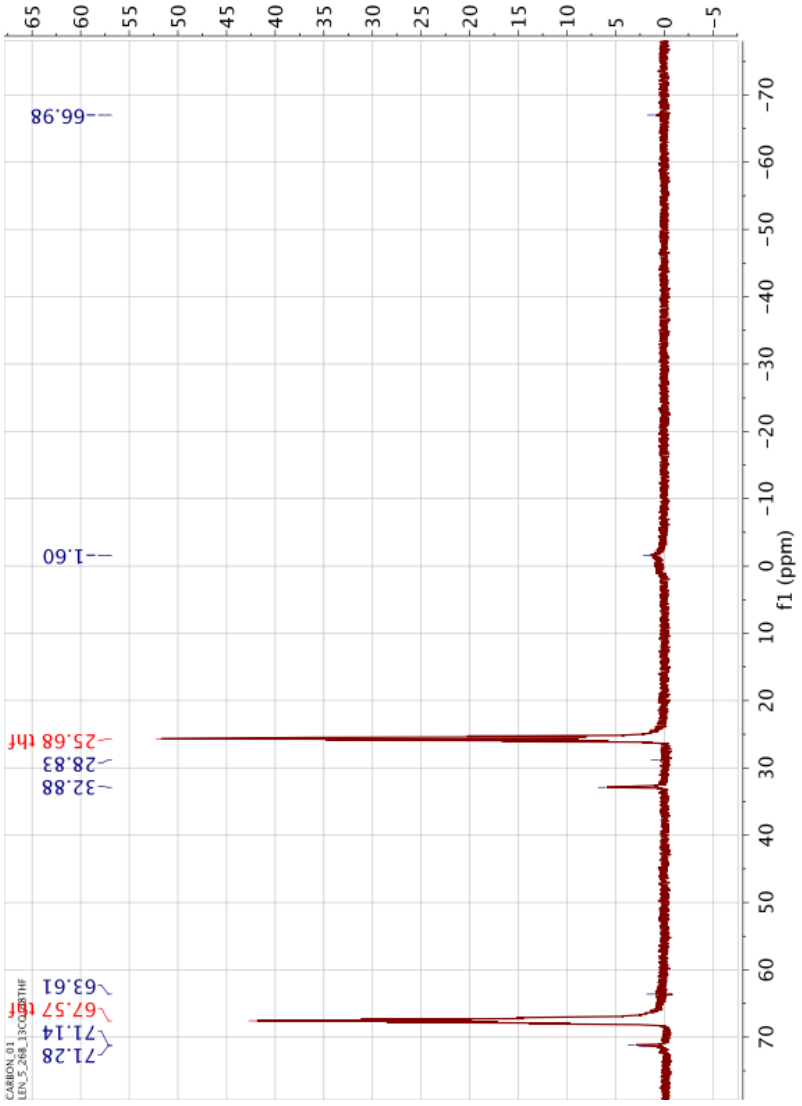

Figure F.17: $^{13}C\{H\}$ NMR for the reaction between K[(U(OSi(O^{t}Bu)$_3$)$_3$)$_2$($\mu-\eta^6$:η^6-tol))] and $^{13}CO/H_2$ at -78 °C Day 1 in d_8-THF

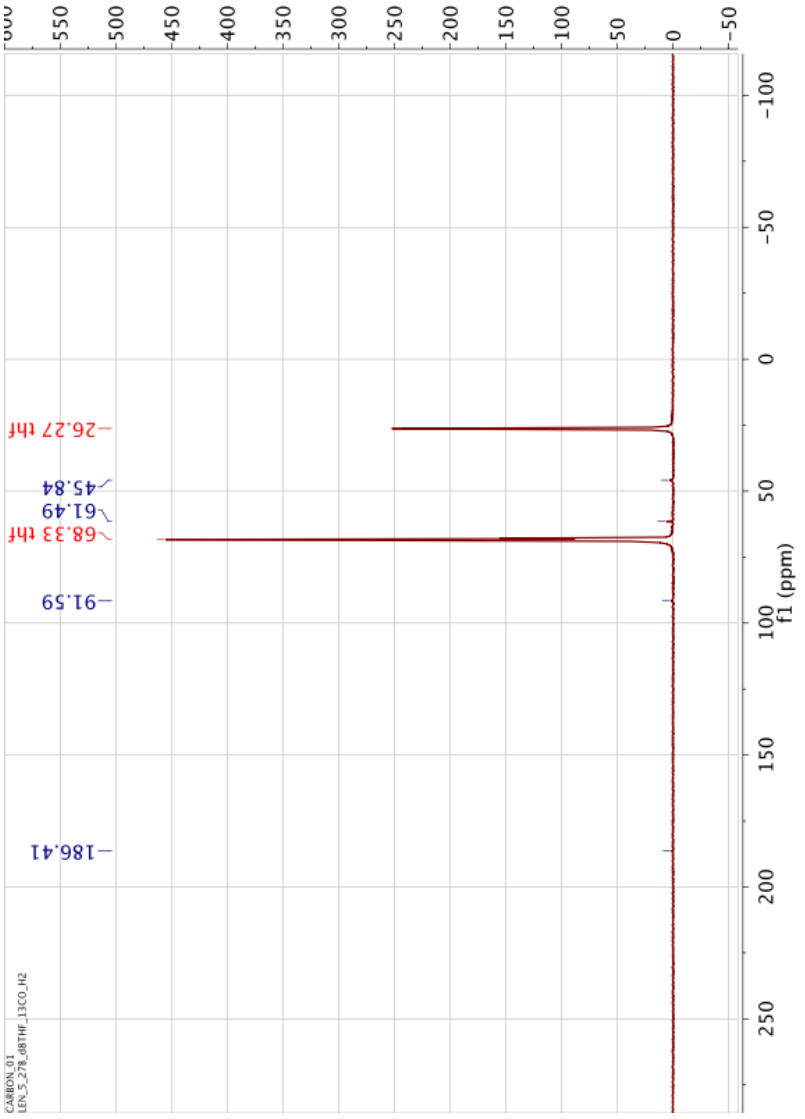

Figure F.18: $^{13}C\{H\}$ NMR for the reaction between K[(U(OSi(O^{t}Bu)$_3$)$_3$)$_2$($\mu-\eta^6:\eta^6$-tol))] and $^{13}CO/H_2$ at -78 °C Day 10 in d_8-THF

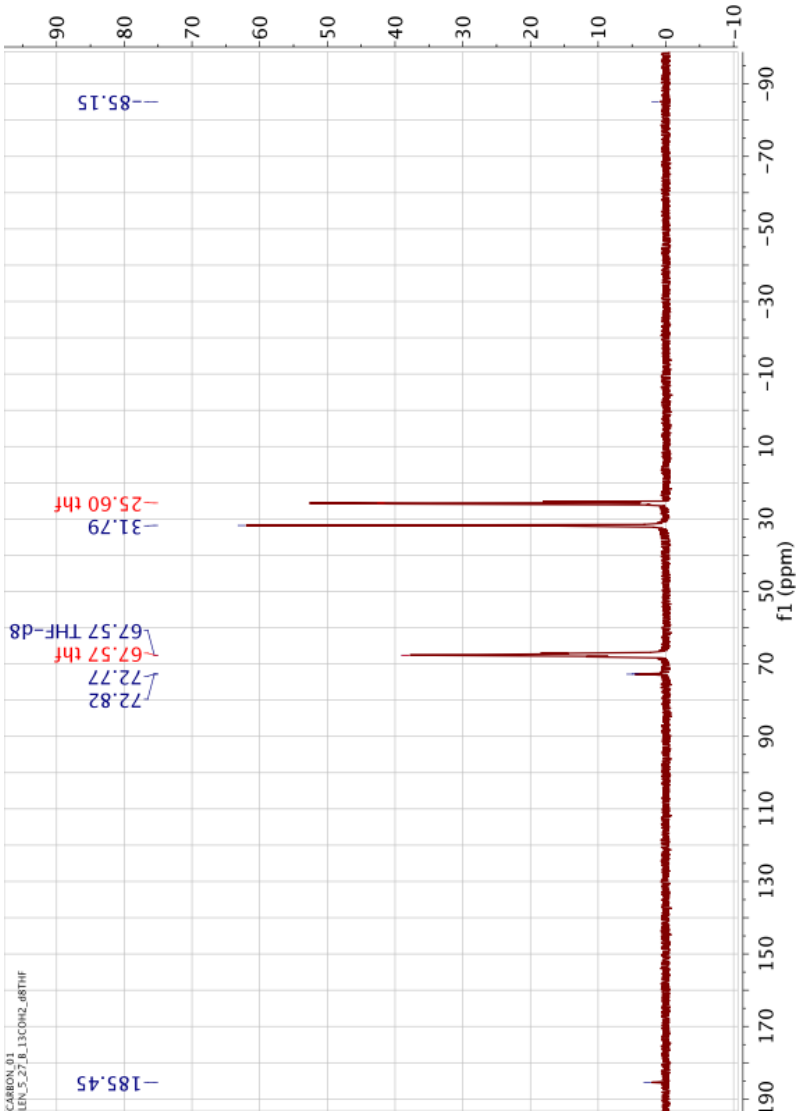

Figure F.19: $^{13}C\{H\}$ NMR for the reaction between K[(U(OSi(O^{t}Bu)$_3$)$_3$)$_2$($\mu-\eta^6:\eta^6$-tol))] and $^{13}CO/H_2$ at -78 °C Day 11 in d_8-THF

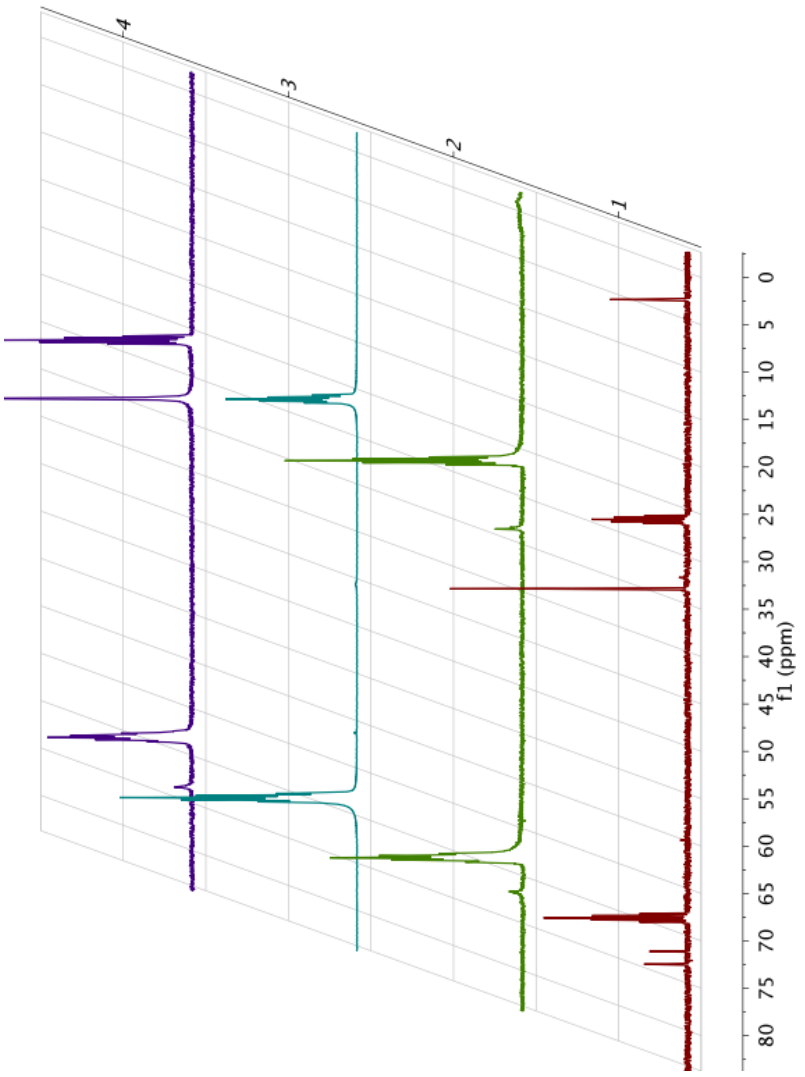

Figure F.20: Stacked $^{13}C\{H\}$ NMR for the reaction between K[(U(OSi(O^{t}Bu)$_3$)$_3$)$_2$(μ–η^6:η^6-tol))] and $^{13}CO/H_2$ in d_8-THF

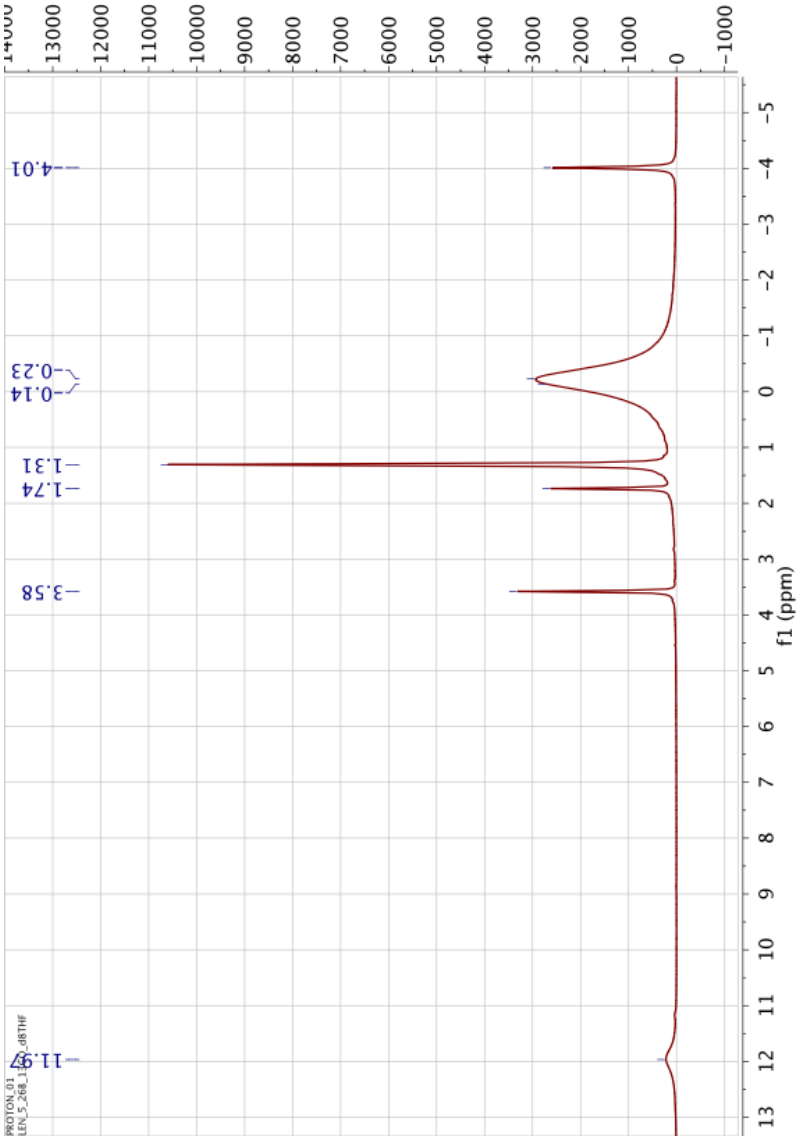

Figure F.21: ^{1}H NMR for the reaction between K[(U(OSi(O^{t}Bu)$_3$)$_3$)$_2$($\mu-\eta^6$:η^6-tol))] and ^{13}CO/H$_2$ at -78 °C Day 1 in d_8-THF

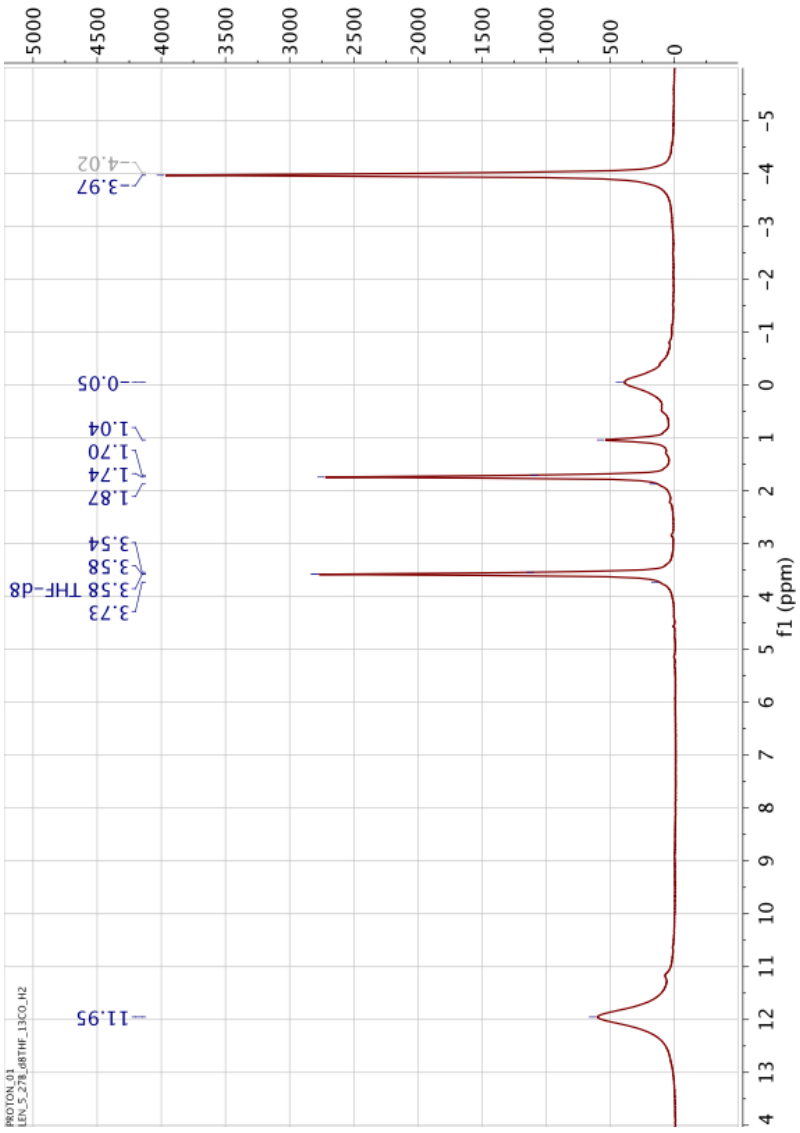

Figure F.22: ^{1}H NMR for the reaction between K[(U(OSi(O^{t}Bu)$_3$)$_3$)$_2$($\mu-\eta^6$:η^6-tol))] and ^{13}CO/H$_2$ at -78 °C Day 10 in d_8-THF

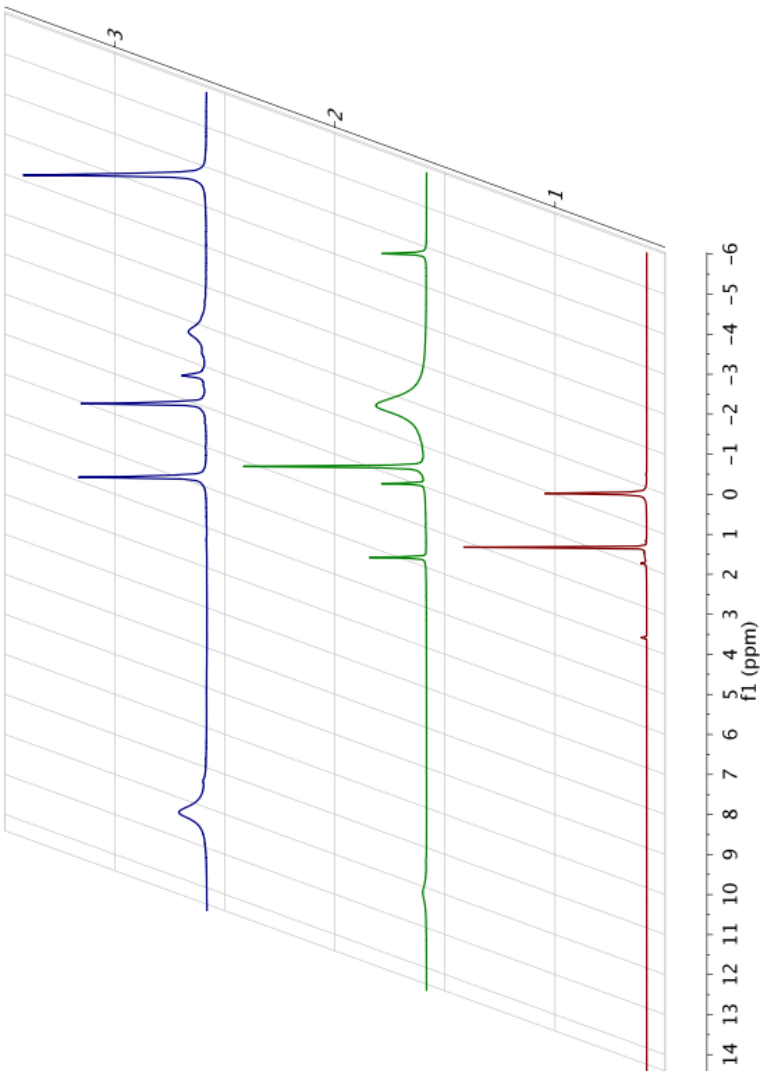

Figure F.23: Stacked ^{1}H NMR for the reaction between K[(U(OSi(O^{t}Bu)$_3$)$_3$)$_2$(μ−η^6:η^6-tol))] and ^{13}CO/H$_2$ in d_8-THF

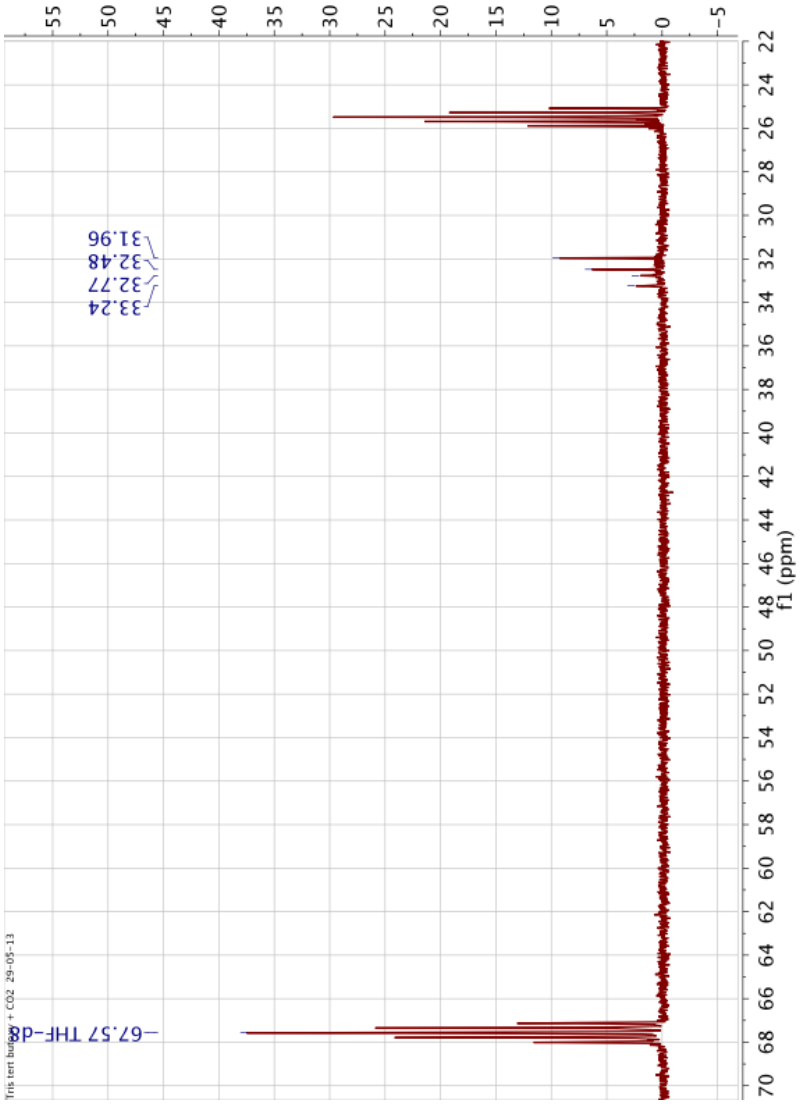

Figure F.24: $^{13}C\{H\}$ NMR for the reaction between K[(U(OSi(O^{t}Bu)$_3$)$_3$)$_2$($\mu-\eta^6$:η^6-tol))] and $^{13}CO_2$ Day 1 in d_8-THF

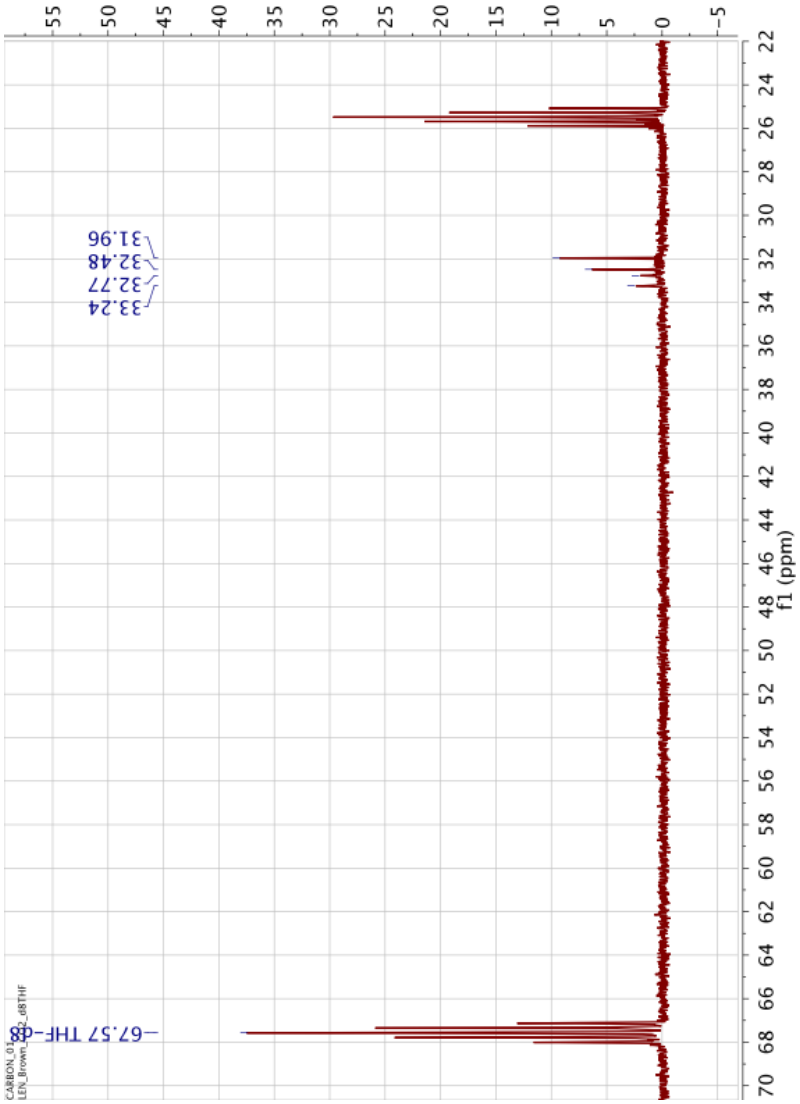

Figure F.25: $^{13}C\{H\}$ NMR for the reaction between K[(U(OSi(O^{t}Bu)$_3$)$_3$)$_2$($\mu-\eta^6$:η^6-tol))] and $^{13}CO_2$ Day 2 in d_8-THF

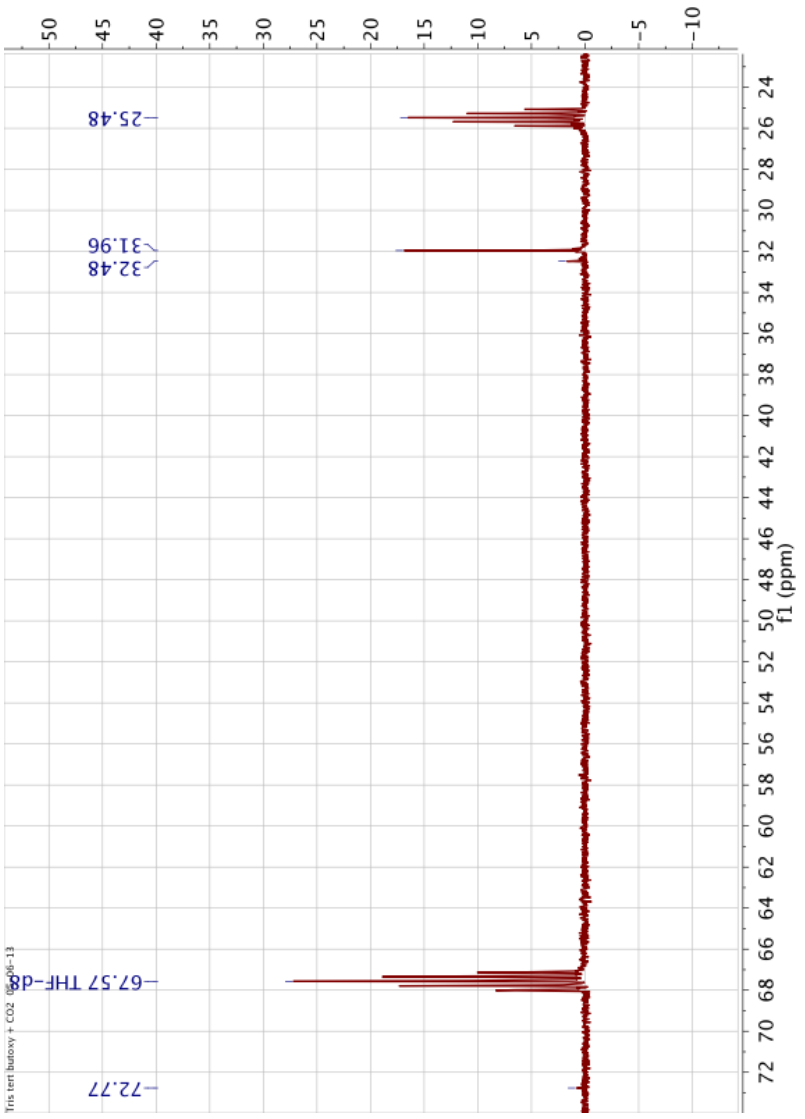

Figure F.26: $^{13}C\{H\}$ NMR for the reaction between K[(U(OSi(O^{t}Bu)$_3$)$_3$)$_2$($\mu-\eta^6$:η^6-tol))] and $^{13}CO_2$ Day 7 in d_8-THF

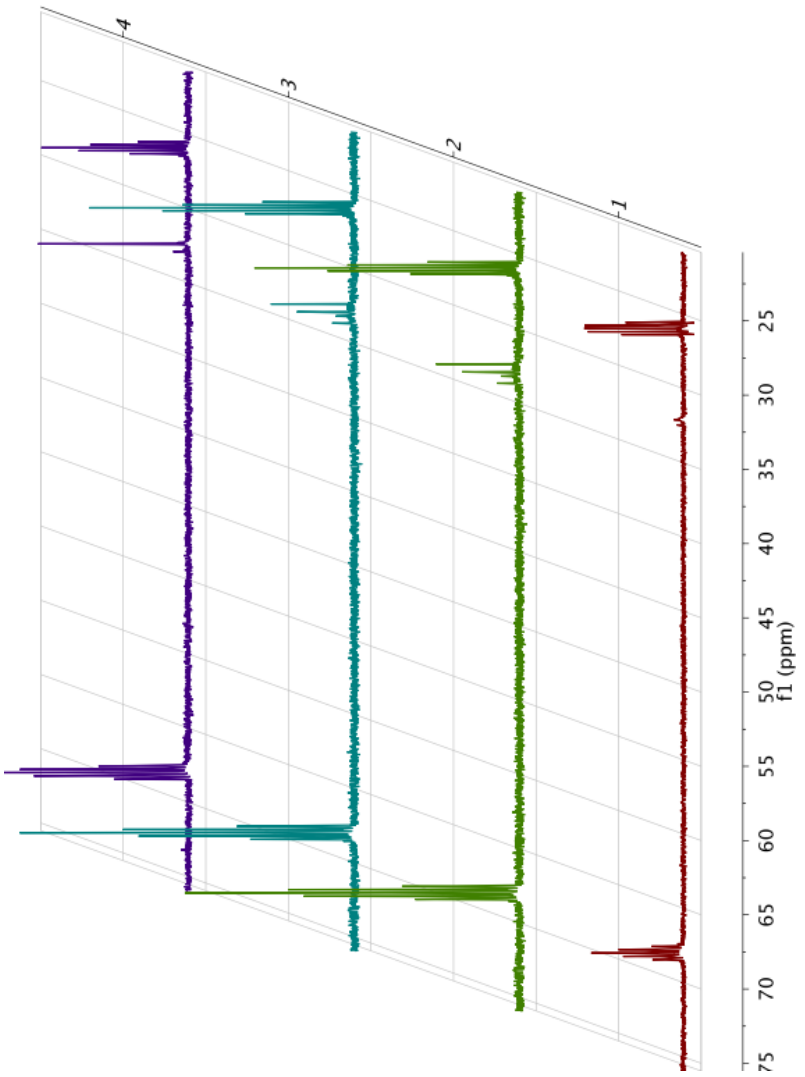

Figure F.27: $^{13}C\{H\}$ NMR for the reaction between K[(U(OSi(O^{t}Bu)$_3$)$_3$)$_2$($\mu-\eta^6$:η^6-tol))] and $^{13}CO_2$ stacked spectra d_8-THF

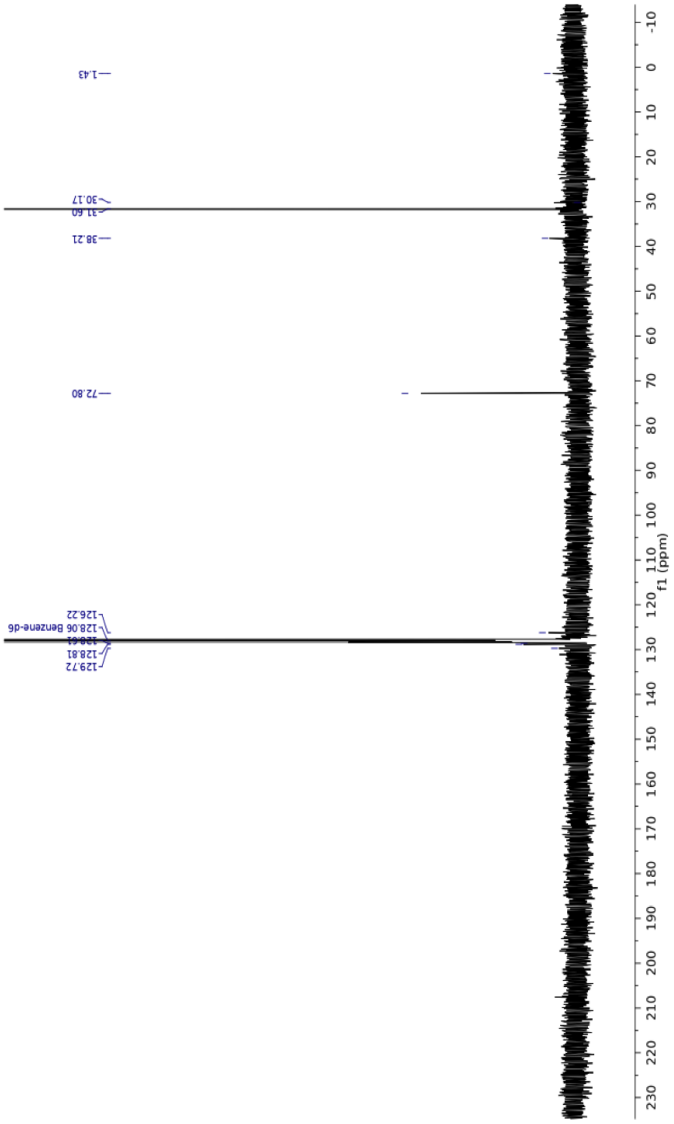

Figure F.28: $^{13}C\{H\}$ NMR for $K[U(CH_2Ph)_2(OSi(O^tBu)_3)_3]$ in d_6-benzene

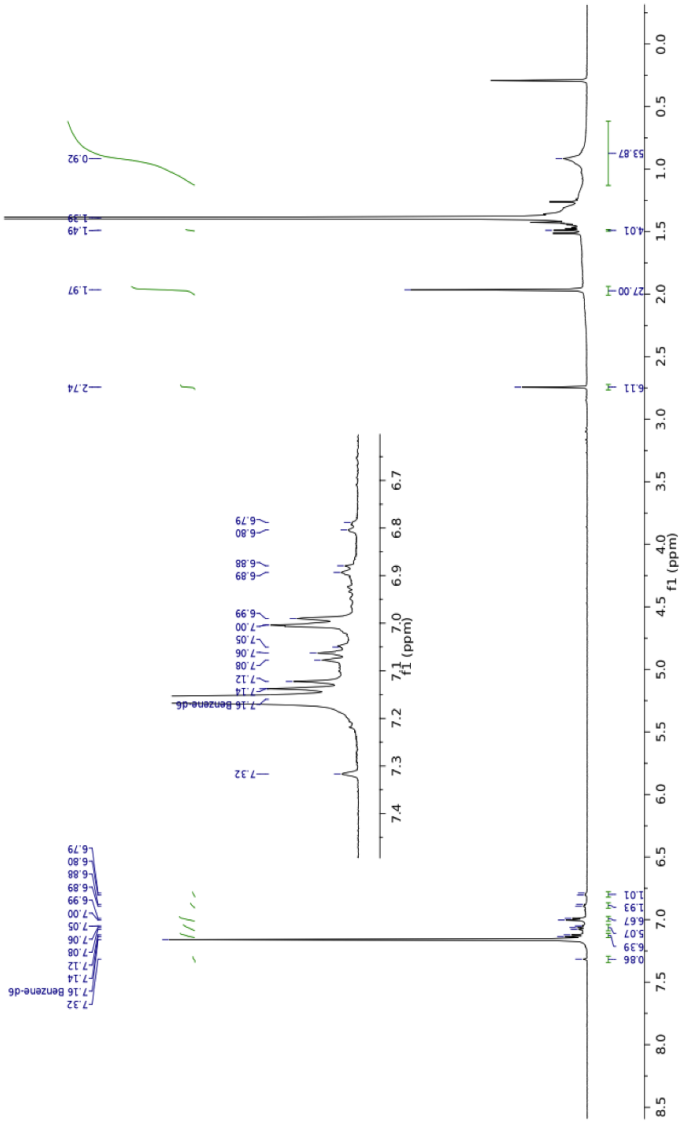

Figure F.29: ^{1}H NMR for K[U(CH$_2$Ph)$_2$(OSi(O^{t}Bu)$_3$)$_3$] in d_6-benzene

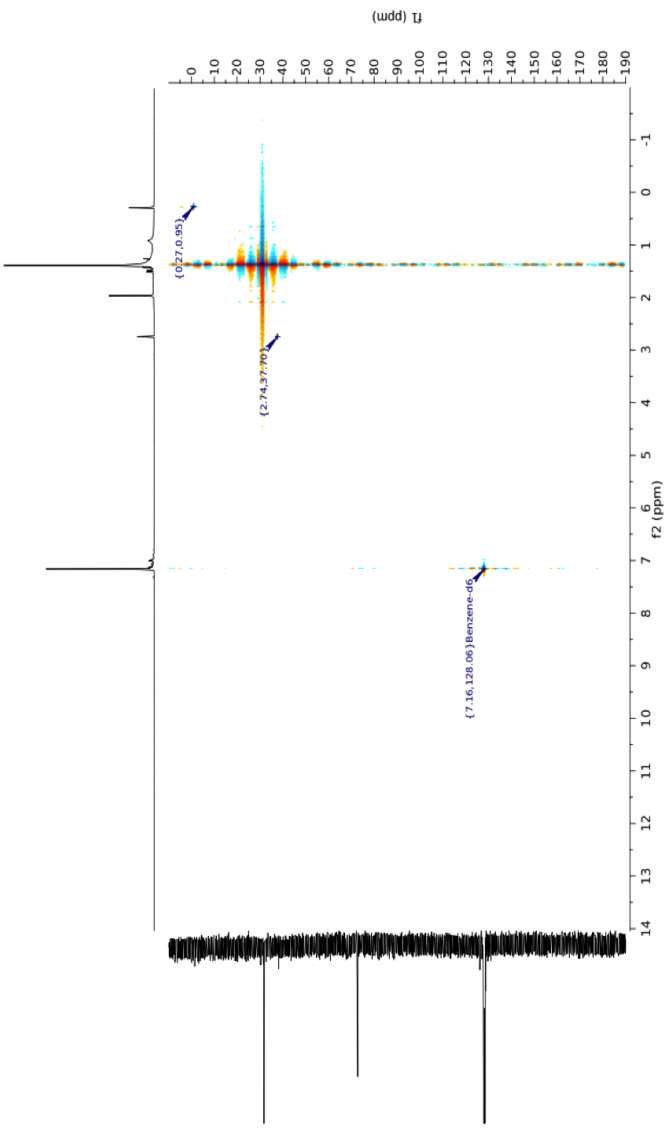

Figure F.30: HMBC NMR for $K[U(CH_2Ph)_2(OSi(O^tBu)_3)_3]$ in d_6-benzene

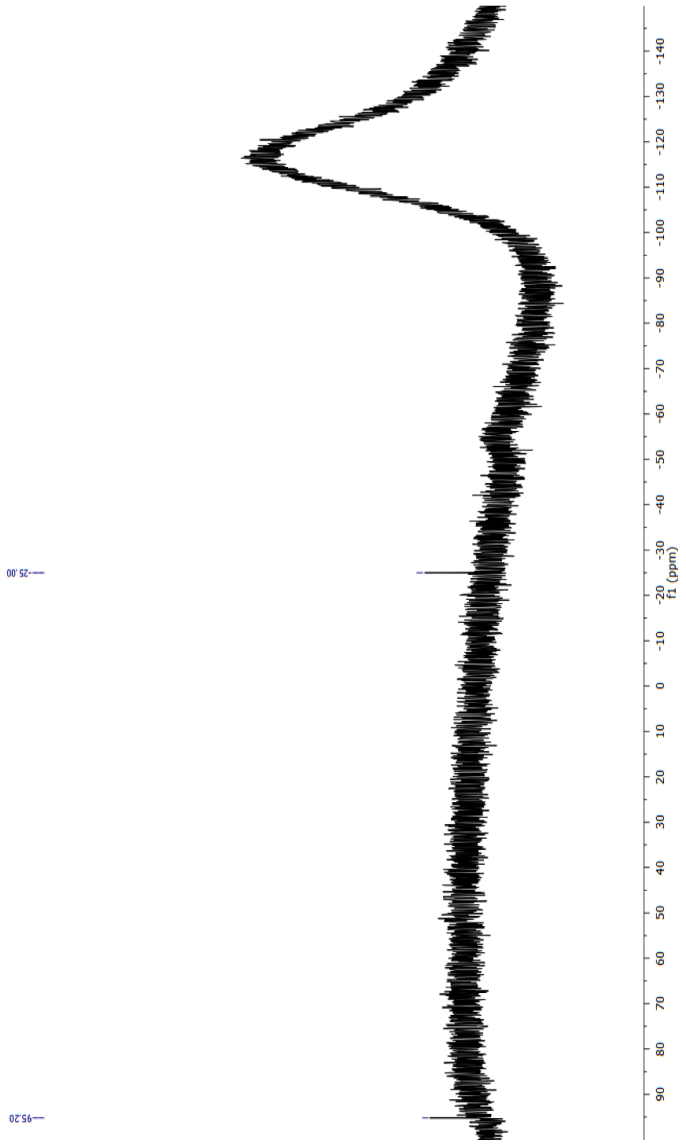

Figure F.31: ^{29}Si NMR for K[U(CH_2Ph)$_2$(OSi(O^{t}Bu)$_3$)$_3$] in d_6-benzene

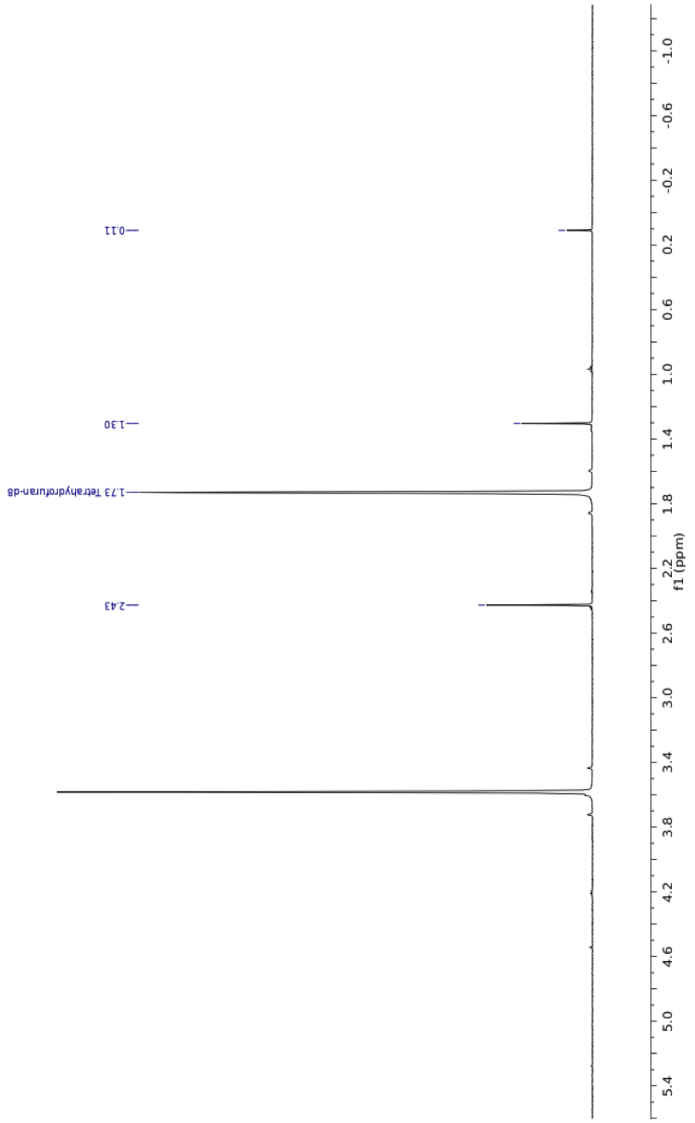

Figure F.32: ^{1}H NMR for the reaction between U(OSi(O^{t}Bu)$_3$)$_4$ and O_2 in d_8-THF

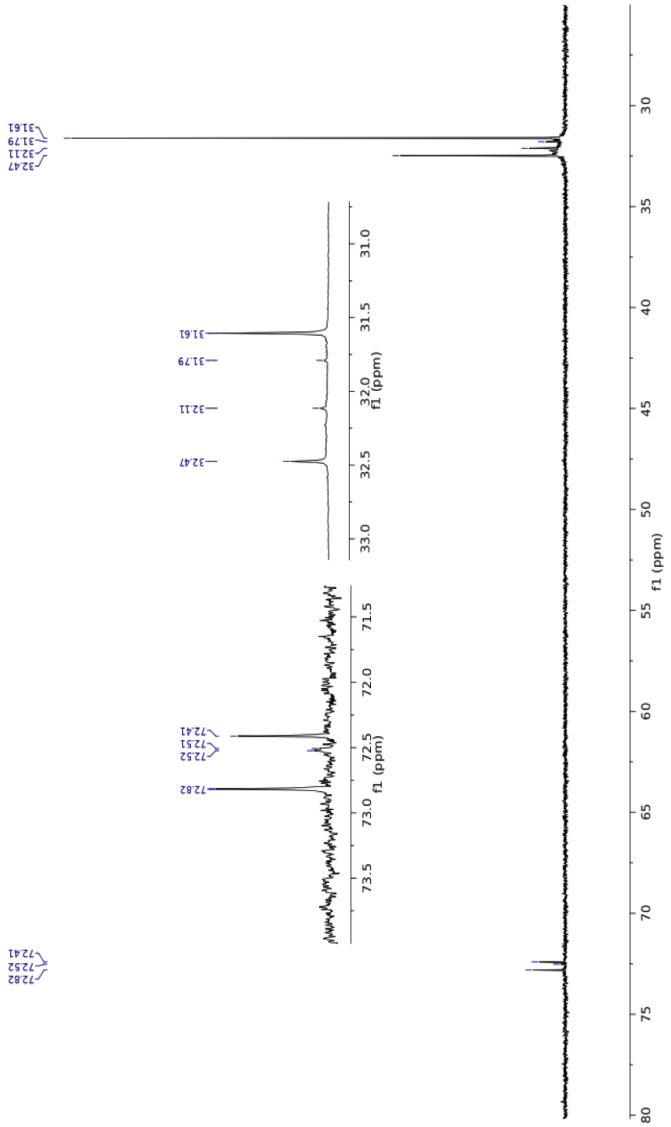

Figure F.33: $^{13}C\{H\}$ NMR for $U(\mu^2-O_2)(OSi(O^tBu)_3)_4(THF)$ in d_6-benzene

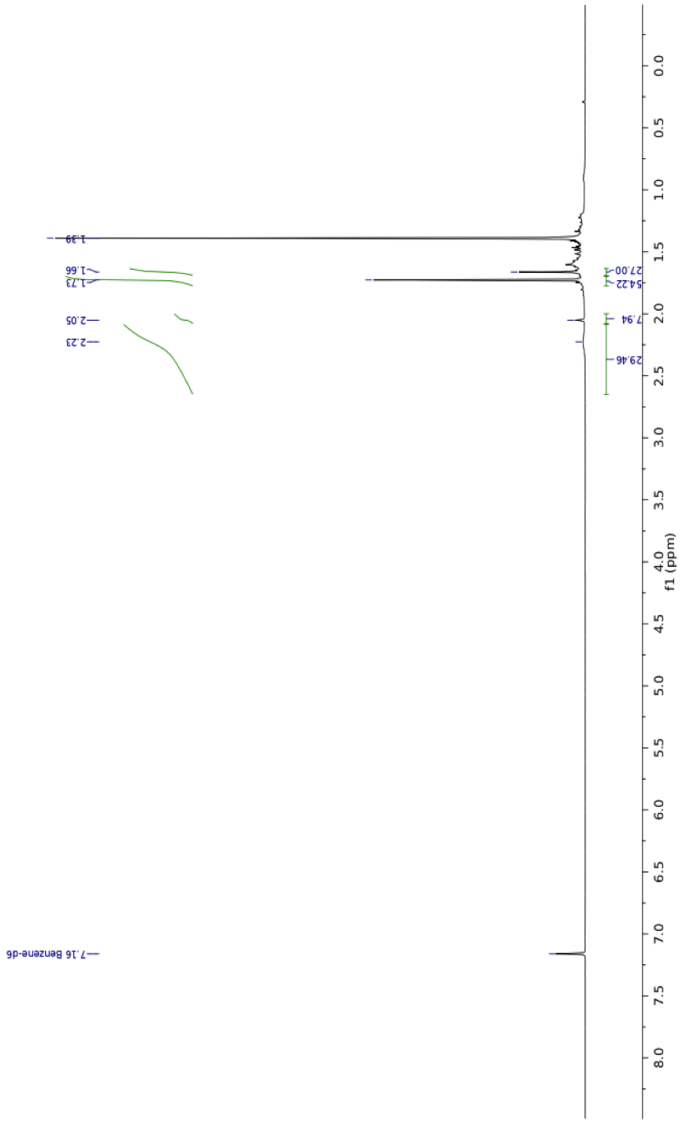

Figure F.34: ^{1}H NMR for U(μ^2-O_2)(OSi(O^{t}Bu)$_3$)$_4$(THF) in d_6-benzene

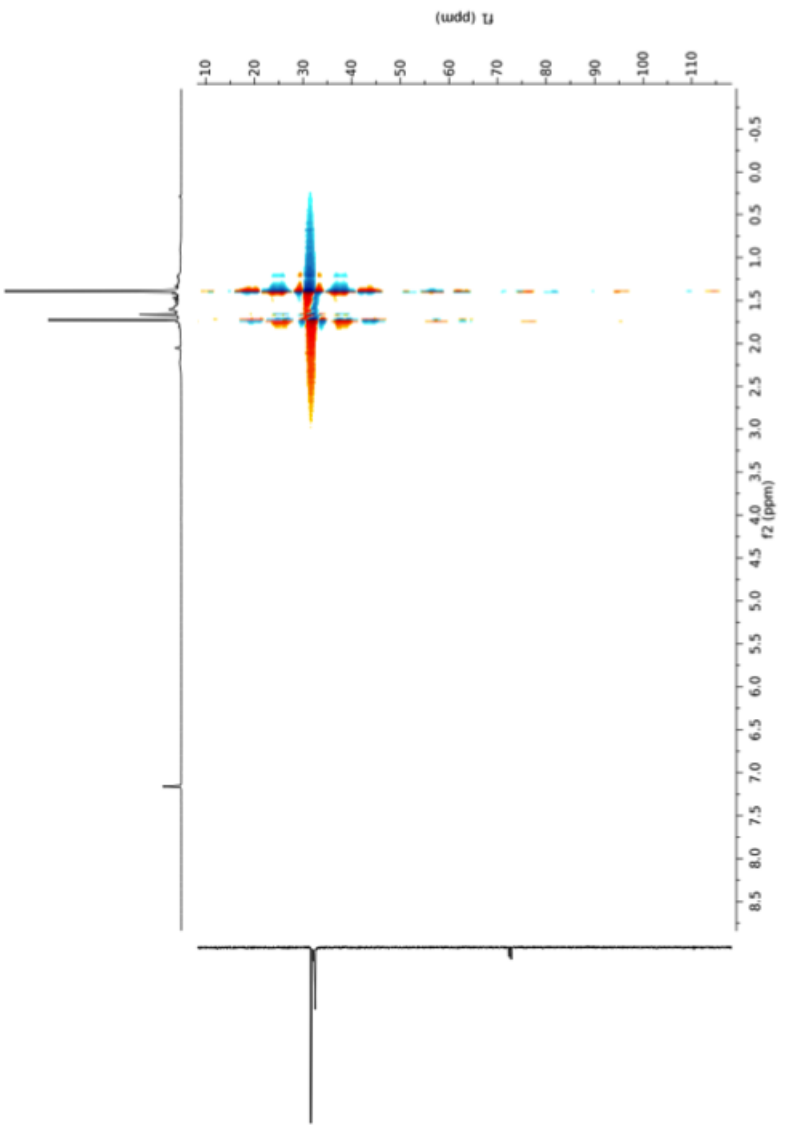

Figure F.35: HMBC NMR for U(μ^2-O_2)(OSi(O^{t}Bu)$_3$)$_4$(THF) in d_6-benzene

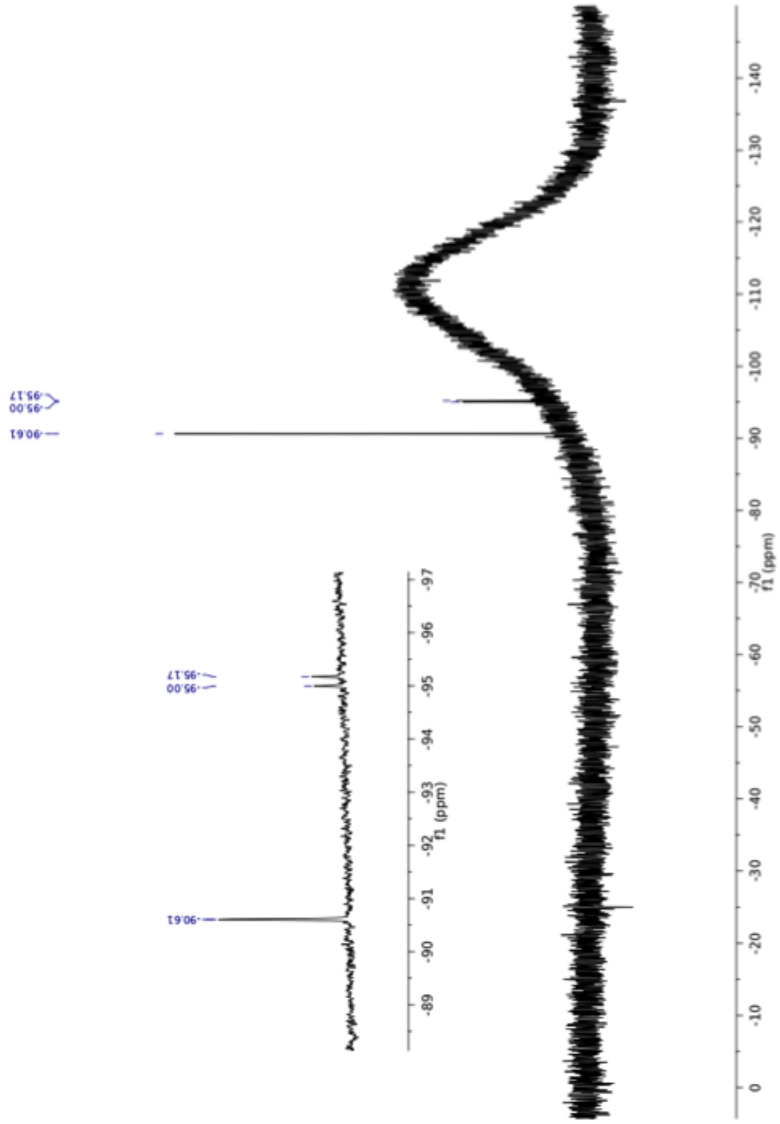

Figure F.36: ^{29}Si NMR for U(μ^2-O_2)(OSi(O^{t}Bu)$_3$)$_4$(THF) in d_6-benzene

Appendix G

Mass spectra - silanol synthesis

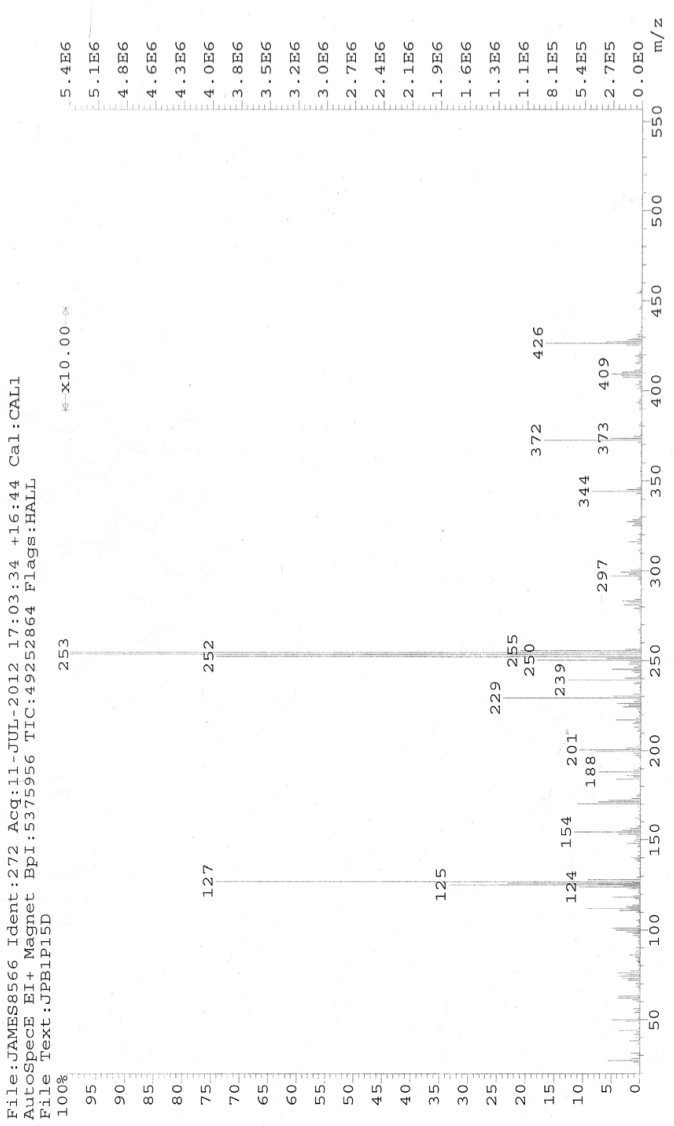

Figure G.1: EI mass spectrum for (1-napthyl)$_3$silanol[80]

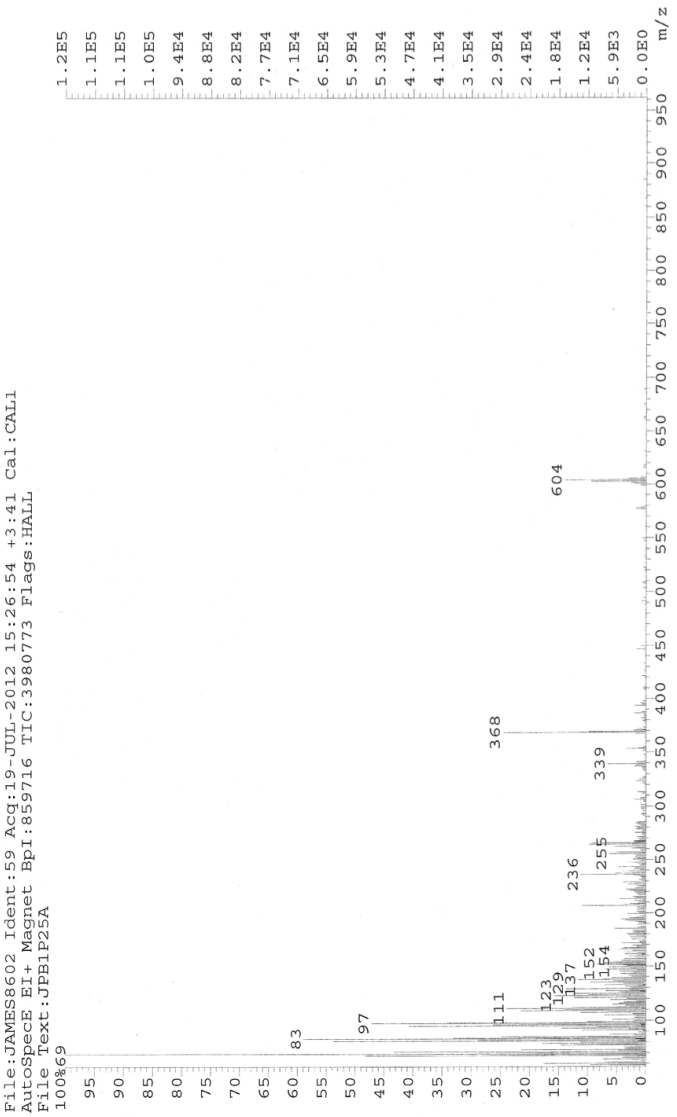

Figure G.2: EI mass spectrum for (4-biphenyl)$_3$silanol[80]

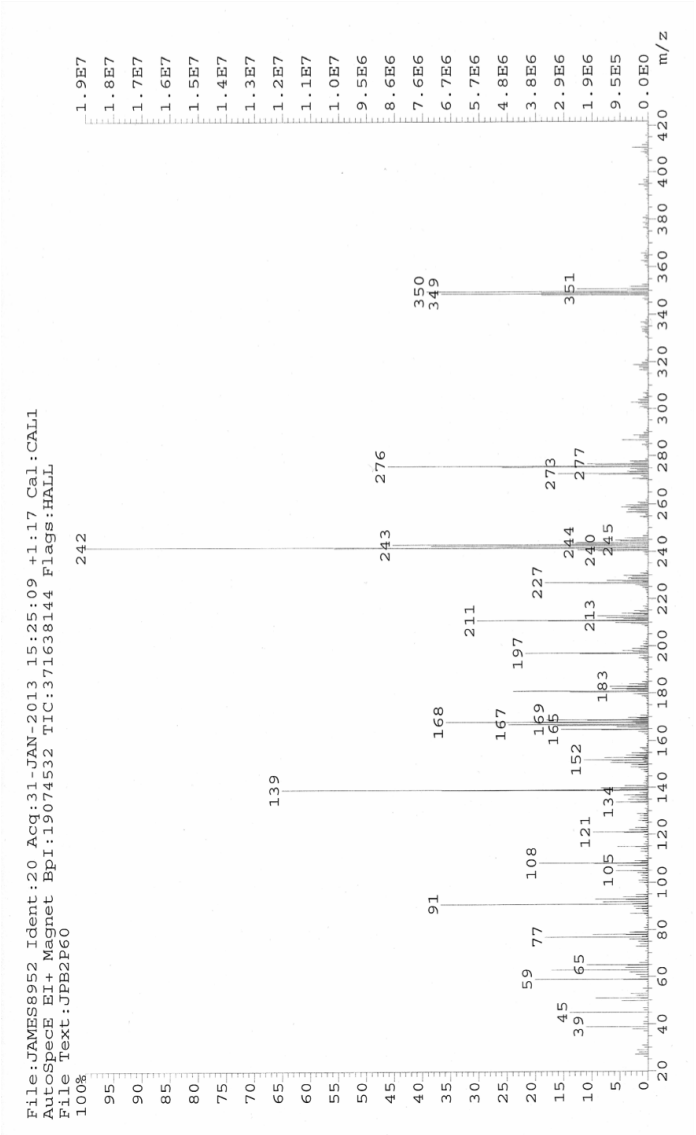

Figure G.3: EI mass spectrum for (1-anisyl)$_3$silanol[80]

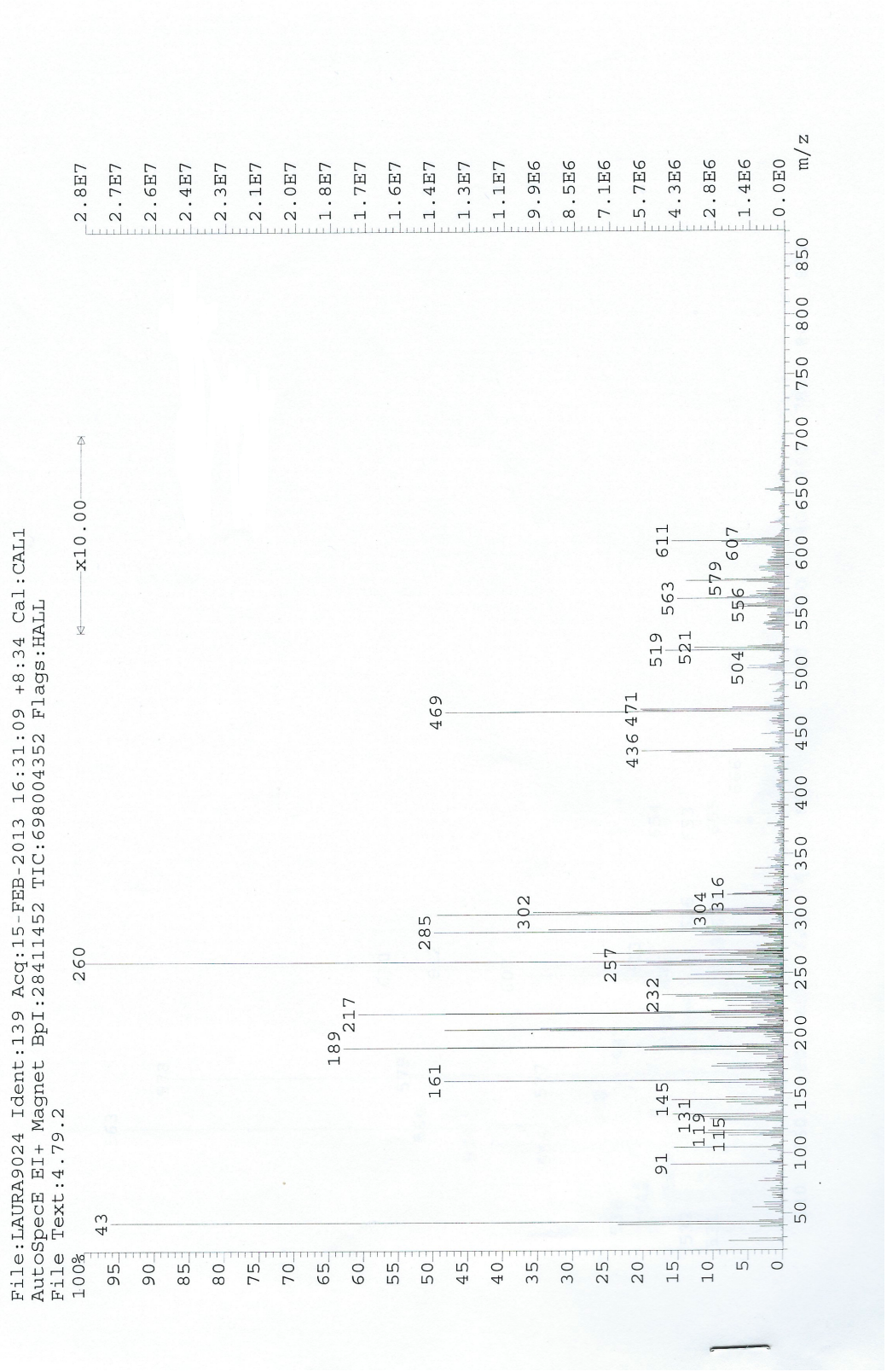

Figure G.4: EI mass spectrum for (2,4,6-triisopropylbenzene)$_3$silanol

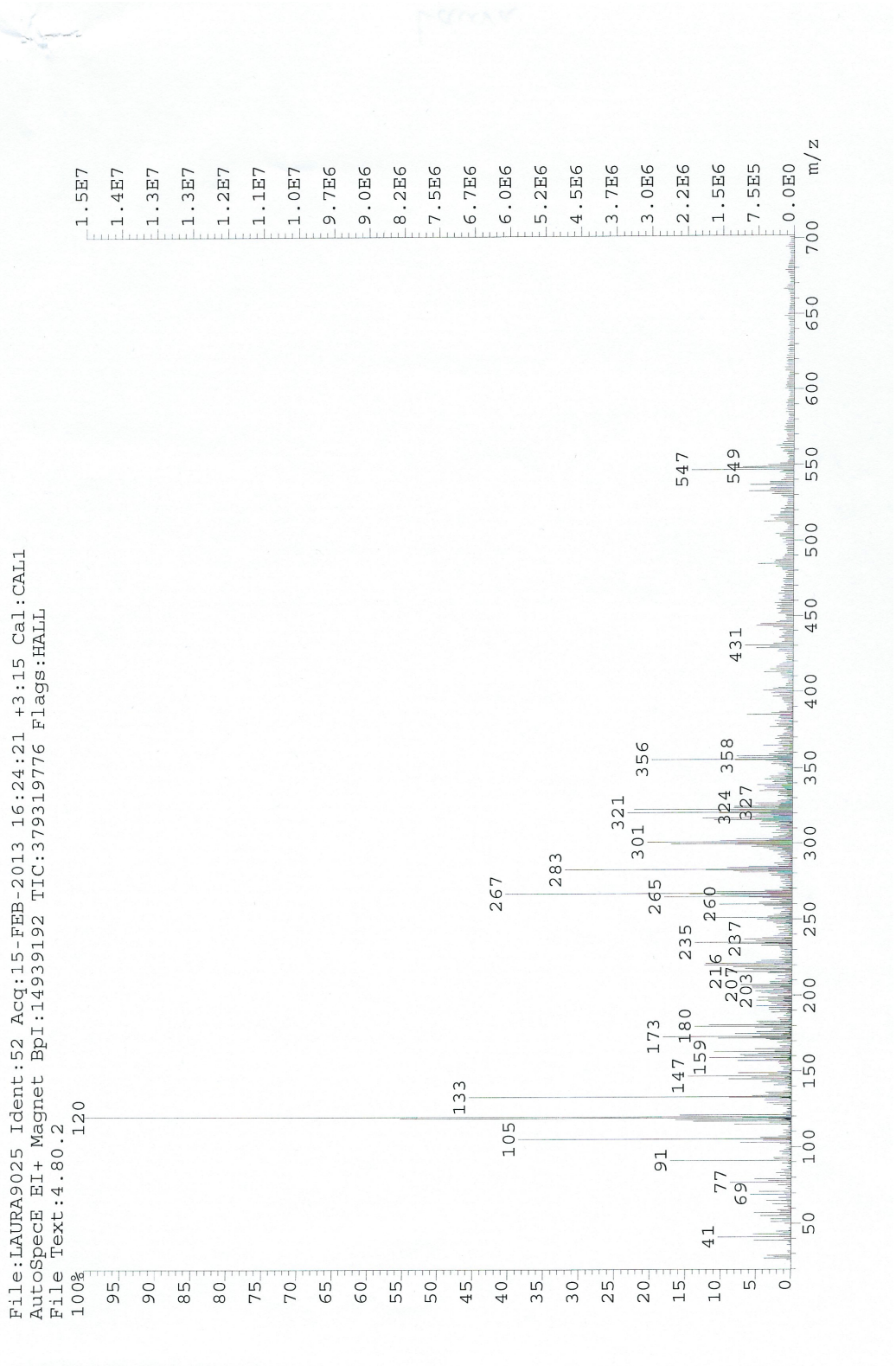

Figure G.5: EI mass spectrum for (mesitylene)$_3$silanol

Appendix H

Mass spectra - triphenylsiloxide ligands

Generic Display Report

Analysis Info

Analysis Name	D:\Data\Alinanoneg\LAURA_8272_000003.d	Acquisition Date	14/12/2011 12:52:06
Method	neg200906024esi_calibrated	Operator	Administrator
Sample Name	neg esi UCL4ADDED 1 OF L	Instrument	apex-III
Comment			

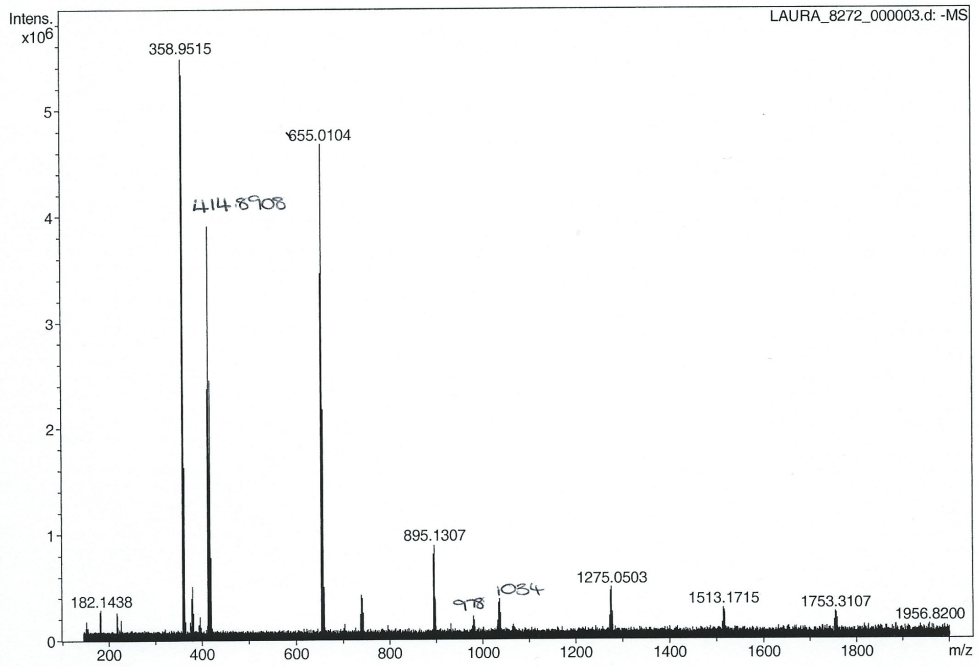

Table 'GenFormulaResults' could not be found in this analysis

Figure H.1: Negative ion HRMS ESI UCl_4 and 1 eq. Ph_3SiOK

Generic Display Report

Analysis Info

Analysis Name	D:\Data\Alinanoneg\LAURA_8272_000003.d	Acquisition Date	14/12/2011 12:52:06
Method	neg200906024esi_calibrated	Operator	Administrator
Sample Name	neg esi UCL4ADDED 1 OF L	Instrument	apex-III
Comment			

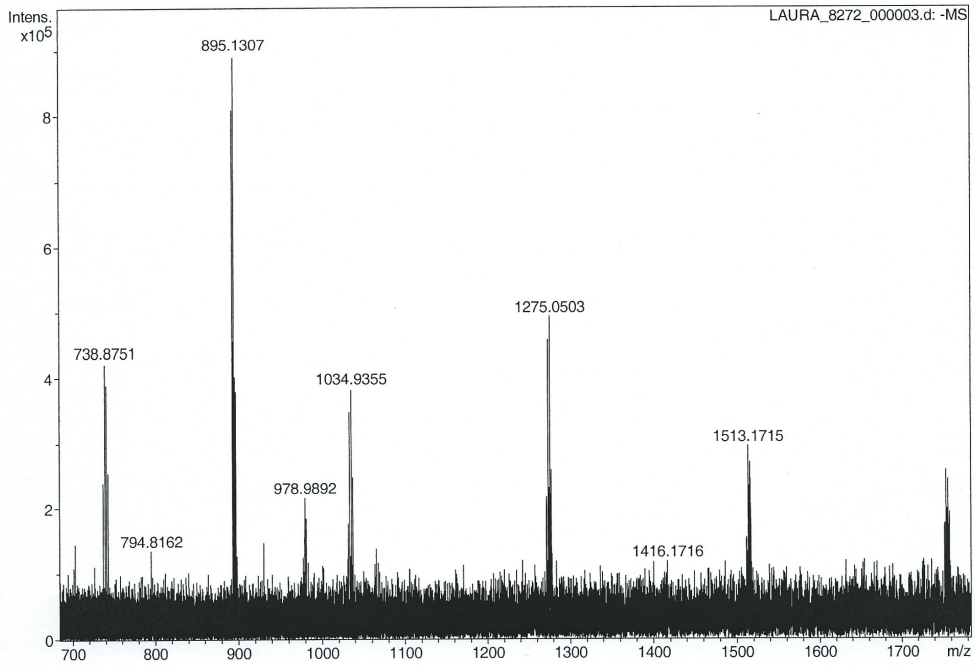

Table 'GenFormulaResults' could not be found in this analysis

Figure H.2: Negative ion HRMS ESI UCl_4 and 1 eq. Ph_3SiOK

Generic Display Report

Analysis Info

Analysis Name	D:\Data\Alinanoneg\LAURA_8272_000003.d	Acquisition Date	14/12/2011 12:52:06
Method	neg200906024esi_calibrated	Operator	Administrator
Sample Name	neg esi UCL4ADDED 1 OF L	Instrument	apex-III
Comment			

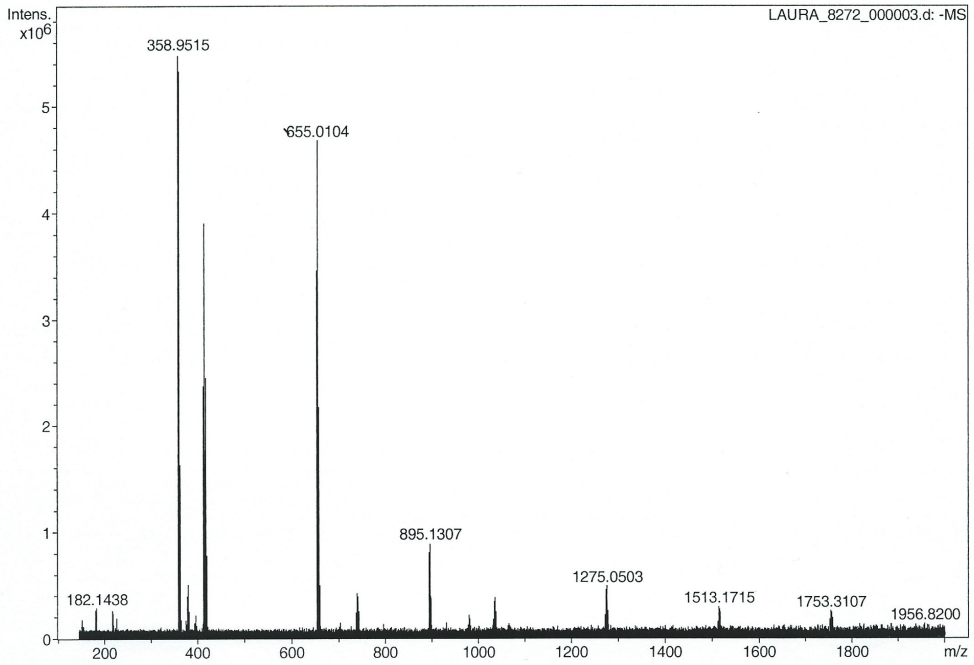

Table 'GenFormulaResults' could not be found in this analysis

Figure H.3: Negative ion HRMS ESI UCl_4 and 1 eq. Ph_3SiOK

Generic Display Report

Analysis Info

Analysis Name	D:\Data\Alinanoneg\LAURA_8273_000002.d	Acquisition Date	14/12/2011 14:37:36
Method	neg200906024esi_calibrated	Operator	Administrator
Sample Name	neg esi UCL4ADDED 1.5 OF L	Instrument	apex-III
Comment			

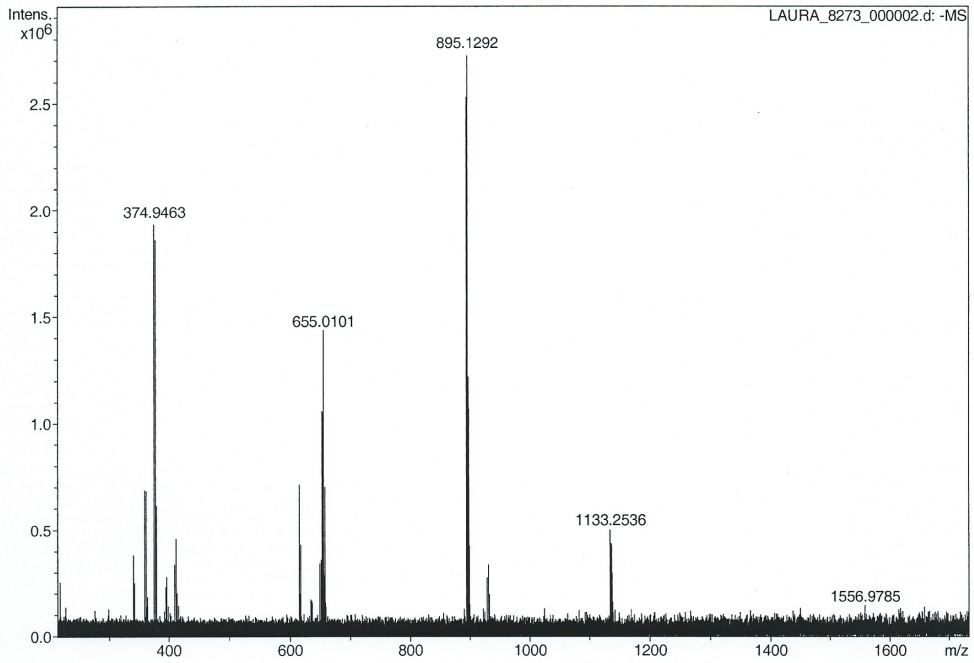

Table 'GenFormulaResults' could not be found in this analysis

Figure H.4: Negative ion HRMS ESI UCl_4 and 1.5 eq. Ph_3SiOK

Generic Display Report

Analysis Info

Analysis Name	D:\Data\Alinanoneg\LAURA_8273_000003.d	Acquisition Date	14/12/2011 14:39:02
Method	neg200906024esi_calibrated	Operator	Administrator
Sample Name	neg esi UCL4ADDED 1.5 OF L	Instrument	apex-III
Comment			

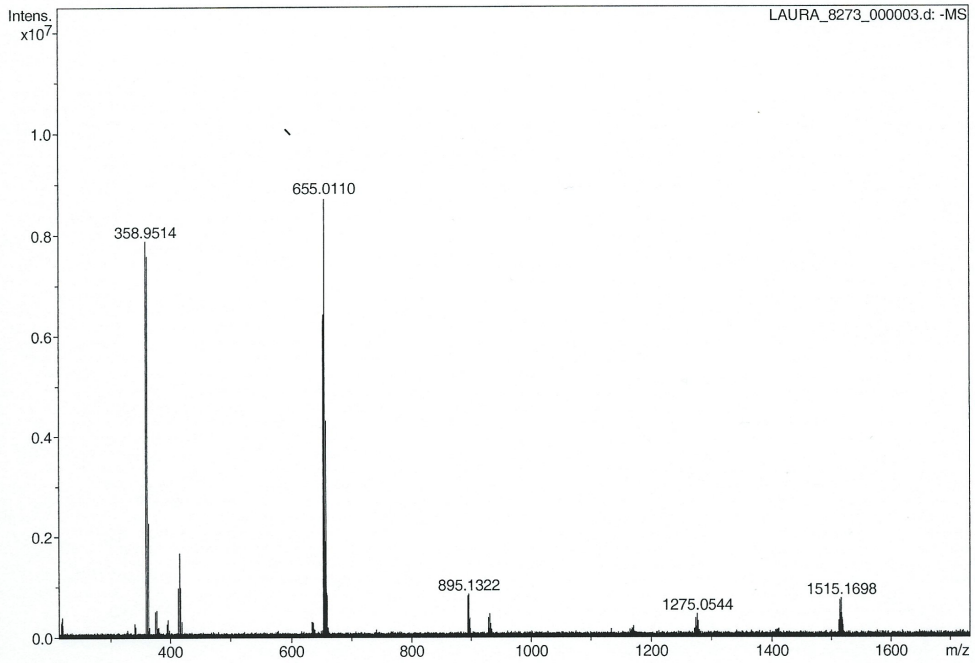

Table 'GenFormulaResults' could not be found in this analysis

Figure H.5: Negative ion HRMS ESI UCl_4 and 1.5 eq. Ph_3SiOK

Generic Display Report

Analysis Info

Analysis Name	D:\Data\Alinanoneg\LAURA_8273_000003.d	Acquisition Date	14/12/2011 14:39:02
Method	neg200906024esi_calibrated	Operator	Administrator
Sample Name	neg esi UCL4ADDED 1.5 OF L	Instrument	apex-III
Comment			

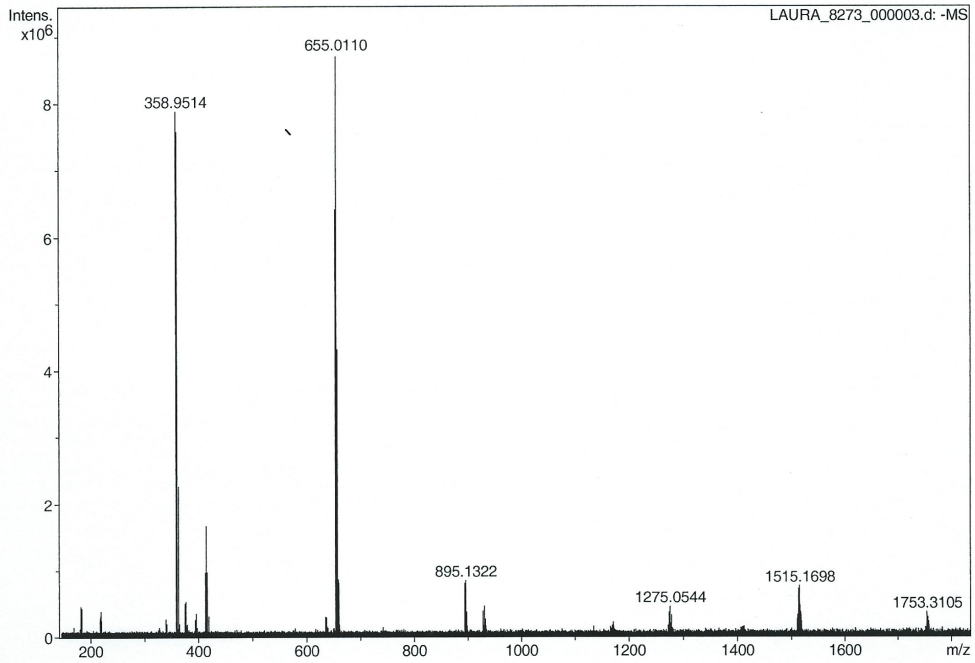

Table 'GenFormulaResults' could not be found in this analysis

Figure H.6: Negative ion HRMS ESI UCl_4 and 1.5 eq. Ph_3SiOK

Generic Display Report

Analysis Info

Analysis Name	D:\Data\Alinanoneg\LAURA_8274_000003.d	Acquisition Date	14/12/2011 14:56:50
Method	neg200906024esi_calibrated	Operator	Administrator
Sample Name	neg esi UCL4ADDED 2 OF L	Instrument	apex-III
Comment			

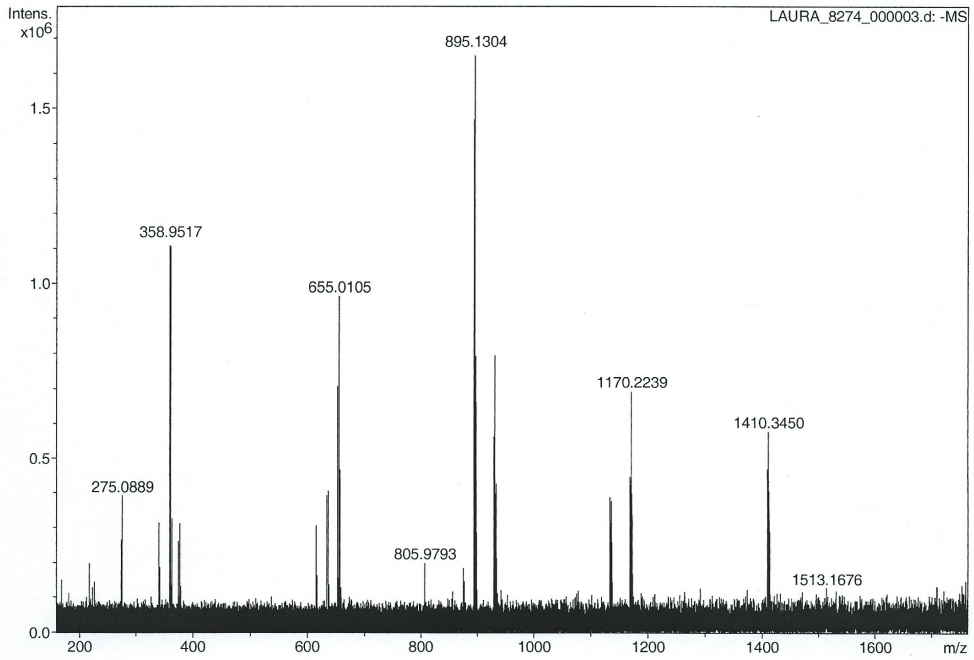

Table 'GenFormulaResults' could not be found in this analysis

Figure H.7: Negative ion HRMS ESI UCl_4 and 2 eq. Ph_3SiOK

Generic Display Report

Analysis Info

Analysis Name	D:\Data\Alinanoneg\LAURA_8275_000003.d	Acquisition Date	14/12/2011 15:14:52
Method	neg200906024esi_calibrated	Operator	Administrator
Sample Name	neg esi UCL4ADDED 3 OF L	Instrument	apex-III
Comment			

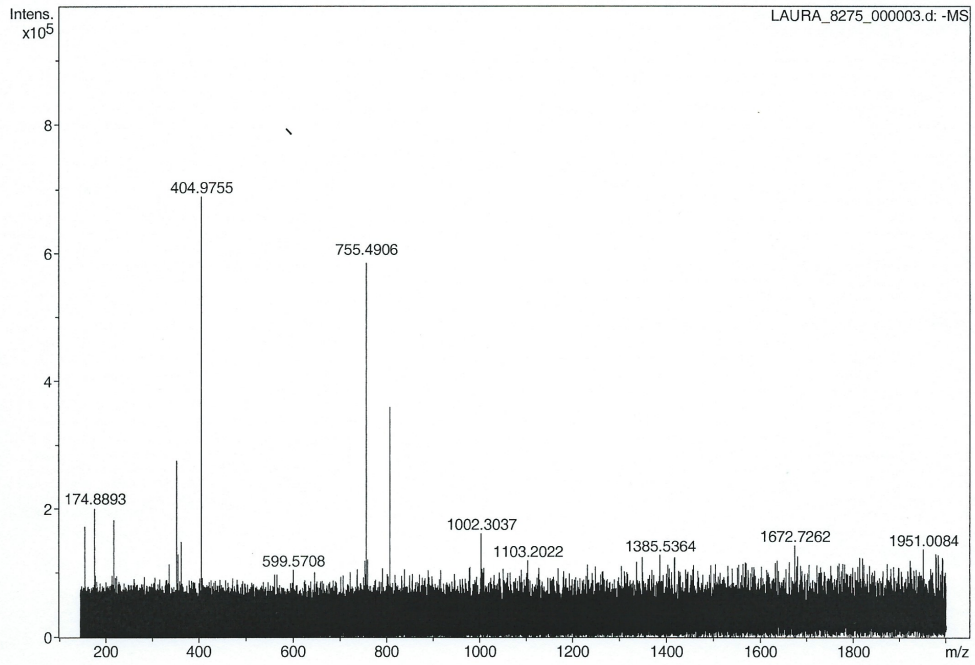

Table 'GenFormulaResults' could not be found in this analysis

Figure H.8: Negative ion HRMS ESI UCl_4 and 3 eq. Ph_3SiOK

Generic Display Report

Analysis Info

Analysis Name	D:\Data\Alinanoneg\LAURA_8275_000004.d	Acquisition Date	14/12/2011 15:16:09
Method	neg200906024esi_calibrated	Operator	Administrator
Sample Name	neg esi UCL4ADDED 3 OF L	Instrument	apex-III
Comment			

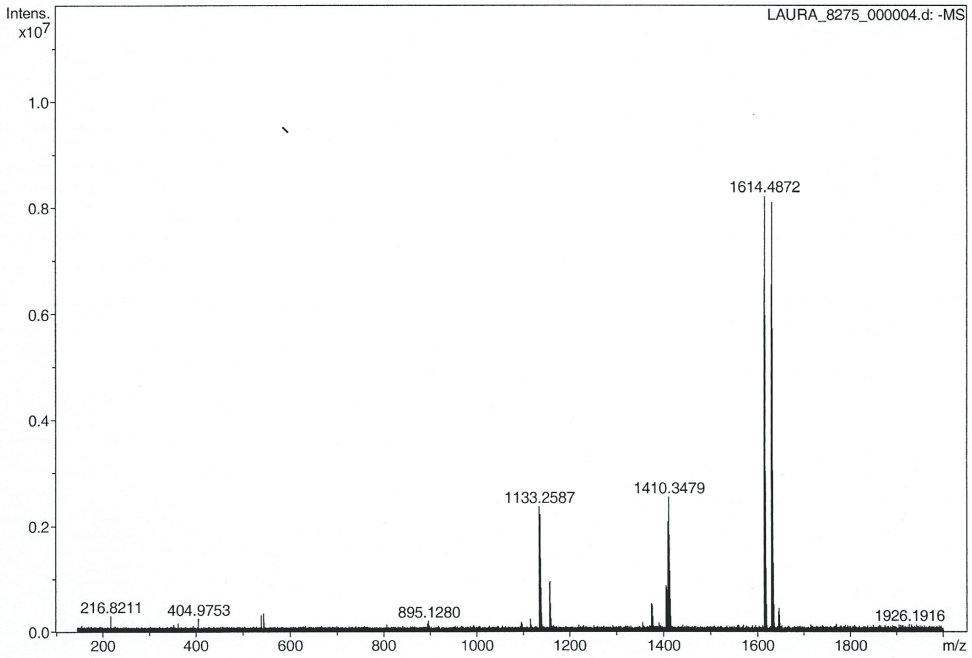

Table 'GenFormulaResults' could not be found in this analysis

Bruker Daltonics DataAnalysis 3.4 printed: 14/12/2011 15:17:27 Page 1 of 1

Figure H.9: Negative ion HRMS ESI UCl_4 and 3 eq. Ph_3SiOK

Generic Display Report

Analysis Info

Analysis Name	D:\Data\Alinanoneg\LAURA_8276_000002.d	Acquisition Date	14/12/2011 15:31:05
Method	neg200906024esi_calibrated	Operator	Administrator
Sample Name	neg esi UCL4ADDED 4OF L	Instrument	apex-III
Comment			

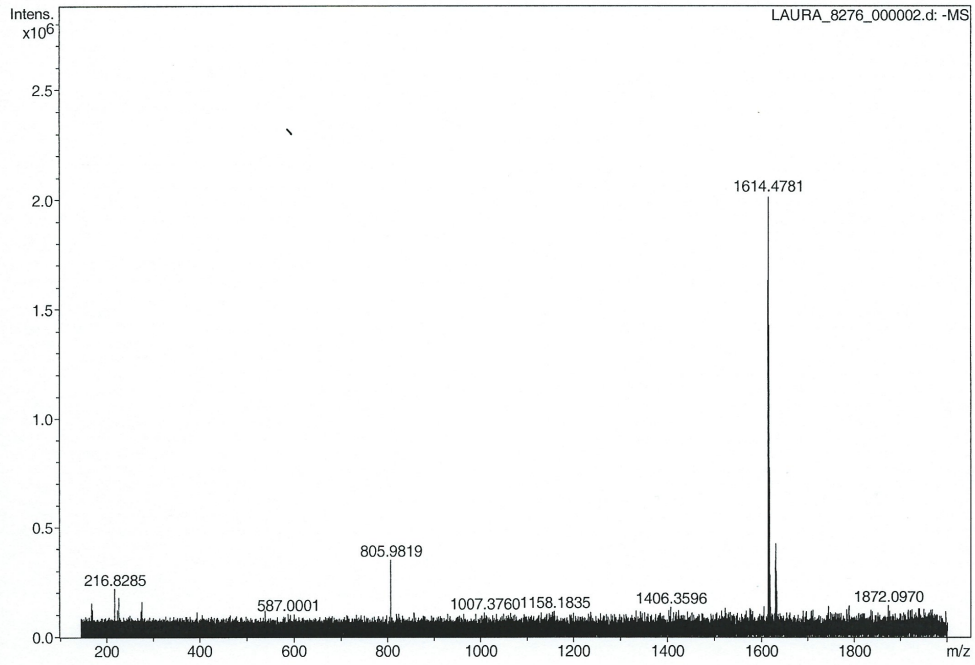

Table 'GenFormulaResults' could not be found in this analysis

Figure H.10: Negative ion HRMS ESI UCl_4 and 4 eq. Ph_3SiOK

Generic Display Report

Analysis Info

Analysis Name	D:\Data\Alinanoneg\SARAH_99999_000001.d	Acquisition Date	25/04/2012 11:56:05
Method	neg200906024esi_calibrated	Operator	Administrator
Sample Name	neg esi 2.82	Instrument	apex-III
Comment			

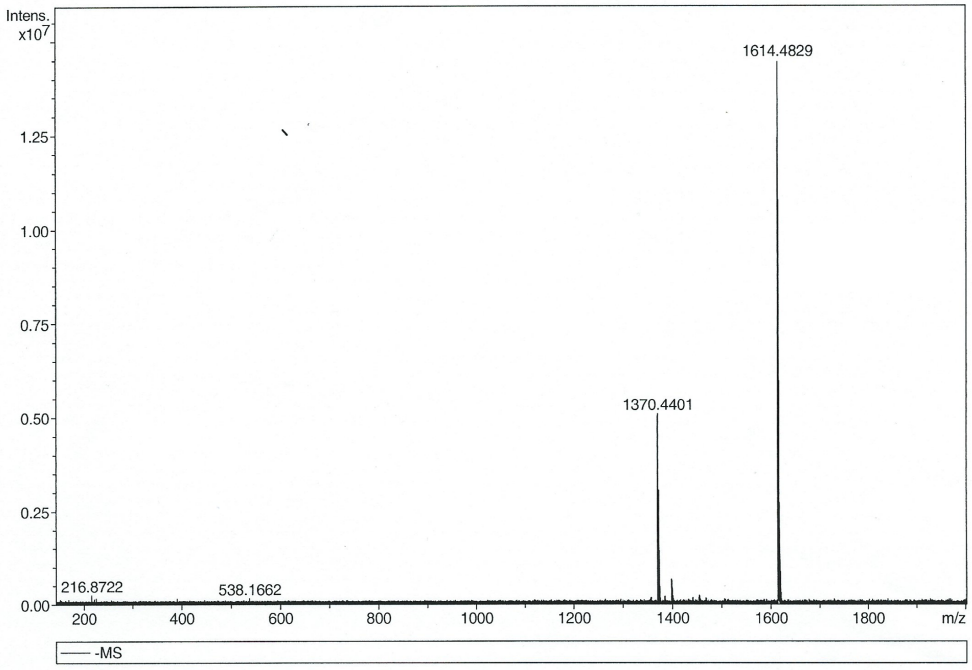

Table 'GenFormulaResults' could not be found in this analysis

Figure H.11: Negative ion HRMS ESI UCl_4 and 5 eq. Ph_3SiOK

Generic Display Report

Analysis Info

Analysis Name	D:\Data\Alinanoneg\LAURA_8277_000002.d	Acquisition Date	14/12/2011 16:00:24
Method	neg200906024esi_calibrated	Operator	Administrator
Sample Name	neg esi UCL4ADDED 6OF L	Instrument	apex-III
Comment			

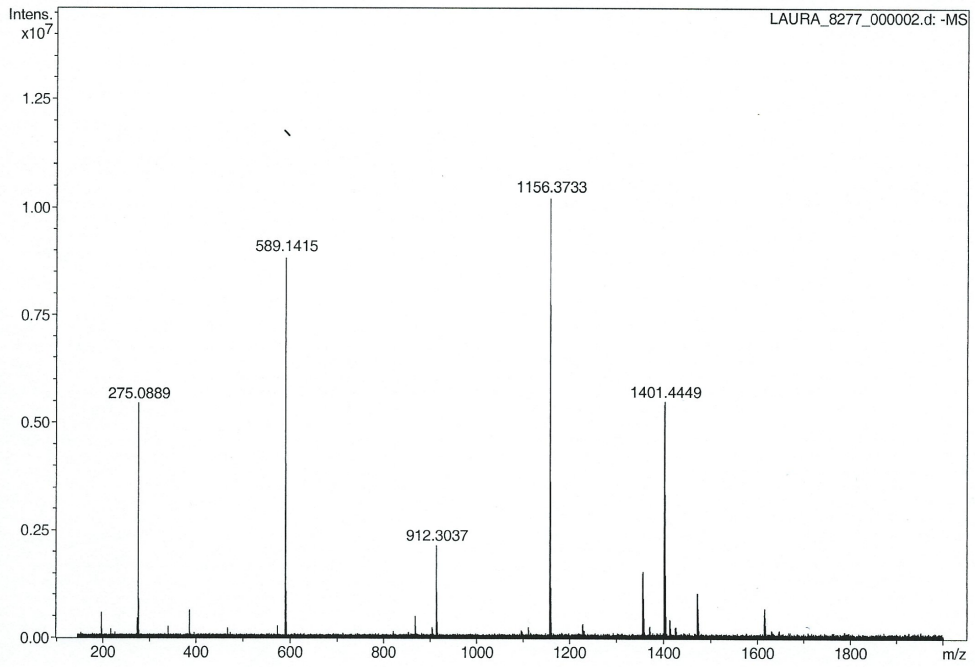

Table 'GenFormulaResults' could not be found in this analysis

Figure H.12: Negative ion HRMS ESI UCl_4 and 6 eq. Ph_3SiOK

Appendix I

Mass spectra - reactions with TMSOTf

Generic Display Report

Analysis Info

Analysis Name	D:\Data\Alinanoneg\SARAH_99999_000001.d	Acquisition Date	25/04/2012 11:56:05
Method	neg200906024esi_calibrated	Operator	Administrator
Sample Name	neg esi 2.82	Instrument	apex-III
Comment			

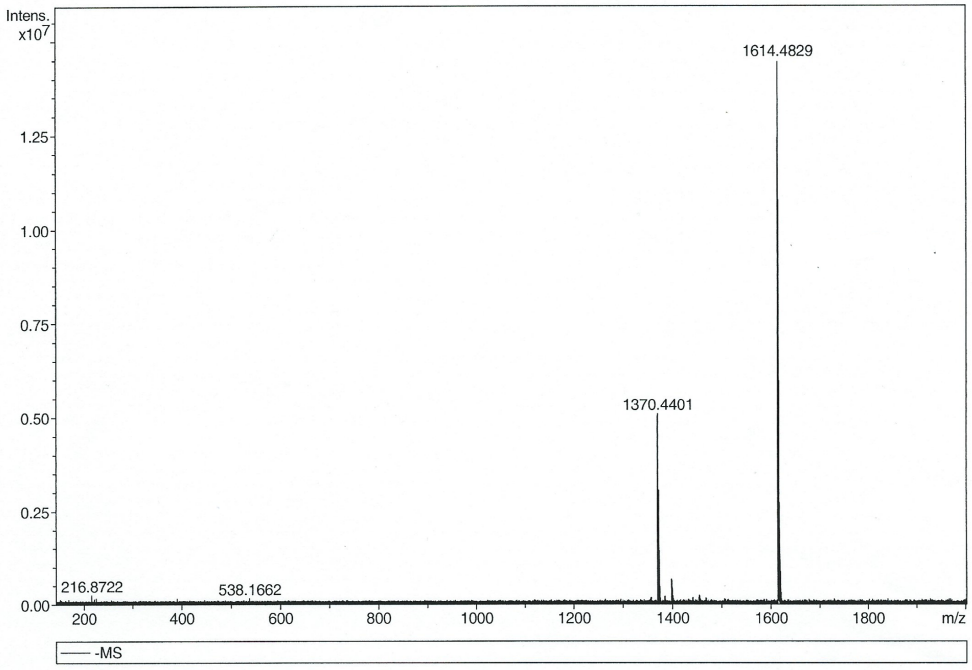

Table 'GenFormulaResults' could not be found in this analysis

Figure I.1: Negative ion HRMS ESI $K[(Ph_3SiO)_5U(THF)]$ and 0 eq. TMSOTf

Generic Display Report

Analysis Info

Analysis Name	D:\Data\Alinanoneg\SARAH_99991_000005.d	Acquisition Date	25/04/2012 12:15:25
Method	neg200906024esi_calibrated	Operator	Administrator
Sample Name	neg esi 2.82 plus 1	Instrument	apex-III
Comment			

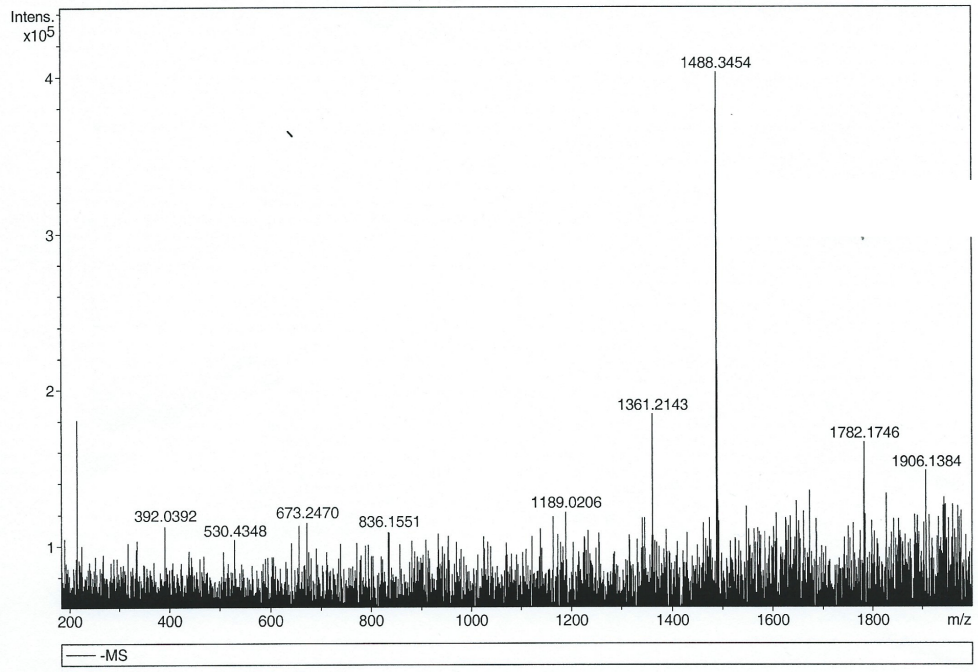

Table 'GenFormulaResults' could not be found in this analysis

Bruker Daltonics DataAnalysis 3.4 printed: 25/04/2012 12:16:39 Page 1 of 1

Figure I.2: Negative ion HRMS ESI $K[(Ph_3SiO)_5U(THF)]$ and 1 eq. TMSOTf

Generic Display Report

Analysis Info

Analysis Name	D:\Data\Alinanoneg\SARAH_99992_000004.d	Acquisition Date	25/04/2012 12:27:37
Method	neg200906024esi_calibrated	Operator	Administrator
Sample Name	neg esi 2.82 plus 2	Instrument	apex-III
Comment			

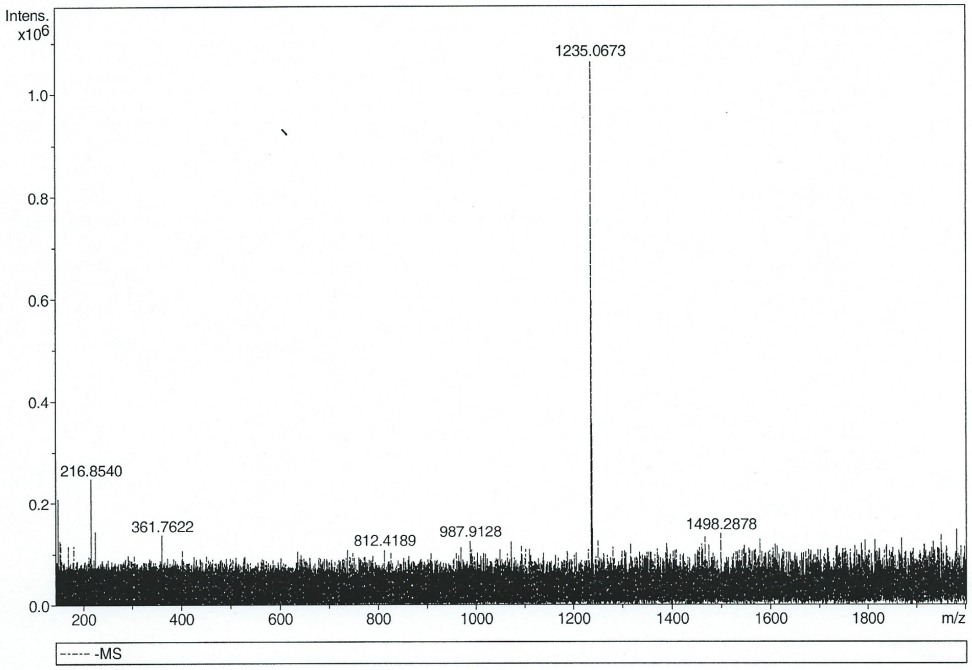

Table 'GenFormulaResults' could not be found in this analysis

Bruker Daltonics DataAnalysis 3.4 printed: 25/04/2012 12:28:27 Page 1 of 1

Figure I.3: Negative ion HRMS ESI $K[(Ph_3SiO)_5U(THF)]$ and 2 eq. TMSOTf

Generic Display Report

Analysis Info

Analysis Name	D:\Data\Alinanopos\LAURA_2079_000001.d	Acquisition Date	20/03/2012 15:38:10
Method	pos20090608esi	Operator	Administrator
Sample Name	POS ESI u PETACYLOXY k	Instrument	apex-III
Comment			

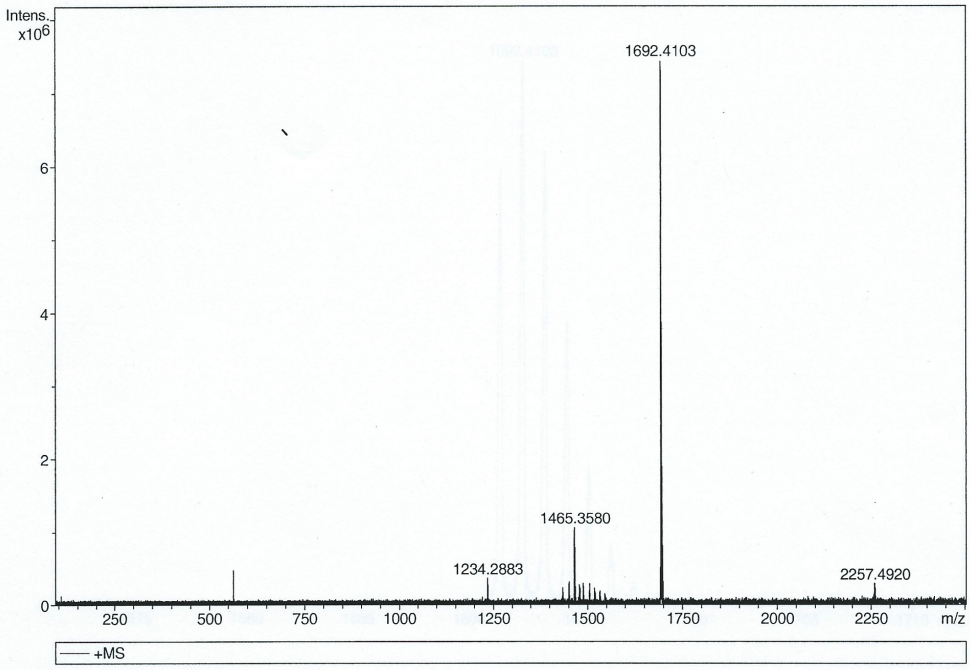

Table 'GenFormulaResults' could not be found in this analysis

Figure I.4: Positive ion HRMS ESI $K[(Ph_3SiO)_5U(THF)]$ and 0 eq. TMSOTf

Generic Display Report

Analysis Info

Analysis Name	D:\Data\Alinanopos\LAURA999_000001.d	Acquisition Date	20/03/2012 15:54:22
Method	pos20090608esi		
Sample Name	POS ESI U COMPLEX 1 EQU OF TMS	Operator	Administrator
Comment		Instrument	apex-III

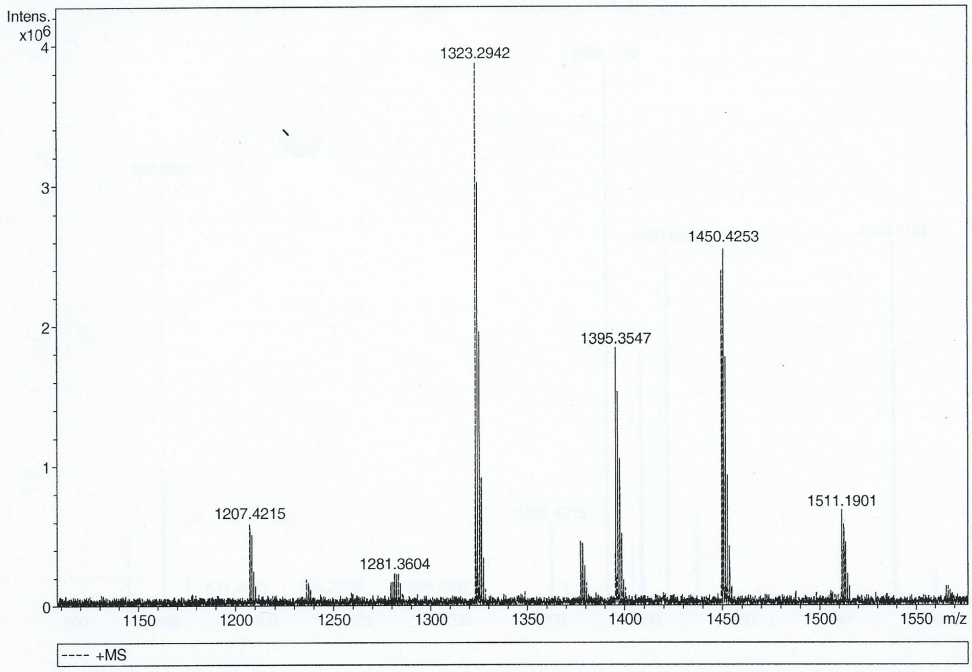

Table 'GenFormulaResults' could not be found in this analysis

Bruker Daltonics DataAnalysis 3.4 printed: 20/03/2012 15:55:19 Page 1 of 1

Figure I.5: Positive ion HRMS ESI $K[(Ph_3SiO)_5U(THF)]$ and 1 eq. TMSOTf

Generic Display Report

Analysis Info

Analysis Name	D:\Data\Alinanopos\LAURA_9090_000001.d	Acquisition Date	20/03/2012 16:09:05
Method	pos20090608esi	Operator	Administrator
Sample Name	POS ESI U COMPLEX 2 EQU TO TMS	Instrument	apex-III
Comment			

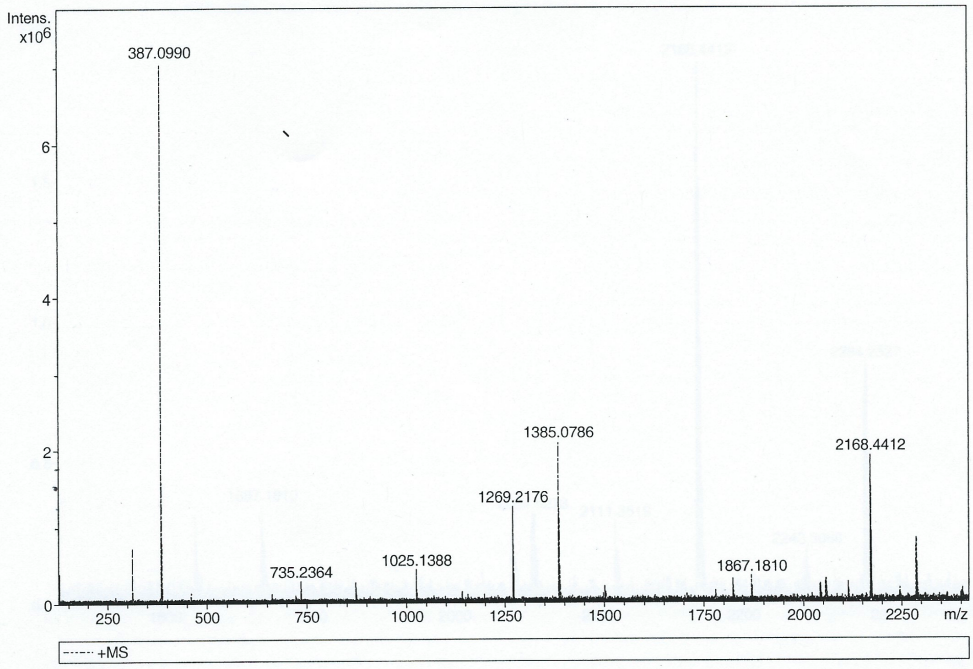

Table 'GenFormulaResults' could not be found in this analysis

Figure I.6: Positive ion HRMS ESI $K[(Ph_3SiO)_5U(THF)]$ and 2 eq. TMSOTf

Appendix J

Mass spectra - triphenysiloxide ligands reactivity studies

Generic Display Report

Analysis Info

Analysis Name	D:\Data\Alinanoneg\LAURA_111_000004.d	Acquisition Date	13/06/2013 11:38:40
Method	neg200906024esi_calibrated	Operator	Administrator
Sample Name	neg esi 5.12	Instrument	apex-III
Comment			

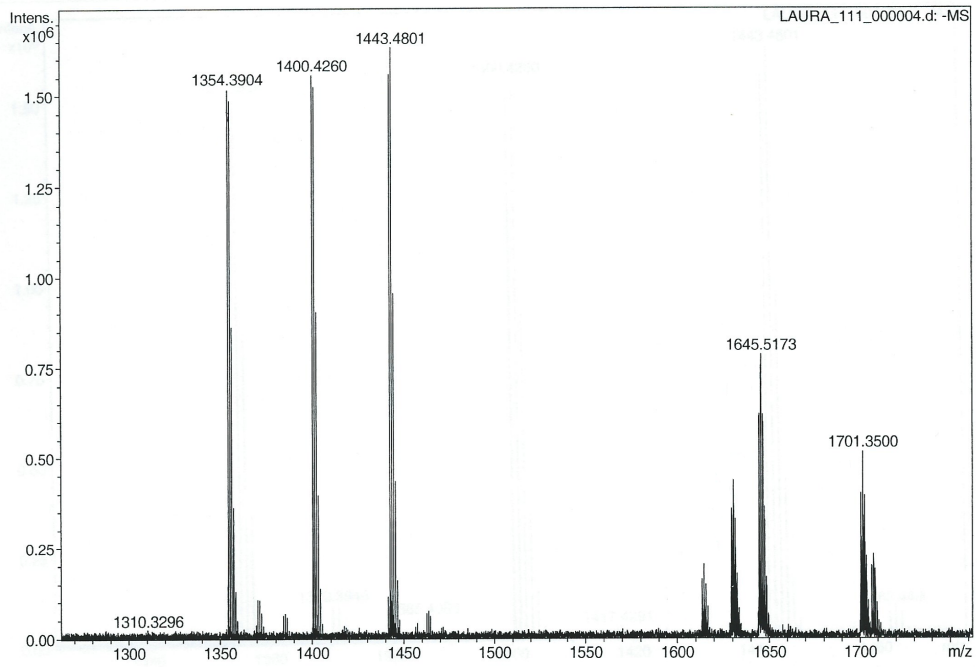

Figure J.1: Negative ion HRMS ESI $K[(Ph_3SiO)_5U(THF)]$ and 0.5 eq. O_2

Generic Display Report

Analysis Info

Analysis Name	D:\Data\Alinanoneg\LAURA_111_000004.d	Acquisition Date	13/06/2013 11:38:40
Method	neg200906024esi_calibrated	Operator	Administrator
Sample Name	neg esi 5.12	Instrument	apex-III
Comment			

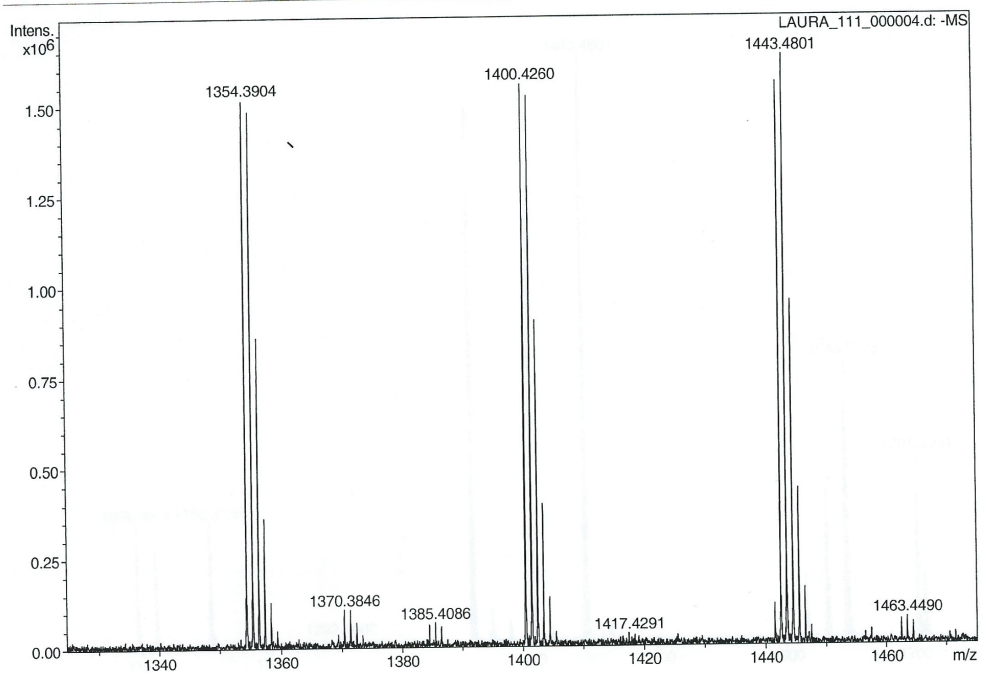

Table 'GenFormulaResults' could not be found in this analysis

Bruker Daltonics DataAnalysis 3.4 printed: 13/06/2013 11:40:22 Page 1 of 1

Figure J.2: Negative ion HRMS ESI $K[(Ph_3SiO)_5U(THF)]$ and 0.5 eq. O_2

Appendix K

UV-Vis spectra

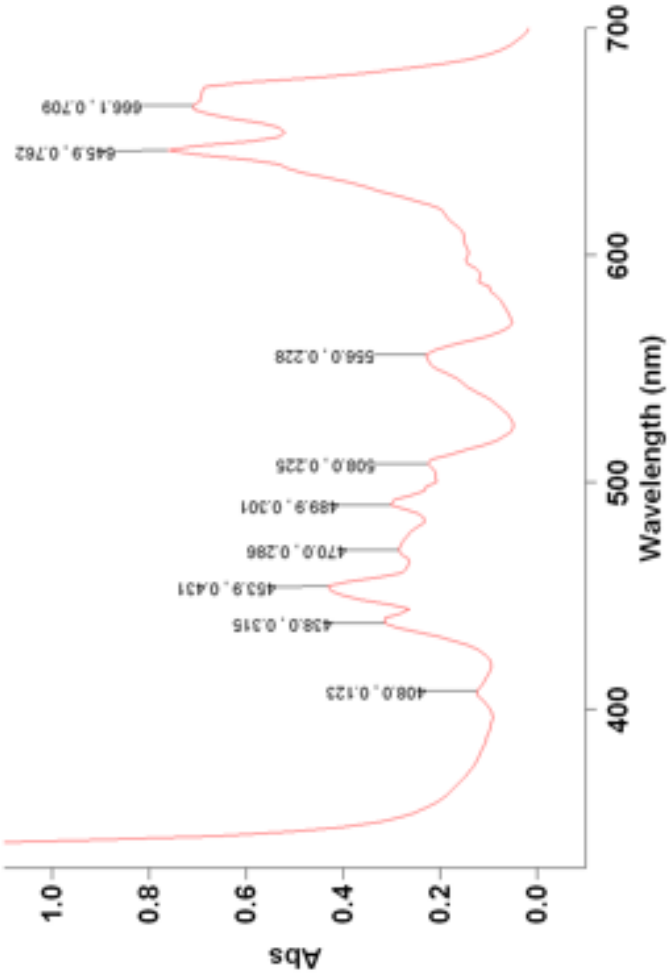

Figure K.1: UV-Vis spectrum for UCl_4 in THF

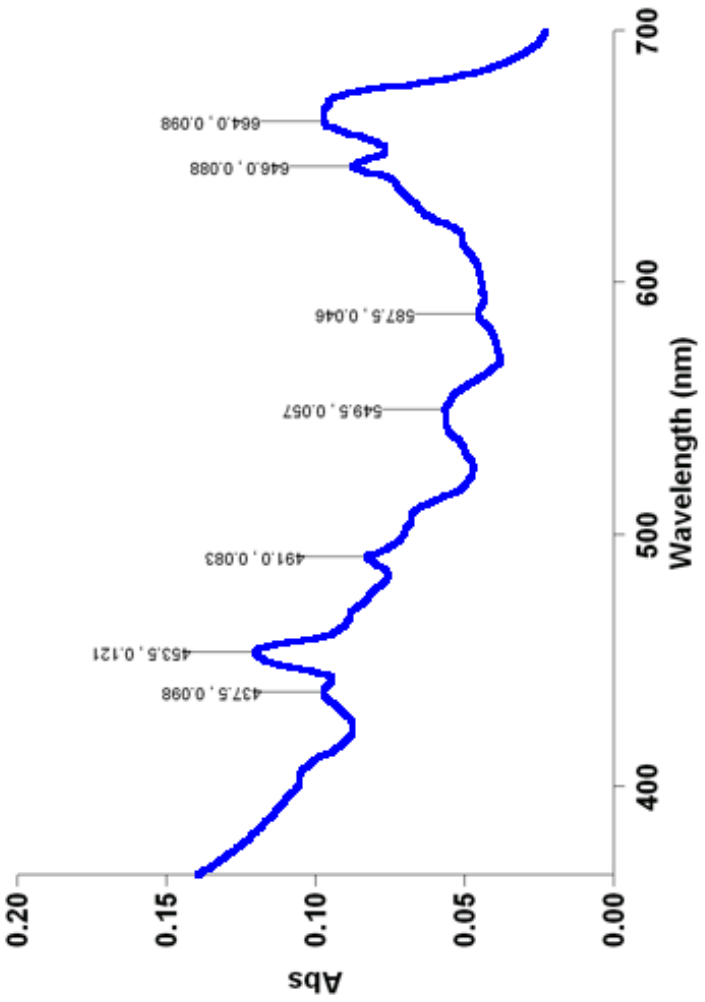

Figure K.2: UV-Vis spectrum for UCl_4 in Toluene

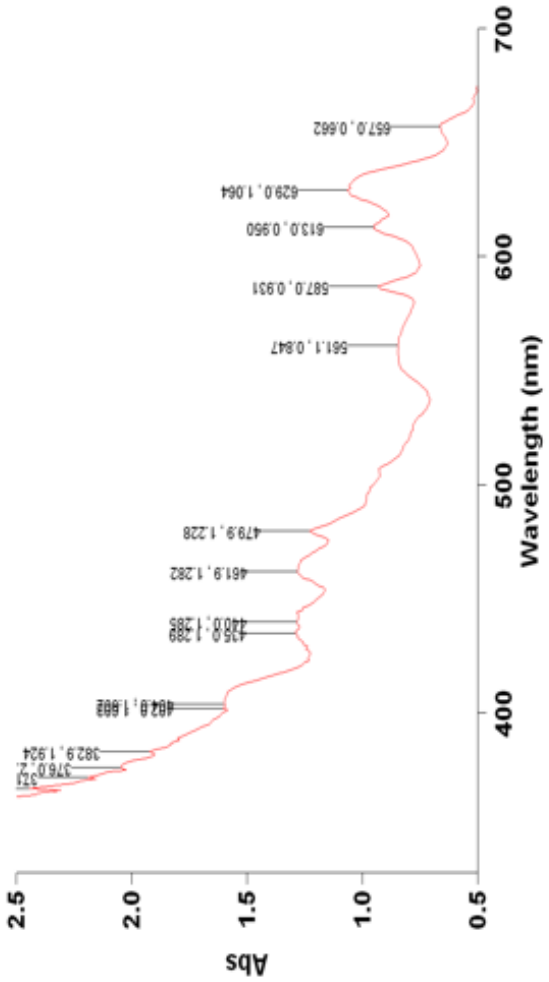

Figure K.3: UV-Vis spectrum for UCl_4 and 1 eq. of Ph_3SiOK in THF

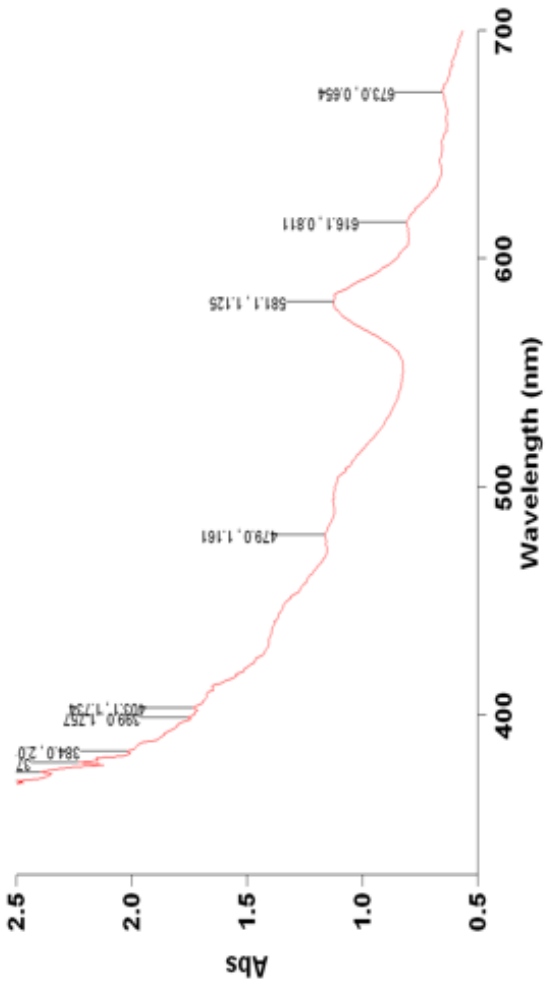

Figure K.4: UV-Vis spectrum for UCl_4 and 2 eq. of Ph_3SiOK in THF

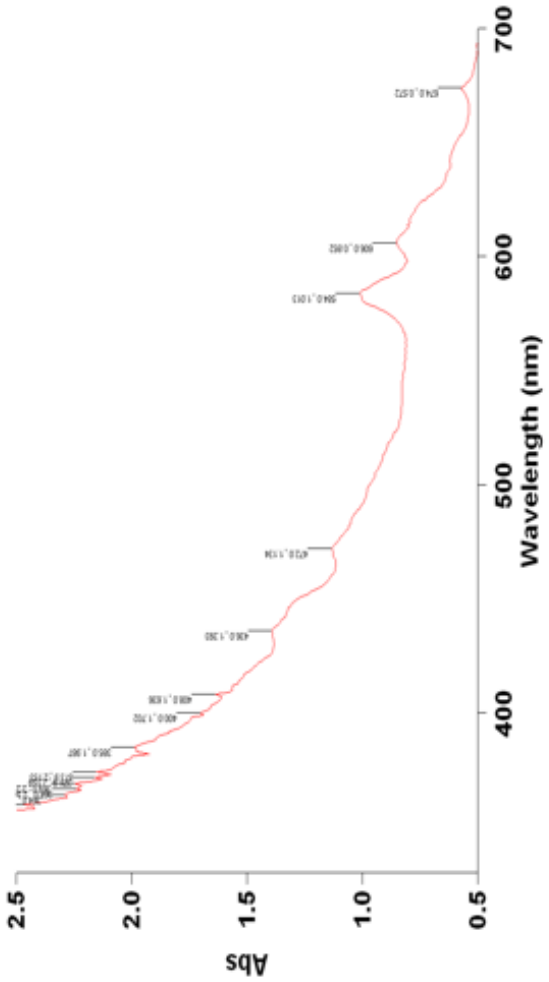

Figure K.5: UV-Vis spectrum for UCl_4 and 3 eq. of Ph_3SiOK in THF

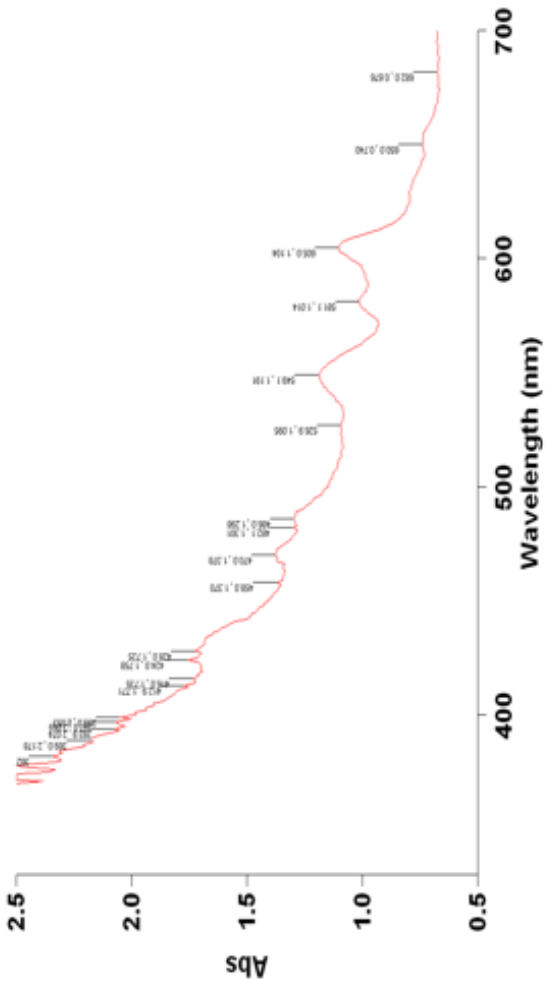

Figure K.6: UV-Vis spectrum for UCl_4 and 4 eq. of Ph_3SiOK in THF

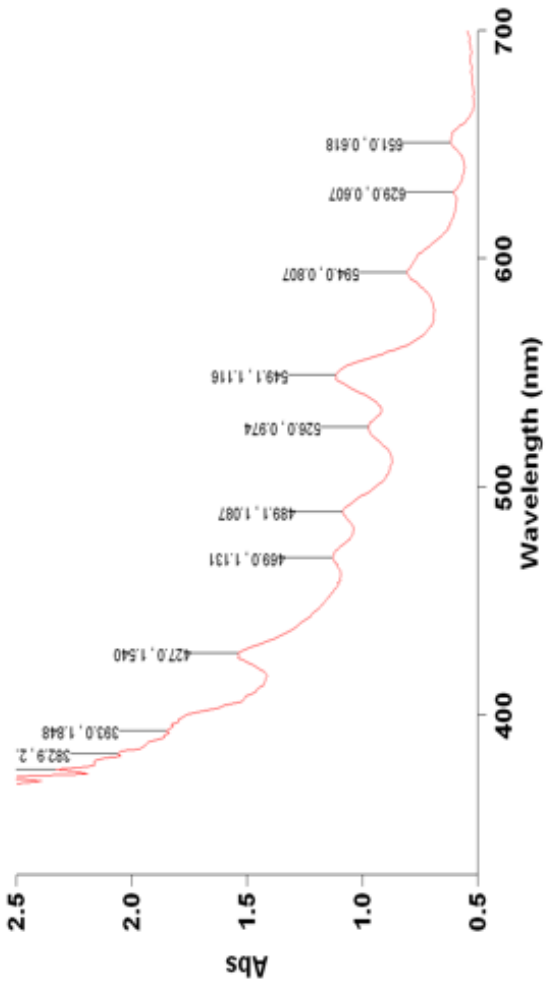

Figure K.7: UV-Vis spectrum for UCl_4 and 5 eq. of Ph_3SiOK in THF

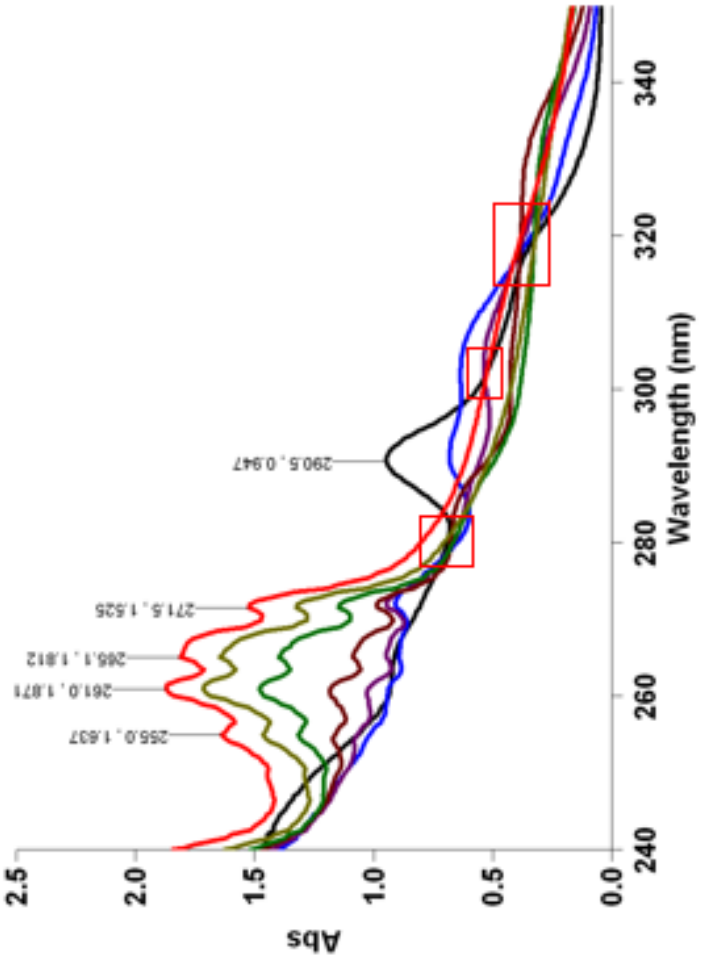

Figure K.8: UV-Vis spectrum of UCl_4 and the addition of Ph_3SiOH in one equivalent aliquots (Black=UCl_4; Blue=1eq; Purple=2eq; Brown=3eq; Green=4eq; Olive=5eq; Red=6eq) with isosbestic points

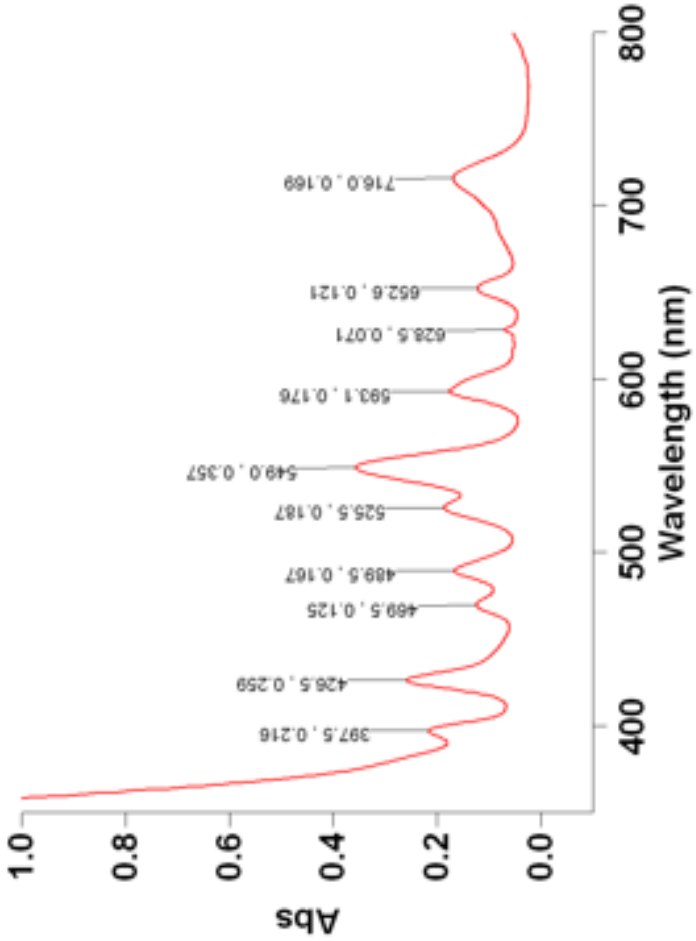

Figure K.9: UV-Vis spectrum for $K[(Ph_3SiO)_5U(THF)]$ in THF

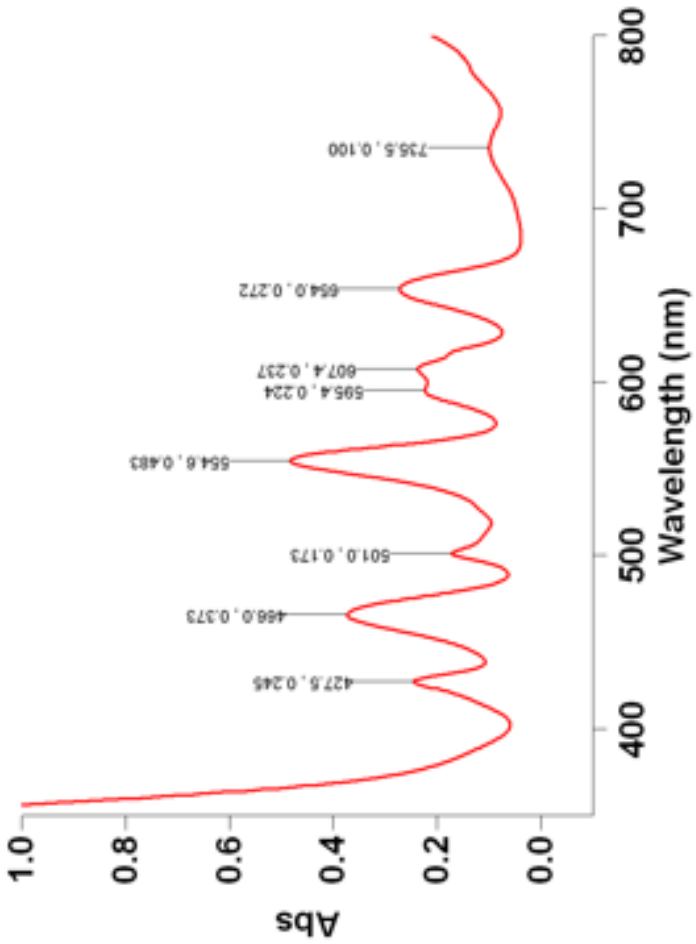

Figure K.10: UV-Vis spectrum for $K[U(OSiPh_3)_5]$ in Toluene

Appendix L

Important bond lengths and angles for molecular structures

See attached files

Appendix M

Useful information on uranium

Atomic Properties	Value
Oxidation States	6, 5, 4, 3
Covalent Radius	196 pm
Atomic Radius	156 pm
Van der Waals Radius	186 pm
1st Ionisation Energy	584 kJ/mol
2nd Ionisation Energy	1420 kJ/mol
3rd Ionisation Energy	1900 kJ/mol
4th Ionisation Energy	3145 kJ/mol
Electronegativity (Pauling Scale)	1.38
Electronic Configuration	[Rn] $5f^3$ $6d^1$ $7s^2$

Table M.1: Atomic Properties of Uranium[2]

Physical Properties	Value
Standard State	Solid
Density @ r.t.	19.1 g/cm^3
Liquid Density @ m.p.	17.3 g/cm^3
Specific Heat Capacity	27.665 J/mol^{-1}K
Heat of Fusion	9.14 kJ/mol
Heat of Vaporisation	417.1 kJ/mol
Melting Point	1132°C
Boiling Point	4131°C

Table M.2: Physical Properties of Uranium[2]

Reduction Potentials of Uranium	E°/V
$M^{3+} + 3e \rightarrow M$	-1.8
$M^{4+} + 4e \rightarrow M$	-1.38
$M^{3+} + e \rightarrow M^{2+}$	-4.7
$M^{4+} + e \rightarrow M^{3+}$	-0.63

Table M.3: Reduction Potentials of Uranium[2]